Implementation, Validation and Application of New Density Functionals for the Computation of Nuclear Magnetic Resonance Parameters

vorgelegt von
M. Sc.
Caspar Jonas Schattenberg

an der Fakultät II - Mathematik und Naturwissenschaften
der Technischen Universität Berlin
zur Erlangung des akademischen Grades

Doktor der Naturwissenschaften
– Dr. rer. nat. –

genehmigte Dissertation

Promotionsausschuss:

Vorsitzender:	Prof. Dr. Andreas Grohmann
Gutachter:	Prof. Dr. Martin Kaupp
Gutachter:	Prof. Dr. Stephan P. A. Sauer

Tag der wissenschaftlichen Aussprache: 21.11.2022

Berlin 2022

Danksagungen

Zunächst möchte ich Prof. Dr. Martin Kaupp für die Gelegenheit zu dieser Arbeit und die damit verbundenen großen Freiheiten in der Ausgestaltung meiner Promotion danken. Mein Dank gilt auch den aktiven und ehemaligen Mitgliedern des Arbeitskreises Kaupp für die angenehme und kollegiale Arbeitsatmosphäre und die vielen Jahre des Austausches. Hier gilt mein besonderer Dank Marc Reimann, für viele wertvolle Kommentare in den letzten Zügen dieser Dissertation, außerdem Dr. Sascha Klawohn und Susanne Fürst, die verlässliche Gesprächs- und Diskussionspartner für mich waren und sich in großer Regelmäßigkeit meine Gedanken angehört und diese mit mir erörtert haben. Außerdem möchte ich Dr. Robin Grotjahn für die angenehme Büroatmosphäre und Dr. Sebastian Gohr für die Vermittlung fundamentaler Wahrheiten über die Quantenchemie hinaus danken.
Ein besonderer Dank gilt Cordula Wittekind, für Optimismus und Zuversicht, sowie die vielen investierten Stunden und damit verbundenen Randnotizen. Des Weiteren möchte ich meinen aktuellen und ehemaligen Mitbewohnern, vor allem Elias Brunken und Doro Wolter, für gemeinsame Abende, Gespräche und die Fähigkeiten über den Rand der Momentaufnahme hinauszublicken danken.
An dieser Stelle möchte ich außerdem meinen Eltern und Großeltern einen besonderen Dank für die vielen aufbauenden und warmen Worte und den Glauben an mich aussprechen. Auch danke ich meinen Freunden und Freundinnen, für ihre Geduld, die gemeinsame Zeit und die verbundenen Zerstreuungen. Zu guter Letzt möchte ich Kristin Pazina für die vielen gemeinsamen Jahre und die Lehren für das Leben danken.

Abstract

Within the course of the present work, the implementation of a new class of density functionals, so-called local hybrid functionals (LHs), for the calculation of nuclear magnetic resonance (NMR) shieldings and spin–spin coupling constants was carried out. First, the relevant equations for the quantum chemical calculation of NMR parameters with LHs were derived and subsequently these equations were implemented into the quantum chemical program package TURBOMOLE. It was shown that despite additional terms caused by the presence of a local mixing function (LMF) in the LHs an efficient semi-numerical implementation can be obtained with a similar computational effort as a comparable implementation of conventional hybrid functionals with constant exact-exchange admixture. In addition, higher derivatives of the density, i.e. the Laplacian and the Hessian of the density, were implemented in a quantum chemical program for the first time in this work. Likewise, a current-density-dependent gauge correction of the kinetic energy density (τ_D) was implemented, which was not available in any program code in the context of linear-response theory.

These developments allowed the first self-consistent validation of a set of meta-GGA functionals for the current-density-corrected approach using τ_D and more importantly, the first systematic validation of LHs for NMR parameters in a coupled-perturbed scheme on the basis of gauge-including atomic orbitals. After initial evaluations for shielding constants, two large validation studies on shieldings and shifts, and a first validation for spin–spin couplings where carried out. In this initial assessment, LHs ranked among the most successful DFT approximations in both test sets for main-group and transition-metal shieldings and shifts, respectively. High accuracy of certain LHs was also demonstrated in the assessment of spin–spin couplings constants, often on par with the best alternative density functionals. Furthermore, a significant dependence of the calculated NMR parameters on the chosen LMF models was demonstrated within the validation studies, indicating further potential for improvements of LH functionals using new and poten-

tially better suited LHs and mixing functions. This suggests further investigation of LHs in connection with magnetic resonance properties.
Finally, the accurate performance of various LH functionals in NMR parameter calculations renders them particularly suitable for application studies. Initially, this was demonstrated by the calculation of fluorine NMR parameters for a small set for fluorohalogenates ($[XF_n]^-$, X=Cl, Br, I; n = 2, 4, 6). In case of n = 2, the applied LH functionals showed much larger deviations with respect to the experimental reference than expected from the prior benchmark studies. These deviations were traced to explicit solvent-solute interactions, specifically, remarkably strong H$\cdots$F hydrogen bonds between the acetonitrile solvent and the $[XF_2]^-$ species. Further analyses, including other fluoride-containing compounds and the free fluoride anion in solution, confirmed explicit orbital interactions as the source of the deviations between computed gas-phase and experimental solution NMR shifts.

Zusammenfassung

Das Thema der vorliegenden Arbeit ist die Verbindung einer neuen Funktionalklasse der Dichtefunktionaletheorie, den sogenannten lokalen Hybridfunktionalen (LHs), und der Kernmagnetresonanz-Spektroskopie (NMR): Im Zuge der vorliegenden Arbeit wurden zunächst die relevanten Gleichungen hergeleitet, welche einer quantenchemische Berechnung der NMR Parameter wie Kernabschirmungen und Spin–Spin Kopplungen mit LHs zugrunde liegen. Im Anschluss wurden diese in das quantenchemische Rechenprogramm Turbomole unter Verwendung eines effizienten semi-numerischen Ansatzes implementiert. Es konnte gezeigt werden, dass trotz neuer Terme, die durch die Präsenz einer lokalen Mischfunktion (LMF) in den LHs hervorgerufen werden, eine effiziente Implementierung erreicht werden kann, deren Rechenaufwand sich kaum von einer seminumerischen Implementierung herkömmlicher Hybridfunktionale unterscheidet. Zusätzlich wurden im Laufe dieser Arbeit erstmals höhere Ableitungen der Dichte, d.h. der Laplacian und Hessian der Dichte, in ein quantenchemisches Rechenprogramm implementiert. Genauso wurde eine stromdichteabhängige Eichursprungskorrektur der kinetischen Energiedichte (τ_D) implementiert, die vorher in keinem Programmcode im Kontext der linearen Antworttheorie verfügbar war.
Diese Arbeiten erlaubten somit die erste selbstkonsistente Validierung einer Reihe von meta-GGAs und weiteren von der kinetischen Energiedichte anhängigen Funktionalen für den stromdichtekorrigierten Ansatz über τ_D und außerdem die erste systematische Validierung von LHs für NMR-Parameter auf der Basis sogenannter Londonorbitale ("gauge-including atomic orbitals") in einem gekoppelten Störungsschema. In zwei großen Validierungsstudien zu NMR Abschirmungskonstanten und chemischen Verschiebungen, sowie einer ersten Validierung für Spin–Spin Kopplungen konnte das große Potential der LHs demonstriert werden. Sowohl in den Studien zu Hauptgruppen-, als auch Übergangsmetallkernen gehörten einzelne LHs zu den erfolgreichsten Dichtefunktionalen in der Berechnung von Kernabschirmungskonstanten bzw. Verschiebungen. Auch in den Spin–Spin-Kopplungen konnte eine hohe Genauigkeit einzelner LH Funktionale demonstriert werden,

die häufig mit den besten alternativen Dichtefunktionalen gleichauf lag. Aus den Daten zeigte sich außerdem eine große Abhängigkeit der Ergebnisse von der gewählten LMF, was auf zusätzliche Verbesserungsmöglichkeiten durch neuere LH Funktionale und angepasste Mischfunktionen schließen lässt und weitere Untersuchungen der LHs im Zusammenhang mit Magnetresonanzeigenschaften nahelegt.
Die in den Benchmarkstudien nachgewiesene hohe Genauigkeit verschiedener LH Funktionale für die Berechnung von NMR-Parametern prädestiniert diese Funktionalklasse außerdem im Besonderen für anwendungsbezogene Arbeiten. Dies wurde anhand der Berechnung von chemischen Verschiebungen für einen Satz kleiner Fluorhalogenate ($[XF_n]^-$, X=Cl, Br, I; $n = 2, 4, 6$) demonstriert, wobei für den Fall $n = 2$ deutlich größere Abweichungen der Berechnungen zur experimentellen Referenz beobachtet wurden, als aus den Validierungsarbeiten zu erwarten waren. Diese Abweichungen konnten auf explizite Wechselwirkungen zwischen dem Lösungsmittel und dem Ion, genauer, auf auffallend starke $H\cdots F$ Wasserstoffbrückenbindungen zwischen den $[XF_2]^-$ Spezies und dem Lösungsmittel Acetonitril zurückgeführt werden. Weitergehende Analysen, auch unter Einbezug weiterer fluoridhaltiger Spezies und dem freien Fluoridion in Lösung, bestätigten explizite Orbitalwechselwirkungen als Ursprung dieser großen Abweichungen zwischen berechneten Verschiebungen in der Gasphase und den experimentellen Werten in Lösung.

List of Publications

Publications Included in the Present Thesis

[I] C. J. Schattenberg, K. Reiter, F. Weigend and M. Kaupp, "*An Efficient Coupled-Perturbed Kohn–Sham Implementation of NMR Chemical Shift Computations with Local Hybrid Functionals and Gauge-Including Atomic Orbitals*", *J. Chem. Theory Comput.*, **2020**, *16*, 931–943.

[II] F. Mack, C. J. Schattenberg, M. Kaupp and F. Weigend, "*Nuclear Spin-Spin Couplings: Efficient Evaluation of Exact Exchange and Extension to Local Hybrid Functionals*", *J. Phys. Chem. A*, **2020**, *124*, 8529–8539.

[III] C. J. Schattenberg and M. Kaupp, "*Effect of the Current Dependence of Tau-Dependent Exchange-Correlation Functionals on Nuclear Shielding Calculations*", *J. Chem. Theory Comput.*, **2021**, *17*, 1469–1479.

[IV] C. J. Schattenberg and M. Kaupp, "*Implementation and Validation of Local Hybrid Functionals with Calibrated Exchange-Energy Densities for Nuclear Shielding Constants*", *J. Phys. Chem. A*, **2021**, *125*, 2697–2707.

[V] C. J. Schattenberg and M. Kaupp, "*Extended Benchmark Set of Main-Group Nuclear Shielding Constants and NMR Chemical Shifts and Its Use to Evaluate Modern DFT Methods*", *J. Chem. Theory Comput.*, **2021**, *17*, 7602–7621.

[VI] C. J. Schattenberg, M. Lehmann, M. Bühl and M. Kaupp, "*Systematic Evaluation of Modern Density Functional Methods for the Computation of NMR Shifts of 3d Transition-Metal Nuclei*", *J. Chem. Theory Comput.*, **2022**, *18*, 273–292.

[VII] P. Pröhm, J. R. Schmid, K. Sonnenberg, P. Voßnacker, S. Steinhauer, C. J. Schattenberg, R. Müller, M. Kaupp and S. Riedel, "*Improved Access to Organo-Soluble Di- and Tetrafluoridochlorate(I)/(III) Salts*", *Angew. Chem. Int. Ed.*, **2020**, *59*, 16002–16006.

[VIII] M. Kaupp, C. J. Schattenberg, R. Müller and M. Reimann, "*Unusually Large Effects of Charge-assisted C–H$\cdots$F Hydrogen Bonds to Anionic Fluorine in Organic Solvents: Computational Study of ^{19}F NMR Shifts versus Thermochemistry*", *ChemistryOpen*, **2022**, e202200146.

Personal Contributions to the Publications

[I] Derivation, implementation, computations, analysis and interpretation of the testset-data, except for the contributions related to open-MP parallelization were performed by the author. The initial draft of the manuscript was written by the author (except for the part related to the open-MP parallelization).

[II] LH related derivations and implementation of the LH related PSO contribution to the spin–spin-coupling calculation, analysis of the test-set data with LH functionals, as well as the contributions to the manuscript regarding the initial draft of the LH part within the manuscript were done by the author.

[III] Derivation, implementation, computations, analysis and interpretation of the data, as well as the initial draft of the manuscript were done by the author.

[IV] Derivation, implementation, computations, analysis and interpretation of the data, as well as the initial draft of the manuscript were done by the author.

[V] Initial conception of the test set, computations and analysis of the data were done by the author. The initial draft of the manuscript was written by the author. Prof. Dr. Martin Kaupp gave helpful suggestions on the conception of the final NS372 benchmark set.

[VI] Initial computations and analyses on a smaller benchmark set where performed by Morten Lehmann in the course of his Bachelor thesis based on structures provided by Prof. Dr. Michael Bühl. The benchmark set was extended including further complexes of the former studies and unified in terms of the computational level by the author. Subsequent extensions, computations of the final benchmark set and the adjusted analyses of the benchmark data was conducted by the author. The initial draft of the manuscript was written by the author. Prof. Dr. Martin Kaupp, and Prof. Dr. Michael Bühl gave helpful suggestions on the conception of the benchmark set.

[VII] Computations, analysis and presentation of the NMR shifts of the fluorohalides within the paper draft were done by the author.

[VIII] Computations regarding the construction of most of the acetonitrile related solvent-solute cluster models, IR spectra and NMR chemical shifts, and related parts of the analysis and presentation of the resulting data within the paper draft were done by the author.

The selection and presentation of the scientific data within the submitted (and subsequently published) paper-drafts were significantly influenced by discussions and suggestions of Prof. Dr. Martin Kaupp, who also contributed parts of the final wording.

Further Non-Contributing Publications

[1] C. J. Schattenberg, T. M. Maier and M. Kaupp, "*Lessons from the Spin-Polarization/Spin-Contamination Dilemma of Transition-Metal Hyperfine Couplings for the Construction of Exchange-Correlation Functionals*", *J. Chem. Theory Comput.*, **2018**, *14*, 5653–5672.

[2] T. Utesch, A. de Miguel Catalina, C. J. Schattenberg, N. Paege, P. Schmieder, E. Krause, Y. Miao, J. A. McCammon, V. Meyer, S. Jung and M. A. Mroginski, "*A Computational Modeling Approach Predicts Interaction of the Antifungal Protein AFP from Aspergillus giganteus with Fungal Membranes via Its γ-Core Motif*", *mSphere*, **2018**, *3*, e00377-18.

Talks and Posters

The work within the present thesis has been presented and discussed on 4 international conferences in 3 talks and 1 poster presentations.

Talks

[1] "*Magnetic Resonance and Local Hybrid Functionals*", XIIth Workshop on Modern Methods in Quantum Chemistry (MMQC), Mariapfarr, **2019**.

[2] "*Systematic evaluation of local hybrid functionals for the calculation of NMR shielding constants (and spin-spin coupling constants).*", XIIIth Workshop on Modern Methods in Quantum Chemistry (MMQC), Mariapfarr, **2020**.

[3] "*New Developments in NMR Parameter Calculations with Local Hybrid Functionals.*", XIVth Workshop on Modern Methods in Quantum Chemistry (MMQC), Online, **2021**.

Posters

[1] "*Lessons from the spin polarization/spin contamination dilemma of transition metal hyperfine couplings for the construction of new functionals*", 54th Symposium on Theoretical Chemistry (STC), Halle (Saale) , **2018**.

Copyright

Transition-Metal Nuclei", *J. Chem. Theory Comput.*, **2022**, *18*, 273–292. Copyright 2021 American Chemical Society.

- The original publication (Section P-VII of Chapter 6), parts of the discussion of Chapter 5 and contents of Section A.6 are reprinted and adapted from P. Pröhm, J. R. Schmid, K. Sonnenberg, P. Voßnacker, S. Steinhauer, C. J. Schattenberg, R. Müller, M. Kaupp and S. Riedel, "*Improved Access to Organo-Soluble Di- and Tetrafluoridochlorate(I)/(III) Salts*", *Angew. Chem. Int. Ed.*, **2020**, 59, 16002–16006, distributed under the terms of the Creative Commons CC BY license.

- The original publication (Section P-VIII of Chapter 6), parts of the discussion of Chapter 5 and contents of Section A.7 are reprinted and adapted from M. Kaupp, C. J. Schattenberg, R. Müller and M. Reimann, "*Unusually Large Effects of Charge-assisted C–H$\cdots$F Hydrogen Bonds to Anionic Fluorine in Organic Solvents: Computational Study of ^{19}F NMR Shifts versus Thermochemistry*", *ChemistryOpen*, **2022**, e202200146, distributed under the terms of the Creative Commons CC BY license.

List of Abbreviations

AC	adiabatic connection
AO	atomic orbital
AE	atomization energy
BO	Born–Oppenheimer
CAS	complete active space
CC	coupled cluster
CDFT	current-density functional theory
CI	configuration interaction
COM	center of mass
COS(-J/K)	chain-of-spheres (for the Coulomb/exchange contribution)
COSMO	conductor-like screening model
COSMO-RS	conductor-like screening model for real solvents
CPMD	Car–Parrinello molecular dynamics
CSGT	continuous set of gauge transformations
D-COSMO-RS	direct conductor-like screening model for real solvents
DDH	dielectric dependent hybrid
DFA	density functional approximation
DFT	density functional theory
DH	double hybrid
DLPNO	domain-based local pair natural orbital
DORI	density overlap region indicator
DSD	dispersion-corrected spin-component-scaled double hybrid
DSO	diamagnetic spin-orbit
EA	electron affinity
EEF	exchange enhancement factor
Eq.	equation
Eqs.	equations
EXX	exact-exchange admixture
FC	Fermi contact
Fig.	figure
Figs.	figures
GEA	gradient expansion approximation
GGA	generalized gradient approximation

GH	global hybrid
GIAO	gauge-including atomic orbital
GKS	generalized Kohn–Sham
GMTKN	(benchmark database for) general main group thermochemistry, kinetics, and non-covalent interactions
HF	Hartree–Fock
HK	Hohenberg–Kohn
IGAIM	individual gauges for atoms in molecules
IGLO	individual gauges for localized orbitals
IP	ionization potential
KS	Kohn–Sham
LCAO	linear combination of atomic orbitals
LH	local hybrid
LORG	localized-orbitals local origin
LMF	local mixing function
LMO	localized molecular orbital
LR	long-range
L(S)DA	local (spin-)density approximation
MAD	mean absolute deviation
MAE	mean absolute error
MAPD	mean absolute percentage deviation
MARE	mean absolute relative deviation
MARI	multipole accelerated resolution of the identity
Max.AD	maximum absolute deviation
MCSCF	multiconfigurational self-consistent field
meta-GGA	meta generalized gradient approximation
MO	molecular orbital
MPn	Møller-Plesset perturbation theory of order n
MSD	mean signed deviation
MSE	mean signed error
NDC	non-dynamical correlation
NMR	nuclear magnetic resonance
OEP	optimized effective potential
PA	proton affinity
PCM	polarizable continuum model
PES	potential energy surface

pig	partial integration gauge
PSO	paramagnetic spin-orbit
PT	perturbation theory
RAS	restricted active space
Ref.	reference
Refs.	references
RHF	restricted Hartree–Fock
RI(-J/K)	resolution of the identity (for the Coulomb/exchange contribution)
RISM	reference interaction site model
RKS	restricted Kohn–Sham
RPA	random-phase approximation
RS	range separated
RSH	range-separated hybrid
SCF	self-consistent field
SD	spin-dipolar
Sec.	section
Secs.	sections
SlD	Slater-determinant
SR	short-range
StD	standard deviation
SIE	self-interaction error
SIF	self-interaction free
SIR	self-interaction reduced
SSCC	spin–spin coupling constant
Tab.	table
Tabs.	tables
UEG	uniform electron gas
UHF	unrestricted Hartree–Fock
UKS	unrestricted Kohn–Sham
XC	exchange correlation
X2C	exact two-component

Contents

1 Introduction

Nuclear magnetic resonance (NMR) spectroscopy is probably one of the most widely applied experimental methods in the structure elucidation of diamagnetic target species today. In the years since the pioneering experiments in 1946,[1–4] a huge amount of empirical data and experience has been accumulated.[5–7] Nevertheless, quantum-chemical calculations are nowadays routinely performed to support experimental work, either to guide the experiment with theoretical insight, or to assist in the final assignment of the resulting spectra.[8] This was on the one hand made possible by the rapid development of computer technology, which nowadays allows calculations of small- to medium-sized systems even on home computers. Also appropriate infrastructure, such as computation clusters or high-performance computing centers with huge computational power, becomes more and more available. On the other hand, it was the development of accurate and efficient quantum-chemical computation packages which made accurate calculations possible in the first place. These developements have been an active field of research in the past decades resulting in a selection of computational software packages (partly varying in focus and specialized applications) such as Turbomole,[9] Cfour[10] or Orca,[11–13] which were used to calculate NMR properties throughout this thesis.

The developments of theoretical and subsequently computational NMR spectroscopy started with the pioneering work of Norman F. Ramsey, who derived the interactions of an external magnetic field with the wave function of a target system in a series of consecutive papers.[14–17] On the basis of this theory, first calculations of NMR properties have been published already in the 1950s.[18,19] However, due to initially limited computational capacities, the work focused on small molecules and/or methods with likewise limited accuracy. Later, the interest for computational NMR properties rose once again in the 1980s and 1990s, when the foundations for today's routine computations were laid, i.e. with work concerned with the gauge ambiguity of the vector potential of the magnetic field,[20–23] computational implementation[23–29] as well as initial validation studies.[30,31]

Clearly, the highest computational accuracy can be achieved with wave-function approaches, such as coupled cluster or configuration interaction, which in principle converge to the exact solution.[32–35] If zero-point vibration and temperature corrections are included, good accuracy in comparison to experimental gas-phase shielding data can be achieved for small light-atom compounds.[36–39] However, such calculations are cost-intensive, and still today only small molecules of limited relevance in chemical research are accessible.

Approaches based on a perturbational treatment of electron correlation, such as Møller Plesset (MP) perturbation theory[40,41] or double hybrid functionals, which contain a MP2-like correlation contribution, are accurate in main group shielding calculations as well.[42] However, due to their inability to reproduce static correlation, error margins increase significantly if these contributions become sizeable.[42] Such methods are already less costly than the highest-level wave-function methods described above. However, larger molecules or the need to perform many (consecutive) calculations, remain a challenge, even for efficiency-increasing implementations using approximations such as the domain-based local pair natural orbital (DLPNO).[43]

One example where possibly many calculations have to be processed is a recently proposed computational protocol that combines a conformer-rotamer sampling with DFT calculations of NMR shieldings and spin–spin coupling constants to generate complete Bolzmann-weighted NMR spectra.[44] Consequently, all energetically relevant structures have to be included, which potentially results in a large number of total calculations and accordingly limits the applicability of the above described set of methods.

Therefore, in many cases more approximative approaches have been established as standard computational protocols. In particular density functional theory (DFT),[45] in its incarnation due to Kohn and Sham (KS),[46] is used in many applications due to its remarkable cost/performance ratio: DFT takes electron correlation into account by using an (approximate) exchange-correlation (XC) functional,[47,48] while still being applicable to systems containing hundreds of atoms on modern computers. Importantly, the XC energy gathers all approximated contributions of the KS-DFT approach and therefore determines the final accuracy of the calculations.[49,50] For that reason, an actively pursued search for a generally applicable and accurate functional resulted in a plethora of available density functional approximations, which were constructed and proposed over the years on the basis of partly very different philosophies.[51]

Starting with just a dependence on the density,[46,52] functionals including correcting terms based on the gradient or higher derivatives of the density evolved.[53–57] A further cornerstone in the development of modern density functionals was the inclusion of exact-

exchange of Hartree–Fock theory,[58,59] which can help to reduce spurious self-interaction of semi-local functionals.[60] However, in the calculation of NMR parameters such semi-local DFT functionals and (global) hybrid methods show a mixed accuracy in shieldings and shifts[13,61–67] as well as spin–spin coupling constants,[28,29,68–72] with a strong dependence on the target species. That is, molecules and complexes containing transition metals, lone pairs, double and/or triple bonds can be a significant challenge for typical density functionals due to potentially large correlation contributions, which are not always captured sufficiently. Early on, the shortcomings of KS-DFT in NMR-shielding calculations were attributed to the lack of a correct description of the arising current-density response in the presence of external magnetic fields, as the method was derived in the field-free limit.[73] However, in initial studies the tested methods including current dependencies were typically less accurate than their non-current-dependent counterparts, which suggested that the underlying XC functionals were not sufficiently accurate after all.[26,74] For this reason the development of more accurate and robust XC functionals for NMR-parameter computations has remained an active field of research to this day.

Within the present work, these efforts have been extended to the class of local hybrid (LH) functionals, for which only few data existed: in initial work on LHs in connection with NMR parameters, shieldings were computed in terms of a localized-local-hybrid exchange-correlation potentials,[75] an approach similar to the optimized effective potential (OEP). The OEP approach gained some interest due to its comparably good performance in shielding and shift caluculations.[76–80] However, the construction of such multiplicative potentials is not a trivial task (and hence time-consuming),[81,82] and more importantly, the gain in performance in the calculation of response properties, such as shielding constants, was traced to an insufficient quality of the resulting multiplicative potential due to numerical instabilities.[83]

For that reason, the first GIAO-based self-consistent implementation of LHs within a coupled-perturbed scheme is reported within the present work. The relevant equations to cover additionally arising terms occurring for LHs were derived and subsequently implemented into the Turbomole program code on the basis of efficient semi-numerical integration techniques. The scheme was furthermore extended to cover spin–spin coupling constants and the current-density response using an alternative gauge correction of the kinetic energy density (τ_D), which likewise was not available self-consistently before in the context of linear-response theory. The implementation extends the applicability of LH functionals in Turbomole to second order magnetic resonance parameters and provides CDFT variants of other kinetic-energy density dependent functionals, both features no other quantum-chemical computation package provides to date.

1.1 Outline of the Present Thesis

The further chapters in this thesis are organized as follows: In Chapter 2, the theoretical outline of the basics of quantum chemistry, density-functional theory (with an emphasis on KS-DFT), functional development, local-hybrid functionals and computational methodology is given. This is followed by a brief outline of the theory of magnetic resonance parameters, their derivation and the connection between DFT and NMR parameter calculations. Chapter 4 covers the relevant computational infrastructure in the TURBOMOLE program code and in Chapter 5 the relevant aspects of the papers making up the present thesis are revisited. This is followed by a brief outlook on further developments and potential pathways of future investigations. Finally, in Chapter 6 the original papers are reprinted, followed by an Appendix gathering the relevant data from the supporting informations of the presented publications and further relevant data.

2 Theoretical Background – Quantum-Chemical Methods

In the present chapter, fundamental equations of quantum chemistry, Hartree–Fock theory and density-functional theory especially in its Kohn–Sham formulation will be briefly introduced. Having established the fundamental theoretical outline (in the field free limit), a more detailed introduction on density functional approximations will be given. The focus lies on functionals used in the studies of the present thesis and especially local hybrid functionals.

2.1 Basic Concepts of Quantum Chemistry

In the non-relativistic limit, the electronic structure of any many-particle system is embedded in the time-independent Schrödinger equation [84]

$$\widehat{H}\Psi = E\Psi. \tag{2.1}$$

Here, Ψ is the (likewise time-independent) wave function and E is the eigenvalue, i.e. the energy of the system described by the Hamilton operator $\widehat{H}$, itself gathering the kinetic and potential energy contributions of the system. In principle, the Hamiltonian, as well as the wave function, contain contributions from nuclei and electrons. However, due to the significant difference in mass and hence velocity of these particles, formally the contributions can be separated [84]

$$\widehat{H} = \widehat{H}_e + \widehat{H}_N, \tag{2.2}$$

$$\Psi = \Psi_e \cdot \Psi_N. \tag{2.3}$$

The electronic wave function depends on the positions of the nuclei parametrically and only describes the motion of the electrons explicitely.[84] Subsequently the two problems can be solved separately within the electronic and nuclear Schrödinger equations, respectively. In the first, the electrons are assumed to move in a potential of fixed nuclei. Therefore, within this approximation, the kinetic energy of the nuclei vanishes and the nuclear Coulomb repulsion gives a constant contribution to the total energy of the system[84]

$$E_N = \sum_{K<L}^{N_N} \frac{Z_K Z_L}{|\mathbf{R}_K - \mathbf{R}_L|}, \tag{2.4}$$

where N_N is the number of nuclei with charge Z_K at position $\mathbf{R}_K$. This approximation is commonly known as the Born-Oppenheimer approximation.[84,85] In atomic units (used throughout the present work) the electronic Hamiltonian is given by[84,86]

$$\widehat{H}_e = \widehat{T}_e + \widehat{V}_{ee} + \widehat{V}_{Ne} \tag{2.5}$$

$$= -\frac{1}{2}\sum_{i}^{N} \nabla_i^2 + \sum_{i<j}^{N} \frac{1}{|\mathbf{r}_i - \mathbf{r}_j|} - \sum_{i,K}^{N,N_N} \frac{Z_K}{|\mathbf{r}_i - \mathbf{R}_K|}. \tag{2.6}$$

Here, $\widehat{T}_e$ is the kinetic energy, $\widehat{V}_{ee}$ the electron-electron repulsion and $\widehat{V}_{eN}$ the electron-nuclear attraction for a system with N electrons at the positions $\mathbf{r}_i$ and $\mathbf{r}_j$. A similar equation can be formulated for the motion of the nuclei using a nuclear Hamiltonian (instead of its electronic counterpart), which describes the motion of the nuclei in an averaged field of the electron cloud.[84] The (graph of the) energy as function of the nuclear coordinates is then known as the potential energy surface (PES). However, in the remaining part of this work only solutions of the electronic Schrödinger equation are discussed, thus the subscript e for the Hamiltonian and for the operator of the kinetic energy is dropped for the following chapters.
Using the electronic Hamiltonian and a complete set of trial wave functions ($|\Psi_i\rangle$), the energy of a certain state can be obtained by multiplication with $\langle\Psi_j|$ and assuming orthonormality ($\langle\Psi_i|\Psi_j\rangle = \delta_{ij}$) via

$$\langle\Psi_j|\widehat{H}_e|\Psi_i\rangle = E_i\delta_{ij}, \qquad \text{with} \quad E_0 \leq E_1 \leq \cdots \leq E_i \leq \ldots. \tag{2.7}$$

The solution with the lowest energy E_0, the ground state (GS) of the system, is obtained with the GS (i.e. exact) wave function $|\Psi_0\rangle$. The fact, that the exact wave function minimizes the energy expression given in Eq. 2.7 is called the variational prin-

ciple.[86,87] However, the search for the this wave function is practically impossible due to the large number of possible trial functions and exact analytical solutions of the electronic Schrödinger equation are only known for simple systems such as the hydrogen atom. Therefore, in practice, suitable approximations usually have to be employed to solve the Schrödinger equation.

2.1.1 Hartree–Fock Theory

One approximation of conceptual importance is the Hartree–Fock (HF) theory.[88] On the one hand, it provides a starting point for highly accurate post-HF methods (i.e. methods which include electron correlation on the basis of a HF solution, see Sec. 2.1.2 for a brief discussion of such approaches). On the other hand, the concepts outlined within this chapter will become important for density functional theory in its Kohn–Sham formulation, which will be discussed in later chapters of this thesis. In the HF method the system's N-electron wave function is expanded in a set of $M \geq N$ orthonormal one-electron wave functions, so called spin orbitals ($\chi_i(\mathbf{x})$). These are composed of a spatial part ($\varphi_i(\mathbf{r})$), the so called molecular orbital (MO), and a spin contribution $\sigma(s)$ (of $\alpha(s)$ or $\beta(s)$ spin)[84]

$$\chi_i(\mathbf{x}) = \varphi_{i,\sigma}(\mathbf{r})\sigma(s). \tag{2.8}$$

Here, $\alpha(s)$ and $\beta(s)$ are associated with spins $\frac{1}{2}$ and $-\frac{1}{2}$, respectively, and they form an orthonormal basis ($\langle\alpha|\beta\rangle = \delta_{\alpha\beta}$). For that reason, the spatial functions $\varphi_{i,\sigma}(\mathbf{r})$ of α and β spin are in principle independent, as orthonormality of the spin orbitals is guaranteed by the associated spin functions. Hence, such spatial orbitals form an unrestricted basis. A calculation using a basis of unrestricted spatial orbitals is called unrestricted Hartree–Fock (UHF). However, in the case of closed-shell singlet states (or restricted open-shell approaches) the condition $\varphi_{i,\alpha} = \varphi_{i,\beta}$ can be imposed and the same spatial orbitals are employed for both spin channels, i.e. they form a basis of restricted spatial orbitals, associated with restricted Hartree–Fock (RHF) or restricted open-shell HF calculations. In the following, the subscripts $i, j, \ldots$ denote occupied, $a, b, \ldots$ unoccupied or virtual, and $p, q, \ldots$ general MOs. For the spins, either α and β as explicit, as well as σ and ς as general (independent) spin labels are used, whereas a primed entity, e.g. σ', denotes the opposite spin to σ.

The requirement of antisymmetry (i.e. the Pauli exclusion principle[89]) and the principle of indistinguishability of the wave function of fermions (such as electrons) are satisfied

by arranging the molecular spin orbitals in an anti-symmetrized product called the Slater determinant (SlD)[84]

$$\Psi = \Phi_{\mathrm{SlD}}(\mathbf{x}_1, \mathbf{x}_2, ..., \mathbf{x}_N) = \frac{1}{\sqrt{N!}} \begin{vmatrix} \chi_1(\mathbf{x}_1) & \chi_1(\mathbf{x}_2) & \cdots & \chi_1(\mathbf{x}_N) \\ \chi_2(\mathbf{x}_1) & \chi_2(\mathbf{x}_2) & \cdots & \chi_2(\mathbf{x}_N) \\ \vdots & \vdots & \ddots & \vdots \\ \chi_N(\mathbf{x}_1) & \chi_N(\mathbf{x}_2) & \cdots & \chi_N(\mathbf{x}_N) \end{vmatrix}. \tag{2.9}$$

Using such an arbitrary SlD, the expectation value (after integration of the orthonormal spin functions) according to Eq. 2.7 is

$$E_{\mathrm{SlD}}\left[\{\varphi_{i,\sigma}\}\right] = T\left[\{\varphi_{i,\sigma}\}\right] + E_{Ne}\left[\{\varphi_{i,\sigma}\}\right] + J\left[\{\varphi_{i,\sigma}\}\right] + E_X\left[\{\varphi_{i,\sigma}\}\right]. \tag{2.10}$$

Here, $\mathscr{O}\left[\{\varphi_{i,\sigma}\}\right]$ denotes the implicit dependence of the entity (operator or functional) $\mathscr{O}$ on the set of occupied MOs. The one-electron contributions of the kinetic energy $T\left[\{\varphi_{i,\sigma}\}\right]$ and the Coulomb attraction of the nuclei and electrons $E_{Ne}\left[\{\varphi_{i,\sigma}\}\right]$ are conveniently combined in one expression

$$T\left[\{\varphi_{i,\sigma}\}\right] + E_{Ne}\left[\{\varphi_{i,\sigma}\}\right] = \sum_{\sigma}\sum_{i}\int \varphi^*_{i,\sigma}(\mathbf{r})\widehat{h}(\mathbf{r})\varphi_{i,\sigma}(\mathbf{r})\mathrm{d}\mathbf{r}, \tag{2.11}$$

where the one-electron core-Hamiltonian is defined as[84]

$$\widehat{h}(\mathbf{r}) = -\frac{1}{2}\nabla^2 - \sum_K \frac{Z_K}{|\mathbf{r} - \mathbf{R}_K|}. \tag{2.12}$$

The Coulomb repulsion, $J\left[\{\varphi_{i,\sigma}\}\right]$, is given by

$$J\left[\{\varphi_{i,\sigma}\}\right] = \frac{1}{2}\sum_{\sigma}\sum_{ij}\int \varphi^*_{i,\sigma}(\mathbf{r})\left[\widehat{J}_{j,\sigma}(\mathbf{r}) + \widehat{J}_{j,\sigma'}(\mathbf{r})\right]\varphi_{i,\sigma}(\mathbf{r})\mathrm{d}\mathbf{r} \tag{2.13}$$

and $E_X\left[\{\varphi_{i,\sigma}\}\right]$ is the exchange energy

$$E_X\left[\{\varphi_{i,\sigma}\}\right] = \frac{1}{2}\sum_{\sigma}\sum_{ij}\int \varphi^*_{i,\sigma}(\mathbf{r})\left[\widehat{K}_{j,\sigma}(\mathbf{r})\right]\varphi_{i,\sigma}(\mathbf{r})\mathrm{d}\mathbf{r}, \tag{2.14}$$

which is a non-classical contribution arising solely due to the antisymmetry of the employed SlD. Moreover, exchange occurs only for electron pairs with same spin and it corrects for spurious self-interaction of the Coulomb operator (in case of $j = i$),[90] otherwise known as the self-interaction error.[60] Both contributions are defined in terms of the

Coulomb and exchange operators, best understood by their action on an arbitrary MO ($\varphi_{i,\sigma}(\mathbf{r})$)

$$\widehat{J}_{j,\varsigma}(\mathbf{r})\varphi_{i,\sigma}(\mathbf{r}) = \varphi_{i,\sigma}(\mathbf{r}) \int \frac{\varphi^*_{j,\varsigma}(\mathbf{r}')\varphi_{j,\varsigma}(\mathbf{r}')}{|\mathbf{r}-\mathbf{r}'|}\mathrm{d}\mathbf{r}', \tag{2.15}$$

$$\widehat{K}_{j,\varsigma}(\mathbf{r})\varphi_{i,\sigma}(\mathbf{r}) = \varphi_{j,\varsigma}(\mathbf{r}) \int \frac{\varphi^*_{j,\varsigma}(\mathbf{r}')\varphi_{i,\sigma}(\mathbf{r}')}{|\mathbf{r}-\mathbf{r}'|} \cdot \delta_{\varsigma\sigma}\mathrm{d}\mathbf{r}'. \tag{2.16}$$

The variational flexibility of the energy according to Eq. 2.10 is embedded in the choice of the set of the N spin orbitals the equation is composed of.[84] In other words, the optimal set which minimizes the energy, is found by application of the variational principle with respect to the set of occupied molecular orbitals, subject to the constraint of orthonormality. Using this approach, the resulting equations can be rewritten as the canonical Hartree–Fock equations.[88] In the MO basis, these are given as

$$\left[\widehat{h}(\mathbf{r}) + v^{HF}_{\sigma}(\mathbf{r})\right] \varphi_{i,\sigma}(\mathbf{r}) = \varepsilon_{i,\sigma}\varphi_{i,\sigma}(\mathbf{r}), \tag{2.17}$$

where $\varepsilon_{i,\sigma}$ is an energy eigenvalue, interpreted as the orbital energy of ith MO of the σ spin channel and $\widehat{h}(\mathbf{r})$ is the core-Hamiltonian of Eq. 2.12. The HF potential contains the Coulomb and exchange operators

$$v^{HF}_{\sigma}(\mathbf{r}) = \sum_{\varsigma}\sum_{j}\left[\widehat{J}_{j,\varsigma}(\mathbf{r}) + \widehat{K}_{j,\sigma}(\mathbf{r})\right]. \tag{2.18}$$

As the HF potential itself depends on the set of MOs, which are the subject of variation within the approach, the HF equations have to be computed iteratively. In practice a first set of orbitals is generated as solution of Eq. 2.17, e.g. via the core-Hamiltonian under neglect of the Hartree–Fock potential. Then in each iteration the HF potential is determined by the orbitals of the previous iteration, generating a new set of orbitals. This procedure is repeated until convergence of the resulting HF energy and thus the involved MOs, i.e. a self-consistent field (SCF) of the potential is achieved.

2.1.2 Electron Correlation and Its Explicit Description

Except for the simplest problems with only one electron, the HF method never provides the exact GS solution of the Schrödinger equation according to Eq. 2.7. The reason for this shortcoming is that HF is a mean-field theory, i.e. the electrons are treated as moving in an averaged potential of the other $N-1$ electrons of the system (pictorially speaking,

the electrons are on average too close to each other in HF theory).[90,91] The deviation

$$E_C = E_0 - E_{HF} \tag{2.19}$$

from the HF energy to the exact ground-state energy is referred to as electron correlation.[92,93] Hence, E_C, as defined in Eq. 2.19, captures all contributions to the total GS energy that cannot be represented by a single SlD. Conceptually, the correlation energy can be separated into the so-called (i) dynamic and (ii) static (also called non-dynamic) correlation (NDC).[94,95] However, the distinction is not clear-cut and methods aimed at recovering correlation in almost all cases account for fractions of both contributions to some degree.[96] Nevertheless, different methods are usually employed to compute the individual contributions:

(i) Dynamic correlation is understood as an energy correction of a dominant single determinant.[95] Practically, it can either be recovered by means of perturbation theory (PT), e.g. the MP2 method by Møller and Plesset (later generalized to MPn, where n is the perturbation order),[97,98] or by single-reference wave-function methods like configuration interaction (CI) or coupled cluster (CC) theory.[99,100] Note that CI and CC are constructed as an expansion of excited determinants of the HF ground state. Extrapolated to the basis set limit, CI and CC calculations can in principle converge to the exact solution of the Schrödinger equation and hence include all correlation contained in E_C. However, such appraoches are computationally costly and limit their applicability to small molecules.[99] Thus in practice, contributions that go beyond a particular excitation order (single, double, triple, etc.) are often truncated, as significant fractions of the correlation are nevertheless recovered.[91] Combinations of CI/CC with perturbation theory are also possible, i.e. CCSD(T) is a coupled cluster calculation with explicit inclusion of all singly and doubly excited determinants and a perturbation theoretical correction of the triply excited contributions.[101]

In contrast, (ii) non-dynamical correlation is best understood by near degeneracies of the occupied and virtual MOs, respectively, near degeneracy of determinants of the HF solution.[95] Such systems with (near) degenerate reference states are also referred to as being of multi-reference character. In practice, in HF theory parts of the static correlation can already be recovered by an unconstrained approach, however, at the cost of a spin-contaminated solution (i.e. the solution is not an eigenvector of the $\widehat{S}^2$ operator anymore).[94] The existence of such lower-energy UHF solutions in singlet systems is referred to as triplet instability.[102] However, such an approach is highly erratic and by no means captures all static correlation or is guaranteed to include even a rele-

vant fraction.[94] Systematic solutions have been established in wave-function theory by means of multi-reference approaches such as the multiconfigurational self-consistent field model (MCSCF).[103] Here, the wave function is expanded in a linear combination of determinants (usually those considered to be of importance for the problem or model to be described[104]), whereas the flexibility is further increased by simultaneous optimization of the involved spin orbitals.[96] Typically, the method is applied within a complete (CASSCF) or restricted active space (RASSCF), where only excitations within the active space are included in the MCSCF wave function. The other orbitals are either doubly occupied ("inactive") or remain vacant ("secondary").[96,104] In addition to the mostly static contribution provided by such approaches, methods to effectively recover dynamic correlation can be applied on top of the multi-reference wave functions, e.g. in methods such as multi-reference CI (MRCI)[91] or CASPT, which applies perturbation theory on top of the CASSCF solution (e.g. CASPT2).[101]

The above described methods successfully recover the correlation contributions. As mentioned, however, they are often costly to compute and therefore can be applied to few systems of interest in chemical research. Thus, for quick and routine applications usually more time-efficient methods with an acceptable error margin have to be employed, such as density functional theory, outlined in further detail in the following.

2.2 The Electron Density and Foundations of Density Functional Theory

In the outline of HF theory, the multi-electron wave function was reformulated in terms of single-electron wave functions, solved in the mean field of the remaining electrons of the system. An alternative to the wave function and its complexity, reducing the electronic problem to just 3 spatial coordinates, is the electron density $\rho(\mathbf{r})$, given by[105,106]

$$\rho(\mathbf{r}) = N \int \Psi^*(\mathbf{x}_1, \ldots, \mathbf{x}_N)\Psi(\mathbf{x}_1, \ldots, \mathbf{x}_N)\mathrm{d}s_1\mathrm{d}\mathbf{x}_2 \ldots \mathrm{d}\mathbf{x}_N, \tag{2.20}$$

Within the Born–Oppenheimer approximation, the density can be understood as the probability to find one of the electrons with arbitrary spin in an infinitesimally small volume element for a given nuclear geometry. Therefore, integration of the electron density over the real space gives the total number of electrons[105]

$$\int \rho(\mathbf{r})\mathrm{d}\mathbf{r} = N. \tag{2.21}$$

Furthermore, the density decays exponentially and vanishes at positions far from the nuclei (i.e. in infinity)[105]

$$\rho(\mathbf{r} \longrightarrow \infty) = 0. \tag{2.22}$$

The foundation of DFT was provided in the 1960s by Hohenberg and Kohn (HK):[45] Considering the Hamiltonian of Eq. 2.5, it is apparent that it is completely determined by the number of electrons and an external potential (i.e. for molecules in the BO approximation the potential V_{Ne}, which is determined by the position of the nuclei). For the first Hohenberg–Kohn theorem it was proven by "reductio ad absurdum", that the external potential uniquely determines the electron density and vice versa.[45] It is therefore possible to formulate a unique energy functional of the electron density, for which the variational principle has been formulated in the second HK theorem, similar to the variational principle in wave function theory.[45] Assuming ρ_0 to be the ground state density and ρ to be any trial density it can be written as

$$E\left[\rho_0\right] \leq E\left[\rho\right] = F_{HK}[\rho] + \int \widehat{V}_{Ne}\rho(\mathbf{r})\mathrm{d}\mathbf{r} = F_{HK}\left[\rho\right] + E_{Ne}\left[\rho\right], \tag{2.23}$$

where

$$F_{HK}[\rho] = T[\rho] + E_{ee}[\rho] = \langle\Psi|\widehat{T} + \widehat{V}_{ee}|\Psi\rangle \tag{2.24}$$

is the exact contribution from the kinetic-energy and electron-electron repulsion operators, if ρ equals the ground state density, i.e. $\rho = \rho_0$.

$E_{Ne}\left[\rho\right]$, $T[\rho]$ and $E_{ee}[\rho]$ are the explicit density functionals of the electron-nuclear attraction, kinetic energy and electron-electron repulsion, respectively. The latter contains the classical Coulomb term as well as a non-classical contribution due to electron correlation and exchange. It is given by

$$E_{ee}[\rho] = \frac{1}{2}\iint \frac{\rho\left(\mathbf{r}\right)\rho\left(\mathbf{r}'\right)}{|\mathbf{r}-\mathbf{r}'|}\mathrm{d}\mathbf{r}\,\mathrm{d}\mathbf{r}' + E_{ncl}\left[\rho\right] = J\left[\rho\right] + E_{ncl}\left[\rho\right]. \tag{2.25}$$

The functional $F_{HK}[\rho]$ is universal, i.e. it is independent of the external potential. However, its exact form as well as those of $T[\rho]$ and $E_{ncl}[\rho]$ remain unknown to date. A systematic approach to its solution was later formulated by Levy's constrained search approach. However, the need to construct a set of wave functions explicitly led to an unbearable cost.[107,108]

The central task of DFT in the formulation by HK is thus to find approximations of the universal functional and subsequently the success of the method depends decisively on the accuracy of these approximations. In particular, the kinetic energy is crucial because it has the same magnitude as the total molecular energy, as evident from the virial theorem. However, the development of accurate expressions just in terms of the density remains a difficult task.[109] Functionals such as the Thomas–Fermi model for the kinetic energy provide impressive evidence for this, as it cannot bind molecular systems.[50,110] Over the years, other more elaborate approximations were proposed within the HK framework,[111,112] but the accuracy was still insufficient for general chemical applications.[113] For this reason, an alternative approach evolved into today's most widely used branch of DFT: Kohn–Sham density functional theory.[46]

2.2.1 Kohn–Sham DFT

In the Kohn–Sham (KS) method,[46,114] some of the simplicity of the HK approach is sacrificed, as KS (re-)introduces molecular orbitals into the approach to provide a reasonable starting point for the calculation of the kinetic energy

$$T_S\left[\{\varphi_{i,\sigma}\}\right] = -\frac{1}{2}\sum_{\sigma}\sum_{i}\int \varphi^*_{i,\sigma}(\mathbf{r})\nabla^2\varphi_{i,\sigma}(\mathbf{r})\mathrm{d}\mathbf{r}. \tag{2.26}$$

The MOs are arranged in a SlD, which, as outlined in HF theory, is the wave function of the mean-field approximation. In the context of DFT this limiting case is connected with the so-called non-interacting (correlation-free) reference system. Thus, T_S is not the kinetic energy of the real interacting system, as it lacks a small but important residual correction.[115] The non-interacting system is linked to the fully interacting one by enforcing the density, constructed from the MOs as

$$\rho(\mathbf{r}) = \sum_{\sigma}\rho_\sigma(\mathbf{r}) = \sum_{\sigma}\sum_{i}|\varphi^*_{i,\sigma}(\mathbf{r})\varphi_{i,\sigma}(\mathbf{r})|, \tag{2.27}$$

to be equal in both the fictitious ($\rho_{KS,\sigma}(\mathbf{r})$) and real ($\rho_\sigma(\mathbf{r})$) reference systems. This is achieved by means of an external potential, which ensures the constraint $\rho_{KS,\sigma}(\mathbf{r}) = \rho_\sigma(\mathbf{r})$. The total energy of the KS approach is given by[114]

$$E\left[\rho_\sigma\right] = T_S[\{\varphi_{i,\sigma}\}] + E_{Ne}[\rho_\sigma] + J[\rho_\sigma] + E_{XC}[\rho_\sigma]. \tag{2.28}$$

Here, the exchange-correlation (XC) functional

$$E_{XC}[\rho_\sigma] = (T[\rho_\sigma] - T_S[\{\varphi_{i,\sigma}\}]) + E_{ncl}\,[\rho_\sigma] \tag{2.29}$$

captures the residual contribution of the kinetic energy as well as the electron-electron interactions not mapped by the classical Coulomb repulsion (E_{ncl}, see Eq. 2.25). Like the universal HK functional $F\,[\rho]$ (Eq. 2.24), the exact form of the XC functional is unknown to date. KS-DFT therefore shifts the complications of HK theory associated with the construction of $F\,[\rho]$ to the approximative construction of $E_{XC}[\rho_\sigma]$. However, the latter represents a significantly lower fraction of the total energy.

Comparing Eqs. 2.10 and 2.28 reveals a close resemblance of the HF and KS approaches. Indeed, in the framework of generalized Kohn–Sham (GKS) theory, which introduces partially interacting reference systems and allows the inclusion of non-local potentials in the calculation, HF can be regarded as a special case of KS-DFT (in the limit $E_{XC} \longrightarrow E_X$).[116] It is therefore not surprising, that the variational minimization of the KS energy equation with respect to the molecular orbitals results in a set of one-electron equations similar to the ones in HF theory[114]

$$\left[\widehat{h}(\mathbf{r}) + \nu_\sigma^{KS}(\mathbf{r})\right] \varphi_{i,\sigma}^*(\mathbf{r}) = \varepsilon_{i,\sigma}\varphi_{i,\sigma}(\mathbf{r}). \tag{2.30}$$

However, there is a distinct difference: the Kohn–Sham potential ν_σ^{KS}, given by

$$v_\sigma^{KS}(\mathbf{r}) = \sum_\varsigma \int \frac{\rho_\varsigma(\mathbf{r}')}{|\mathbf{r} - \mathbf{r}'|}\mathrm{d}\mathbf{r}' + v_{XC,\sigma}(\mathbf{r}), \tag{2.31}$$

is, as stated above, defined by the constraint $\rho_{KS}(\mathbf{r}) = \rho(\mathbf{r})$ and thus generates MOs which, according to Eq. 2.27, should give the exact density of the fully interacting system and finally its exact energy via Eq. 2.28. Hence, the MOs of HF and KS-DFT are similar but not the same. Finally, the exchange correlation potential[114]

$$v_{XC,\sigma}(\mathbf{r}) = \frac{\delta E_{XC}\,[\rho_\sigma]}{\delta\rho_\sigma(\mathbf{r})}, \tag{2.32}$$

is defined as the functional derivative of the XC energy with respect to the electron density. However, since it is derived from the approximative (see below) XC functional, the potential in KS-DFT also remains an approximation.

Conceptually, the XC energy can be separated into the exchange and correlation contributions[117]

$$E_{XC}\left[\rho_\sigma\right] = E_X\left[\rho_\sigma\right] + E_C\left[\rho_\sigma\right]. \tag{2.33}$$

Exchange is interpreted as the exchange energy arising from a SlD of KS orbitals (it is therefore different from exchange in HF theory) and is typically a much larger contribution than the correlation.[118] The latter describes the remaining non-classical energy contribution (therefore, it also contains the missing fraction of the kinetic energy). Furthermore, the XC energy can be expressed either in terms of the exchange-correlation energy density ($e_{X/C}$) or its counterpart per particle ($\varepsilon_{X/C}$) weighted by the density[117]

$$E_{X/C}\left[\rho_\sigma\right] = \sum_\sigma \int e_{X/C,\sigma}\left[\rho_\sigma\right] \mathrm{d}\mathbf{r} = \sum_\sigma \int \rho_\sigma(\mathbf{r}) \varepsilon_{X/C,\sigma}\left[\rho_\sigma\right] \mathrm{d}\mathbf{r}. \tag{2.34}$$

Spin-neutral definitions of the XC energy were also proposed (related to the spin-density formulation via the spin-scaling relation $E[\rho] = 1/2\left(E[2\rho_\alpha] + E[2\rho_\beta]\right)$).[54] Others defined functionals in terms of the density and spin polarization ($E[\rho, \zeta]$)[119,120]

$$\zeta(\mathbf{r}) = \frac{\rho_\alpha(\mathbf{r}) - \rho_\beta(\mathbf{r})}{\rho(\mathbf{r})}. \tag{2.35}$$

However, as shown by the spin-scaling relation, these are equivalent and only the spin-dependent formulations will be used throughout this work.

2.2.2 Assessment of Approximate XC Functionals

In the derivation of KS-DFT the existence of a universal exchange-correlation functional was proven, which, if it was known and if its functional derivative was constructable, would provide an exact solution to the electronic Schrödinger equation. However, the exact form of the XC functional or how it might be constructed is not apparent from the KS-DFT derivation. A prescription, to some extent, is provided by the adiabatic connection (AC)[119,121–123] and the exchange and correlation holes.[105,124,125] The AC connects the non-interacting reference system to the fully interacting ("real") one and gives an exact prescription of the exchange-correlation energy by means of the XC hole.[109] However, for the XC hole and its exchange and correlation counterparts separately, exact constraints have been derived, such as cusp and integration conditions ("sum rules"),[118,126] which can be used to guide the development of new functionals.

Nevertheless, the performance of density functional approximations (DFAs) is usually assessed by statistical measures generated from comparison of the approximate DFT calculations against (near-)exact test-set data bases. Standardized test sets have been used throughout the DFA development. Early examples of such data bases are the G1 benchmark set and its successors by Pople and co-workers.[127–129] However, such early attempts often relied heavily on a few properties (largely atomization energies (AE), but also ionization potentials (IP), electron – (EA) and proton affinities (PA)) and therefore did not necessarily provide a representative assessment of the overall performance of the tested methods.[130] To better account for robustness (i.e. the applicability of a certain methods to all tested properties, with the constraint of the absence of severe outliers) in the testing of DFAs, in one attempt randomized testing was proposed.[131] Truhlar and co-workers used diverse benchmark sets covering a range of chemical properties,[132] later also using a combined statistical measure.[133,134] In a similar attempt, Grimme and co-workers combined a total 55 test sets in the largest main-group energetics benchmark set to date, the GMTKN55 test set,[135] which is the latest offspring of the GMTKN series of benchmark data bases.[136,137]

Whereas test sets have been used to evaluate functionals for more than two decades, different philosophies in constructing XC functionals have also evolved: while some groups tried to satisfy as many of the (known) exact constraints as possible, that way building non-empirical XC functionals, a (semi-)empirical branch also emerged, where the parameters of the functional were optimized with respect to experimental and (in the beginning atomic) theoretical data. Later, this approach was taken further and some groups constructed functionals with many empirical parameters fitted to extended molecular training-sets (see below). Recently, the topic gained attention due to a study by Medvedev *et al.* in which it was argued, that modern functionals and/or their development, respectively, might have already lost their path towards the "exact" functional.[138,139] In the study, the authors ranked a set of functionals by deviations in atomic densities and found the performance of semi-empirical and highly parametrized functionals to fall behind DFAs constructed in a non-empirical fashion. However, the chosen test set (containing partly highly charged, thus chemically less meaningful atomic species) and method (e.g. bias in the chosen functionals and the selected data) was critically reviewed shortly after with partly differing results.[140,141]

In the following, such approaches and test-set data will not be discussed in detail and will only briefly be mentioned where it suits the discussion of the different DFAs.

2.2.3 Local Approximate XC Functionals

The Local Density Approximation The simplest possible approximation for a density functional can be based on the uniform electron gas (UEG). The UEG is a model of a homogeneous electron distribution of N electrons in a volume (V) neutralized by a uniform background charge (such that $V \to \infty$, $N \to \infty$ and $\rho = N/V$).[117,142] The exact analytical expression of the exchange part of the UEG model for the XC functional, the previously mentioned Slater (S) exchange, reads[52,143]

$$E_X^{UEG}[\rho_\sigma] = -\frac{3}{2}\left(\frac{3}{4\pi}\right)^{1/3} \sum_\sigma \int \rho_\sigma^{4/3}(\mathbf{r})\mathrm{d}\mathbf{r}. \tag{2.36}$$

(Note, the inclusion of a simple scaling factor into the UEG model was termed the $X\alpha$ functional.[115])

Corresponding correlation functionals were derived by means of fitting analytical expressions to numerical quantum Monte-Carlo simulations,[144] resulting in differently parametrized constructions like VWN[120] or PW92.[145,146] Since these models can all be expressed solely in terms of the density,[45] or the spin densities,[119,147] these approximations are called local-(spin-)density approximation (L(S)DA) (the term LSDA will be used synonymously throughout).

Even though the model is a drastic approximation in molecular calculations (due to rapid changes in the local densities in such systems), the performance is relatively accurate,[118,148–150] which was attributed to constraint satisfaction with regard to the XC hole.[119,126] However, the applicability is limited, i.e. exchange energies are underestimated,[151] whereas correlation energies are overestimated due to the overestimation of same-spin correlation in molecular systems[152,153] and hence the LSDA is far from the regime of chemical accuracy (typically 1kcal/mol).[91]

The Generalized Gradient Approximation A straightforward extension of the LSDA is the introduction of the gradient of the density ($\nabla\rho_\sigma$) into the exchange-correlation functional. However, initial attempts of such DFAs were shown to violate important constraints of the exchange and correlation holes[53,154–156] and showed further shortcomings (i.e. the potential was shown to diverge in regions of small densities and the prefactor of the gradient correction was not universal).[55] Today, these inital attempts are referred to as gradient expansion approximations (GEAs),[117] to clearly separate them from later approaches.

DFAs enforcing the violated constraints of the GEA model, first introduced by Perdew and Becke,[53–55,157] are collectively termed generalized gradient approximations (GGAs).[118]

In a shorthand notation, the GGA exchange functional can be expressed as

$$E_X^{GGA}[\rho_\sigma] = \sum_\sigma \int e_{X,\sigma}^{LSDA}[\rho_\sigma] f_{X,\sigma}[\rho_\sigma, \nabla\rho_\sigma] \,\mathrm{d}\mathbf{r}, \tag{2.37}$$

where $f_{X,\sigma}[\rho_\sigma, \nabla\rho_\sigma]$ is the exchange enhancement factor (EEF) or inhomogeneity correction factor (ICF),[51] which can also be expressed in terms of a dimensionless reduced gradient of the density

$$s_\sigma(\mathbf{r}) = \frac{1}{k}\frac{|\nabla\rho_\sigma(\mathbf{r})|}{\rho_\sigma^{4/3}(\mathbf{r})}, \tag{2.38}$$

with $k = 2(3\pi^2)^{1/3}$, giving $f_{X,\sigma}[\rho_\sigma, s_\sigma]$. Clearly, for $f_{X,\sigma}(0) = 1$ such a functional reduces to the LSDA. In 1997 Becke introduced a generalized form of the EEF[158]

$$f_{X,\sigma}[\rho_\sigma, s_\sigma] = \sum_{i=0}^{m} c_{X,i} u_{X,\sigma}^i[\rho_\sigma, s_\sigma]. \tag{2.39}$$

However, the popular GGA models B86,[55] B88[159] and PBE[160] share a simpler model, equal to cutting off the expansion after the first correcting term ($m = 1$, $f_{X,\sigma}[s_\sigma] = 1 + c_{X,1}u_{X,\sigma}[s_\sigma]$). As an example, the EEFs of such models (here shown for B88 and PBE) read

$$f_{X,\sigma}^{B88}[\rho_\sigma, s_\sigma] = 1 + a_1\frac{2}{3}\left(\frac{4\pi}{3}\right)^{1/3}\left(\frac{k_F^2 s_\sigma^2(\mathbf{r})}{1 + 6a_1 k_F s_\sigma(\mathbf{r})\sinh^{-1}(k_F s_\sigma(\mathbf{r}))}\right), \tag{2.40}$$

$$f_{X,\sigma}^{PBE}[\rho_\sigma, s_\sigma] = 1 + \frac{b_1 b_2 s_\sigma^2(\mathbf{r})}{b_1 + b_2 s_\sigma^2(\mathbf{r})}. \tag{2.41}$$

The different philosophies of obtaining the optimal exchange-enhancement factors were employed in such models: whereas Becke's B86 and B88 rely on semi-empiricism and therefore their parameters (i.e. $a_1 = 0.0042$) were fitted to (exact) HF atomic exchange data,[55,159] the functional PBE is constructed with non-empirical (i.e. physically motivated) constants based on the Lieb–Oxford bound and the linear response of the spin unpolarized UEG ($b_1 = 0.804$ and $b_2 = 0.21951$).[160,161]

More recent approaches using higher orders of the expansion of Eq. 2.39 like the HCTH functionals ($m = 4$)[162,163] rely on parametrization using molecular test sets and contain up to 15 empirical parameters for exchange and correlation. A step further to semi-empirical fitting was taken by Truhlar and co-workers, who published exchange-correlation

GGAs like N12 with overall 30 empirical parameters, adjusted in a sophisticated fitting procedure with a large set of training-data.[164]

Specialized constructions like the KT series of functionals (KT1–KT3) have a particular importance for the present work: these functionals were optimized with respect to (near-exact) potentials, which were shown to be accurate in NMR shielding calculations shortly before,[165] in order to reproduce nuclear shieldings and the respective shifts.[166,167] The main difference between the three models lies in a successively enhanced flexibility (by introducing further optimized parameters, respectively, a more evolved functional form in KT3) in order to simultaneously reproduce molecular properties beyond nuclear shieldings. However, in comparison to other GGAs even the most flexible KT3 is overall less successful in the application to reaction barriers and total electronic energies.[167] In fact, it was shown that GGA exchange can never simultaneously reproduce the correct asymptotic behaviour of its potential and its energy density.[168] Therefore, optimization of the EEF with respect to the potential in order to enhance the performance in shielding constants necessarily (at least to some extent) violates the asymptotic limit of the exchange energy density, whereas this limit was connected to the performance with respect to the calculation of energy differences.[168]

Correlation models of the GGA approach are for example LYP[169] by Lee, Yang and Parr, or P86,[170] PW91[171,172] and PBE[160] by Perdew and co-workers. The first is the density functional of the Colle and Salvetti correlation model, which was derived from the HF second-order density matrix and was fitted to the Helium atom.[173] This correlation model was for example later combined with B88 exchange, resulting in the famous BLYP functional.[174] The latter functionals of the above list, however, follow a similar philosophy as the exchange functionals of the same authors, i.e. they are based on non-empirical arguments and constraint satisfaction.[109] Unlike the LYP functional, these models (also HCTH and N12 are in line here) provide exchange and correlation models simultaneously. Thus, a calculation using "PBE" usually refers to PBE exchange and correlation, but they may also be employed separately (e.g. BP86 and BPW91 combine B88 exchange with either P86 or PW91 correlation).

The meta-Generalized Gradient Approximation DFAs involving higher derivatives of the density, such as the Laplacian[175] and/or the kinetic energy density

$$\tau_\sigma(\mathbf{r}) = \frac{1}{2}\sum_i \nabla^{\mathrm{T}}\varphi^*_{i,\sigma}(\mathbf{r})\nabla\varphi_{i,\sigma}(\mathbf{r}) \tag{2.42}$$

are termed meta-GGAs (or mGGAs). The latter quantity is more commonly chosen due to enhanced numerical stability.[109]

In accordance with Eq. 2.37, meta-GGAs can generally be expressed using an extended EEF [176]

$$E_X^{mGGA}[\rho_\sigma] = \sum_\sigma \int e_{X,\sigma}^{LSDA}[\rho_\sigma]\, f_{X,\sigma}[\rho_\sigma, \nabla\rho_\sigma, \tau_\sigma]\, \mathrm{d}\mathbf{r}. \tag{2.43}$$

Typically, the form of such EEFs is less instructive than for the GGAs, as more parameters and more evolved functions are usually chosen. The advantage, however, is that the introduction of additional semi-local ingredients and parameters into the functional enhances its flexibility and subsequently allows for the satisfaction of more of the (known) constraints simultaneously. [177]

This approach was, as for the GGAs, largely explored by Perdew and co-worker, who published XC functionals like TPSS [178] and its predecessor PKZB, [176] which both can be viewed as attempts to improve upon the PBE functional. [109,178] Both share the general form of the EEF employed in PBE (Eq. 2.41), but with a substitution in the semi-local parameter using a τ_σ-dependent function x_σ (not discussed in detail here) instead of the reduced density gradient s_σ (see Eq. 2.38) ($s_\sigma[\rho_\sigma, \nabla\rho_\sigma] \longrightarrow x_\sigma[\rho_\sigma, \nabla\rho_\sigma, \tau_\sigma]$). Finally, the approach was pushed further in the developement of the strongly constrained and appropriately normed (SCAN) functional, which was explicitly constructed with full constraint satisfaction in mind. [179] On the semi-empirical branch, meta-GGAs like VSXC, [180] τ-HCTH, [181] M06-L [182] or M15-L [183] have been constructed. For these 16 (VSXC), 21 (τ-HCTH), 37 (M06-L) and up to 58 (MN15-L) empirical parameters were fitted to (partly extended) molecular data sets.

Closing Remarks DFT functionals are termed "local" if the computation of their potential $v_{XC,\sigma}(\mathbf{r})$ at point $\mathbf{r}$ only requires information related to this specific point in space. Nevertheless, the gradient and kinetic energy density contain information about the immediate vicinity of the reference point. Therefore, the term "semi-local" is employed for these functionals to oppose them to purely local LSDAs.

Furthermore, the three models discussed up to this point represent the first three rungs on the so called "Jacob's ladder" proposed by Perdew and Schmidt (pictorally connecting the "Hartree World" to the "(heaven of) chemical accuracy"). [184] The scheme uses the semi-local DFT ingredients to categorize DFAs, i.e. LSDA with just the density describes the first, GGAs with additionally using the (reduced) gradient of the density the second and meta-GGAs incorporating also the kinetic energy density (or other variants of the second-order correction) the third rung.

2.2.4 Non-Local Approximate XC Functionals

Within the present section, approaches going beyond semi-local DFT are discussed. Local hybrid functionals are a non-local approximation to the exchange-correlation contribution as well. However, due to their central importance for this thesis these are discussed separately (see Sec. 2.3).

Hybrid Functionals The forth rung of the "ladder" of Perdew and Schmidt is represented by the so-called hyper-GGAs, which contain a non-local contribution from the (KS) orbitals in form of the exact exchange (see Eq. 2.14).[a] The simplest representative of these functionals are (global) hybrid (GH) functionals, which can expressed as

$$\begin{aligned} E_{XC}^{GH}\left[\rho_\sigma\right] &= \sum_\sigma \left[\int \left\{ a_X \cdot e_{X,\sigma}^{exact}\left[\left\{\varphi_{i,\sigma}\right\}\right] + (1-a_X)\cdot e_{X,\sigma}^{DFT}\left[\rho_\sigma\right] \right\} \mathrm{d}\mathbf{r} \right] + E_C^{DFT}\left[\rho_\sigma\right] \\ &= a_X \cdot E_X^{exact}\left[\left\{\varphi_{i,\sigma}\right\}\right] + (1-a_X)\cdot E_X^{DFT}\left[\rho_\sigma\right] + E_C^{DFT}\left[\rho_\sigma\right], \end{aligned} \tag{2.44}$$

where a_X is a constant and $e_{X,\sigma}^{exact}\left[\left\{\varphi_{i,\sigma}\right\}\right]$ is the exact-exchange energy density

$$e_{X,\sigma}^{exact}\left[\left\{\varphi_{k,\sigma}\right\}\right] = -\frac{1}{2}\sum_{ij}\varphi_{i,\sigma}^*(\mathbf{r})\varphi_{j,\sigma}(\mathbf{r})\int\frac{\varphi_{j,\sigma}^*(\mathbf{r}')\varphi_{i,\sigma}(\mathbf{r}')}{|\mathbf{r}-\mathbf{r}'|}\mathrm{d}\mathbf{r}', \tag{2.45}$$

dependent on the set of occupied KS orbitals $\{\varphi_{k,\sigma}\}$. Clearly, the integration requires the sampling of a second spatial variable ($\mathbf{r}'$) and accordingly the potential of such approaches becomes $v_{XC,\sigma}(\mathbf{r},\mathbf{r}')$. The evaluation of such non-local potentials hence requires a treatment via the GKS scheme (see also Sec. 2.2.1). It is noted in passing, that a transformation of $v_{XC,\sigma}(\mathbf{r},\mathbf{r}')$ into an OEP is possible, which recovers the local KS-DFT approach.[185,186] However, such schemes are not discussed in further detail within the present work.

The introduction of exact exchange was rationalized on the one hand by the localization properties of the exchange hole.[50] On the other hand, it can help to reduce spurious self-interaction present in typical DFAs. This error arises, as for such functionals the exchange-correlation contribution does not fully cancel the self-interaction present in the Coulomb contribution.[51,60,187]

However, Becke rationalized the approach using the AC and initially assumed a linear interpolation between the non-interacting (described by exact exchange) and the fully

[a] It should be noted that the exchange is calculated from the KS orbitals, not their HF counterpart and is therefore not "exact" in the sense of HF theory. The expression is nevertheless used throughout this work.

interacting limit (in his model approximated by the LSDA), which resulted in a "half and half" mixing form.[58] Later, this approach was slightly adjusted to the BHLYP functional using B88 exchange and LYP correlation.[188] Other popular functionals with a similar approach are for example TPSSh, with 10% exact-exchange admixture (EXX) on top of TPSS[189] or PBE0, with 25% EXX on top of PBE.[190,191] The exchange admixture in PBE0, however, was argued to be non-empirical as the parameter was fixed with arguments based on perturbation theory (the lowest order of PT which provides a realistic shape of the XC-energy curve within the adiabatic connection).[192] However, using similar arguments, also different prefactors were derived,[193] even with an enhanced performance.[194] In the same year as the simple one parameter hybrids, Becke also proposed the (semi-empirical) three-parameter B3PW91 functional.[59] Replacing PW91 by LYP correlation finally gave the popular B3LYP,[195] probably the most commonly used DFA in chemistry to date,[49] for which the exchange and correlation contributions according to Eq. 2.44 are

$$E_X^{DFT} \longrightarrow E_X^{LSDA} + \frac{b}{(1-a)} \cdot E_X^{B88}, \tag{2.46}$$

$$E_C^{DFT} \longrightarrow (1-c) \cdot E_C^{LSDA} + c \cdot E_C^{LYP}. \tag{2.47}$$

However, the functional uses the same parameters ($a = 0.20$, $b = 0.72$ and $c = 0.81$) as the initial model proposed by Becke.[59] B3PW91 was also the first functional, which was ever optimized using molecular test-set data.[50] Later, the approach was rationalized to some extent by Csonka *et al.*, who pointed out that no additional exact constraints can be satisfied with a constant exchange admixture and hence EXX must always be estimated (semi-)empirically.[196]

Further approaches in that direction include the B97 functional, which explored the optimal GGA (never intended to give reasonable results without EXX) to mix with exact-exchange in terms of the EEF expansion scheme (Eq. 2.39). In the final functional, the order $m = 2$ was employed, as for higher orders signs of overfitting were observed, giving in total 10 optimized parameters.[158,197] Also Truhlar and co-workers proposed (highly parametrized) (semi-)empirical GHs, such as M06, M06-2X and M06-HF with 27%, 54% and 100% exact exchange, respectively,[134,198] or the M08[199] series of functionals as well as DFAs such as MN15.[200]

Range-Separated Hybrid Functionals An early extension of the global hybrid scheme and still on rung four of Perdew's ladder, are the range-separated (RS) hybrid functionals, which use a substitution of the Coulomb operator in order to split the exchange interac-

tion into a short and long-range contribution.[201,202] Among other possible choices,[203] a common version of the splitting operator uses the error function

$$\frac{1}{|\mathbf{r}-\mathbf{r}'|} \equiv \frac{\operatorname{erfc}(\omega|\mathbf{r}-\mathbf{r}'|)}{|\mathbf{r}-\mathbf{r}'|} + \frac{\operatorname{erf}(\omega|\mathbf{r}-\mathbf{r}'|)}{|\mathbf{r}-\mathbf{r}'|}. \tag{2.48}$$

Here, the first term on the right-hand side describes the short-range (SR), the second term the long-range (LR) electron-electron interaction. The parameter ω defines the transition between the two domains, which becomes more rapid, the larger the value of ω is chosen. In the simplest RS hybrids the SR domain is dominated by DFT exchange, to benefit from the description of the exchange-correlation hole and the error compensation between the semi-local exchange and correlation functionals, whereas the LR domain is typically represented by exact exchange in order to properly describe the long-range behavior of the potential and to benefit from self-interaction correction in one-electron regions. Typical examples for such functionals are the long-range corrected (LC) versions of popular semi-local constructions such as LC-BLYP, LC-PBE[204] or the more recent ωB97.[205] Following arguments used in the construction of GHs, admixture of exact exchange was also introduced into the short-range part, as in ωB97X[205] or CAM-B3LYP.[206] The latter uses a generalization of the splitting operator of Eq. 2.48, termed Coulomb-attenuation method (CAM), providing a more flexible mixing of semi-local and exact exchange in the SR and LR domains.[206]

In optimally-tuned RS hybrids, the non-empirical system-dependent determination of the RS parameter in the course of the calculation was suggested (instead of using a fixed ω, irrespective of the application).[207–209] Recently, this approach was also extended to NMR property calculations, however, with limited success.[210]

London Dispersion London dispersion interactions are a long-range and hence non-local correlation effect. While short-ranged to medium-ranged dispersion interactions are to some extent captured within the parametrization of the correlation models of many DFAs, the long-range part is impossible to describe by purely local constructions due to its non-local nature.[211] In the context of this work, two types of corrections were applied: (i) semi-empirical schemes, which often apply a correction to the energy and (ii) non-local density-based schemes, which introduce a correction to the potential itself.[211]

Practical examples of (i) are dispersion corrections such as D2,[212] its successor D3[213] and related models.[214,215] Corrections of that type are calculated directly from the nuclear coordinates without the need of any knowledge of the electronic structure. Therefore, such models can be used as a post-SCF correction (with empirical parameters fit to the individual functionals) at low computational cost. To avoid double counting of correlation (in

DFAs which may already contain some dispersion contributions as described above),[211] intrinsically dispersion corrected functionals such as B97-D[212] or ωB97X-D[216] have been constructed, both using the D2 dispersion model.

As an example of type (ii), the non-local dispersion functional by Vydrov and Van Voorhis is considered.[217] Here, the dispersion is calculated by means of a non-local correlation kernel, parametrized to capture the missing fraction of the dispersion energy directly from the electron density. It was later shown, that similar to the above discussed corrections of type (i), the empirical parameters in VV10 can also be fitted to suit a range of DFAs, allowing the correction to be applied on top of common XC functionals.[218] However, functionals such as the meta-GGA B97M-V[219] as well as the RS hybrids ωB97X-V[220] and ωB97M-V[221] have been parametrized with VV10 dispersion correction explicitly included.

Rung Five Functionals The fifth rung of Perdew's ladder is defined by the additional incorporation of contributions dependent on virtual KS orbitals.[184] This covers methods with contributions from wave-function theory involving excited SlDs (see above), the random-phase approximation (RPA)[222,223] and different approaches based on perturbation theory.[186,224–227] However, the focus here is on so-called double-hybrid (DH) functionals.[228,229] DHs extend the idea of the GHs to the correlation contribution by introducing a fraction of second-order perturbative correlation into the DFT correlation functional, in the simplest form expressed as[228]

$$\begin{aligned} E_{XC}^{DH}\left[\rho_\sigma\right] =& a_X \cdot E_X^{exact}\left[\left\{\varphi_{i,\sigma}\right\}\right] + (1-a_X)\cdot E_X^{DFT}\left[\rho_\sigma\right] \\ &+ a_C \cdot E_C^{PT2}\left[\left\{\varphi_{p,\sigma}\right\}\right] + (1-a_C)\, E_C^{DFT}\left[\rho_\sigma\right]. \end{aligned} \tag{2.49}$$

Here, $E_C^{PT2}\left[\left\{\varphi_{p,\sigma}\right\}\right]$ is the second-order contribution derived from perturbation theory, which in addition to the occupied block includes an implicit dependence on the set of virtual KS orbitals $\left\{\varphi_{a,\sigma}\right\}$. The term was first used in Grimme's B2PLYP functional, which (as in B3LYP) combines B88 exchange and LYP correlation. The hybrid mixing parameters ($a_X = 0.53$ and $a_C = 0.27$) have been fitted to a small thermochemical test set.[230,231] A later refit, the B2GP-PLYP functional, uses the same exchange and correlation functionals but larger mixing parameters of $a_X = 0.65$ and $a_C = 0.36$.[232] The DH scheme was further extended by introducing dispersion corrections (see above) and by separating the PT correlation contribution to same and opposite-spin contributions

with individual (adjustable) parameters

$$a_C \cdot E_C^{PT2}\left[\{\varphi_{p,\sigma}\}\right] \longrightarrow c_S \cdot E_C^{SS-PT2}\left[\{\varphi_{p,\sigma}\}\right] + c_O \cdot E_C^{OS-PT2}\left[\{\varphi_{p,\sigma}\}\right]. \tag{2.50}$$

One example of such functionals is the dispersion-corrected spin-component-scaled double hybrid with PBE exchange and P86 correlation (DSD-PBEP86), which was the result of a search for the best possible DSD-DFT combination by Kozuch and Martin.[233] As for DFT and hybrid methods, many DH functionals were proposed (see Refs. 228 and 229 as well as references therein), including approaches to non-empirical DHs based on the AC[234] or combinations with range separation in the exchange part.[235] However, such functionals will not be discussed in further detail here.

2.3 Local Hybrid Functionals

Another generalization of global hybrid functionals as shown in Eq. 2.44, and still on rung four of Perdew's ladder, are local-hybrid functionals (LHs).[236,237] For this class of hybrids, a real-space function, the local mixing function (LMF) $g_\sigma(\mathbf{r})$, is employed to control the exact-exchange admixture position dependently in the target species. Consistent with the expression for GHs, a general expression for LH functionals is given by[238]

$$\begin{aligned} E_{XC}^{LH}[\rho_\sigma] = \sum_\sigma \Bigg\{ &\int g_\sigma(\mathbf{r}) e_{X,\sigma}^{exact}[\{\varphi_{i,\sigma}\}]\,\mathrm{d}\mathbf{r} \\ &+ \int (1 - g_\sigma(\mathbf{r}))\left(e_{X,\sigma}^{DFT}[\rho_\sigma] + G_\sigma(\mathbf{r})\right)\mathrm{d}\mathbf{r}\Bigg\} + E_C^{DFT}[\rho_\sigma], \end{aligned} \tag{2.51}$$

where the global admixture of exact exchange is interchanged with the LMF ($a \longrightarrow g_\sigma(\mathbf{r})$), $e_{X,\sigma}^{exact}$ is the exact-exchange energy density as defined in Eq. 2.45 and $G_\sigma(\mathbf{r})$ is the so called gauge or calibration function (see below). Compared to GHs, for such LHs two new quantities arise: (i) the LMF ($g_\sigma(\mathbf{r})$) and (ii) the gauge or calibration function ($G_\sigma(\mathbf{r})$), which both will be addressed in more detail in the following.

2.3.1 Local Mixing Functions

The LMF governs the position-dependent admixture of exact exchange in the functional, therefore usually $0 \leq g(\mathbf{r}) \leq 1$ is chosen. A set of constraints of the real space behavior of the LMF were derived.[238] These are based on general considerations: (i) in one-electron regions, that is, regions dominated by single exponential decays, exchange dominates

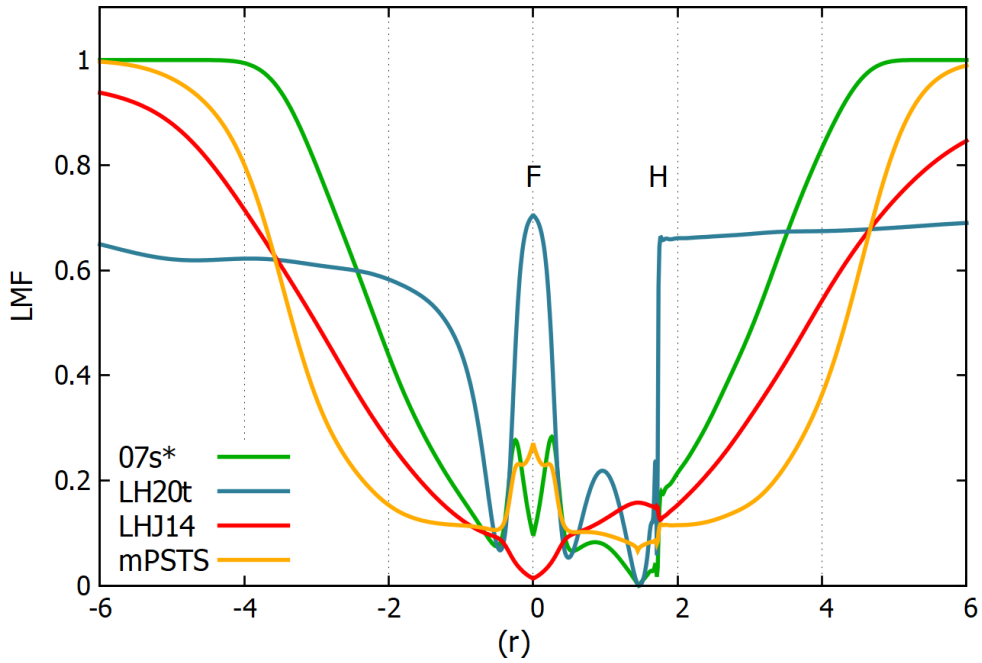

Figure 2.1.: Plots of real-space exact-exchange admixture along the F–H bond in the HF molecule for various LH functionals using different models for the LMF. Here, F is located at the origin of ($\mathbf{r}$) and H at the position ($\mathbf{r}$) = 1.729; *07s corresponds to LH07s-SVWN.

correlation and therefore the admixture of exact exchange is employed to compensate self-interaction. Hence, pure exact exchange is desirable ($g_\sigma(\mathbf{r}) \longrightarrow 1$).[239] This constraint is best associated with the asymptotic region far outside the molecule. However, the exact constraints for the transition to the asymptotic region are unknown.[238] (ii) A similar constraint also holds for the high-density limit and is related to the scaling properties of the exchange and correlation contributions.[238] The high-density limit is associated with the core region of the molecules. However, height (i.e. the on top value) and shape (i.e. representation of the core shell structure) are dependent on the nuclei and the limiting case is more likely met in heavier elements, as the core density increases with the nuclear charge.[238] (iii) In the homogeneous limit the implicit description of NDC and error compensation between the semi-local exchange and correlation functionals is beneficial, hence admixture of exact-exchange should vanish or be comparably low ($g_\sigma(\mathbf{r}) \longrightarrow 0$).[238] In the molecular case, this limit is best associated with the bonding region, where NDC is a crucial aspect.[238]

A set of different LMF models has been proposed. However, the focus here will be on the models employed in the context of the present work, exemplarily plotted for the HF molecule in Fig. 2.1. Starting with the pioneering work of Jaramillo *et al.*, the ratio

between the von-Weizsäcker kinetic energy density

$$\tau_{W,\sigma}(\mathbf{r}) = \frac{1}{8}\frac{\gamma_{\sigma\sigma}(\mathbf{r})}{\rho_\sigma(\mathbf{r})}, \qquad \text{with} \quad \gamma_{\sigma\varsigma}(\mathbf{r}) = \nabla^{\mathrm{T}}\rho_\sigma(\mathbf{r})\nabla\rho_\varsigma(\mathbf{r}), \tag{2.52}$$

and its KS counterpart was used as their initial LMF.[237] The same quantity was formerly also employed as the inhomogeneity parameter in different (non-empirical) meta-GGA functionals.[176,178,240] In these, it was typically employed as an iso-orbital indicator,[241] i.e. it was exploited, that the von-Weizsäcker kinetic energy density reduces to the KS kinetic energy density for isolated orbitals (which are typically associated with one-electron regions). Later, an empirical prefactor (a) was introduced, which resulted in enhanced performance, utilized in a variety of LH functionals (see below).[242–245] The resulting (scaled) t-LMF is given by (blue line in Fig. 2.1, using $a = 0.715$)[242,246]

$$g^{\mathrm{t}}_\sigma(\mathbf{r}) = a \cdot \frac{\tau_{W,\sigma}(\mathbf{r})}{\tau_\sigma(\mathbf{r})}. \tag{2.53}$$

Furthermore, Kaupp and co-workers proposed the s-LMF[247]

$$g^{\mathrm{s}}_\sigma(\mathbf{r}) = \mathrm{erf}(b \cdot s_\sigma(\mathbf{r})), \tag{2.54}$$

which uses the (scaled) reduced spin-density gradient, subsequently mapped by the error function to obtain $0 \leq g^{\mathrm{s}}_\sigma(\mathbf{r}) \leq 1$. The first version used the spin density gradient of Eq. 2.38. Later, a slightly different definition was employed using $k = 2(6\pi^2)^{1/3}$. However, the versions are interchangeable by adapting the empirical parameter b (green line in Fig. 2.1, using $b = 0.22$, respectively, $b = 0.277$, see below).[238]

Johnson proposed another model mapped with the error function, which is based on the (same-spin) correlation-length ($z_{\sigma\varsigma}$),[248] in the following termed z-LMF (red line in Fig. 2.1, using $c = 0.096$)[249]

$$g^{z}_\sigma(\mathbf{r}) = \mathrm{erf}(c \cdot z_{\sigma\sigma}(\mathbf{r})). \tag{2.55}$$

Here,

$$z_{\sigma\varsigma}(\mathbf{r}) = c_{\sigma\varsigma}\left[\frac{1}{|\varepsilon_X\left[\rho_\sigma\right]|} + \frac{1}{|\varepsilon_X\left[\rho_\varsigma\right]|}\right] \tag{2.56}$$

is defined in terms of the exchange-energy density per particle (see Eq. 2.34) and $c_{\sigma\varsigma}$ are empirical parameters, fitted to atomic correlation energies.[249]

Perdew and co-workers published a sophisticated LMF to satisfy as many exact constraints as possible in their attempt to construct a LH based on TPSS exchange and correlation, the PSTS functional.[239] The LMF is constructed from two parts (note, originally the LMF was given in a spin-free formulation. The mPSTS version (see below) is plotted as the yellow line in Fig. 2.1)

$$g_\sigma^p(\mathbf{r}) = 1 - (1 - g_{1,\sigma}(\mathbf{r}))(1 - g_{2,\sigma}(\mathbf{r})), \tag{2.57}$$

where $g_{1,\sigma}(\mathbf{r})$ is used to identify one-electron, rapidly varying and high-density regions, and $g_{2,\sigma}(\mathbf{r})$ is used to identify regions of strongly fluctuating electron numbers. In the original publication both are associated with the need of high exact-exchange admixture (termed "abnormal", see also above).[239] The two functions, $g_{1,\sigma}(\mathbf{r})$ and $g_{2,\sigma}(\mathbf{r})$, are defined as

$$g_{1,\sigma}(\mathbf{r}) = \frac{1}{1 + d_1 \cdot \ln(1 + d_2 u_\sigma(\mathbf{r}))}, \tag{2.58}$$

$$g_{2,\sigma}(\mathbf{r}) = \left(\frac{d_3 \left(\zeta^2(\mathbf{r}) \cdot r_s^{-1}\right)}{1 + d_4 \left(\zeta^2(\mathbf{r}) \cdot r_s^{-1}\right)} \right) \cdot f\left[v_\sigma\right], \tag{2.59}$$

where $d_1, \ldots, d_4$ are empirical parameters, ζ is the spin polarization (Eq. 2.35) and r_s is the Seitz radius. In a first approach, the function $f[v_\sigma]$ was given by

$$f[v_\sigma] = \begin{cases} 1, & v_\sigma(\mathbf{r}) \leq d_5, \\ \frac{1}{1+\exp\left[1/(1-v_\sigma(\mathbf{r}))^F - 1/\left(v_\sigma(\mathbf{r})-d_5\right)^F\right]}, & d_5 < v_\sigma(\mathbf{r}) < 1, \\ 0, & v_\sigma(\mathbf{r}) \geq 1, \end{cases} \tag{2.60}$$

where $F = -3/(2\ln[(1-d_5)/2]) > 0$ and d_5 is an additional empirical parameter. Finally, the quantities

$$u_\sigma(\mathbf{r}) = \frac{\varepsilon_C^{GL2-TPSS}\left[\rho_\sigma\right]}{\varepsilon_X^{LSDA}\left[\rho_\sigma\right]}, \tag{2.61}$$

$$v_\sigma(\mathbf{r}) = \frac{\varepsilon_X^{exact}\left[\{\varphi_{i,\sigma}\}\right]}{\varepsilon_X^{TPSS}\left[\rho_\sigma\right]} \tag{2.62}$$

are constructed from various exchange-energy densities, i.e. the Görling-Levy second-order limit of TPSS correlation,[224] LSDA exchange, exact exchange and TPSS exchange.

Further LMF models have been proposed: Kaupp and co-workers introduced the AC-LMFs, derived using the adiabatic-connection formula[250] as well as spin-polarized models of the t-LMF and s-LMF.[251] Corminbeuf *et al.* proposed an LMF based on the density-overlap region indicator (DORI).[252,253] Furthermore, Schmidt *et al.* used the orbital indicator of the t-LMF scaled by the square of the spin polarization in connection with a reduced density gradient.[254] Various approaches were also published by Scuseria and co-workers using similarity metrics of exact and LSDA exchange (spin-)density matrices,[255,256] or defining the LH as a perturbation of the underlying GH.[257]
To this point, the LMFs have been formulated in their spin-channel representation, i.e. in principle a different LMF is employed in the α and β channel, if spin-polarized systems are targeted (for unpolarized closed shell systems both reduce to the same contribution). However, a reformulation of the LH energy expression in terms of a non-dynamical correlation correction to an exact-exchange and correlation functional

$$\begin{aligned} E_{XC}^{LH}\left[\rho_\sigma\right] = E_X^{exact}\left[\left\{\varphi_{i,\sigma}\right\}\right] \\ + \int \left[\left(1-g_\sigma\right)\left(e_{X,\sigma}^{DFT}\left[\rho_\sigma\right] + G_\sigma(\mathbf{r}) - e_{X,\sigma}^{exact}\left[\left\{\varphi_{i,\sigma}\right\}\right]\right)\right] \mathrm{d}\mathbf{r} + E_C^{DFT}\left[\rho_\sigma\right] \end{aligned} \tag{2.63}$$

reveals the role of the LMF as a local scaling factor of the NDC contribution which in principle should contain cross-terms between the two spin channels.[244] These considerations motivated the construction of common instead of spin-channel LMFs, constructed from total quantities instead of their spin-resolved counterparts. Exemplarily, the common t-LMF can be written as

$$g^t(\mathbf{r}) = a \cdot \frac{1}{8}\frac{\gamma(\mathbf{r})}{\rho(\mathbf{r})\cdot\tau(\mathbf{r})}, \tag{2.64}$$

where $\tau = \tau_\alpha + \tau_\beta$, $\rho = \rho_\alpha + \rho_\beta$ and $\gamma = \gamma_{\alpha\alpha} + 2\gamma_{\alpha\beta} + \gamma_{\beta\beta}$.

2.3.2 The Calibration Function

The use of gauge or calibration functions (CFs)[258] in the context of LH functionals is motivated by the following considerations: an energy density as defined by Eq. 2.34 is only uniquely defined up to an integrable function $G_\sigma(\mathbf{r})$, which itself is defined by the condition

$$\int G_\sigma(\mathbf{r})\mathrm{d}\mathbf{r} = 0. \tag{2.65}$$

Hence, for semi-local and GH functionals

$$E_{X,\sigma}\left[\rho_\sigma\right] = \int e_{X,\sigma}\left[\rho_\sigma\right] \mathrm{d}\mathbf{r} = \int \left(e_{X,\sigma}\left[\rho_\sigma\right] + G_\sigma(\mathbf{r})\right) \mathrm{d}\mathbf{r} = \int e'_{X,\sigma}\left[\rho_\sigma\right] \mathrm{d}\mathbf{r}, \tag{2.66}$$

the "uncalibrated" ($e_{X,\sigma}(\mathbf{r})$) and "calibrated" ($e'_{X,\sigma}(\mathbf{r}) = e_{X,\sigma}(\mathbf{r}) + G_\sigma(\mathbf{r})$, where $G_\sigma(\mathbf{r})$ is accordingly called the CF) energy densities integrate to the same energy contribution.

However, if a local mixing function is used, a (potentially non-vanishing) contribution to the LH energy remains[244]

$$E_{XC}^{LH}\left[\rho_\sigma\right] = \tilde{E}_{XC}^{LH}\left[\rho_\sigma\right] - \int g_\sigma(\mathbf{r}) \cdot G_\sigma(\mathbf{r}) \mathrm{d}\mathbf{r}, \tag{2.67}$$

where $\tilde{E}_{XC}^{LH}\left[\rho_\sigma\right]$ is the uncalibrated counterpart of the LH energy expression of Eq. 2.51.[244]

Therefore, as shown in Eq. 2.63, for LHs the CF enters as a correction or scaling factor of the NDC term and allows to tune the difference of the energy densities to a "matching gauge" (i.e. adjusting the LHs behavior, e.g. in the bond dissociation of noble-gas dimers).[245] LHs using a CF are accordingly termed calibrated. If certain constraints are fulfilled, e.g. the CF should vanish for the uniform electron gas, be totally symmetric, decay in the asymptotic limit and exhibit the proper coordinate scaling (see also Ref. 244), it is possible to obtain a physically meaningful representation of the non-dynamical correlation contribution for such LHs.[259]

Among earlier attempts,[236,258] Kaupp and co-workers suggested a semi-local model for the CF, based on the divergence of a vector field[244]

$$G_\sigma(\mathbf{r}) = \nabla \cdot \left[a \cdot \frac{\nabla \rho_\sigma(\mathbf{r})}{\rho_\sigma^{1/3}(\mathbf{r})} \cdot f[s_\sigma] \right]. \tag{2.68}$$

Here, $f[s_\sigma]$ is a damping or cut-off function, for which exemplarily a Gaussian function ($f[s_\sigma] = \exp\left[-b \cdot s_\sigma^2(\mathbf{r})\right]$) was chosen in the original publication.[244] Application of such CF models resulted in a significantly enhanced performance of GGA based LH functionals due to the reduction of spurious positive NDC contributions,[244] when used in a PBE-based LH functional competitive to contemporary functionals.[260]

As an extension, in a relatively recent approach by Maier *et al.* the CF was directly constructed from integration by parts of the underlying semi-local exchange functionals.[261]

The resulting CF can generally be written as

$$G_\sigma^{(N)}(\mathbf{r}) = \sum_{m=1}^{N} \left[\prod_{n=1}^{m} a_n \right] \cdot \nabla^{\mathrm{T}} \left[\frac{\nabla \rho_\sigma(\mathbf{r}) s_\sigma^{X(m-1)}(\mathbf{r})}{\rho_\sigma^{1/3}(\mathbf{r})} \frac{d^{m-1} f\left[Q_\sigma\right]}{dQ_\sigma^{m-1}(\mathbf{r})} \right]. \tag{2.69}$$

In this equation, a_n are adjustable empirical parameters, $X = 1$ in GGA and $X = 2$ in meta-GGA functionals and $Q_\sigma(\mathbf{r})$ is an inhomogeneity parameter present in the EEF ($f\left[Q_\sigma\right]$) of the semi-local XC functional the LH is based on (for examples of such EEFs see Sec. 2.2.3. However, a slightly different definition of the EEF was employed in Ref. 261, using $E_X^{GGA}\left[\rho_\sigma\right] = E_X^{LSDA}\left[\rho_\sigma\right] - \sum_\sigma \int \rho_\sigma^{4/3}(\mathbf{r}) s_\sigma^2(\mathbf{r}) f\left[s_\sigma\right] \mathrm{d}\mathbf{r}$). The superscript (N) denotes the order of the CFs and accordingly the first-order calibration model derived from a GGA functional $G_\sigma^{(1)}(\mathbf{r})$ was termed pig1 (partial integration gauge (pig) of first order), the second-order model $G_\sigma^{(2)}(\mathbf{r})$ termed pig2 (pig of second order). If a meta-GGA functional was used in the construction the term "τ-dependent partial integration gauge" (tpig) was suggested. Furthermore, the Nth order CF is derived from a partial integration based on the $(N-1)$th order term, hence, the higher order CFs can be regarded as corrections to the former and should thus be applied hierarchically on top of the former contributions. Importantly, due to the partial integration, higher-order derivatives of the density arise in such CFs, which results in an implicit dependence of the pig1 and pig2 models on the Laplacian ($l_\sigma(\mathbf{r})$) and Hessian ($\eta_{\varsigma,\sigma\vartheta}(\mathbf{r})$) of the density

$$l_\sigma(\mathbf{r}) = \Delta \rho_\sigma(\mathbf{r}), \tag{2.70}$$

$$\eta_{\varsigma,\sigma\vartheta}(\mathbf{r}) = \nabla^{\mathrm{T}} \rho_\sigma(\mathbf{r}) \nabla \nabla^{\mathrm{T}} \rho_\varsigma(\mathbf{r}) \nabla \rho_\vartheta(\mathbf{r}). \tag{2.71}$$

Additionally, the tpig1 is dependent on a reduced quantity containing the gradient of the kinetic energy density ($\nabla \tau_\sigma(\mathbf{r})$). However, the gauge problem was recognized to be less severe if LSDA, instead of GGA or meta-GGA semi-local functionals were employed.[244] Thus, until suitable CFs were available, most LH functionals were based on LSDA semi-local exchange and correlation (with the exception of PSTS, see also below).

2.3.3 Local Hybrid Functionals in Turbomole

In the present work, a set of LH models have been used, primarily those implemented in Turbomole (usually fixed by a keyword within the program code). These are collected in Tab. 2.1 (similarly to Ref. 263). The list contains LSDA based spin-channel LHs such as the LH07s-SVWN using the s-LMF with prefacor $b = 0.22$ (or $b = 0.277$, depending on

Table 2.1.: LH functionals implemented in Turbomole and employed in the present work

LMF	Specification	Ref.
LH07t-SVWN	spin-channel t-LMF ($a = 0.48$), Slater exchange and VWN correlation	246
LH07s-SVWN	spin-channel s-LMF ($b = 0.22$, respectively, $b = 0.277$), Slater exchange and VWN correlation	238,247
LH12ct-SsirPW92	common t-LMF ($a = 0.646$), Slater-exchange and sicPW92 correlation ($\omega = 0.8$, $\lambda = 0.646$)	243
LH12ct-SsifPW92	common t-LMF ($a = 0.709$), Slater-exchange and sicPW92 correlation ($\omega = 0.8$, $\lambda = 1.0$)	243
LH14t-calPBE	spin-channel t-LMF ($a = 0.5$), pig1-CF ($a_1 = -0.1446$, $b = 0.190488$), 0.49Slater+0.51PBE-exchange and 0.55PW92+0.45PBE correlation	244
LHJ14	spin-channel z-LMF ($c = 0.096$), B88 exchange and correlation	249
LH20t	common t-LMF ($a = 0.715$), pig2-CF ($a_1 = -0.9361$, $a_2 = 0.2034$, and $\beta = 0.004936$ (contained in the damping function)), 0.22Slater+0.78PBE-exchange and modified B95 correlation (using parameters $c_{\sigma\sigma} = 0.0954$, $c_{opp.} = 0.00499$, $d_{\sigma\sigma} = 0.82$, and $d_{opp.} = 1.23$)	245
mPSTS	modified PSTS functional (see Eq. 2.57), TPSS exchange and correlation	239,262

the definition of k) within the reduced spin-density gradient (see above)[238,247] and LH07t-SVWN using a prefactor of $a = 0.48$.[246] Furthermore, the functionals LH12ct-SsirPW92 and LH12ct-SsifPW92 combine a common t-LMF (using a prefactor of $a = 0.646$ and $a = 0.709$, respectively) with LSDA and a short-range self-correlation correction (either self-interaction free (SIF) or self-interaction reduced (SIR)) of the form

$$E_{C,\omega}^{SR-LSDA} = \int \Bigg\{ e_{C,\omega}^{SR-LSDA}\left[\rho_\alpha, \rho_\beta\right] - \lambda \left[\left(\frac{\tau_{W,\alpha}}{\tau_\alpha} \right) e_{C,\omega}^{SR-LSDA}\left[\rho_\alpha, 0\right] - \left(\frac{\tau_{W,\beta}}{\tau_\beta} \right) e_{C,\omega}^{SR-LSDA}\left[0, \rho_\beta\right] \right] \Bigg\} \mathrm{d}\mathbf{r}. \quad (2.72)$$

The scaling factor $\lambda = 1$ is used for the SIF version, whereas generally $0 \leq \lambda \leq 1$ for the SIR case (practically, in LH12ct-SsirPW92 $\lambda = 0.646$ is chosen). The t-LMF based LH14t-calPBE[244] (spin-channel t-LMF with prefactor $a = 0.5$) and LH20t[245] (common t-LMF with prefactor $a = 0.715$) are two examples of calibrated GGA based functionals using PBE exchange and (modified) B95 correlation, in connection with the pig1 and pig2 CFs, respectively.

The LHJ14 functional uses B88[159] exchange and correlation as well as the z-LMF, which in the original work was fitted to G3 atomization energies with a resulting prefactor of $c = 0.1$.[264] However, here an adjusted version is used, with a prefactor of $c = 0.096$, as implemented in the course of Ref. 262. In the same work, Holzer *et al.* identified numerical instabilities related to the function $f[v_\sigma]$ in the PSTS LMF model and proposed a modification for the function of Eq. 2.60

$$f[v_\sigma] = \frac{1}{2} - \frac{1}{2}\tanh\left(\frac{v_\sigma(\mathbf{r}) - \frac{1}{2}(1+d)}{0.017}\right), \tag{2.73}$$

where d is an empirical parameter.[262] The resulting functional was termed mPSTS, which shares TPSS exchange and correlation as well as the empirical parameters (fitted to atomic and molecular test-set data) with the original PSTS model.[239]

2.3.4 Density Matrices and the LH Potential

In the context of publications related to LH functionals, a generalized way to express semi-local quantities was employed,[238] using density matrices already in the MO basis, given by

$$D_{ij,\sigma} = \delta_{ij}, \tag{2.74}$$
$$D_{ia,\sigma} = D_{ai,\sigma} = D_{ab,\sigma} = 0. \tag{2.75}$$

Semi-local quantities, here shown as an example the density, using such density matrices hence become

$$\rho_\sigma(\mathbf{r}) = \sum_{pq} D_{pq,\sigma}\varphi^*_{p,\sigma}(\mathbf{r})\varphi_{q,\sigma}(\mathbf{r}). \tag{2.76}$$

The advantage of this fomulation is a straight-forward derivative scheme in terms of the density matrices, with which the LH potential in the MO basis is defined as[238]

$$\begin{aligned} V_{XC,pq,\varsigma}^{LH} =& \frac{\partial E_{XC}^{LH}}{\partial D_{pq,\varsigma}} \\ =& -\frac{1}{2}\sum_{rs} D_{rs,\varsigma} \int g_{\varsigma}(\mathbf{r}) \left(\varphi_{r,\varsigma}(\mathbf{r})\varphi_{q,\varsigma}(\mathbf{r})A_{ps,\varsigma}(\mathbf{r}) + \varphi_{p,\varsigma}(\mathbf{r})\varphi_{s,\varsigma}(\mathbf{r})A_{rq,\varsigma}(\mathbf{r})\right) \mathrm{d}\mathbf{r} \\ &+ \sum_{\sigma} \int \widehat{d}_{pq,\varsigma} g_{\sigma}(\mathbf{r}) \cdot \left[e_{X,\sigma}^{exact}\left[\{\varphi_{t,\sigma}\}\right] - e_{X,\sigma}^{DFT}\left[\rho_{\sigma}\right]\right] \mathrm{d}\mathbf{r} \\ &+ \sum_{\sigma} \int \left[1 - g_{\sigma}(\mathbf{r})\right] \widehat{d}_{pq,\varsigma} e_{X,\sigma}^{DFT}\left[\rho_{\sigma}\right] \mathrm{d}\mathbf{r} + \int \widehat{d}_{pq,\varsigma} e_{C}^{DFT}\left[\rho_{\sigma}\right] \mathrm{d}\mathbf{r}. \end{aligned} \tag{2.77}$$

Here,

$$A_{pq,\sigma}(\mathbf{r}) = \int \frac{\varphi_{p,\sigma}^{*}(\mathbf{r}')\varphi_{q,\sigma}(\mathbf{r}')}{|\mathbf{r} - \mathbf{r}'|} \mathrm{d}\mathbf{r}' \tag{2.78}$$

is the two center A-matrix and the exact-exchange energy density in terms of the density matrix reads

$$e_{X,\sigma}^{exact}\left[\{\varphi_{p,\sigma}\}\right] = -\frac{1}{2}\sum_{pqrs} D_{pq,\sigma} D_{rs,\sigma} \varphi_{p,\sigma}^{*}(\mathbf{r})\varphi_{s,\sigma}(\mathbf{r})A_{rq,\sigma}(\mathbf{r}). \tag{2.79}$$

Next, $\widehat{d}_{pq,\sigma}$ is a differential operator, defined as

$$\widehat{d}_{pq,\sigma} = \sum_{Q \varepsilon \mathbb{Q}} \int \frac{\partial Q(\mathbf{r}')}{\partial D_{pq,\sigma}} \frac{\delta}{\delta Q(\mathbf{r}')} \mathrm{d}\mathbf{r}' \tag{2.80}$$

and second order derivatives of such operators are given by

$$\begin{aligned} \widehat{d}_{rs,\varsigma}\widehat{d}_{pq,\sigma} =& \sum_{Q,Q' \varepsilon \mathbb{Q}} \iint \frac{\partial Q(\mathbf{r}')}{\partial D_{pq,\sigma}} \frac{\partial Q'(\mathbf{r}'')}{\partial D_{rs,\varsigma}} \frac{\delta^2}{\delta Q(\mathbf{r}')\delta Q'(\mathbf{r}'')} \mathrm{d}\mathbf{r}''\mathrm{d}\mathbf{r}' \\ &+ \sum_{Q \varepsilon \mathbb{Q}} \int \frac{\partial^2 Q(\mathbf{r}')}{\partial D_{pq,\sigma}\partial D_{rs,\varsigma}} \frac{\delta}{\delta Q(\mathbf{r}')} \mathrm{d}\mathbf{r}'. \end{aligned} \tag{2.81}$$

Here, Q and Q' run over the set of (semi-local) quantities present in the functional or function ($\mathbb{Q} = \{\rho_{\sigma}, \gamma_{\sigma\sigma}, \tau_{\sigma}, \dots\}$), of which the derivatives are taken. Explicitly, such a

derivative, here as an example for a general function $f = f[\rho_\sigma, \gamma_{\sigma\sigma}, \tau_\sigma])$, reads

$$\begin{aligned}\widehat{d}_{pq,\sigma} f =& \varphi^*_{p,\sigma}\varphi_{q,\sigma}\frac{\delta f}{\delta \rho_\sigma} + \frac{1}{2}\nabla^{\mathrm{T}}\varphi^*_{p,\sigma}\nabla\varphi_{q,\sigma}\frac{\delta f}{\delta \tau_\sigma} \\ &+ \nabla^{\mathrm{T}}\left[\varphi^*_{p,\sigma}\varphi_{q,\sigma}\right]\left(2\nabla\rho_\sigma\frac{\delta f}{\delta \gamma_{\sigma\sigma}} + \nabla\rho_{\sigma'}\frac{\delta f}{\delta \gamma_{\sigma\sigma'}}\right).\end{aligned} \tag{2.82}$$

2.4 Computational Methodology

2.4.1 Atomic Orbitals

To this point, all equations have been shown in the MO basis. However, in molecular calculations the MOs are usually expanded in a linear combination of atomic orbitals (LCAO).[265] Such an expansion results in the Roothaan–Hall equations for restricted[266,267] and Pople–Nesbet equations for unrestricted calculations.[268] Explicitly, the expansion is given as

$$\varphi_{i,\sigma}(\mathbf{r}) = \sum_\mu c_{\mu i,\sigma}\phi_\mu(\mathbf{r}), \tag{2.83}$$

where $c_{\mu i}$ is the orbital coefficient and $\phi_\mu(\mathbf{r})$ is the AO. Note that throughout this work the subscripts $\mu, \nu, \ldots$ on the variable ϕ denote atomic orbitals. The expansion coefficients are conveniently arranged in the (spin resolved) AO density matrices, given by

$$D_{\mu\nu,\sigma} = \sum_{pq} c^*_{\mu p,\sigma} c_{\nu q,\sigma} D_{pq,\sigma}. \tag{2.84}$$

The AOs can themselves either be constructed from a contracted primitive basis

$$\phi_\mu(\mathbf{r}) = \sum_n a_{n\mu}\gamma_n(\mathbf{r}), \tag{2.85}$$

or in the special case of uncontracted basis sets, all AOs are constructed from just one primitive and the corresponding contraction coefficient $a_{1\mu} = 1$.
The AOs and the primitive functions $\gamma_n(\mathbf{r})$ are usually centered on the associated atoms and either Slater-type orbitals or (more frequently) Gaussian-type orbitals are used. The latter can generally be written as[269]

$$\gamma_n(\mathbf{r}) = x^i y^j z^k \exp(-\alpha_n r^2). \tag{2.86}$$

Here, α_n is the related exponent of the individual primitive, the exponents of the so-called monomials i, j and k define the angular quantum number $l = i + j + k$ and x, y, z are the Cartesian components of the vector $\mathbf{r}$. Each contracted set of basis functions (according to Eq. 2.85) of a certain l-quantum number is called a shell and accordingly, AOs of the same l-quantum number share the shell's coefficients ($a_{n\mu}$) and exponents (α_n). It is noted in passing, that the product of two interacting Gaussian primitives may itself be expressed in terms of a single Gaussian function via the "Gaussian product rule", which allows for efficient integral evaluation using standardized techniques (see below).[270]

2.4.2 Integral Evaluation

Throughout the chapter, the evaluation of molecular quantities was expressed in terms of integration over spatial coordinates, where formally three different types of integrals can be distinguished. (I) Relatively simple two-center one-electron integrals, such as for the overlap and the kinetic energy, (II) integrals involving the semi-local exchange-correlation energy and (III) four-center two-electron integrals involving the Coulomb operator.

(I) The "simple"[269] two-center integrals can be solved using well established integral evaluation techniques such as Gauss–Hermite or the recurrence-related Obara–Saika and McMurchie–Davidson schemes.[269] However, such integrals have never been altered within the course of the present thesis and therefore are not discussed in further detail.

(II) Focussing next on the semi-local quantities, analytic integration of the exchange-correlation terms can in general be difficult due to the partly sophisticated form of the involved functionals. Therefore the integration over the spatial coordinates can be reformulated in terms of a sum over a numerical grid, generally expressed as[271]

$$F = \int f(\mathbf{r})\mathrm{d}\mathbf{r} \approx \sum_g w_g f(\mathbf{r}_g), \tag{2.87}$$

where w_g is a grid-weighting factor and $\mathbf{r}_g$ are the spatial coordinates of the respective grid points. Assuming, that the function f is implicitly dependent on a set of molecular quantities $\mathbb{Q} = \{\rho_\sigma, \nabla\rho_\sigma, \tau_\sigma, \dots\}$, its evaluation requires the computation of these quantities on the integration grid. For example the density (Eq. 2.27) in terms of the AOs at

individual grid points ($\phi_\mu(\mathbf{r}_g)$) is given by

$$\begin{aligned}\rho_\sigma(\mathbf{r}_g) &= \sum_{\mu\nu} D_{\mu\nu,\sigma}\phi^*_\mu(\mathbf{r}_g)\phi_\nu(\mathbf{r}_g) \\ &= \sum_\mu \phi^*_\mu(\mathbf{r}_g) \sum_\nu D_{\mu\nu,\sigma}\phi_\nu(\mathbf{r}_g) \\ &= \boldsymbol{\phi}_g^{\mathrm{T}}\mathbf{D}\boldsymbol{\phi}_g. \end{aligned} \tag{2.88}$$

These semi-local quantities are evaluated straightforwardly in terms of matrix-vector products on the numerical integration grid.

The difficulty associated with numerical integration is to provide the balance between molecular grids, which on the one hand result in near analytical error margins, but on the other hand are sufficiently small to enable efficient evaluation of molecular properties. Therefore, in TURBOMOLE standardized schemes for the grid construction were implemented, such as Becke partitioning in connection with approaches by Lebedev for the spherical grid and by Chebyshev for the radial grid construction.[271–273]

(III) The evaluation of the four-center integrals

$$(\phi_\mu\phi_\nu|\phi_\kappa\phi_\lambda) = \iint \frac{\phi^*_\mu(\mathbf{r})\phi_\nu(\mathbf{r})\phi^*_\kappa(\mathbf{r}')\phi_\lambda(\mathbf{r}')}{|\mathbf{r}-\mathbf{r}'|}\mathrm{d}\mathbf{r}'\mathrm{d}\mathbf{r} \tag{2.89}$$

is the most time consuming step in common KS-DFT and HF calculations due to its formal N^4 scaling. Hence, the implementation of efficient algorithms to reduce the computational cost is crucial to obtain efficient and applicable tools.

To reduce the cost of integral evaluation, (i) a simplification of the analytical integrals can be employed, i.e. reformulation of the four-center integrals in order to reduce their complexity, number or cost, and (ii) the development of numerical methods to efficiently solve the resulting integrals is required.

Examples of (i) are the resolution of the identity (RI) and chain-of-spheres (COS) approximations, which can be applied both to the Coulomb (RI-J, COS-J) and exchange integrals (RI-K, COS-X). While for the Coulomb part the RI-J scheme was found to be more efficient than the COS-J scheme (especially, if its multipole-accelerated variant (MARI-J)[274] is chosen),[275] for exchange COS-X outperforms the RI-K approximation (due to a favorable scaling with system size).[13,276]

For the RI-J approximation the Gaussian-type orbitals are expanded in a set of pre-fitted auxiliary basis functions $P(\mathbf{r})$ [277,278]

$$\sum_{\mu\nu} D_{\mu\nu}\phi_\mu^*(\mathbf{r})\phi_\nu(\mathbf{r}) \approx \sum_P c_P P(\mathbf{r}) = \tilde{\rho}(\mathbf{r}). \tag{2.90}$$

These are constructed from a suitable scheme such as minimizing the self-repulsion of the residual density.[265] That way, the complexity of the four-center integrals is reduced to the three-center entities[278,279]

$$(\phi_\mu\phi_\nu|\phi_\kappa\phi_\lambda)_{RI} = \sum_{PQ}(\phi_\mu\phi_\nu|Q)(Q|P)^{-1}(P|\phi_\kappa\phi_\lambda), \tag{2.91}$$

with a formal reduction of the scaling to be proportional to $N_{\text{aux.}} \cdot N^2$ (where $N_{\text{aux.}}$ is the number of basis functions in the auxiliary basis set and N is the number of basis functions).

For the multipole-accelerated variant the additional steps taken involve the separation of the Coulomb integrals into short-range ("near-field") interactions, calculated with the RI-J approximation as shown in Eq. 2.91, and a long-range ("far-field") interaction, where the Coulomb interactions are evaluated in terms of charge distributions instead of the explicit four-center integrals.[274,280,281]

Efficient implementations of four-center exchange integrals can be obtained by algorithms such as COS-X, which is based on a semi-numerical approach[275]

$$\begin{aligned} K_{\mu\nu} = -\frac{1}{2}\sum_{\kappa\lambda} D_{\kappa\lambda}(\phi_\mu\phi_\lambda|\phi_\kappa\phi_\nu) &\approx -\frac{1}{2}\sum_{\kappa\lambda,g} w_g \cdot \phi_\mu^*(\mathbf{r}_g) A_{\nu\kappa,g} D_{\kappa\lambda}\phi_\lambda(\mathbf{r}_g) \\ &= -\frac{1}{2}\sum_g w_g \cdot \phi_\mu^*(\mathbf{r}_g) \sum_\kappa A_{\nu\kappa,g} \sum_\lambda D_{\kappa\lambda}\phi_\lambda(\mathbf{r}_g) \\ &= -\frac{1}{2}\boldsymbol{\phi}^{\mathrm{T}}\mathbf{AD}\boldsymbol{\phi}. \end{aligned} \tag{2.92}$$

Here, the explicit integral over the outer vector $\mathbf{r}$ in the four-center term is replaced by numerical integration, as outlined in Eq. 2.87. However, the two-center A-matrix elements ($A_{\mu\nu,g}$, see Eq. 2.93 below) are solved analytically, thus formally the overall scaling reduces to $n_g \cdot N^2$, where n_g is the number of grid points. Again, the second line of the right-hand side of Eq. 2.92 shows the potential step-wise contraction of the expressions by means of the matrix-vector products, as schematically outlined in the last line. Here, additionally implicit summation (Einstein notation) over the weighted grid points is employed. It is noted in passing, that the approach to this point is similar to the

pseudo-spectral methods developed by Friesner and co-workers.[282–284] As the most time consuming step within such semi-numerical schemes is the evaluation of the two-center A-matrix integrals, the crucial step to arrive at the COS-X scheme is to introduce efficient pre-screening of the basis-function overlap ("S-junction") or density-matrix elements ("P-junctions"), used to decided which four-center integrals have to be evaluated (see also below).[275] Recently, further pre-evaluation based on an asymptotic integral estimate ("F-junction") was suggested for the modified COS-X (mCOS-X) method.[285] Here, the spatial expansion of the current grid batch is approximated by a sphere comprising all grid-points of the said batch, and based on the minimal distance of the sphere to the center of a basis-function pair (outside the sphere) an estimate of the integral is calculated as an upper bound for the integrals of the basis-function pair on any point of the grid batch. Finally, the evaluation of the A-matrix elements for such a basis-function pair is skipped if this upper bound is below a chosen threshold. In large-scale calculations, the combined pre-screening for the COS-X (respectively, mCOS-X) scheme potentially results in linear scaling, as the number of interacting pairs (basis and density-matrix) converges.[275,286] Furthermore, semi-numerical implementation is also well suited for the evaluation of non-standard integrals such as the LMF weighted exchange (see e.g. Eq. 2.51) arising in LH functionals,[238] as the analytic evaluation of LMF-dependent integrals can be circumvented and instead the LMF and its derivatives are constructed from semi-local ingredients on the numerical grid.

(ii) In standard GH functionals the four-center integrals Eq. 2.89 are usually solved using well established integration techniques, such as the recurrence-related McMurchie–Davidson and Obara–Saika schemes or a direct approach such as Rys-quadrature,[269] which all can also be applied in connection with the RI approximation (see Eq. 2.91). In the context of the present work especially the two center A-matrices ($A_{\mu\nu,g}$) of Eq. 2.92 are of importance, which contain the interaction between two basis functions over the Coulomb operator involving the evaluated point on the numerical grid[287]

$$A_{\mu\nu,g} = \int \frac{\phi^*_\mu(\mathbf{r}')\phi_\nu(\mathbf{r}')}{|\mathbf{r}_g - \mathbf{r}'|}\mathrm{d}\mathbf{r}'. \tag{2.93}$$

However, in the implementations reported in Sec. 5.3 such repulsion integrals were evaluated using well established, formerly implemented integral evaluation schemes within TURBOMOLE.[273] These use an Boys-function based approach up to f-f basis function pairs and Rys-quadrature for higher l-quantum numbers.[288]

3 Theoretical Background – Nuclear Magnetic Resonance

Chapter 2 has so far focused on KS-DFT in its field-free limit. In this chapter, the fundamental theory of nuclear magnetic resonance is introduced, a general description of the calculation of magnetic properties via perturbation theory and the central equations derived by Ramsey are presented and the extension of the Hamiltonian to cover magnetic interactions is derived. Furthermore, the coupled perturbed equations, central to the derivation in later chapters, are discussed and finally the formal extension of KS-DFT to current-carrying states is outlined.

3.1 Linking Experiment and Theory

3.1.1 The Effective Spin-Hamiltonian

In NMR experiments, the probe is placed within a external magnetic field ($\mathbf{B}$), which interacts with the nuclear magnetic moments of the nuclei and induces a Zeeman splitting of associated energy levels.[289] Importantly, due to induced electric currents in the electronic structure of the sample, the local magnetic field strength is dependent on the electronic environment.[290] Hence, the method is sensitive to the local electronic structure of the target molecules. The local magnetic field at the position of nucleus K is defined by

$$\mathbf{B}_{K,\text{loc.}} = (1 - \boldsymbol{\sigma}_K)\,\mathbf{B}, \tag{3.1}$$

introducing the nuclear shielding tensor $\boldsymbol{\sigma}_K$, which is related to the interaction of the nuclear magnetic moment with the external field, described by the Hamiltonian

$$\begin{aligned} H^{\mathbf{B}} &= -\mathbf{M}_K \cdot \mathbf{B}_{K,\text{loc.}} \\ &= -\mathbf{M}_K(1-\boldsymbol{\sigma}_K)\mathbf{B}. \end{aligned} \tag{3.2}$$

$\mathbf{M}_K$ is the nuclear magnetic dipole moment

$$\mathbf{M}_K = \gamma_K \hbar \mathbf{I}_K, \tag{3.3}$$

itself related to the gyromagnetic ratio γ_K and the nuclear spin $\mathbf{I}_K$ (with the spin quantum numbers $m_I = -I, -I{+}1, \ldots, I{-}1, I$). Note that $\mathbf{M}_K$ and $\mathbf{B}$ are both vectors, whereas $\boldsymbol{\sigma}_K$ is a second rank tensor, containing in principle nine independent contributions. However, in a freely tumbling molecule typically just the isotropic contribution is measured, which is given by[289]

$$\sigma_{K,iso.} = \frac{1}{3}\text{Tr}\left(\boldsymbol{\sigma}_K\right). \tag{3.4}$$

Applying an electromagnetic pulse at the so-called observation frequency (ν_K) induces transitions between the energy levels and the absorbed wave length (typically radio-waves) can subsequently be detected.[290] The corresponding ν_K is itself dependent on the nuclear shielding (here fixed in direction of the magnetic field, chosen as the z-direction)[289]

$$\nu_K = \frac{\gamma_K\left(1-\sigma_{K,zz}\right)B_z}{2\pi}. \tag{3.5}$$

Finally, the chemical shift, expressed as the difference to a reference compound, is related to the observation frequency via[289]

$$\begin{aligned} \delta_K &= \frac{\nu_K - \nu_{K,\text{ref.}}}{\nu_{K,\text{ref.}}} = \frac{\sigma_{K,\text{iso.,ref.}} - \sigma_{K,\text{iso.}}}{1-\sigma_{K,\text{iso.,ref.}}} \\ &\approx \sigma_{K,\text{iso.,ref.}} - \sigma_{K,\text{iso.}}. \end{aligned} \tag{3.6}$$

A second interaction observed in NMR spectra is due to the coupling of the nuclear spins, the spin–spin coupling. As (parts of) these contributions can also be detected in freely tumbling molecules, it was concluded that these are not due to a direct interaction of the magnetic dipoles (direct coupling, $\mathbf{D}_{KL}$), but mediated by the electronic structure in the molecules ((reduced) indirect coupling, $\mathbf{K}_{KL}$).[291] These two distinct contributions can

be collected in the Hamiltonian

$$H^{\mathbf{I}} = \frac{1}{2}\gamma_K\gamma_L\hbar^2\mathbf{I}_K\left(\mathbf{K}_{KL} + \mathbf{D}_{KL}\right)\mathbf{I}_L, \tag{3.7}$$

where, just as the shielding tensor, $\mathbf{K}_{KL}$ and $\mathbf{D}_{KL}$ have in principle nine independent components, depending on the Cartesian directions of the vectors $\mathbf{I}_K$ and $\mathbf{I}_L$. The direct coupling (as stated above) vanishes in freely tumbling molecules and just the isotropic contribution of the indirect coupling is obtained in these spectra, given by [292]

$$K_{KL,iso.} = \frac{1}{3}\mathrm{Tr}\left(\mathbf{K}_{KL}\right). \tag{3.8}$$

Typically the indirect spin–spin coupling tensor $\mathbf{J}_{KL}$ is reported instead of its reduced counterpart $\mathbf{K}_{KL}$, given by

$$\mathbf{J}_{KL} = h\frac{\gamma_K}{2\pi}\frac{\gamma_L}{2\pi}\mathbf{K}_{KL}. \tag{3.9}$$

Using the quantities discussed above,[a] experimental NMR spectra can be fit by an effective spin-Hamiltonian, written as [292,293]

$$H_{\text{eff.}} = -\sum_K \gamma_K\hbar\mathbf{B}^{\mathrm{T}}\left(1 - \boldsymbol{\sigma}_K\right)\mathbf{I}_K + \frac{1}{2}\sum_{K\neq L}\gamma_k\gamma_L\hbar^2\mathbf{I}_K\left(\mathbf{K}_{KL} + \mathbf{D}_{KL}\right)\mathbf{I}_L. \tag{3.10}$$

Compared to electronic energy differences, the perturbation due to the experimental external magnetic fields and the nuclear spins are small. [292] Therefore, perturbation theory (PT) is a suitable tool to link the effective spin-Hamiltonian and quantum-chemical computations, as discussed in the following.

3.1.2 Molecular Properties via Perturbation Theory

As outlined by the effective spin-Hamiltonian (Eq. 3.10), the application of the external magnetic field and the nuclear magnetic moments induces changes in the molecular electronic states of the target system. These changes are the so-called magnetic responses of the system and can subsequently be identified with the molecular properties associated with the applied perturbations. If these response-energies in comparison to the ground-state energy are small, PT (here shown for the non-degenerate and time-independent

[a] Further contributions, such as nuclear quadrupole couplings, which would be present for nuclei with $I > 1/2$ and manifest themselves as a splitting of the NMR signals in the spectrum, [293] were never analysed within this work and are therefore neglected.

limits) is a suitable starting point for their calculation.[292] Using Rayleigh–Schrödinger PT,[91,294] the corrections to the energy are obtained from a power series expansion of the energy, Hamiltonian and wave function. In double perturbation theory, two perturbation factors ($\boldsymbol{\lambda}$ and $\boldsymbol{\kappa}$) are applied simultaneously, giving

$$E = E_0 + \boldsymbol{\lambda}E^{(10)} + \boldsymbol{\kappa}E^{(01)} + \boldsymbol{\lambda}^2E^{(20)} + \boldsymbol{\lambda}\boldsymbol{\kappa}E^{(11)} + \boldsymbol{\kappa}^2E^{(02)} + \ldots, \tag{3.11}$$

$$H = H_0 + \boldsymbol{\lambda}H^{(10)} + \boldsymbol{\kappa}H^{(01)} + \boldsymbol{\lambda}^2H^{(20)} + \boldsymbol{\lambda}\boldsymbol{\kappa}H^{(11)} + \boldsymbol{\kappa}^2H^{(02)} + \ldots \tag{3.12}$$

and

$$\Psi = \Psi_0 + \boldsymbol{\lambda}\Psi^{(10)} + \boldsymbol{\kappa}\Psi^{(01)} + \boldsymbol{\lambda}^2\Psi^{(20)} + \boldsymbol{\lambda}\boldsymbol{\kappa}\Psi^{(11)} + \boldsymbol{\kappa}^2\Psi^{(02)} + \ldots. \tag{3.13}$$

These switch the system from unperturbed at $\boldsymbol{\lambda} = \boldsymbol{\kappa} = 0$ to fully perturbed at $\boldsymbol{\lambda} = \boldsymbol{\kappa} = 1$ and are associated with the perturbation order, where terms of the form $\boldsymbol{\lambda}^l\boldsymbol{\kappa}^kE^{(lk)}$ denote the $(k+l)$th order perturbation.

Molecular properties of a certain order can be connected with derivatives of the molecular ground-state energy. The general expression for the energy as a function of the perturbations $\boldsymbol{\lambda}$ and $\boldsymbol{\kappa}$ is given by[295,296]

$$E = E(\boldsymbol{\lambda}, \boldsymbol{\kappa}, c(\boldsymbol{\lambda}, \boldsymbol{\kappa})), \tag{3.14}$$

where c denotes the wave-function parameters, e.g. the MO coefficients. The first derivative of the energy at the point of a vanishing perturbation

$$\left.\frac{dE}{d\boldsymbol{\lambda}}\right|_{\lambda=0} = \frac{\partial E}{\partial \boldsymbol{\lambda}} + \frac{\partial E}{\partial c}\frac{\partial c}{\partial \boldsymbol{\lambda}} \tag{3.15}$$

contains an explicit derivative with respect to $\boldsymbol{\lambda}$ as well as the implicit variation via the wave-function parameters on the right-hand side. In case of variational wave functions, such as the ones obtained from HF-theory and KS-DFT, the GS energy is a stationary point with respect to c, therefore

$$\frac{dE}{dc} = \frac{\partial E}{\partial c} = 0, \tag{3.16}$$

and the second term on the right-hand side of Eq. 3.15 vanishes. This result is related to the Hellmann–Feynman theorem,[297,298] which states that a molecular property of first order $E^{(1)}$ (without the explicit dependence of the wave function on the perturbation) can be obtained from the ground state wave function and the first-order perturbed Hamiltonian.

This leads to a simple explicit expression of Eq. 3.15:

$$E^{(10)} = \langle \Psi_0 | \widehat{H}^{(10)} | \Psi_0 \rangle \,. \tag{3.17}$$

The (symmetrized) second derivative is given by[292]

$$\left.\frac{d^2E}{d\boldsymbol{\lambda} d\boldsymbol{\kappa}}\right|_{\boldsymbol{\lambda}=\boldsymbol{\kappa}=0} = \frac{\partial^2 E}{\partial \boldsymbol{\lambda} \partial \boldsymbol{\kappa}} + \frac{\partial^2 E}{\partial c \partial \boldsymbol{\lambda}} \frac{\partial c}{\partial \boldsymbol{\kappa}} + \frac{\partial^2 E}{\partial c \partial \boldsymbol{\kappa}} \frac{\partial c}{\partial \boldsymbol{\lambda}} + \frac{\partial^2 E}{\partial c \partial c} \frac{\partial c}{\partial \boldsymbol{\lambda}} \frac{\partial c}{\partial \boldsymbol{\kappa}}. \tag{3.18}$$

Similar to the first-order equation, the last term on the right-hand side vanishes for variational wave functions due to the condition shown in Eq. 3.16. Alternatively, a step-wise differentiation of Eq. 3.15 results in a reduced variant of the above equation

$$\left.\frac{d^2E}{d\boldsymbol{\lambda} d\boldsymbol{\kappa}}\right|_{\boldsymbol{\lambda}=\boldsymbol{\kappa}=0} = \frac{\partial^2 E}{\partial \boldsymbol{\lambda} \partial \boldsymbol{\kappa}} + \frac{\partial^2 E}{\partial c \partial \boldsymbol{\lambda}} \frac{\partial c}{\partial \boldsymbol{\kappa}}. \tag{3.19}$$

However, the second derivative of Eq. 3.19 results in a reduced (but usually sufficient) numerical accuracy in comparison to Eq. 3.18.[292] As stated by the interchange theorem, the order of the derivatives in Eq. 3.19 is interchangeable.[299] Using

$$\left.\frac{d^2E}{d\boldsymbol{\kappa} d\boldsymbol{\lambda}}\right|_{\boldsymbol{\lambda}=\boldsymbol{\kappa}=0} = \frac{\partial^2 E}{\partial \boldsymbol{\kappa} \partial \boldsymbol{\lambda}} + \frac{\partial^2 E}{\partial c \partial \boldsymbol{\kappa}} \frac{\partial c}{\partial \boldsymbol{\lambda}} \tag{3.20}$$

therefore results in the same perturbed energy contribution as Eq. 3.19. However, the order may have an (significant) influence on the overall efficiency of the PT scheme (see also Sec. 3.2.1).

In terms of the second-order correction of the energy and Hamiltonian, the second-order energy correction for a mixed derivative is given by

$$E^{(11)} = \langle \Psi_0 | \widehat{H}^{(11)} | \Psi_0 \rangle + 2 \sum_a \frac{\langle \Psi_0 | \widehat{H}^{(10)} | \Phi_a^{(01)} \rangle \, \langle \Phi_a^{(10)} | \widehat{H}^{(01)} | \Psi_0 \rangle}{E_a - E_0}, \tag{3.21}$$

which is the so-called sum-over-states (SOS) expression of double-perturbation theory. The left-hand side is built from the ground-state wave function and is therefore a simple expectation value of the second-order Hamiltonian. However, the construction of the right-hand side contribution requires the perturbed wave function of first order. It is noted in passing, that Eq. 3.21 is obtained by assuming that the perturbed wave function of first order can be expanded in a basis of the excited states of its ground state ($\Psi^{(10)} = \sum_a c_a^{(10)} \Phi_a^{(10)}$). However, in order to calculate the second-order correction to the energy, the first-order response of the wave function is sufficient. This was generally expressed

by Wigner's $2n+1$ theorem stating that the nth order correction to the wave function is sufficient to calculate $(2n+1)$th order properties.[295,300]

As the exact wave function and its expansion in virtual states is in most cases not available, especially in approximate calculations based on a single SlD,[292] molecular properties are usually calculated using a different ansatz than the SOS. Suitable schemes are outlined further below (see Sec. 3.2.1). Comparing the spin-Hamiltonian (Eq. 3.10) with the outlined perturbation scheme, the quantities $\boldsymbol{\lambda}$ and $\boldsymbol{\kappa}$ can be associated with the magnetic field $\mathbf{B}$ and the nuclear magnetic moment of nucleus K, $\mathbf{M}_K$, in case of NMR shielding constants, or the magnetic moments $\mathbf{M}_K$ and $\mathbf{M}_L$ for SSCCs. In this case, the contributions of the SOS equation are often termed diamagnetic (on the left-hand side) and paramagnetic (on the right-hand side), respectively. Furthermore, the pure electronic Hamiltonian of Eq. 2.6 is insufficient as it lacks contributions dependent on the magnetic field and it has to be adjusted accordingly to describe such interactions properly. After introducing general definitions regarding the magnetic field, the derivation of a suitable quantum-chemical Hamiltonian including magnetic interactions is outlined in the following.

3.1.3 The Magnetic Field and Its Vector Potential

The magnetic field ($\mathbf{B}$) and the corresponding magnetic vector potential ($\mathbf{A}$) are interrelated with the electric field, the charge density, the current density and the electric vector potential via Maxwell's equations and related reformulations.[301] In the context of the present work, however, only the interconnection of both magnetic quantities is briefly revisited. The magnetic field vector can be defined as the curl of the a vector potential

$$\mathbf{B} = \nabla \times \mathbf{A}, \tag{3.22}$$

which by construction obeys the constraint of the absence of free magnetic poles ($\nabla \cdot \mathbf{B} = 0$).[301] From the definition of 3.22 the corresponding vector potential ($\mathbf{A}$) is not uniquely defined, as readily shown by choosing $\mathbf{A}' = \mathbf{A} + \nabla\Lambda$ (where Λ is an arbitrary function)

$$\mathbf{B}' = \nabla \times \mathbf{A}' = \nabla \times (\mathbf{A} + \nabla\Lambda) = \nabla \times \mathbf{A} + \nabla \times \nabla\Lambda = \mathbf{B}. \tag{3.23}$$

In the absence of sources (thus for a vanishing scalar potential), a convenient choice is the so-called Coulomb gauge,[292,301] i.e. a divergence-free vector potential

$$\nabla \cdot \mathbf{A} = 0. \tag{3.24}$$

Other possiblities such as the Lorentz gauge have been considered,[301] however, for time-independent vector and scalar potentials, as assumed throughout the present work, the choices are indistinguishable.[302]
An explicit form of the vector potential associated with a uniform external magnetic field is[292]

$$\mathbf{A}_G(\mathbf{r}) = \frac{1}{2}\mathbf{B} \times (\mathbf{r} - \mathbf{R}_G)\,, \tag{3.25}$$

where $\mathbf{R}_G$ is the gauge origin of the magnetic vector potential.
Considering NMR experiments, the magnetic induction ($\mathbf{B}^{\text{tot.}}(\mathbf{r})$) and the corresponding vector potential ($\mathbf{A}^{\text{tot.}}(\mathbf{r})$), arise from the external magnetic field induced within the spectrometer, as well as the magnetic field due to the magnetic moments of the nuclei

$$\mathbf{B}^{\text{tot.}}(\mathbf{r}) = \mathbf{B} + \sum_K \mathbf{B}_K(\mathbf{r}), \tag{3.26}$$

$$\mathbf{A}^{\text{tot.}}(\mathbf{r}) = \mathbf{A}_G(\mathbf{r}) + \sum_K \mathbf{A}_K(\mathbf{r}). \tag{3.27}$$

Here,[292]

$$\mathbf{A}_K(\mathbf{r}) = \alpha^2 \frac{\mathbf{M}_K \times \mathbf{r}_K}{r_K^3} \tag{3.28}$$

is the vector potential induced by nucleus K and its corresponding magnetic field is given by[292]

$$\mathbf{B}_K(\mathbf{r}) = -\alpha^2 \frac{r_K^2 \mathbb{1} - 3\mathbf{r}_K \mathbf{r}_K^{\mathrm{T}}}{r_K^5} \mathbf{M}_K + \frac{8\pi\alpha^2}{3} \delta(\mathbf{r}_K)\, \mathbf{M}_K. \tag{3.29}$$

In both equations α is the fine structure constant, which is the inverse of the velocity of light in atomic units ($\alpha \approx 137^{-1}$) and $r_K = |\mathbf{r}_K| = |\mathbf{r} - \mathbf{R}_K|$ is the distance with regard to the position of nucleus K. Note that explicitly taking the curl of the vector potential associated with the nuclei gives rise to the Dirac δ-function in the expression for the magnetic field. This is due to a singularity of $\mathbf{A}_K(\mathbf{r})$ at the point of the nucleus ($r_K \to 0$), which requires the differentiation in a distribution sense.[303,304]

3.1.4 The Magnetic Hamiltonian

The Dirac equation describes the relativistic interactions of an electron in a (time-independent) magnetic field.[302,305,306] Following an ansatz by Fukui,[291,307] the equation in block form

for a single electron without the presence of nuclear charges is given by

$$\left(\alpha^{-1}\begin{pmatrix}0 & \boldsymbol{\sigma}\\ \boldsymbol{\sigma} & 0\end{pmatrix}\boldsymbol{\pi} + \alpha^{-2}\begin{pmatrix}\mathbb{1} & 0\\ 0 & -\mathbb{1}\end{pmatrix}\right)\begin{pmatrix}\Psi^L\\ \Psi^S\end{pmatrix} = E_{\text{rel.}}\begin{pmatrix}\Psi^L\\ \Psi^S\end{pmatrix}. \tag{3.30}$$

Here, $\boldsymbol{\sigma}$ is the vector of the 2×2 Pauli spin matrices, $\boldsymbol{\pi}$ is the kinetic momentum ($\boldsymbol{\pi} = -i\nabla + \mathbf{A}$), $\mathbb{1}$ the 2×2 identity matrix and $E_{\text{rel.}}$ is the relativistic energy. Furthermore, Ψ^S and Ψ^L are the small and large components of the wave function, respectively.
Equation 3.30 contains two uncoupled linear equations for Ψ^S and Ψ^L. The small component of the wave function can be eliminated by insertion, resulting in the equation

$$\left[\frac{\alpha^{-2}\left(\boldsymbol{\sigma}\cdot\boldsymbol{\pi}\right)^2}{E_{\text{rel.}} - \alpha^{-2}} + \alpha^{-2} - E_{\text{rel.}}\right]\Psi^L = 0, \tag{3.31}$$

from which an expression for the relativistic energy can be extracted

$$E_{\text{rel.}} = \pm\left(\alpha^{-4} + \alpha^{-2}(\boldsymbol{\sigma}\cdot\boldsymbol{\pi})^2\right)^{1/2}. \tag{3.32}$$

The Hamiltonian for the electronic states is obtained in terms of a power-series expansion of the positive energy contribution

$$H_{rel.} = \alpha^{-2} + \frac{1}{2}(\boldsymbol{\sigma}\cdot\boldsymbol{\pi})^2 - \frac{\alpha^2(\boldsymbol{\sigma}\cdot\boldsymbol{\pi})^4}{8} + \ldots, \tag{3.33}$$

where the first contribution is related to the rest-mass energy and the higher-order terms ($\mathscr{O}(\alpha^2 + \ldots)$) contain relativistic corrections (which vanish in the non-relativistic limit). However, the second term on the right-hand side contains the non-relativistic contributions. By using the Dirac identity ($(\boldsymbol{\sigma}\cdot\boldsymbol{\pi})^2 = \boldsymbol{\pi}^2 + i\boldsymbol{\sigma}\cdot(\boldsymbol{\pi}\times\boldsymbol{\pi})$)[308] and inspecting its right-hand side[309]

$$(\boldsymbol{\pi}\times\boldsymbol{\pi}) = (-i\nabla + \mathbf{A})\times(-i\nabla + \mathbf{A}) = -i\mathbf{B}, \tag{3.34}$$

a non-relativistic Hamiltonian is obtained, given by

$$\begin{aligned}\widehat{H}_{\text{spin}} &= \frac{1}{2}\boldsymbol{\pi}^2 + \frac{1}{2}\boldsymbol{\sigma}\cdot\mathbf{B}\\ &= \frac{1}{2}\nabla^2 - i\mathbf{A}\cdot\nabla + \widehat{\mathbf{s}}\cdot\mathbf{B} + \frac{1}{2}|\mathbf{A}|^2.\end{aligned} \tag{3.35}$$

Here, the second line is obtained by invoking the Coulomb gauge (see Eq. 3.24) and $\widehat{\mathbf{s}} = \frac{1}{2}\boldsymbol{\sigma}$ is the spin operator.

The Hamiltonian of Eq. 3.35 is known as the Pauli Hamiltonian, which is suitable for the Pauli equation, i.e. the Schrödinger equation with an additional spin-dependent term to describe the interactions of one electron with an external magnetic field.[302]

The Pauli Hamiltonian, however, is a one-electronic Hamiltonian but can be extended to the N-electronic case by introducing the summation over all electrons and adding pairwise electronic and nuclear Coulomb interactions. Finally, the resulting Hamiltonian can be decomposed into contribution of different orders in the magnetic field and the corresponding vector potential, resulting in[310]

$$H = H^{(0)} + H^{(1)} + H^{(2)}. \tag{3.36}$$

Here, $H^{(0)}$ is the (unperturbed) electronic Hamiltonian (Eq. 2.6) and

$$H^{(1)} = -i \sum_k \mathbf{A}(\mathbf{r}_k) \cdot \nabla_k + \sum_k \mathbf{B}(\mathbf{r}_k) \cdot \widehat{\mathbf{s}}_k, \tag{3.37}$$

$$H^{(2)} = \frac{1}{2} \sum_k |\mathbf{A}(\mathbf{r}_k)|^2, \tag{3.38}$$

where $H^{(1)}$ is the linear paramagnetic contribution and $H^{(2)}$ is the diamagnetic contribution. The paramagnetic contribution is composed of the orbital paramagnetic term (first term), which couples the external magnetic field to the orbital motion of the electrons, and the spin paramagnetic term (second term), which couples the field to the spin of the electrons.

3.1.5 Explicit Contributions to the Magnetic Hamiltonian

With the definitions of the magnetic field and vector potential in Eqs. 3.22 – 3.29, the contributions entering the explicit expressions for NMR shielding and spin–spin couplings can be derived. This results in the set of equations reported by Ramsey in the 1950s.[14–17]

Starting with contributions of first order in the magnetic field, first the external magnetic field (Eq. 3.22) and the corresponding vector potential (Eq. 3.25) are inserted into the adjusted Hamiltonian (Eq. 3.37)

$$\begin{aligned} H_{\mathbf{B}}^{(1)} &= \sum_k \big(-i\mathbf{A}_G(\mathbf{r}_k) \cdot \nabla_k + \mathbf{B} \cdot \widehat{\mathbf{s}}_k \big) \\ &= \mathbf{B}\big(\mathbf{h}_{\mathbf{B}}^{\text{orb.}} + \mathbf{h}_{\mathbf{B}}^{\text{spn.}}\big). \end{aligned} \tag{3.39}$$

The contributions to the Hamiltonian are[292]

$$\mathbf{h}_{\mathbf{B}}^{\text{orb.}} = \frac{1}{2}\sum_{k} \mathbf{l}_{kG}, \tag{3.40}$$

$$\mathbf{h}_{\mathbf{B}}^{\text{spn.}} = \sum_{k} \widehat{\mathbf{s}}_{k}, \tag{3.41}$$

where $\mathbf{l}_{kG} = -i\mathbf{r}_{kG} \times \nabla_k$ is the orbital angular momentum operator with respect to the gauge origin $\mathbf{R}_G$.

Contributions arising from the nuclear magnetic moments are likewise obtained by inserting in the magnetic field (Eq. 3.29) and vector potential (Eq. 3.28) due to the nuclear magnetic moments

$$\begin{aligned} H_{\mathbf{M}}^{(1)} &= \sum_{k,K} \left(-i\mathbf{A}_K(\mathbf{r}_k) \cdot \nabla_k + \mathbf{B}_K(\mathbf{r}_k) \cdot \widehat{\mathbf{s}}_k \right) \\ &= \sum_{K} \mathbf{M}_K \left(\mathbf{h}_{K,\mathbf{M}}^{\text{FC}} + \mathbf{h}_{K,\mathbf{M}}^{\text{SD}} + \mathbf{h}_{K,\mathbf{M}}^{\text{PSO}} \right), \end{aligned} \tag{3.42}$$

with[292,310]

$$\mathbf{h}_{K,\mathbf{M}}^{\text{FC}} = \alpha^2 \frac{8\pi}{3} \sum_{k} \delta\left(r_{kK}\right) \widehat{\mathbf{s}}_k, \tag{3.43}$$

$$\mathbf{h}_{K,\mathbf{M}}^{\text{SD}} = \alpha^2 \sum_{k} \frac{3\mathbf{r}_{kK}\mathbf{r}_{kK}^{\text{T}} - r_{kK}^2 \mathbb{1}_{3\times 3}}{r_{kK}^5} \widehat{\mathbf{s}}_k, \tag{3.44}$$

$$\mathbf{h}_{K,\mathbf{M}}^{\text{PSO}} = \alpha^2 \sum_{k} \frac{\mathbf{l}_{kK}}{r_{kK}^3}. \tag{3.45}$$

Here, FC denotes the Fermi-contact, SD the spin-dipolar and PSO paramagnetic spin-orbit operator, respectively.

Finally, for the second-order contributions the total vector potential (Eq. 3.27) is inserted into the second-order Hamiltonian Eq. 3.38, giving

$$\begin{aligned} H_{\mathbf{B},\mathbf{M}}^{(2)} &= \frac{1}{2}\sum_{k} \left(\mathbf{A}_G^{\text{T}}(\mathbf{r}_k) + \sum_{K} \mathbf{A}_K^{\text{T}}(\mathbf{r}_k) \right) \cdot \left(\mathbf{A}_G(\mathbf{r}_k) + \sum_{L} \mathbf{A}_L(\mathbf{r}_k) \right) \\ &= \mathbf{B}^{\text{T}} \mathbf{h}_{\mathbf{BB}}^{\text{dia.}} \mathbf{B} + \sum_{K} \mathbf{B}^{\text{T}} \mathbf{h}_{K,\mathbf{BM}}^{\text{dia.}} \mathbf{M}_K + \sum_{K,L} \mathbf{M}_K^{\text{T}} \mathbf{h}_{KL,\mathbf{MM}}^{\text{DSO}} \mathbf{M}_L, \end{aligned} \tag{3.46}$$

with [292,310]

$$\mathbf{h}^{\text{dia.}}_{\mathbf{BB}} = \frac{1}{8}\sum_k \mathbb{1}_{3\times3} r^2_{kG} - \mathbf{r}_{kG}\mathbf{r}^{\mathrm{T}}_{kG}, \tag{3.47}$$

$$\mathbf{h}^{\text{dia.}}_{K,\mathbf{BM}} = \frac{\alpha^2}{2}\sum_k \frac{\mathbf{r}^{\mathrm{T}}_{kG}\mathbf{r}_{kK}\mathbb{1}_{3\times3} - \mathbf{r}_{kK}\mathbf{r}^{\mathrm{T}}_{kG}}{r^3_{kK}}, \tag{3.48}$$

$$\mathbf{h}^{\text{DSO}}_{KL,\mathbf{MM}} = \frac{\alpha^4}{2}\sum_k \frac{\mathbf{r}^{\mathrm{T}}_{kK}\mathbf{r}_{kL}\mathbb{1}_{3\times3} - \mathbf{r}_{kK}\mathbf{r}^{\mathrm{T}}_{kL}}{r^3_{kK}r^3_{kL}}. \tag{3.49}$$

Using these explicit operators of the magnetic-field dependent Hamiltonian, the final expressions, as formulated by Ramsey, can be obtained from the general expression of the SOS (Eq. 3.21). These are given by [14,292]

$$\left.\frac{d^2E}{d\mathbf{B}d\mathbf{M}_K}\right|_{\mathbf{B}=\mathbf{M}_K=0} = \langle\Psi_0|\mathbf{h}^{\text{dia.}}_{K,\mathbf{BM}}|\Psi_0\rangle - 2\sum_a^S \frac{\langle\Psi_0|\mathbf{h}^{\text{orb.}}_{\mathbf{B}}|\Phi^S_a\rangle\,\langle\Phi^S_a|(\mathbf{h}^{\text{PSO}}_{K,\mathbf{M}})^{\mathrm{T}}|\Psi_0\rangle}{E^S_a - E_0}, \tag{3.50}$$

for NMR shielding constants and [15,16,292]

$$\begin{aligned}\left.\frac{d^2E}{d\mathbf{M}_K d\mathbf{M}_L}\right|_{\mathbf{M}_K=\mathbf{M}_L=0} &= \langle\Psi_0|\mathbf{h}^{\text{DSO}}_{KL,\mathbf{MM}}|\Psi_0\rangle - 2\sum_a^S \frac{\langle\Psi_0|\mathbf{h}^{\text{PSO}}_{K,\mathbf{M}}|\Phi^S_a\rangle\,\langle\Phi^S_a|(\mathbf{h}^{\text{PSO}}_{L,\mathbf{M}})^{\mathrm{T}}|\Psi_0\rangle}{E^S_a - E_0} \\ &\quad - 2\sum_a^T \frac{\langle\Psi_0|\mathbf{h}^{\text{FC}}_{K,\mathbf{M}} + \mathbf{h}^{\text{SD}}_{K,\mathbf{M}}|\Phi^T_a\rangle\,\langle\Phi^T_a|(\mathbf{h}^{\text{FC}}_{L,\mathbf{M}})^{\mathrm{T}} + (\mathbf{h}^{\text{SD}}_{L,\mathbf{M}})^{\mathrm{T}}|\Psi_0\rangle}{E^T_a - E_0},\end{aligned} \tag{3.51}$$

for spin–spin coupling constants, respectively.
The superscripts S and T denote excitations into singlet and triplet states, which arise due to the symmetries of the involved operators. [292] No contributions in shielding and SSCC calculations arise from the operators $\mathbf{h}^{\text{spn.}}_{\mathbf{B}}$ and $\mathbf{h}^{\text{dia.}}_{\mathbf{BB}}$, which are included only for the sake of completeness. That is because (i) the operator $\mathbf{h}^{\text{spn.}}_{\mathbf{B}}$ (Eq. 3.41) vanishes for singlet states due to the involved spin operator and (ii) $\mathbf{h}^{\text{dia.}}_{\mathbf{BB}}$ involves the second derivatives with respect to the external magnetic field, which in the presented PT-approach represents the diamagnetic contribution to magnetizabilities.

3.1.6 The Gauge-Origin Problem

On closer examination, the (NMR-related) operators of Eq. 3.40 and 3.48 are implicitly dependent on the gauge origin as introduced in Eq. 3.25. Hence, a gauge transformation of the vector potential ($\mathbf{A}' = \mathbf{A} + \nabla\Lambda$) affects the Hamiltonian ($H \longrightarrow H'$) and its

eigenfunctions ($\Psi \longrightarrow \Psi'$)[292] as well as the dia- and paramagnetic contribution separately.[311] However, for exact wave functions it does not affect its eigenvalues[302] and the gauge invariance of the property is maintained, i.e.[292]

$$\langle \Psi' | H' | \Psi' \rangle = \langle \Psi | H | \Psi \rangle \,. \tag{3.52}$$

Furthermore, the two wave functions describe the same physical state[292]

$$|\Psi'(\mathbf{r})|^2 = |\Psi(\mathbf{r})|^2. \tag{3.53}$$

However, the introduced gauge transformation of the Hamiltonian induces a compensating phase factor within the wave function[292,302]

$$\Psi'(\mathbf{r}) = \exp\left(-\frac{i}{2c}\mathbf{B} \times (\mathbf{R}_G - \mathbf{R}_{G'}) \cdot \mathbf{r}\right) \Psi(\mathbf{r}). \tag{3.54}$$

The transformation of Eq. 3.54 is exact for exact wave functions, but this condition does not necessarily hold for approximate calculations and subsequently an (unpysical) dependence on the chosen gauge origin may remain.[292] A natural choice for the gauge in atomic systems is the position of the nucleus for which the wave function is exact to first order in the magnetic field.[292] However, in molecular calculations no such a-priori defined position exists and any choice of such a common gauge origin may result in a significant gauge dependence of the calculation, unless a sufficiently flexible basis (with a typically slow convergence to the complete basis-set (CBS) limit) is employed.[290,312]

To enhance the convergence to the CBS limit, the distribution of gauge origins throughout the molecule was suggested: an initial successful approach by Kutzelnigg and co-workers termed "individual-gauges for localized-orbitals" (IGLO) attached a similar phase factor to that of Eq. 3.54 to the center of the electronic charge of localized molecular orbitals (LMOs).[20–22] Later, Hansen and Bouman introduced their "localized-orbitals local origin" (LORG) ansatz in the context of RPA.[295,313] However, the close relation of the LORG to the IGLO approach was later pointed out by Kutzelnigg.[22] Further approaches such as the "individual gauges for atoms in molecules" (IGAIM) method[314] or the related "continuous set of gauge transformations" (CSGT)[315] aimed at recovering the local current density in order to calculate the local magnetic field (and hence related NMR properties) by distribution of the gauge origins.

In the "gauge-including atomic orbitals" (GIAOs) ansatz,[8,312,316] the phase factor is directly integrated into the atomic-orbital basis

$$\omega_\mu(\mathbf{r},\mathbf{B}) = \exp\left(-\frac{i}{2c}\mathbf{B}\times(\mathbf{R}_\mu-\mathbf{R}_G)\cdot\mathbf{r}\right)\phi_\mu(\mathbf{r}), \tag{3.55}$$

as initially introduced by London in the study of aromatic hydrocarbons (the original paper is written in french and included just for the sake of completeness).[317] Most importantly, GIAOs provide a smooth and fast convergence with respect to basis-set size.[30] However, as discussed below (see Sec. 3.2.1), a drawback of GIAOs are additional integrals arising in the corresponding HF and DFT approaches due to the explicit dependence of the orbitals on the perturbing external magnetic field. For that reason, their broad success was closely connected to the avaiability of efficient implementations, first reported in the 1990s.[23]

An initial implementation of the GIAO approach on HF level was reported by Ditchfield in the 1970s,[318,319] whereas a first implementation for DFT was reported by Friedrich *et al.*, at the time limited to the $X\alpha$ method.[320] Later, the approach was extended to different program packages covering a variety of density functionals by different groups.[25,26,30,321] The derivative of a GIAO with respect to the magnetic field is given by

$$\frac{\partial\omega_\mu(\mathbf{r},\mathbf{B})}{\partial(\mathbf{B})_k} = -\frac{i}{2c}\left(\mathbf{R}_\mu\times(\mathbf{r}-\mathbf{R}_G)\right)_k\phi_\mu(\mathbf{r}), \tag{3.56}$$

where $\mathbf{R}_\mu$ is the center of the AO $\phi_\mu(\mathbf{r})$ and $\mathbf{R}_G$ is the position of the gauge of the magnetic vector potential. However, the explicit presence of the gauge origin in Eq. 3.56 vanishes for the derivative of the GIAO pair

$$\frac{\partial\left(\omega^*_\mu(\mathbf{r},\mathbf{B})\omega_\nu(\mathbf{r},\mathbf{B})\right)}{\partial(\mathbf{B})_k} = \frac{i}{2c}\left(\mathbf{R}_{\mu\nu}\times\mathbf{r}\right)_k\left(\phi^*_\mu(\mathbf{r})\phi_\nu(\mathbf{r})\right). \tag{3.57}$$

Here, $\mathbf{R}_{\mu\nu} = \mathbf{R}_\mu - \mathbf{R}_\nu$ is the distance vector of the two AOs and since $\mathbf{R}_{\mu\nu} = -\mathbf{R}_{\nu\mu}$ matrices involving such derivatives of GIAOs are skew-symmetric.

3.2 Calculation of NMR Parameters Using DFT

3.2.1 Coupled Perturbed Kohn–Sham Equations

In Sec. 3.1.2 the basic ansatz of perturbation theory to calculate molecular properties was outlined. In the following, this is extended to equations actually solved within KS-

DFT (and thus intrisically HF).[292,322] For both methods, due to their methodological resemblance, underlying considerations and the resulting expressions are similar.[323–325]

The present derivation starts from the energy expression of KS-DFT (Eq. 2.28), augmented with a constant admixture of exact exchange ($E'_{KS} = E_{KS} + c_{ex}E_X^{exact}$). For completeness, the open-shell description is given. To highlight derivatives of the involved (potentially perturbation-dependent) atomic orbitals, equations where such derivatives are present are given in the AO basis. Using these conditions, a generalized expression for the first derivative, i.e. first-order molecular properties, is[322]

$$\begin{aligned}\frac{\partial E'_{KS}}{\partial \boldsymbol{\lambda}} =& \frac{\partial E_{NN}}{\partial \boldsymbol{\lambda}} + \sum_{\mu\nu,\sigma} D_{\mu\nu,\sigma}\left\{\frac{\partial h_{\mu\nu}}{\partial \boldsymbol{\lambda}} + \frac{1}{2}\sum_{\kappa\lambda} D_{\kappa\lambda,\sigma}\frac{\partial\big((\phi_\mu\phi_\nu|\phi_\kappa\phi_\lambda) + c_{ex}(\phi_\mu\phi_\lambda|\phi_\kappa\phi_\nu)\big)}{\partial \boldsymbol{\lambda}}\right.\\ &\left. + \frac{1}{2}\sum_{\kappa\lambda} D_{\kappa\lambda,\sigma'}\frac{\partial(\phi_\mu\phi_\nu|\phi_\kappa\phi_\lambda)}{\partial \boldsymbol{\lambda}} + \int v_{XC,\sigma}\frac{\partial(\phi^*_\mu\phi_\nu)}{\partial \boldsymbol{\lambda}}\mathrm{d}\mathbf{r}\right\} - \sum_{\mu\nu,\sigma} W_{\mu\nu,\sigma}\frac{\partial S_{\mu\nu}}{\partial \boldsymbol{\lambda}},\end{aligned} \tag{3.58}$$

where $v_{XC,\sigma}$ is the XC potential (see Eq. 2.32) and $W_{\mu\nu,\sigma} = \sum_i \varepsilon_{i,\sigma} c^*_{\mu i,\sigma} c_{\nu i,\sigma}$ is the energy weighted density matrix. Equation 3.58 is independent of the perturbed density matrix, due to reformulations of the expression by (i) using[324]

$$-\sum_{\mu\nu} D_{\mu\nu,\sigma} S^{\boldsymbol{\lambda}}_{\mu\nu} = \sum_{\mu\nu} D^{\boldsymbol{\lambda}}_{\mu\nu,\sigma} S_{\mu\nu}, \tag{3.59}$$

which can be derived from the perturbed orthonormality condition (and equivalently holds for the energy weighted density matrix) and (ii)

$$\begin{aligned}\sum_{\mu\nu} W^{\boldsymbol{\lambda}}_{\mu\nu,\sigma} S_{\mu\nu} &= \sum_{\mu\nu} D^{\boldsymbol{\lambda}}_{\mu\nu,\sigma} F_{\mu\nu,\sigma}\\ &= \sum_{\mu\nu} D^{\boldsymbol{\lambda}}_{\mu\nu,\sigma}\Big[h_{\mu\nu} + \sum_{\kappa\lambda} D_{\kappa\lambda,\sigma}\left((\phi_\mu\phi_\nu|\phi_\kappa\phi_\lambda) + c_{ex}(\phi_\mu\phi_\lambda|\phi_\kappa\phi_\nu)\right)\\ &\qquad + \sum_{\kappa\lambda} D_{\kappa\lambda,\sigma'}(\phi_\mu\phi_\nu|\phi_\kappa\phi_\lambda) + \int v_{XC,\sigma}\phi^*_\mu\phi_\nu\mathrm{d}\mathbf{r}\Big],\end{aligned} \tag{3.60}$$

which arises from the Roothaan–Hall equation.[88,266] Hence, the Hellman-Feynman theorem holds. Without the dependence of the orbitals on the perturbation and under the condition of one-electron perturbations, the equation of the gradient with respect to the

perturbation $\boldsymbol{\lambda}$ reduces to

$$\frac{\partial E'_{KS}}{\partial \boldsymbol{\lambda}} = \sum_{\mu\nu,\sigma} D_{\mu\nu,\sigma} \left(\phi_\mu | h^{\boldsymbol{\lambda}} | \phi_\nu\right). \tag{3.61}$$

The generalized expression for the second-order correction to the energy, i.e. the second derivative, is given by[322]

$$\begin{aligned}
\frac{\partial^2 E'_{KS}}{\partial \boldsymbol{\lambda}\partial \boldsymbol{\kappa}} = & \frac{\partial^2 E_{NN}}{\partial \boldsymbol{\lambda}\partial \boldsymbol{\kappa}} \\
& + \sum_{\mu\nu,\sigma} \Bigg\{ D_{\mu\nu,\sigma} \frac{\partial^2 h_{\mu\nu}}{\partial \boldsymbol{\lambda}\partial \boldsymbol{\kappa}} + D_{\mu\nu,\sigma} \int v_{XC,\sigma} \frac{\partial^2 \left(\phi^*_\mu \phi_\nu\right)}{\partial \boldsymbol{\lambda}\partial \boldsymbol{\kappa}} \mathrm{d}\mathbf{r} - W_{\mu\nu,\sigma} \frac{\partial^2 S_{\mu\nu}}{\partial \boldsymbol{\lambda}\partial \boldsymbol{\kappa}} \\
& \quad + \frac{\partial D_{\mu\nu,\sigma}}{\partial \boldsymbol{\kappa}} \frac{\partial h_{\mu\nu}}{\partial \boldsymbol{\lambda}} + \frac{\partial D_{\mu\nu,\sigma}}{\partial \boldsymbol{\kappa}} \int v_{XC,\sigma} \frac{\partial \left(\phi^*_\mu \phi_\nu\right)}{\partial \boldsymbol{\lambda}} \mathrm{d}\mathbf{r} - \frac{\partial W_{\mu\nu,\sigma}}{\partial \boldsymbol{\kappa}} \frac{\partial S_{\mu\nu}}{\partial \boldsymbol{\lambda}} \Bigg\} \\
& + \frac{1}{2} \sum_{\mu\nu\kappa\lambda,\sigma} \Bigg\{ D_{\mu\nu,\sigma} D_{\kappa\lambda,\sigma} \frac{\partial^2 \big((\phi_\mu \phi_\nu | \phi_\kappa \phi_\lambda) + c_{ex} (\phi_\mu \phi_\lambda | \phi_\kappa \phi_\nu)\big)}{\partial \boldsymbol{\lambda}\partial \boldsymbol{\kappa}} \\
& \quad + \frac{\partial \left(D_{\mu\nu,\sigma} D_{\kappa\lambda,\sigma}\right)}{\partial \boldsymbol{\kappa}} \frac{\partial \big((\phi_\mu \phi_\nu | \phi_\kappa \phi_\lambda) + c_{ex} (\phi_\mu \phi_\lambda | \phi_\kappa \phi_\nu)\big)}{\partial \boldsymbol{\lambda}} \\
& \quad + D_{\mu\nu,\sigma} D_{\kappa\lambda,\sigma'} \frac{\partial^2 (\phi_\mu \phi_\nu | \phi_\kappa \phi_\lambda)}{\partial \boldsymbol{\lambda}\partial \boldsymbol{\kappa}} + \frac{\partial \left(D_{\mu\nu,\sigma} D_{\kappa\lambda,\sigma'}\right)}{\partial \boldsymbol{\kappa}} \frac{\partial (\phi_\mu \phi_\nu | \phi_\kappa \phi_\lambda)}{\partial \boldsymbol{\lambda}} \\
& \quad + 2 \sum_{\varsigma} D_{\mu\nu,\sigma} D_{\kappa\lambda,\varsigma} \iint f_{XC,\sigma\varsigma} \frac{\partial \left(\phi^*_\mu(\mathbf{r}) \phi_\nu(\mathbf{r})\right)}{\partial \boldsymbol{\lambda}} \frac{\partial \left(\phi^*_\kappa(\mathbf{r}') \phi_\lambda(\mathbf{r}')\right)}{\partial \boldsymbol{\kappa}} \mathrm{d}\mathbf{r}' \mathrm{d}\mathbf{r} \\
& \quad + 2 \sum_{\varsigma} D_{\mu\nu,\sigma} \frac{\partial D_{\kappa\lambda,\varsigma}}{\partial \boldsymbol{\kappa}} \iint f_{XC,\sigma\varsigma} \frac{\partial \left(\phi^*_\mu(\mathbf{r}) \phi_\nu(\mathbf{r})\right)}{\partial \boldsymbol{\lambda}} \phi^*_\kappa(\mathbf{r}') \phi_\lambda(\mathbf{r}') \mathrm{d}\mathbf{r}' \mathrm{d}\mathbf{r} \Bigg\},
\end{aligned} \tag{3.62}$$

where

$$f_{XC,\sigma\varsigma} = \frac{\delta^2 E_{XC}}{\delta \rho_\sigma(\mathbf{r}) \delta \rho_\varsigma(\mathbf{r}')} \tag{3.63}$$

involves the second functional derivative of the exchange-correlation energy with respect to the density and is known as the exchange-correlation kernel.[322] Without an explicit dependence of the basis functions on either of the perturbations the second-order equation also reduces drastically and we find[322]

$$\frac{\partial^2 E'_{KS}}{\partial \boldsymbol{\lambda}\partial \boldsymbol{\kappa}} = \sum_{\mu\nu,\sigma} \left(D_{\mu\nu,\sigma} \frac{\partial^2 h_{\mu\nu}}{\partial \boldsymbol{\lambda}\partial \boldsymbol{\kappa}} + \frac{\partial D_{\mu\nu,\sigma}}{\partial \boldsymbol{\kappa}} \frac{\partial h_{\mu\nu}}{\partial \boldsymbol{\lambda}} \right). \tag{3.64}$$

However, identifying $\boldsymbol{\kappa}$ with $\mathbf{B}$ and using GIAOs (thus perturbation-dependent basis functions), additionally the paramagnetic-undisturbed-density (PUD) contribution to the shieldings (labelled in the expression below) has to be taken into account

$$\frac{\partial^2 h_{\mu\nu}}{\partial\boldsymbol{\lambda}\partial\boldsymbol{\kappa}} = \left(\omega_\mu\middle|\frac{\widehat{h}}{\partial\boldsymbol{\lambda}\partial\boldsymbol{\kappa}}\middle|\omega_\nu\right) + \left(\frac{\partial\omega_\mu}{\partial\boldsymbol{\kappa}}\middle|\frac{\widehat{h}}{\partial\boldsymbol{\lambda}}\middle|\omega_\nu\right)_{\mathrm{PUD}} + \left(\omega_\mu\middle|\frac{\widehat{h}}{\partial\boldsymbol{\lambda}}\middle|\frac{\partial\omega_\nu}{\partial\boldsymbol{\kappa}}\right)_{\mathrm{PUD}}. \tag{3.65}$$

Furthermore, Eq. 3.64 reveals the importance of the order of derivation with mixed perturbations, as identifying $\boldsymbol{\kappa}$ with either the external magnetic field or the nuclear magnetic moment leads to a different dimensionality of the perturbed density. For $\boldsymbol{\kappa} = \mathbf{B}$ the perturbed density has three Cartesian components, the choice $\boldsymbol{\kappa} = \mathbf{M}_K$ results in $3 \cdot K$ entries for the perturbed density matrix (and additional terms arising due to the use of GIAOs), with an accordingly larger computational burden, if solved for all nuclei. However, to accelerate the shielding calculations for just a small number of nuclei in large molecular systems, such an approach was suggested.[326,327]

The perturbed density can finally be evaluated using the coupled-perturbed Kohn–Sham (CPKS) scheme, which is readily obtained from differentiating the Brillouin condition,[13,88]

$$u^{\boldsymbol{\kappa}}_{ai,\sigma}\left(\varepsilon_{a,\sigma} - \varepsilon_{i,\sigma}\right) = -F^{\boldsymbol{\kappa}}_{ai,\sigma} + \varepsilon_{i,\sigma} S^{\boldsymbol{\kappa}}_{ai,\sigma}. \tag{3.66}$$

The expansion coefficients $u^{\boldsymbol{\kappa}}_{ai,\sigma}$ are typically defined in terms of the expansion of the MO coefficients[322]

$$c^{\boldsymbol{\kappa}}_{\mu i,\sigma} = \sum_p c_{\mu p,\sigma} u^{\boldsymbol{\kappa}}_{pi,\sigma}. \tag{3.67}$$

Likewise they can be related to the set of virtual orbitals ($\varphi^{\boldsymbol{\kappa}}_{i,\sigma}(\mathbf{r}) = \sum_a \varphi_{a,\sigma}(\mathbf{r}) u^{\boldsymbol{\kappa}}_{ai,\sigma}$[328]). However, to solve for $u^{\boldsymbol{\kappa}}_{ai,\sigma}$ or its real and imaginary contribution ($u^{\boldsymbol{\kappa}}_{ai,\sigma} = x^{\boldsymbol{\kappa}}_{ai,\sigma} + i y^{\boldsymbol{\kappa}}_{ai,\sigma}$), the perturbed MO Fock-matrix $F^{\boldsymbol{\kappa}}_{ai,\sigma}$ has to be evaluated. Its explicit derivative results in the final CPKS equations,[322] (i) for the real part

$$\sum_{bj,\varsigma} G^{\mathrm{Re.}}_{aibj,\sigma\varsigma} x^{\boldsymbol{\kappa}}_{bj,\varsigma} = -F^{(\boldsymbol{\kappa})}_{ai,\sigma} + \frac{1}{2} R^{\mathrm{Re.}}_{ai,\sigma}\left(\mathbf{S}^{\boldsymbol{\kappa}}\right) + \varepsilon_i S^{\boldsymbol{\kappa}}_{ai,\sigma}, \tag{3.68}$$

where the real part of the electronic Hessian is given by

$$\begin{aligned} G^{\text{Re.}}_{aibj,\sigma\varsigma} =&(\varepsilon_{a,\sigma} - \varepsilon_{i,\sigma})\delta_{ab}\delta_{ij}\delta_{\varsigma\sigma} + \Big(2(\varphi_{a,\sigma}\varphi_{i,\sigma}|\varphi_{b,\sigma}\varphi_{j,\sigma}) + 2(\varphi_{a,\sigma}\varphi_{i,\sigma}|f_{XC,\sigma\sigma}|\varphi_{b,\sigma}\varphi_{j,\sigma}) \\ &- c_{ex}[(\varphi_{a,\sigma}\varphi_{j,\sigma}|\varphi_{b,\sigma}\varphi_{i,\sigma}) + (\varphi_{a,\sigma}\varphi_{b,\sigma}|\varphi_{j,\sigma}\varphi_{i,\sigma})]\Big)\delta_{\varsigma\sigma} \\ &+ \Big(2(\varphi_{a,\sigma}\varphi_{i,\sigma}|\varphi_{b,\sigma'}\varphi_{j,\sigma'}) + 2(\varphi_{a,\sigma}\varphi_{i,\sigma}|f_{XC,\sigma\sigma'}|\varphi_{b,\sigma'}\varphi_{j,\sigma'})\Big)\delta_{\varsigma\sigma'}, \end{aligned} \tag{3.69}$$

and

$$\begin{aligned} R^{\text{Re.}}_{ai,\sigma}(\mathbf{S}^{\boldsymbol{\kappa}}) = \sum_{jk}\Bigg\{ & S^{\boldsymbol{\kappa}}_{kj,\sigma}\Big(2(\varphi_{a,\sigma}\varphi_{i,\sigma}|\varphi_{k,\sigma}\varphi_{j,\sigma}) + 2(\varphi_{a,\sigma}\varphi_{i,\sigma}|f_{XC,\sigma\sigma}|\varphi_{k,\sigma}\varphi_{j,\sigma}) \\ &- c_{ex}[(\varphi_{a,\sigma}\varphi_{j,\sigma}|\varphi_{k,\sigma}\varphi_{i,\sigma}) + (\varphi_{a,\sigma}\varphi_{k,\sigma}|\varphi_{j,\sigma}\varphi_{i,\sigma})]\Big) \\ &+ S^{\boldsymbol{\kappa}}_{kj,\sigma'}\Big(2(\varphi_{a,\sigma}\varphi_{i,\sigma}|\varphi_{k,\sigma'}\varphi_{j,\sigma'}) + 2(\varphi_{a,\sigma}\varphi_{i,\sigma}|f_{XC,\sigma\sigma'}|\varphi_{k,\sigma'}\varphi_{j,\sigma'})\Big)\Bigg\}. \end{aligned} \tag{3.70}$$

(ii) The imaginary part is given by

$$\sum_{bj} G^{\text{Im.}}_{aibj,\sigma} y^{\boldsymbol{\kappa}}_{bj,\sigma} = -F^{(\boldsymbol{\kappa})}_{ai,\sigma} + \frac{1}{2}R^{\text{Im.}}_{ai,\sigma}(\mathbf{S}^{\boldsymbol{\kappa}}) + \varepsilon_i S^{\boldsymbol{\kappa}}_{ai,\sigma}, \tag{3.71}$$

with

$$G^{\text{Im.}}_{aibj,\sigma} = (\varepsilon_{a,\sigma} - \varepsilon_{i,\sigma})\delta_{ab}\delta_{ij} + c_{ex}\big((\varphi_{a,\sigma}\varphi_{j,\sigma}|\varphi_{b,\sigma}\varphi_{i,\sigma}) - (\varphi_{a,\sigma}\varphi_{b,\sigma}|\varphi_{j,\sigma}\varphi_{i,\sigma})\big), \tag{3.72}$$

and

$$R^{\text{Im.}}_{ai,\sigma}(\mathbf{S}^{\boldsymbol{\kappa}}) = \sum_{jk} S^{\boldsymbol{\kappa}}_{kj,\sigma} c_{ex}\big((\varphi_{a,\sigma}\varphi_{j,\sigma}|\varphi_{k,\sigma}\varphi_{i,\sigma}) - (\varphi_{a,\sigma}\varphi_{k,\sigma}|\varphi_{j,\sigma}\varphi_{i,\sigma})\big). \tag{3.73}$$

$F^{(\boldsymbol{\kappa})}_{ai,\sigma}$ contains all contributions of the one-electron part ($h^{\kappa}_{ai,\sigma}$) and involves derivatives of the atomic orbitals,

$$\begin{aligned} F^{(\boldsymbol{\kappa})}_{ai,\sigma} = c_{\mu a,\sigma}\Bigg(& h^{\boldsymbol{\kappa}}_{\mu\nu} + \int v_{XC} \frac{\partial(\phi^*_\mu(\mathbf{r})\phi_\nu(\mathbf{r}))}{\partial\boldsymbol{\kappa}} \mathrm{d}\mathbf{r} \\ & + \sum_{\kappa\lambda} D_{\kappa\lambda,\sigma} \left\{ \frac{\partial\big((\phi_\mu\phi_\nu|\phi_\kappa\phi_\lambda) + c_{ex}(\phi_\mu\phi_\lambda|\phi_\kappa\phi_\nu)\big)}{\partial\boldsymbol{\kappa}} + \left(\phi_\mu\phi_\nu \middle| f_{XC,\sigma\sigma} \middle| \frac{\partial(\phi_\kappa\phi_\lambda)}{\partial\boldsymbol{\kappa}}\right)\right\} \\ & + \sum_{\kappa\lambda} D_{\kappa\lambda,\sigma'} \left\{ \frac{\partial(\phi_\mu\phi_\nu|\phi_\kappa\phi_\lambda)}{\partial\boldsymbol{\kappa}} + \left(\phi_\mu\phi_\nu \middle| f_{XC,\sigma\sigma'} \middle| \frac{\partial(\phi_\kappa\phi_\lambda)}{\partial\boldsymbol{\kappa}}\right)\right\}\Bigg) c_{\nu i,\sigma}. \end{aligned} \tag{3.74}$$

Due to the implicit dependence of Eqs. 3.69 and 3.72 on the expansion coefficients the CPKS equations have to be solved iteratively. In case of semi-local functionals, however, the imaginary contribution $R^{\mathrm{Im.}}_{ai,\sigma}$ vanishes, as it only contains contributions from exact-exchange, i.e. the expansion coefficients are directly accessible (the approach is uncoupled) and no iterative procedure is required. Without any dependence of the orbitals on the perturbation, contributions dependent on $\mathbf{S}^{\boldsymbol{\lambda}}$ vanish and in Eq. 3.74 only the perturbed one-electron contribution $h^{\boldsymbol{\kappa}}_{ai,\sigma}$ survives. However, in case of $\boldsymbol{\kappa} = \mathbf{B}$ and the use of GIAOs, only the kernel-dependent contributions (right hand side) vanish, due to the symmetry of the involved matrices. Thus, similar to Eq. 3.65, additional GIAO-dependent four-center integrals have to be computed

$$\frac{\partial(\omega_\mu\omega_\nu|\omega_\kappa\omega_\lambda)}{\partial(\mathbf{B})_k} = \left(\frac{\partial(\omega_\mu\omega_\nu)}{\partial(\mathbf{B})_k}\middle|\omega_\kappa\omega_\lambda\right) + \left(\omega_\mu\omega_\nu\middle|\frac{\partial(\omega_\kappa\omega_\lambda)}{\partial(\mathbf{B})_k}\right). \tag{3.75}$$

The evaluation of the four-center integrals is (similar to the ground-state SCF) the most time consuming step in NMR-parameter calculations, hence, efficient implementations have also been developed in this context. Examples of such are RI-J[13,281] and its multipole-accelerated variant MARI-J,[281] pseudospectral methods[329] and COS-X (see Sec. 2.4.2 for further details).[13] It is noted in passing, that within the GIAO-dependent perturbed COS-X exchange-contribution

$$\begin{aligned} K_{\mu\nu}[\omega^{\mathbf{B}}] &= \sum_{\kappa\lambda,g} D_{\kappa\lambda} w_g \left\{ \left(\omega^*_\mu\omega_\lambda\right)^{\mathbf{B}} A_{\kappa\nu,g} + \omega^*_\mu\omega_\lambda \left(A_{\kappa\nu,g}\right)^{\mathbf{B}} \right\} \\ &= \sum_{\kappa\lambda,g} D_{\kappa\lambda} w_g \left\{ \left(\omega^*_\mu\omega_\lambda\right)^{\mathbf{B}} A_{\kappa\nu,g} + \left(\omega^*_\kappa\omega_\nu\right)^{\mathbf{B}} A_{\mu\lambda,g} \right\}, \end{aligned} \tag{3.76}$$

the second equality is obtained by interchange of the involved arguments $\mathbf{r} \longrightarrow \mathbf{r}'$. Hence, for global hybrid functionals the evaluation of the perturbed A-matrix elements can be circumvented using the COS-X approximation.

It should ne noted, that Eqs. 3.69 and 3.72 are presented in a generalized, spin-resolved form. In case of closed shell systems, as assumed throughout the present work, the two separate density matrices are equal ($D_{\mu\nu,\alpha} = D_{\mu\nu,\beta}$). However, the conditions for describing singlet and triplet states separate the equations into their singlet and triplet counterparts,[330] where the triplet description is required in the calculation of the FC and SD contributions.[292]

With the computed perturbed densities, according to Eq. 3.64 shieldings and SSCCs in the AO basis are then obtained via

$$\boldsymbol{\sigma}_K = \frac{\partial^2 E'_{KS}}{\partial \mathbf{B} \partial \mathbf{M}_K} = \sum_{\mu\nu,\sigma} \left(D_{\mu\nu,\sigma} \mathbf{h}^{\text{dia.}}_{\mu\nu,\mathbf{BM}} + \mathbf{D}^{\text{orb.}}_{\mu\nu,\sigma} \left(\mathbf{h}^{\text{PSO}}_{\mu\nu,\boldsymbol{M}} \right)^{\text{T}} \right) \tag{3.77}$$

and[330]

$$\mathbf{K}_{KL} = \frac{\partial^2 E'_{KS}}{\partial \mathbf{M}_K \partial \mathbf{M}_L} = \sum_{\mu\nu,\sigma} \Bigg(D_{\mu\nu,\sigma} \mathbf{h}^{\text{DSO}}_{\mu\nu,\mathbf{MM}} + \mathbf{D}^{\text{PSO}}_{\mu\nu,\sigma} \left(\mathbf{h}^{\text{PSO}}_{\mu\nu,\boldsymbol{M}} \right)^{\text{T}} + \mathbb{1}_{3\times3} D^{\text{FC}}_{\mu\nu,\sigma} h^{\text{FC}}_{\mu\nu,\boldsymbol{M}} + D^{\text{FC}}_{\mu\nu,\sigma} \mathbf{h}^{\text{SD}}_{\mu\nu,\boldsymbol{M}} + \mathbf{D}^{\text{SD}}_{\mu\nu,\sigma} h^{\text{FC}}_{\mu\nu,\boldsymbol{M}} + \mathbf{D}^{\text{SD}}_{\mu\nu,\sigma} \mathbf{h}^{\text{SD}}_{\mu\nu,\boldsymbol{M}} \Bigg). \tag{3.78}$$

In both equations, the superscripts on the perturbed densities indicate the right hand side one-electron contribution within the CPKS scheme and the one-electron integrals are obtained from the operators shown in Eqs. 3.40, 3.43 – 3.45, 3.48, and 3.49. For example the diamagnetic contribution to the shielding constants (neglecting the PUD contribution) is given by

$$\mathbf{h}^{\text{dia.}}_{\mu\nu,\mathbf{BM}} = \frac{\alpha^2}{2} \int \phi^*_\mu(\mathbf{r}) \frac{\mathbf{r}_G^{\text{T}} \mathbf{r}_K \mathbb{1}_{3\times3} - \mathbf{r}_K \mathbf{r}_G^{\text{T}}}{r_K^3} \phi_\nu(\mathbf{r}) \text{d}\mathbf{r}. \tag{3.79}$$

The following dimensions of the operators and perturbed densities have to be taken into account:[330] (i) $\mathbf{D}^{\text{orb.}}_{\mu\nu,\sigma}$, $\mathbf{D}^{\text{PSO}}_{\mu\nu,\sigma}$ and $\mathbf{h}^{\text{PSO}}_{\mu\nu,\boldsymbol{M}}$ are vectors with one entry for each Cartesian component of the magnetic fields due to the externally applied field and the magnetic moment of the involved nucleus, respectively. (ii) The FC contributions are scalar, as the operator involves the delta function and takes into account just the contribution at the position of the nuclei. (iii) The SD perturbed density ($\mathbf{D}^{\text{SD}}_{\mu\nu,\sigma}$) and one-electron terms ($\mathbf{h}^{\text{SD}}_{\mu\nu,\boldsymbol{M}}$) in principle contain 9 entries per nucleus due to the involved spin operator, which

itself has three Cartesian components. However, the matrices are symmetric and therefore only 6 individual contributions have to be taken into account.
Finally, due to the triplet symmetry of both the FC and SD operators, cross-terms between both contributions have to be taken into account (see also Eq. 3.51). However, the resulting contribution to the reduced spin–spin coupling constant is traceless and therefore such cross-terms only contribute to the anisotropy of the SSCCs.

3.2.2 Current Density Functional Theory

As outlined in Sec. 2.2.1, the general formulation of KS-DFT considers electrons in an arbitrary external potential, but neglects any external magnetic fields.[331,332] In their presence, the local magnetic field is a superposition of the external and local field strength (see also Eq. 3.1), whereas the local field, according to the Biot–Savart law,[299,333] is caused by the current density.[290] Hence, the proper formulation of a current-density functional theory (CDFT) requires an implicit dependence of the XC functional on an additional parameter to describe the arising interactions.[290] The rigorous CDFT was formulated by Vignale *et al.*[73] and extended to the spin-dependent formulation by the same authors shortly after,[332] replacing the density by a current-density functional

$$E_{XC}\left[\rho_\sigma\right] \longrightarrow E_{XC}\left[\rho_\sigma, \mathbf{j}_{p,\sigma}\right] = E_{XC}\left[\rho_\sigma, \mathbf{v}_{p,\sigma}\right]. \tag{3.80}$$

Here,

$$\mathbf{j}_{p,\sigma}(\mathbf{r}) = \frac{i}{2}\sum_{ij} D_{ij,\sigma}\left(\varphi_{j,\sigma}(\mathbf{r})\nabla\varphi^*_{i,\sigma}(\mathbf{r}) - \varphi^*_{i,\sigma}(\mathbf{r})\nabla\varphi_{j,\sigma}(\mathbf{r})\right) \tag{3.81}$$

is the paramagnetic current density and

$$\mathbf{v}_{p,\sigma}(\mathbf{r}) = \nabla \times \left(\frac{\mathbf{j}_{p,\sigma}(\mathbf{r})}{\rho_\sigma(\mathbf{r})}\right) \tag{3.82}$$

is the vorticity, which was introduced as a gauge-independent alternative to the paramagnetic current density.[73] For closed-shell molecules in the absence of a magnetic field

$$\mathbf{j}_{p,\sigma}(\mathbf{r})\big|_{\mathbf{B}=0} = 0. \tag{3.83}$$

The first implementation using CDFT in connection with response equations for NMR parameter calculations was reported by Lee *et al.*[26] Later, explicit finite-field dependent implementations have been published.[334]

As shown in the context of Eq. 3.71, the CPKS equations of NMR shielding calculations using semi-local current-free KS-DFT remain uncoupled, i.e. there is no response of the density nor the XC potential, if an external magnetic field is applied. However, within the CDFT scheme, the electronic Hessian (Eq. 3.72) is no longer diagonal. Therefore, the approach includes a response of the exchange-correlation term to the external magnetic field, formerly neglected in uncoupled DFT.[290]

In the context of the present work $\mathbf{j}_{p,\sigma}$ only arises via the kinetic energy density, which in the presence of the magnetic field is not gauge invariant.[241] This can be shown from the compensating gauge transformation of the MOs

$$\varphi_{i,\sigma}(\mathbf{r}) \longrightarrow \varphi'_{i,\sigma}(\mathbf{r}) = \varphi_{i,\sigma}(\mathbf{r}) \exp\left(-i\Lambda(\mathbf{r})\right) \tag{3.84}$$

in case of a gauge transformation of the vector potential of the magnetic field ($\mathbf{A} \longrightarrow \mathbf{A'} = \mathbf{A} + \nabla\Lambda$, see Secs. 3.1.3 and 3.1.6), in which case the kinetic energy density takes the form[241,335]

$$\tau'_\sigma(\mathbf{r}) = \tau_\sigma(\mathbf{r}) - \nabla\Lambda(\mathbf{r})\mathbf{j}_{p,\sigma}(\mathbf{r}) + \frac{1}{2}|\nabla\Lambda(\mathbf{r})|^2\rho_\sigma(\mathbf{r}). \tag{3.85}$$

Gauge-invariant models have been proposed. First Maximoff *et al.* identified $\Lambda(\mathbf{r}) = \frac{1}{c}\mathbf{A}_G(\mathbf{r})$ and therefore[335]

$$\tilde{\tau}_{MS,\sigma}(\mathbf{r}) = \tau_\sigma(\mathbf{r}) - \frac{\mathbf{A}_G^{\mathrm{T}}(\mathbf{r})}{c}\mathbf{j}_{p,\sigma}(\mathbf{r}) + \frac{|\mathbf{A}_G(\mathbf{r})|^2}{2c^2}\rho_\sigma(\mathbf{r}). \tag{3.86}$$

Here, the vector potential of the magnetic field and the paramagnetic current density are present simultaneously, which keeps the Hessian in the evaluation of the CPKS equations diagonal, i.e. despite the presence of $\mathbf{j}_{p,\sigma}(\mathbf{r})$ no current response in the sense of CDFT arises for τ_{MS}.

Another gauge-corrected form of $\tau_\sigma(\mathbf{r})$ arises from the generalization of the spherically-averaged exchange hole in case of non-zero currents, first derived in the context of the work of Dobson,[336,337]

$$\tilde{\tau}_{D,\sigma}(\mathbf{r}) = \tau_\sigma(\mathbf{r}) - \frac{|\mathbf{j}_{p,\sigma}(\mathbf{r})|^2}{2\rho_\sigma(\mathbf{r})}. \tag{3.87}$$

It is noted in passing, that Becke and Tao *et al.* also explored this generalized variant in the development of current-dependent functional models.[338–340]

Both of these gauge-invariant models for $\tau_\sigma(\mathbf{r})$ depend on the paramagnetic current density and therefore any τ-dependent density functional gains an implicit dependence on $\mathbf{j}_{p,\sigma}(\mathbf{r})$. In principle, the presence of the current density in the XC functional requires the extension of the field-free KS equations (Eq. 2.30) to cover these arising current densities within the functional. As stated above, however, in the context of this work the dependence only arises from the gauge corrections of the kinetic energy densities and therefore [334]

$$\begin{aligned} E_{XC}\left[\rho_\sigma, \mathbf{j}_{p,\sigma}\right] &= \int e_{XC}\left[\rho_\sigma, \nabla\rho_\sigma, \tau_\sigma, \mathbf{j}_{p,\sigma}\right] \mathrm{d}\mathbf{r} \\ &= \int e_{XC}\left[\rho_\sigma, \nabla\rho_\sigma, \tilde{\tau}_\sigma\right] \mathrm{d}\mathbf{r}. \end{aligned} \tag{3.88}$$

Hence, the corresponding contributions to the functional derivative entering the XC potential is given by

$$\frac{\delta e_{XC}}{\delta \mathbf{j}_{p,\sigma}} = \frac{\delta e_{XC}}{\delta \tilde{\tau}_\sigma} \frac{\partial \tilde{\tau}_\sigma}{\partial \mathbf{j}_{p,\sigma}}, \tag{3.89}$$

where in the absence of the magnetic field, and thus in the limit of vanishing current-density contributions

$$\left.\frac{\delta e_{XC}}{\delta \tilde{\tau}_\sigma}\right|_{j_{p,\sigma}=0} = \frac{\delta e_{XC}}{\delta \tau_\sigma}. \tag{3.90}$$

4 Turbomole Program Structure

All developments throughout this work were implemented into the TURBOMOLE quantum chemical calculation package using a local developers' version, which was regularly updated to the most current published version. All developments shown in this work are available in the TURBOMOLE program code starting from version 7.5.[9] In the following, a short outline of the relevant aspects of the program structure for the present work is given with an emphasis on developments in the context of LH functionals.

4.1 Ground-State SCF

Property calculations with the TURBOMOLE program package are built upon converged SCF solutions, which can be obtained via the DSCF and RIDFT programs,[273] i.e. full analytic four-center Coulomb or RI-J adjusted approaches, respectively. LH functionals have been implemented in a semi-numerical fashion in both routines by Bahmann *et al.*,[287] who also introduced central LH specific infrastructure into the TURBOMOLE program package. The current versions of these routines are (i) the ONDES_X routines, specifically ONDES_KS for the symmetric contraction of the basis-function vector with the density matrix ($\mathbf{D}\boldsymbol{\phi}$) and ONDES_2AS for a similar asymmetric contraction. (ii) The LMF_X routines constructing the LMF value (X=U0, R0) and derivatives (X=U1, R1, for first derivatives; X=U2, R2 for second derivatives, ...) on the numerical grid, for restricted (RX) and unrestricted (UX) calculations, respectively. Finally, (iii) the LOCHYB_X routines (where X is denoted just as in the LMF routines), which construct the exchange-correlation contribution of the LH and its derivatives (on the numerical integration grid)

$$O^{LH}_{XC,g} = w_g \sum_{Q \varepsilon \mathbb{Q}} \left(\frac{\partial g_g}{\partial Q} \left(e^{exact}_{X,g} - e^{DFT}_{X,g} \right) + \frac{\partial e^{DFT}_{X,g}}{\partial Q} \left(1 - g_g \right) + \frac{\partial e^{DFT}_{C,g}}{\partial Q} \right), \tag{4.1}$$

which in a final step is contracted with the AO basis-function vectors to the LMF-dependent potential contribution.

Furthermore, the evaluation of the two-center A-matrix was introduced using similar pre-screening techniques as outlined for the COS-X approach (see Sec. 2.4.2).[275,287] These are (i) the S-junctions, for which the radial extent of the shells around the nuclei (until its value falls below the chosen threshold) is probed. Only shell-pairs with overlapping radii are considered in the A-matrix evaluation. (ii) the P-junctions, where the entries of the F-vectors (the weighted contraction of the density matrix with the basis-function vectors, $F_{\mu g} = \sum_\nu {w_g}^{1/2} D_{\mu\nu}\phi_\nu(\mathbf{r}_g)$) are compared to a threshold value. In this case, the evaluation of the A-matrix is omitted, if the F-vectors of both shells are below this chosen threshold. However, it was later pointed out, that in the limit of an infinite grid the use of $F_{\mu g}$ in the P-junction evaluation results in full neglect of any A-matrix evaluation, as the grid weights in that case become infinitesimally small. Therefore, within the junction evaluation, the use of the non-weighted contraction of the density matrix and the basis-function vector was suggested.[285]

Gradients used in the optimization of molecular structures are implemented in the GRAD and RDGRAD subroutines, for full analytical and RI-J approximative calculations, respectively. Adjustments for LH functionals were later added by Klawohn *et al.*[341] Within this work, recurrence relations for the basis-function gradients were employed,[269] which subsequently required the evaluation of two-center A-matrices with adjusted azimuthal (orbital angular momentum)-quantum numbers of the Gaussian primitives ($\mathbf{A}'$). These are handled in the A_MATRICES routines.

4.2 The MPSHIFT Routine

The calculation of NMR shielding constants in TURBOMOLE is available via the subroutine MPSHIFT, developed by Häser *et al.*[342] Prior to the present work, the routine supported calculations with semi-local and global hybrid functionals,[343] as well as MP2 on the basis of gauge-including atomic orbitals.[344,345] The use of implicit solvation using the conductor-like screening model (COSMO) is supported.[281,346] Furthermore, multipole-accelerated RI-J was implemented and reported recently.[281] The existing (implicit) treatment of relativistic effects by the use of effective core potentials (ECPs)[347,348] was extended by a two-component scalar-relativistic implementation using the exact two-component (X2C) Hamiltonian.[349] In the context of the work of Refs. 281 and 349 additional parts of the MPSHIFT code were revisited and adapted prior to this work. Parallel to the present work, a semi-numerical scheme for GH functionals was implemented and

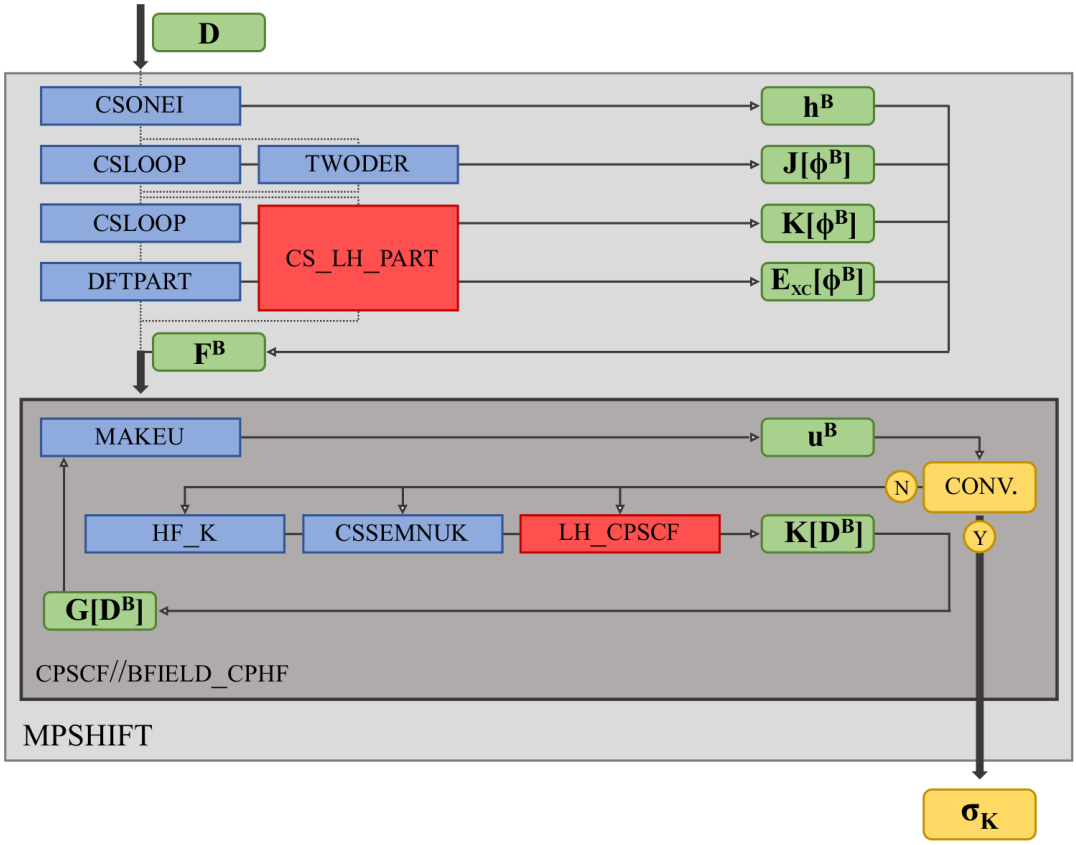

Figure 4.1.: Schematic work-flow diagram of the MPSHIFT routine. The LH specific subroutines introduced in the present work are highlighted in red.

shortly after the initial implementation of LHs in the context of this work, the response code was restructured, which further enhanced the efficiency (also of the LH implementation).[262] Additional DFAs were introduced via linking external exchange and correlation functional libraries such as LIBXC.[350,351]

In Fig. 4.1 a schematic (and simplified) work-flow diagram of the MPSHIFT routine for non-relativistic DFT and HF calculations is shown. The program is roughly structured in two parts: (i) a pre-loop section, where the one-electron contributions ($\mathbf{h}^{\mathbf{B}}$) and GIAO dependent terms are calculated (marked with $\phi^{\mathbf{B}}$ to point to derivatives of GIAOs) and (ii) a section handling the construction of the perturbed density, in the uncoupled case either directly or via the coupled-perturbed iterations, if exact exchange or the paramagnetic current density is present (see also Eqs. 3.71–3.74 for details of the terms). As pointed out above, the calculations are based on a converged SCF solution. The ground-state density matrix ($\mathbf{D}$) is therefore assumed to be available as an input parameter.

In (i) the one-electron integrals ($\mathbf{h}^{\mathbf{B}}$), (undisturbed-density) exact exchange ($\mathbf{K}\left[\phi^{\mathbf{B}}\right]$), the Coulomb contribution ($\mathbf{J}\left[\phi^{\mathbf{B}}\right]$) and the GIAO-dependent XC potential contribution

($\mathbf{E}_{XC}\left[\phi^{\mathbf{B}}\right]$) are calculated and directly written onto the perturbed Fock-matrix ($\mathbf{F}^{\mathbf{B}}$). The corresponding subroutines are CSONEI, CSLOOP or TWODER (the latter is employed in case of the RI and MARI adjusted Coulomb terms) and DFTPART. The exact exchange and DFT contributions for LH functionals are, however, handled separately within CS_LH_PART.

Program section (ii) is organized either by the subroutine CPSCF or its recently restructured counterpart BFIELD_CPHF.[262] However, the schematic work flow (outlined in the gray box) is fairly similar and therefore not depicted separately in Fig. 4.1. Initially, the perturbed Fock-matrix is handed over into the MAKEU subroutine, which returns an initial set of expansion coefficients ($\mathbf{u}^{\mathbf{B}}$). These are restructured to the perturbed MO coefficients ($\mathbf{c}^{\mathbf{B}}$) and organized in the perturbed density matrix ($\mathbf{D}^{\mathbf{B}}$). In the diagram, these reformulations are skipped for conciseness. In an uncoupled approach, the perturbed density matrix is directly used to calculate the final shielding result. If exact exchange is present, the perturbed density (i.e. the expansion coefficients) is handed into the HF_K (analytic exact exchange) or CSSEMNUK (semi-numerical exact exchange) subroutines to calculate the respective contribution and obtain a new set of coefficients. However, for a LH functional the exact-exchange contribution is calculated within LH_CPSCF. The procedure is then iterated until convergence, followed by calculation of the final shielding results ($\boldsymbol{\sigma}_K$).

Within the work-flow diagram, the new LH specific subroutines are marked in red. They each replace the exact-exchange and DFT routines in the pre-loop and loop sections, respectively. Their content is discussed in more detail in Sec. 5.3.

4.3 The ESCF Routine

The ESCF[352] subroutine was extended to LH functionals by Maier *et al.*[353,354] In the later work the LH functionals were embedded within the routine DF2ND_LOCHYB which is called within DF2ND (itself a wrapper differentiating semi-local functionals). However, in the schematic work-flow diagram in Fig. 4.2, these routines are shown in parallel to highlight that the output parameters of RSHLOP and DF2ND in the semi-local and GH case are replaced by the LH-specific routine. Since there are no Coulomb contributions, neither in the real triplet nor in the imaginary (singlet or triplet) cases,[330] these are skipped within the schematic overview.

The extension to SSCCs was achieved by replacing the right-hand side vectors by the one-electron vectors ($\mathbf{h}^{\mathbf{M}_K}$) of the FC and SD contribution for the real-triplet and PSO term for the imaginary-singlet case. These are calculated within the subroutine MKNCINTS

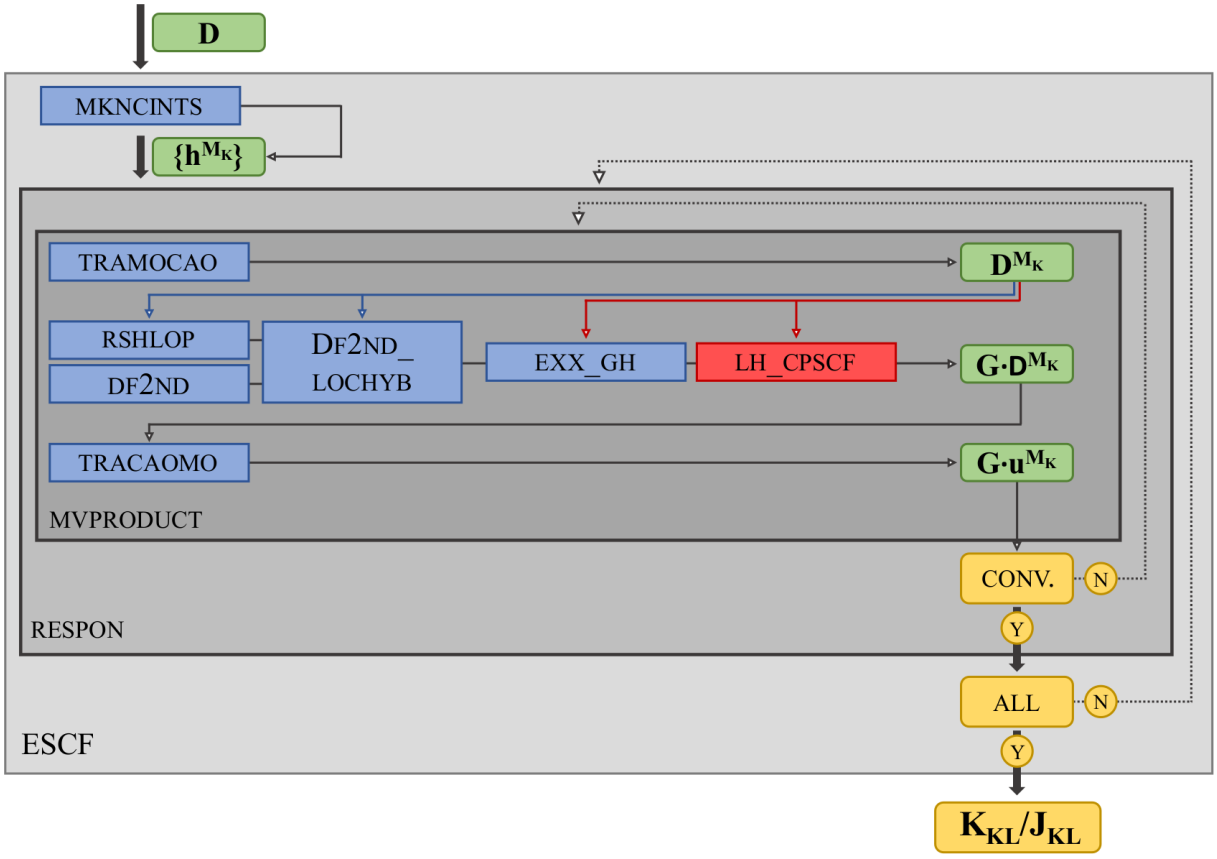

Figure 4.2.: Schematic work-flow diagram of the ESCF routine. The LH specific subroutines introduced in the present work are highlighted in red.

according to Eq. 3.74 using the operators of Eqs. 3.43 – 3.45 (note that without a dependence of the orbitals on the perturbation, only the one-electron contribution remains). For semi-local and GH functionals, the electronic Hessians were constructed as outlined in Eqs. 3.69 and 3.72, similarly to RPA or time-dependent DFT (TDDFT) calculations. Corresponding extentions of these equations for LH functionals were published in Refs. 353 and 354.

The three contributions to the SSCC (FC, SD and PSO) are constructed separately within a loop over the RESPON routine (marked with ALL within the work-flow diagram). This routine calculates the matrix-vector products of the electronic Hessian and the perturbed densities (see Eq. 3.68 and 3.71) within the MVPRODUCT subroutine.

Within the subroutine MVPRODUCT, the input density in the MO basis is initially transformed into the AO basis via TRAMOCAO for all contributing terms. However, the overall work flow is different for the real and imaginary contributions. Therefore, these are separated in Fig. 4.2 by either the blue (for the real-triplet case) or the red arrows (for the imaginary-singlet case). For the real contribution (blue arrows), exact exchange and

semi-local contributions are calculated either via RSHLOP and DF2ND (in the GH case) or via DF2ND_LOCHYB (in case of a LH functional). The construction of these contributions remained unaltered within the present thesis.
The construction of the imaginary triplet contribution (red arrows) only requires the evaluation of exact exchange, as for the GH case shown in Eq. 3.72. Therefore, in the initial hybrid implementation the DFT part via DF2ND was skipped entirely, as the exact-exchange contribution is calculated either via RSHLOP, or SENEX_AS_OMP for semi-numerical exchange. Both routines are collectively termed EXX_GH within the work-flow diagram.
However, the PSO contribution was not evaluated properly for LHs because the exact-exchange contribution for local hybrids is embedded in DF2ND_LOCHYB (called within DF2ND), which was skipped in the initial implementation. Its evaluation was implemented externally of DF2ND and parallel to the semi-numerical GH subroutine via LH_CPSCF. The subroutine was formerly implemented to handle the paramagnetic contribution of NMR shielding constant (see above), which as the PSO contribution is of imaginary-singlet character. Therefore, the routine required only minor adjustments for the extension to the PSO in SSCCs, i.e. it was altered to handle the $3 \cdot K$ (instead of 3 as in the shielding case) perturbed densities simultaneously (see also Sec. 3.2.1 for further details). The newly implemented subroutine is marked in red, for which further details are outlined in Sec. 5.3.
Finally, the matrix-vector product is transformed into the MO basis (via TRACAOMO) and MVPRODUCT is iterated until the expansion coefficients of all perturbed densities are converged. For the final output the contributions are gathered on the reduced spin–spin coupling tensor $\mathbf{K}_{KL}$ and reformulated into its counterpart $\mathbf{J}_{KL}$ using the corresponding nuclear magnetic moments of the computed nuclei tabulated within the program code.

5 NMR Property Calculations with Local Hybrid Functionals

The general theory of semi-local and GH functionals, and the calculation of NMR properties by means of perturbation theory using the CPKS equations has been outlined in chapters 2 and 3, which in the context of this work was extended to cover local hybrid functionals. The details of this work were published within the enclosed manuscripts reprinted after the present chapter. In the following, the main results and interconnections between the respective publications will be highlighted.
The chapter begins with a short summary of generalized computational details intended to cover programs, functionals, methods, basis sets and computational setups used throughout the presented work. This is followed by a short review of the most important steps of the project regarding the derivation, implementation, validation and application of local hybrid functionals for NMR properties such as shieldings, chemical shifts and spin–spin coupling constants. Where necessary, the discussions of the publications have been supplemented and extended. Finally, the chapter is closed by a brief summary of the main conclusions and an outlook of further research, which might build on the presented work. Throughout, the reprinted publications are referred to as P-X, whereas data published in the supporting information (SI) of the respective publications is referred to as SI-X. In both cases, X is the number of the respective publication within the present work. It should be noted that due to the extensive data collection in some of the SIs, only parts are reprinted in this work.

5.1 Computational Details

Calculations using DFT functionals up to rung 4 on Perdew's ladder were performed using a developers' version of TURBOMOLE updated regularly during the developments until version 7.5.[9] In some cases comparative calculations were performed using the GAUSSIAN

Table 5.1.: Pre-defined functionals and methods used throughout P-I – P-VIII. In case of GHs the exact-exchange admixture, for RSHs the short and long range EXX as well as their RS parameter ω and for DHs the exact-exchange admixture and (same and opposite spin) correlation contributions is given (see also Eqs. 2.49 and 2.50). For LHs further details are given in Table 2.1 and Figure 2.1.

LSDA	SVWN[52,120]
GGA	BP86,[159,170,361] BLYP,[159,169] PBE,[160] KT1,[166] KT2,[166] KT3,[167] HCTH[162,362] and B97D[212]
m-GGA	TPSS,[178,363] VSXC,[180] τ-HCTH,[181] M06-L,[182] MN15-L,[183] B97M-V,[219] SCAN,[179] rSCAN[364] and r^{2}SCAN[365,366]
GH	TPSSh (10 %),[189] B3LYP (20 %),[59,195] B97-2 (21 %),[165] PBE0 (25 %),[190,191] M06 (27 %),[134] PW6B95 (28 %),[367] MN15 (44 %),[200] BHLYP (50 %)[58,188] and M06-2X (54 %)[134]
RSH	CAM-B3LYP (19 % $\rightarrow$ 65 %, ω = 0.33),[206] ωB97X-D (22 % $\rightarrow$ 100 %, ω = 0.2),[216] ωB97X-V (17 % $\rightarrow$ 100 %, ω = 0.3)[220] and ωB97M-V (15% $\rightarrow$ 100 %, ω = 0.3)[221]
LH	LH07s-SVWN,[247] LH07t-SVWN,[242] LH12ct-SsirPW92,[243] LH12ct-SsifPW92,[243] LH14t-calPBE,[244] LH20t[245], LHJ14[249] and mPSTS[239,262]
DH	B2PLYP (a_X=53 %, a_C=27 %),[230] B2GP-PLYP (a_X=65 %, a_C=36 %)[232] and DSD-PBEP86 (a_X=70 %, c_o= 53 %, c_s =25 %)[233,368]
methods	Hartree–Fock, MP2, CCSD and CCSD(T)

program, either Gaussian09, revision D.01,[355] or Gaussian16, revision A.03.[356] Double hybrid and MP2 shielding calculations were performed using Orca, version 4.2.1,[11–13] whereas coupled-cluster optimizations and property calculations used the Cfour program code, version 1.2,[10] in some cases extended to further CC diagnostics using Molpro.[357] Analysis of contributions to NMR shieldings tensors were computed using ReSpect.[358] Tight-binding based calculations were performed using the xTB program code,[359] whereas the sampling of molecular structure spaces was performed using the conformer-rotamer ensemble sampling tool (CREST).[360]

Throughout P-I – P-VIII, the pre-defined functionals and methods listed in Tab. 5.1 were used. Furthermore, a few adjusted LH models have been employed: 07ct, 07tx and 07ctx, which are related to the LH07t-SVWN functional using either a common LMF, an enlarged prefactor ($a = 0.709$), or both. The two functionals LH14t-nc and LH20t-nc use the same set of parameters as LH14t-calPBE and LH20t, but are constructed without the respective CFs.

Where required, D3 dispersion corrections[213,369] in combination with Becke–Johnson damping (denoted D3(BJ))[370–372] were employed. The prefix "c" is used for function-

als employing the current-corrected τ_D model for the kinetic energy density for shielding or spin–spin coupling calculations. In some computations, the resolution of the identity for the Coulomb contribution (RI-J) has been employed,[278] partly in its multipole-accelerated variant (MARI-J).[274,281] Furthermore, implicit solvent models COSMO and the direct COSMO for real solvents (D-COSMO-RS) have been used.[346,373–375]
Optimizations were performed either with the def2-X[376,377] (X = TZVP, TZVPD) or the correlation-consistent cc-pVXZ[378–381] (X = T, Q) basis sets. NMR-property calculations employed specifically optimized basis sets as published by Jensen, using pcSseg-X[382] (X = 3, 4) for shieldings and pcJ-4[383] for spin–spin coupling constants. In P-VII additionally the ANO-RCC basis set was used for I.[384] In some cases uncontracted basis sets were employed marked with the suffix "unc". If the RI-J or subsequently the MARI-J approximations are employed, "universal" auxiliary basis sets have been used throughout.[385]
Statistical quantities such as the standard deviation (StD), mean signed (MSE) and mean absolute errors (MAE) are reported. In cases where statistical data is calculated from reference data, which is not of benchmark quality, the term "deviation" instead of "error" (MSD, MAD) is employed. Partly relative quantities are compared, termed either "mean absolute relative error" (MARE) or "mean absolute percentage deviation" (MAPD). The definition of these quantities is also shown in Sec. S1 of SI-I, reprinted in Sec. A.1.1. In P-V and P-VI relative quantities were normalized by the shielding and shift ranges provided by the references for individual nuclei. These quantities are marked with the prefix "rel.", whereas for maximum values the prefix "max." is used.
For further details on computational methodology, grid setting and computational convergence criteria see also the individual computational details of P-I – P-VIII.

5.2 Derivation

The general derivation of NMR property calculations using LH functionals is reported in P-I and P-II, in which the coupled-perturbed, respectively, response schemes for shielding and SSCC calculations are outlined. Extensions to that work, including the current-dependent implementation of the Dobson variant of the kinetic-energy density (Eq. 3.87) and second-order derivatives of the density, are reported in P-III and P-IV.
The derivation of second-order NMR properties for LH functionals can be started from the expression of the perturbed Fock matrix (see also Eq. (12) of P-I). Compared to the GH scheme only the LH-specific exchange-correlation potential is altered by the LMF and therefore requires adjustments. Importantly, also the LMF-dependent exact-exchange

contribution is gathered within this term. The first step was thus to derive a generalized expression for the perturbed LH potential (the direct derivative of the potential, Eq. 2.77, with respect to the perturbation), which with respect to an arbitrary perturbation is given by

$$\begin{aligned}
\frac{\partial V^{LH}_{XC,\mu\nu,\varsigma}}{\partial \boldsymbol{\lambda}} = &-\frac{1}{2}\sum_{\kappa\lambda}\Bigg[D^{\boldsymbol{\lambda}}_{\kappa\lambda,\varsigma}\int g_\varsigma(\mathbf{r})\left(\phi^*_\kappa(\mathbf{r})\phi_\nu(\mathbf{r})A_{\mu\lambda}(\mathbf{r})+\phi^*_\mu(\mathbf{r})\phi_\lambda(\mathbf{r})A_{\kappa\nu}(\mathbf{r})\right)\mathrm{d}\mathbf{r}\\
&+D_{\kappa\lambda,\varsigma}\int \widehat{d}_{\boldsymbol{\lambda}}g_\varsigma(\mathbf{r})\left(\phi^*_\kappa(\mathbf{r})\phi_\nu(\mathbf{r})A_{\mu\lambda}(\mathbf{r})+\phi^*_\mu(\mathbf{r})\phi_\lambda(\mathbf{r})A_{\kappa\nu}(\mathbf{r})\right)\mathrm{d}\mathbf{r}\\
&+D_{\kappa\lambda,\varsigma}\int g_\varsigma(\mathbf{r})\left(\phi^*_\kappa(\mathbf{r})\phi_\nu(\mathbf{r})A_{\mu\lambda}(\mathbf{r})+\phi^*_\mu(\mathbf{r})\phi_\lambda(\mathbf{r})A_{\kappa\nu}(\mathbf{r})\right)^{\boldsymbol{\lambda}}\mathrm{d}\mathbf{r}\Bigg]\\
&+\sum_\sigma\Bigg[\int \widehat{d}_{\boldsymbol{\lambda}}\widehat{d}_{\mu\nu,\varsigma}g_\sigma(\mathbf{r})\cdot\left[e^{exact}_{X,\sigma}\left[\{\phi_\tau\}\right]-e^{DFT}_{X,\sigma}\left[\rho_\sigma\right]\right]\mathrm{d}\mathbf{r}\\
&+\int \widehat{d}_{\mu\nu,\varsigma}g_\sigma(\mathbf{r})\cdot\widehat{d}_{\boldsymbol{\lambda}}e^{exact}_{X,\sigma}\left[\{\phi_\tau\}\right]\mathrm{d}\mathbf{r}-\int \widehat{d}_{\mu\nu,\varsigma}g_\sigma(\mathbf{r})\cdot\widehat{d}_{\boldsymbol{\lambda}}e^{DFT}_{X,\sigma}\left[\rho_\sigma\right]\mathrm{d}\mathbf{r}\\
&-\int \widehat{d}_{\boldsymbol{\lambda}}g_\sigma(\mathbf{r})\widehat{d}_{\mu\nu,\varsigma}e^{DFT}_{X,\sigma}\left[\rho_\sigma\right]\mathrm{d}\mathbf{r}+\int\left[1-g_\sigma(\mathbf{r})\right]\widehat{d}_{\boldsymbol{\lambda}}\widehat{d}_{\mu\nu,\varsigma}e^{DFT}_{X,\sigma}\left[\rho_\sigma\right]\mathrm{d}\mathbf{r}\Bigg]\\
&+\int \widehat{d}_{\boldsymbol{\lambda}}\widehat{d}_{\mu\nu,\varsigma}e^{DFT}_{C}\left[\rho_\sigma\right]\mathrm{d}\mathbf{r}. \qquad (5.1)
\end{aligned}$$

Here, $\widehat{d}_{\boldsymbol{\lambda}}$ describes the derivative of the semi-local quantities with respect to the arbitrary perturbation $\boldsymbol{\lambda}$ using the chain rule.
Without a dependence of the basis functions on the perturbation (in the context of this work the condition holds for the calculation of SSCCs) the derivative operators in Eq. 5.1 can be rewritten in terms of derivatives with respect to the density matrices as outlined in Eqs. 2.80 and 2.81

$$\widehat{d}_{\boldsymbol{\lambda}}\big|_{(\phi^{\boldsymbol{\lambda}}=0)} = \sum_{\mu\nu}\sum_\sigma D^{\boldsymbol{\lambda}}_{\mu\nu,\sigma}\widehat{d}_{\mu\nu,\sigma}, \qquad (5.2)$$

$$\widehat{d}_{\boldsymbol{\lambda}}\widehat{d}_{\mu\nu,\sigma}\big|_{(\phi^{\boldsymbol{\lambda}}=0)} = \sum_{\kappa\lambda}\sum_\varsigma D^{\boldsymbol{\lambda}}_{\kappa\lambda,\varsigma}\widehat{d}_{\kappa\lambda,\varsigma}\widehat{d}_{\mu\nu,\sigma}. \qquad (5.3)$$

Using these adjusted operators, the response equations for SSCCs are obtained, as presented in Eqs. (10), (11), (16) and (17) of P-II. However, in P-II the equations were directly reported in form of the electronic Hessians, as outlined for GHs in Eqs. 3.68 and 3.71. As shown in Eq. 3.78, for SSCCs the real FC and SD as well as imaginary PSO perturbations are present. These are reflected in symmetric and skew-symmetric perturbed density matrices, giving rise to the two different definitions of the Hessian in the real (Eqs. (11) and (16) of P-II) and imaginary cases (eq. (17) of P-II). It is noted in

passing, that the final expressions for the Hessians resemble those which were derived in the context of LH functionals in the framework of TDDFT.[353,354]

If a CDFT functional via τ_D is chosen, the current response enters only in the imaginary PSO contribution due to skew-symmetry of the perturbed density matrix. Details are outlined in the discussion of paramagnetic contributions below.

For NMR shielding constants (initially derived without current contributions) the dependence of the orbitals on the perturbation had to be taken into account. In that case, the corresponding generalization of the derivative operators is not as instructive as shown for SSCCs. Therefore, the present discussion uses references to the respective equations in the original publications.

The contributing terms for shielding constants without the current response were shown in Eq. (16) of P-I. This expression is obtained by considering that the paramagnetic contribution is imaginary and the involved perturbed density matrices as well as matrices of the GIAO pairs (see Eq. 3.57) are skew-symmetric. For that reason, the direct derivatives of semi-local quantities in Eq. 5.1 vanish.

However, due to the involved GIAOs, the shielding calculation requires contributions contracted with the unperturbed density, which are calculated just once (pre-loop), as well as contributions dependent on the perturbed density, which are constructed within the CPKS iterations, as also outlined in Sec. 4.2.

Within the pre-loop part, the most important steps to adjust the coupled-perturbed scheme for LHs involved the derivation of a suitable expression for the pre-loop exact-exchange contribution, which requires the contruction of the perturbed A-matrix, as outlined in Eq. (20) of P-I. As shown, the quantity can be constructed from the A-matrices with an increased l-quantum number, similar to the schemes derived for molecular gradients.[341] However, circumventing the perturbed A-matrix, as shown for GHs (see Eq. 3.76), is impractical for LHs due to the presence of the LMF: interchanging $\mathbf{r} \longrightarrow \mathbf{r}'$ results in explicit dependence of the analytic A-matrix integrals on the (potentially sophisticated) LMF, which might lead to integrals without analytical solution. Further details of the derivation of the perturbed A-matrix were given in Sec. S3 of SI-I, see also Sec. A.1.2.

The derivation also required the perturbed LMF-dependent potential contribution, as shown in Eq. (28) of P-I. Within the initial implementation, the focus was on uncalibrated LH models (see Sec. 2.3.2 for further details) with a dependence on the density, gradient of the density and kinetic energy density. In the course of the work published in P-IV, second derivatives of the density such as the Laplacian (Eq. 2.70) and the Hessian of the density (Eq. 2.71) were included (see Eqs. (20)–(22) of P-IV), which enter due to the presence of the calibration functions (Eq. 2.69). The inclusion into the previously outlined potential

contribution was straightforward (see also Eq. (28) of P-I). In this context, expressions for the gradient of the kinetic energy density in their gauge-independent representations via the Maximoff–Scuseria (Eq. 3.86) and Dobson (Eq. 3.87) models were derived, see Eqs. (29) and (30) of P-IV. These would enter for calibrated meta-GGA-based LHs (see Sec. 2.3.2). However, no LH functionals using this quantity have been reported to date.
The perturbed-density-dependent exchange contribution, given in Eq. (29) of P-I, resembles the Hessian for the imaginary PSO contribution in SSCCs (Eq. (17) in P-II). Both are reflected in the first term on the right-hand side of Eq. 5.1.
If a current-density functional via τ_D (see Eq. 3.87) is chosen in a shielding calculation, the related expression due to the perturbed paramagnetic current density is outlined in Eq. (18) of P-III. The equation contains a contribution dependent on the perturbed and unperturbed densities. For these contributions the condition of Eq. 3.89 applies. It should be noted that the potential contribution for an arbitrary $f\left[\tilde{\tau}\right]$ with $\tilde{\tau} \to \tau_D$ can be derived using

$$\left.\frac{\partial^2 f}{\partial \mathbf{j}_p^2}\right|_{\mathbf{j}_p=0} = -\frac{1}{\rho}\frac{\partial f}{\partial \tau}. \tag{5.4}$$

The work related to the gauge correction of the kinetic energy density was made necessary due to paramagnetic artefacts arising within the τ_{MS}-model. These already occurred in the application to second-period noble-gas atoms (see P-III for further details). These additional contributions were traced to an orbital rotation-operator, which was derived from the expression of the potential contribution for the kinetic energy using the τ_{MS}-model (see Eqs. (23) and (24) of P-III, as well as Sec. S1 in SI-III and Sec. A.3.1). Therefore, various models for the kinetic energy density were revisited in P-III, including a gauge-dependent construction allowing to choose the gauge origin of the kinetic energy density within the calculation (typically, it was placed at the center-of-mass (COM)) and an ad-hoc corrected variant, which was derived to resemble the model implemented in the ORCA program code. The exact forms of the latter two models are outlined in Sec. S2 of SI-III and Sec. A.3.2 of the present work.

5.3 Implementation

The implementation within the CPKS scheme for LH functionals was reported in P-I and P-II for shieldings and SSCCs, respectively. Extensions to the initial implementation covering the paramagnetic current density and the Laplacian and Hessian terms were reported in P-III and P-IV. The matrix-vector notation as introduced in Sec. 2.4.2 is used

throughout this section. In the following, the implementation as reported in the publications (without consideration of later changes within the program code not conducted by the author) are revisited and further details of the program structure and interconnections to other LH related implementations are outlined.

The shielding extension in TURBOMOLE was implemented into the MPSHIFT program code (see also Fig. 4.1), whereas SSCCs were obtained from implementations within the ESCF routine (Fig. 4.2). As shown in Fig. 4.1, LH specific extensions to MPSHIFT bypass the exchange and semi-local contributions of common semi-local and hybrid functionals. Within the the pre-loop part the routines CSLOOP and DFTPART are replaced with CS_LH_PART and within the loop the routines HF_K (for analytical exchange) or cssemnuk (for semi-numerical exchange) are replaced with LH_CPSCF. In calculations of SSCCs using LHs, the real triplet contribution due to the FC and SD operators (Eqs. (5) and (6) in P-II, see also Eqs. 3.43 and 3.44 of the present work) utilizes the resemblance to TDDFT derivations (see Refs. 353 and 354, as well as Sec. 5.2) by adjusting the right-hand-side vector with the according perturbed one-electron contribution (Eq. (11) in P-II or Eq. 3.74 of the present work). This part of the program required no additional modifications of the available LH-TDDFT program code. Only the LH-specific PSO contribution (Eq. (7) in P-II, see also Eq. 3.45) had to be introduced (as the DF2ND routines are skipped within the PSO loop, see Sec. 4.3). This was achieved by implementing the LH_CPSCF routine (which required just slight adjustments, see below), available from the related work on NMR shieldings.

In Figs. 5.1 and 5.2, the main subroutines of the newly implemented CS_LH_PART and LH_CPSCF routines are outlined in a schematic pseudo-code representation. The relevant output of the subroutines is shown on the right-hand side. Both subroutines use the arguments *cdft* and *lh_func*. The first represents changes within the program due to the presence of the paramagnetic current density via τ_D (see Eq. 3.87). The second variable describes additional steps involved with LH functionals, as the routine is also used for the semi-numerical solution of GH models within the pre-loop section (within the loop, the CSSEMNUK routine is used for GHs).

The CS_LH_PART Routine The initialization of the program contains the division of the numerical grid into batches (typically up to 100 grid points per batch) in order to reduce memory demands within the calculation and enable efficient parallelization by subdivision of grid-batches to multiple CPUs. Within the program loops over the grid batches are used and within these loop the working subroutines are called. The program is structured to hierarchically construct the semi-local XC and non-local exchange quantities, beginning with the AO values as well as their first and second derivatives (if they are

CS_LH_PART()

initialization
for *number of grid batches* **do**
  call funct() ... $\boldsymbol{\phi}$, $\nabla\boldsymbol{\phi}$, $\nabla^{\mathrm{T}}\nabla\boldsymbol{\phi}$
  call ondes_ks() ... $\mathbf{D}\boldsymbol{\phi}$, $\mathbf{Q}$
  call cs_ondes(*cdft*) ... $\mathbf{D}\boldsymbol{\phi}^{\mathbf{B}}$, $\mathbf{j}_p^{\mathbf{B}}$
  if *lh_func* **then**
    call lmf_r1() ... $\mathbf{g}$, $\mathbf{g}'$
  end
  call calc_ftg_B() ... $\mathbf{F}$, $\mathbf{F}^{\mathbf{B}}$
  call cs_gvg(*lh_func*) ... $\mathbf{G}$, $\mathbf{G}^{\mathbf{B}}$, $\mathbf{G}^{\mathbf{A}^B}$
  call cs_kmat(*lh_func*) ... $\mathbf{K}^{\mathbf{B}}$
  if *lh_func* **then**
    calc_exx() ... $\mathbf{e}_X^{exact}$
    call lochyb_r1() ... $\mathbf{O}$
    if *cdft* **then**
      call scal_jpb() ... $\mathbf{j}_p^{\mathbf{B}}\boldsymbol{\rho}^{-1}$
    end
    call cslh_mgga(*cdft*) ... $\mathbf{F}_{XC}^{\mathbf{B}}$
  end
end

Figure 5.1.: Simplified algorithm of the newly implemented CS_LH_PART routine (neglecting grid and junction construction for conciseness).

required by the chosen functional) on the grid, arranged as a vector by the FUNCT routines. These vectors are contracted with the input density matrix ($\mathbf{Z} = \mathbf{D}\boldsymbol{\phi}$) within ONDES_KS. In the same subroutine the semi local quantities Q ($Q\varepsilon\mathbb{Q}$, $\mathbb{Q} = \mathbb{Q}\{\boldsymbol{\rho}, \nabla\boldsymbol{\rho}, \boldsymbol{\tau}, \dots\}$; except $\mathbf{j}_p$) present in the chosen functional or LMF (see also Sec. 4.1) are also constructed. Essentially, the CS_ONDES subroutine is a rework of the ONDES_KS routine. Within the routine, the prefactor of the derived GIAOs (Eq. 3.56) is multiplied with the basis function and afterwards the former product is contracted with the unperturbed density to obtain the $\mathbf{Z}^{\mathbf{B}}$-vectors, where $\mathbf{Z}^{\mathbf{B}} = \mathbf{D}\boldsymbol{\phi}^{\mathbf{B}}$. If a current-dependent density functional (under use of τ_D) is chosen, the unperturbed-density contribution of the paramagnetic current density ($\mathbf{j}_p^{\mathbf{B}}$) is also constructed, as outlined by the right hand side of Eq. (18), and represented by the three vectors outlined in Eqs. (20)–(22) in P-III.

As outlined in Sec. 4.1, in LMF_R1 the LMF and its first derivatives with respect to the semi-local quantities are constructed. These are later used to scale the exchange contri-

bution in CS_KMAT and in the construction of the semi-local contribution in CSLH_MGGA (see also Eqs. (26) and (28) of P-I).

Within the CALC_FTG_B subroutine, the unperturbed and perturbed vectors $\mathbf{F}$ and $\mathbf{F}^{\mathbf{B}}$ are calculated,[a] as shown in Eq. (21) of P-I. The resulting vectors are then contracted with the $\mathbf{A}$ and $\mathbf{A}^{\mathbf{B}}$-matrices[b] (Eqs. (14) and (20) of P-I, see also Eq. 2.93 in this work) within the CS_GVG subroutine to provide the corresponding unperturbed $\mathbf{G}$, perturbed $\mathbf{G}^{\mathbf{B}}$ and $\mathbf{G}^{\mathbf{A}^{\mathbf{B}}}$ vectors (Eqs. (22) and (23) of P-I), respectively. The direct contraction of the A-matrices reduces the memory demand significantly, as the A-matrices are never stored explicitly within the routine. As previously discussed for Eq. (20) of P-I, the $\mathbf{A}^{\mathbf{B}}$-matrices require an increased l-quantum number, similar to the recurrence relation arising in the derivation of molecular gradients.[269,341] However, the schematic work-flow of CS_GVG is similar to the outline of refs. 341 and 288 and is not discussed in further detail here. To enhance the efficiency of the implementation, the S- (pre-constructed within the MPSHIFT routine and handed down), P- (constructed from the $\mathbf{Z}$ and $\mathbf{Z}^{\mathbf{B}}$ vectors within CS_LH_PART) and F-junctions (constructed on the fly within CS_GVG) are evaluated within the subroutine. A detailed discussion of the pre-screenings was included in P-I (for details see the related discussion in P-I, or Sec. 4.1 for S- and P-junctions and Sec. 2.4.2 for F-junctions, respectively). The final exchange contribution is constructed within the CS_KMAT subroutine according to Eq. (26) (or in case of a GH Eq. (27)) of P-I and written on the perturbed Fock matrix, which is the output of the routine.

In case of a GH, the semi-numerical exact-exchange contribution is fully evaluated at this point and the routine is left as the semi-local DFT contributions are evaluated externally within the routine DFTPART (see Fig. 4.1). However, in case of a LH the exact-exchange energy density ($\mathbf{e}_X^{exact}$) and subsequently the $\mathbf{O}$ vectors according to Eq. 4.1 are constructed via CALC_EXX and LOCHYB_R1. Finally, these vectors are contracted with the basis functions within CSLH_MGGA, according to Eq. (28) of P-I, or in case of the presence of the Laplacian or Hessian of the density Eqs. (18)–(23) of P-IV.

If a current-density dependent functional via τ_D is chosen, the contribution of the kinetic-energy density to the semi-local potential is altered according to Eq. (15) of P-III. In that case the initial product $\mathbf{j}_p^{\mathbf{B}} \cdot \boldsymbol{\rho}^{-1}$ is calculated externally within the SCAL_JPB routine, whereas the final contraction of the reduced perturbed paramagnetic current density with the basis-function pairs ($\mathbf{j}_p^{\mathbf{B}} \cdot \boldsymbol{\rho}^{-1} (\boldsymbol{\phi}\nabla\boldsymbol{\phi} - \boldsymbol{\phi}\nabla\boldsymbol{\phi})$) is likewise performed in the CSLH_MGGA

[a] These are the weighted contractions $w_g^{1/2}\mathbf{D}\boldsymbol{\phi}$ and $w_g^{1/2}\mathbf{D}\boldsymbol{\phi}^{\mathbf{B}}$, not to be confused with the Fock matrix, and its derivative.

[b] Not to be confused with the magnetic vector potential.

LH_CPSCF()

initialization
for *number of grid batches* **do**
  call funct() ... $\boldsymbol{\phi}$, $\nabla\boldsymbol{\phi}$, $\nabla^{\mathrm{T}}\nabla\boldsymbol{\phi}$
  call ondes_ks() ... $\mathbf{D}^{\boldsymbol{\kappa}}\boldsymbol{\phi}$, $\mathbf{Q}$
  for *perturbed density matrices* **do**
    call ondes_2as(*cdft*) ... $\mathbf{D}^{\boldsymbol{\kappa}}\boldsymbol{\phi}$, $\mathbf{j}_p\left[\mathbf{D}^{\boldsymbol{\kappa}}\right]$
  end
  call lmf_r1() ... $\mathbf{g}$, $\mathbf{g}'$
  if *cdft* **then**
    call calc_ftg() ... $\mathbf{F}\left[\mathbf{D}\right]$
  end
  for *perturbed density matrices* **do**
    call calc_ftgB() ... $\mathbf{F}\left[\mathbf{D}^{\boldsymbol{\kappa}}\right]$
  end
  call cs_gvg_cpscf(*cdft*) ... $\mathbf{G}\left[\mathbf{D}\right]$, $\mathbf{G}\left[\mathbf{D}^{\boldsymbol{\kappa}}\right]$
  if *cdft* **then**
    call calc_exx() ... $\mathbf{e}_X^{exact}$
  end
  call cs_kmat_cpscf() ... $\mathbf{K}\left[\mathbf{D}^{\boldsymbol{\kappa}}\right]$
  if *cdft* **then**
    call lochyb_r1() ... $\mathbf{O}$
    call scaljpb() ... $\mathbf{j}_p\left[\mathbf{D}^{\boldsymbol{\kappa}}\right]\boldsymbol{\rho}^{-1}$
    call cslh_jpb() ... $\mathbf{F}_{XC}\left[\mathbf{D}^{\boldsymbol{\kappa}}\right]$
  end
end

Figure 5.2.: Simplified algorithm of the newly implemented LH_CPSCF routine (neglecting grid and junction construction for conciseness).

subroutine. As for the exact-exchange contribution above, the resulting semi-local contribution is written on the perturbed Fock-matrix and passed to the MPSHIFT routine.

The LH_CPSCF Routine The CPKS loops of the paramagnetic term of the shieldings and the PSO contribution in SSCCs are equivalently handled within the LH_CPSCF routine. As for CS_LH_PART, the *cdft* argument was implemented to separate DFT and CDFT cases (for the latter, the connected contributions are outlined in Eqs. (12), (15) and (19) of P-III). If no current dependency is present, the subroutine only controls the construction of the perturbed-density-dependent exact-exchange contribution (Eq. (29) in P-I and Eq. (17) in P-II, respectively). A recurring element within the subroutine is the loop over the perturbed density matrices. In case of shielding calculations 3 (one for

each direction of the magnetic field) and in case of SSCCs $3 \cdot K$ matrices (the Cartesian components for each nucleus individually) are handled.

Equivalently to CS_LH_PART, within LH_CPSCF loops over grid batches are used and initially the basis-function vector and its derivatives are constructed via the FUNCT routines. Also, semi-local contributions are computed via ONDES_KS. The LMF values and the corresponding derivatives are obtained via LMF_R1. Technically, the derivatives are only required in the CDFT case. However, LMF_R0 and LMF_R1 are almost equivalently fast, and no distinction of the cases was built in. Due to the skew-symmetry of the perturbed density matrices, their contraction with the basis functions ($\mathbf{D}^{\boldsymbol{\kappa}}\boldsymbol{\phi}$) is handled within ONDES_2AS, the asymmetric counterpart to the ONDES_KS routine. This subroutine was implemented by Maier *et al.* in the course of the TDDFT implementation (see Refs. 353 and 354) and can also be used to construct the perturbed-density-dependent paramagnetic current density ($\mathbf{j}_p\left[\mathbf{D}^{\boldsymbol{\kappa}}\right]$) if the *cdft* option is set.

If no current dependency is present, only the perturbed density dependent $\mathbf{F}\left[\mathbf{D}^{\boldsymbol{\kappa}}\right]$, $\mathbf{G}\left[\mathbf{D}^{\boldsymbol{\kappa}}\right]$ and $\mathbf{K}\left[\mathbf{D}^{\boldsymbol{\kappa}}\right]$ are constructed within LH_CPSCF. This is done in a similar fashion as the corresponding quantities outlined for the CS_LH_PART routine above. However, in these steps the subroutines CALC_FTGB, CS_GVG_CPSCF and CS_KMAT_CPSCF are employed, as in contrast to the pre-loop contributions, the CPSCF specific routines handle the 3, respectively, $3 \cdot K$ vectors arising due to the perturbed densities simultaneously. Prescreening is employed via the S- and the (loop-specific) PL- and FL-junctions. The PL- and FL-junctions are constructed similarly to their P- and F-junction counterparts. However, due to the presence of the perturbed densities, a separate threshold value was introduced to compensate for the observed higher sensitivity of the CPKS-loops on the junction-settings. An additional gain in efficiency (with an acceptable error margin) was obtained by introducing non-standard coarse numerical grids within the loop section (see below). Details on these pre-screenings and efficiency-related technicalities are outlined in P-I.

In case of a CDFT functional via τ_D, an additional semi-local contribution is present. In that case $\mathbf{F}\left[\mathbf{D}\right]$, $\mathbf{G}\left[\mathbf{D}\right]$ and subsequently $\mathbf{e}_X^{exact}$ have to be constructed to build the $\mathbf{O}$ vectors in LOCHYB_R1. These contributions are calculated taking similar steps as for the pre-loop part described above, i.e. the (perturbed-density dependent) paramagnetic current density is scaled by the density within SCALJPB and finally contracted with the basis functions in CSLH_JPB. Here, CSLH_JPB is a reduction of CSLH_MGGA as only the current-dependent contribution has to be evaluated (see Eq. (19) in P-III).

Table 5.2.: Mean absolute deviations (MAD) of NMR shielding constants (in ppm) using different coarse grid settings (see text) in comparison to calculations using grid setting 5 for the test-set data of Ref. 13 (GIAO-DFT/pcSseg-3 results).

		LH07t-SVWN						LH20t					
		τ_{MS}			τ_D			τ_{MS}			τ_D		
	grid	1	1	1	1	1	1	1	1	1	1	1	1
	cpksgrid	–	0	-1	–	0	-1	–	0	-1	–	0	-1
MAD	^{1}H	0.001	0.001	0.001	0.001	0.001	0.001	0.001	0.001	0.002	0.001	0.001	0.002
	^{13}C	0.02	0.03	0.09	0.02	0.03	0.12	0.02	0.05	0.15	0.02	0.05	0.07
	^{15}N	0.02	0.04	0.30	0.02	0.04	0.35	0.03	0.06	0.47	0.05	0.05	0.28
	^{17}O	0.04	0.05	0.15	0.04	0.05	0.17	0.03	0.16	0.26	0.04	0.15	0.27
	^{19}F	0.01	0.10	0.08	0.01	0.10	0.09	0.02	0.15	0.13	0.03	0.12	0.11
	^{31}P	0.07	0.12	0.20	0.07	0.12	0.18	0.13	0.21	0.36	0.14	0.25	0.38
rel. MAD	^{1}H	0.01	0.01	0.01	0.01	0.01	0.01	0.02	0.02	0.03	0.02	0.02	0.03
	^{13}C	0.01	0.01	0.04	0.01	0.01	0.05	0.01	0.02	0.07	0.01	0.02	0.03
	^{15}N	0.00	0.01	0.04	0.00	0.01	0.05	0.00	0.01	0.07	0.01	0.01	0.04
	^{17}O	0.01	0.01	0.02	0.01	0.01	0.02	0.00	0.02	0.03	0.00	0.02	0.03
	^{19}F	0.00	0.01	0.01	0.00	0.01	0.01	0.00	0.02	0.02	0.00	0.02	0.02
	^{31}P	0.01	0.02	0.03	0.01	0.02	0.03	0.02	0.03	0.06	0.02	0.04	0.06

5.3.1 Efficiency and Grid Convergence

The efficiency of the semi-numerical implementation (see Sec. S2 of SI-I or Eq. 2.92 and the related discussion within this work) relies on integral pre-screening via the S-, P-, and F-junctions (as well as their loop-section counterparts), as outlined above. However, the implementation also crucially depends on the employed integration grid (see also Sec. 2.4.2). To further increase the efficiency of the implementation, coarse integration grids have been evaluated within the loop section of the shielding calculations (for the definitions of TURBOMOLE grid settings see Tab. 1 in P-I), where in comparison to the pre-loop part of the calculation a lower sensitivity on the grid size was detected (see Fig. S2 within SI-I, reprinted in Fig. A.1 of the present work). These initial measures have been tested and reported in P-I.

However, the initial implementation, for which the timings and grid-dependencies of the coarse-grid approach have been tested, used the τ_{MS}-model for the kinetic energy density. Therefore, the loop section contained only the perturbed exact exchange and was independent of any semi-local contributions. This changes with the introduction of τ_D. Due to the potential sensitivity of such semi-local quantities on the chosen grid, the error margins of the separate grid settings for the CPKS loops have been re-evaluated for the CDFT variants of the LHs. Fig. 5.2 gathers the MAD and relative MAD of calculations using various coarse grid settings in comparison to a set of shieldings obtained with grid size 5 (internal TURBOMOLE setting) for the benchmark set reported by Stoychev *et al.* (GIAO-DFT/pcSseg-3 level of theory is employed, see Tab. A.27 for the full data).[13] The data for the individual nuclei is reported for two t-LMF based LH models, LH07t-

SVWN and LH20t, as examples for uncalibrated and calibrated LH functionals. However, the error margins in the CDFT case are insignificantly larger in comparison to the initial implementation. Therefore, the conclusions of P-I regarding the grid-dependencies still hold for the CDFT-LH variants.
A similar pre-screening as for shieldings is also available for SSCCs. However, thorough testing was provided elsewhere.[353] As visible from Tab. S10 in SI-II (reprinted in Tab. A.2.1), calculation of SSCCs appears to be more sensitive to the chosen grids and therefore the coarse grids have not been employed.

5.4 Validation

5.4.1 Validity of the Implementation

The implementations reported above have been carefully tested. However, a thorough validation as provided by numerical differentiation, i.e. finite-field methods, is not available in the one-component code of TURBOMOLE. Therefore, the validation used implicit rather then explicit arguments, i.e. it relied on a comparison between LH related code segments and testing of GH vs. GH-via-LH (calculations of GH results using the LH code) approaches, which was executed in P-I – P-IV for all newly implemented extensions.
The implemented $\mathbf{A}'$ routines were tested by computing both expressions of Eq. 3.76 (with and without the exchange $\mathbf{r} \longrightarrow \mathbf{r}'$), as outlined for the Hartree–Fock results in Tab. S1 of the SI-I (reprinted in Tab. A.1). As shown, the error margins are within numerical accuracy. The same holds for the GH and GH-via-LH comparison, which provides a simultaneous test of the semi-local implementation and the CPKS-loop computation, as shown for B3LYP (and further GHs) in the same table.
Furthermore, gauge-independence was proven for the implementations, which is an important physical property in NMR parameter calculations (see also Sec. 3.1.6). The corresponding data is provided in Tabs. S2 and S3 of the SI-I (see also Tab. A.2) as well as Tab. S2 (and for further partly gauge-variant version in Tab. S3) of SI-III, reprinted in Tab. A.9 of the present work. As an example for calibrated LHs, similar data is provided for LH20t, see Tab. A.26. In all cases translation and rotation of a trial-molecule (NH_3) was tested.
The implicit measures were also employed for the validation of SSCCs. Nevertheless, in the initial implementation the author set an incorrect prefactor: due to the modularity of the TURBOMOLE program code, the definition of the GS density matrix is inconsistent within the individual subroutines of the code. In some routines the off-diagonal elements are pre-

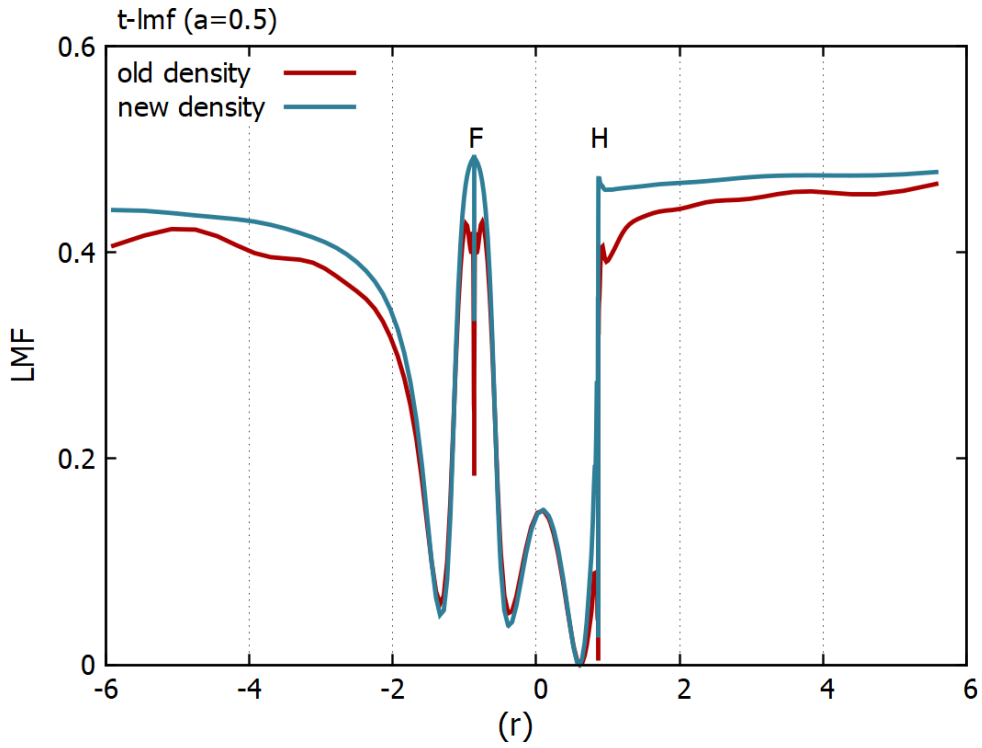

Figure 5.3.: Plot of the real-space exact-exchange admixture, as controlled by the t-LMF with prefactor $a = 0.5$, due to the two definitions of the density matrix (see text) along the H–F bond; F is placed at the origin and H at $(r) = 1.729$.

multiplied by a factor 2 to include both ij and ji matrix elements in loops over upper or lower triangular matrices. Such a difference is also present within the MPSHIFT and ESCF subroutines, but it was missed in the initial transfer of the LH_CPSCF subroutine for the calculation of SSCCs. As outlined above, the routine is involved within the construction of the PSO contribution to the SSCCs. Without the use of a current-density functional (as for the initial implementation) the GS density matrix only enters in the construction of the LMF, which weights the LH exact-exchange contribution. In case of GH functionals via the LH code a constant is provided and the direct comparison of the two codes (GH and GH-via-LH) matched exactly. Nevertheless, the initial LH results use an additional prefactor of 1/2 for the unperturbed density matrices used in the construction of the LMF, which subsequently controls the exact-exchange admixture within the PSO contribution. The correct prefactor was set in the course of Ref. 386. However, the impact on the resulting SSCCs is comparably small. On the one hand this is due to the overall small contribution of the PSO in comparison to the total coupling constants. On the other hand, it should be noted that no one-to-one mapping between the LMF and the (prefactor of the) density-matrix exists and therefore significant parts of the LMF are almost identical

Table 5.3.: Mean absolute percentage deviations (in %) of SSCCs obtained with various DFAs in comparison to the combined test set of Refs. 387 and 388. On the left, the initially published data of P-II, and on the right the data computed with the corrected PSO contribution (see text) and the CDFT variants of various density functionals are shown.

	$^{1}\mathrm{J}^{a}$	$^{2/3}\mathrm{J}^{a,b}$	$^{1}\mathrm{J}$	$^{2/3}\mathrm{J}^{b}$
TPSS	34.37	33.87	34.37	33.87
cTPSS	–	–	34.78	35.08
TPSSh	29.67	28.10	29.67	28.14
cTPSSh	–	–	30.05	29.45
B3LYP	22.94	21.89	22.95	21.87
PBE0	22.09	19.56	22.09	19.57
BHLYP	26.65	27.63	26.65	27.55
LH07t-SVWN	19.80	15.64	20.17	16.65
cLH07t-SVWN	–	–	20.27	16.92
LH12ct-SsirPW92	–	–	31.19	28.75
cLH12ct-SsirPW92	–	–	31.19	28.78
LH12ct-SsifPW92	31.70	28.23	32.26	29.34
cLH12ct-SsifPW92	–	–	32.23	29.26
LH14t-calPBE	15.38	16.27	15.77	17.49
cLH14t-calPBE	–	–	15.82	17.62
LH20t	–	–	17.90	22.79
cLH20t	–	–	17.75	22.41

[a] Reprinted original data published in P-II; [b] Couplings with absolute values smaller than 5 Hz have been excluded from the statistical evaluation.

with both definitions of the density matrix (with distinct differences in asymptotic and high density limits), see Fig. 5.3. For that reason, the main conclusions of P-II are still valid for the corrected scaling of the exact-exchange admixture. The original data is given in SI-II (the total SSCCs are reprinted in Tab. A.4). The corrected data for the same data set is given in Tabs. A.29 and A.30 of the present work.

5.4.2 Validation of NMR Spin–Spin Coupling Constants

The initial validation of SSCCs in the course of P-II was based on a mixed main-group benchmark set of MCSCF/BS2 and CC3/aug-ccJ-pVTZ levels of theory providing 80 SSCCs in 23 small main-group molecules, taken from Refs. 387 and 388.[c]

Within the main discussion of P-II, the MAPD of the ^{1}J and $^{2/3}$J SSCCs was provided as an initial assessment of the DFAs performance. Otherwise, the data of particularly challenging $^{1}\mathrm{J}_{\mathrm{CF}}$ coupling constants and their individual contributions was provided as an initial test for the newly implemented LHs. Besides these limited discussions in the main text, further aspects of the functionals performance have been outlined in a more detailed discussion in SI-II, reprinted in the present work in Sec. A.2.3.

[c] Throughout, SSCCs between nuclei K and L separated by n bonds are reported as $^{n}\mathrm{J}_{KL}$.

To summarize the main findings, (i) none of the provided models performs outstandingly for all SSCCs. However, the statistical mean, as provided in Tab. 5.3, revealed the comparatively broad accuracy of the t-LMF based LHs with lower EXX and the calibrated models within such main-group coupling constants. Furthermore, these LHs show a comparably robust performance, i.e. even in cases less well described the deviations are never among the worst performing methods. Therefore, such LHs outperform also established GH methods, which are frequently applied and have been shown to perform well compared to (approximate) wave-function based appraoches for (certain) SSCCs.[70,389,390] (ii) In the computation of the $^1J_{CF}$ couplings the FC contribution in many cases dominated the overall SSCCs (see also Ref.[71]) and the DSO contribution is usually small to negligible. However, also the PSO and SD contributions may become sizeable and decisively influence the overall performance of the DFAs. In particular, the PSO contribution for t-LMF-based LHs with higher exact-exchange admixture is outstandingly accurate. In comparison to established DFAs this results in SSCCs comparable to the quality of BHLYP, formerly found as the best performing DFA in the calculation of coupling constants involving fluorine (a more detailed discussion of these aspects is provided in P-II).[391]

As outlined above, these initial results for the LH functionals use an incorrect scaling of the exact-exchange admixture in the PSO contribution. For that reason, the corrected data for the employed functionals of P-II is presented in Tabs. A.29 – A.31 using the same computational settings as in the former calculations. However, the direct comparison of both data sets shows relatively small deviations in most SSCCs with a MAD below 0.5 Hz for all LH models. Again, this finding can be rationalized by noting the overall small PSO contributions in the SSCCs of the test-set data and the relatively small impact of the factorized density matrix on the final EXX (see above). Nevertheless, larger deviations of -63.5 Hz in $^2J_{FF}(OF_2)$, as well as 19.4 Hz and 31.1 Hz for the $^1J_{OF}$ couplings in OF_2 and OHF are observed for LH12ct-SsifPW92. However, on a relative scale these barely exceed 5 % in comparison to the reference value. The small overall deviations are also preserved for the $^1J_{CF}$ coupling constants, particularly for the individual PSO contributions, which in the original publication was traced as the source of the accurate performance of certain LH models. The related conclusions of the discussion within P-II therefore remain valid. The corrected data is shown in Tab. A.32.

In Tabs. A.29 – A.31 the CDFT versions of the kinetic-energy dependent LHs and meta-GGA functionals via τ_D are reported as well. These were not available at the time of P-II. The current contribution likewise enters just the PSO term due to the symmetry of the involved density matrices. Overall, small deviations are observed due to τ_D in the DFT

Table 5.4.: Mean signed (MSD), mean absolute (MAD) and maximum absolute deviations (MaxAD) in Hz of the DFT vs. CDFT (via τ_D) data sets for various density functionals.

	TPSS	TPSSh	07t	12sir	12sif	14t	LH20t
MSD	0.41	0.33	0.06	0.00(4)	-0.03	0.02	-0.06
MAD	1.69	1.53	0.39	0.13	0.22	0.12	0.65
Max.AD	56.5	49.0	10.0	1.8	4.7	2.4	16.8

[a] abbreviations 07t=LH07t-SVWN, 12sir=LH12ct-SsirPW92, 12sif=LH12ct-SsifPW92, 14t=LH14t-calPBE, respectively

vs. CDFT data and the relative performance is largely preserved, as shown by the mean statistical data provided in Tab. 5.3. However, a slight tendency of all methods except the LHs with larger exact-exchange admixture to larger deviations with respect to the reference data is observed upon inclusion of τ_D. Significant deviations in the SSCC data due to the presence of the current density in the PSO contribution are rare. This is also reflected in the MSD of the DFT vs. the CDFT variants (see Tab. 5.4), which is below 0.5 Hz in all employed functionals, for the LHs even significantly lower (between -0.06 Hz in LH20t and 0.06 Hz in LH07t-SVWN). The largest changes are again found for $^1J_{OF}$ SSCC in OHF and the SSCCs in OF_2. Interestingly (and different to shielding calculations, see below), the largest deviations are observed for the TPSS and TPSSh functionals (up to 56.5 Hz). In comparison, the maximum deviation of the LHs are observed for LH20t with a maximum of -16.8 Hz for the $^2J_{OF}$ in OF_2. However, on a relative scale, these changes barely exceed 5 % and the main conclusions of P-II also hold in case of the current-density correction within the PSO contribution.

Furthermore, the discussion of P-II lacks the analysis of the influence of the CFs, semi-local functionals and the choice between spin-channel and common LMFs.[d] To better understand some of these aspects, several LH models were modified separately, starting with the cLH07t-SVWN model. In a first step the original prefactor was increased from $a = 0.48$ to $a = 0.709$, matching the prefactor used in the cLH12ct-SsifWP92 functional. In a second step, the spin-channel LMF was replaced by a common-LMF, both for the smaller and the larger prefactor. These changes on the one hand allowed the study of the influence of the common vs. spin-channel variants of the LMF and of exact-exchange admixture, and on the other hand also probed the role of the short-range self-interaction corrected PW92 LSDA correlation in cLH12ct-SsifPW92 in comparison to VWN LSDA correlation in the modified cLH07t-SVWN version using the same admixture of exact exchange. The role of the CF was probed by switching off the pig1 and pig2 models in cLH14t-calPBE, and cLH20t. The uncalibrated variants are termed cLH14t-nc and

[d] Different to the shielding case (see below) the presence of the triplet operators in the FC and SD contributions generates a spin cross-term dependency via the common LMF (see Eq. 2.64)

Table 5.5.: Mean signed errors (MSE) in Hz from reference SSCC data of Refs. 387 and 388 for a variety of LH models (see text).

		c07t[a]	c07ct[a]	c07tx[a]	c07ctx[a]	c12sif[a]	c14t[a]	c14t-nc[a]	c20t[a]	c20t-nc[a]
MSE	$^{1}J_{HC}$	-6.43	-19.19	3.84	-17.12	-30.04	4.69	-0.14	-11.00	-4.51
	$^{1}J_{CC}$	0.60	-12.69	8.00	-14.27	-20.87	8.52	3.93	-4.45	-5.65
	$-^{1}J_{CO/CN}$	-6.73	-10.55	-2.34	-8.90	-10.50	-4.35	-6.95	-5.76	-5.98
	$^{1}J_{CF}$	-93.52	-81.19	-81.66	-62.74	-59.88	-96.39	-103.51	-59.70	-58.59
	$^{2}J_{HH}$	-0.90	2.52	-3.79	1.81	1.49	1.46	-1.21	2.06	2.85
	$^{2}J_{HC}$	0.08	0.91	-1.25	0.92	0.40	0.79	0.05	1.68	2.13
	$^{3}J_{HH}$	-0.49	-1.59	0.77	-1.39	-1.83	-0.26	0.07	-1.51	-1.05

[a] abbreviations of LH functionals c07t = cLH07t-SVWN, c12sif = cLH12ct-SsfiPW92, c14t = LH14t-calPBE, c20t = cLH20t; "t" vs. "ct" mark the spin-channel and common t-LMF, "x" denotes functionals with a non standard prefactor ($a = 0.709$), and "nc" is used for uncalibrated models.

cLH20t-nc. It is noted in passing, that the resulting cLH14t-nc is also a PBE analogue of the LH07t-SVWN, with just a slight difference in the LMF prefactor.

The evaluation of these changes uses a subset of the initial SSCC benchmark data, subdivided into individual classes of coupling constants (C–H, C–C, C–N/C–O, C–F and H–H), with at least 6 elements. Further statistical data is gathered in Tab. A.28, whereas here primarily the MSE of just the CDFT variants of the respective LHs is discussed, as shown in Tab. 5.5. Due to the negative gyromagnetic ratios of the ^{17}O and ^{15}N nuclei, the negative of the C–N/C–O coupling MSE were included for easier comparison.

Focusing on the spin-channel variant of cLH07t-SVWN first, the increase of the prefactor is observed to systematically increase the MSE (the negative MSE for C–N/C–O) for the ^{1}J couplings by 7-12 Hz (4.4 Hz for C–N/C–O). The agreement with the reference data does not change dramatically and only notably improves for C–F. An increased MSE is also observed for $^{3}J_{HH}$, changing the sign, while the two-bond couplings decrease, deteriorating somewhat agreement with the reference data. However, the same increase of the prefactor applied to the common t-LMF has a much smaller and non-systematic effect on all the one-bond couplings except for $^{1}J_{CF}$, which increase even more (by ca. 17 Hz) than for the spin-channel LMF (where it reduces absolute deviations). Effects on the $^{2/3}J$ couplings are much smaller than in the spin-channel case. This shows that $^{1}J_{CF}$ SSCCs behave distinctly different than the other ^{1}J coupling constants evaluated.

Directly comparing the spin-channel and common LMF variants for a given prefactor, the $^{1}J_{CH}$ and $^{1}J_{CC}$ MSEs as well as the negative of the MSE of $^{1}J_{CN/CO}$ are observed to decrease, even more so if a larger prefactor is employed. The MSEs in these cases become too negative, indicating a systematic underestimation of the corresponding SSCCs. Only the MSE for $^{1}J_{CF}$ increases (improving the agreement with the reference data), consistent with the distinctly different behavior identified for this type of coupling (see above). Furthermore, replacing the spin-channel with a common LMF increases the ^{2}J and decreases the ^{3}J couplings, whereas the size of the change again correlates with the chosen prefac-

tor. As mentioned above, it should be noted that the spin-channel and common LMFs are identical for closed-shell ground states and therefore reduce to the same models, e.g. in nuclear shielding calculations (see below). However, they affect the triplet response terms involved in SSCCs, i.e. the FC and SD contributions. It is often argued that the spin cross-terms introduced by the common LMFs introduce non-dynamical correlation to some extent, which lacks in the spin-channel LH models. In the present context, such terms seem particularly beneficial for the C–F couplings, reducing their systematic underestimate significantly, but at the same time they appear to cause also the deterioration of the other ^{1}J couplings.

The c07ctx functional model differs from cLH12ct-SsifPW92 only in the correlation functional, hence their comparison provides an estimate of the influence of such correlation models: replacing VWN by sifPW92 (see Eq. 2.72) further decreases the ^{1}J MSEs (-MSE for $^1J_{CN/CO}$), and provides a small increase for $^1J_{CF}$. As a result, the cLH12ct-SsifPW92 functional exhibits the most negative MSEs for all one-bond couplings, except C–F, for which the smallest deviation of the so far discussed functionals is observed (only topped by cLH20t, see below), however, with still a significant systematic underestimation in comparison to the reference data. The replacement of the correlation functional results also in somewhat smaller ^{2}J and ^{3}J couplings. Hence, the performance of cLH12ct-SsifPW92 can be rationalized by a combination of a common t-LMF with large prefactor (and thus local exact-exchange admixture) combined with its modified correlation functional. These aspects appear to be beneficial for the C–F couplings but also account for the observed systematic underestimate of the other SSCCs, which results in a mediocre performance in the overall evaluation as given in P-II (see also Tab. 5.3).

Finally, to inspect the influence of the CFs more closely, cLH14t-calPBE and cLH20t are compared with their uncalibrated variants. First, removing the CF in cLH14t-calPBE decreases all ^{1}J coupling MSEs (-MSE for $^1J_{CN/CO}$) by about 3-7 Hz, with a mixed impact on the agreement with the reference data (performance in H–C and C–C improves, but deteriorates in C–F and C–N/C–O). However, the ^{2}J coupling MSEs are decreased (with a change in the sign of the H–H coupling constant MSE), while the $^3J_{HH}$ are increased, yet the changes are smaller (between -2.7 Hz – 0.7 Hz). The cLH14t-nc functional is furthermore a close analogue of cLH07t-SVWN, replacing LSDA contributions in the latter by PBE exchange and correlation. However, differences in the MSEs of the ^{1}J couplings are moderate, with cLH07t-SVWN performing better for C–C and C–F couplings but worse for C–H couplings (C–N/C–O coupling MSEs are similar) and overall negligible in ^{2}J and ^{3}J coupling MSEs. Removing the CF in cLH20t, however, results in a moderate decrease of the $^1J_{HC}$ MSE (6.5 Hz) whereas the changes in the other ^{1}J, ^{2}J and ^{3}J coupling

MSEs are much smaller and range from -1.2 Hz to 0.8 Hz. It appears that the correction in cLH20t is smaller than in cLH14t-calPBE, i.e. it has a smaller impact on the resulting SSCCs.

5.4.3 Validation of NMR Shielding Constants

Initial Studies – P-I, P-III and P-IV The initial validation of LH functionals for shieldings in P-I (uncalibrated LHs), P-III (CDFT variants) and P-IV (calibrated LH models) used a smaller benchmark set compiled by Stoychev *et al.* based on GIAO-CCSD(T)/pcSseg-4 reference data,[13] containing 34 (8 ^{1}H, 7 ^{13}C, 5 ^{15}N, 6 ^{17}O, 5 ^{19}F and 3 ^{31}P) shielding constants in 15 molecules.

In that context P-I provided a limited set of LHs containing the first-generation, uncalibrated LSDA based approaches, LH07s-SVWN, LH07t-SVWN and the LH12ct-series of functionals in comparison to the HF method and a few common semi-local and GH functionals (such as BLYP, TPSS, TPSSh, B3LYP and BHLYP). The latter were also studied by Stochev *et al.* and therefore provided a basis of comparison of the newly implemented functionals.[13] This initial analysis of the LHs revealed (i) the s-lmf based LH07s-SVWN to show a comparable performance to the applied GH models and (ii) the t-LMF based models to perform comparably accurate, especially for the heavier nuclei of the test set, if a larger prefactor as in the LH12ct-functionals is chosen. However, (iii) the t-LMF based models showed a relatively large deviation in the application to ^{1}H shielding constants (also rising with the prefactor of the LMF), which at the time was attributed to the shape of the mixing function when approaching the hydrogen along the bond axis (see Fig. 2.1). It was then argued that the interplay of the steep increase in connection with a large prefactor may deteriorate the results in such cases.

However, in the course of P-III four different models for the kinetic-energy density, including the explicitly current-dependent τ_D (Eq. 3.87) were revisited and applied in connection with meta-GGAs and other τ-dependent functionals such as the LHs. This approach revealed that the deviations of the t-LMF based LH functionals described in P-I can be traced to spurious artefacts (caused by a arising orbital-rotation operator, see also in Sec. 5.2) due to the formerly implemented τ_{MS}-model. An analysis of these artefacts was attempted in terms of atomic systems such as helium and neon (see Tab. 1 in P-III), and the $\sigma_{\parallel}^{p}$-components of the paramagnetic contribution to the shielding tensors in a set of linear diatomic molecules (see Tab. 2 in P-III). Comparably large deviations were found not only in the LHs (increasing with the prefactor) but also in the M06-L and M06 functionals, while TPSS and TPSSh were much less affected. However, the model provided

by Maximoff and Scuseria was the first approach to implement meta-GGA functionals in a gauge-independent way and is the standard approach in many quantum-chemical calculation packages such as GAUSSIAN or (before the present work) TURBOMOLE. Another aspect which was already noticed in P-I, but clearly rationalized not until P-III, was the much better performance of the TPSS and M06-L functionals in Ref. 13 compared to the τ_{MS}-data provided in P-I, which was due to an ad-hoc corrected version of τ within the ORCA program code.

Evaluation of the τ_D-dependent shielding constants for a similar set of (τ-dependent) functionals as in P-I revealed a significant increase of the performance of the cLH12ct-series of functionals. For these a decrease of the MAE and StD was observed, accompanied by an increase of the MSE (still the lowest of the tested methods). Similarly, the performance of the cLH07t-SVWN functional in ^{1}H shieldings improved. This was, however, accompanied by a slight decrease of the description of the heavier nuclei. Finally, a significant increase in the StD of the CDFT variant of the formerly well performing meta-GGA M06-L was observed. This was attributed to error compensation of the non-current dependent models of the kinetic energy density within this highly parametrized semi-empirical functional. Other meta-GGAs, such as TPSS or TPSSh, were much less affected by different choices for the kinetic energy density. As a result of these deviations, the cLH12ct-series of functionals (cLH12ct-SsirPW92, and cLH12ct-SsifPW92 performed overall very similar) were now the top performers of the tested methods for the small shielding benchmark set.

Within P-IV the analysis was then extended to the calibrated LH functionals cLH14t-calPBE and cLH20t, which showed an excellent overall performance of the calibrated models for ^{1}H shielding constants, and a comparable performance in the heavier nuclei (i.e. ^{13}C and heteronuclei such as ^{15}N, ^{17}O, ^{19}F and ^{31}P provided in the test-set) for the calibrated models and the uncalibrated LHs with a similar prefactor. However, a slight offset of the calibrated models was observed. While this makes the cLH12ct-series of functionals still the best choice for heavier nuclei, in a simultaneous calculation of multiple nuclei including hydrogen cLH20t was observed as the probably most robust choice.

Drawbacks of the small test set employed within these initial analyses are the potential dominance of a few shielding constants in the statistical evaluations. This was exemplified by the exclusion of PN from the statistical data (see Fig. 1 in P-IV), as this particular molecule is a major challenge for typical DFAs due to its significant (static-)correlation contribution.[35] Furthermore, the small sample of data complicates reliable statistical measures for the individual nuclei. To construct a statistically meaningful test set, the combination of previously compiled reference data (see e.g. Refs. 13,35–39,64,392 for

shielding and Refs. 62,65–67 for shift data sets) has been considered. However, such an approach suffers from the inconsistent description of the benchmark data as well as the implicit need to carefully trace errors due to the chosen methods and basis sets (in optimization, shielding and corresponding shift calculations, respectively). The magnitude of such deviations can be estimated from the data collection of Tabs. S4 and S5 in SI-V (see also Tabs. A.10 and A.11), which shows that especially the effect due to optimized structures can amount to deviations of several ppm.

Systematic Validations – P-V and P-VI As reported in P-V, a benchmark data set of consistent quality was compiled for validation of main-group shieldings and shifts. Throughout, structure optimization was based on CCSD(T)/cc-pVQZ calculations (partly also CCSD(T)/cc-pVTZ structures were computed for comparison) and shielding constants on GIAO-CCSD(T)/pcSseg-3 calculations (for a significant subset additional GIAO-CCSD(T)/pcSseg-4 data was provided). Finally, the benchmark comprised 372 evaluated shieldings constants (124 ^{1}H, 15 ^{11}B, 93 ^{13}C, 43 ^{15}N, 33 ^{17}O, 49 ^{19}F, 14 ^{31}P, and 6 ^{33}S) and shifts, respectively.

In Sec. 5.1 and 5.2 of P-V, the residual error of the test-set data was carefully estimated by assessing the basis-set and method errors (see also S4 and S5 in SI-V). Furthermore, the reliability of the single-reference benchmark data was analysed by suitable diagnostic tools to exclude severe multi-reference cases (see S3 in SI-V). Further estimates of relativistic (spin-orbit) contributions were provided by four-component calculations for a subset of molecules. These, however, play no role in the direct QM-QM (i.e. QM=quantum mechanic) comparison at the non-relativistic limit as provided throughout P-V (and would become important just in case of QM-experiment comparisons). Due to the exclusive computational benchmark data, also the estimation of vibrational and environmental effects was circumvented, which likewise would become important for direct comparison to experimental data.

To furthermore include electronically challenging test-set data, a benchmark of 3d transition-metal (TM) nuclei was constructed, as published within P-VI, using a combination (and partly extension) of data sets of the systematic studies by Bühl *et al.*[393–400] Due to the size of the systems and significant static-correlation contributions, a wave-function based approach to construct the reference data was not pursued in this case. The data set contains 70 evaluated complexes (12 ^{49}Ti, 10 ^{51}V, 10 ^{53}Cr, 11 ^{55}Mn, 9 ^{57}Fe, 9 ^{59}Co and 9 ^{61}Ni nuclei) with carefully selected experimental reference data (see Tab. S1 of SI-VI; data not shown in the present thesis). It should be noted, that due to the direct comparison with experimental shifts, further steps were included to validate the comparability of the calculated vs. experimental reference data: these steps include careful estimates of

solvent and environmental effects, including an estimate of the donor properties of organic solvents such as acetonitrile (see Sec. S3 in SI-VI, reprinted in Sec. A.5.1), as well as (scalar-)relativistic effects (see Sec. S6 in SI-VI, or Sec. A.5.2 of the present work). Furthermore, in the original publications partly truncated model system were included and the influences of the truncated vs. full ligand systems have been estimated carefully (see Sec. S7 of SI-VI, reprinted in Sec. A.5.3). Also, the choice of the reference standard for the calculation of NMR shifts (see Eq. 3.6) was analyzed. A "best estimate" approach via the y-intercept of the linear regression of computed shielding constants at a given level against the experimental shift data was employed (comparisons of statistical data using either a referenced or the y-intercept approach are provided in Sec. S8 of SI-VI, reprinted in Tabs A.17 – A.19 in Sec. A.5.4 of the present work). Further steps in the preparation of the data set included the unification of the optimized structures and the careful estimation of the residual errors due to the chosen DFT approach in the optimization. However, a negligible effect on the relative statistics throughout the employed DFAs was observed for different approaches for the input structure (a plot of the statistical data and selected data sets of the shift results with different input structures are included in Sec. S2 in SI-VI, in the context of this work only the plot of the statistical data is reprinted, see Fig. A.5). Also, the influence of triplet instabilities was estimated. These were traced to become severe for methods with large EXX (and subsequently are the reason for a very poor performance of MP2 and the DHs), but were shown to be of lower importance for typical DFAs (see Sec. S4 in SI-VI, reprinted in Sec. A.5.6).

In P-V, 45 methods and density functionals were included. These comprise Hartree–Fock, MP2, CCSD and DFAs from all rungs of Perdew's ladder such as semi-local functionals, GHs, RSHs, LHs and DHs (see also the set of DFAs and methods outlined in Sec. 5.1). Of these, 41 were also evaluated within the TM test set of P-VI, excluding only the regularized and re-regularized SCAN models (which in P-V were observed to perform fairly similar to SCAN) as well as B2GP-PLYP (due to the overall poor performance of DHs) and CCSD (too computationally demanding). Furthermore, in both studies the four different models for τ, as outlined in P-III, were included for meta-GGAs and other functionals dependent on the kinetic energy density. Within the main studies, the focus was on the current-dependent τ_D. However, the performance of the widely applied τ_{MS} as well as the COM and ad-hoc corrected models of the kinetic energy density were also compared (see the related discussions in the contexts of Fig. 3 of P-V and Fig. 4 of P-VI). Furthermore, estimates of the paramagnetic artefacts due to τ_{MS} by means of iso-electronic diamagnetic TM ions and atoms (see Tab. 1 of P-VI) were included in P-VI, similar to the data provided in P-III.

This resulted in 111 individual data sets in the main-group benchmark (not counting shieldings and shifts individually) and 101 data sets for the TM benchmark, respectively. The analyses in both studies contained averaged statistical measures, in the case of P-V for shieldings and shifts (see the discussions in connection with Figs. 1 and 4 of P-V as well as Fig. 1 of P-VI). Furthermore, both studies contained analyses of the performances regarding the individual nuclei (see the corresponding sections within the publications as well as Secs. S1 and S2 in SI-V, reprinted in Secs. A.4.1 and A.4.2 of the present work). As a measure for robustness the maximum errors have been included (see Fig. 1 in P-V and Sec. S3 in SI-V (reprinted in Sec. A.4.4 and the related Fig. A.2) as well as Sec. S5 in P-VI (reprinted in Sec. A.5.7 and Fig. A.6)). Furthermore, in P-VI the role of exact exchange was discussed in detail, providing further insights into the performance of individual DFAs with regard to the nuclei of the benchmark set (see Figs. 2 and 3 and the related discussion in P-VI).

Collecting common results from both studies: strikingly, CDFT meta-GGAs and LHs such as cB97M-V and cmPSTS provide an outstanding accuracy and relative robustness over the range of nuclei and partly challenging test cases presented in the benchmark data of P-V and P-VI. Also the calibrated LH models cLH14t-calPBE and cLH20t provide a similar performance. For the latter functionals, only the ^{53}Cr subset is an exception, which was shown to be notoriously sensitive to EXX and therefore error margins comparable to common GH functionals are observed for these LH models.

A few more functionals were identified with an overall robust performance, but showed already larger error margins in either one or both subsets. These are DFAs such as the HCTH and B97D GGAs, which in both studies were typically more accurate than older functionals of the same rung (e.g. BLYP or PBE). Furthermore, CDFT meta-GGAs such as cM06-L or cVSXC combined a relatively stable performance in the main-group data, with an outstanding performance in the TM benchmark set. Within this category also GHs and RSHs such as cTPSSh, B97-2, ωB97X-V and ωB97M-V, as well as the first-generation LSDA based cLH07t-SVWN can be collected, which are among the best hybrid functionals in both benchmark sets. However, these DFAs are typically already outperformed by CDFT meta-GGAs and also the best CDFT LH functionals. It is also noteworthy that cTPSSh (similar to cmPSTS) is more accurate for shifts than shieldings due to a pronounced error compensation. Furthermore, of the tested GHs B3LYP was observed to be the best for the transition-metal benchmark set due to a successful balance of the individual subset errors (while it is less successful in main-group shieldings and shifts). To a lesser extent, also the t-LMF based cLH12ct-series of functionals can be included within this group as these performed comparable to typical

GHs within the TM benchmark, but were outstandingly accurate within the main-group test set. In particular, the cLH12ct-SsifPW92 provided the overall best relative MAE for the main-group shielding data and within the ^{19}F test set performed similar to the best DH functionals of the set.
As a next category, DFAs and methods are collected with an outstanding performance in one of the benchmark sets, but clearly larger error margins in the other. This category includes the specialized KT series of functionals, which were parametrized with shieldings and shifts in mind, but trained using main-group species. Likely for that reason, their good performance within the main-group test set was not preserved in the TM test-set data, where these functionals were outperformed by common GGAs. Also cMN15-L was very accurate in the evaluation of P-V but had to be excluded from closer statistical evaluation of the TM benchmark due to its extremely large error margins. MP2 and the DHs, particularly DSD-PBEP886, provide overall outstanding results in the main-group case (in fact DSD-PBEP86 is the best functional up to rung 5 for the main-group benchmark). Nevertheless, due to triplet instabilities (and significant static correlation that is not properly reproduced), these methods are largely useless for the calculation of TM shifts. Another drawback of MP2 and the DHs is the high computational cost due to the perturbation-dependent correlation contribution.
Some functionals are less well to categorize. One example is BHLYP, which on the one hand performs remarkably accurate for some main-group nuclei such as ^{1}H or ^{19}F. On the other hand, it shows large error margins in the TM benchmark set due to significant triplet instabilities (except the less critical nuclei such as ^{49}Ti or ^{51}V) and a mediocre performance considering the combined statistical measures for the main-group benchmark set.
Finally, methods which cannot be recommended for general use in shielding and shift computations are largely comprised of GHs with larger exact-exchange admixture, such as the Minnesota series of functionals (M06, M06-2X and MN15). These DFAs were commonly observed among the methods with the largest error margins in P-V and P-VI.

5.5 Application to ^{19}F Shifts

On the basis of the systematic validation of various DFAs and wave-function based methods, the comparably high robustness and accuracy of various LH models in the application for NMR properties was shown (see also the conclusions below). Especially the cLH12ct-series of functionals were observed to perform remarkably well for ^{19}F shieldings (even on par with the tested DH functionals) and, e.g., C–F SSCCs. This predestines these functionals also in the application to fluorine-specific problems. Such applications were

carried out in P-VII and P-VIII. The present summary of these aspects focuses on the contributions conducted by the author within these collaborative works.

In the initial study in P-VII, the NMR shifts of a set of fluorohalogenates ($[XF_n]^-$ with X=Cl, Br, I and $n = 2, 4, 6$) were calculated to support the experimental conclusions with regard to the synthesis of the individual species. However, while the deviations of the computational results with respect to the experimental data were within the expected error margins of the benchmark of P-V for the four- and six-coordinated species, much larger deviations were observed in case of two-coordinated $[XF_2]^-$ (see Tab. 1 of P-VII, and Tabs. S3 and S4 of SI-VII, reprinted in Tabs. A.22 and A.23).

Therefore, in P-VIII the solvent-induced ^{19}F shifts were analyzed in detail for a set of fluorine containing compounds, including the initial $[ClF_2]^-$ and $[ClF_4]^-$ (the latter to provide a comparison of a less affected system) as well as $[FHF]^-$ and the fluoride anion (F^-). Throughout P-VII, experiments were conducted in acetonitrile. The solvent-solute interactions of the two-coordinated species, as well as of the fluoride and bifluoride anions, were significantly underestimated by implicit solvent modeling via COSMO (published in P-VII, see Tabs. S3 and S4 in SI-VII, reprinted in Tabs. A.22 and A.23), D-COSMO-RS and the three-dimensional reference interaction site model (3D-RISM; those calculations were not conducted by the author). This is why the corresponding NMR shifts were far from the experimental reference results. Therefore, up to 12 explicit acetonitrile molecules were added successively to the calculations. For the resulting micro-solvated clusters between 2–8 ($[ClF_2]^-$, $[ClF_4]^-$), 8–9 (F^-) and up to 10 ($[FHF]^-$) explicit CH$\cdots$F hydrogen bonds were observed within the CREST and DFT optimized systems (see Tab. S1 of SI-VIII, reprinted in Tab. A.24), close to the results which were also suggested by the 3D-RISM model. It was shown that the number of formed hydrogen bonds correlates with the solvation free energy, which in turn correlates with the strength of the formed bonds due to the negative charge on fluorine ("charge-assisted hydrogen bond"). Subsequent calculations of the ^{19}F NMR shifts revealed a significant solvent shift of 50-60 ppm for $[ClF_2]^-$, about 80 ppm in $[FHF]^-$ and up to 227 ppm for the micro-solvated F^- (see Tab. S4 in SI-VIII, reprinted in Tab. A.25).

Further analysis of two model systems ($[F(MeCN)_8]^-$ and a symmetrically coordinated water cluster $[F(H_2O)_6]^-$) showed that the solvent shifts are induced by charge transfer from the anion to the solvent molecules. Within the acetonitrile micro-cluster this primarily involves the σ^*(C–H) MOs (schematically shown in Fig. 3 of P-VIII). This charge transfer was furthermore observed to induce a distinct red-shifted fingerprint in the infrared spectrum of (computationally) high intensity for the C–H stretching mode (see Fig. 4 of P-VIII) in comparison to a $(MeCN)_8$ cluster system. In spite of the overall higher

experimental and computed solvation free energy in water compared to acetonitrile, the experimental and computed solvent effect on the ^{19}F shifts in the latter solvent is found to be larger. This was traced back in the analyses to arise from the overall larger average number of hydrogen bonds (ca. 8–9 in acetonitrile compared to ca. 4–5 in water).

5.6 Conclusions and Outlook

In the present work, the derivation, implementation and validation of local hybrid functionals for the calculation of NMR properties, such as shieldings and spin–spin coupling constants, was reported. It was shown that despite the presence of a local mixing function within the LHs, an efficient implementation is possible on the basis of semi-numerical integration. In comparison to standard global hybrid functionals, such an approach results in just a small increase of the prefactor of the pre-loop section within the CPKS equations caused by the unavoidable presence of the perturbed two-center A-matrix integrals. If calibrated LHs are included, higher derivatives of the density, such as the Laplacian and Hessian, are additionally required. However, the derivation and implementation was shown to be straightforward and with a negligible additional computational burden.
Initial validation using small benchmark sets for shieldings constants revealed the comparably accurate and robust performance of LHs. However, an unexpectedly large error margin for relatively small and electronically less challenging species was detected. These deviations were observed in particular for the t-LMF dependent LH functionals with an implicit dependence on the kinetic energy density and were finally traced to unphysical paramagnetic artefacts caused by the Maximoff–Scuseria model for the gauge-correction of τ in the presence of a magnetic field. It was furthermore shown that these artefact are not exclusively present in LH functionals, but can also be observed in other functionals with a dependence on τ. The impact on the overall performance is, however, significantly different. For that reason, the gauge corrections of τ were revisited and a physically motivated model proposed by Dobson (τ_D) was implemented. Using τ_D, no artefacts as for τ_{MS} were observed and subsequently the deviations in the initial LH models were reduced significantly. The model also renders the functionals implicitly current dependent. Hence, the implementation of τ_D also enabled the first CPKS-based self-consistent evaluation of common meta-GGA functionals and methods dependent on the kinetic-energy density in the CDFT framework via τ_D.
For spin–spin coupling constants, the final equations are similar to those derived in the LH-TDDFT framework, which was exploited for the FC and SD contributions. Adaptations were only required for the PSO contribution. However, due to its resemblance to the

paramagnetic contribution in NMR shieldings, its implementation was relatively straight forward and could be based on routines previously implemented in the course of this work. The initial validation of SSCCs revealed a comparably accurate and robust performance of the t-LMF based LHs with lower exact-exchange admixtures, as well as the calibrated models, also on par with the best performing alternative DFAs on the challenging $^1J_{CF}$ coupling constants. It was later observed, that an erroneous prefactor had been included in the initial implementation. However, the impact on the results was small and the respective discussion and conclusions of P-II hold for the corrected data set. The analysis of the current-dependent DFAs via τ_D in the PSO contribution revealed a small impact on the resulting SSCC data, likely due to the small overall contribution of the term in comparison to the total SSCCs.

A detailed analysis of the influencing factors of the performance of the LHs revealed a significant impact of the inclusion of non-dynamical correlation within the SSCC calculations, as it affects the often dominant FC (and also SD) contributions. Also, a significant sensitivity to exact-exchange admixture was observed. As in LHs the exact-exchange admixture is controlled by the LMF, this sensitivity suggests further research into potentially better suited mixing functions with an enhanced performance. However, the initially employed test set comprised just a small number of SSCCs. In particular, a statistically still too small number of data points for the individual coupling constants was provided. Further evaluation with larger benchmark data sets might therefore sharpen the presented analyses and help to draw a conclusive picture on the capability of the DFAs, the impact of the current contributions and further aspects of the LHs such as semi-local ingredients, CFs or the LMFs.

The performance in NMR shielding and shift calculations was assessed in two large benchmark studies for main-group as well as 3d transition-metal nuclei. Each of the test sets contained the largest combined benchmark data for shieldings and shifts to date and thus allowed for an unprecedentedly detailed validation of the applied methods and DFAs. The set of 3d transition-metal shifts was based on experimental data and combined to a large extent earlier sets of individual nuclei, but treated computationally at a consistent level. The new, unprecedentedly large and diverse NS372 main-group shielding/shift benchmark, however, is based on newly generated, extremely demanding but accurate coupled-cluster calculations carried out by the author.

Remarkably, several CDFT meta-GGAs and LHs are among the most robust and best performing functionals and methods for the combined test-set data and are hence also frequently found among the most accurate methods for individual nuclei. Such an outstanding performance was also exploited in the analysis of solvent-induced NMR shifts in

a set of small fluorine-containing compounds, which further illustrates the applicability of these newly implemented LHs. However, as for SSCCs above, throughout the validation studies a significant dependence of the performance on the chosen semi-local ingredients and, more importantly, LMFs was observed, which suggests further research along these lines.

Finally, the comparably accurate performance of the LHs in NMR shieldings and SSCCs also suggests the extension of the implementation to NMR-parameters for open-shell species, which to date is not yet provided in TURBOMOLE. Moreover, further properties in the context of magnetic resonance, such as magnetizabilities, could be explored in order to gain further insights into the performance of the LHs and potential future pathways of their development. Overall, this work has provided advances in DFT methodologies to compute NMR parameters that should be useful when aiming at the complete first-principles-based prediction and evaluation of NMR spectra.

6 Contributing Publications

I

C. J. Schattenberg, K. Reiter, F. Weigend and M. Kaupp,
"*An Efficient Coupled-Perturbed Kohn–Sham Implementation of NMR Chemical Shift Computations with Local Hybrid Functionals and Gauge-Including Atomic Orbitals*",
J. Chem. Theory Comput., **2020**, *16*, 931–943.
DOI: 10.1021/acs.jctc.9b00944

JCTC Journal of Chemical Theory and Computation

pubs.acs.org/JCTC Article

An Efficient Coupled-Perturbed Kohn–Sham Implementation of NMR Chemical Shift Computations with Local Hybrid Functionals and Gauge-Including Atomic Orbitals

Caspar Jonas Schattenberg, Kevin Reiter, Florian Weigend, and Martin Kaupp*

Cite This: J. Chem. Theory Comput. 2020, 16, 931–943 Read Online

ACCESS | Metrics & More | Article Recommendations | Supporting Information

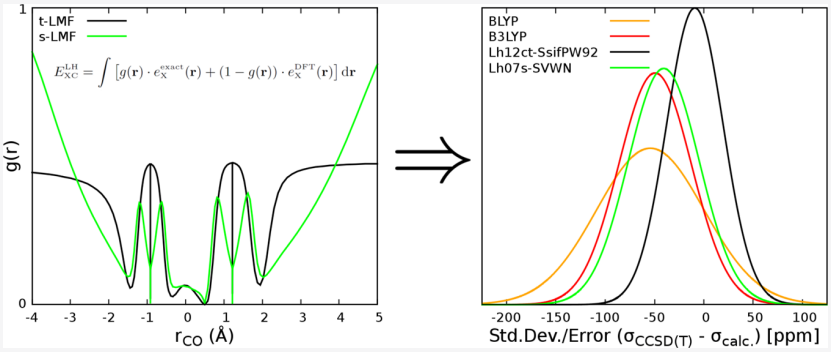

ABSTRACT: Nuclear shielding calculations for local hybrid (LH) functionals with position-dependent exact-exchange admixtures within a coupled-perturbed Kohn–Sham (CPKS) framework have been implemented into the TURBOMOLE code using efficient seminumerical integration techniques to deal with two-electron integrals. When using gauge-including atomic orbitals, LHs generate additional terms within the "pre-loop" section of the CPKS scheme compared to global hybrid (GH) functionals, related to perturbed electron-repulsion integrals. These terms have been implemented and tested in detail, together with dependencies on grid sizes and integral screening procedures. Even with relatively small grids, a seminumerical treatment of GHs reproduces analytical GH results with high accuracy while improving scaling with system and basis-set sizes significantly. The extra terms generated by LHs in the pre-loop part increase the scaling of that contribution slightly, but the advantages compared to the analytical scheme are largely retained, in particular for the typically large basis sets used in NMR shift calculations, allowing for a very efficient computational scheme. An initial comparison of four first-generation LHs based on LDA exchange for a shielding test set of 15 small main-group molecules against high-level CCSD(T) benchmark data indicates a substantial reduction of the systematically underestimated shieldings compared to semilocal functionals or GHs for non-hydrogen nuclei when a so-called t-LMF is used to control the position dependence of the exact-exchange admixture. In contrast, proton shieldings are underestimated with this LMF, while an LH with a so-called s-LMF performs much better. These results are discussed in the context of experience for other properties, and they suggest directions for further improvements of LHs regarding nuclear shieldings.

1. INTRODUCTION

The fundamental importance of NMR spectroscopy in many areas of natural science and the central role that chemical shifts often play in the characterization of chemical compounds can hardly be overemphasized. It is therefore natural that the quantum-chemical computation of nuclear shieldings and thus of NMR chemical shifts has become an important tool in the hands of researchers in various fields, for example, in catalysis research, biophysics, or materials sciences. In this context, Kohn–Sham density functional theory (KS-DFT) is the most widely used approach, given its favorable scaling with system size compared to more sophisticated post-Hartree–Fock methodologies[1] (see ref 2 for a review of the latter). However, the accuracy of DFT calculations depends crucially on the approximate exchange-correlation (XC) functional used. Nuclear shieldings are quite sensitive in this context. While DFT is widely used to compute them, limitations in accuracy have been documented and discussed (see, e.g., refs 1, 3, 6. and the references therein). Standard functionals are known to often underestimate absolute shieldings, in particular for systems with smaller excitation energy gaps.[3,7,8] Efforts toward improved performance for nuclear shieldings involved initially

Received: September 24, 2019
Published: January 3, 2020

https://dx.doi.org/10.1021/acs.jctc.9b00944
J. Chem. Theory Comput. 2020, 16, 931–943

some ad hoc corrections[9−12] and subsequently the use of hybrid functionals with a constant exact-exchange (EXX) admixture[4,13,14] (in the following termed "global hybrids", GHs) or explicit empirical parametrization of semilocal functionals for shieldings.[15,16] While GHs and parametrized functionals like Tozer's KT2 or KT3 may improve performance[15−17] over simpler semilocal functionals in some cases, they are by no means a panacea for improving upon the limited accuracy of DFT for sensitive shielding cases,[18,19] and some highly parametrized GHs in fact perform poorly for core-related properties.[17,20] While range-separated functionals are particularly popular for other linear-response properties such as TDDFT excitation energies, they also so far have not been found to be a notable improvement.[21,22] Double hybrid functionals, which contain a fraction of MP2 correlation, have been screened for the nuclear shieldings of a set of small main-group molecules.[23] Double hybrids performed very well in comparison to CCSD(T) benchmark data, but the MP2 part in combination with large basis sets and gauge-including atomic orbitals (GIAOs) renders the computational effort of such calculations rather demanding.

One likely origin for the deficiencies of approximate DFT in the computation of shieldings is the neglect of induced current terms in the XC functional. As has been demonstrated recently based on functionals extracted from accurate densities,[18] the neglected current terms are typically shielding (except possibly for a small negative contribution to proton shieldings). Their contributions reached up to 11 ppm for the ^{13}C shielding in CO and 13 ppm for the ^{15}N shielding in N_2. The importance of such current terms had been suspected earlier and had been used to justify the use of EXX admixture in hybrid functionals as exact nonlocal Hartree−Fock exchange does provide a current response.[24] The studies in ref 18 analyzed also individual contributions to the dia- and paramagnetic shielding parts and emphasized errors of typical XC functionals in the core region as well as error cancellation between these two parts (for example, in the empirical KT2 functional). Unfortunately, the current corrections in ref 18 require CCSD(T) computations and an extraction of KS-orbitals from the coupled-cluster densities, and they can thus be applied only to small molecules for benchmark purposes.

The present work will focus on yet another type of hybrid functionals, so-called local hybrids (LHs) with a position-dependent EXX admixture.[25] An enhanced EXX admixture of LHs in the core region near nuclei can address, to some extent, the description of core densities, and the non-local exchange may alleviate the errors from the neglected current terms. The potentially good performance of LHs for core-related properties has been demonstrated recently for hyperfine coupling constants[20] and for core excitations at the TDDFT level,[26] albeit the local mixing functions (LMFs) used to control the position dependence were still of rather modest complexity and most of the LHs studied were based on LDA exchange. It seems nevertheless clear that LHs should provide a possible way forward toward improved nuclear shieldings given that suitable implementations become available. Such an implementation is the purpose of the present work, which details the development and implementation of a coupled-perturbed Kohn−Sham (CPKS) treatment of nuclear shieldings with LHs within a generalized KS framework (i.e., using nonlocal Hartree−Fock exchange) with GIAOs. We had earlier attempted to use approximations to the multiplicative and local optimized-effective potential (OEP) of exact exchange to arrive at an uncoupled KS perturbation theory for nuclear shieldings for GHs[27] and LHs.[28] However, it was later found for GHs that the usual approximations to the OEP (including the localized Hartree−Fock approach used in refs 27, 28) are not of a sufficient quality for subtle response properties like shieldings.[29−33] The only previous CPKS treatment of magnetic properties for LHs in a generalized KS framework has been done for g-tensors.[34] Implementation in that case benefited from the use of a common gauge origin that removed most of the additional terms arising for LHs. For nuclear shieldings, the use of GIAOs or other distributed-gauge treatments is mandatory, and we thus derive and implement the CPKS terms in the GIAO basis using seminumerical integration techniques to obtain an efficient code. We report the implementation into the mpshift module of the TURBOMOLE[35] program code and provide a preliminary evaluation of computed shifts with LHs for some typical test sets.

2. THEORY

2.1. Local Hybrid Functionals. Replacing the constant amount ($0 \le a_0 \le 1$) of EXX admixture in GHs

$$E_{XC} = \sum_{\sigma} \{a_0 E_X^{ex} + (1 - a_0) E_X^{sl}\} + E_C^{sl} \tag{1}$$

by a position-dependent admixture in LHs,[36] governed by the LMF $g_\sigma(\mathbf{r})$, gives the form[25]

$$E_{XC}^{LH} = \sum_{\sigma} \int [g_\sigma(\mathbf{r}) e_{X,\sigma}^{ex}(\mathbf{r}) + (1 - g_\sigma(\mathbf{r}))(e_{X,\sigma}^{sl}(\mathbf{r}) + G_\sigma(\mathbf{r}))]\mathrm{d}\mathbf{r} + E_C^{sl} \tag{2}$$

E_C^{sl} represents some semilocal correlation contribution to the energy, and $e_{X,\sigma}^{sl}$ and $e_{X,\sigma}^{ex}$ are the (spin-resolved) semilocal and exact-exchange energy density, respectively. $e_{X,\sigma}^{ex}$ is constructed from a set of occupied molecular spin orbitals $\{\varphi_{i,\sigma}\}$

$$e_{X,\sigma}^{ex}(\mathbf{r}) = -\frac{1}{2} \sum_{ij} \varphi_{i,\sigma}^{*} \varphi_{j,\sigma} \int \frac{\varphi_{j,\sigma}^{*} \varphi_{i,\sigma}}{|\mathbf{r} - \mathbf{r}'|} \mathrm{d}\mathbf{r}' \tag{3}$$

$G_\sigma(\mathbf{r})$ represents the so-called calibration function (CF), having the property $\int G_\sigma(\mathbf{r})\mathrm{d}\mathbf{r} = 0$. The CF accounts for the ambiguity of the exchange-energy densities (the so-called gauge problem).[37] Proper introduction of a CF to provide a better match between the semilocal and exact-exchange energy density[38] reduces gauge-related spurious nondynamical correlation contributions and notably improves upon weak noncovalent interactions.[37,39,40] In this first CPKS implementation of nuclear shieldings with LHs, we neglect the CF. We therefore also restrict our initial evaluations to LDA-based "uncalibrated" LHs only. An implementation for calibrated exchange-energy densities, which requires derivatives with respect to the density Hessian and Laplacian in the CPKS scheme, will be reported elsewhere. We note in passing that initial tests for hyperfine couplings suggested an only modest influence of calibration for such core-related properties.[20] We note also that the present work deals with closed-shell systems only, and thus any distinctions between "spin-channel" and "common" LMFs[25,41] are irrelevant for the purpose of the present work.

While the number of different LMF forms suggested has increased over the past years,[25] in this initial assessment, we

https://dx.doi.org/10.1021/acs.jctc.9b00944
J. Chem. Theory Comput. 2020, 16, 931−943

will mainly focus only on two simple types: (a) so-called "t-LMFs" based on the scaled ratio of the von Weizsäcker kinetic energy density and the Pauli kinetic energy density[36,42,43]

$$g_\sigma(\mathbf{r}) = a\cdot\frac{\tau_{W,\sigma}(\mathbf{r})}{\tau_\sigma(\mathbf{r})}, \quad \tau_\sigma = \frac{1}{2}\sum_i \nabla\varphi_{i,\sigma}^*\nabla\varphi_{i,\sigma}, \quad \tau_{W,\sigma} = \frac{\nabla\rho_\sigma\nabla\rho_\sigma}{8\cdot\rho_\sigma} \tag{4}$$

and (b) an "s-LMF"[44] formulated as

$$g_\sigma(\mathbf{r}) = \mathrm{erf}(b\cdot s_\sigma), \quad s_\sigma = \frac{1}{k}\frac{\nabla\rho_\sigma}{\rho_\sigma^{4/3}}, \quad k = 2(3\pi^2)^{1/3} \tag{5}$$

where $\rho_\sigma = \sum_i \varphi_{i,\sigma}^*\varphi_{i,\sigma}$ is the electron density. a and b are the adjustable parameters of t- and s-LMFs, respectively ($0 \le a \le 1$ and $0 \le b \le 1$), typically optimized for thermochemistry and reaction barriers (see explicit parametrizations in the Computational Details below).

2.2. Extension of the Coupled-Perturbed Equations for Nuclear Shieldings to Local Hybrid Functionals. The theory background of the coupled-perturbed Hartree−Fock equations and their extension to GHs can be found in detail elsewhere.[1,5,45] As a basis for the formulation of the CPKS scheme for LHs, we only introduce the main aspects and the notation. The nuclear shielding tensor $\boldsymbol{\sigma}$ (not to be confused with the spin label σ) may be identified as the second derivative of the energy with respect to the magnetic field $\mathbf{B}$ and the nuclear magnetic moment of nucleus K, $\mathbf{m}^K$,

$$\sigma_{kl}^K = \left.\frac{\mathrm{d}^2E}{\mathrm{d}B_k\mathrm{d}m_l^K}\right|_{B_k=m_l^K=0}, \quad k,l = x,y,z \tag{6}$$

For a variational wave function describing the unperturbed closed-shell ground state (GS), this mixed derivative may be written in terms of the GS density matrix in the atomic-orbital (AO) basis, $D_{\mu\nu} = 2\sum_i c_{\mu i}^* c_{\nu i}$, as

$$\sigma_{kl}^K = \sum_{\mu\nu}\left[D_{\mu\nu}\frac{\mathrm{d}^2H_{\mu\nu}}{\mathrm{d}B_k\mathrm{d}m_l^K} + \frac{\mathrm{d}D_{\mu\nu}}{\mathrm{d}B_k}\frac{\mathrm{d}H_{\mu\nu}}{\mathrm{d}m_l^K}\right]_{B_k=m_l^K=0} \tag{7}$$

where $H_{\mu\nu}$ is an element of the molecular Hamiltonian in the same basis. We require the first-order response of the density matrix (and hence of the wave function) to solve for $\boldsymbol{\sigma}$. This response is constructed from the perturbed coefficients, which in turn are expressed in terms of unperturbed states, weighted by expansion coefficients $u_{ia}^{B_k}$,

$$c_{\mu i}^{B_k} = \sum_a u_{ia}^{B_k} c_{\mu a} \tag{8}$$

The expansion coefficients may be obtained from direct differentiation of the Brillouin condition or of the Roothaan−Hall equations, which leads to the coupled-perturbed equations (CPE)

$$u_{ia}^{B_k} = \frac{F_{ia}^{B_k} - \varepsilon_i S_{ia}^{B_k}}{\varepsilon_i - \varepsilon_a} \tag{9}$$

where $F_{ia}^{B_k}$ is the derivative of the Fock matrix (in the MO basis) with respect to the magnetic field. For a local and multiplicative KS potential (i.e., in the absence of nonlocal Hartree−Fock exchange or of current contributions to the XC potential), the CPE may be solved in one step as they are uncoupled. For the Hartree−Fock method or for hybrid functionals, the corresponding potential depends implicitly on the expansion coefficients $u_{ia}^{B_k}$, and the iterative CPHF or CPKS scheme is required. We will use GIAOs to deal with the gauge dependence in a finite basis set[46−48]

$$\omega_\mu[\mathbf{r},\mathbf{B}] = \phi_\mu(\mathbf{r})\exp\left[-\frac{i}{2c}(\mathbf{B}\times\mathbf{R}_\mu)\mathbf{r}\right] \tag{10}$$

where ϕ_μ is an atom-centered basis function with its center at position $\mathbf{R}_\mu$.

Usually, we consider derivatives with respect to GIAO pairs

$$[\omega_\mu^*\omega_\lambda]^{B_k}\Big|_{B_k=0} = \frac{i}{2c}[\mathbf{R}_{\mu\nu}\times\mathbf{r}]_k\phi_\mu\phi_\nu \tag{11}$$

where $\mathbf{R}_{\mu\nu} = \mathbf{R}_\mu - \mathbf{R}_\nu$ is the distance vector between the two basis functions ϕ_μ and ϕ_ν.

In the following, we (mostly) suppress spin labels for the sake of simplicity as we deal with closed-shell systems only. Equation 9 contains the derivative of the Fock matrix with respect to the magnetic field. As the Fock matrix depends on the HF or generalized KS potential V^{XC}, as well as on the exact-exchange admixture (a_0 for a GH, $g_\sigma(\mathbf{r})$ for an LH, see eqs 1 and 2), these derivatives clearly depend on the functional used. For LHs, the derivative (marked by superscript B) may be expressed as

$$[F_{ij}^{\mathrm{LH}}]^{\mathbf{B}} = [h_{ij} + J_{ij} + V_{ij}^{\mathrm{LH,XC}}]^{\mathbf{B}} \tag{12}$$

where exact exchange is part of the exchange-correlation potential $V_{ij}^{\mathrm{LH,\,XC}} = V_{ij}^{\mathrm{LH,\,XC}}[\rho, e_{\mathrm{X}}^{\mathrm{ex}}]$ as we mix energy densities (see eq 2) rather than integrated energy quantities. Note that the Coulomb term contributes only due to the use of GIAOs and would vanish otherwise for the direct derivative with respect to the magnetic field.[49] Dropping the dependencies on coordinate $\mathbf{r}$, the LH exchange-correlation potential in the AO basis reads:[25]

$$V_{\mu\nu}^{\mathrm{LH,XC}} = -\frac{1}{2}\int g\cdot\sum_{\kappa\lambda} D_{\kappa\lambda}(\phi_\kappa\phi_\nu\mathbf{A}_{\mu\lambda} + \phi_\mu\phi_\lambda\mathbf{A}_{\kappa\nu})\mathrm{d}\mathbf{r} + \int[1-g]\hat{d}_{\mu\nu}e_{\mathrm{x}}^{\mathrm{sl}}\mathrm{d}\mathbf{r} + \int\hat{d}_{\mu\nu}e_{\mathrm{C}}^{\mathrm{sl}}\mathrm{d}\mathbf{r} + \int d_{\mu\nu}g\cdot[e_{\mathrm{X}}^{\mathrm{ex}} - e_{\mathrm{X}}^{\mathrm{sl}}]\mathrm{d}\mathbf{r} \tag{13}$$

introducing the $\mathbf{A}$ matrix

$$\mathbf{A}_{\mu\nu}(\mathbf{r}) = \int\frac{\phi_\mu(\mathbf{r}')\phi_\nu(\mathbf{r}')}{\mathbf{r}-\mathbf{r}'}\mathrm{d}\mathbf{r}' \tag{14}$$

as well as the potential operator

$$\hat{d}_{\mu\nu} = \sum_{Q\in\mathcal{Q}}\int\frac{\partial Q(\mathbf{r}')}{\partial D_{\mu\nu}}\frac{\partial}{\partial Q(\mathbf{r}')}\mathrm{d}\mathbf{r}' \tag{15}$$

where $\mathcal{Q} = \{\rho, \nabla\rho, \tau, ...\}$ is a set of all quantities considered in the LMF or LH of choice (a detailed description may be found in ref 25).

Next, we have to evaluate the direct derivatives of the potential with respect to the Cartesian components of the magnetic field $\mathbf{B} = (B_x, B_y, B_z)$

https://dx.doi.org/10.1021/acs.jctc.9b00944
J. Chem. Theory Comput. 2020, 16, 931−943

$$[V_{\mu\nu}^{\mathrm{LH,XC}}]^{\mathbf{B}} = -\frac{1}{2}\sum_{\kappa\lambda}\int \{gD_{\kappa\lambda}^{\mathbf{B}}(\omega_\kappa^* \omega_\nu A_{\mu\lambda} + \omega_\lambda^* \omega_\mu A_{\kappa\nu}) + gD_{\kappa\lambda}(\omega_\kappa^* \omega_\nu A_{\mu\lambda} + \omega_\lambda^* \omega_\mu A_{\kappa\nu})^{\mathbf{B}}\}\mathrm{d}\mathbf{r} + \int (\hat{d}_{\mu\nu} g)^{\mathbf{B}} \cdot [e_{\mathrm{XX}} - e_{\mathrm{X}}^{\mathrm{sl}}]\mathrm{d}\mathbf{r} + \int (1-g)(\hat{d}_{\mu\nu} e_{\mathrm{X}}^{\mathrm{sl}})^{\mathbf{B}}\mathrm{d}\mathbf{r} + \int (\hat{d}_{\mu\nu} e_{\mathrm{C}}^{\mathrm{DFT}})^{\mathbf{B}}\mathrm{d}\mathbf{r} \tag{16}$$

The first two lines represent the EXX contribution to the potential, multiplied by the LMF prefactor, relatable to the somewhat simpler, well-known CPKS scheme for GHs. The first line represents the exchange response involving the perturbed wave function (via the perturbed density matrix), which contributes to the coupling terms of the CPKS scheme. Exchange and correlation energy densities do not depend directly on the magnetic field and contribute to the response Fock matrix only via their contributions to the perturbed potential terms (see lines four and five). The same holds for the LMF, which itself does not depend on the perturbation but contributes as part of an additional perturbed potential term (lines three and four). The latter contributions may be viewed as arising from a nondynamical correlation (NDC) term, the second term on the RHS of 17. This is a rewritten formulation of the LH energy functional (without a CF, see above)[50,51] where this NDC term corrects 100% exact exchange (first term) and is combined with the dynamical correlation (third term):

$$E_{\mathrm{XC}}^{\mathrm{LH}} = E_{\mathrm{X}}^{\mathrm{ex}} + \sum_\sigma \int [(1 - g_\sigma(\mathbf{r})) \times (e_{\mathrm{X},\sigma}^{\mathrm{sl}}(\mathbf{r}) - e_{\mathrm{X},\sigma}^{\mathrm{ex}}(\mathbf{r}))]\mathrm{d}\mathbf{r} + E_{\mathrm{C}}^{\mathrm{sl}} \tag{17}$$

The LMF or the semilocal XC contributions may depend on the kinetic energy density, which is not a priori gauge invariant. Following ref 52, we restore the gauge independence by using the finite-external-field kinetic energy density

$$\tilde{\tau} = \sum_{\mu\nu} D_{\mu\nu}\left(i\nabla + \frac{1}{c}\mathbf{A}\right)\omega_\mu \cdot \left(-i\nabla + \frac{1}{c}\mathbf{A}\right)\omega_\nu \tag{18}$$

rather than the zero-field kinetic energy density τ ($\mathbf{A} = \frac{1}{2}\mathbf{B} \times \mathbf{r}$ is the vector potential).

Line 2 in eq 16 contains the exact-exchange contribution arising from the ground-state density $D_{\mu\nu}$, giving

$$K_{\mu\nu,g}^{\mathbf{B}}[D] = -\frac{1}{2}\int \sum_{\kappa\lambda} gD_{\kappa\lambda} \cdot \{(\omega_\kappa \omega_\nu)^{\mathbf{B}} A_{\mu\lambda} + \omega_\kappa \omega_\nu \mathbf{A}_{\mu\lambda}^{\mathbf{B}} + \ldots\}\mathrm{d}\mathbf{r} \tag{19}$$

(shown here only for the first set of indices).

Due to the presence of the LMF, we may not simply interchange the integration indices and sum up as we also change the position of the LMF ($g_\sigma(\mathbf{r}) \rightarrow g_\sigma(\mathbf{r}')$ for $\mathbf{r} \rightarrow \mathbf{r}'$).

That is, the perturbed $\mathbf{A}$ matrix has to be computed explicitly. For example, we find for the x component of the perturbed $\mathbf{A}$ matrix (using eqs 10 and 11)

$$A_{\mu\nu,g}^{B_x} = \frac{i}{2c}\left(R_{\mu\nu,y}\int z \cdot \frac{[\phi_\mu \phi_\nu]}{|\mathbf{r}_g - \mathbf{r}|}\mathrm{d}\mathbf{r} - R_{\mu\nu,z}\int y \cdot \frac{[\phi_\mu \phi_\nu]}{|\mathbf{r}_g - \mathbf{r}|}\mathrm{d}\mathbf{r}\right) = \frac{i}{2c}(R_{\mu\nu,y}(A_{\mu\nu,g}^{m+1} + R_{\mu,z}A_{\mu\nu,g}) - R_{\mu\nu,z}(A_{\mu\nu,g}^{k+1} + R_{\mu,y}A_{\mu\nu,g})) \tag{20}$$

and analogous results for the other components (see Section S3 in the Supporting Information for more details).

Note that $z - R_{\mu,z} = z_\mu$ is just a Cartesian prefactor of a given Gaussian primitive (indicated by the superscripts m for the z component and k for the y component).[53] Hence, the remaining integrals over $\mathrm{d}\mathbf{r}$ (the $\mathbf{A}$ as well as the $\mathbf{A}^{\mathbf{B}}$ matrices) can be solved straightforwardly by standard techniques involving incremented l quantum numbers. The perturbed $\mathbf{A}$ matrices are furthermore exclusively connected to the unperturbed density matrix as only the first-order response has to be considered. We therefore have to solve them only once before the CPKS iterations. The additional effort for LHs compared to GHs is thus limited to the "pre-loop part".

2.3. Seminumerical Integration Techniques. We and others have found seminumerical integration techniques to be uniquely suited to implement LHs[54−58] as the LMF contributions in an LH are readily included. Seminumerical schemes like RIJ-COSX,[59] which are a simplification of Friesner's so-called pseudospectral methods,[60] in addition offer general scaling advantages for exact-exchange integration also for GHs and post-Hartree−Fock methods as the approach scales formally as $n \cdot N_{\mathrm{bas}}^2$ compared to an N_{bas}^4 scaling of analytical four-center integrals (n is the number of grid points and N_{bas} the number of basis functions). In general, seminumerical methods replace the outer integration of two-electron integrals by quadrature on a set of (weighted) grid points, while the inner integration is done analytically (these two-center electron repulsion integrals constitute the $\mathbf{A}$ matrix that has to be computed at each grid point). We note in passing that the nuclear-shielding implementation for GHs in the ORCA code uses RIJ-COSX.[59] Here, we will follow the notation of our SCF and TDDFT implementations of LHs (see refs 54, 56). The underlying basic equations are provided in the Supporting Information (eqs S5−S9) so that here we can focus exclusively on the additional equations needed for the CPKS treatment of nuclear shieldings in a GIAO basis.

Due to the derivation of the GIAOs wrt the magnetic field B_k ($k = x, y, z$), three additional perturbed $F_{\kappa,g}$ matrices involving the GIAO prefactor

$$F_{\kappa,g}^{B_k} = \frac{i}{2c}\sum_\lambda \sqrt{w_g} \cdot D_{\kappa\lambda}(\mathbf{R}_\lambda \times \mathbf{r})_k \phi_{\lambda,g} \tag{21}$$

and six perturbed $G_{\nu,g}$ matrices

$$G_{\nu,g}^{B_k} = \sum_\kappa A_{\nu\kappa,g} F_{\kappa,g}^{B_k} \tag{22}$$

$$G_{\nu,g}^{\mathbf{A}^{B_k}} = \sum_\kappa A_{\nu\kappa,g}^{B_k} F_{\kappa,g} \tag{23}$$

have to be constructed.

In contrast to the symmetric unperturbed $\mathbf{A}$ matrices, the perturbed $\mathbf{A}$ matrices are skew-symmetric (as are the perturbed density matrices). However, due to the presence of the perturbed density, we additionally have to construct $\mathbf{F}$ matrices depending on $D_{\mu\nu}^{\mathbf{B}}$

$$F_{\kappa,g}^{D^{B_k}} = \sum_\lambda \sqrt{w_g} \cdot D_{\kappa\lambda}^{B_k} \phi_{\lambda,g} \tag{24}$$

as well as the resulting $\mathbf{G}$ matrices

$$G_{\nu,g}^{D^{B_k}} = \sum_\kappa A_{\nu\kappa,g} F_{\kappa,g}^{D^{B_k}} \tag{25}$$

https://dx.doi.org/10.1021/acs.jctc.9b00944
J. Chem. Theory Comput. 2020, 16, 931−943

$F_{\kappa,g}^{D^{B_k}}$ and, hence, $G_{\nu,g}^{D^{B_k}}$ only contribute within the CPKS loop, while the other **F** and **G** matrices (eqs 21−23) only need to be evaluated once before the iterations.

2.3.1. Integral Screening (S-, P-, and F-Junctions). The timing of the seminumerical procedure is determined by the calculation of the **A** matrix elements, and savings in the computational effort are possible by prescreening of **A** matrix elements using so-called S-junctions (based on an overlap criterion of spherical shells) and P-junctions (based on density matrices contracted with the basis-function vectors to the **F** matrices),[59] as well as F-junctions (based on an integral estimate in the asymptotic limit, as recently proposed in ref 61). We follow the S-junction criteria of ref 54. Regarding both the P- and F-junctions, we need to screen not only unperturbed but also perturbed **F** matrices. This screening is done once before the CPKS iterations and takes into account $F_{\mu,g}$ (eq S7) and $F_{\mu,g}^{B_k}$ (eq 21). For the P-junctions, **A** matrix elements are neglected if all (non-weighted) values of F ($F_{\mu,g}$ and $F_{\mu,g}^{B_k}$) are below the given threshold, while for elements with negligible $F_{\mu,g}$ but non-negligible $F_{\mu,g}^{B_k}$, at least the calculation of the perturbed **A** matrix can be skipped for the given grid-point batch (saving more than with unperturbed matrices due to the incremented angular momentum). In the case of the F-junctions, computation of the current grid batch is skipped if the contraction of an asymptotic integral estimate and the maximum value $F_{\mu,g}$ (considering $F_{\mu,g}$ and $F_{\mu,g}^{B_k}$) of that grid batch is below the chosen threshold.

Within the CPKS loop, the (non-weighted) elements $F_{\kappa,g}^{D^{B_k}}$ are probed, and again the evaluation of the **A** matrix for the given grid-point batch may be skipped if all values are below the threshold. In principle, the same holds for the F-junctions. These considerations show that different thresholds may be suitable in the pre-loop (P- and F-junctions) and in the loop (PL- and FL-junctions, respectively) parts of the CPKS scheme as the magnitudes of $D_{\mu\nu}$ and $D_{\mu\nu}^{\mathbf{B}}$ may differ significantly (see Section 4 for more details).

2.4. Implementation. Starting from the most recent GH shielding implementation in TURBOMOLE,[62] adjustments for LHs and for seminumerical integration of GHs have been made. We distinguish in the following between those contributions to the perturbed Fock matrix that depend on the perturbed density (i.e., the contributions obtained iteratively) and those we have to calculate just once (pre-loop). The first pre-loop contributions come from the LMF-weighted exact exchange, treated seminumerically (see above). After computing the perturbed **A** matrices according to eq 20, this contribution is calculated as

$$K_{\mu\nu}^{B_k}[D] = -\frac{i}{4c}\sum_{\kappa\lambda}\sum_{g} w_g g_g \cdot [\phi_{\nu,g}(G_{\mu,g}^{B_k} + G_{\mu,g}^{A^{B_k}}) - \phi_{\mu,g}(G_{\nu,g}^{B_k} + G_{\nu,g}^{A^{B_k}}) + (R_\mu \times \mathbf{r})_k \phi_{\mu,g} G_{\nu,g} - (R_\nu \times \mathbf{r})_k \phi_{\nu,g} G_{\mu,g}] \quad (26)$$

For $g(\mathbf{r}) = a_0 = \text{const}$, we obtain the GH seminumerical scheme

$$K_{\mu\nu}^{B_k}[D] = -\frac{i}{2c}a_0\sum_{\kappa\lambda}\sum_{g} w_g \cdot [\phi_{\nu,g} G_{\mu,g}^{B_k} - \phi_{\mu,g} G_{\nu,g}^{B_k} + (R_\mu \times \mathbf{r})_k \phi_{\mu,g} G_{\nu,g} - (R_\nu \times \mathbf{r})_k \phi_{\nu,g} G_{\mu,g}] \quad (27)$$

which does not require the evaluation of perturbed **A** matrices.

The second additional pre-loop contribution arises from the LMF-weighted semilocal exchange part. Here, the direct derivatives of the LMF do not contribute. The semilocal correlation contributions are in any case unaltered and not shown here. Overall, the additional contributions to the Fock matrix read:

$$F_{\mu\nu}^{\mathrm{XC},\mathbf{B}} = \sum_{Q\in\mathcal{Q}} \int \mathrm{d}\mathbf{r}\left\{\left[\frac{\partial g}{\partial Q}(e_{\mathrm{X}}^{\mathrm{ex}} - e_{\mathrm{X}}^{\mathrm{sl}}) + \frac{\partial e_{\mathrm{X}}^{\mathrm{sl}}}{\partial Q}(1-g)\right]\left[\frac{\partial Q}{\partial D_{\mu\nu}}\right]^{\mathbf{B}}\right\}, \quad \text{with} \quad \mathcal{Q} = \{\rho, \nabla, \tau, ...\} \quad (28)$$

$\mathcal{Q}$ contains all quantities occurring in the LMF and in the semilocal exchange functional. Having multiplied the derivatives of the LMF with respect to those quantities by the difference between exact and semilocal exchange-energy densities, as well as the derivative of the semilocal exchange by $1 - g$, we are left with the evaluation of the perturbed orbital pairs, which are comparable to standard DFT routines (if the set $\mathcal{Q}$ does only involve the density, the gradient of the density, and the kinetic-energy density), as outlined in detail elsewhere.[52]

The GIAO contribution arising from the Coulomb term remains unaltered (cf. the recent update to include the MARI-J[62] approximation for this term).

Within the loop section, we finally have to account for the LMF-weighted EXX contribution depending of the perturbed density $D_{\mu\nu}^{\mathbf{B}}$

$$K_{\mu\nu}^{B_k}[D^{B_k}] = -\frac{1}{2}\sum_{\kappa\lambda}\sum_{g} w_g g_g \cdot [\phi_{\mu,g} A_{\nu\kappa} D_{\kappa\lambda}^{B_k} \phi_{\lambda,g} - \phi_{\nu,g} A_{\mu\lambda} D_{\lambda\kappa}^{B_k} \phi_{\kappa,g}] \quad (29)$$

Here, the analytical integration is replaced by the seminumerical integration scheme, leaving the other program segments (e.g., the construction of the perturbed density matrix from the expansion coefficients) unaltered.

3. COMPUTATIONAL DETAILS

The above equations have been implemented into a local developers' version of the TURBOMOLE program package, release 7.3.[35] Computational efficiency has been tested on a single CPU core (Intel(R) Xeon(R) CPU X5650 @2.67GHz, and TURBOMOLE has been compiled using Intel Fortran Compiler version *ifort 17.0.2-20170213*). All calculations have used the RI-J approximation in the SCF-calculation, with energy convergence criteria set to 10^{-9} a.u., as well as the MARI-J approximation for the GIAO Coulomb shielding contribution,[62] with shift convergence (convergence of the Euclidean norm of the residual vectors) set to 10^{-7}.

Throughout this work, we use standard TURBOMOLE integration grids (Lebedev angular grids and Chebyshev radial grids), constructed as outlined in ref 63 using Becke partitioning.[64] Table 1 provides the grid definitions. The first column gives the standard settings (grid size X = 1, 2, 3, 4, 5), except for the largest grid where additionally the keyword "radsize 25" was employed to enlarge the radial Chebyshev grid. For some parts of the algorithm, we also examined very small non-standard grids marked as grid −1 and grid 0.

Timings and scaling with system and basis-set sizes of the shielding computations have been evaluated comparing seminumerical treatments of LHs (eq 26) and GHs (eq 27)

https://dx.doi.org/10.1021/acs.jctc.9b00944
J. Chem. Theory Comput. 2020, 16, 931−943

Table 1. TURBOMOLE Grid Settings[a]

setting	angular pts.	radial pts.
−1[b]	50	10 (H−He)
		15 (Li−Ne)
		20 (Na−Ar)
		≡(10/15/20)
0[b]	50	(15/20/25)
1	110	(20/25/30)
2	194	(25/30/35)
3	302	(30/35/40)
4	434	(40/45/50)
5	590	(55/60/65)
7/25	1202	(140/145/150)

[a]"Angular" is synonymous for Lebedev grids with the indicated grid points, while "radial" grids use the indicated number of Chebyshev grid points, depending on atom type (illustrated for grid −1). [b]Non-standard grid settings; see text for details.

to the existing analytical GH implementation of the code. In these comparisons, the TPSSh GH[65] and the Lh07t-SVWN LH[42] were used. The effects of prescreening (S-, P-, F-, PL-, and FL-junctions) on efficiency and accuracy have been evaluated for the all-*trans* $C_{10}H_{12}$ polyene (all-*trans* decene).

Performance comparison of different XC functionals is done for a small set of 15 molecules (overall 34 shielding values) taken from ref 59 (structures are also taken from that work) against benchmark CCSD(T) data for ^{1}H, ^{13}C, ^{15}N, ^{17}O, ^{19}F, and ^{31}P nuclei. As in that work, extended pcSseg-4 basis sets are used.[66] In addition to LHs (see below), we include BLYP[67,68] as an example for a GGA functional, TPSS as meta-GGA,[69] and the GHs TPSSh,[65] B3LYP,[70] and BHLYP,[71] (providing 10, 20, and 50% EXX admixtures, respectively), as well as Hartree−Fock (HF) calculations. On the LH side, for this initial comparison, we include the simple LDA-based functionals Lh07s-SVWN[44] (s-LMF, eq. 5, b = 0.22) and Lh07t-SVWN[42] (t-LMF, eq. 4, a = 0.48). Functionals Lh12ct-SsirPW92[41] and Lh12ct-SsifPW92[41] use t-LMFs (a = 0.646 and a = 0.709, respectively) with PW92[72] correlation modified to reduce or eliminate, respectively, short-range self-correlation. Statistical measures employed are mean signed errors (MSEs), mean absolute errors (MAEs), and standard deviations (SDs) (see eqs S1−S3 in the Supporting Information).

4. ACCURACY AND EFFICIENCY OF THE IMPLEMENTATION

Before going into an assessment of grid dependencies, we note that we have carefully evaluated for GH and HF calculations that seminumerical EXX integration with (eq 26) and without (eq 27) accounting for perturbed **A** matrices gave identical results and data in excellent agreement with the standard analytical EXX integration (data are provided in Table S1 in the Supporting Information). Additionally, gauge independence of the implementation has been confirmed by rotation and translation of a simple test system for both global and local hybrids (cf. Supporting Information, Table S2 for the structures and Table S3 for full results).

4.1. Dependence of Accuracy and Efficiency on Grid Sizes. As the efficiency of the seminumerical scheme benefits from using smaller grids, we need to evaluate the accuracy and efficiency achieved with different grid sizes (cf. Table 1 for the TURBOMOLE grid settings used). This is done at the Lh07t-SVWN/pcSseg-4 level for the full set of 15 molecules described in the Computational Details. Evaluations for the ground-state SCF and for the pre-loop part of the CPKS scheme compared standard grid sizes 1−5 as the same grid is used here for the seminumerical integration of two-electron integrals and for the integration of semilocal functionals (where we cannot afford to reduce the grid size further[59]). Within the loop section where no semilocal functionals are integrated, we also evaluate still coarser grids denoted grid 0 and grid −1. Convergence of the density matrix is set to 10^{-7} a.u. in these evaluations. Following ref 59, throughout this work, we report ^{1}H and ^{13}C results separately from those for the other nuclei (^{13}N, ^{17}O, ^{19}F, ^{31}P) to account for the somewhat different shielding ranges covered. Accuracy is measured against an extremely large grid (grid 7/25, see above). Effects of grid size on accuracy and efficiency for the different parts of the code were screened independently for each part of the code while keeping the large grid 5 for the other two parts.

Deviations from the super-large grid 7/25 results are plotted in Figure S2 in the Supporting Information (see also Tables S5−S7 for detailed evaluations). The accuracy converges very quickly with increasing grid sizes. Already for the combination of the smallest grid 1 for SCF and the pre-loop part and grid 0 for the loop part, ^{1}H shieldings deviate only by an MAE of 0.001 ppm, ^{13}C shieldings by 0.041 ppm, and the other nuclei by 0.097 ppm (see Table S8 in the Supporting Information). That is, any of the grid combinations evaluated, except the use of grid −1 in the loop part, provides clearly sufficient accuracy compared, for example, to errors arising from different functionals. The possibility of using such relatively small grids does of course aid the efficiency of the computations compared to the standard analytical integration scheme for GHs. This gain in computational efficiency for smaller grid sizes is shown in Figure 1 for timings of a typical shielding

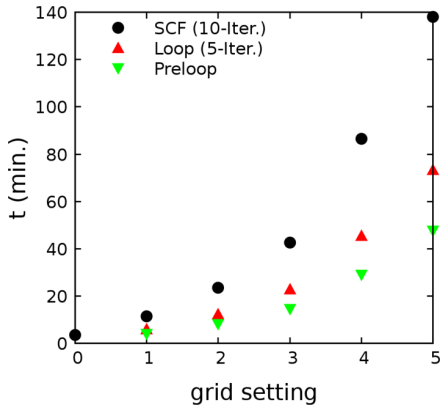

Figure 1. Grid dependence of the timings of different parts of the code for the calculation of shieldings for $C_{10}H_{12}$ in a def2-TZVP basis using the Lh07t-SVWN functional.

computation on $C_{10}H_{12}$ in a def2-TZVP basis, assuming 10 SCF cycles and a typical value of 5 CPKS iterations. General timing comparisons of different approaches are provided further below.

4.2. Effects of Integral Screening. As S-, P-, F-, PL-, and FL-junctions can be used to further speed up the seminumerical integrations (see the Implementation section), we need to evaluate their influence on the accuracy. This is done

https://dx.doi.org/10.1021/acs.jctc.9b00944
J. Chem. Theory Comput. 2020, 16, 931−943

by varying individually the threshold for one type of junction while not screening by the other criteria (and using grid 5). Results are shown in Table 2 (see Tables S9–S14 in the Supporting Information for more detailed evaluations). Even at very loose thresholds for the S- and P-junctions, deviations are similarly small as discussed above for the grid errors. Only if we choose extremely large values of 10^{-2} for S- and P-junctions, we get larger errors and even convergence failure in some cases. Regarding the F-junctions, reasonable accuracy seems to be afforded at a threshold of 10^{-6}, but since we expect F-jupctions to affect larger systems more strongly, we suggest 10^{-7} as a reasonable lower cutoff. Tighter thresholds are required for the CPKS loops (PL- and FL-junctions). For the PL-junctions, 10^{-5} is needed to arrive at similarly small errors as obtained with 10^{-3} P-junction settings in the pre-loop part. For the FL-junctions, convergence can only be guaranteed for thresholds of 10^{-9}. This reflects the fact that in the CPKS loop part, we screen the (much smaller) perturbed density matrices.

Table 2. Mean Absolute Shielding Errors (in ppm) Caused by Different Screening Thresholds for S-, P-, F-, P-Loop-, and F-Loop-Junctions (PL/FL) for the Full Set of 15 Small Molecules and Total CPU Times and Deviations from Unscreened Results Using Grid 5 (Lh07t-SVWN/def2-TZVP) for $C_{10}H_{12}$

	$\Delta\sigma_{av.}$			$\Delta\sigma_{max}$		
type	^{1}H	^{13}C	other	^{1}H	^{13}C	other
S-Junc.						
2	partly unconverged results					
3	0.000	0.024	0.024	0.001	0.114	0.094
4	0.000	0.001	0.005	0.000	0.006	0.038
5	0.000	0.000	0.000	0.000	0.000	0.000
P-Junc.						
2	0.102	2.851	6.558	0.274	11.619	34.570
3	0.003	0.070	0.203	0.011	0.286	0.930
4	0.000	0.001	0.004	0.000	0.005	0.016
5	0.000	0.000	0.000	0.000	0.000	0.000
PL-Junc.						
3	partly unconverged results					
4	0.016	1.537	3.935	0.036	4.505	12.538
5	0.007	0.069	0.326	0.010	0.295	1.103
6	0.001	0.002	0.013	0.002	0.009	0.056
7	0.000	0.000	0.000	0.000	0.000	0.002
F-Junc.						
4	0.048	1.035	1.261	0.106	3.865	7.334
5	0.021	0.250	0.419	0.080	0.812	2.027
6	0.007	0.064	0.117	0.028	0.185	0.421
7	0.002	0.015	0.025	0.006	0.036	0.090
8	0.000	0.003	0.005	0.001	0.007	0.020
9	0.000	0.001	0.001	0.000	0.002	0.004
FL-Junc.						
8	partly unconverged results					
9	0.001	0.012	0.028	0.002	0.019	0.081
10	0.000	0.003	0.006	0.001	0.005	0.018
11	0.000	0.001	0.001	0.000	0.001	0.004

$C_{10}H_{12}$	MAE ^{1}H	MAE ^{13}C	time [s]
unscreened			9009
high thresh.[b]	0.005	0.024	6376
low thresh.[b]	0.022	0.075	5426

[b]Thresholds are as follows: (i) low S-/P-j. 10^{-3}, PL-j. 10^{-5}, F-j. 10^{-7}, FL-j. 10^{-9}; (ii) high S-/P-j. 10^{-4}, PL-j. 10^{-6}, F-j. 10^{-8}, FL-j. 10^{-10}

Settings 10^{-4} for S- and P-junctions, 10^{-8} for F-junctions, 10^{-6} for PL-junctions, and 10^{-10} for FL-junctions guarantee essentially converged results if we aim at MAEs close to 0.001 ppm for ^{1}H shieldings and at approximately 0.01 ppm for the other nuclei. Combining these settings in the same calculation leads to closely similar deviations (see Table S15 in the Supporting Information). We may use even more aggressive thresholds by up to one order of magnitude (10^{-3} for S- and P-junctions, 10^{-7} for F-junctions, 10^{-5} for PL-junctions, and 10^{-9} for FL-junctions). The resulting somewhat lower accuracy will likely still be reasonable for many applications. Comparison of the higher and lower settings for $C_{10}H_{12}$ (bottom of Table 2) indicates significant speedups while conserving good accuracy (see Table S16 in the Supporting Information for more detailed evaluations). In the following, we will use 10^{-4} for S- and P-junctions, 10^{-8} for F-junctions, 10^{-6} for PL-junctions, and 10^{-10} for FL-junctions as standard thresholds (marked as high threshold).

4.3. Overall Timings. Starting with the basis-set dependence for ethylene as an example for a small molecule, Figure 2 compares analytical and seminumerical treatments for a GH (TPSSh) and the seminumerical scheme for an LH (Lh07t-SVWN) as a function of increasing the basis set within the TURBOMOLE def2-X (X = SVP, TZVP, TZVPD, QZVP, QZVPD) and Dunning's cc-pVXZ, aug-cc-pVXZ, and d-aug-cc-pVXZ (with X = D, T, Q, 5) families (grid 1 for the pre-loop and grid 0 for the loop part have been used). Presentation on a logarithmic scale helps to evaluate scaling with basis-set size (linear fits were done on the logarithmized data set). Consistent with similar evaluations for TDDFT calculations of excitation energies[56] and as expected from the theoretical underpinnings,[59] these plots reveal roughly N^2 scaling of both pre-loop and loop timings with basis-set size in the semi-numerical schemes compared to an N^4 scaling for the analytical GH computations. Additional efforts for the LH compared to the GH in the seminumerical scheme, pertaining to perturbed **A** matrices (cf. Section 2), occur only in the pre-loop part. For the given (small) molecule, these contributions increase the scaling exponent of the pre-loop part very slightly, while the prefactor obtained in the fit is even slightly lower (likely due to the effect of F-junctions). This leads to a somewhat earlier crossover with basis-set size compared to the analytical treatment of GHs for GHs than for LHs (Figure 2), but only moderately so. The CPKS iterations are not affected. Note that the crossover is observed for basis sets of double to triple zeta quality, which is near or below the lower limit of basis sets required for accurate shielding computations (see Figure S1 in the Supporting Information).[5]

Moving on to the dependence on system size, we use a "worst-case scenario" for seminumerical integration in comparison to analytical four-center integrals[56] by looking at polyene chains (the same set of all-*trans* $C_{2n}H_{2n+2}$; $n = 1 - 10$ as discussed above) with moderate def2-TZVP basis sets. Such linear systems are best suited for standard integral screenings in the analytical scheme while offering no advantages for seminumerical integration. Figure 3 shows CPU times for full NMR shielding calculations (normalized to 5 CPKS iterations, while for $n = 2 - 6$, usually 3 to 4 iterations suffice for convergence) obtained with the standard grid and the high-threshold screening settings discussed above. As expected from the above basis-set studies, the semi-numerical scheme outperforms the analytical one even for very short chains and increasingly so for longer ones, when looking at the TPSSh

https://dx.doi.org/10.1021/acs.jctc.9b00944
J. Chem. Theory Comput. 2020, 16, 931−943

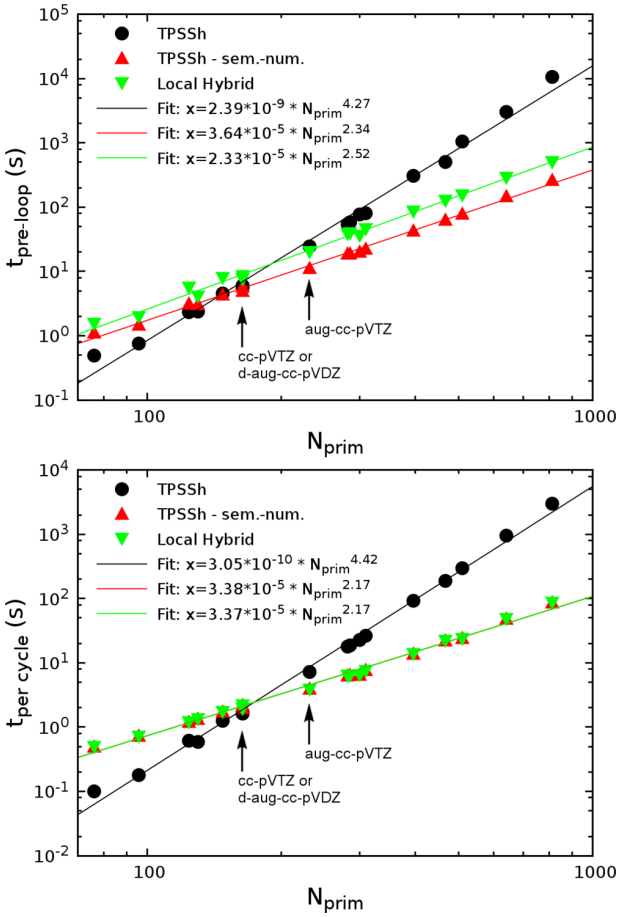

Figure 2. Comparison of timings for pre-loop (top) and CPKS loop part (bottom) of nuclear shielding calculations on ethylene using analytical and seminumerical treatments of the TPSSh GH and the seminumerical treatment for the lh07t-svwn LH functional. def2-X (X = SVP, TZVP, TZVPD, QZVP, QZVPD) and ((d)-aug-)cc-pVXZ (X = D, T, Q, 5) basis sets are compared. Settings were grid 1 (grid 0 for CPKS loops) and high thresholds (see text) in seminumerical integration. The logarithmized data set has been used for linear fits (Table S4 gives the N_{prim} of all basis sets).

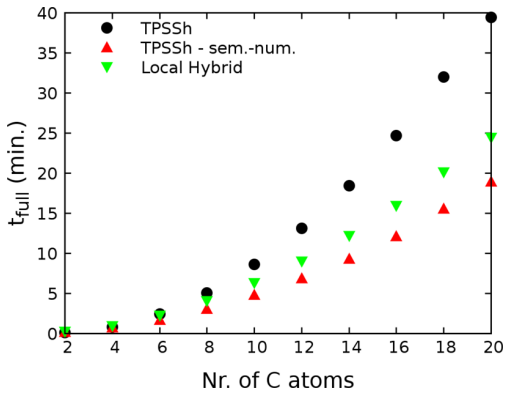

Figure 3. Comparison of timings for full nuclear shielding calculations on polyalkenes (def2-TZVP basis, normalized to five CPKS iterations) using analytical and seminumerical treatments of the TPSSh GH and the seminumerical treatment for the lh07t-svwnLH functional. Settings were grid 1 (grid 0 for CPKS loops) and high thresholds (see text) in seminumerical integration.

GH. For this worst-case scenario, the extra work for the LH in the pre-loop part is moderate, and the increase with chain length is also faster. However, except for the shortest chains, these LH computations still outperform the analytical GH scheme. As typically larger, often weakly contracted basis sets are employed for nuclear-shielding calculations, this advantage of the seminumerical scheme will be even more pronounced for practical applications.

The code has been SMP-parallelized. Preliminary test calculations for the $C_{10}H_{12}$ system on one node provide a speedup of approximately 3.9 (4 CPUs), 7.1 (8 CPUs), and 9.6 (12 CPUs), reducing the full computational time from 153 min (1 CPU) to 39 min (4 CPUs), 21.5 min (8 CPUs), and 16 min (12 CPUs) when using grid 5 without pre-screening in the seminumerical integration.

5. EVALUATION OF LOCAL HYBRID FUNCTIONALS

As a first assessment of the accuracy of a limited set of first-generation local-hybrid functionals (LDA-based without CF), we look at the CCSD(T)/psSseg-4-based benchmark data set for 15 small main-group species of ref 59 in comparison with a few standard functionals that include one GGA (BLYP), one meta-GGA (TPSS), and three GHs with increasing amounts of EXX admixture. The direct comparison against CCSD(T) gas-phase computations eliminates the need to correct for environmental or for ro-vibrational effects (also for relativistic effects). To eliminate basis-set errors, we use the same large psSseg-4 basis as the benchmark computations. Table 3 provides the data, including statistical analyses. The latter have to be viewed with some care due to the small sample sizes (8 entries for ^{1}H, 7 for ^{13}C, and 19 for the combined ^{15}N, ^{17}O, ^{19}F, and ^{31}P set, following the separation used also in ref 59), but they nevertheless provide some useful insights. While we provide results obtained using grid setting 5 and without pre-screening, identical conclusions can be drawn from data using smaller grids and standard screening thresholds as discussed above (see also Table S17 in the Supporting Information).

We start with the mean signed errors (MSEs) and mean absolute errors (MAEs) of non-hydrogen main-group nuclei: as is well known (see, e.g., ref 8), semilocal functionals systematically underestimate nuclear shieldings in such test sets, as indicated by the negative MSE for BLYP and TPSS being equal to the negative of the MAE. As discussed in the introduction, this may in part be attributed to the neglect of current-density terms in the XC functional for the non-hydrogen atoms.[18] This systematic underestimate holds also for the GHs, and it is not notably diminished (e.g., TPSS gives smaller MAEs than the global hybrids, except for TPSSh). Interestingly, HF theory exhibits smaller negative MSEs but notably large MAEs, suggesting a less systematic underestimate but significant statistical scattering. Turning to the LHs, we see that Lh07s-SVWN (07s) with s-LMF performs essentially like the GHs, with the MSEs being the negative of the MAEs. This changes as we move on to t-LMFs.

While the simplest and earliest LDA-based functional Lh07t-SVWN (07t) features only a small reduction of the negative MSEs compared to the MAEs, the errors are indeed reduced. As we increase the prefactor of the t-LMF and thereby bring in a more position-dependent EXX admixture with Lh12ct-SsirPW92 (12sir) and Lh12ct-SsifPW92 (12sif), the errors get noticeably smaller, and the (still negative) MSEs deviate more from the MAEs. This shows that, while we still underestimate to some extent the shieldings for the non-hydrogen nuclei with

https://dx.doi.org/10.1021/acs.jctc.9b00944
J. Chem. Theory Comput. 2020, 16, 931−943

Table 3. Comparison of Isotropic Shielding Constants (in ppm) Computed with Different Functionals against CCSD(T)/pcSseg-4 Reference Values[a]

nuclei	molecule	HF	BLYP	TPSS	TPSSh	B3LYP	BHLYP	07s	07t	12sir	12sif	Ref.
^{1}H	furan (C2/5)	24.27	24.02	24.15	24.19	24.00	24.03	23.74	23.68	23.52	23.42	24.03
	furan (C3/4)	25.30	25.03	25.22	25.25	25.00	25.03	24.68	24.63	24.45	24.33	25.02
	$(CH_3)_2CO$	29.94	29.53	29.66	29.72	29.57	29.71	29.37	29.28	29.19	29.11	29.53
	CH_4	31.63	31.65	31.72	31.69	31.59	31.55	31.45	31.31	31.19	31.12	31.39
	NH_3	31.57	31.83	31.94	31.88	31.72	31.59	31.57	31.33	31.17	31.09	31.44
	H_2O	30.49	31.29	31.37	31.37	31.04	30.84	30.84	30.47	30.28	30.18	30.65
	HF	28.11	29.80	29.82	29.75	29.33	28.87	29.06	28.55	28.28	28.16	28.82
	PH_3	29.67	29.69	29.67	29.67	29.63	29.65	29.40	29.25	29.12	29.03	29.46
^{13}C	furan (C2/5)	36.85	25.17	35.65	37.00	26.50	29.19	33.23	38.02	42.06	43.44	47.36
	furan (C3/4)	74.50	59.62	69.21	70.80	61.63	65.45	67.00	72.32	76.39	77.79	81.67
	$(CH_3)_2\underline{C}O$	−24.94	−42.28	−30.25	−28.05	−39.81	−33.55	−33.00	−30.31	−25.88	−24.34	−10.84
	$(\underline{C}H_3)_2CO$	162.51	145.05	151.26	153.43	148.84	154.87	154.09	159.38	163.67	165.35	162.88
	CH_4	195.11	186.47	188.76	189.89	188.82	191.66	193.51	199.85	203.92	205.78	199.39
	CF_4	77.81	36.06	45.57	49.16	44.64	57.19	51.53	53.40	58.82	60.81	65.96
	CO	−28.05	−19.19	−9.04	−9.71	−22.93	−25.02	−16.92	−13.20	−10.87	−10.32	2.56
^{15}N	N_2	−116.04	−89.97	−79.18	−83.12	−97.20	−106.03	−92.03	−81.59	−78.74	−78.12	−61.16
	NH_3	262.07	258.45	259.26	259.99	259.68	261.06	263.88	275.84	280.43	282.39	270.4
	N<u>N</u>O	−35.78	−7.60	1.57	−0.28	−14.52	−21.84	−6.41	−1.52	0.70	1.64	11.74
	<u>N</u>NO	60.94	85.31	91.09	89.41	79.01	72.20	85.89	94.44	97.76	99.00	106.22
	PN	−510.99	−425.30	−398.73	−405.87	−447.50	−470.04	−428.60	−401.71	−395.99	−394.92	−344.71
^{17}O	furan	58.20	8.09	22.46	27.25	15.03	28.78	22.03	37.55	44.76	46.62	64.82
	$(CH_3)_2CO$	−333.47	−350.97	−320.59	−320.08	−356.21	−348.90	−342.33	−316.52	−306.17	−304.12	−297.91
	H_2O	327.59	325.50	326.55	327.64	326.53	328.11	331.06	349.49	354.87	356.91	337.63
	CO	−91.92	−83.89	−71.10	−70.67	−88.07	−87.78	−81.43	−64.96	−60.21	−59.42	−55.42
	OF_2	−448.18	−646.56	−561.91	−536.98	−593.76	−524.56	−583.15	−538.32	−511.64	−504.24	−446.32
	NNO	173.28	172.21	172.30	173.52	171.30	172.31	175.54	191.34	196.51	198.46	198.77
^{19}F	HF	414.32	409.95	411.23	412.42	411.49	413.76	414.79	437.04	442.80	444.75	419.91
	F_2	−173.98	−279.70	−236.89	−226.64	−259.92	−223.67	−252.35	−215.67	−198.22	−192.91	−192.76
	CF_4	281.95	229.96	241.17	246.15	241.33	257.09	247.97	262.88	271.40	273.89	267.58
	OF_2	19.74	−105.06	−73.39	−58.59	−76.60	−36.31	−58.08	−34.20	−16.18	−10.03	−24.28
	PF_3	255.53	182.74	196.38	205.27	199.15	223.36	209.21	227.02	238.06	240.94	231.81
^{31}P	PH_3	583.04	553.28	569.98	574.07	560.99	569.90	580.93	598.97	615.34	623.43	604.51
	PF_3	255.41	149.12	180.59	189.07	168.07	200.24	181.29	189.24	204.92	210.03	224.8
	PN	−109.37	−48.52	−7.85	−18.03	−70.30	−92.05	−72.30	−44.89	−40.28	−40.39	51.61
MSE (^{1}H)			0.08	0.31	0.40	0.40	0.19	0.12	−0.03	−0.23	−0.39	−0.49
MSE (^{13}C)			−7.88	−22.58	−13.98	−12.35	−20.18	−15.60	−14.22	−9.93	−5.84	−4.35
MSE (other)			−26.05	−54.22	−33.91	−30.67	−49.41	−39.56	−40.60	−21.20	−11.96	−9.12
MAE (^{1}H)			0.30	0.32	0.40	0.40	0.21	0.12	0.18	0.23	0.39	0.49
MAE (^{13}C)			11.27	22.58	13.98	12.35	20.18	15.60	14.22	10.06	7.36	6.88
MAE (other)			39.89	54.22	33.91	30.67	49.41	39.56	40.60	24.83	20.29	20.15
SD (^{1}H)			0.34	0.33	0.30	0.27	0.18	0.08	0.20	0.10	0.13	0.14
SD (^{13}C)			12.08	5.96	3.79	3.07	5.82	7.24	5.21	6.35	6.50	6.75
SD (other)			54.26	43.89	24.77	21.25	36.73	36.98	36.03	29.81	28.29	28.67

[a]Results with pcSseg-4 basis sets, grid 5, and without pre-screening. Abbreviations: 07s = Lh07s-SVWN, 07t = Lh07t-SVWN, 12sir = LH12ct-SsirPW92, 12sif = LH12ct-SsifPW92, Ref. = CCSD(T)/pcSseg-4.[59]

those t-LMF-based LHs, the underestimate is overall appreciably less pronounced than with GHs and semilocal functionals, and the deviations become more statistical. This is interesting given the very simple structure of these LHs, but it aligns with the good performance of the Lh12ct-SsirPW92 and Lh12ct-SsifPW92 functionals in TDDFT computations of different types of excitation energies.[26,73] Looking at the standard deviations for the non-hydrogen nuclei is also instructive: these are in fact the smallest for TPSS and TPSSh and not for the LHs, indicating that the distributions for the former two functionals are narrower than for the others even though they are shifted to distinctly too low shielding values. This is confirmed by the normal distributions shown in Figure 4 (middle and right panels). Note that the distributions for the LHs with t-LMF are also somewhat wider than that for the LH with s-LMF but shifted closer to the origin.

Closer analyses of non-hydrogen shieldings of different systems (Table 3) provide some explanations for the

https://dx.doi.org/10.1021/acs.jctc.9b00944
J. Chem. Theory Comput. 2020, 16, 931−943

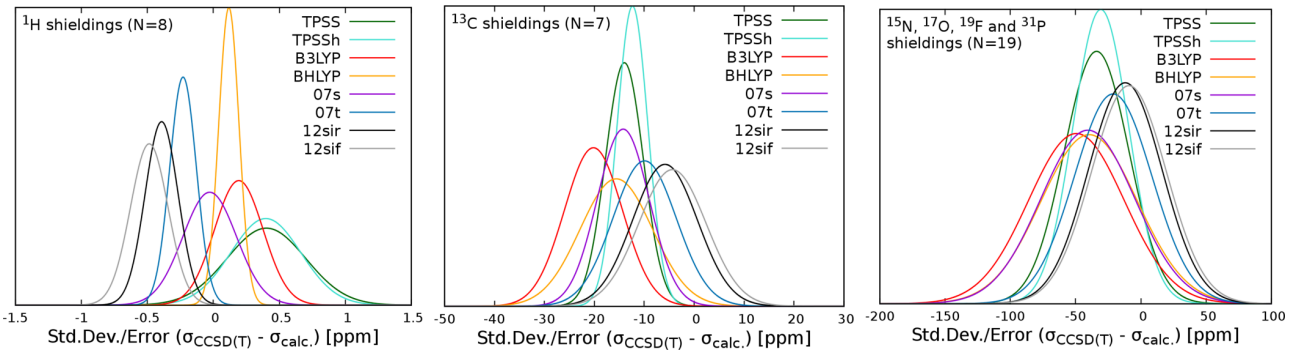

Figure 4. Normal error distributions of absolute shielding constants (ppm) obtained with different functionals relative to the CCSD(T) reference data from ref 59. The computations used pcSseg-4 basis sets, the MARI-J approximation for the Coulomb contributions, grid 5, and no pre-screening (see text).

somewhat wider distributions of the LHs with t-LMF: results for systems with relatively large nondynamical correlation effects and smaller band gaps are improved most notably; for example, several fluorine and oxygen shifts (where lone-pair repulsions can be important), as well as unsaturated systems such as CO, N_2 or N_2O. This may suggest that LHs with t-LMF indeed bring in a certain amount of extra nondynamical correlation (cf. eq 17). In contrast, atoms bonded to hydrogen atoms tend to be described more poorly by the t-LMF-based LHs, and the "heavy-atom" shielding in these systems (NH_3, H_2O, HF, PH_3) is overestimated by those functionals. This explains at least in part the wider error distributions.

Matters are rather different for the ^{1}H shieldings (Table 3). Now, the LHs having a t-LMF clearly underestimate the shieldings systematically by similar amounts as the semilocal functionals overestimate them. In contrast, Lh07s-SVWN with an s-LMF now is among the best-performing functionals, together with BHLYP and B3LYP. However, note that the latter two functionals give systematically too shielded ^{1}H values, while the errors of Lh07s-SVWN are largely statistical. The relatively poor performance of the t-LMF for proton shieldings may be linked to the peculiar shape of this type of LMFs near hydrogen atoms as the ratio $\frac{\tau_{W,\sigma}(\mathbf{r})}{\tau_{\sigma}(\mathbf{r})}$ (eq 4) goes to 1 near hydrogen atoms (consistent with these spatial regions being dominated by a single hydrogen 1 s orbital).[25,74] This suggests that, while t-LMFs perform well for the second- and third-period atoms studied here, modifications of the LMF may be needed to properly account for proton shieldings. These results are furthermore consistent with observations for binding energies involving hydrogen atoms when using t-LMFs.[25] Obviously, an increased prefactor of the t-LMF, as in Lh12ct-SsirPW92 and Lh12ct-SsifPW92, is in this case detrimental rather than beneficial. Interestingly, for proton shieldings the normal distributions of the LH results with t-LMF are among the most narrow of all functionals (except for BHLYP, see SDs in Table 3 and distribution in Figure 4, left panel), suggesting that the underestimated shieldings are largely due to a systematic error for all species. We should emphasize that, while fulfilling the one-orbital limit may be a useful exact constraint on an LMF for one-electron regions, the constancy of $\frac{\tau_{W,\sigma}(\mathbf{r})}{\tau_{\sigma}(\mathbf{r})} = 1$ applies equally to closed-shell s orbital-dominated situations as in H_2, or for parts of the E−H bonding regions in molecules of the present test set (see Figure S3 in the Supporting Information). In the latter case, this leads to a sudden rise of the LMF as we approach the hydrogen-atom position. This likely does not adequately model left−right correlation in the E−H bond.

To evaluate to which extent it is the large EXX admixture near hydrogen and to what extent the steep increase toward hydrogen, which is responsible for the too deshielded ^{1}H values obtained with t-LMFs, we have tested GHs constructed from two of the t-LMF-based LHs by simply using the maximum EXX admixture provided by the given t-LMF prefactor (Table S18 in the Supporting Information). For both cases, the ^{1}H values for the GHs are also too deshielded with respect to the CCSD(T) reference values, but somewhat less so than for the underlying LH. In fact, for most molecules, the differences between LH and GH are very similar (0.10−0.15 ppm for Lh07t-SVWN and 0.13−0.18 ppm for Lh12ct-SsirPW92). Only for the most polar E−H bonds, there is either a smaller shielding increase for the associated GH (0.07 and 0.08 ppm, respectively, for H_2O) or there is an extra deshielding (−0.05 and −0.07 ppm, respectively, for HF). These results suggest that the very large EXX admixture near the hydrogen nucleus is part of the problem with the t-LMFs for ^{1}H shieldings but the steep increase and thus the shape of the LMF also may contribute. The results for the non-hydrogen shieldings obtained with these specially constructed GHs are much poorer than those of the underlying LHs (Table S18), roughly comparable to the data for BHLYP, which exhibits similar EXX admixtures (Table 3).

The present results with LHs cannot yet compete with the results for double hybrid (DH) functionals given in ref 23. While the MSE and MAE for ^{13}C shieldings with t-LMF are comparable to the best DH results, those for the other non-hydrogen nuclei are overall inferior to those for the best DH evaluated (DSD-PBEP86).[59] The standard deviations for DHs indicate clearly more narrow distributions. Also, of course, the LH results with t-LMFs for proton shieldings are not competitive for the reasons outlined above. However, the small main-group molecules of the present test set are ideal cases for DHs, while the MP2 correlation term contained in DHs is likely to cause problems for systems exhibiting large nondynamical correlation effects (e.g., for the ^{17}O shieldings in ozone or in d^0 oxo complexes where MP2 is known to fail completely[19]). It seems likely that improved LMFs may render LHs competitive with the best DHs for systems like those studied here while performing better for systems with strong nondynamical correlation at lower computational cost than required for DHs.

https://dx.doi.org/10.1021/acs.jctc.9b00944
J. Chem. Theory Comput. 2020, 16, 931−943

We note in passing that our results using TPSS for non-hydrogen nuclei are rather different (lower) than those in ref 59 where TPSS and M06L were the best-performing functionals apart from DHs. We have repeated these calculations for τ-dependent meta-GGA functionals with the Gaussian09 code[75] and obtained results very close to our own data for TPSS but very different from the results of ref 59 for TPSS and M06L (see Table S19 in the Supporting Information). It appears that the different results in ref 59 arise from the neglect of current terms caused by the τ contributions (cf. eq 18).

6. CONCLUSIONS

To be able to tap the potential of local hybrid functionals with position-dependent exact-exchange admixture for the computation of NMR chemical shifts, this work has reported the first implementation of a coupled-perturbed Kohn−Sham scheme with local hybrids for nuclear shieldings within a generalized Kohn−Sham framework using gauge-including atomic orbitals. The additional contributions to the shielding tensor resulting for local hybrids compared to global hybrids have been derived and implemented using efficient seminumerical integration techniques for the terms arising from exact exchange, as well as current-density contributions for mixing functions and meta-GGA contributions depending on local kinetic energy densities. Efficiency and accuracy of this scheme depend on the required integration grid sizes. Gratifyingly, rather small grid sizes for the different program parts have been found to be sufficient to obtain accurate nuclear shieldings, and efficiency can be further enhanced by different integral screening techniques. This leads to a CPKS scheme for global hybrids that exhibits more favorable scaling with system and basis-set sizes than standard analytical integration schemes (as has been shown previously), and the additional effort required for the computation of perturbed **A** matrices with local hybrids, restricted to the pre-loop part of the CPKS algorithm, increases the CPU time only moderately and does not affect the basis-set scaling. As the advantages of the seminumerical scheme are particularly notable for large basis sets as typically used for nuclear-shielding calculations, this allows the straightforward application of local and global hybrid functionals to the computation of NMR chemical shifts for large molecules.

A preliminary evaluation of the performance of four first-generation local hybrids based on LDA exchange in comparison with some standard GGA, meta-GGA, and global hybrid functionals against CCSD(T) reference data for a test set of 34 shielding values of 15 small, light main-group compounds has been carried out. Local hybrids with local mixing functions based on the ratio between von Weizsäcker and Pauli kinetic energy densities (t-LMFs) provide a substantial improvement for the shieldings of the non-hydrogen nuclei, reducing the systematic underestimate of these shieldings by semilocal functionals and global hybrids. These improvements pertain particularly to systems with large nondynamical correlation and small band gaps, while atoms bonded to hydrogen are treated less accurately by these t-LMF-based local hybrids. For proton shieldings, these same functionals provide systematically underestimated shieldings, suggesting that the unique shape of t-LMFs in one-orbital regions around hydrogen is unfavorable in this context. A local hybrid with a local mixing function based on the reduced density gradient (s-LMF) in contrast performs more closely aligned with standard global hybrids, that is, less accurately for non-hydrogen shieldings (except when bonded to hydrogen) and more accurately for proton shieldings. These results point to the crucial role of the LMF and of its shape in different spatial regions for local hybrids, suggesting areas for improvement as the development of this class of functionals continues actively. That is, we pursue LMFs that respect the high-density homogeneous coordinate scaling limit relevant for the core regions of heavy atoms and also exhibit the correct shape in areas dominated by hydrogen 1 s orbitals. Having an efficient implementation for nuclear shielding computations with local hybrids will allow an in-depth investigation of these and other aspects, together with evaluations for other magnetic and electric properties for which variable exact-exchange admixture in different regions in space may also be beneficial.

■ ASSOCIATED CONTENT

Supporting Information

The Supporting Information is available free of charge at https://pubs.acs.org/doi/10.1021/acs.jctc.9b00944.

Definition of statistical quantities, details on the seminumerical integration scheme, consideration of magnetic-field derivatives of the LMF, explicit formulations of perturbed **A** matrices, as well as additional tables and figures containing tests of gauge invariance, grid and junction dependencies, comparison of different codes and plots of the t-LMF along the element-hydrogen bond axes (PDF)

This material is available free of charge via the Internet at http://pubs.acs.org.

■ AUTHOR INFORMATION

Corresponding Author

Martin Kaupp − *Technische Universität Berlin, Institut für Chemie, Berlin D-10623, Germany;* orcid.org/0000-0003-1582-2819; Email: martin.kaupp@tu-berlin.de

Other Authors

Caspar Jonas Schattenberg − *Technische Universität Berlin, Institut für Chemie, Berlin D-10623, Germany*

Kevin Reiter − *Karlsruher Institut für Technologie (KIT), Institut für Nanotechnologie, Karlsruhe D-76021, Germany*

Florian Weigend − *Karlsruher Institut für Technologie (KIT), Institut für Nanotechnologie, Karlsruhe D-76021, Germany;* orcid.org/0000-0001-5060-1689

Complete contact information is available at: https://pubs.acs.org/10.1021/acs.jctc.9b00944

Notes

The authors declare no competing financial interest.

■ ACKNOWLEDGMENTS

This work has been funded by Deutsche Forschungsgemeinschaft within project KA1187/14-1. C.J.S. is grateful for a PhD scholarship provided by Studienstiftung des deutschen Volkes. K.R. acknowledges financial support from SFB 1176, project Q5.

■ REFERENCES

(1) Kaupp, M.; Bühl, M.; Malkin, V. G. *Calculation of NMR and EPR Parameters: Theory and Applications*; 1st ed.; Wiley-VCH: Weinheim, 2004.

(2) Gauss, J.; Stanton, J. F. Electron-Correlated Methods for the Calculation of NMR Chemical Shifts. *Adv. Chem. Phys.* **2002**, 355.
(3) Lee, A. M.; Handy, N. C.; Colwell, S. M. The density functional calculation of nuclear shielding constants using London atomic orbitals. *J. Chem. Phys.* **1995**, *103*, 10095−10109.
(4) Cheeseman, J. R.; Trucks, G. W.; Keith, T. A.; Frisch, M. J. A comparison of models for calculating nuclear magnetic resonance shielding tensors. *J. Chem. Phys.* **1996**, *104*, 5497−5509.
(5) Helgaker, T.; Jaszuński, M.; Ruud, K. Ab Initio Methods for the Calculation of NMR Shielding and Indirect Spin-Spin Coupling Constants. *Chem. Rev.* **1999**, *99*, 293−352.
(6) Harding, M. E.; Lenhart, M.; Auer, A. A.; Gauss, J. Quantitative prediction of gas-phase ^{19}F nuclear magnetic shielding constants. *J. Chem. Phys.* **2008**, *128*, 244111.
(7) Mulder, F. A. A.; Filatov, M. NMR chemical shift data and ab initio shielding calculations: emerging tools for protein structure determination. *Chem. Soc. Rev.* **2010**, *39*, 578−590.
(8) Teale, A. M.; Lutnæs, O. B.; Helgaker, T.; Tozer, D. J.; Gauss, J. Benchmarking density-functional theory calculations of NMR shielding constants and spin−rotation constants using accurate coupled-cluster calculations. *J. Chem. Phys.* **2013**, *138*, No. 024111.
(9) Malkin, V. G.; Malkina, O. L.; Casida, M. E.; Salahub, D. R. Nuclear Magnetic Resonance Shielding Tensors Calculated with a Sum-over-States Density Functional Perturbation Theory. *J. Am. Chem. Soc.* **1994**, *116*, 5898−5908.
(10) Fadda, E.; Casida, M. E.; Salahub, D. R. Time-Dependent Density Functional Theory as a Foundation for a Firmer Understanding of Sum-Over-States Density Functional Perturbation Theory: "Loc.3" Approximation. *Int. J. Quantum Chem.* **2003**, *91*, 67−83.
(11) Fadda, E.; Casida, M. E.; Salahub, D. R. NMR shieldings from sum-over-states density-functional-perturbation theory: Further testing of the "Loc.3" approximation. *J. Chem. Phys.* **2003**, *118*, 6758−6768.
(12) Xin, D.; Sader, C. A.; Chaudhary, O.; Jones, P.-J.; Wagner, K.; Tautermann, C. S.; Yang, Z.; Busacca, C. A.; Saraceno, R. A.; Fandrick, K. R.; Gonnella, N. C.; Horspool, K.; Hansen, G.; Senanayake, C. H. Development of a ^{13}C NMR Chemical Shift Prediction Procedure Using B3LYP/cc-pVDZ and Empirically Derived Systematic Error Correction Terms: A Computational Small Molecule Structure Elucidation Method. *J. Org. Chem.* **2017**, *82*, 5135−5145.
(13) Alipour, M. In search of the appropriate theoretically justified mixing coefficient in parameter-free hybrid functionals for computing the NMR parameters. *RSC Adv.* **2015**, *5*, 4737−4746.
(14) Kupka, T. H_2O, H_2, HF, F_2 and F_2O nuclear magnetic shielding constants and indirect nuclear spin−spin coupling constants (SSCCs) in the BHandH/pcJ-n and BHandH/XZP Kohn−Sham limits. *Magn. Reson. Chem.* **2009**, *47*, 959−970.
(15) Keal, T. W.; Tozer, D. J. The exchange-correlation potential in Kohn−Sham nuclear magnetic resonance shielding calculations. *J. Chem. Phys.* **2003**, *119*, 3015−3024.
(16) Keal, T. W.; Tozer, D. J. A semiempirical generalized gradient approximation exchange-correlation functional. *J. Chem. Phys.* **2004**, *121*, 5654−5660.
(17) Kupka, T.; Stachów, M.; Nieradka, M.; Kaminsky, J.; Pluta, T. Convergence of Nuclear Magnetic Shieldings in the Kohn-Sham Limit for Several Small Molecules. *J. Chem. Theory Comput.* **2010**, *6*, 1580−1589.
(18) Reimann, S.; Ekström, U.; Stopkowicz, S.; Teale, A. M.; Borgoo, A.; Helgaker, T. The importance of current contributions to shielding constants in density-functional theory. *Phys. Chem. Chem. Phys.* **2015**, *17*, 18834−18842.
(19) Kaupp, M.; Malkina, O. L.; Malkin, V. G. The calculation of ^{17}O chemical shielding in transition metal oxo complexes. I. Comparison of DFT and ab initio approaches, and mechanisms of relativity-induced shielding. *J. Chem. Phys.* **1997**, *106*, 9201−9212.
(20) Schattenberg, C. J.; Maier, T. M.; Kaupp, M. Lessons from the Spin-Polarization/Spin-Contamination Dilemma of Transition-Metal Hyperfine Couplings for the Construction of Exchange-Correlation Functionals. *J. Chem. Theory Comput.* **2018**, *14*, 5653−5672.
(21) Aquino, F.; Govind, N.; Autschbach, J. Scalar Relativistic Computations of Nuclear Magnetic Shielding and g-Shifts with the Zeroth-Order Regular Approximation and Range-Separated Hybrid Density Functionals. *J. Chem. Theory Comput.* **2011**, *7*, 3278−3292.
(22) Iron, M. A. Evaluation of the Factors Impacting the Accuracy of ^{13}C NMR Chemical Shift Predictions using Density Functional Theory − The Advantage of Long-Range Corrected Functionals. *J. Chem. Theory Comput.* **2017**, *13*, 5798−5819.
(23) Stoychev, G. L.; Auer, A. A.; Neese, F. Efficient and Accurate Prediction of Nuclear Magnetic Resonance Shielding Tensors with Double-Hybrid Density Functional Theory. *J. Chem. Theory Comput.* **2018**, *14*, 4756−4771.
(24) van Wüllen, C. *Calculation of NMR and EPR Parameters: Theory and Applications*; 1st ed.; Kaupp, M.; Bühl, M.; Malkin, V. G., Eds.; Chapter 6: Chemical Shifts with Hartree−Fock and Density Functional Methods; Wiley-VCH: Weinheim, 2006;, p 98ff.
(25) Maier, T. M.; Arbuznikov, A. V.; Kaupp, M. Local Hybrid Functionals: Theory, Implementation, and Performance of an Emerging New Tool in Quantum Chemistry and Beyond. *Wiley Interdiscip. Rev.: Comput. Mol. Sci.* **2019**, *9*, No. e1378.
(26) Maier, T. M.; Bahmann, H.; Arbuznikov, A. V.; Kaupp, M. Validation of local hybrid functionals for TDDFT calculations of electronic excitation energies. *J. Chem. Phys.* **2016**, *144*, No. 074106.
(27) Arbuznikov, A. V.; Kaupp, M. Construction of local hybrid exchange-correlation potentials and their evaluation for nuclear shielding constants. *Chem. Phys. Lett.* **2004**, *386*, 8−16.
(28) Arbuznikov, A. V.; Kaupp, M. Nuclear shielding constants from localized local hybrid exchange-correlation potentials. *Chem. Phys. Lett.* **2007**, *442*, 496−503.
(29) Wilson, P. J.; Tozer, D. J. Varying the fraction of orbital exchange in density functional theory: Influence on nuclear magnetic resonance shielding constants. *J. Chem. Phys.* **2002**, *116*, 10139−10147.
(30) Teale, A. M.; Tozer, D. J. Exchange representations in Kohn−Sham NMR shielding calculations. *Chem. Phys. Lett.* **2004**, *383*, 109−114.
(31) Teale, A. M.; Cohen, A. J.; Tozer, D. J. Transition metal NMR chemical shifts from optimized effective potentials. *J. Chem. Phys.* **2007**, *126*, No. 074101.
(32) Peach, M. J. G.; Kattirtzi, J. A.; Teale, A. M.; Tozer, D. J. Shielding Constants and Chemical Shifts in DFT: Influence of Optimized Effective Potential and Coulomb-Attenuation. *J. Phys. Chem. A* **2010**, *114*, 7179−7186.
(33) Krykunov, M.; Ziegler, T. On the Use of the Exact Exchange Optimized Effective Potential Method for Static Response Properties. *Int. J. Quantum Chem.* **2009**, *109*, 3246−3258.
(34) Arbuznikov, A. V.; Kaupp, M. Coupled-Perturbed Scheme for the Calculation of Electronic g-Tensors with Local Hybrid Functionals. *J. Chem. Theory Comput.* **2009**, *5*, 2985−2995.
(35) *Local version derived from Turbomole version 7.3, Turbomole GmbH, 2017*. Turbomole is a development of University of Karlsruhe and Forschungszentrum Karlsruhe 1989-2007, Turbomole GmbH since 2007.
(36) Jaramillo, J.; Scuseria, G. E.; Ernzerhof, M. Local hybrid functionals. *J. Chem. Phys.* **2003**, *118*, 1068−1073.
(37) Maier, T. M.; Haasler, M.; Arbuznikov, A. V.; Kaupp, M. New approaches for the calibration of exchange energy densities in local hybrid functionals. *Phys. Chem. Chem. Phys.* **2016**, *18*, 21133−21144.
(38) Tao, J.; Staroverov, V. N.; Scuseria, G. E.; Perdew, J. P. Exact-exchange energy density in the gauge of a semilocal density-functional approximation. *Phys. Rev. A* **2008**, *77*, No. 012509.
(39) Arbuznikov, A. V.; Kaupp, M. Towards improved local hybrid functionals by calibration of exchange-energy densities. *J. Chem. Phys.* **2014**, *141*, 204101.
(40) Theilacker, K.; Arbuznikov, A. V.; Kaupp, M. Gauge effects in local hybrid functionals evaluated for weak interactions and the GMTKN30 test set. *Mol. Phys.* **2016**, *114*, 1118−1127.

(41) Arbuznikov, A. V.; Kaupp, M. Importance of the correlation contribution for local hybrid functionals: Range separation and self-interaction corrections. *J. Chem. Phys.* **2012**, *136*, No. 014111.
(42) Kaupp, M.; Bahmann, H.; Arbuznikov, A. V. Local hybrid functionals: An assessment for thermochemical kinetics. *J. Chem. Phys.* **2007**, *127*, 194102.
(43) Bahmann, H.; Rodenberg, A.; Arbuznikov, A. V.; Kaupp, M. A thermochemically competitive local hybrid functional without gradient corrections. *J. Chem. Phys.* **2007**, *126*, No. 011103.
(44) Arbuznikov, A. V.; Kaupp, M. Local hybrid exchange-correlation functionals based on the dimensionless density gradient. *Chem. Phys. Lett.* **2007**, *440*, 160−168.
(45) Neese, F. Prediction of molecular properties and molecular spectroscopy with density functional theory: From fundamental theory to exchange-coupling. *Coord. Chem. Rev.* **2009**, *253*, 526−563.
(46) London, F. Théorie quantique des courants interatomiques dans les combinaisons aromatiques. *J. Phys. Radium* **1937**, *8*, 397−409.
(47) Ditchfield, R. Self-consistent perturbation theory of diamagnetism. *Mol. Phys.* **1974**, *27*, 789−807.
(48) Wolinski, K.; Hinton, J. F.; Pulay, P. Efficient Implementation of the Gauge-Independent Atomic Orbital Method for NMR Chemical Shift Calculations. *J. Am. Chem. Soc.* **1990**, *112*, 8251−8260.
(49) Reviakine, R. Development of reliable methods of NMR and EPR parameters calculations and their application to transition metal complexes. Dissertation, Slovak Academy of Sciences, 2002.
(50) Arbuznikov, A. V.; Bahmann, H.; Kaupp, M. Local Hybrid Functionals with an Explicit Dependence on Spin Polarization. *J. Phys. Chem. A* **2009**, *113*, 11898−11906.
(51) Perdew, J. P.; Staroverov, V. N.; Tao, J.; Scuseria, G. E. Density functional with full exact exchange, balanced nonlocality of correlation, and constraint satisfaction. *Phys. Rev. A.* **2008**, *78*, No. 052513.
(52) Maximoff, S. N.; Scuseria, G. E. Nuclear magnetic resonance shielding tensors calculated with kinetic energy density-dependent exchange-correlation functionals. *Chem. Phys. Lett.* **2004**, *390*, 408−412.
(53) Helgaker, T.; Jørgensen, P.; Olsen, J. *Molecular Electronic-Structure Theory*; 1st ed.; John Wiley & Sons Ltd.: Chichester, 2000.
(54) Bahmann, H.; Kaupp, M. Efficient Self-Consistent Implementation of Local Hybrid Functionals. *J. Chem. Theory Comput.* **2015**, *11*, 1540−1548.
(55) Klawohn, S.; Bahmann, H.; Kaupp, M. Implementation of Molecular Gradients for Local Hybrid Density Functionals Using Seminumerical Integration Techniques. *J. Chem. Theory Comput.* **2016**, *12*, 4254−4262.
(56) Maier, T. M.; Bahmann, H.; Kaupp, M. Efficient Seminumerical Implementation of Global and Local Hybrid Functionals for Time-Dependent Density Functional Theory. *J. Chem. Theory Comput.* **2015**, *11*, 4226−4237.
(57) Laqua, H.; Kussmann, J.; Ochsenfeld, C. Efficient and Linear-Scaling Seminumerical Method for Local Hybrid Density Functionals. *J. Chem. Theory Comput.* **2018**, *14*, 3451−3458.
(58) Plessow, P.; Weigend, F. Seminumerical Calculation of the Hartree−Fock Exchange Matrix: Application to Two-Component Procedures and Efficient Evaluation of Local Hybrid Density Functionals. *J. Comput. Chem.* **2012**, *33*, 810−816.
(59) Stoychev, G. L.; Auer, A. A.; Izsák, R.; Neese, F. Self-Consistent Field Calculation of Nuclear Magnetic Resonance Chemical Shielding Constants Using Gauge-Including Atomic Orbitals and Approximate Two-Electron Integrals. *J. Chem. Theory Comput.* **2018**, *14*, 619−637.
(60) Ko, C.; Malick, D. K.; Braden, D. A.; Friesner, R. A.; Martínez, T. J. Pseudospectral time-dependent density functional theory. *J. Chem. Phys.* **2008**, *128*, 104103.
(61) Maier, T. M.; Ikabata, Y.; Nakai, H. Efficient Semi-Numerical Implementation of Relativistic Exact Exchange within the Infinite-Order Two-Component Method Using a Modified Chain-of-Spheres Method. *J. Chem. Theory Comput.* **2019**, *15*, 4745−4763.
(62) Reiter, K.; Mack, F.; Weigend, F. Calculation of Magnetic Shielding Constants with meta-GGA Functionals Employing the Multipole-Accelerated Resolution of the Identity: Implementation and Assessment of Accuracy and Efficiency. *J. Chem. Theory Comput.* **2018**, *14*, 191−197.
(63) Treutler, O.; Ahlrichs, R. Efficient molecular numerical integration schemes. *J. Chem. Phys.* **1995**, *102*, 346−354.
(64) Becke, A. D. A multicenter numerical integration scheme for polyatomic molecules. *J. Chem. Phys.* **1988**, *88*, 2547−2553.
(65) Staroverov, V. N.; Scuseria, G. E.; Tao, J.; Perdew, J. P. Comparative assessment of a new nonempirical density functional: Molecules and hydrogen-bonded complexes. *J. Chem. Phys.* **2003**, *119*, 12129−12137.
(66) Jensen, F. Segmented Contracted Basis Sets Optimized for Nuclear Magnetic Shielding. *J. Chem. Theory Comput.* **2015**, *11*, 132−138.
(67) Lee, C.; Yang, W.; Parr, R. G. Development of the Colle-Salvetti correlation-energy formula into a functional of the electron density. *Phys. Rev. B* **1988**, *37*, 785−789.
(68) Becke, A. D. Density-functional exchange-energy approximation with correct asymptotic behavior. *Phys. Rev. A* **1988**, *38*, 3098−3100.
(69) Tao, J.; Perdew, J. P.; Staroverov, V. N.; Scuseria, G. E. Climbing the Density Functional Ladder: Nonempirical Meta−Generalized Gradient Approximation Designed for Molecules and Solids. *Phys. Rev. Lett.* **2003**, *91*, 146401.
(70) Becke, A. D. Density-functional thermochemistry. III. The role of exact exchange. *J. Chem. Phys.* **1993**, *98*, 5648−5652.
(71) Becke, A. D. A new mixing of Hartree−Fock and local density-functional theories. *J. Chem. Phys.* **1993**, *98*, 1372−1377.
(72) Perdew, J. P.; Wang, Y. Accurate and simple analytic representation of the electron-gas correlation energy. *Phys. Rev. B: Condens. Matter Mater. Phys.* **1992**, *45*, 13244−13249.
(73) Grotjahn, R.; Maier, T. M.; Michl, J.; Kaupp, M. Development of a TDDFT-Based Protocol with Local Hybrid Functionals for the Screening of Potential Singlet Fission Chromophores. *J. Chem. Theory Comput.* **2017**, *13*, 4984−4996.
(74) Arbuznikov, A. V.; Kaupp, M.; Bahmann, H. From local hybrid functionals to "localized local hybrid" potentials: Formalism and thermochemical tests. *J. Chem. Phys.* **2006**, *124*, 204102.
(75) *Gaussian 09*, Revision D.01, Frisch, M. J., Trucks, G. W., Schlegel, H. B., Scuseria, G. E., Robb, M. A., Cheeseman, J. R., Scalmani, G., Barone, V., Mennucci, B., Petersson, G. A., Nakatsuji, H., Caricato, M., Li, X., Hratchian, H. P., Izmaylov, A. F., Bloino, J., Zheng, G., Sonnenberg, J. L., Hada, M., Ehara, M., Toyota, K., Fukuda, R., Hasegawa, J., Ishida, M., Nakajima, T., Honda, Y., Kitao, O., Nakai, H., Vreven, T., Montgomery, J. A., Jr., Peralta, J. E., Ogliaro, F., Bearpark, M., Heyd, J. J., Brothers, E., Kudin, K. N., Staroverov, V. N., Keith, T., Kobayashi, R., Normand, J., Raghavachari, K., Rendell, A., Burant, J. C., Iyengar, S. S., Tomasi, J., Cossi, M., Rega, N., Millam, J. M., Klene, M., Knox, J. E., Cross, J. B., Bakken, V., Adamo, C., Jaramillo, J., Gomperts, R., Stratmann, R. E., Yazyev, O., Austin, A. J., Cammi, R., Pomelli, C., Ochterski, J. W., Martin, R. L., Morokuma, K., Zakrzewski, V. G., Voth, G. A., Salvador, P., Dannenberg, J. J., Dapprich, S., Daniels, A. D., Farkas, O., Foresman, J. B., Ortiz, J. V., Cioslowski, J., Fox, D. J., Gaussian, Inc., Wallingford CT, 2013.

https://dx.doi.org/10.1021/acs.jctc.9b00944
J. Chem. Theory Comput. 2020, 16, 931−943

II

Reprinted with permission from

F. Mack, C. J. Schattenberg, M. Kaupp and F. Weigend,
"*Nuclear Spin-Spin Couplings: Efficient Evaluation of Exact Exchange and Extension to Local Hybrid Functionals*",
J. Phys. Chem. A, **2020**, *124*, 8529–8539.
DOI: 10.1021/acs.jpca.0c06897

THE JOURNAL OF PHYSICAL CHEMISTRY A

pubs.acs.org/JPCA Article

Nuclear Spin−Spin Couplings: Efficient Evaluation of Exact Exchange and Extension to Local Hybrid Functionals

Fabian Mack,[⊥] Caspar J. Schattenberg,[⊥] Martin Kaupp,* and Florian Weigend*

Cite This: J. Phys. Chem. A 2020, 124, 8529−8539 Read Online

ACCESS | Metrics & More | Article Recommendations | Supporting Information

ABSTRACT: We present an efficient implementation for the computation of nuclear spin−spin coupling tensors within density functional theory into the TURBOMOLE software suite. Emphasis is put on methods to efficiently evaluate the Hartree−Fock exchange needed for hybrid functionals: resolution of the identity and seminumerical evaluation on a grid. Our algorithm allows for the selection of specific nuclei for the reduction of calculation times. Further, the accuracy of locally dense basis sets in the density functional theory framework is investigated. These features allow for the routine computation of coupling constants in systems comprising about 100 carbon atoms within less than one day on a single CPU and within a few hours when using the OpenMP variant. Based on seminumerical integration, the first implementation of local hybrid functionals for spin−spin couplings is reported. This has allowed a preliminary evaluation of position-dependent exact-exchange admixture in three local hybrid functionals for a set of 80 isotropic spin−spin couplings in 23 small main-group molecules against CC3 and MCSCF reference data. Two of the local hybrids (LH14t-calPBE and LH07t-SVWN) are the top performers in the overall statistical evaluation compared to several standard functionals (TPSS, TPSSh, B3LYP, PBE0, and BHLYP), in particular, as they do not exhibit notable outliers for specific coupling types.

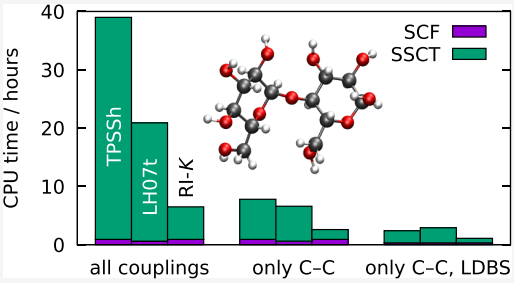

INTRODUCTION

Nuclear magnetic resonance (NMR) is one of the most powerful tools in chemistry to analyze geometric and electronic structures in molecules, solutions, and solids.[1−4] In addition to nuclear magnetic shieldings, which relate to chemical shifts, nuclear spin−spin coupling tensors (SSCTs) are one of the most important NMR parameters. In isotropic media (e.g., in fluids), the isotropic spin−spin coupling constant (SSCC, trace of the SSCT) is usually measured. The SSCT anisotropy can provide additional information and is accessible in certain solid-state or gas-phase measurements.[5,6] To aid the interpretation of the experimental data and to make predictions,[7,8] reliable yet efficient quantum-chemical methods for the calculation of SSCTs are needed. The large size of many relevant molecules, which may easily consist of hundreds of atoms, presently often prohibits the use of precise wave function-based methods, such as coupled cluster theory.[9−12] Density functional theory (DFT) is a popular choice to fill this gap. Often, hybrid functionals, which include a constant amount of exact exchange ("global hybrids"), perform better for SSCCs than pure density functionals.[13−20]

As the exact exchange dominates the computational requirements of the coupled-perturbed Kohn−Sham treatment of SSCTs using hybrid functionals, the first main aim of the present work is its efficient treatment. The computation of the exact-exchange contribution scales as $O(N_{bf}^4)$ per perturbation (N_{bf} is the number of basis functions). Therefore, the calculation of SSCTs scales effectively with system size N as $O(N^5)$. We will present several methods to improve upon both formal scaling and prefactor, including the selection of perturbed and responding nucleus, a systematic use of locally dense basis sets (LDBSs), as well as the efficient evaluation of exact exchange using a resolution of the identity (RI-K) or seminumerical integration on a grid.

The second main aim of this work is to use the seminumerical integration of exact exchange to implement and evaluate for the first time local hybrid functionals ("local hybrids", LHs) for the computation of SSCTs. LHs replace the constant amount of exact-exchange admixture of global hybrids by a position-dependent admixture, governed by a local mixing function (LMF).[21] The increased flexibility of local hybrids compared to global hybrids offers the promise of an accurate treatment of properties that depend on different areas of space, for example, near nuclei, in bonding regions or in the low-density asymptotics of a molecule. In addition to various other ground- and excited-state properties that have been reviewed,[21] this enhanced potential of LHs has already been evaluated also

Received: July 28, 2020
Revised: September 18, 2020
Published: September 21, 2020

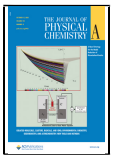

https://dx.doi.org/10.1021/acs.jpca.0c06897
J. Phys. Chem. A 2020, 124, 8529−8539

for some magnetic-resonance parameters. In particular, the possibility of balancing of core- and valence-shell spin polarization by having more exact exchange in the core region has been found promising for hyperfine couplings (HFCs) of transition-metal complexes[22] and may likely be improved further by LMFs respecting the high-density limit.[23] Our very recent nuclear-shielding implementation of LHs also provided very promising results, even though room for improvement of the functionals was identified for proton shieldings and for nuclei bound to hydrogen.[24] Given the large role of the Fermi-contact (FC) term, which can be related to HFCs, and of the paramagnetic spin−orbit (PSO) term that is analogous to paramagnetic shielding, one may expect also the advantages of position-dependent exact-exchange admixture for SSCTs.

The paper is organized as follows: first, we briefly review the theory of SSCTs and discuss the extension to LHs. We then present our implementation along with a description of the RI-K and seminumerical integration algorithms we use. Afterward, small examples are provided to highlight the correctness, timing, and usefulness of the new implementation features. This is followed by the first evaluation and analysis of LH functionals for SSCTs. We close with our conclusions.

THEORY

The theoretical framework for the calculation of SSCTs has been described elsewhere in detail.[11,12,25−28] We focus here on the key points necessary to understand the described treatments of exact exchange and the extension to LHs.

The reduced indirect nuclear spin−spin coupling tensor $\mathbf{K}_{KL}$ is the second derivative of the electronic energy E with respect to the magnetic dipole moments $\boldsymbol{M}$ of the coupling nuclei

$$\mathbf{K}_{KL} = \left.\frac{\mathrm{d}E}{\mathrm{d}\boldsymbol{M}_K\,\mathrm{d}\boldsymbol{M}_L}\right|_{\boldsymbol{M}_I=0\,\forall\, I} \tag{1}$$

The isotropic and the anisotropic part

$$K_{KL}^{\mathrm{iso}} = \frac{1}{3}\mathrm{tr}(\mathbf{K}_{KL}) \tag{2}$$

$$K_{KL}^{\mathrm{anis}} = \sqrt{\frac{3}{2}\left(\frac{1}{4}\sum_{\alpha\beta}((K_{KL})_{\alpha\beta} + (K_{KL})_{\beta\alpha})^2 - 3(K_{KL}^{\mathrm{iso}})^2\right)} \tag{3}$$

are invariant under rotation of the molecule in space. By multiplying with the isotope-specific gyromagnetic ratio γ, the observable quantities J_{KL}^{iso} and J_{KL}^{anis} are obtained

$$J_{KL}^{\mathrm{iso}} = h\frac{\gamma_K}{2\pi}\frac{\gamma_L}{2\pi}K_{KL}^{\mathrm{iso}} \tag{4}$$

and similar for J_{KL}^{anis}.

We note in passing that the choice for the anisotropic part is not unique.[29] For reasons of consistency, here, the same definition was chosen as for the anisotropy in chemical shielding tensors.[30]

According to Ramsey's theory,[31] four terms contribute to the SSCTs: the FC, spin−dipole (SD), PSO, and diamagnetic spin−orbit (DSO) interactions

$$\hat{h}_K^{\mathrm{FC}} = \frac{8\pi\alpha^2}{3}\sum_i \delta(\boldsymbol{r}_{iK})\boldsymbol{s}_i \tag{5}$$

$$\hat{h}_K^{\mathrm{SD}} = \alpha^2\sum_i \frac{3\boldsymbol{r}_{iK}^{\mathrm{T}}\boldsymbol{s}_i\boldsymbol{r}_{iK} - r_{iK}^2\boldsymbol{s}_i}{r_{iK}^5} \tag{6}$$

$$\hat{h}_K^{\mathrm{PSO}} = -\mathrm{i}\alpha^2\sum_i \frac{\boldsymbol{r}_{iK}\times\nabla_i}{r_{iK}^3} \tag{7}$$

$$\hat{h}_{KL}^{\mathrm{DSO}} = \alpha^4\sum_i \frac{\boldsymbol{r}_{iK}^{\mathrm{T}}\boldsymbol{r}_{iL}\mathbf{I}_3 - \boldsymbol{r}_{iK}\boldsymbol{r}_{iL}^{\mathrm{T}}}{r_{iK}^3 r_{iL}^3} \tag{8}$$

$\alpha \approx 1/137$ is the fine structure constant, $\delta(\boldsymbol{r}_{iK})$ denotes the Dirac delta distribution, $\boldsymbol{s}_i$ is the spin of electron i, and $\mathbf{I}_3$ is the (3×3) identity matrix.

Carrying out the derivative in eq 1 yields

$$\mathbf{K}_{KL} = \frac{\partial^2 E}{\partial\boldsymbol{M}_K\partial\boldsymbol{M}_L} + \frac{\partial^2 E}{\partial\boldsymbol{M}_K\partial\kappa}\frac{\partial\kappa}{\partial\boldsymbol{M}_L} = \frac{\partial^2 E}{\partial\boldsymbol{M}_K\boldsymbol{M}_L} + \boldsymbol{R}_K\boldsymbol{\lambda}_L \tag{9}$$

where κ is the set of parameters that determine the wave function. The right-hand side integrals $\boldsymbol{R}_K$ (for FC, SD, and PSO terms) can be calculated easily from the operators, eqs 5−7. The response of the wavefunction λ_L can be obtained by solving the linear system of equations for each nucleus L

$$\sum_{bj} G_{ai,bj}\lambda_{L,bj} = -R_{L,ai} \tag{10}$$

where $\mathbf{G}$ is an electronic Hessian. In the context of SSCTs, two different Hessians are needed

$$G_{ai,bj}^{\mathrm{rt}} = \delta_{ij}\delta_{ab}(\varepsilon_a - \varepsilon_i) + (ab|f_{\mathrm{XC}}|ji) + (aj|f_{\mathrm{XC}}|bi) \tag{11}$$

$$G_{ai,bj}^{\mathrm{is}} = \delta_{ij}\delta_{ab}(\varepsilon_a - \varepsilon_i) - \gamma\iint(w_{abji} - w_{ajbi})\,\mathrm{d}\boldsymbol{r}_1\,\mathrm{d}\boldsymbol{r}_2 \tag{12}$$

where the labels r, i, s, and t stand for real, imaginary, singlet, and triplet, respectively. ε_p denotes the energy of orbital p.

$$(pq|f_{\mathrm{XC}}|rs) = \int\hat{d}_{ps}\hat{d}_{rq}e_{\mathrm{C}}^{\mathrm{sl}}\,\mathrm{d}\boldsymbol{r}_1 - \gamma\iint w_{pqrs}\,\mathrm{d}\boldsymbol{r}_1\,\mathrm{d}\boldsymbol{r}_2 + (1-\gamma)\int\hat{d}_{ps}\hat{d}_{rq}e_{\mathrm{X}}^{\mathrm{sl}}\,\mathrm{d}\boldsymbol{r}_1 \tag{13}$$

are the DFT kernel integrals, where γ is the portion of exact exchange in global hybrid functionals, $e_{\mathrm{X}}^{\mathrm{sl}}$ and $e_{\mathrm{C}}^{\mathrm{sl}}$ are the semilocal exchange and correlation energy densities, respectively (defined by $E_{\mathrm{X/C}}^{\mathrm{sl}} = \int e_{\mathrm{X/C}}^{\mathrm{sl}}\,\mathrm{d}\boldsymbol{r}_1$). The differential operator $\hat{d}_{\mathrm{ps}}$ is defined as

$$\hat{d}_{ps} = \sum_{Q\in\mathbf{Q}}\frac{\partial Q}{\partial D_{ps}}\frac{\partial}{\partial Q} \tag{14}$$

where Q runs over all quantities present in the functional of choice (e.g., $\mathbf{Q} = \{\rho, \nabla\rho, \tau\}$ for meta-GGA functionals) and D_{ps} is an element of the density matrix.

The four-center products are defined as

$$w_{pqrs} = \phi_p^*(\boldsymbol{r}_1)\phi_q(\boldsymbol{r}_1)r_{12}^{-1}\phi_r^*(\boldsymbol{r}_2)\phi_s(\boldsymbol{r}_2) \tag{15}$$

For LH functionals, the constant amount of exact exchange γ in eqs 12 and 13 is replaced by an LMF $g(\boldsymbol{r})$. As a result, the four-center integrals depend on an additional semilocal function, whose derivatives have to be accounted for as well, leading to additional terms within the potential and kernel integrals.

https://dx.doi.org/10.1021/acs.jpca.0c06897
J. Phys. Chem. A 2020, 124, 8529−8539

For the sake of simplicity, we limit ourselves to a general LH exchange kernel integral. The second term in eq 13 is then replaced by

$$
\begin{aligned}
(pq|f_{\mathrm{X}}^{\mathrm{LH}}|rs) = -\frac{1}{2}\iint\Big\{&[g(\boldsymbol{r}_1)+g(\boldsymbol{r}_2)]w_{pqrs}\\
&+\hat{d}_{ps}[g(\boldsymbol{r}_1)+g(\boldsymbol{r}_2)]\sum_k w_{kqrk}\\
&+\hat{d}_{rq}[g(\boldsymbol{r}_1)+g(\boldsymbol{r}_2)]\sum_k w_{pkks}\\
&+\hat{d}_{ps}\hat{d}_{rq}[g(\boldsymbol{r}_1)+g(\boldsymbol{r}_2)]\sum_{kl} w_{kllk}\Big\}\mathrm{d}\boldsymbol{r}_1\,\mathrm{d}\boldsymbol{r}_2\\
&+\int[(1-g(\boldsymbol{r}_1))\hat{d}_{ps}\hat{d}_{rq}e_{\mathrm{X}}^{\mathrm{sl}}(\boldsymbol{r}_1)\\
&-\hat{d}_{ps}\hat{d}_{rq}g(\boldsymbol{r}_1)e_{\mathrm{X}}^{\mathrm{sl}}(\boldsymbol{r}_1)]\,\mathrm{d}\boldsymbol{r}_1\\
&-\int[\hat{d}_{ps}g(r_1)\hat{d}_{rq}e_{\mathrm{X}}^{\mathrm{sl}}(r_1)+\hat{d}_{rq}g(r_1)\hat{d}_{ps}e_{\mathrm{X}}^{\mathrm{sl}}(r_1)]\mathrm{d}\boldsymbol{r}_1
\end{aligned}
\tag{16}
$$

Similar real triplet kernel integrals have to be solved in the context of linear-response time-dependent DFT, and detailed derivations for LHs can be found in ref 32.

The imaginary singlet Hessian, eq 12, becomes

$$
\begin{aligned}
G_{ai,bj}^{\mathrm{is,LH}} &= \delta_{ij}\delta_{ab}(\varepsilon_a-\varepsilon_i)\\
&\quad-\frac{1}{2}\iint(g(\boldsymbol{r}_1)+g(\boldsymbol{r}_2))(w_{abji}-w_{ajbi})\mathrm{d}\boldsymbol{r}_1\,\mathrm{d}\boldsymbol{r}_2
\end{aligned}
\tag{17}
$$

The PSO operator is a purely imaginary singlet operator (hence requiring $\mathbf{G}^{\mathrm{is}}$) and does therefore not interact with the FC and SD operators (which are real and triplet operators). The contributions of the latter two are both obtained from $\mathbf{G}^{\mathrm{rt}}$ and therefore form a cross term which can be written equivalently in two forms

$$
\begin{aligned}
\mathbf{K}_{KL}^{\mathrm{FC/SD}} &= \sum_{ai}\lambda_{ai,K}^{\mathrm{FC}}\mathbf{R}_{ai,L}^{\mathrm{SD}}+\sum_{ai}\mathbf{R}_{ai,K}^{\mathrm{SD}}\lambda_{ai,L}^{\mathrm{FC}}\\
&= \sum_{ai}\lambda_{ai,K}^{\mathrm{FC}}\mathbf{R}_{ai,L}^{\mathrm{SD}}+\sum_{ai}\boldsymbol{\lambda}_{ai,K}^{\mathrm{SD}}R_{ai,L}^{\mathrm{FC}}
\end{aligned}
\tag{18}
$$

This matrix is traceless and does therefore not contribute to the SSCC, but it is in many cases the dominant contribution to the SSCT anisotropy.

The DSO contribution

$$
\begin{aligned}
\mathbf{K}_{KL}^{\mathrm{DSO}} &= \frac{\partial^2 E}{\partial\boldsymbol{M}_K\partial\boldsymbol{M}_L}\\
&= 4\alpha^4\sum_i\int\phi_i(\boldsymbol{r})r_K^{-3}r_L^{-3}(\boldsymbol{r}_K^{\mathrm{T}}\boldsymbol{r}_L\mathbf{I}_3-\boldsymbol{r}_K\boldsymbol{r}_L^{\mathrm{T}})\phi_i(\boldsymbol{r})\,\mathrm{d}\boldsymbol{r}
\end{aligned}
\tag{19}
$$

is a ground-state expectation value and thus does not require solution of linear-response equations.

The complete reduced coupling tensor is given by

$$
\begin{aligned}
\mathbf{K}_{KL} = \mathbf{K}_{KL}^{\mathrm{DSO}}&+\sum_{ai}\boldsymbol{\lambda}_{ai,K}^{\mathrm{PSO}}(\mathbf{R}_{ai,L}^{\mathrm{PSO}})^{\mathrm{T}}+\mathbf{K}_{KL}^{\mathrm{FC/SD}}\\
&+\mathbf{I}_3\sum_{ai}\lambda_{ai,K}^{\mathrm{FC}}R_{ai,L}^{\mathrm{FC}}+\sum_{ai}\boldsymbol{\lambda}_{ai,K}^{\mathrm{SD}}\mathbf{R}_{ai,L}^{\mathrm{SD}}
\end{aligned}
\tag{20}
$$

IMPLEMENTATION

DSO Term. The DSO integral in eq 19 cannot be solved analytically. Instead, it is rewritten as suggested in ref 33 and is then solved by one analytical integration and one Gauss–Legendre quadrature on 24 gridpoints. For the transformation of the integral bounds, $m = 0.75$ was chosen, in accordance with ref 33.

Response. The response eq 10 are solved for FC, SD, and PSO individually, using an iterative non-orthonormal Krylov subspace method.[34,35]

The trial vectors are read from a file in the basis of molecular orbitals (MO basis, Latin indices) and transformed to the basis of atomic basis functions (AO basis, Greek indices). They are then contracted with the two-electron integrals,[36,37] which are calculated on the fly using the Obara–Saika scheme

$$
R_{\mu\nu} = \sum_{\kappa\lambda} g_{\mu\nu\kappa\lambda}\lambda_{\kappa\lambda} \tag{21}
$$

$$
g_{\mu\nu\kappa\lambda} = \iint\phi_\mu^*(\boldsymbol{r}_1)\phi_\nu(\boldsymbol{r}_1)r_{12}^{-1}\phi_\kappa^*(\boldsymbol{r}_2)\phi_\lambda(\boldsymbol{r}_2)\,\mathrm{d}\boldsymbol{r}_1\,\mathrm{d}\boldsymbol{r}_2 \tag{22}
$$

The matrix–vector products are transformed back to the MO basis and stored on disk for the convergence check.

RI-*K*. For Coulomb integrals, an efficient and accurate approximation has been developed.[38−40] Due to its formal similarity to the resolution of the identity, it has been termed RI-*J*. In the context of SSCTs, however, there are no Coulomb terms. A similar approach, RI-*K*, exists for the exchange integrals.[41] In contrast to RI-*J*, it does not reduce the formal scaling, albeit the prefactor is reduced.

Within the RI-*K* approximation, the four-center integrals for exchange are calculated as

$$
g_{\mu\nu\kappa\lambda}^{\mathrm{RI}} = \frac{1}{2}\sum_{PQR}(\mu\nu|P)(P|R)^{-1/2}(R|Q)^{-1/2}(Q|\kappa\lambda) \tag{23}
$$

To solve the response eq 10, the integrals need to be contracted with the trial vector λ_{bj}. Instead of transforming it to the AO basis in every iteration, the three-center integrals $(\mu\nu|P)$ are transformed to the MO basis once after construction, and the quantity

$$
B_{pq}^{Q} = \sum_P(pq|P)(P|Q)^{-1/2} \tag{24}
$$

is stored on disk. Within the solver iterations, these quantities are read and contracted with λ_{bj}, yielding

$$
\tilde{B}_{aj}^{Q} = \sum_b B_{ab}^{Q}\lambda_{bj} \tag{25}
$$

In the final step

$$
R_{ai} = \sum_{jQ} B_{ji}^{Q}\tilde{B}_{aj}^{Q} \tag{26}
$$

is obtained.

Seminumerical Integration. As an alternative, we implemented the seminumerical (sn) integration of the four-center integrals on a grid[42−44]

$$
R_{\mu\nu}^{\mathrm{sn}} = \sum_g X_{\mu g}\sum_\lambda A_{\nu\lambda g}\sum_\kappa\lambda_{\kappa\lambda}X_{\kappa g} \tag{27}
$$

here, g indexes the grid points at position $\boldsymbol{r}_g$ with weights w_g and

https://dx.doi.org/10.1021/acs.jpca.0c06897
J. Phys. Chem. A 2020, 124, 8529−8539

$$X_{\mu g} = w_g^{1/2} \phi_\mu(\boldsymbol{r}_g) \tag{28}$$

$$A_{\nu\lambda g} = \int \frac{\phi_\nu(\boldsymbol{r}_g)\phi_\lambda(\boldsymbol{r}_g)}{|\boldsymbol{r} - \boldsymbol{r}_g|} \, \mathrm{d}\boldsymbol{r} \tag{29}$$

Like in ground state calculations, $A_{\nu\lambda g}$ is evaluated by an exact quadrature scheme. Equation 26 is most efficiently evaluated right-to-left. The loop over the grid points is executed in batches to reduce memory demands.

Extension to Local Hybrids. A similar seminumerical integration scheme has been used to implement LH functionals. As outlined above, due to the presence of the LMF, the four-center exchange integrals depend on an additional semilocal function, rendering an analytical implementation demanding, if not impossible. Yet the seminumerical scheme allows a straightforward solution, where the LMF is constructed from molecular properties on a grid and is included in the quadrature part of the integration.

The extension of the existing code to match the requirement of SSCCs is done taking the following steps: (i) the electronic (LH) Hessian of eq 11 is used, as described in ref 32, where only the right-hand sides are exchanged to correspond to the contributions of eqs 5 and 6. (ii) The Hessian of the PSO contribution, which is comparable to the paramagnetic contribution to nuclear shieldings (as both are imaginary, they depend only on the exact-exchange contribution), is solved by adjusting the dimensions of the involved perturbed density matrices in the routines of our recent nuclear shielding implementation for LHs in TURBOMOLE (cf. ref 24), and exchange of the right-hand sides to match eq 7. We note that for SSCTs, a larger number of perturbed contributions have to be computed compared to shielding calculations (overall $3{\cdot}N$, where N is the number of non-symmetry-equivalent nuclei, instead of the 3 perturbations by the external magnetic field for shieldings).

Nuclei Selection Schemes. As is evident from eq 20, it is sufficient to solve the response equations for one coupling partner in order to obtain the coupling tensor between that atom and any other atom. For the latter, it suffices to calculate the right-hand side. Since there is a separate set of eq 10 for each atom, excluding some $\mathbf{R}_K$ does not alter the solution vector λ_L and therefore leaves the resulting SSCT untouched. This can be utilized via a nuclei selection scheme, where the response is calculated only for a few, user-selected, nuclei. This can be readily combined with the idea of LDBSs,[45] that is, by employing different types of basis sets for the atom/region of interest and the remainder of the molecule, which is carefully investigated for the present context below.

The form given in the first line of eq 18 requires both λ_K^{FC} and λ_L^{FC}, that is, the response equations need to be solved for both coupling atoms. This prohibits the full use of the nuclei selection, but it avoids the six response equations of the SD term. The form given in the second line requires λ_K^{FC} and λ_K^{SD} and is preferred if the SD terms are calculated anyway, as no response equations for nucleus L need to be solved. If one wants, for example, to obtain the ^{13}C NMR spectrum of a compound $C_nA_mX_k$, where A stands for coupling nuclei and X for non-coupling ones, then only $10(n + m)$ RHS vectors need to be calculated and $10n$ response equations to be solved, instead of $10(n + m + k)$. The factor $10 = 1 + 6 + 3$ describes the individual contributions of the FC, SD, and PSO term.

Further, molecular symmetry may be exploited for D_{2h} symmetry and subgroups, and solvent effects may be included by the conductor-like screening models COSMO[46] and D-COSMO-RS.[47] All features are available in TURBOMOLE V7.5.[48−51]

RESULTS AND DISCUSSION

Technical Performance of the Implementation. *Settings.* For the computations in this section, the wave function has been converged with an energy threshold of 10^{-8} Ha and the response vectors with a residual norm of 10^{-6}, which is enough to obtain a precision in the coupling tensors of typically 10^{-2} Hz.

The computation times were recorded on an Intel Xeon CPU E5-2687W v4 (3.00 GHz).

Nuclei Selection and Locally Dense Basis Sets. The time savings when calculating the coupling tensors of only a subset of atom pairs have been investigated exemplarily using porphyrin. At B3LYP[52,53]/pcJ-2[54−56] (grid[57] size 3) level without symmetry, the calculation of all tensors takes 72 h on one core. All hydrogen−hydrogen coupling tensors can be calculated within 21 h and a particular nitrogen−nitrogen coupling tensor within 3 h using nuclei selection, without loss of accuracy. An obvious complement to this feature is the idea of so-called "locally dense basis sets" (LDBSs), that is, the combination of larger basis sets for the atom/region of interest and smaller ones for the remainder of the molecule, as for SSCTs, only the electronic structure of the coupling atoms and their immediate vicinity matters. This concept was first employed in the calculation of chemical shifts.[45,58−60] It has been applied to SSCCs as well, mainly using the second order polarization propagator approximation.[61−64] Although LDBS have been used with DFT methods,[65,66] little investigation on the reliability of such a method has been done.[67]

We have investigated the LDBS scheme on 15 molecules: adamantane, Al_4Me_4, $AlH_2PMe_2CF_3$, AlH_2PMe_3, allene, B_4Me_4, bicyclo[1.1.1]pentane, butane, C_2H_2, C_2H_6, EtMgCl·2THF, HCN, $MgMe_2$, naphthalene, and OF_2. For these compounds in particular, it is not always clear which nuclei to include into a chemically meaningful surrounding of the coupling atoms as this would require a priori knowledge of the system. In preliminary investigations, we found that it is usually sufficient to use LDBS at the coupling partners only. Our results are summarized in Table 1, the complete list can be found in Supporting Information (Tables S1−S4). We used the basis set combinations "pcJ-n/m" (meaning pcJ-m for the coupling atoms and an attenuated basis set pcJ-n for the remainder of the system) and "XVP/pcJ-m" (X = S, TZ), where we employed the def2-XVP basis set[68] as the attenuated basis. In this article, we restrict ourselves to $m = 2$ and use pcJ-2 as a reference. We used the TPSS[69] and the B3LYP functional with grid 3. The isotropic and anisotropic part of the

Table 1. Number of Couplings That Deviate More Than 0.1 Hz from the pcJ-2 Reference Result (First Number) and Maximum Deviation Therefrom (Second Number, in Hz)

measured quantity	pcJ-1/2	TZVP/pcJ-2	SVP/pcJ-2
TPSS, isotropy	25/−12.2	29/−12.2	47/−57.5
B3LYP, isotropy	24/−10.6	29/−11.5	45/−54.3
TPSS, anisotropy	29/14.6	31/6.1	40/18.8
B3LYP, anisotropy	27/16.2	28/7.8	40/22.0

https://dx.doi.org/10.1021/acs.jpca.0c06897
J. Phys. Chem. A 2020, 124, 8529−8539

SSCT in most cases differ by less than 5 Hz (for pcJ-2) between these two functionals, but large deviations up to 240 Hz have been found for OF_2. However, all basis set combinations are affected in a similar way (as can be seen from the maximum deviation in Table 1), and we are therefore confident that our findings hold for other density functionals as well.

The distribution of errors is highly non-Gaussian, and the usual statistical methods such as calculating the standard deviation are not meaningful. For instance, the smallest attenuated basis set, def2-SVP, produces the largest deviation from the pcJ-2 result, 57.5 Hz for the F−F coupling in OF_2. We therefore use the number of coupling constants that differ by more than 0.1 Hz from their reference value as a primary criterion; other thresholds give similar results. With pcJ-1/2, we find 24−29 (depending on the functional and whether isotropy or anisotropy is considered) such outliers in the 51 coupling constants investigated, and the combination TZVP/pcJ-2 yields similar values (28−31). With SVP/pcJ-2, many coupling constants (40−47) differ by more than 0.1 Hz from pcJ-2. We find no clear indication that either the isotropic or the anisotropic contribution is described worse with LDBS. It is noteworthy that most SSCTs are only slightly affected if the attenuated basis set is used instead of the large one. For example, with TZVP/pcJ-2, only three coupling constants deviate by more than 2 Hz from pcJ-2. Of the three combinations investigated here, we deem the methods pcJ-1/2 and TZVP/pcJ-2 eligible.

As a practical example, we calculated the P−H and P−C coupling constants of SIMesPH [SIMes = 1,3-bis(2,4,6-trimethylphenyl)imidazolin-2-ylidene] as well as its tBu$_2$AlCl and tBu$_2$GaCl adducts, in the following labeled SIMesPH·Al and SIMesPH·Ga, respectively. In Table 2, we compare the computed coupling constants (using B3LYP/grid 3) with the experimentally obtained ones from ref 70, from where we also obtained the optimized Cartesian coordinates. We used COSMO to simulate the solvent effect, using ε = 2.28 (benzene). All three calculation protocols yield almost the same result, reproducing the experimental trends fairly well. Note that the experiment does not indicate the sign of the coupling constants. If a negative sign for J_{PC} is assumed, the calculated values are consistently about 25 Hz smaller than the measured ones. The agreement between the three computation methods shows that the use of mixed basis sets pcJ-1/2 and TZVP/pcJ-2 is valid also beyond the sample test set and that basis set errors are much smaller than the differences to the experiment.

Table 2. Comparison of Experimentally Measured ("Exp.", Sign Unkown) Coupling Constants (in Hz) with the Ones Calculated with Different Basis Set Combinations (at the B3LYP Level)[a]

	SIMesPH		SIMesPH·Al		SIMesPH·Ga	
	J_{PH}	J_{PC}	J_{PH}	J_{PC}	J_{PH}	J_{PC}
Exp.	163	72.7	211	68.9	215	65.6
pcJ-2	139.1	−103.1	188.8	−96.3	192.3	−92.2
pcJ-1/2	137.2	−105.1	188.0	−97.4	191.1	−93.4
TZVP/pcJ-2	138.5	−103.4	188.7	−96.3	192.3	−92.2

[a]For Ga, pcJ-1 and pcJ-2 were replaced by def2-SVP and def2-TZVP, respectively.

Grids for the Seminumerical Integration and LHs. The size of the grid for the numerical integration is a tradeoff between the errors made and the computational effort. To find a suitable grid size, we investigated the 276 coupling tensors of the α-D-glucose monomer (generated with the SWEET tool[71]) with the pcJ-2 basis set.

The seminumerical calculation of the exact exchange was examined using Hartree−Fock. We found that the TURBOMOLE grid size 1 yields maximum errors of 0.03 and 0.05 Hz for the isotropic and anisotropic part, respectively.

The error margins of LH functionals using the smallest integration grids (grid setting 1) are tested with respect to very large grid settings (TURBOMOLE grid 7 with enlarged radial grid setting to 25), giving a maximal deviation of 0.12 Hz with an averaged deviation of 0.01 Hz for LH07t-SVWN.[72] Due to the presence of the gauge function, deviations are larger for LH14t-calPBE,[73] giving a maximal deviation of 2.44 Hz and an average deviation of 0.18 Hz. However, increasing the radial grid size slightly (radial grid setting 3 instead of the default setting of 1) reduces the deviations to 0.27 Hz (max.) and 0.01 Hz (av.), with only a moderate increase of grid points (increase from a total of 30,797 to 43,596 grid points, see also Table S10 in Supporting Information).

Efficiency. To demonstrate the efficiency of our implementation, we investigated chains consisting of n α-D-glucose units, denoted (amylose)$_n$, n = 4, 8, 16, 32, 48, 64, which were generated with the SWEET tool. Our setup (PBE[74]/pcJ-1, TURBOMOLE grid 1, one core) is very close to the parameters used in ref 75. The wall times obtained in this manner (without approximations) are listed in Table 3. For ease of comparison with ref 75, we report only the time needed for the calculation of **R** and $\boldsymbol{\lambda}$, disregarding overhead, for example for reading the MO data. We achieve a favorable scaling of $n^{2.3}$ between n = 16 and n = 32, close to that in ref 75 ($n^{2.4}$) but with a lower prefactor. Factoring in the thermal design power of the CPUs, we find that our implementation consumes about half the energy.

Table 3. Wall Times on One Core (in minutes) for Setting up the RHS and Solving the Necessary Response Equations for the Calculation of a Single Coupling Tensor in a Chain of n Glucose Units Employing PBE/pcJ-1

n	wall time
4	1
8	2
16	6
32	28
48	78
64	174

Benefit of the Implemented Features. In the following, we compare timings for RI-K (using the def2-TZVP auxiliary basis[76]) and the seminumerical integration (for which a grid size of 1 was used) with the unapproximated exchange. For this, we use TPSSh[77] and grid 3 for the exchange−correlation functional. For comparison, we include the LH07t-SVWN functional (using a grid size of 1 for the exchange−correlation functional as discussed above). We investigated four setups: (amylose)$_2$ with a pcJ-2 basis, where we are able to calculate all SSCTs in less than two days, and the larger system (amylose)$_4$ in a pcJ-3 basis, where we only calculate a single SSCT, to test the other extreme. For the first system, we also investigated the

https://dx.doi.org/10.1021/acs.jpca.0c06897
J. Phys. Chem. A 2020, 124, 8529−8539

Table 4. Wall Times (in hours) on Four Cores[a]

			TPSSh				LH07t-SVWN	
molecule	basis set	response	SCF	no approx.	RI-*K*	seminumerical	SCF	SSCT
$(amylose)_2$	pcJ-2	all	0.9	38.1	5.6	12.9	0.6	20.3
	pcJ-2	all C	0.9	6.9	1.7	3.4	0.6	6.0
	pcJ-1/2	all C	0.3	2.1	0.8	1.6	0.3	2.6
$(amylose)_4$	pcJ-3	one C	35.2	21.3	14.9	9.1	10.2	17.7

[a]In the third row, a LDBS scheme was used. The column "response" indicates for which atoms the response equations had been solved. For TPSSh, grid 3 has been used. The seminumerical integration was carried out with grid 1. For LH07t-SVWN, grid 1 has been used throughout.

effect of the nuclei selection and LDBS. The times given are wall times on four cores. The wave function was optimized using the RI-*J* approximation only (in all cases) starting from a Hückel guess.

For $(amylose)_2$, the SCF procedure is faster than solving the response equations for all three approximations (cf. Table 4). When calculating all coupling constants, in the TPSSh case, about 2.1 h are spent outside the four-center integral routines (this time is included in Table 4), mainly computing the density functional derivatives. The remainder of the time (i.e., the larger part) is brought down from 36.0 to 10.8 h with the seminumerical integration and even to 3.5 h with RI-*K*, meaning a speedup of the exchange integrals by one order of magnitude.

If only C−C coupling tensors are to be calculated, much less response equations have to be solved, and therefore, the computation time is greatly reduced. The time of the SCF procedures is not affected. If additionally the pcJ-1/2 LDBS combination (as described above) is employed, the times for both the SCF and the SSCT step are reduced.

In these three cases, RI-*K* is the fastest method of the three investigated. This is because pcJ-2 is a rather large basis set, where RI-*K* performs well, if enough memory is available.

Similar time savings can be seen for the LH functional LH07t-SVWN. While it requires slightly more computational effort than the seminumerical approximation for the global hybrid, the use of smaller grids remedies this drawback, rendering the computation times for C−C-only couplings similar to the unapproximated TPSSh case. If a large number of couplings are to be calculated, the effect of the small grid prevails.

For $(amylose)_4$, the SCF procedure with TPSSh takes 35.2 h, which is significantly longer than the response equations for one SSCT. These take 21.3 h without approximation, where again most time (20.9 h) is spent for the exact exchange. With RI-*K*, this reduces to 14.4 h, but a significant amount (5.4 h) is spent preparing the B^{Q}_{pq} intermediates. Their computational effort is always the same, independent of the number of SSCTs to be calculated. The seminumerical integration does not suffer from such an overhead and is the fastest method of the three for this case, evaluating the four-center integrals in 8.6 h. It is well known that the seminumerical integration (and hence the LHs as well) scales better than analytical exact exchange with basis set size;[42,43] therefore, this scheme becomes more competitive as larger basis sets (e.g., pcJ-4) are chosen. With LH07t-SVWN, the wavefunction can be computed faster than with TPSSh due to the seminumerical treatment of exact exchange. Computing the TPSSh wave function with similar parameters as LH07t-SVWN only takes 7.9 h but results in an error of about 4 Hz. The response part with LH07t-SVWN is about as fast as with TPSSh.

Parallelization. Most computation times so far were obtained on four cores using the OpenMP parallelization scheme. It is therefore worthwhile to examine the efficiency when calculating all SSCTs of $(amylose)_2$/pcJ-1 and one SSCT of $(amylose)_3$/pcJ-2, using grid settings as discussed above. As can be seen from Table 5, with TPSSh, a speedup of 3.7 is achieved on four cores in the first case and 3.2 in the latter. Examining the approximations, we find a speedup of 3.8 for the seminumerical integration for both molecules. The RI-*K* method seems to be slightly worse, with a speedup of about 3. The good performance of the seminumerical integration translates to the LH functionals LH07t-SVWN and LH14t-calPBE (3.6−3.8). The overall longer time of LH14t-calPBE compared to LH07t-SVWN can be explained by the larger grid (radial grid size 3 instead of 1), containing about 40% more grid points.

Table 5. Computation Times in Hours on One and Four Cores Using Different Methods[a]

	$(amylose)_2$/pcJ-1			$(amylose)_4$/pcJ-2		
	1 core	4 cores	speedup	1 core	4 cores	speedup
TPSSh	9.3	2.5	3.7	5.8	1.8	3.2
TPSSh (sn)	9.8	2.6	3.8	6.8	1.8	3.8
TPSSh (RI-*K*)	4.4	1.3	3.3	8.5	3.0	2.9
LH07t-SVWN	14.4	4.0	3.6	14.8	3.9	3.7
LH14t-calPBE	20.1	5.5	3.7	21.0	5.6	3.8

[a]For TPSSh, grid 3 has been used. The seminumerical integration was carried out with grid 1. For LH07t-SVWN, grid 1 has been used throughout. LH14t-calPBE has been computed with a spherical grid size of 1 and a radial grid size of 3.

Performance of Local Hybrid Functionals. *Settings.* For this first preliminary evaluation of LHs in the computation of isotropic SSCCs, we focus on a combined benchmark set of 23 small main-group species (H_2O, HOF, OF_2, C_2H_4, C_2H_6, C_2H_2, CFCH, C_2F_2, NH_3, N_2, C_3H_4, CH_4, CH_3F, CO, CO_2, H_2CO, HFCO, F_2CO, HCN, FCN, FNO, HD, and HF), with overall 80 SSCCs of diverse nucleus combinations against CC3/aug-ccJ-pVTZ and MCSCF/BS2 data from refs 78 and 79, respectively, which avoids complications from environmental or rovibrational effects included in experimental values. For consistency, structures from these studies have been used without reoptimization at the given DFT level. The reference data are of either CC3/aug-ccJ-pVTZ or MCSCF/BS2 quality. Where references and structures are available in both benchmark sets (H_2O, C_2H_2, HCN, and CO), we use the more recently published CC3 SSCCs from ref 79 (yet structures and SSCC benchmark data from both works are almost identical). pcJ-4 basis sets, energy convergence thresholds of 10^{-9} Ha, and density matrix convergence thresholds of 10^{-7} were used for the evaluation of LHs and

https://dx.doi.org/10.1021/acs.jpca.0c06897
J. Phys. Chem. A 2020, 124, 8529−8539

Table 6. Comparison of MAPD (in %) of Computed SSCCs for Various Density Functionals Compared to the Reference Data

coupling	TPSS	TPSSh	B3LYP	PBE0	BHLYP	LH07t	LH12ct	LH14t
^{1}J	34.37	29.67	22.94	22.09	26.65	19.80	31.70	15.38
$^{2/3}J^{a}$	33.87	28.10	21.89	19.56	27.63	15.64	28.23	16.27

[a]Couplings with absolute values smaller than 5 Hz have been excluded from the statistical evaluation.

Table 7. Comparison of Computed Contributions to the $^{1}J_{CF}$ SSCCs with Various Density Functionals against CC3/aug-ccJ-pVTZ Data

		Exp.[a]	CC3[a]	TPSS	TPSSh	B3LYP	PBE0	BHLYP	LH07t[b]	LH12ct[b]	LH14t[b]
C_2F_2	FC		−241.57	−400.36	−384.67	−357.81	−355.82	−308.95	−348.08	−323.51	−349.35
	SD		−7.52	−13.41	−15.32	−14.00	−15.91	−19.60	−11.04	−7.92	−12.76
	PSO		−8.08	−11.27	−14.26	−18.04	−19.12	−26.29	−13.98	−14.58	−14.43
	DSO		0.59	0.59	0.59	0.58	0.58	0.58	0.58	0.58	0.58
	Σ	−287.3	−256.58	−424.45	−413.66	−389.28	−390.26	−354.26	−372.52	−345.44	−375.96
F_2CO	FC		−256.94	−394.57	−375.72	−355.19	−346.15	−298.65	−342.54	−311.56	−342.84
	SD		0.00	−0.91	−1.42	−1.46	−1.97	−2.78	−1.12	−0.62	−1.48
	PSO		−38.61	−44.14	−44.74	−47.63	−46.71	−47.89	−42.84	−41.32	−43.22
	DSO		1.17	1.17	1.17	1.16	1.16	1.15	1.16	1.16	1.16
	Σ	−308	−294.39	−438.45	−420.71	−403.13	−393.67	−348.15	−385.34	−352.34	−386.38
CFCH	FC		−247.47	−398.12	−381.47	−356.20	−353.56	−305.58	−349.14	−323.82	−349.57
	SD		−9.73	−16.60	−18.81	−17.40	−19.64	−24.34	−14.31	−10.72	−16.34
	PSO		−20.96	−24.81	−27.92	−32.86	−33.96	−41.81	−28.08	−29.10	−28.38
	DSO		0.49	0.49	0.49	0.48	0.48	0.47	0.47	0.47	0.48
	Σ		−277.68	−439.04	−427.71	−405.99	−406.69	−371.26	−391.07	−363.17	−393.82
FCN	FC		−365.36	−556.46	−527.63	−493.85	−484.74	−418.39	−477.93	−432.60	−478.88
	SD		−9.67	−14.78	−17.42	−16.98	−18.73	−25.59	−14.04	−11.26	−16.08
	PSO		−28.55	−31.23	−34.72	−39.91	−41.11	−50.47	−35.33	−36.54	−35.84
	DSO		0.57	0.57	0.56	0.55	0.56	0.54	0.55	0.55	0.55
	Σ		−403	−601.90	−579.21	−550.19	−544.01	−493.90	−526.75	−479.85	−530.25
HFCO	FC		−314.6	−427.18	−413.57	−397.83	−387.22	−357.29	−374.17	−333.84	−379.56
	SD		1.18	−0.54	−1.13	−1.06	−1.68	−2.66	−0.64	0.07	−0.96
	PSO		−39.7	−51.07	−50.22	−52.17	−50.89	−48.35	−46.47	−43.65	−46.58
	DSO		0.72	0.72	0.72	0.71	0.72	0.71	0.71	0.71	0.71
	Σ	369	−352.41	−478.08	−464.21	−450.35	−439.08	−407.59	−420.58	−376.70	−426.38

[a]See ref 79. [b]LH07t-SVWN, LH12ct-SsifPW92, LH14t-calPBE.

the other functionals in that comparison. To ensure convergence for this initial evaluation for LHs, we enhanced the grids to the large TURBOMOLE standard setting 5, albeit tests show that the grid dependence for LHs and meta-GGA global hybrid functionals is essentially the same (see Table S10 in Supporting Information). The ground-state SCF for LHs uses the seminumerical implementation of ref 44.

While more uniform DFT results with smaller deviations from experimental SSCCs can be obtained when these are evaluated at structures obtained with the same DFT functional,[12] we rely here on the structures provided in the benchmark studies to concentrate exclusively on the performance of a given functional in the perturbation treatment of the coupling constants.

All employed LH models are based on the so called t-LMF,[80] defined as the (scaled) ratio of the von-Weizsäcker and Pauli kinetic energy densities ($g(\boldsymbol{r}) = b\cdot\frac{\tau_W(\boldsymbol{r})}{\tau(\boldsymbol{r})}$), with $\tau_W(\boldsymbol{r}) = \frac{1}{8}\frac{|\nabla\rho(\boldsymbol{r})|^2}{\rho(\boldsymbol{r})}$). We include the LDA-based LH07t-SVWN with a prefactor b = 0.48 for its spin-channel t-LMF, LH12ct-SsifPW92[81] with a larger prefactor of b = 0.709 of its common t-LMF, and a short-range modified (self-interaction-free − sif) PW92 correlation functional, and LH14t-calPBE (b = 0.50 for its spin-channel t-LMF). The latter functional is based on PBE exchange and correlation and serves as a first example of using exchange-energy densities calibrated by a gauge function to account for their ambiguity (further functionals based on such an approach are currently developed).

Performances are statistically compared by reporting mean absolute percentage deviations (MAPDs) $\left(\mathrm{MAPD} = \frac{1}{N}\left(\sum_i^N \frac{|J_i - J_{\mathrm{Ref},i}|}{|J_{\mathrm{Ref},i}|}\cdot 100\right)\right)$. For comparison with the LH results (see below), we include the meta-GGA TPSS and its global hybrid version TPSSh (which both often perform well in NMR shielding calculations[82]), together with the global hybrids B3LYP, PBE0,[83] and BHLYP[84] (the latter has been found to perform well for the challenging C−F SSCCs[85] and for H−F SSCCs[86]).

https://dx.doi.org/10.1021/acs.jpca.0c06897
J. Phys. Chem. A 2020, 124, 8529−8539

Statistical Data Evaluation. It is tempting to condense the rather extensive data analysis of these two test sets by using statistical analyses. This is made difficult by the rather diverse types of SSCCs with rather different sizes and signs, requirements regarding the different terms, and general behavior. Table 6 makes an attempt to nevertheless obtain an impression of the general performances of different functionals by providing MAPDs. This allows a better comparison of small and large, positive and negative SSCCs. We provide separate statistics for one-bond couplings and for two-/three-bond couplings. We see that for the one-bond couplings, LH14t-calPBE provides the lowest relative deviations, followed by LH07t-SVWN and the PBE0 and B3LYP global hybrids. In spite of its top performance for some of the types of couplings (see below), BHLYP exhibits only a middle place in this evaluation. LH12ct-SsifPW92, which also performs best for some of the couplings, ranks even lower due to problems for other cases. The TPSS meta-GGA provides the largest MAPD. This holds also for the two-/three-bond couplings. Here, the LH07t-SVWN LH gives slightly lower deviations than LH14t-calPBE and ranks first. PBE0 and B3LYP again rank third and fourth, respectively, while BHLYP and LH12ct-SsifPW92 perform again only moderately well. We note in passing that coupled-perturbed Hartree−Fock calculations (sometimes referred to as RPA in this context) give much larger MAPD values between 200 and 400%, even if we exclude cases where the Hartree−Fock wave function exhibits triplet instabilities.

More Detailed Evaluations. In the interest of conciseness and clarity, we refer the reader to Supporting Information for a more detailed, somewhat tedious comparison of the various functionals for different classes of SSCCs. Full data are provided in Table S11 (individual FC, SD, PSO, and DSO terms are analyzed in Tables S12−S15). This is an attempt to understand the statistical results better by discussing different types of couplings in turn, focussing in particular on one-bond couplings for different combinations of nuclei.

Here, we select only the $^1J_{CF}$ SSCCs for closer scrutiny, as they behave rather differently than most other couplings. It is important to note that these types of couplings are considered a major challenge to DFT. Indeed, the accuracy achieved for many other couplings is much better (see Table S11 in Supporting Information). As for $^1J_{FH}$ in the HF monomer and dimer,[86] the large negative $^1J_{CF}$ SSCCs (six occurrences in the test sets) are known to be underestimated appreciably by most functionals, with BHLYP having been found to perform best[85] (or even larger exact-exchange admixture being superior[17]). While the PSO contribution also exhibits some dependence on the functional,[17−19,87] the FC term is again the main culprit here (see Table 7 for closer analysis). Our computations confirm the relatively good performance of BHLYP, but LH12ct-SsifPW92 performs even slightly better (except for F_2CO). Interestingly, this may be attributed to a clearly better description of the PSO term by the LH (reminiscent of its good performance for non-hydrogen nuclear shieldings[24]), while BHLYP benefits from a somewhat less negative FC contribution. This highlights that the different terms, in this case FC and PSO, present different requirements to the functional. For couplings involving atoms with lone pairs, it appears that the large constant exact-exchange admixture of BHLYP may be favorable for reducing the underestimate of the FC contribution, but it increases the underestimate of the PSO term. The couplings obtained with the other two LHs (LH14t-calPBE, LH07t-SVWN) are only moderately more negative than the BHLYP and LH12ct-SsifPW92 ones, followed by the PBE0 results. The most negative values are obtained with TPSS and TPSSh, that is, the present LH results do improve upon $^1J_{CF}$ SSCCs but do not eliminate their systematic underestimate by DFT approaches completely.

The overall detailed analyses (see Supporting Information) confirm that no functional evaluated here is fully satisfactory for all SSCCs of the two test sets, even if we keep in mind the somewhat heterogeneous reference data (CC3 and MCSCF, which deviate also a bit from the available experimental data). This confirms previous evaluations for global hybrids (see, e.g., ref 17). Some functionals perform best in some situations but may exhibit serious shortcomings in others. Picking, for example, BHLYP, our computations not only confirm its leading performance for $^1J_{CF}$ and $^1J_{FH}$[85,88] but also show it performs best for $^1J_{CO}$ (and for $^1J_{OH}$). Yet this top performance is offset by cases where high constant exact-exchange admixture is detrimental, such as the C−H, C−C, C−N, O−F, and N−F one-bond couplings. The O−F and N−F couplings highlight that some cases with appreciable static correlation may not tolerate the large admixture, and the C−N couplings and the C−C couplings in acetylenes tell a similar story for some of the couplings across multiple bonds.[17] These are some of the reasons that prevent BHLYP from being a top performer across the entire test set. We can make analogous arguments for the LH12ct-SsifPW92 LH. While this performs very well for some of the couplings (C−F, N−F, O−F) and seems to tolerate static correlation cases, it underestimates reduced couplings for many of the seemingly simpler cases such as C−H or C−C couplings. The LH14t-calPBE and LH07t-SVWN LHs that top the overall ranking (Table 6) are most often among the top performers. However, even when they are not, they never exhibit extreme deviations. One may say the same, but to a lesser extent, about the PBE0 and B3LYP global hybrids.

Further evaluations of the different aspects that may affect the performance of a given LH functional will be needed to proceed toward a more complete understanding that will also aid in the development and validation of improved functionals. Such evaluations, which are outside the scope of the present work and will be pursued separately, will involve the role of the LMF and calibration function and the role of induced-current contributions to the response equations resulting from the occurrence of the local kinetic energy density in the t-LMF and conceivably in more sophisticated mixing functions.

■ CONCLUSIONS

The implementation of the calculation of spin−spin coupling tensors at Hartree−Fock, semi-local DFT (including meta-GGA functionals), global hybrid and, for the first time, LH DFT level in the TURBOMOLE code has been presented. The two described approximations to treat exact exchange, RI-*K* and seminumerical integration, both reduce the computation time significantly. On the $(amylose)_2$ molecule investigated, the calculation with RI-*K* was about seven times as fast as full analytical integration, with negligible loss in accuracy. The SSCCs of all 45 atoms can be calculated in less than 6 h. Symmetry exploitation and a nuclei selection scheme may further reduce the computational effort.

We have confirmed that LDBS can be used within DFT for both the isotropic and the anisotropic contribution to the spin−spin coupling. We were able to obtain a speedup of more

https://dx.doi.org/10.1021/acs.jpca.0c06897
J. Phys. Chem. A 2020, 124, 8529−8539

than 14 with this approximation, which will increase if even larger systems are investigated.

Using seminumerical integration has also allowed the extension of the code to be able to use LH functionals for the computation of spin−spin couplings for the first time, complementing a recent implementation of nuclear shieldings in the same code. This permits studies of the effects of position-dependent exact-exchange admixture on the quality of computed spin−spin coupling tensors. A first assessment of three first-generation LHs in comparison with some standard functionals in wider use against CC3 and MCSCF benchmark isotropic couplings of small main-group molecules has provided insights into the performance. Two of the LHs (LH14t-calPBE and LH07t-SVWN) were the top performers in a general statistical evaluation. They often performed well and, most notably, never exhibited extreme deviations. Other functionals, such as BHLYP, perform well in some types of couplings but deliver substantial errors in others. This holds also for the third LH in the comparison, LH12ct-SsifPW92; while it performs particularly well for the challenging $^{1}J_{CF}$ couplings (competitive with BHLYP) and for some other SSCCs, including cases with substantial static correlation, it exhibits notable underestimates for seemingly simpler couplings.

In view of the overall promising performance of LHs in this initial evaluation, without a truly exceptional quality of the results across the entire test suite, further work in the development of this class of functionals certainly seems warranted. A more systematic evaluation of the various aspects of a LH functional that may affect the quality of computed SSCCs (LMF, calibration function, and semi-local ingredients of both exchange and correlation parts of the functional) should provide indications of where further improvements are to be expected. Such evaluations will involve more extensive benchmarking and further functionals. The availability of an efficient implementation, as reported here, provides the opportunity of in-depth investigations of such aspects.

■ ASSOCIATED CONTENT

Supporting Information

The Supporting Information is available free of charge at https://pubs.acs.org/doi/10.1021/acs.jpca.0c06897.

All investigated isotropic and anisotropic coupling contributions with different basis set combinations; short discussion of point group symmetry; Cartesian coordinates of molecules used for this, three SIMesPH compounds, porphyrin, and the cubane molecule; grid dependence of LH results and detailed LH data, including different SSCC terms; and further statistical analyses (PDF)

■ AUTHOR INFORMATION

Corresponding Authors

Martin Kaupp − *Institut für Chemie, Theoretische Chemie/Quantenchemie, Technische Universität Berlin, 10623 Berlin, Germany;* orcid.org/0000-0003-1582-2819; Email: martin.kaupp@tu-berlin.de

Florian Weigend − *Institute of Nanotechnology, Karlsruhe Institute of Technology (KIT), 76344 Eggenstein-Leopoldshafen, Germany; Fachbereich Chemie, Philipps-Universität Marburg, 35032 Marburg, Germany;* orcid.org/0000-0001-5060-1689; Email: florian.weigend@chemie.uni-marburg.de

Authors

Fabian Mack − *Institute of Physical Chemistry, Karlsruhe Institute of Technology (KIT), 76131 Karlsruhe, Germany*

Caspar J. Schattenberg − *Institut für Chemie, Theoretische Chemie/Quantenchemie, Technische Universität Berlin, 10623 Berlin, Germany*

Complete contact information is available at: https://pubs.acs.org/10.1021/acs.jpca.0c06897

Author Contributions

⊥F.M. and C.J.S. contributed equally to this work.

Notes

The authors declare no competing financial interest.

■ ACKNOWLEDGMENTS

We are grateful to Christof Holzer and to Yannick J. Franzke for technical improvements of the implementation and to the authors of ref 79 for providing input structures. F.M. acknowledges financial support from the Deutsche Forschungsgemeinschaft (German Research Foundation) through the CRC 1176 (Project Q5). C.J.S. acknowledges funding via a Ph.D. scholarship of Studienstiftung des deutschen Volkes. Work in Berlin has also received funding by the German Research Foundation (Deutsche Forschungsgemeinschaft, DFG) within project KA1187/14-1 and furthermore by project-ID 387284271-SFB 1349 (Gefördert durch die Deutsche Forschungsgemeinschaft (DFG)—project-ID 387284271-SFB 1349).

■ REFERENCES

(1) Wüthrich, K. NMR Studies of Structure and Function of Biological Macromolecules (Nobel Lecture). *Angew. Chem., Int. Ed.* **2003**, *42*, 3340−3363.

(2) Mason, E. J. *Multinuclear NMR*; Springer: Hamburg, 1987.

(3) Krivdin, L. B.; Kalabin, G. A. Structural applications of one-bond carbon−carbon spin−spin coupling constants. *Prog. Nucl. Magn. Reson. Spectrosc.* **1989**, *21*, 293−448.

(4) Juranic, N.; Ilich, P. K.; Macura, S. Hydrogen Bonding Networks in Proteins As Revealed by the Amide $^{1}J_{NC'}$ Coupling Constant. *J. Am. Chem. Soc.* **1995**, *117*, 405−410.

(5) Harris, R. K.; Wasylishen, R. E. *Encyclopedia of NMR*; Wiley VCH, 2012; pp 2075−2083.

(6) Faucher, A.; Wasylishen, R. E. In *Gas Phase NMR*; Jackowski, K., Jaszuński, M., Eds.; The Royal Society of Chemistry, 2016; Chapter 2, pp 52−94.

(7) Maciel, G. E.; McIver, J. W.; Ostlund, N. S.; Pople, J. A. Approximate self-consistent molecular orbital theory of nuclear spin coupling. III. Geminal proton-proton coupling constants. *J. Am. Chem. Soc.* **1970**, *92*, 4151−4157.

(8) Wu, A.; Cremer, D.; Auer, A. A.; Gauss, J. Extension of the Karplus Relationship for NMR Spin-Spin Coupling Constants to Nonplanar Ring Systems: Pseudorotation of Cyclopentane. *J. Phys. Chem. A* **2002**, *106*, 657−667.

(9) Perera, S. A.; Sekino, H.; Bartlett, R. J. Coupled-cluster calculations of indirect nuclear coupling constants: The importance of non-Fermi contact contributions. *J. Chem. Phys.* **1994**, *101*, 2186−2191.

(10) Teale, A. M.; Lutnæs, O. B.; Helgaker, T.; Tozer, D. J.; Gauss, J. Benchmarking density-functional theory calculations of NMR shielding constants and spin−rotation constants using accurate coupled-cluster calculations. *J. Chem. Phys.* **2013**, *138*, 024111.

(11) Helgaker, T.; Jaszuński, M.; Ruud, K. Ab Initio Methods for the Calculation of NMR Shielding and Indirect Spin-Spin Coupling Constants. *Chem. Rev.* **1999**, *99*, 293−352.
(12) Helgaker, T.; Jaszuński, M.; Pecul, M. The quantum-chemical calculation of NMR indirect spin-spin coupling constants. *Prog. Nucl. Magn. Reson. Spectrosc.* **2008**, *53*, 249−268.
(13) Helgaker, T.; Watson, M.; Handy, N. C. Analytical calculation of nuclear magnetic resonance indirect spin−spin coupling constants at the generalized gradient approximation and hybrid levels of density-functional theory. *J. Chem. Phys.* **2000**, *113*, 9402−9409.
(14) Keal, T. W.; Helgaker, T.; Sałek, P.; Tozer, D. J. Choice of exchange-correlation functional for computing NMR indirect spin−spin coupling constants. *Chem. Phys. Lett.* **2006**, *425*, 163−166.
(15) Bally, T.; Rablen, P. R. Quantum-Chemical Simulation of ^{1}H NMR Spectra. 2. Comparison of DFT-Based Procedures for Computing Proton−Proton Coupling Constants in Organic Molecules. *J. Org. Chem.* **2011**, *76*, 4818−4830.
(16) Maximoff, S. N.; Peralta, J. E.; Barone, V.; Scuseria, G. E. Assessment of Density Functionals for Predicting One-Bond Carbon-Hydrogen NMR Spin-Spin Coupling Constants. *J. Chem. Theory Comput.* **2005**, *1*, 541−545.
(17) Sychrovský, V.; Gräfenstein, J.; Cremer, D. Nuclear magnetic resonance spin−spin coupling constants from coupled perturbed density functional theory. *J. Chem. Phys.* **2000**, *113*, 3530−3547.
(18) Malkina, O. L.; Salahub, D. R.; Malkin, V. G. Nuclear magnetic resonance spin−spin coupling constants from density functional theory: Problems and results. *J. Chem. Phys.* **1996**, *105*, 8793−8800.
(19) Vaara, J. Theory and computation of nuclear magnetic resonance parameters. *Phys. Chem. Chem. Phys.* **2007**, *9*, 5399−5418.
(20) Kupka, T.; Nieradka, M.; Stachów, M.; Pluta, T.; Nowak, P.; Kjær, H.; Kongsted, J.; Kaminsky, J. Basis Set Convergence of Indirect Spin-Spin Coupling Constants in the Kohn−Sham Limit for Several Small Molecules. *J. Phys. Chem. A* **2012**, *116*, 3728−3738.
(21) Maier, T. M.; Arbuznikov, A. V.; Kaupp, M. Local Hybrid Functionals: Theory, Implementation, and Performance of an Emerging New Tool in Quantum Chemistry and Beyond. *Wiley Interdiscip. Rev.: Comput. Mol. Sci.* **2019**, *9*, No. e1378.
(22) Schattenberg, C. J.; Maier, T. M.; Kaupp, M. Lessons from the Spin-Polarization/Spin-Contamination Dilemma of Transition-Metal Hyperfine Couplings for the Construction of Exchange-Correlation Functionals. *J. Chem. Theory Comput.* **2018**, *14*, 5653−5672.
(23) Wodyński, A.; Kaupp, M. Noncollinear Relativistic Two-Component X2C Calculations of Hyperfine Couplings Using Local Hybrid Functionals. Importance of the High-Density Coordinate Scaling Limit. *J. Chem. Theory Comput.* **2020**, *16*, 314−325.
(24) Schattenberg, C. J.; Reiter, K.; Weigend, F.; Kaupp, M. An Efficient Coupled-Perturbed Kohn−Sham Implementation of NMR Chemical Shift Computations with Local Hybrid Functionals and Gauge-Including Atomic Orbitals. *J. Chem. Theory Comput.* **2020**, *16*, 931−943.
(25) Helgaker, T.; Coriani, S.; Jørgensen, P.; Kristensen, K.; Olsen, J.; Ruud, K. Recent Advances in Wave Function-Based Methods of Molecular-Property Calculations. *Chem. Rev.* **2012**, *112*, 543−631.
(26) Cremer, D.; Gräfenstein, J. Calculation and analysis of NMR spin-spin coupling constants. *Phys. Chem. Chem. Phys.* **2007**, *9*, 2791−2816.
(27) Kaupp, M.; Bühl, M.; Malkin, V. G. *Calculation of NMR and EPR Parameters: Theory and Applications*; Wiley-VCH Verlag GmbH & Co. KGaA: Weinheim, 2004.
(28) Bühl, M.; van Mourik, T. NMR spectroscopy: quantum-chemical calculations. *Wiley Interdiscip. Rev.: Comput. Mol. Sci.* **2011**, *1*, 634−647.
(29) Harris, R. K.; Becker, E. D.; De Menezes, S. M. C.; Granger, P.; Hoffman, R. E.; Zilm, K. W. Further Conventions for NMR Shielding and Chemical Shifts (IUPAC Recommendations 2008). *Magn. Reson. Chem.* **2008**, *46*, 582−598.
(30) Kollwitz, M.; Gauss, J. A direct implementation of the GIAO-MBPT(2) method for calculating NMR chemical shifts. Application to the naphthalenium and anthracenium ions. *Chem. Phys. Lett.* **1996**, *260*, 639−646.
(31) Ramsey, N. F. Electron Coupled Interactions between Nuclear Spins in Molecules. *Phys. Rev.* **1953**, *91*, 303−307.
(32) Maier, T. M.; Bahmann, H.; Kaupp, M. Efficient Seminumerical Implementation of Global and Local Hybrid Functionals for Time-Dependent Density Functional Theory. *J. Chem. Theory Comput.* **2015**, *11*, 4226−4237.
(33) Matsuoka, O.; Aoyama, T. Molecular integral of diamagnetic contribution to nuclear spin-spin coupling constant. *J. Chem. Phys.* **1980**, *73*, 5718−5720.
(34) Stratmann, R. E.; Scuseria, G. E.; Frisch, M. J. An efficient implementation of time-dependent density-functional theory for the calculation of excitation energies of large molecules. *J. Chem. Phys.* **1998**, *109*, 8218−8224.
(35) Furche, F.; Krull, B. T.; Nguyen, B. D.; Kwon, J. Accelerating molecular property calculations with nonorthonormal Krylov space methods. *J. Chem. Phys.* **2016**, *144*, 174105.
(36) Bauernschmitt, R.; Ahlrichs, R. Treatment of electronic excitations within the adiabatic approximation of time dependent density functional theory. *Chem. Phys. Lett.* **1996**, *256*, 454−464.
(37) Weiss, H.; Ahlrichs, R.; Häser, M. A direct algorithm for self-consistent-field linear response theory and application to C_{60}: Excitation energies, oscillator strengths, and frequency-dependent polarizabilities. *J. Chem. Phys.* **1993**, *99*, 1262−1270.
(38) Vahtras, O.; Almlöf, J.; Feyereisen, M. W. Integral approximations for LCAO-SCF calculations. *Chem. Phys. Lett.* **1993**, *213*, 514−518.
(39) Feyereisen, M.; Fitzgerald, G.; Komornicki, A. Use of approximate integrals in ab initio theory. An application in MP2 energy calculations. *Chem. Phys. Lett.* **1993**, *208*, 359−363.
(40) Bauernschmitt, R.; Häser, M.; Treutler, O.; Ahlrichs, R. Calculation of excitation energies within time-dependent density functional theory using auxiliary basis set expansions. *Chem. Phys. Lett.* **1997**, *264*, 573−578.
(41) Weigend, F. A fully direct RI-HF algorithm: Implementation, optimised auxiliary basis sets, demonstration of accuracy and efficiency. *Phys. Chem. Chem. Phys.* **2002**, *4*, 4285−4291.
(42) Neese, F.; Wennmohs, F.; Hansen, A.; Becker, U. Efficient, approximate and parallel Hartree-Fock and hybrid DFT calculations. A 'chain-of-spheres' algorithm for the Hartree-Fock exchange. *Chem. Phys.* **2009**, *356*, 98−109.
(43) Plessow, P.; Weigend, F. Seminumerical calculation of the Hartree-Fock exchange matrix: Application to two-component procedures and efficient evaluation of local hybrid density functionals. *J. Comput. Chem.* **2012**, *33*, 810−816.
(44) Bahmann, H.; Kaupp, M. Efficient Self-Consistent Implementation of Local Hybrid Functionals. *J. Chem. Theory Comput.* **2015**, *11*, 1540−1548.
(45) Chesnut, D. B.; Moore, K. D. Locally dense basis sets for chemical shift calculations. *J. Comput. Chem.* **1989**, *10*, 648−659.
(46) Klamt, A.; Schüürmann, G. COSMO: a new approach to dielectric screening in solvents with explicit expressions for the screening energy and its gradient. *J. Chem. Soc., Perkin Trans. 2* **1993**, 799−805.
(47) Klamt, A.; Jonas, V.; Bürger, T.; Lohrenz, J. C. W. Refinement and Parametrization of COSMO-RS. *J. Phys. Chem. A* **1998**, *102*, 5074−5085.
(48) *TURBOMOLE* V7.5 2020, a Development of University of Karlsruhe and Forschungszentrum Karlsruhe GmbH, 1989−2007, TURBOMOLE GmbH, since 2007; available from http://www.turbomole.com.
(49) Ahlrichs, R.; Bär, M.; Häser, M.; Horn, H.; Kölmel, C. Electronic structure calculations on workstation computers: The program system turbomole. *Chem. Phys. Lett.* **1989**, *162*, 165−169.
(50) Furche, F.; Ahlrichs, R.; Hättig, C.; Klopper, W.; Sierka, M.; Weigend, F. Turbomole. *Wiley Interdiscip. Rev.: Comput. Mol. Sci.* **2014**, *4*, 91−100.

https://dx.doi.org/10.1021/acs.jpca.0c06897
J. Phys. Chem. A 2020, 124, 8529−8539

(51) Balasubramani, S. G.; Chen, G. P.; Coriani, S.; Diedenhofen, M.; Frank, M. S.; Franzke, Y. J.; Furche, F.; Grotjahn, R.; Harding, M. E.; Hättig, C.; et al. TURBOMOLE: Modular program suite for ab initio quantum-chemical and condensed-matter simulations. *J. Chem. Phys.* **2020**, *152*, 184107.
(52) Becke, A. D. Density-functional thermochemistry. III. The role of exact exchange. *J. Chem. Phys.* **1993**, *98*, 5648−5652.
(53) Lee, C.; Yang, W.; Parr, R. G. Development of the Colle-Salvetti correlation-energy formula into a functional of the electron density. *Phys. Rev. B: Condens. Matter Mater. Phys.* **1988**, *37*, 785−789.
(54) Jensen, F. The Basis Set Convergence of Spin-Spin Coupling Constants Calculated by Density Functional Methods. *J. Chem. Theory Comput.* **2006**, *2*, 1360−1369.
(55) Jensen, F. The optimum contraction of basis sets for calculating spin−spin coupling constants. *Theor. Chem. Acc.* **2010**, *126*, 371−382.
(56) Aggelund, P. A.; Sauer, S. P. A.; Jensen, F. Development of polarization consistent basis sets for spin-spin coupling constant calculations for the atoms Li, Be, Na, and Mg. *J. Chem. Phys.* **2018**, *149*, 044117.
(57) Treutler, O.; Ahlrichs, R. Efficient molecular numerical integration schemes. *J. Chem. Phys.* **1995**, *102*, 346−354.
(58) Chesnut, D. B.; Rusiloski, B. E.; Moore, K. D.; Egolf, D. A. Use of locally dense basis sets for nuclear magnetic resonance shielding calculations. *J. Comput. Chem.* **1993**, *14*, 1364−1375.
(59) Krivdin, L. B. Computational ^{1}H NMR: Part 1. Theoretical background. *Magn. Reson. Chem.* **2019**, *57*, 897−914.
(60) Reid, D. M.; Kobayashi, R.; Collins, M. A. Systematic Study of Locally Dense Basis Sets for NMR Shielding Constants. *J. Chem. Theory Comput.* **2014**, *10*, 146−152.
(61) Provasi, P. F.; Aucar, G. A.; Sauer, S. P. A. The use of locally dense basis sets in the calculation of indirect nuclear spin−spin coupling constants: The vicinal coupling constants in H_3C-CH_2X (X=H, F, Cl, Br, I). *J. Chem. Phys.* **2000**, *112*, 6201−6208.
(62) Rusakov, Y. Y.; Rusakova, I. L.; Fedorov, S. V.; Gray, G. A.; Krivdin, L. B. Stereochemical Dependences of ^{31}P−^{13}C Spin−Spin Coupling Constants of Heterocyclic Phosphines. *J. Phys. Chem. A* **2019**, *123*, 6298−6303.
(63) Provasi, P. F.; Aucar, G. A.; Sanchez, M.; Alkorta, I.; Elguero, J.; Sauer, S. P. A. Interaction Energies and NMR Indirect Nuclear Spin-Spin Coupling Constants in Linear HCN and HNC Complexes. *J. Phys. Chem. A* **2005**, *109*, 6555−6564.
(64) Provasi, P. F.; Aucar, G. A.; Sauer, S. P. A. Large Long-Range F-F Indirect Spin-Spin Coupling Constants. Prediction of Measurable F-F Couplings over a Few Nanometers. *J. Phys. Chem. A* **2004**, *108*, 5393−5398.
(65) Rusakov, Y. Y.; Krivdin, L. B. One-bond ^{29}Si-^{1}H spin-spin coupling constants in the series of halosilanes: benchmark SOPPA and DFT calculations, relativistic effects, and vibrational corrections. *Magn. Reson. Chem.* **2013**, *51*, 557−561.
(66) Rusakov, Y. Y.; Krivdin, L. B.; Sauer, S. P. A.; Levanova, E. P.; Levkovskaya, G. G. Structural trends of ^{77}Se−^{1}H spin−spin coupling constants and conformational behavior of 2-substituted selenophenes. *Magn. Reson. Chem.* **2010**, *48*, 44−52.
(67) Martínez, F. A.; Aucar, G. A. Intermolecular magnetic interactions in stacked DNA base pairs. *Phys. Chem. Chem. Phys.* **2017**, *19*, 27817−27827.
(68) Weigend, F.; Ahlrichs, R. Balanced basis sets of split valence, triple zeta valence and quadruple zeta valence quality for H to Rn: Design and assessment of accuracy. *Phys. Chem. Chem. Phys.* **2005**, *7*, 3297−3305.
(69) Tao, J.; Perdew, J. P.; Staroverov, V. N.; Scuseria, G. E. Climbing the Density Functional Ladder: Nonempirical Meta−Generalized Gradient Approximation Designed for Molecules and Solids. *Phys. Rev. Lett.* **2003**, *91*, 146401.
(70) Lemp, O.; Balmer, M.; Reiter, K.; Weigend, F.; von Hänisch, C. An NHC−phosphinidenyl as a synthon for new group 13/15 compounds. *Chem. Commun.* **2017**, *53*, 7620−7623.
(71) Bohne, A.; Lang, E.; von der Lieth, C. W. SWEET - WWW-based rapid 3D construction of oligo- and polysaccharides. *Bioinformatics* **1999**, *15*, 767−768.
(72) Kaupp, M.; Bahmann, H.; Arbuznikov, A. V. Local hybrid functionals: An assessment for thermochemical kinetics. *J. Chem. Phys.* **2007**, *127*, 194102.
(73) Arbuznikov, A. V.; Kaupp, M. Towards improved local hybrid functionals by calibration of exchange-energy densities. *J. Chem. Phys.* **2014**, *141*, 204101.
(74) Perdew, J. P.; Burke, K.; Ernzerhof, M. Generalized Gradient Approximation Made Simple. *Phys. Rev. Lett.* **1996**, *77*, 3865−3868.
(75) Luenser, A.; Kussmann, J.; Ochsenfeld, C. Computation of indirect nuclear spin−spin couplings with reduced complexity in pure and hybrid density functional approximations. *J. Chem. Phys.* **2016**, *145*, 124103.
(76) Weigend, F.; Häser, M.; Patzelt, H.; Ahlrichs, R. RI-MP2: optimized auxiliary basis sets and demonstration of efficiency. *Chem. Phys. Lett.* **1998**, *294*, 143−152.
(77) Staroverov, V. N.; Scuseria, G. E.; Tao, J.; Perdew, J. P. Comparative assessment of a new nonempirical density functional: Molecules and hydrogen-bonded complexes. *J. Chem. Phys.* **2003**, *119*, 12129−12137.
(78) San Fabián, J.; Díez, E.; García de la Vega, J. M.; Suardíaz, R. Approximating correlation effects in multiconfigurational self-consistent field calculations of spin-spin coupling constants. *J. Chem. Phys.* **2008**, *128*, 084108.
(79) Faber, R.; Sauer, S. P. A.; Gauss, J. Importance of Triples Contributions to NMR Spin−Spin Coupling Constants Computed at the CC3 and CCSDT Levels. *J. Chem. Theory Comput.* **2017**, *13*, 696−709.
(80) Jaramillo, J.; Scuseria, G. E.; Ernzerhof, M. Local hybrid functionals. *J. Chem. Phys.* **2003**, *118*, 1068−1073.
(81) Arbuznikov, A. V.; Kaupp, M. Importance of the correlation contribution for local hybrid functionals: Range separation and self-interaction corrections. *J. Chem. Phys.* **2012**, *136*, 014111.
(82) Stoychev, G. L.; Auer, A. A.; Izsák, R.; Neese, F. Self-Consistent Field Calculation of Nuclear Magnetic Resonance Chemical Shielding Constants Using Gauge-Including Atomic Orbitals and Approximate Two-Electron Integrals. *J. Chem. Theory Comput.* **2018**, *14*, 619−637.
(83) Adamo, C.; Barone, V. Toward reliable density functional methods without adjustable parameters: The PBE0 model. *J. Chem. Phys.* **1999**, *110*, 6158−6170.
(84) Becke, A. D. A new mixing of Hartree−Fock and local density-functional theories. *J. Chem. Phys.* **1993**, *98*, 1372−1377.
(85) Gryff-Keller, A.; Szczeciński, P. An efficient DFT method of predicting the one-, two- and three-bond indirect spin−spin coupling constants involving a fluorine nucleus in fluoroalkanes. *RSC Adv.* **2016**, *6*, 82783−82792.
(86) San Fabián, J.; Omar, S.; García de la Vega, J. M. Towards quantifying the role of exact exchange in the prediction hydrogen bond spin-spin coupling constants involving fluorine. *J. Chem. Phys.* **2016**, *145*, 084301.
(87) Lantto, P.; Vaara, J.; Helgaker, T. Spin−spin coupling tensors by density-functional linear response theory. *J. Chem. Phys.* **2002**, *117*, 5998−6009.
(88) Fabián, J. S.; García de la Vega, J. M.; San Fabián, E. Improvements in DFT Calculations of Spin-Spin Coupling Constants. *J. Chem. Theory Comput.* **2014**, *10*, 4938−4949.

https://dx.doi.org/10.1021/acs.jpca.0c06897
J. Phys. Chem. A 2020, 124, 8529−8539

III

Reprinted with permission from

C. J. Schattenberg and M. Kaupp,
"*Effect of the Current Dependence of Tau-Dependent Exchange-Correlation Functionals on Nuclear Shielding Calculations*",
J. Chem. Theory Comput., **2021**, *17*, 1469–1479.
DOI: 10.1021/acs.jctc.0c01223

JCTC Journal of Chemical Theory and Computation

pubs.acs.org/JCTC Article

Effect of the Current Dependence of Tau-Dependent Exchange-Correlation Functionals on Nuclear Shielding Calculations

Caspar Jonas Schattenberg and Martin Kaupp*

Cite This: J. Chem. Theory Comput. 2021, 17, 1469−1479 Read Online

ACCESS | Metrics & More | Article Recommendations | Supporting Information

ABSTRACT: Exchange-correlation functionals that depend on the local kinetic energy τ are widely used in many fields. This includes meta-generalized gradient approximation (GGA) functionals and their global hybrid versions as well as local hybrid functionals with τ-dependent local mixing functions to determine position-dependent exact-exchange admixture. Under the influence of an external magnetic field, τ becomes dependent on the gauge of the magnetic vector potential and should thus be extended to a gauge-invariant formulation. The currently most widely used extension for nuclear shielding calculations is that suggested by Maximoff and Scuseria (Maximoff, S. N.; Scuseria, G. E. *Chem. Phys. Lett.* **2004**, *390*, 408). Using the recent first implementation of local hybrids in this framework, we have found unphysical paramagnetic contributions, which are most clearly identified for atoms but are also present in molecules. These τ_{MS} artifacts are small for the TPSS or TPSSh functionals, significantly deshielding in the case of nonhydrogen nuclei for the M06-L and M06 functionals and significantly shielding in those cases for the first-generation τ-dependent local hybrids LH07t-SVWN and LH12ct-SsifPW92. We have therefore implemented an extension of a linear-response nuclear shielding code to the proper current-density functional version of τ suggested by Dobson (Dobson, J. F. *J. Chem. Phys.* **1993**, *98*, 8870). Using τ_D eliminates the gauge dependence as well as the unphysical contributions introduced by τ_{MS}. A first evaluation of this implementation for a set of main-group nuclear shieldings against CCSD(T) benchmark data indicates rather small effects for the TPSS and TPSSh functionals but significant changes for the other functionals studied: the previously observed remarkable performance of the highly parameterized meta-GGA functional M06-L is found to be the result of error compensation with the lack of an explicit current dependence. Results for the M06 functional are improved somewhat but are still overall of relatively low accuracy. In contrast, too low proton shieldings found recently for τ-dependent local hybrids are improved significantly within the τ_D current-density functional framework while preserving the outstanding performance of these functionals for other nuclei.

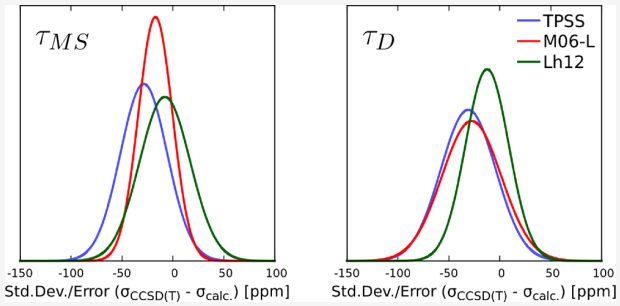

1. INTRODUCTION

In view of the central importance of nuclear magnetic resonance (NMR) spectroscopy in many research fields, the quantum-chemical computation of its parameters is an active and growing endeavor, providing central insights into molecular and electronic structure.[1] Nuclear shieldings and the related NMR chemical shifts are the focus of the present work. Despite the shortcomings of currently available approximate exchange-correlation (XC) functionals, Kohn−Sham density functional theory (KS-DFT) is the most widely used approach to compute NMR parameters. Yet, the accuracy achieved with standard XC functionals leaves substantial room for improvement,[2,3] more so than for simpler properties like energetics or structures. Among the various directions for improvement pursued, we mention specialized functionals parameterized specifically for shieldings,[4,5] which, however, are based on extensive error compensation,[6] likely also limiting their predictive power. The currently most accurate DFT results for shieldings of many main-group species are obtained with double-hybrid functionals (DH).[7] Apart from possible problems for systems with appreciable static correlation, the MP2-like correlation part of DHs renders shielding calculations computationally much more demanding than with simpler functionals on the lower rungs of the Jacob's ladder of XC functionals.[8] Improvements for functionals on these lower rungs (1−4) are thus highly desirable.

A central problem with KS-DFT identified for shieldings and other magnetic properties[9−11] is that standard XC functionals lack a dependence on the paramagnetic current density. This was recently demonstrated most clearly in ref 6 based on XC functionals extracted from accurate coupled-cluster electron densities. Inclusion of current terms reduced overestimated

Received: November 24, 2020
Published: February 25, 2021

https://dx.doi.org/10.1021/acs.jctc.0c01223
J. Chem. Theory Comput. 2021, 17, 1469−1479

paramagnetic shielding contributions for all nuclei studied except hydrogen.[6] The earliest attempts to include current dependencies of XC functionals into shielding computations for the local density approximation (LDA), i.e., the lowest rung of the ladder, gave negligible contributions and thus no improvements,[12] and so far, no improvements for shieldings have been found when introducing currents[9] on the second rung, the generalized gradient approximation (GGA).

Introduction of the non-interacting KS kinetic-energy density

$$\tau = \frac{1}{2}\sum_i \nabla\psi_i^*\nabla\psi_i \tag{1}$$

on the third meta-GGA rung without current dependency is, however, known to violate the required invariance with respect to the gauge of the vector potential of the external magnetic field.[13−17] To correct for this, essentially all implementations of nuclear shieldings with τ-dependent functionals to date (but see below) use a modified local kinetic energy suggested by Maximoff and Scuseria (τ_{MS})[13]

$$\tau \rightarrow \tau_{MS} = \tau + \frac{\mathbf{A}_G}{c}\mathbf{j}_p + \frac{|(\mathbf{A}_G)|^2}{2c^2}\rho \tag{2}$$

where $\mathbf{j}_p$ is the paramagnetic current density

$$\mathbf{j}_p = \frac{i}{2}\sum_i (\psi_i\nabla\psi_i^* - \psi_i^*\nabla\psi_i) \tag{3}$$

and $\mathbf{A}_G = \frac{1}{2}\mathbf{B}\times(\mathbf{r}-\mathbf{R}_G)$ is the vector potential of the magnetic field $\mathbf{B}$ for an arbitrary gauge origin $\mathbf{R}_G$. This holds for meta-GGA functionals like TPSS[18] or M06-L,[19] which have been found to perform relatively well in shielding computations,[20,21] or for meta-GGA-based global hybrid (GH) functionals on the fourth rung, such as TPSSh[22] or M06.[23] It holds also for the first nuclear shielding implementation with local hybrid (LH) functionals[24] having position-dependent exact-exchange admixtures (still on rung 4), needed here because of the predominant use of a τ-dependent local mixing function (LMF) to determine the position dependence (see the Theory section).

The MS treatment removes the gauge dependence of the XC contribution while keeping the magnetic Hessian diagonal, i.e., no coupling terms enter the paramagnetic shielding contributions that would occur for a proper current density functional. This helps to avoid an iterative treatment of the perturbed Kohn−Sham scheme in the case of meta-GGAs. We will show here that the price paid for this advantage is unphysical paramagnetic contributions that may become significant for some of the relevant functionals. We note that coupling terms arise in any case for GHs or LHs. Indeed, it has been pointed out that the formulation of τ_{MS} in terms of the full physical current and its resulting explicit dependence on the magnetic vector potential renders it non-universal[6,16,25,26] (cf. also refs[9−11]). Moreover, τ_{MS} does not constitute a proper iso-orbital indicator like τ does in the absence of a magnetic field.[27]

A gauge-invariant extension of τ that provides proper current density functionals depending not on the full physical current but only on the paramagnetic orbital current has been introduced by Dobson[28,29]

$$\tau \rightarrow \tau_D = \tau - \frac{\mathbf{j}_p^2}{2\rho} \tag{4}$$

Here, the current density is not mixed with the magnetic field, and the model introduces an explicit dependence on the current density into the exchange-correlation contribution to the magnetic-field response in the shielding calculations (and to the full exchange-correlation functional for current-carrying states, see below). This ansatz not only provides a field-free gauge correction to τ, it also recovers the iso-orbital constraint and satisfies the second-order gradient expansion of the kinetic-energy density for slowly varying densities and current densities.[25] τ_D has been used for reducing unphysical symmetry breaking in current-carrying atomic states[14] and for the proper gauge-invariant implementation of meta-GGAs for TDDFT calculations of excitation energies[16] (also for LHs[30]). It has furthermore been used in finite-field treatments of molecules in strong magnetic fields using meta-GGA functionals.[31] Application of τ_D to nuclear shieldings so far has been very limited. This includes a small set of shieldings obtained with the TPSS and B98[32] meta-GGAs[31] and a comparison of the current-free τ vs τ_{MS} and τ_D for TPSS.[6] Relatively small differences between results for these approaches were found in the latter work, but we will show here that this does not hold true for all τ-dependent XC functionals. Both of these studies used a finite-field approach, and we are not aware of any linear-response implementation of shieldings based on τ_D. We will close this gap in the present work, where we will point out problems with approaches based on τ_{MS} and compare explicitly shieldings obtained with τ, τ_{MS}, and τ_D for meta-GGAs, meta-GGA-based GHs, and two LHs with a t-LMF.

2. THEORY

Using perturbation theory, the shielding tensor is expressed as the second derivative of the total energy of the system with respect to the (external) magnetic field B_k and the nuclear magnetic moment μ_l^K of the nucleus K in the Cartesian directions $k, l = x, y, z$[1,33]

$$\sigma_{kl}^K = \left.\frac{\partial^2 E}{\partial B_k \partial \mu_l^K}\right|_{B_k=\mu_l^K=0} = \sum_{\mu\nu}\left[D_{\mu\nu}\frac{\partial^2 h_{\mu\nu}}{\partial B_k \partial \mu_l^K} + \frac{\partial D_{\mu\nu}}{\partial B_k}\frac{\partial h_{\mu\nu}}{\partial \mu_l^K}\right]\Bigg|_{B_k=\mu_l^K=0} \tag{5}$$

The first term on the right-hand side of eq 5 (diamagnetic shielding) is a simple expectation value of the ground-state wave function or the density matrix (the latter formulation is chosen here). In contrast, the paramagnetic shielding contribution (second term of eq 5)

$$\sigma_{kl}^p = \sum_{\mu\nu}\frac{\partial D_{\mu\nu}}{\partial B_k}\langle\phi_\mu^*|\frac{[-i\nabla\times(\mathbf{r}-\mathbf{R}_K)]}{r_K^3}|\phi_\nu\rangle \tag{6}$$

is formulated here in terms of the atomic-orbital (AO) basis $\{\phi_\mu\}$ and the density matrix perturbed to the first order in the external magnetic field

$$\frac{\partial D_{\mu\nu}}{\partial B_k} = \sum_{ia} u_{ai}^{B_k}(c_{\mu i}^* c_{\nu a} - c_{\mu a}^* c_{\nu i}) - \sum_{ij} c_{\mu i}^* S_{ij}^{B_k} c_{\nu j} \tag{7}$$

https://dx.doi.org/10.1021/acs.jctc.0c01223
J. Chem. Theory Comput. 2021, 17, 1469−1479

where $S_{ij}^{B_k}$ is the perturbed overlap matrix, and $u_{ai}^{B_k}$ are the expansion coefficients to be solved for within the coupled perturbed equations

$$u_{ai}^{B_k} = \frac{F_{ai}^{B_k} - \varepsilon_i S_{ai}^{B_k}}{\varepsilon_i - \varepsilon_a} \tag{8}$$

We generally use i and j to denote occupied and a and b for virtual MOs, while μ and ν denote AOs.

The first-generation LH functionals that we will evaluate here do not contain a so-called calibration function to deal with the ambiguity of exchange-energy densities[34] and may be formulated as

$$E_{XC}^{LH} = \int [g(\mathbf{r})\cdot e_X^{ex}(\mathbf{r}) + (1 - g(\mathbf{r}))e_X^{sl}(\mathbf{r})]\, d\mathbf{r} + E_C^{sl} \tag{9}$$

where $g(\mathbf{r})$ is the local-mixing function (LMF) that governs the position-dependent exact-exchange admixture, $e_X^{sl}(\mathbf{r})$ is the (semi)local energy density, and $e_X^{ex}(\mathbf{r})$ is the exact-exchange energy density

$$e_X^{ex}(\mathbf{r}) = -\frac{1}{2}\sum_{ij}\psi_i^*\psi_j \int \frac{\psi_j^*\psi_i}{|\mathbf{r} - \mathbf{r}'|}\, d\mathbf{r}' \tag{10}$$

and E_C^{sl} is some (semi)local correlation functional.

While a substantial number of LMFs have already been proposed (see ref 34 and references therein), the currently most widely used constructions are the so-called t-LMFs, defined as the (scaled) ratio of the von-Weizsäcker and Pauli kinetic-energy densities

$$g = a\cdot\frac{\tau_W}{\tau}, \quad \text{with} \quad \tau_W = \frac{1}{8}\frac{|\nabla\rho|^2}{\rho} \tag{11}$$

The extension of the CPKS scheme for nuclear shieldings to such LH functionals was reported recently.[24] The central equation needed here to understand extensions to τ_D vs τ_{MS} is the XC contribution (eq 28 of ref 24 to the perturbed Fock matrix

$$F_{\mu\nu}^{XC,B_k} = \sum_{Q\varepsilon\mathcal{J}}\int\left[\frac{\partial g}{\partial Q}(e_X^{ex} - e_X^{sl}) + \frac{\partial e_X^{sl}}{\partial Q}(1 - g) + \frac{\partial e_C^{sl}}{\partial Q}\right]\left[\frac{\partial Q}{\partial D_{\mu\nu}}\right]^{B_k} d\mathbf{r} \tag{12}$$

Here, Q defines the set of (local) quantities used in the respective LMF or (semi)local functional, e.g., $Q = \{\rho, \nabla\rho, \tilde{\tau}\}$ for a meta-GGA.

Letting $g \to a_0 = const.$, we obtain the GH expression for the perturbed Fock matrix. Likewise, $g \to a_0 = 0.0$ defines the (semi)local limit. Choosing $Q = \{\tau_{MS}\}$, the contributions arising from the term $\left[\frac{\partial Q}{\partial D_{\mu\nu}}\right]^{B_k}$ are

$$\left[\frac{\partial \tau_{MS}}{\partial D_{\mu\nu}}\right]^{B_k} = \left[\frac{1}{2}\nabla\omega_\mu^*\nabla\omega_\nu + \frac{i}{2c}\mathbf{A}_G(\omega_\nu\nabla\omega_\mu^* - \omega_\mu^*\nabla\omega_\nu)\right]^{B_k} \tag{13}$$

omitting the terms depending on the magnetic field to the second order ($\mathbf{A}^2$) in eq 2 in the derivative since these vanish for $\mathbf{B} = 0$. Here, the gauge dependence of the kinetic energy is corrected due to the presence of the gauge within the vector potential but at the cost of introducing an explicit dependence on the magnetic vector potential into the functional, as discussed in the Introduction.

Choosing instead $Q = \{\tau_D\}$ and neglecting the term to the second order in $\mathbf{j}_p$ since

$$\mathbf{j}_p\Big|_{B_k=0} = 0 \tag{14}$$

we get

$$\left[\frac{\partial \tau_D}{\partial D_{\mu\nu}}\right]^{B_k} = \left[\frac{1}{2}\nabla\omega_\mu^*\nabla\omega_\nu - \frac{i}{2\rho}\mathbf{j}_p(\omega_\nu\nabla\omega_\mu^* - \omega_\mu^*\nabla\omega_\nu)\right]^{B_k} \tag{15}$$

The second terms on the r.h.s. of eqs 13 and 15 correct for the gauge dependence of $\frac{1}{2}[\nabla\omega_\mu^*\nabla\omega_\nu]^{B_k}$, which itself corresponds to the uncorrected and thus gauge-dependent contribution from the kinetic-energy density. In all equations, ω_μ and ω_ν denote gauge-including atomic orbitals (GIAOs) used throughout[35,36]

$$\omega_\mu = \phi_\mu \exp\left(-\frac{i}{2c}[\mathbf{B}\times(\mathbf{R}_\mu - \mathbf{R}_G)]\mathbf{r}\right) \tag{16}$$

We note in passing that for current-carrying ground states (e.g., certain open-shell species or potentially atoms and molecules in a strong magnetic field treated variationally[14,31,37]), use of τ_D leads explicitly to a current-density functional theory (CDFT) framework,[9−11] i.e.,

$$E_{XC}[\rho] \to E_{XC}[\rho, \mathbf{j}_p] \tag{17}$$

Within the present linear-response treatment of the magnetic perturbations and in the absence of ground-state currents, there is no dependence of the ground state on $\mathbf{j}_p$ (cf. eq 14), and the corrections from eq 15 will contribute just to the XC response. That is, we have to construct

$$\begin{aligned}\mathbf{j}_p^{B_k} &= \frac{i}{2}\sum_{\mu\nu}\left[D_{\mu\nu}(\omega_\nu\nabla\omega_\mu^* - \omega_\mu^*\nabla\omega_\nu)\right]^{B_k} \\ &= \frac{i}{2}\sum_{\mu\nu}\Bigg[D_{\mu\nu}^{B_k}(\omega_\nu\nabla\omega_\mu^* - \omega_\mu^*\nabla\omega_\nu) \\ &\quad + \frac{i}{2c}D_{\mu\nu}\Big([(\mathbf{B}\times(\mathbf{R}_\mu - \mathbf{R}_G))^{B_k} \\ &\quad + (\mathbf{B}\times(\mathbf{R}_\nu - \mathbf{R}_G))^{B_k}]\phi_\mu^*\phi_\nu \\ &\quad + (\mathbf{R}_{\mu\nu}\times\mathbf{r})_k(\phi_\nu\nabla\phi_\mu^* - \phi_\mu^*\nabla\phi_\nu)\Big)\Bigg]\end{aligned} \tag{18}$$

The first term depends of the perturbed density, constructed from the expansion coefficients. That is, coupling terms enter also for pure meta-GGA functionals even in the absence of exact exchange, and thus, the perturbation equations have to be solved iteratively, when τ_D is used (see below). Note that eq 18 still depends on the gauge of the magnetic vector potential. However, as shown before,[31] the terms arising from τ_D now cancel the gauge dependence of the original equations for a gauge-dependent τ. While the correction of the gauge vectors $\mathbf{R}_G$ is immediately visible for the τ_{MS} case, for τ_D the gauge corrections arise within the iterative solution of the equations.

https://dx.doi.org/10.1021/acs.jctc.0c01223
J. Chem. Theory Comput. 2021, 17, 1469−1479

Table 1. Diamagnetic (σ^{d}, Equal for Both τ Models) and Paramagnetic (σ^{p}) Contributions to Shieldings in He and Ne Comparing the τ_{MS} (Equation 2) and τ_{D} (Equation 4) Models for Various Functionals

		CCSD(T)[a]		TPSS	M06-L	TPSSh	M06	LH07t[b]	LH12ct[b]
^{3}He	σ^{d}	59.9	σ^{d}	60.0	60.1	60.0	60.1	59.6	59.7
	σ^{p}	0.0	$\sigma^{p,MS}$	0.0	0.0	0.0	0.0	0.0	0.0
			$\sigma^{p,D}$	0.0	0.0	0.0	0.0	0.0	0.0
^{21}Ne	σ^{d}	552.0	σ^{d}	552.2	552.4	552.2	552.4	551.1	551.3
	σ^{p}	0.0	$\sigma^{p,MS}$	−0.7	−11.5	−0.5	−20.9	18.8	24.1
			$\sigma^{p,D}$	0.0	0.0	0.0	0.0	0.0	0.0

[a]GIAO-CCSD(T)/aug-cc-pVQZ data.[6] [b]LH07t = LH07t-SVWN and LH12ct = LH12ct-SsifPW92.

However, the gauge invariance has been ascertained in both cases (see below).

If we neglect the second term in eq 13, which depends on the vector potential, or the second term in eq 15, which depends on the paramagnetic current density, we arrive at a treatment for the uncorrected, gauge-dependent τ. In the finite-difference work of ref 6, a common gauge at the center of mass was applied to these terms. We will in the following call this model τ_C. Our numerical tests suggest that the default version in the widely used ORCA code[21,38,39] simply removes the gauge-dependent terms in this approach (see the Supporting Information), as has been confirmed by the authors. We will term this *ad hoc* gauge-invariant approximation τ_{GI} and will also include its results, as well as those with τ_C, mostly in the Supporting Information.

2.1. Implementation of the τ_D-Dependent Contributions. Analogous to the CPKS treatment for hybrid functionals, we may divide new contributions to $\mathbf{j}_p^{B_k}$ arising from eq 18 into two parts. The first part depends of the perturbed density $D_{\mu\nu}^{B_k}$, which is solved for iteratively within the CPKS loops (note that $D_{\nu\mu}^{B_k} = -D_{\mu\nu}^{B_k}$ is skew-symmetric)

$$\mathbf{j}_p[\omega, D^{B_k}] = -\frac{1}{2}\sum_{\mu\nu}[\phi_\nu D_{\nu\mu}^{B_k}\nabla\phi_\mu^* + \phi_\mu^* D_{\mu\nu}^{B_k}\nabla\phi_\nu] \tag{19}$$

The remaining "pre-loop" part ($\mathbf{j}_p[\omega^{B_k}, D]$) is constructed from the three vectors

$$\chi_1 = \sum_\kappa \nabla\phi_\kappa \sum_\lambda D_{\kappa\lambda}((\mathbf{R}_\lambda - \mathbf{R}_G)\times\mathbf{r})_k\phi_\lambda \tag{20}$$

$$\chi_2 = \sum_\kappa \phi_\kappa \sum_\lambda D_{\kappa\lambda}(\mathbf{B}\times(\mathbf{R}_\lambda - \mathbf{R}_G))^{B_k}\phi_\lambda \tag{21}$$

$$\chi_3 = \sum_\kappa \phi_\kappa \sum_\lambda D_{\kappa\lambda}((\mathbf{R}_\lambda - \mathbf{R}_G)\times\mathbf{r})_k\nabla\phi_\lambda \tag{22}$$

resulting in a separate vector of $\mathbf{j}_p$ for each Cartesian component of the magnetic field. The additional computational effort required for (local or global) hybrid functionals is minor (see Table S1 in the Supporting Information). Due to the presence of the perturbed density, an iterative solution is also needed for semilocal meta-GGA functionals. This adds some computational burden over the τ_{MS} treatment, but the remaining computational effort is still appreciably smaller than that for hybrid functionals (Table S1).

3. COMPUTATIONAL DETAILS

Extensions of τ-dependent meta-GGA, GH, and LH functionals to use τ_D (as well as τ_C and τ_{GI}) have been added to the *mpshift* nuclear shielding module[17] of a developers' version of the Turbomole program package, based on release 7.5,[40,41] into which LHs were implemented recently (so far based on τ_{MS}).[24] While we thus mainly report results obtained with Turbomole, we also provide some data that have been obtained with the ORCA[21,38,39] and Gaussian[42] program packages (see the Supporting Information), based on τ_{MS}. This ensures comparability to other codes. All shieldings are computed using gauge-including atomic orbitals (GIAOs) and large pcSseg-4 basis sets. We also implemented the uncorrected gauge-dependent τ_C and the *ad hoc* gauge-independent τ_{GI} models discussed at the end of the Theory section (see Section S2 in the Supporting Information for more details).

Initial analyses focus on the He and Ne atoms, compared to recent GIAO-CCSD(T)/aug-cc-pVQZ[43−45] reference data,[6] followed by some small molecular systems. To obtain statistically relevant insights into the performances of different functional forms, we compare our results to GIAO-CCSD(T)/pcSseg-4[46] reference data of main-group molecules from ref 21, as done recently for a variety of LHs in the τ_{MS} formulation.[24] We compare data for two meta-GGAs, TPSS and M06-L, the meta-GGA GHs TPSSh and M06, and the two LHs LH07t-SVWN[47,48] and LH12ct-SsifPW92[49] based on t-LMFs (some data with the related LH12ct-SsirPW92 functional[49] are included in the Supporting Information).

Unless noted otherwise, all calculations using Turbomole employ grids of size 5 (internal setting) and are performed without any integral prescreening within the seminumerical treatment of the LHs. SCF convergence criteria in TBM were set to 10^{-9}, with additionally ensuring convergence by enforcing the convergence of the density matrix to 10^{-7}. Convergence of the Euclidean norm of the residual vectors within the shielding calculations was likewise set to 10^{-7}. Computational timings as reported in Table S1 have been recorded on an AMD EPYC 7302 16-Core CPU. Calculations in Gaussian use the options *verytight* for the SCF convergence and *ultrafine* for the grid setup, while in ORCA, we used *VeryTightSCF* and the internal setting *Grid6* with a convergence tolerance for the shielding calculations of 10^{-12}. We note in passing that we have numerically checked the gauge invariance of both our τ_{MS} and τ_D implementations (see, e.g., Table S2 in the Supporting Information, which includes also gauge-invariant τ_{GI} data). Tests for a larger molecule (eicosane, data not shown) confirm these conclusions. A gauge-dependent τ results in appreciable overall gauge dependence (cf. Table S3 in the Supporting Information) even though the choice of placing the gauge at the center of mass (τ_C), as done in ref 6, still provides overall reasonable shieldings.

https://dx.doi.org/10.1021/acs.jctc.0c01223
J. Chem. Theory Comput. 2021, 17, 1469−1479

Table 2. Components of the Paramagnetic Shielding Tensor for Three Linear Molecules, Comparing Different Functionals and Models for τ

			τ_{MS}		τ_D		τ_C		τ_{GI}	
			$\sigma^p_\perp$	$\sigma^p_\parallel$	$\sigma^p_\perp$	$\sigma^p_\parallel$	$\sigma^p_\perp$	$\sigma^p_\parallel$	$\sigma^p_\perp$	$\sigma^p_\parallel$
LiH	^{1}H	PBE[a]			−0.39	0.00				
		TPSS	−2.60	0.00	−2.58	0.00	−2.84	0.00	−2.58	0.00
		M06-L	0.04	0.00	0.07	0.00	−0.36	0.00	0.01	0.00
		TPSSh	−2.62	0.00	−2.60	0.00	−2.83	0.00	−2.60	0.00
		M06	0.31	0.00	0.34	0.00	0.29	0.00	0.25	0.00
		LH07t	−1.66	0.00	−1.66	0.00	−1.65	0.00	−1.61	0.00
		LH12sif	−1.95	0.00	−1.97	0.00	−1.67	0.00	−1.90	0.00
	^{7}Li	PBE[a]			−18.3	0.0				
		TPSS	−17.2	0.0	−17.3	0.0	−16.5	0.0	−16.9	0.0
		M06-L	−20.2	0.0	−19.9	0.0	−19.0	0.0	−19.5	0.0
		TPSSh	−17.2	0.0	−17.2	0.0	−16.5	0.0	−16.9	0.0
		M06	−16.8	0.0	−16.5	0.0	−18.0	0.0	−18.1	0.0
		LH07t	−16.8	0.0	−16.8	0.0	−15.6	0.0	−15.8	0.0
		LH12sif	−15.9	0.0	−15.9	0.0	−15.0	0.0	−14.9	0.0
HF	^{1}H	PBE[a]			2.92	0.00				
		TPSS	2.80	−0.08	2.62	0.00	2.31	0.00	2.96	0.00
		M06-L	10.85	−0.26	10.56	0.00	9.96	0.00	11.51	0.00
		TPSSh	2.72	−0.07	2.56	0.00	2.29	0.00	2.88	0.00
		M06	6.55	−0.22	6.19	0.00	6.28	0.00	6.08	0.00
		LH07t	2.49	0.14	2.87	0.00	2.72	0.00	3.07	0.00
		LH12sif	2.41	0.20	2.99	0.00	2.91	0.00	3.12	0.00
	^{19}F	PBE[a]			−85.9	0.0				
		TPSS	−86.7	−1.1	−86.9	0.0	−85.6	0.0	−82.9	0.0
		M06-L	−82.7	−10.4	−76.1	0.0	−71.0	0.0	−65.6	0.0
		TPSSh	−85.4	−0.9	−85.6	0.0	−84.5	0.0	−81.9	0.0
		M06	−96.4	−24.1	−73.2	0.0	−72.8	0.0	−75.5	0.0
		LH07t	−57.0	19.9	−75.0	0.0	−74.4	0.0	−72.1	0.0
		LH12sif	−47.8	25.6	−70.3	0.0	−69.7	0.0	−67.9	0.0
F_2	^{19}F	PBE[a]			−1106.7	0.0				
		TPSS	−1051.0	−0.7	−1064.2	0.0	−1037.0	0.0	−1033.0	0.0
		M06-L	−994.3	−7.6	−1049.1	0.0	−958.9	0.0	−942.8	0.0
		TPSSh	−1041.1	−0.6	−1052.7	0.0	−1028.6	0.0	−1024.9	0.0
		M06	−1152.8	−16.0	−1151.9	0.0	−1149.4	0.0	−1147.1	0.0
		LH07t	−1025.7	15.1	−1028.6	0.0	−1022.4	0.0	−1023.6	0.0
		LH12sif	−993.8	19.3	−993.7	0.0	−994.3	0.0	−997.0	0.0

[a]No τ dependence for this GGA functional.

4. RESULTS

4.1. Unphysical Paramagnetic Contributions from τ_{MS} for Atoms. During our careful evaluations of results within the τ_{MS} formalism in ref 24, we had noted that the data for t-LMF-based LHs tended to deviate more than expected from the CCSD(T) reference data for proton shieldings and for the shieldings of some heavier nuclei in seemingly simple cases, where low paramagnetic contributions were expected. We assumed at that time that the specific form of the t-LMF along element-hydrogen bonds[34] may have been responsible for these deviations, as results for an s-LMF (based on the reduced density gradient) aligned more closely with GH results.[24] However, subsequent analyses have made us suspect that the τ_{MS} formalism may be responsible for some of the deviations when dealing with t-LMFs. We first illustrate the problem by comparing shieldings for simple spherical closed-shell atomic systems, where paramagnetic shielding contributions clearly should not be sustained, independent of any gauge issues, for the exact and approximate wave functions and also for DFT approaches.[50]

Table 1 provides data for the He and Ne atoms with meta-GGAs, meta-GGA-based GHs, and LHs, comparing τ_{MS} and τ_D. Diamagnetic shielding contributions depend on the functional (Table 1) but not on the model, so we may concentrate on the paramagnetic part. Both models give exactly zero σ^p contributions for He. This can be traced back to the absence of any occupied orbital with angular momentum. Turning to Ne, however, we see notable differences: τ_{MS} now generates non-negligible σ^p values. These artifacts are negative and below 1 ppm for TPSS and TPSSh, also negative but an order of magnitude larger for M06-L and M06, and significantly positive for the two LHs. The latter positive contributions are fully consistent with the too shielded values

https://dx.doi.org/10.1021/acs.jctc.0c01223
J. Chem. Theory Comput. 2021, 17, 1469−1479

that we found with t-LMF-based LHs for nonhydrogen nuclei in seemingly simple electronic situations.[24] In contrast, τ_D provides zero σ^p contributions, as it should, and thus overall much better agreement with the CCSD(T) value for Ne. While the unphysical σ^p contributions with τ_{MS} might be considered only a small issue for TPSS and TPSSh, they clearly are a problem for the other four functionals.

To clarify the origin of these artificial paramagnetic terms due to τ_{MS}, we start from the contribution to the perturbed Fock matrix with τ_{MS} for a meta-GGA functional, written in the AO basis

$$F_{\mu\nu,XC}^{\tau_{MS},B_k} = \frac{i}{4c}\int \frac{\partial f}{\partial \tau}[(R_{\mu\nu}\times \mathbf{r})_k \nabla\phi_\mu^* \nabla\phi_\nu + \phi_\nu((\mathbf{r}-R_\nu)\times\nabla\phi_\mu^*)_k - \phi_\mu^*((\mathbf{r}-R_\mu)\times\nabla\phi_\nu)_k]\,d\mathbf{r} \quad (23)$$

For a free atom at the gauge origin, the equation reduces to

$$F_{\mu\nu,XC}^{\tau_{MS},B_k} = \frac{i}{4c}\int \frac{\partial f}{\partial \tau}[\phi_\nu(\mathbf{r}\times\nabla\phi_\mu^*)_k - \phi_\mu^*(\mathbf{r}\times\nabla\phi_\nu)_k]\,d\mathbf{r} \quad (24)$$

but the contributions to the Fock matrix do not vanish, as they do in the LDA and GGA case or when using the uncorrected τ in τ-dependent functionals (τ_C and τ_{GI} approaches, see above). Inspecting the operator $\mathbf{r}\times\nabla$ acting on the second basis function, we note that it is a simple rotation around the direction of the magnetic field, as soon as the magnetic quantum number $m_l \geq 1$ for the AO involved (see more details in the Supporting Information). We note in passing that the one-electron contributions to the perturbed Fock matrix depend on a closely similar operator

$$h_{\mu\nu}^{B_k}[\omega, h^{B_k}] = \langle\phi_\mu^*|-(\mathbf{r}\times\nabla)_k|\phi_\nu\rangle \quad (25)$$

and they also contribute to the perturbed Fock matrix for the exact same entries (following the rotation pattern). However, in contrast to the additional contributions from the τ_{MS} model, these contributions cancel completely within the occupied-virtual block of the expansion coefficients and thus do not contribute to the final perturbed density matrix. Therefore, no net paramagnetic contributions arise. The entries in the perturbed Fock matrix due to the τ_{MS} model are typically an order of magnitude smaller for TPSS or TPSSh compared to the other four functionals, explaining the smaller impact on the shielding tensors. Any entries arising from τ_D are orders of magnitude smaller, below the level of numerical noise determined by the inherent integration accuracies.

We should also note that the present meta-GGA or meta-GGA-based GH results using τ_{MS} in Turbomole agree almost perfectly with data obtained within the same model but with the ORCA[38,39] or Gaussian[42] program packages (see Table S4 in the Supporting Information; the same holds for molecules). That is, the unphysical σ_p contributions are clearly not an artifact of any particular implementation but intrinsic to the τ_{MS} model itself.

4.2. Extension of the Analyses to Simple Linear Molecules. For molecular systems, proper paramagnetic contributions naturally arise as well, and so, the artifactual σ^p contributions generated by τ_{MS} are less visible. However, we see them clearly in the parallel shielding tensor contributions in linear molecules, e.g., for the parallel ^{19}F shielding tensor component in HF (see Table 2), where σ^p clearly should also vanish (see, e.g., ref 51 and references therein). Here, magnitudes and sizes for the different functionals are closely analogous to what we saw above for Ne. Looking at the perpendicular tensor component in HF, where sizable regular paramagnetic contributions are present, a comparison between τ_{MS} and τ_D suggests that similar artifacts for the former contribute also here. This reflects the relatively ionic F−H bond, which renders the fluorine environment still relatively similar to that of a free fluoride ion. As we switch to the more covalent situation in F_2, we still get similar, albeit somewhat smaller, parallel contributions for τ_{MS} as in HF, with the same dependence on the functional as for HF or for Ne. However, now, the differences between τ_{MS} and τ_D for the much larger (negative) perpendicular components behave very differently. That is, differences are larger for TPSS, M06-L, and TPSSh but smaller for M06 and the LHs. This shows that the artifacts of τ_{MS} are not easily separable from the overall paramagnetic terms and of course also from the current contributions, which enter for τ_D.

No numerically significant artifacts of the τ_{MS} model are seen for the parallel ^{7}Li shielding component in LiH (Table 2), confirming our conclusion for He that the artifacts are linked to orbitals on the atoms of interest with angular momentum. These contribute apparently rather little to the lithium shielding in this case, as confirmed also by the very small differences between τ_{MS} and τ_D for $\sigma_\perp^p$. The same holds for both components of the ^{1}H paramagnetic shielding tensor. This contrasts to the small but notable artifacts for $\sigma_\parallel^p$ (^{1}H) in HF. These artifacts are again negative for TPSS and TPSSh, negative and somewhat larger for M06-L and M06, and positive by similar amounts for the LHs. One might thus expect too large ^{1}H shieldings for the LHs. However, this trend for $\sigma_\parallel^p$ is outweighed by the two more deshielded $\sigma_\perp^p$ components with τ_{MS} compared to τ_D, explaining the observations in ref 24 of too deshielded isotropic ^{1}H values with LHs. In contrast, now, τ_{MS} provides increased $\sigma_\perp^p$ compared to τ_D for the other four functionals, to varying extents. This then leads to more positive isotropic ^{1}H shieldings for τ_{MS} vs τ_D in the case of these other functionals. Despite the rather transferable effects between atoms and the parallel tensor components in linear molecules, we thus find that we cannot anymore fully disentangle the artifacts of the τ_{MS} treatment from current contributions when larger paramagnetic terms come into play.

This holds also, for example, for the ^{13}C and ^{17}O shieldings in CO and the ^{15}N shieldings in N_2 (cf. Table S6 in the Supporting Information). In those cases, not all of the abovementioned dependencies on the functional hold for the parallel component. While the artifacts due to τ_{MS} are still positive for the LHs in all cases, some variations of sign and magnitude are seen for the other four functionals. That is, the artifacts are deshielding for M06-L and M06 but shielding for TPSS and TPSSh in the case of the parallel ^{17}O and ^{15}N values, whereas matters are reversed for the ^{13}C shielding (with smaller absolute values). As seen above for F_2, the differences between τ_{MS} and τ_D for $\sigma_\perp^p$ behave differently (Table S6) from those for $\sigma_\parallel^p$.

Table 2 and Table S6 provide additional paramagnetic shielding contributions for the two models based on an uncorrected kinetic-energy density, the gauge-dependent τ_C and the *ad hoc* τ_{GI} model (see the Theory section). Here, no contributions to the parallel component in these linear

https://dx.doi.org/10.1021/acs.jctc.0c01223
J. Chem. Theory Comput. 2021, 17, 1469−1479

Table 3. Comparison of Statistical Deviations with Respect to GIAO-CCSD(T)/pcSseg-4 Reference Data for the Main-Group Shielding Set from Reference 21 for Six Density Functionals Using Either the τ_{MS} or the τ_D Model

			TPSS	M06-L	TPSSh	M06	LH07t[a]	LH12ct[a]
^{1}H	τ_{MS}	SD	0.30	0.24	0.23	0.16	0.10	0.14
		MSE	0.40	0.28	0.34	0.24	−0.23	−0.49
		MAE	0.40	0.29	0.34	0.25	0.23	0.49
	τ_D	SD	0.27	0.19	0.20	0.16	0.10	0.13
		MSE	0.36	0.34	0.30	0.16	−0.09	−0.27
		MAE	0.36	0.34	0.30	0.21	0.10	0.27
^{13}C	τ_{MS}	SD	3.8	2.1	3.2	9.0	6.3	6.8
		MSE	−14.0	−12.1	−13.2	−28.7	−9.9	−4.4
		MAE	14.0	12.1	13.2	28.7	10.1	6.9
	τ_D	SD	4.0	4.4	3.7	9.5	5.4	5.3
		MSE	−13.9	−14.0	−13.2	−27.4	−10.4	−4.8
		MAE	13.9	14.0	13.2	27.4	10.4	5.8
heteronuclei[b]	τ_{MS}	SD	24.8	19.2	22.3	59.1	29.8	28.7
		MSE	−33.9	−19.0	−32.7	−79.7	−21.2	−9.1
		MAE	33.9	22.4	32.7	79.7	24.8	20.1
	τ_D	SD	29.0	32.6	26.6	61.6	27.4	24.1
		MSE	−37.2	−32.7	−35.8	−72.6	−26.9	−15.2
		MAE	37.2	32.7	35.8	72.6	26.9	17.0
all	τ_{MS}	SD	23.6	16.4	21.8	56.1	24.1	22.0
		MSE	−21.7	−13.0	−20.9	−50.4	−14.0	−6.1
		MAE	21.9	15.1	21.1	50.5	16.0	12.8
	τ_D	SD	27.1	28.1	25.2	55.7	23.6	19.3
		MSE	−23.6	−21.1	−22.6	−46.2	−17.2	−9.6
		MAE	23.8	21.2	22.8	46.2	17.2	10.8

[a]LH07t−LH07t-SVWN and LH12ct−LH12ct-SsifPW92. [b]Combining ^{15}N, ^{17}O, ^{19}F, and ^{31}P shielding constants.

molecules arise, as expected. We may thus focus only on $\sigma_\perp^p$ where, however, current contributions clearly matter. Taking the τ_D model as the correct reference, we cannot see clear-cut trends or advantages of one over the other of the simpler models. Starting with Table 2, differences tend again to be relatively small for both ^{1}H and ^{7}Li shieldings in LiH, where current contributions from p orbitals are minor. Deviations from the τ_D results are the largest for $\sigma_\perp^p$ in F_2. This is not surprising, as the effects of a current density functional should be the most notable for the largest paramagnetic currents.

Interestingly, for this system, the deviations are the most sizable for the semilocal M06-L functional and the smallest for the LHs. This may be rationalized as follows: in the semilocal functional, all of the current dependence of the functional arises from the τ_D contributions. In contrast, in the LHs, most of the current contributions likely are provided by the position-dependent nonlocal exchange admixture (which is relatively large in the most decisive semicore region[24]), while only some further contributions come from τ_D occuring in the LMF. The same observation holds for the $\sigma_\perp^p$ contributions in CO and N_2 (Table S6), where clearly the largest effect of τ_D compared to the uncorrected τ_C and τ_{GI} models (larger deshielding) is seen with M06-L and the smallest with the LHs. These observations are expected to be of general relevance for the nonhydrogen nuclei (see below).

4.3. Broader Evaluation for a Main-Group Isotropic Shielding Benchmark Set. We evaluate now the performance of the same set of six functionals with τ_{MS} vs τ_D on the main-group isotropic shielding benchmark set of ref 21, which contains 15 molecules and overall 34 shielding constants for ^{1}H, ^{13}C, ^{15}N, ^{17}O, ^{19}F, and ^{31}P of GIAO-CCSD(T)/pcSseg-4 quality. This set was also used for the recent first evaluation of LH shielding computations, using τ_{MS}.[24] Statistics with respect to the CCSD(T) reference data are provided in Table 3, grouped into ^{1}H, ^{13}C, and heteroatom (^{15}N, ^{17}O, ^{19}F, plus ^{31}P) shieldings. Full isotropic shielding data for all functionals, including also results with the τ_C and τ_{GI} models, are provided in Tables S7−S10 in the Supporting Information.

Note that in addition to the evaluation of LHs within the τ_{MS} framework,[24] TPSS and M06-L had also been screened before using the same model and were generally found to perform well.[20,21] Before starting a more detailed discussion, we note that the effects of going from τ_{MS} to τ_D on the overall statistics are small for TPSS and TPSSh but in part significant for the other functionals, as one might have expected from the atomic and linear-molecule results discussed above.

If we take first a bird's eye view on the statistical performance for all nuclei, switching from τ_{MS} to τ_D causes a slight deterioration of the performance for TPSS and TPSSh and a more significant one for M06-L. While the latter functional performs remarkably well within the τ_{MS}, τ_C, and τ_{GI} models, as found previously for τ_{MS}[20] and τ_{GI},[21] deviations are much larger using τ_D. This suggests that the previously observed good performance of this highly parameterized semilocal functional may to some extent indicate the right answer for the wrong reason, i.e., an error compensation involving the lack of current dependencies. In contrast, the rather poor performance of M06 improves slightly when using the τ_D model (but with a slightly wider distribution of errors). In this rough bird's eye view, the effects of changing to τ_D

https://dx.doi.org/10.1021/acs.jctc.0c01223
J. Chem. Theory Comput. 2021, 17, 1469−1479

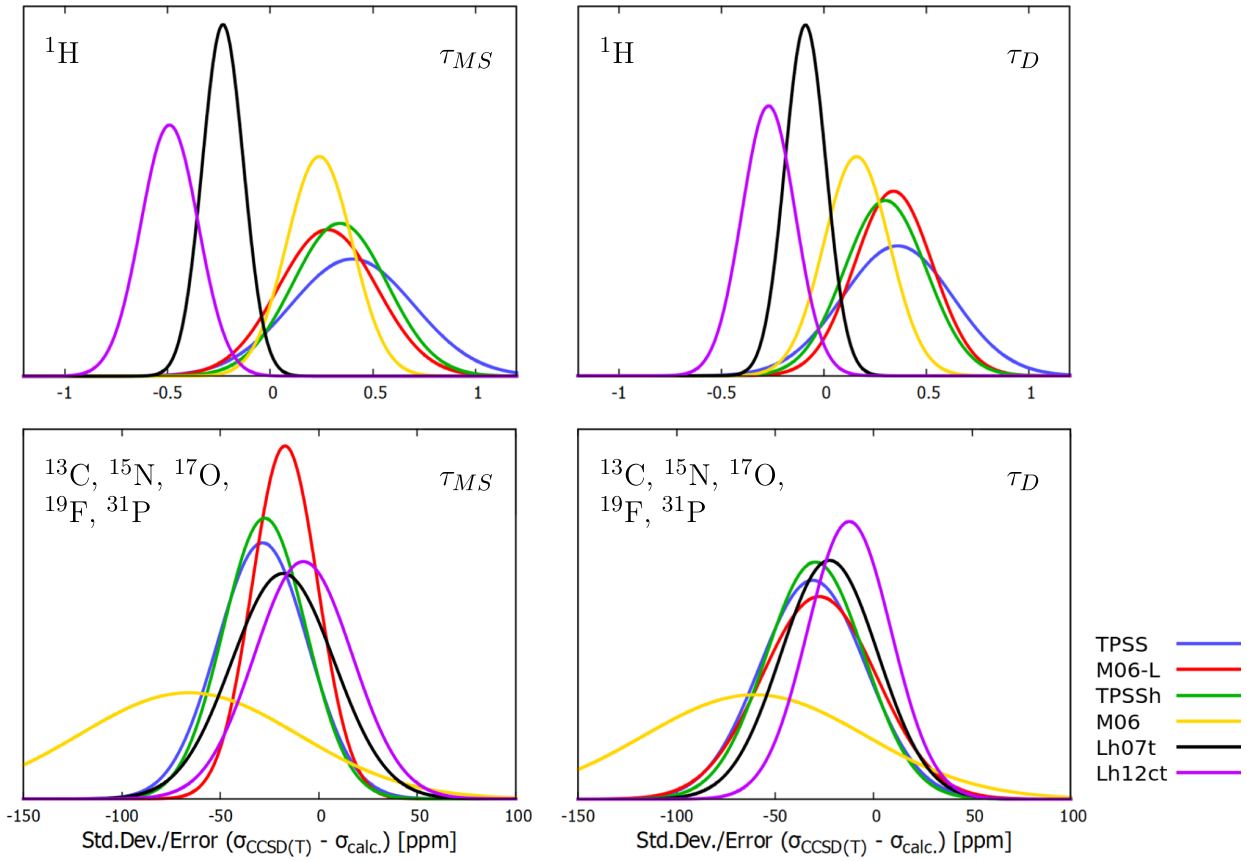

Figure 1. Normal error distributions of absolute shielding constants (ppm) for (top) ^{1}H and (bottom) ^{13}C, ^{15}N, ^{17}O, ^{19}F, and ^{31}P nuclei obtained with different functionals relative to GIAO-CCSD(T)/pcSseg-4 benchmark data,[21] comparing the τ_{MS} (left) and τ_D (right) models.

would also seem relatively minor for the already relatively good performance of the two LHs. However, it is preferable to analyze these observations separately for the different subsets of nuclei.

Starting with the ^{13}C shieldings, the differences between the models are essentially negligible for TPSS and TPSSh, and the changes also are rather modest for the other functionals (e.g., the top performance of LH12ct-SsifPW92 for MSE and MAE is not affected). This is different for the heteronuclei, where the performance of TPSS and TPSSh deteriorates slightly with τ_D, that for M06-L worsens more significantly, and the very poor performance of M06 improves somewhat (but with a slightly increased SD). For the very simple LH07t-SVWN local hybrid, the error distribution narrows, but the moderate systematic underestimation of the shieldings increases slightly. For the newer LH12ct-SsifPW92, similar trends are observed, i.e., an even more notable narrowing of the distribution and a slightly more negative MSE, but the overall MAE is now reduced somewhat. Given the much worse performance of M06-L within the τ_D model, LH12ct-SsifPW92 is now even more clearly the best-performing functional for the heteronuclei.

The most notable effects of the model for the LHs, however, are seen for the ^{1}H shieldings. In contrast to all other functionals compared in ref 24, LHs had been found to underestimate proton shieldings significantly, even though the overall performance for other nuclei was outstanding (see above). This can also be seen here for both LHs, particularly for LH12ct-SsifPW92, when using τ_{MS}. Most of this negative deviation is removed with τ_D for LH07t-SVWN, and the negative MSE for LH12ct-SsifPW92 is reduced almost by half. We can thus conclude that at least part of the previously observed poor performance of t-LMF-based LHs for proton shieldings is not caused by the specific form of the t-LMF, as we had assumed, but by the artifacts of the τ_{MS} model. Changes of the proton shieldings from τ_{MS} to τ_D are much smaller for the other functionals, with the slight exception of M06, where the MSE decreases, while the SD remains the same. We note also the very different performances and dependences on the treatment of τ of the at first sight closely related functionals M06-L and M06. That is, despite their generally similar functional form, predictions are rendered difficult by the highly parameterized nature of these functionals. M06-L and M06 were also found recently to provide very different descriptions of core−shell spin polarization in the context of transition-metal hyperfine couplings.[52]

It is also instructive to compare graphically the distribution of errors when moving from τ_{MS} to τ_D (Figure 1): in the case of the ^{1}H shieldings, the distributions narrow slightly (except those for M06-L and TPSSh, which widen). Consistent with the above discussion, the maxima of the curves move closer to the origin, except for M06-L, most notably so for M06 and the LHs, coming from opposite directions. With τ_D, LH07t-SVWN clearly provides the narrowest error distribution and particularly small systematic errors as well. For the non-hydrogen nuclei, the most notable features of going from τ_{MS} to τ_D are the pronounced broadening of the distribution for M06-L and the less pronounced sharpening for LH12ct-SsifPW92, which is now even more clearly the best-performing

https://dx.doi.org/10.1021/acs.jctc.0c01223
J. Chem. Theory Comput. 2021, 17, 1469−1479

of the functionals evaluated, despite the slightly more negative MSE. We note in passing that within the τ_C and τ_{GI} models, the LH performance differs only moderately from the τ_D data, consistent with a reduced role of the explicit current dependence compared to M06-L (see above).

5. CONCLUSIONS

We have identified appreciable unphysical paramagnetic contributions to nuclear shieldings for a number of exchange-correlation functionals based on the KS kinetic energy, when applying the widely used Maximoff−Scuseria model to remove the gauge dependence of τ. These artifacts can be identified most clearly for spherical atoms and for the parallel tensor component in linear molecules. While the effects are rather small for the TPSS meta-GGA and its TPSSh global hybrid variant, they become much larger for the M06-L and M06 functionals and for local hybrid functionals with τ-dependent local mixing functions. For these local hybrids, the artifactual paramagnetic contributions for atoms are deshielding; for the other functionals, they are shielding. We have traced these unphysical contributions to entries in the magnetically perturbed Fock matrix arising from the rotation of orbitals with angular momentum.

Such unphysical contributions are eliminated when instead using Dobson's explicit current-density functional extension of τ. Here, τ_D has been included for the first time into a linear-response nuclear shielding code. For meta-GGA functionals, this adds somewhat to the computational effort by requiring an iterative coupled-perturbed Kohn−Sham treatment, while for global or local hybrid functionals, the already higher computational requirements are affected very little. The τ_D scheme ensures the gauge invariance of the XC functionals and simultaneously eliminates the unphysical contributions encountered for the τ_{MS} model. The actual impact on the overall shielding results depends on the specific functional form into which the τ_{MS} or τ_D contributions enter. The previously observed outstanding performance of the M06-L functional to some extent has been due to a compensation between intrinsic errors of the density functional and the incomplete (or lacking for the τ_C and τ_{GI} models) treatment of its current-density dependence. That is, M06-L performs less accurately within the τ_D framework.

In contrast, recently observed too negative ^{1}H shieldings with first-generation local hybrid functionals, such as LH07t-SVWN and LH12ct-SsifPW92 studied in this work, were to a significant part due to artifacts within the τ_{MS} implementation used. The more complete treatment using τ_D improves these hydrogen shieldings appreciably while retaining the already outstanding performance for other nuclei. This clearly motivates the further development of local hybrid functionals for nuclear shieldings and related properties, which is underway in our laboratory.

■ ASSOCIATED CONTENT

Supporting Information

The Supporting Information is available free of charge at https://pubs.acs.org/doi/10.1021/acs.jctc.0c01223.

Further data on gauge (in-)dependence, effects of rotation operators on atomic orbitals, comparison between different codes, paramagnetic shielding tensors with different functionals and models for τ, and detailed numerical data on isotropic shieldings (PDF)

■ AUTHOR INFORMATION

Corresponding Author

Martin Kaupp − *Institut für Chemie, Theoretische Chemie/Quantenchemie, Technische Universität Berlin, D-10623 Berlin, Germany;* orcid.org/0000-0003-1582-2819; Email: martin.kaupp@tu-berlin.de

Author

Caspar Jonas Schattenberg − *Institut für Chemie, Theoretische Chemie/Quantenchemie, Technische Universität Berlin, D-10623 Berlin, Germany*

Complete contact information is available at: https://pubs.acs.org/10.1021/acs.jctc.0c01223

Notes

The authors declare no competing financial interest.

■ ACKNOWLEDGMENTS

C.J.S. is grateful for a scholarship provided by Studienstiftung des deutschen Volkes. This work has been funded by the German Research Foundation (Deutsche Forschungsgemeinschaft, DFG) within project KA1187/14-1 and furthermore by Project-ID 387284271 - SFB 1349 (Gefördert durch die Deutsche Forschungsgemeinschaft (DFG) - Project-ID 387284271 - SFB 1349).

■ REFERENCES

(1) Kaupp, M.; Bühl, M.; Malkin, V. G. *Calculation of NMR and EPR Parameters*; 1st ed.; Wiley-VCH: Weinheim, 2004.

(2) Flaig, D.; Maurer, M.; Hanni, M.; Braunger, K.; Kick, L.; Thubauville, M.; Ochsenfeld, C. Benchmarking Hydrogen and Carbon NMR Chemical Shifts at HF, DFT, and MP2 Levels. *J. Chem. Theory Comput.* **2014**, *10*, 572−578.

(3) Maurer, M.; Ochsenfeld, C. Spin Component-Scaled Second-Order Møller-Plesset Perturbation Theory for Calculating NMR Shieldings. *J. Chem. Theory Comput.* **2015**, *11*, 37−44.

(4) Keal, T. W.; Tozer, D. J. The exchange-correlation potential in Kohn-Sham nuclear magnetic resonance shielding calculations. *J. Chem. Phys.* **2003**, *119*, 3015−3024.

(5) Keal, T. W.; Tozer, D. J. A semiempirical generalized gradient approximation exchange-correlation functional. *J. Chem. Phys.* **2004**, *121*, 5654−5660.

(6) Reimann, S.; Ekström, U.; Stopkowicz, S.; Teale, A. M.; Borgoo, A.; Helgaker, T. The importance of current contributions to shielding constants in density-functional theory. *Phys. Chem. Chem. Phys.* **2015**, *17*, 18834−18842.

(7) Stoychev, G. L.; Auer, A. A.; Neese, F. Efficient and Accurate Prediction of Nuclear Magnetic Resonance Shielding Tensors with Double-Hybrid Density Functional Theory. *J. Chem. Theory Comput.* **2018**, *14*, 4756−4771.

(8) Perdew, J. P.; Schmidt, K. Jacob's ladder of density functional approximations for the exchange-correlation energy. *AIP Conf. Proc.* **2001**, *577*, 1−20.

(9) Vignale, G.; Rasolt, M. Density-Functional Theory in Strong Magnetic Fields. *Phys. Rev. Lett.* **1987**, *59*, 2360−2363.

(10) Vignale, G.; Rasolt, M. Current- and spin-density-functional theory for inhomogeneous electronic systems in strong magnetic fields. *Phys. Rev. B* **1988**, *37*, 10685−10696.

(11) Vignale, G.; Rasolt, M.; Geldart, D. J. W. Diamagnetic susceptibility of a dense electron gas. *Phys. Rev. B* **1988**, *37*, 2502−2507.

(12) Lee, A. M.; Handy, N. C.; Colwell, S. M. The density functional calculation of nuclear shielding constants using London atomic orbitals. *J. Chem. Phys.* **1995**, *103*, 10095−10109.

(13) Maximoff, S. N.; Scuseria, G. E. Nuclear magnetic resonance shielding tensors calculated with kinetic energy density-dependent

exchange-correlation functionals. *Chem. Phys. Lett.* **2004**, *390*, 408−412.
(14) Becke, A. D. Current density in exchange-correlation functionals: Application to atomic states. *J. Chem. Phys.* **2002**, *117*, 6935−6938.
(15) Johansson, M. P.; Swart, M. Magnetizabilities at Self-Interaction-Corrected Density Functional Theory Level. *J. Chem. Theory Comput.* **2010**, *6*, 3302−3311.
(16) Bates, J. E.; Furche, F. Harnessing the meta-generalized gradient approximation for time-dependent density functional theory. *J. Chem. Phys.* **2012**, *137*, 164105.
(17) Reiter, K.; Mack, F.; Weigend, F. Calculation of Magnetic Shielding Constants with meta-GGA Functionals Employing the Multipole-Accelerated Resolution of the Identity: Implementation and Assessment of Accuracy and Efficiency. *J. Chem. Theory Comput.* **2018**, *14*, 191−197.
(18) Tao, J.; Perdew, J. P.; Staroverov, V. N.; Scuseria, G. E. Climbing the Density Functional Ladder: Nonempirical Meta-Generalized Gradient Approximation Designed for Molecules and Solids. *Phys. Rev. Lett.* **2003**, *91*, 146401.
(19) Zhao, Y.; Truhlar, D. G. A new local density functional for main-group thermochemistry, transition metal bonding, thermochemical kinetics, and noncovalent interactions. *J. Chem. Phys.* **2006**, *125*, 194101.
(20) Zhao, Y.; Truhlar, D. G. Improved Description of Nuclear Magnetic Resonance Chemical Shielding Constants Using the M06-L Meta-Generalized-Gradient-Approximation Density Functional. *J. Phys. Chem. A* **2008**, *112*, 6794−6799.
(21) Stoychev, G. L.; Auer, A. A.; Izsák, R.; Neese, F. Self-Consistent Field Calculation of Nuclear Magnetic Resonance Chemical Shielding Constants Using Gauge-Including Atomic Orbitals and Approximate Two-Electron Integrals. *J. Chem. Theory Comput.* **2018**, *14*, 619−637.
(22) Staroverov, V. N.; Scuseria, G. E.; Tao, J.; Perdew, J. P. Comparative assessment of a new nonempirical density functional: Molecules and hydrogen-bonded complexes. *J. Chem. Phys.* **2003**, *119*, 12129−12137.
(23) Zhao, Y.; Truhlar, D. G. The M06 suite of density functionals for main group thermochemistry, thermochemical kinetics, noncovalent interactions, excited states, and transition elements: two new functionals and systematic testing of four M06-class functionals and 12 other functionals. *Theor. Chem. Acc.* **2008**, *120*, 215−241.
(24) Schattenberg, C. J.; Reiter, K.; Weigend, F.; Kaupp, M. An Efficient Coupled-Perturbed Kohn−Sham Implementation of NMR Chemical Shift Computations with Local Hybrid Functionals and Gauge-Including Atomic Orbitals. *J. Chem. Theory Comput.* **2020**, *16*, 931−943.
(25) Tao, J. Explicit inclusion of paramagnetic current density in the exchange-correlation functionals of current-density functional theory. *Phys. Rev. B* **2005**, *71*, 205107.
(26) Tao, J.; Perdew, J. P. Nonempirical Construction of Current-Density Functionals from Conventional Density-Functional Approximations. *Phys. Rev. Lett.* **2005**, *95*, 196403.
(27) Sagvolden, E.; Ekström, U.; Tellgren, E. I. Isoorbital indicators for current density functional theory. *Mol. Phys.* **2013**, *111*, 1295−1302.
(28) Dobson, J. F. Spin-density functionals for the electron correlation energy with automatic freedom from orbital self-interaction. *J. Phys.: Condens. Matter* **1992**, *4*, 7877−7890.
(29) Dobson, J. F. Alternative expressions for the Fermi hole curvature. *J. Chem. Phys.* **1993**, *98*, 8870−8872.
(30) Maier, T. M.; Bahmann, H.; Kaupp, M. Efficient Semi-numerical Implementation of Global and Local Hybrid Functionals for Time-Dependent Density Functional Theory. *J. Chem. Theory Comput.* **2015**, *11*, 4226−4237.
(31) Furness, J. W.; Verbeke, J.; Tellgren, E. I.; Stopkowicz, S.; Ekström, U.; Helgaker, T.; Teale, A. M. Current Density Functional Theory Using Meta-Generalized Gradient Exchange-Correlation Functionals. *J. Chem. Theory Comput.* **2015**, *11*, 4169−4181.
(32) Becke, A. D. A new inhomogeneity parameter in density-functional theory. *J. Chem. Phys.* **1998**, *109*, 2092−2098.
(33) Helgaker, T.; Jaszuński, M.; Ruud, K. Ab Initio Methods for the Calculation of NMR Shielding and Indirect Spin-Spin Coupling Constants. *Chem. Rev.* **1999**, *99*, 293−352.
(34) Maier, T. M.; Arbuznikov, A. V.; Kaupp, M. Local Hybrid Functionals: Theory, Implementation, and Performance of an Emerging New Tool in Quantum Chemistry and Beyond. *Wiley Interdiscip. Rev.: Comput. Mol. Sci.* **2019**, *9*, No. e1378.
(35) London, F. Théorie quantique des courants interatomiques dans les combinaisons aromatiques. *J. Phys. Radium* **1937**, *8*, 397−409.
(36) Ditchfield, R. Self-consistent perturbation theory of diamagnetism. *Mol. Phys.* **1974**, *27*, 789−807.
(37) Irons, T. J. P.; Spence, L.; David, G.; Speake, B. T.; Helgaker, T.; Teale, A. M. Analyzing Magnetically Induced Currents in Molecular Systems Using Current-Density-Functional Theory. *J. Phys. Chem. A* **2020**, *124*, 1321−1333.
(38) Neese, F. Software update: the ORCA program system, version 4.0. *Wiley Interdiscip. Rev.: Comput. Mol. Sci.* **2017**, *8*, No. e1327.
(39) Neese, F.; Wennmohs, F.; Becker, U.; Riplinger, C. The ORCA quantum chemistry program package. *J. Chem. Phys.* **2020**, *152*, 224108.
(40) Local version derived from TURBOMOLE version 7.4.1, TURBOMOLE GmbH, 2019. TURBOMOLE is a development of University of Karlsruhe and Forschungszentrum Karlsruhe 1989-2007, TURBOMOLE GmbH since 2007. The modifications described in the present work will be available with the next release version.
(41) Balasubramani, S. G.; Chen, G. P.; Coriani, S.; Diedenhofen, M.; Frank, M. S.; Franzke, Y. J.; Furche, F.; Grotjahn, R.; Harding, M. E.; Hättig, C.; Hellweg, A.; Helmich-Paris, B.; Holzer, C.; Huniar, U.; Kaupp, M.; Marefat Khah, A.; Karbalaei Khani, S.; Müller, T.; Mack, F.; Nguyen, B. D.; Parker, S. M.; Perlt, E.; Rappoport, D.; Reiter, K.; Roy, S.; Ruckert, M.; Schmitz, G.; Sierka, M.; Tapavicza, E.; Tew, D. P.; van Wüllen, C.; Voora, V. K.; Weigend, F.; Wodynski, A.; Yu, J. M. TURBOMOLE: Modular program suite for ab initio quantum-chemical and condensed-matter simulations. *J. Chem. Phys.* **2020**, *152*, 184107.
(42) Frisch, M. J.; Trucks, G. W.; Schlegel, H. B.; Scuseria, G. E.; Robb, M. A.; Cheeseman, J. R.; Scalmani, G.; Barone, V.; Petersson, G. A.; Nakatsuji, H.; Li, X.; Caricato, M.; Marenich, A. V.; Bloino, J.; Janesko, B. G.; Gomperts, R.; Mennucci, B.; Hratchian, H. P.; Ortiz, J. V.; Izmaylov, A. F.; Sonnenberg, J. L.; Williams-Young, D.; Ding, F.; Lipparini, F.; Egidi, F.; Goings, J.; Peng, B.; Petrone, A.; Henderson, T.; Ranasinghe, D.; Zakrzewski, V. G.; Gao, J.; Rega, N.; Zheng, G.; Liang, W.; Hada, M.; Ehara, M.; Toyota, K.; Fukuda, R.; Hasegawa, J.; Ishida, M.; Nakajima, T.; Honda, Y.; Kitao, O.; Nakai, H.; Vreven, T.; Throssell, K.; Montgomery, J. A., Jr.; Peralta, J. E.; Ogliaro, F.; Bearpark, M. J.; Heyd, J. J.; Brothers, E. N.; Kudin, K. N.; Staroverov, V. N.; Keith, T. A.; Kobayashi, R.; Normand, J.; Raghavachari, K.; Rendell, A. P.; Burant, J. C.; Iyengar, S. S.; Tomasi, J.; Cossi, M.; Millam, J. M.; Klene, M.; Adamo, C.; Cammi, R.; Ochterski, J. W.; Martin, R. L.; Morokuma, K.; Farkas, O.; Foresman, J. B.; Fox, D. J. *Gaussiañ16*; Revision A.03. 2016; Gaussian Inc.: Wallingford CT.
(43) Dunning, T. H., Jr. Gaussian basis sets for use in correlated molecular calculations. I. The atoms boron through neon and hydrogen. *J. Chem. Phys.* **1989**, *90*, 1007−1023.
(44) Kendall, R. A.; Dunning, T. H., Jr.; Harrison, R. J. Electron affinities of the first-row atoms revisited. Systematic basis sets and wave functions. *J. Chem. Phys.* **1992**, *96*, 6796−6806.
(45) Woon, D. E.; Dunning, T. H., Jr. Gaussian basis sets for use in correlated molecular calculations. IV. Calculation of static electrical response properties. *J. Chem. Phys.* **1994**, *100*, 2975−2988.
(46) Jensen, F. Segmented Contracted Basis Sets Optimized for Nuclear Magnetic Shielding. *J. Chem. Theory Comput.* **2015**, *11*, 132−138.
(47) Bahmann, H.; Rodenberg, A.; Arbuznikov, A. V.; Kaupp, M. A thermochemically competitive local hybrid functional without gradient corrections. *J. Chem. Phys.* **2007**, *126*, No. 011103.

https://dx.doi.org/10.1021/acs.jctc.0c01223
J. Chem. Theory Comput. 2021, 17, 1469−1479

(48) Kaupp, M.; Bahmann, H.; Arbuznikov, A. V. Local hybrid functionals: An assessment for thermochemical kinetics. *J. Chem. Phys.* **2007**, *127*, 194102.
(49) Arbuznikov, A. V.; Kaupp, M. Importance of the correlation contribution for local hybrid functionals: Range separation and self-interaction corrections. *J. Chem. Phys.* **2012**, *136*, No. 014111.
(50) Malkina, O. L.; Komorovský, S.; Visscher, L.; Malkin, V. G. Note: Counterintuitive gauge-dependence of nuclear magnetic resonance shieldings for rare-gas dimers: Does a natural gauge-origin for spherical atoms exist? *J. Chem. Phys.* **2011**, *134*, No. 086101.
(51) Fukui, H. Theory and calculation of nuclear shielding constants. *Prog. Nucl. Magn. Reson. Spectrosc.* **1997**, *31*, 317−342.
(52) Schattenberg, C. J.; Maier, T. M.; Kaupp, M. Lessons from the Spin-Polarization/Spin-Contamination Dilemma of Transition-Metal Hyperfine Couplings for the Construction of Exchange-Correlation Functionals. *J. Chem. Theory Comput.* **2018**, *14*, 5653−5672.

https://dx.doi.org/10.1021/acs.jctc.0c01223
J. Chem. Theory Comput. 2021, 17, 1469−1479

IV

Reprinted with permission from

C. J. Schattenberg and M. Kaupp,
"*Implementation and Validation of Local Hybrid Functionals with Calibrated Exchange-Energy Densities for Nuclear Shielding Constants*",
J. Phys. Chem. A, **2021**, *125*, 2697–2707.
DOI: 10.1021/acs.jpca.1c01135

THE JOURNAL OF PHYSICAL CHEMISTRY A
A JOURNAL OF THE AMERICAN CHEMICAL SOCIETY

pubs.acs.org/JPCA Article

Implementation and Validation of Local Hybrid Functionals with Calibrated Exchange-Energy Densities for Nuclear Shielding Constants

Published as part of The Journal of Physical Chemistry virtual special issue "Alexander Boldyrev Festschrift".

Caspar Jonas Schattenberg and Martin Kaupp*

Cite This: *J. Phys. Chem. A* 2021, 125, 2697−2707 Read Online

ACCESS | Metrics & More | Article Recommendations | Supporting Information

ABSTRACT: A recently reported coupled-perturbed Kohn−Sham implementation to compute nuclear shielding constants with gauge-including atomic orbitals and local hybrid functionals has been extended to cover higher derivatives of the density in the local mixing function (LMF) of the local hybrid as well as the calibration function (CF) needed to deal with the ambiguity of exchange-energy densities. This allowed the first evaluation of state-of-the-art local hybrids with "calibrated" exchange-energy densities for nuclear shieldings. Compared to previously evaluated simpler local hybrids without a CF, appreciable improvements are found for proton shieldings. Furthermore, the recent LH20t functional is still competitive with the outstanding performance of the uncalibrated LH12ct-SsirSVWN and LH12ct-SsifSVWN LHs for heavier nuclei, suggesting that LH20t is possibly the most robust choice of any rung-four functional for computing the nuclear shieldings of main-group nuclei so far. Interestingly, the presence of a CF in the functional significantly reduces the number of artifacts introduced by the widely used Maximoff−Scuseria framework to treat the local kinetic energy τ. The latter occurs in so-called t-LMFs used in many of the present local hybrids. In any case, the use of Dobson's current-density functional framework is also recommended with more advanced calibrated τ-dependent local hybrid functionals.

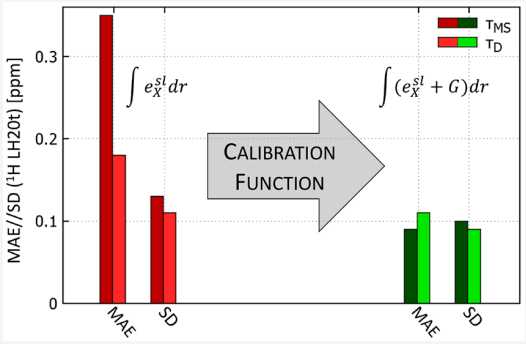

1. INTRODUCTION

Due to the central importance of NMR spectroscopy in chemistry and related fields, the quantum-chemical calculation of NMR parameters has become a tool of appreciable importance and interest.[1] Methodological improvements in this area in terms of the computational efficiency[2,3], accuracy,[4−6] and method validation[7−19] are currently being pursued very actively. With the focus of the present work on nuclear shieldings, we note that Kohn−Sham density functional theory (DFT) is the most widely used methodology in view of its good cost−performance ratio. Yet, the overall accuracy obtained with standard functionals is currently a limiting factor, more so than that for energetics, for example. This is also relevant in regard to efforts toward the automated quantum-chemical computation of full NMR spectra.[20] So far, double-hybrid (DH) functionals are considered to provide the most accurate nuclear shieldings for most main-group species;[5] however, they require computationally expensive MP2 second-derivatives involving gauge-including atomic orbitals (GIAOs[21−23]), limiting their applicability to smaller systems.

Accuracy improvements on the lower rungs of the often-invoked Jacob's ladder of DFT exchange-correlation functionals[24] (double hybrids are on the fifth and highest rung) are thus highly desirable. Our own recent efforts in this context involve local hybrid (LH) functionals[25−27] on the fourth rung. These exhibit a position-dependent Hartree−Fock exchange admixture, which is governed by a so-called local mixing function (LMF). This position-dependent admixture allows a more flexible compromise between a minimization of the self-interaction errors and a simulation of the left−right correlation in different regions of space compared to global hybrid (GH) functionals with a constant admixture. This is also expected to be beneficial for NMR parameters, and the recent first implementations and preliminary evaluations of LHs for nuclear shieldings[28] and spin−spin coupling constants[29] appear to support this assumption. One reason for the expected advantages of LHs for nuclear shieldings is that locally elevated Hartree−Fock exchange admixtures may help bring in some of the dependencies on induced paramagnetic

Received: February 7, 2021
Revised: March 8, 2021
Published: March 18, 2021

https://doi.org/10.1021/acs.jpca.1c01135
J. Phys. Chem. A 2021, 125, 2697−2707

currents that are lacking in standard semilocal functionals. Recent work suggests that at least part of the too low shieldings obtained with the latter for main-group nuclei is related to the missing current terms,[16] and in a broader way GHs are not very effective in curing this deficiency.

Indeed, the first LH implementation of LHs for shieldings[28] has given excellent results for non-hydrogen main-group nuclei when using so-called t-LMFs[26,30,31] based on a scaled ratio of the von Weizsäcker and Kohn−Sham local kinetic energies ($g(\mathbf{r}) = b\cdot\frac{\tau_W}{\tau}$). However, clearly inferior results were found for proton shieldings in addition to unexpected deviations from accurate CCSD(T) data for some seemingly simple molecules with small paramagnetic contributions. We initially suspected that the form of the t-LMF was responsible for the too deshielded proton values,[28] as LHs with an s-LMF based on the reduced density gradient[32] performed more in line with GHs. However, closer analyses showed that another issue affected the proton data specifically:[33] the t-LMF depends on the gauge-dependent local kinetic energy τ. Therefore, the implementation of ref 28 was done within the widely used framework of Maximoff and Scuseria[34] (MS) to render the τ contributions gauge-independent (τ_{MS}). It turned out that the MS scheme introduced artifactual paramagnetic contributions that showed up even for atoms or the parallel shielding tensor contribution of linear molecules.[33] These artifacts were found to be responsible for both a significant part of the too deshielded proton values and the deviations in "simple" cases for other nuclei. Such artifactual contributions from τ_{MS} also appear for other τ-dependent functionals such as meta-GGAs or meta-GGA-based GHs. In some cases (e.g., TPSS and TPSSh), the artifacts were small or even beneficial (M06-L) due to error compensation. This was shown by the implementation[33] of a theoretically more complete treatment based on Dobson's current-density generalization[35,36] of τ (τ_D), which did not exhibit these artifacts. The too negative ^{1}H shieldings of LHs with t-LMF improved significantly in this τ_D-framework, while the other shieldings remained accurate and the overall width of the error distributions narrowed further.[33]

The LH nuclear shielding implementations of refs 28 and 33 are still incomplete in an important aspect: they have been limited to first-generation LHs based on the local spin-density approximation (LSDA) for the exchange-energy density, which lack a so-called calibration function (CF) to deal with the gauge ambiguity of exchange-energy densities.[27,37−39] In particular, the gauge problem manifests in spurious non-dynamical correlation contributions and notably affects weak noncovalent interactions.[27,38−41] Our more recent LHs are thus based on GGA exchange-energy densities that are corrected by a semilocal CF.[38,40] The recent LH20t functional[40] is particularly notable in this context as it has been found to be one of the most accurate rung-four functionals for general main-group energetics and is the first functional of any rung to properly balance localization and delocalization in the MVO-10[42] gas-phase mixed-valence benchmark. The CFs in such calibrated functionals contain terms that depend on the Laplacian and Hessian of the electron density. To evaluate such second-generation LHs for nuclear shieldings, in this work we extend the code to include such terms as well as further terms that involve derivatives of the local kinetic energy. We note in passing that these extensions may enable also the use of either future LMFs that contain higher density derivatives or LHs based on meta-GGA exchange-energy densities. Thus, the main goal of this work is to present the extended implementation of more advanced "calibrated" LHs into the nuclear shielding part of the Turbomole program package and in addition their first evaluation for main-group nuclear shieldings by comparing both τ_{MS} and the more complete τ_D framework.

2. THEORY

2.1. Local Hybrid Functionals Containing Calibration Functions. A relatively general form of a LH reads[38]

$$E_{XC}^{LH} = E_X^{ex} + E_C^{sl} + \sum_\sigma \int [1 - g_\sigma(\mathbf{r})][e_{X,\sigma}^{sl}(\mathbf{r}) - e_{X,\sigma}^{ex}(\mathbf{r}) + G_\sigma(\mathbf{r})]\,d\mathbf{r} \tag{1}$$

where E_X^{ex} is the exact (Hartree−Fock-type) exchange energy, E_C^{sl} is a semilocal correlation energy functional, $e_{X,\sigma}^{sl}(\mathbf{r})$ is the semilocal exchange-energy density, and $e_{X,\sigma}^{ex}(\mathbf{r})$ is the exact exchange-energy density

$$e_{X,\sigma}^{ex}(\mathbf{r}) = -\frac{1}{2}\sum_{ij}\varphi_{i,\sigma}^*(\mathbf{r})\varphi_{j,\sigma}(\mathbf{r})\int\frac{\varphi_{j,\sigma}^*(\mathbf{r}')\varphi_{i,\sigma}(\mathbf{r}')}{|\mathbf{r}-\mathbf{r}'|}\,d\mathbf{r}' \tag{2}$$

constructed from a set of molecular spin−orbitals $\{\varphi_i\sigma(\mathbf{r})\}$. $G_\sigma(\mathbf{r})$ is a calibration function (CF)[43] defined by its basic property $\int G_\sigma(\mathbf{r})\,d\mathbf{r} = 0$. In principle, any function that fulfills this basic constraint may be considered (see ref 37 and the references therein), but here we consider the semilocal CFs as suggested in refs 38 and 39 (see below), which fulfill a number of additional exact constraints.[27,38,39] In the case of $g(\mathbf{r}) = a_0 =$ *constant* i.e. for a GH, the CF integrates out and has thus no effect on the resulting exchange-correlation energy E_{XC}. This is not possible for a proper LH. The CF is adjusted to bring $e_{X,\sigma}^{sl}(\mathbf{r})$ and $e_{X,\sigma}^{ex}(\mathbf{r})$ "into matching gauges". In practice, the CF contains adjustable parameters that can be optimized to remove unphysical nondynamical correlation-energy contributions, e.g., for atoms or weakly bound noble-gas dimers.[38,39]

Ref 39 shows how to derive semilocal CFs from semilocal exchange functionals using one or more partial integrations. We may, for example, consider a GGA functional written as $E_{X,\sigma}^{GGA} = E_{X,\sigma}^{LDA} - \int\Delta e_{X,\sigma}^{GGA}\,d\mathbf{r}$, where $e_{X,\sigma}^{GGA} = \rho_\sigma^{4/3}\cdot\mathcal{F}[s_\sigma]\cdot{s_\sigma}^2$. Here, $s_\sigma(\mathbf{r})$ is the reduced spin-density gradient

$$s_\sigma(\mathbf{r}) = \frac{1}{k}\cdot\frac{{\gamma_{\sigma\sigma}}^{1/2}(\mathbf{r})}{{\rho_\sigma}^{4/3}(\mathbf{r})} \tag{3}$$

where $k = 2(6\pi^2)^{1/3}$, $\rho_\sigma(\mathbf{r})$ is the density, and $\gamma_{\sigma\sigma}(\mathbf{r})$ is the squared density gradient

$$\gamma_{\sigma\varsigma}(\mathbf{r}) = \nabla^T\rho_\sigma(\mathbf{r})\nabla\rho_\varsigma(\mathbf{r}) \tag{4}$$

$\mathcal{F}[s_\sigma]$ is a real-space damping function, which is discussed further below.

A first partial integration leads to a first-order "partial integration gauge" CF (pig1 CF)[39]

$$G_\sigma^{(1)} = f_1\cdot\rho_\sigma^{4/3}\cdot\left[\mathcal{F}[s_\sigma]\cdot\left(q_\sigma - \frac{1}{3}{s_\sigma}^2\right) + s_\sigma\cdot\frac{d\mathcal{F}[s_\sigma]}{ds_\sigma}\cdot\left(p_\sigma - \frac{4}{3}{s_\sigma}^2\right)\right] \tag{5}$$

Another partial integration provides a second-order contribution

https://doi.org/10.1021/acs.jpca.1c01135
J. Phys. Chem. A 2021, 125, 2697−2707

$$G_\sigma^{(2)} = f_1 \cdot f_2 \cdot \rho_\sigma^{4/3} \cdot \left[s_\sigma^2 \cdot \frac{d^2\mathcal{F}[s_\sigma]}{ds_\sigma^2} \cdot \left(p_\sigma - \frac{4}{3} s_\sigma^2 \right) + s_\sigma \cdot \frac{d\mathcal{F}[s_\sigma]}{ds_\sigma} \cdot \left(p_\sigma + q_\sigma - \frac{5}{3} s_\sigma^2 \right) \right] \quad (6)$$

where f_1 and f_2 are adjustable parameters. Combined with the first-order contribution, this leads then to a more complex second-order pig2 CF. In these equations,

$$q_\sigma(\mathbf{r}) = \frac{1}{k^2} \cdot \frac{l_\sigma(\mathbf{r})}{\rho_\sigma^{5/3}(\mathbf{r})} \quad (7)$$

is the reduced density Laplacian and

$$p_\sigma(\mathbf{r}) = \frac{1}{k^2} \cdot \frac{\eta_{\sigma,\sigma\sigma}(\mathbf{r})}{\gamma_{\sigma\sigma}(\mathbf{r}) \cdot \rho_\sigma^{5/3}(\mathbf{r})} \quad (8)$$

is the reduced density Hessian. These contain the density Laplacian

$$l_\sigma(\mathbf{r}) = \Delta\rho_\sigma(\mathbf{r}) \quad (9)$$

(where $\Delta = \nabla^T\nabla$) and the projection of the density Hessian onto the density gradient

$$\eta_{\varsigma,\sigma\vartheta}(\mathbf{r}) = \nabla^T\rho_\sigma(\mathbf{r})\nabla\nabla^T\rho_\varsigma(\mathbf{r})\nabla\rho_\vartheta(\mathbf{r}) \quad (10)$$

We note in passing that ς, σ, and ϑ are individual spin labels of either α- or β-spin and σ' is the *opposite* spin in regard to the spin defined by σ. The underlying damping (or real-space cutoff) functions $\mathcal{F}$ depend on the GGA functional we started with. Two examples present in the functionals we will evaluate here are the damping factor of the B88 functional,[44] which occurs in the pig2 CF[39] of the LH20t functional,[40] and a simple Gaussian damping function, which occurs in the pig1 CF of the earlier LH14t-calPBE functional.[38] The implementation includes also pig1 and pig2 CFs based on the PBE functional.[45] Ref 39 also provides a first-order CF (tpig1) based on the B98 meta-GGA functional,[46] which depends on the gradient of τ. The magnetic-field derivatives and shielding contributions for the latter have also been derived in this work (see Appendix A), albeit no published functional so far uses tpig1.

2.2. Extension of the LH Nuclear Shielding Implementation to Include a Calibration Function. For broader overviews on the theoretical aspects of shielding calculations, we refer to refs 47 and 48. We built on ref 28 for the general formulation of the coupled-perturbed KS scheme to compute nuclear shieldings with LHs and on ref 33 for the extension to the τ_D formalism. In the following, we will thus restrict the exposition mainly to the additional terms arising from a semilocal CF. We thus switch to the AO basis, which is denoted as $\{\phi_\mu\}$, and use $\omega_\mu = \phi_\mu \exp\left(-\frac{i}{2c}[\mathbf{B} \times \mathbf{R}_\mu]\mathbf{r}\right)$ to denote GIAOs. For the sake of simplicity, superscripts denote derivatives with respect to the given quantity, and we omit the argument $\mathbf{r}$ since all employed quantities are local.

The general equation to be solved for shielding constants $\boldsymbol{\sigma}$ can be expressed as

$$\sigma_{kl} = \sum_{\mu\nu,\sigma} \left[D_{\mu\nu}^\sigma \frac{d^2 h_{\mu\nu}}{dB_k d\mu_{l,K}} + \frac{dD_{\mu\nu}^\sigma}{dB_k} \frac{dh_{\mu\nu}}{\mu_{l,K}} \right]_{B_k=\mu_{l,K}=0} \quad (11)$$

where $h_{\mu\nu}$ is a component of the (magnetic-field-dependent) Hamiltonian in the AO basis; k, l = x, y, z are Cartesian components; B_k is a spatial component of the magnetic field; and $\mu_{l,K}$ is a component of the nuclear magnetic moment of nucleus K. The first (diamagnetic) term on the right-hand side involves only the ground-state density matrix for which LHs with a semilocal CF had already been formulated and implemented.[38,39] The new implementation thus pertains exclusively to the second (paramagnetic) term, which involves the perturbed density matrix $[D_{\mu\nu}^{\sigma,B_k} = \frac{\partial}{\partial B_k} \sum_i (c_{\mu i,\sigma}^* c_{\nu i,\sigma})]$ constructed from perturbed MO coefficients $(c_{\mu i}^{B_k})$. The latter may be expanded into a set of virtual unperturbed orbitals, which are weighted by so-called expansion coefficients $(c_{\mu i,\sigma}^{B_k} = \sum_a u_{ai,\sigma}^{B_k} c_{\mu a,\sigma})$. Finally, the expansion coefficients require the solution of the CP equations derived from, for example, the Brillouin condition

$$u_{ai,\sigma}^{B_k} = \frac{F_{ai,\sigma}^{B_k} - \varepsilon_{i,\sigma} S_{ai,\sigma}^{B_k}}{\varepsilon_{i,\sigma} - \varepsilon_{a,\sigma}} \quad (12)$$

where $F_{ai,\sigma}^{B_k}$ and $S_{ai,\sigma}^{B_k}$ are perturbed Fock and overlap matrices, respectively, and the ε_σ terms are MO energies. Additional terms due to the presence of a CF arise in the perturbed Fock matrix. While the CF may be viewed equally well as calibrating either the semilocal exchange-energy density or the exact exchange-energy density,[38] the semilocal nature of the CFs used here make it natural to lump them with the semilocal exchange-energy density and compute these parts together with other semilocal quantities. The former generates a modified semilocal expression

$$e_{X,\sigma}^{sl,G_\sigma} = e_{X,\sigma}^{sl} + G_\sigma \quad (13)$$

As discussed above, this brings in higher derivatives of the density (and potentially the gradient of the kinetic-energy density; see Appendix A), which have to be dealt with. In general, the semilocal parts of a LH, via LMF, $e_{X,\sigma}^{sl}$, or CF, may depend on a variety of quantities

$$f = f[Q] \quad \text{where } Q = \{\rho_\sigma, \gamma_{\sigma\sigma}, l_\sigma, \eta_{\sigma,\sigma\sigma}, \tau_\sigma, ...\} \quad (14)$$

for which derivatives with respect to the magnetic field have to be computed. We note again that τ itself is not gauge-invariant. In this work, we will compare both the gauge-invariant extension by Maximoff and Scuseria[34]

$$\tau_\sigma \to \tau_{MS,\sigma} = \tau_\sigma + \frac{\mathbf{A}^T}{c}\mathbf{j}_{p,\sigma} + \frac{|\mathbf{A}|^2}{2c^2}\rho_\sigma \quad (15)$$

which involves the magnetic vector potential $\mathbf{A}$, and that due to Dobson[35,36]

$$\tau_\sigma \to \tau_{D,\sigma} = \tau_\sigma - \frac{|\mathbf{j}_{p,\sigma}|^2}{2\rho_\sigma} \quad (16)$$

which only brings in the paramagnetic current $\mathbf{j}_{p,\sigma}$. The term $\mathbf{j}_{p,\sigma}$ is defined as

$$\mathbf{j}_{p,\sigma} = \frac{i}{2} \sum_{\mu\nu} D_{\mu\nu}^\sigma (\phi_\nu \nabla\phi_\mu^* - \phi_\mu^* \nabla\phi_\nu) \quad (17)$$

While τ_D also requires the solution of coupled equations for meta-GGA functionals, it has the advantage of being an explicit

https://doi.org/10.1021/acs.jpca.1c01135
J. Phys. Chem. A 2021, 125, 2697−2707

current-density functional. τ_{MS} is computationally more convenient but has the disadvantages of depending on the vector potential,[37] violating the iso-orbital constraint,[49] and generating unphysical paramagnetic contributions.[33] In contrast to τ, the density and the gradient of the density are both implicitly gauge-invariant without modification, and the same holds for higher derivatives such as the Laplacian and Hessian.

The final contributions to the perturbed Fock matrix have the general form

$$F^{B_k}_{\mu\nu,\sigma} = \int \mathrm{d}\mathbf{r}[\hat{d}_{\mu\nu,\sigma} f_\sigma]^{B_k} \tag{18}$$

where

$$[\hat{d}_{\mu\nu,\sigma} f_\sigma]^{B_k}\Big|_{\mathbf{B}=0} = \sum_{Q\in Q}\left[\frac{\partial^2 Q}{\partial D^\sigma_{\mu\nu}\partial B_k}\frac{\partial f_\sigma}{\partial Q}\right]\Bigg|_{\mathbf{B}=0} \tag{19}$$

and Q runs over the set of quantities present in $f[Q]$. Since the contributions from the density, the gradient of the density, and the kinetic-energy density are well-known (e.g., see ref 34), we only give the explicit equations for the Laplacian

$$F^{l,B_k}_{\mu\nu,\sigma} = \int \mathrm{d}\mathbf{r}\left\{\frac{\partial f}{\partial l_\sigma}[\Delta(\omega^*_\mu\omega_\nu)]^{B_k}\right\} \tag{20}$$

and the Hessian

$$\begin{aligned} F^{\eta,B_k}_{\mu\nu,\sigma} = \int \mathrm{d}\mathbf{r}\Bigg\{&\Bigg(\nabla^T\rho_\sigma[\nabla\nabla^T(\omega^*_\mu\omega_\nu)]^{B_k}\times\left(\nabla\rho_\sigma\frac{\partial f}{\partial\eta_{\sigma,\sigma\sigma}} + \nabla\rho_{\sigma'}\frac{\partial f}{\partial\eta_{\sigma,\sigma\sigma'}}\right)\\ &+\nabla^T\rho_{\sigma'}[\nabla\nabla^T(\omega^*_\mu\omega_\nu)]^{B_k}\nabla\rho_{\sigma'}\frac{\partial f}{\partial\eta_{\sigma,\sigma'\sigma'}}\Bigg)\\ &+[\nabla^T(\omega^*_\mu\omega_\nu)]^{B_k}\Bigg(2\nabla\nabla^T\rho_\sigma\nabla\rho_\sigma\frac{\partial f}{\partial\eta_{\sigma,\sigma\sigma}} + \nabla\nabla^T\rho_\sigma\nabla\rho_{\sigma'}\frac{\partial f}{\partial\eta_{\sigma,\sigma\sigma'}}\\ &+2\nabla\nabla^T\rho_{\sigma'}\nabla\rho_\sigma\frac{\partial f}{\partial\eta_{\sigma',\sigma\sigma}}+\nabla\nabla^T\rho_{\sigma'}\nabla\rho_{\sigma'}\frac{\partial f}{\partial\eta_{\sigma',\sigma\sigma'}}\Bigg)\Bigg\} \end{aligned} \tag{21}$$

(see Appendix A for the gradient of the kinetic-energy density). We have to additionally construct

$$[\Delta(\omega^*_\mu\omega_\nu)]^{B_k} = \frac{i}{2c}[2(\mathbf{B}\times\mathbf{R}_{\mu\nu})^{T,B_k}\nabla[\phi^*_\mu\phi_\nu] + (\mathbf{R}_{\mu\nu}\times\mathbf{r})_k\Delta[\phi^*_\mu\phi_\nu]] \tag{22}$$

and

$$\begin{aligned} [\nabla\nabla^T(\omega^*_\mu\omega_\nu)]^{B_k} = \frac{i}{2c}&[(\mathbf{B}\times\mathbf{R}_{\mu\nu})^{B_k}\nabla^T[\phi^*_\mu\phi_\nu]\\ &+\nabla[\phi^*_\mu\phi_\nu](\mathbf{B}\times\mathbf{R}_{\mu\nu})^{T,B_k}\\ &+(\mathbf{R}_{\mu\nu}\times\mathbf{r})_k\nabla\nabla^T[\phi^*_\mu\phi_\nu]] \end{aligned} \tag{23}$$

3. COMPUTATIONAL DETAILS

The developments described in the Theory section have been implemented into the mpshift module of a local developers' version of the Turbomole program package, which was updated to release 7.5,[50] thus extending the LH implementations of refs 28 and 33. Nuclear shielding constants were calculated using GIAOs. To deal with the gauge-dependence of the kinetic-energy density, we compare the τ_{MS} model (eq 15)[34] and the recently implemented[33] and explicitly current-dependent τ_D model (eq 16).[35−37,51] The SCF energy-convergence criterion of 10^{-9} was used in addition to ensuring the convergence of the input density by setting the density convergence to 10^{-7}. Integration grids employed grid setting "5" (internal Turbomole setting) for both the semilocal contributions and seminumerical integrations[52−56] of the exact-exchange contributions. For this benchmarking study, no integral screening methods ("junctions") were used in this work for the exact-exchange terms (see ref 28). The convergence of the CPKS iterations was set to 10^{-7} (convergence of the Euclidean vectors). Unless stated otherwise, we use the RI-J approximation for the Coulomb terms in the SCF calculations and the MARI-J approximation for the GIAO Coulomb shielding contribution.[2]

After initial analyses of the effects of the τ_{MS} framework on the Ne atom and the HF molecule, we evaluated computed shieldings against GIAO−CCSD(T)/pcSseg-4 benchmark data for the main-group test set of ref 3, which contains 15 molecules and 34 shielding constants ($8\times{}^1$H, $7\times{}^{13}$C, $5\times{}^{15}$N, $6\times{}^{17}$O, $5\times{}^{19}$F, and $3\times{}^{31}$P). As in our previous studies,[28,33] we used pcSseg-4 basis sets[57] throughout to essentially eliminate basis-set errors. We employed the auxiliary basis sets ("universal") as specified in ref 58.

The focus of the present evaluations is on LHs with calibrated exchange-energy densities. That is, the LH20t functional[40] based on PBE exchange and B95 correlation, which is augmented by a B88-based pig2 CF, and the earlier LH14t-calPBE functional[38] based on PBE exchange and correlation and a Gaussian-damped pig1 CF are both considered. Both of these LHs use a scaled t-LMF (with prefactors $b = 0.715$ and 0.5, respectively). For comparison, we also include results with uncalibrated first-generation LSDA-based LHs that have previously been evaluated.[28,33] These are the t-LMF-based LH07t-SVWN ($b = 0.48$),[30] the s-LMF-based LH07s-SVWN,[32] and the t-LMF-based LH12ct-SsirPW92 ($b = 0.646$)[59] and LH12ct-SsifPW92 ($b = 0.709$).[59] For the analysis, we also evaluate the effect of removing the CF from the two calibrated LHs while keeping all other parameters fixed. We will denote these modified functionals as LH14t$_{NC}$ and LH20t$_{NC}$. While a larger number of further functionals was previously evaluated for this test set,[3,5,28,33] for conciseness we only include TPSSh here.[60] This meta-GGA-based GH was previously identified as the best non-LH rung-four functional for this set of main-group shieldings.[3,28] Some statistical data for further standard functionals are included in Table S1 in the Supporting Information.

4. RESULTS

Initial work to evaluate the correctness of the implementation focused on the gauge invariance and on other invariances, for example, those regarding spatial symmetries. All of the tests confirmed that the additional terms were implemented correctly. Some timing tests (data not shown) confirmed that the computational effort increased only marginally compared to that for simpler LHs when using the same computational settings.

4.1. Evaluation of the Artifacts of the τ_{MS} Framework for the Ne Atom and HF and F_2 Molecules. We noted above that too deshielded proton values and some artifacts for seemingly simple cases with t-LMF-based first-generation LHs in the initial evaluation of LHs for nuclear shielding[28] were caused to an appreciable part by artifacts of the standard τ_{MS} treatment and notably improved within the τ_D framework.[33] Before we delve into a more general statistical evaluation of

https://doi.org/10.1021/acs.jpca.1c01135
J. Phys. Chem. A 2021, 125, 2697−2707

Table 1. Total Isotropic Shielding Constants and Paramagnetic Shielding Tensor Contributions for Ne, HF, and F_2 In Comparison To CCSD(T) Reference Data When Comparing the τ_{MS} and τ_D Frameworks

				reference[a]	LH07t	LH12sif	LH14t	LH14t$_{NC}$	LH20t	LH20t$_{NC}$
τ_{MS}	Ne	^{21}Ne	σ	552.0	569.9	575.4	561.3	566.1	559.3	569.3
			σ^p	0.0	18.8	24.1	9.6	14.5	7.2	17.2
	HF	^{1}H	σ	28.82	28.55	28.16	28.78	28.64	28.55	28.28
			$\sigma^p_\perp$		2.49	2.41	3.34	2.39	5.16	2.95
			$\sigma^p_\parallel$		0.14	0.20	0.07	0.11	0.05	0.14
		^{19}F	σ	419.91	437.0	444.7	426.9	432.1	426.0	436.8
			$\sigma^p_\perp$		−57.0	−47.8	−69.8	−62.0	−73.7	−57.4
			$\sigma^p_\parallel$		19.9	25.6	9.9	15.3	7.1	18.3
	F_2	^{19}F	σ	−192.76	−215.7	−192.9	−220.3	−218.4	−209.2	−205.6
			$\sigma^p_\perp$		−1025.7	−993.8	−1029.3	−1028.8	−1011.8	−1011.2
			$\sigma^p_\parallel$		15.2	19.3	7.4	11.6	5.2	13.8
τ_D	Ne	^{21}Ne	σ	552.0	551.1	551.3	551.7	551.6	552.1	552.1
			σ^p	0.0	0.0	0.0	0.0	0.0	0.0	0.0
	HF	^{1}H	σ	28.82	28.76	28.48	28.82	28.81	28.52	28.51
			$\sigma^p_\perp$		2.87	2.99	3.43	2.70	5.13	3.36
			$\sigma^p_\parallel$		0.00	0.00	0.00	0.00	0.00	0.00
		^{19}F	σ	419.91	418.4	421.2	418.0	418.1	420.1	420.5
			$\sigma^p_\perp$		−75.0	−70.3	−78.2	−75.4	−79.0	−72.7
			$\sigma^p_\parallel$		0.0	0.0	0.0	0.0	0.0	0.0
	F_2	^{19}F	σ	−192.76	−222.7	−199.3	−222.9	−223.0	−206.1	−206.7
			$\sigma^p_\perp$		−1028.6	−993.7	−1029.5	−1029.9	−1004.6	−1006.0
			$\sigma^p_\parallel$		0.0	0.0	0.0	0.0	0.0	0.0

[a]GIAO−CCSD(T) reference data, cf. refs 3 and 16.

main-group shieldings, it is thus of interest to see how such artifacts were affected by the presence of a CF in the LH20t and LH14t-calPBE functionals. As these contributions are typically overshadowed in the presence of genuinely large paramagnetic terms, it is best to evaluate them for spherical atoms or the $\sigma^p_\parallel$ contributions in linear molecules, where the physical $\sigma^p_\parallel$ terms are zero. Table 1 provides this analysis for the Ne atom and the HF and F_2 molecules, which served a similar purpose before.[33]

We can most favorably compare the results of LH14t-calPBE to those of LH07t-SVWN and the results of LH20t to those LH12ct-SsifPW91, as these pairs exhibit rather similar t-LMF prefactors (see Computational Details). Additionally, we can simply remove the CF from both of the two calibrated LHs. Interestingly, the τ_{MS} artifacts on Ne and those for $\sigma^p_\parallel$ in HF and F_2 that were seen for LH14t-calPBE are smaller by close to a factor of two relative to those for LH07t-SVWN, while the removal of the CF (LH14t$_{NC}$) increases the unphysical terms by part of this difference. In case of the larger t-LMF prefactors of LH20t and LH12ct-SsifPW91, the differences are even more notable. Now, the artifacts of the calibrated LH20t are less than one-third of those for the uncalibrated LH12ct-SsifPW91, and the effect of removing the CF (LH20t$_{NC}$) is likewise larger. Thus, it seems that the use of uncalibrated exchange-energy densities exacerbates the unphysical contributions from τ_{MS} for t-LMFs, and using a CF provides a better starting point. This holds for the Ne atom and for the $\sigma^p_\parallel$ terms of both ^{1}H and ^{19}F shieldings in HF. Nevertheless, some artifacts remain, even for the calibrated functionals. These contributions are absent when using the τ_D current-density functional framework for the τ-dependent terms (Table 1). Paramagnetic contributions for Ne and $\sigma^p_\parallel$ in the two molecules vanish, as they should.

The agreement of the isotropic shieldings with the reference data for Ne and HF largely reflect the unphysical artifacts of τ_{MS}; thus, these systems may be considered "simple cases" for which uncalibrated LHs previously showed unexpectedly large deviations in this framework.[28] The large $\sigma^p_\perp$ and thus the isotropic shielding in F_2 reflect other aspects of the functional and are not necessarily improved by the use of either τ_D or the CF. Such aspects will be more broadly evaluated below for the larger test set of main-group shieldings. As τ occurs also in the B95 meta-GGA correlation functional of LH20t, and the results may be affected by how we render it gauge-invariant, we have evaluated replacing it with PBE GGA correlation. Effects of this substitution are much smaller than those arising from the exchange functionals and are thus not shown in the table.

We want to further demonstrate that the too low ^{1}H shieldings and the too large shieldings for heavy atoms bound to hydrogen in electronically "simple" cases found initially with uncalibrated LHs[28] were caused to a large extent by the τ_{MS} framework[33] and that these artifacts are clearly smaller with calibrated LHs. To this end, Table S2 in the Supporting Information provides shieldings computed for the element hydrides CH_4, NH_3, H_2O, and HF compared to the CCSD(T) reference data.

While the ^{1}H shieldings with TPSSh are generally overestimated, those of the uncalibrated LHs are significantly underestimated within the τ_{MS} treatment, increasingly so from CH_4 to HF and most pronouncedly with a larger prefactor of the t-LMF. Using the physically better-founded τ_D framework, these deviations decrease but do not vanish completely. With the calibrated LHs, the underestimate is only really notable (but much smaller) for HF in the case of LH20t and is not much affected when using τ_D.

Turning to the "heavy" nuclei in these systems, the clear *overestimate* of the shieldings for most of the uncalibrated LHs is obvious with τ_{MS}, again increasingly so for the more polar element−hydrogen bonds up to 25 ppm for HF. The problem

https://doi.org/10.1021/acs.jpca.1c01135
J. Phys. Chem. A 2021, 125, 2697−2707

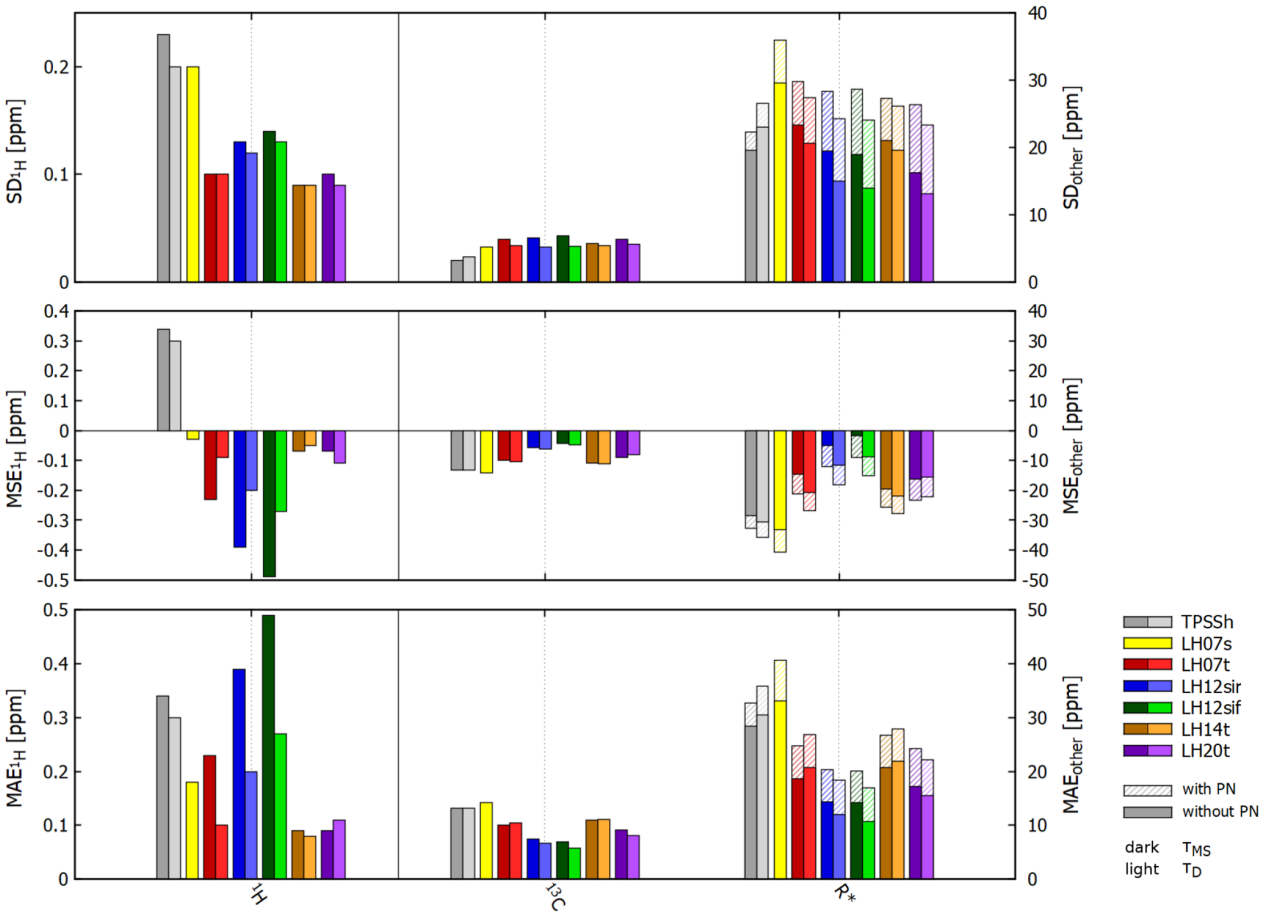

Figure 1. Statistical evaluation for various LH functionals and the TPSSh GH with the pcSseg-4 basis sets compared to the CCSD(t)/pcSseg-4 reference data from ref 3. R* stands for all heteronuclei. In that case, the PN molecule caused a large part of the deviations; therefore, the solid bars indicate the statistics obtained when excluding PN.

disappears when using τ_D. The artifacts arising with τ_{MS} for the calibrated LHs are again much smaller, while the removal of the CF increases them. Differences between the different LHs and relative to the CCSD(T) values are very small within the τ_D framework, now almost irrespective of the presence of a CF in the functional. We note in passing that the TPSSh GH gives somewhat too low shieldings irrespective of the treatment of τ, which is in line with previous observations for this and other standard functionals.

Statistical Evaluations for Main-Group Shieldings. To extend the study of nuclear shieldings with first-generation LHs in refs 28 and 33 to the more sophisticated calibrated LH14t-calPBE and LH20t functionals, we turn to the statistical evaluation of the main-group shielding benchmark from ref 3. As done previously, we grouped the shieldings into ^{1}H, ^{13}C, and heteronuclei (combining ^{15}N, ^{17}O, ^{19}F, and ^{31}P). For each subset, we evaluated the standard deviation (SD), the mean signed error (MSE), and the mean absolute error (MAE). For the subset of heteronuclei, we found that the PN molecule dominated the deviations of the LHs and for that matter any hybrid functional with larger exact-exchange admixtures[3,28] (TPSSh has only 10% and is thus somewhat less sensitive). This reflects the particularly large static correlation effects of this diatomic molecule.[61] Our statistical evaluations in Figure 1 thus provide results with PN either excluded (solid bars) or included (hatched bars). For comparison, we give also the data for the first generation uncalibrated LHs (including LH07s-SVWN, which is based on an s-LMF) and TPSSh. We furthermore compare the τ_{MS} (darker color tone) and τ_D (lighter tone) treatments of the local kinetic energy for all τ-dependent functionals. The full set of isotropic shielding constants is provided in Tables S3 and S4 in the Supporting Information. We note in passing that we deliberately compared them to CCSD(T) rather than to the corrected experimental data. This may introduce a very small bias, as the benchmark data show some small but notable deviations from the experiment for systems with an appreciable static correlation, such as OF_2, F_2, N_2O, or the ^{31}P shielding of PN. However, comparing them instead directly to the experimental data for the subgroup of systems for which these are available (Tables S3 and S4) would not notably alter the statistical evaluation.

Starting with the somewhat less critical ^{13}C shieldings (middle of Figure 1), we see relatively small differences between the functionals and the treatments of τ. Most of the LHs (except the s-LMF-based LH07s-SVWN) give lower MAEs and less negative MSEs than TPSSh, while their standard deviations are slightly larger (particularly with τ_{MS} and less so with τ_D). Indeed, the smallest MAEs were found with the two uncalibrated LHs LH12ct-SsifPW91 and LH12ct-SsirPW91. LH20t, which has a similarly large t-LMF prefactor

https://doi.org/10.1021/acs.jpca.1c01135
J. Phys. Chem. A 2021, 125, 2697−2707

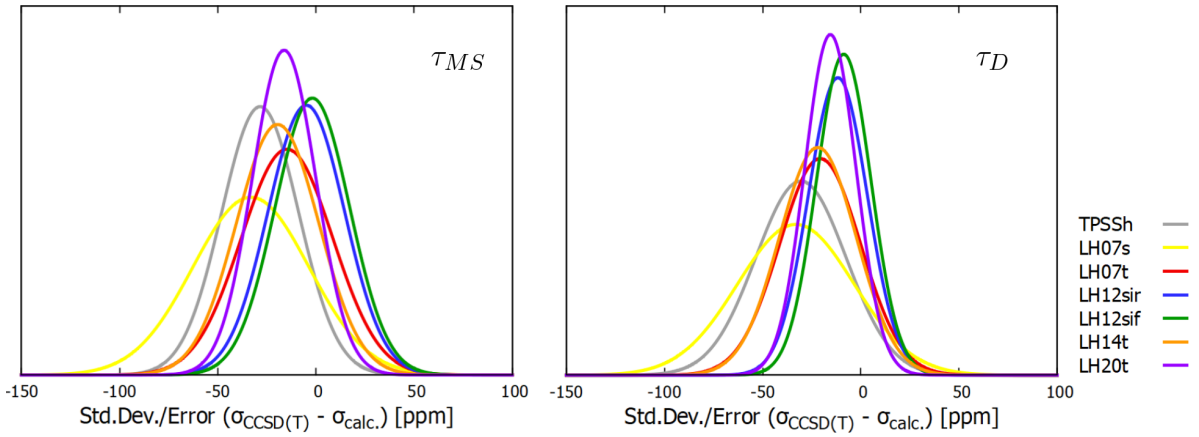

Figure 2. Normal distribution plot of the deviations of heteronuclear shieldings (combining ^{15}N, ^{17}O, ^{19}F, and ^{31}P, excluding PN) relative to the CCSD(T) reference data.

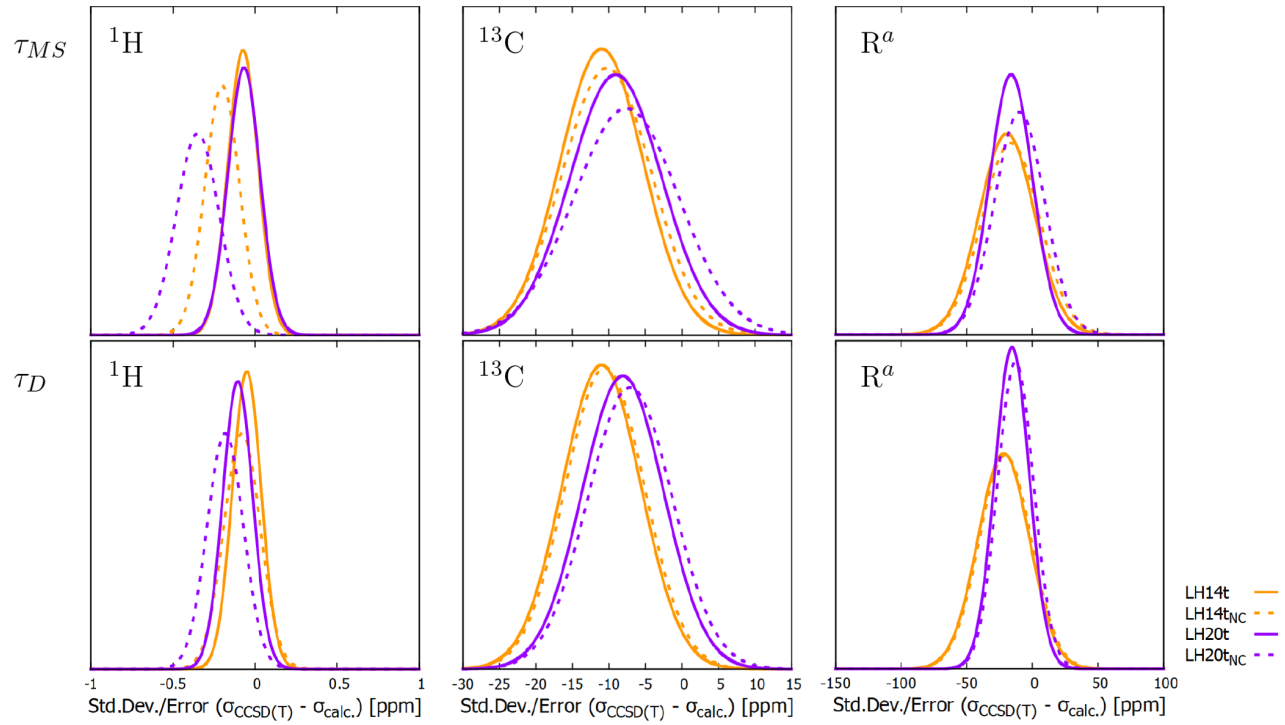

Figure 3. Normal distribution plot of the deviations of shieldings computed with LH14t-calPBE (orange) and LH20t (purple) as well as those computed without the respective CF (dotted lines) using either τ_{MS} (top) or τ_D (bottom) relative to the CCSD(T) reference data. R^a combines the ^{15}N, ^{17}O, ^{19}F, and ^{31}P shieldings (excluding PN).

compared to those two functionals (see Computational Details), is only slightly worse but shows a somewhat more negative MSE. Importantly, the treatment of τ only moderately affects the overall performance of even uncalibrated LHs. That is, the τ_{MS} artifacts identified for "simple" cases such as CH_4 (see above) are small relative to the overall paramagnetic contributions that arise in many of the molecules involved in the ^{13}C shielding subset considered.

In contrast, the most striking differences were seen for the ^{1}H shieldings (left of Figure 1, note the different scale). Uncalibrated t-LMF-based LHs were previously found to clearly underestimate these values with τ_{MS}, but were improved within the τ_D framework (with LH07t-SVWN performing the best). LH07s-SVWN had small systematic errors but comparably large statistical scatter, while many GHs, including TPSSh, tended to overestimate the ^{1}H shieldings. Here, the performances of the two calibrated LHs are striking, in particular for LH20t; with both τ_{MS} and τ_D, LH20t and LH14t-calPBE perform excellently. This confirms the findings for the simplest hydrides discussed above.

Finally, the heteronuclei shieldings (right side of Figure 1) offer some of the most notable advantages when using t-LMF-based LHs over standard functionals such as TPSSh (the s-LMF-based LH07s-SVWN is inferior). While use of τ_{MS} gives less negative MSEs than τ_D for the uncalibrated LHs, likely indicating some error compensation, the MAEs and SDs were

https://doi.org/10.1021/acs.jpca.1c01135
J. Phys. Chem. A 2021, 125, 2697−2707

clearly improved upon switching to τ_D. These effects were again somewhat diminished for the two calibrated LHs. In this case, the older LH14t-calPBE performs somewhat worse than the best-performing uncalibrated LH12ct-SsifPW91 and LH12ct-SsirPW91 and comparable to LH07t-SVWN, which has a similar t-LMF prefactor. The more recent LH20t, which has a larger prefactor, is almost on par with the best performers in this case. However, it retains a somewhat larger fraction of the typically too large deshielding of standard functionals. Given the much better results for proton shieldings compared to those of the LH12ct functionals, LH20t may nevertheless be the most robust choice overall if one aims at hydrogen and non-hydrogen shieldings simultaneously. Obviously, the still relatively large exact-exchange admixture of this LH may still hamper the accuracy for cases with a strong static correlation, such as PN. As LH20t is currently the best LH for general main-group energetics, indeed one of the best rung-four functionals overall, and has further advantages for both ground and excited states,[40] these first results for nuclear shieldings are encouraging. If one aims mostly at non-hydrogen shieldings, LH12ct-SsirPW91 and particularly LH12ct-SsifPW91 are so far the best choices overall. Used with τ_D, their errors for proton shieldings may also be acceptable.

Further insight into the error distributions of the heteronuclei subset are provided by the plots of the deviations in Figure 2 (distributions including PN are provided in Figure S1 in the Supporting Information). The top performances of LH12ct-SsifPW91 and LH12ct-SsirPW91, followed by LH20t, are apparent, as is the notable narrowing of the curves for the two former uncalibrated LHs when using τ_D (right side). LH20t provides the narrowest distribution of errors but a slight systematic shift to too-low shieldings. Note, however, that this shift is small compared to that of any GH studied previously for this test set[28,33] and is inferior only to that of the best double hybrid studied so far, DSD-PBEP86.[5]

Overall, the removal of the CF for LH20t or LH14t-calPBE modifies the overall statistical performance relatively little but still is most notable for proton shieldings. Figure 3 shows that the CF helps to narrow the ^{1}H distributions for both LH14t-calPBE and LH20t (the distribution for heteronuclei with PN is given as Figure S2 in the Supporting Information). While it also corrects the overall too negative shieldings, this effect becomes less pronounced when moving from τ_{MS} to the τ_D framework. In the ^{13}C case, the narrowing is less pronounced and the systematic negative shift is even very slightly increased. Finally, the effects are rather small for the heteronuclei, particularly when using τ_D. Numerical data underlying these distributions are provided in Table S4 in the Supporting Information.

We finally note that, while TPSSh was previously identified as the best rung-four functional for this main-group shielding test set, the rung-three meta GGA M06-L gave even slightly better statistics when used within the τ_{MS} framework.[5] We showed in ref 33 that this reflects the error compensation with missing current terms. For completeness, Table S1 in the Supporting Information gives some gross statistical data for the entire test set for a set of additional functionals, including M06-L with τ_{MS} and τ_D. This shows that several local hybrids indeed outperform all the previously studied functionals on rungs one to four for this test set, particularly when using the t-LMF within the τ_D current-density functional framework.

5. CONCLUSIONS

A recent coupled-perturbed Kohn−Sham implementation for the computation of nuclear shieldings with local hybrid functionals and GIAOs has been extended to account for higher derivatives of the electron density (and the gradient of the local kinetic energy). This has allowed the first evaluation of more advanced constructions of local hybrids that include a semilocal calibration function to deal with the "gauge problem", i.e., with the ambiguity of exchange-energy densities, and allow the use of GGA or meta-GGA contributions. Two functionals of this more advanced type were implemented, namely, LH14tcal-PBE and the most recent LH20t. The latter was previously found to be superior to all earlier local hybrids as one of the overall best rung-four functionals for main-group energetics (GMTKN55 set) and the first functional to simultaneously describe the most extreme delocalized and localized cases of mixed-valence systems. Indeed, the first evaluations for a moderate-sized main-group shielding test set show that the "calibrated" local hybrids provide substantial improvements over the uncalibrated ones for proton shieldings while maintaining a high accuracy for the other nuclei. Behind the best of the significantly more computationally demanding double hybrid functionals studied recently (DSD-PBEP86), the data suggest that LH20t is currently one of the overall most robust choices for the computation of main-group shielding constants and thus NMR chemical shifts, being clearly superior to standard rung one through four functionals.

This underlines the potential of the position-dependent exact-exchange admixture in local hybrids for properties that depend on different regions of space. Ongoing work in our laboratory is aimed at evaluating this methodology for a much wider range of shieldings for both main-group and transition-metal systems. At the same time, more advanced local mixing functions and other extensions of the local hybrid methodology are expected to provide further improvements in accuracy. More detailed comparisons of local hybrids with double hybrids and other functionals will be explored elsewhere for a much larger benchmark test set.

Interestingly, the artifacts introduced by the gauge-invariant Maximoff−Scuseria extension of the local kinetic energy, which occur in the most widely used local mixing functions (t-LMFs) of local hybrids so far, is substantially diminished for the more advanced calibrated functionals. Nevertheless, use of Dobson's current-density functional extension, which does not introduce any artifacts but also ensures the gauge-invariance of τ, is recommended as the most accurate and physically justified methodology.

APPENDIX A

In ref 39, a first-order calibration function for meta-GGA functionals (tpig1) was proposed as follows:

$$G_\sigma^{(1)} = f_1 \cdot \rho_\sigma^{4/3} \cdot F(\tilde{Q}_\sigma) \cdot \left(q_\sigma - \frac{1}{3} s_\sigma^2\right) + \frac{10}{3} f_1 \cdot \rho_\sigma^{4/3} \cdot \frac{dF(\tilde{Q}_\sigma)}{d\tilde{Q}_\sigma} \times \left(\frac{5}{6} p_\sigma s_\sigma^2 + 2r_\sigma - \frac{10}{9} s_\sigma^4 - \frac{1}{4} \frac{\tau_\sigma}{\tau_{TF,\sigma}} s_\sigma^2\right) \quad (24)$$

Here, $\tilde{Q}_\sigma$ is the inhomogeneity parameter

$$\tilde{Q}_\sigma = \frac{1}{2} \frac{\tau_\sigma}{\tau_{TF,\sigma}} + \frac{25}{18} s_\sigma^2 - \frac{1}{2} \quad (25)$$

https://doi.org/10.1021/acs.jpca.1c01135
J. Phys. Chem. A 2021, 125, 2697−2707

where

$$\tau_{\mathrm{TF},\sigma} = \frac{3}{40}k^2\rho_\sigma^{5/3} \tag{26}$$

is the Thomas−Fermi kinetic-energy density, and

$$r_\sigma = \frac{1}{k^4}\frac{\iota_{\sigma\sigma}}{\rho_\sigma^{10/3}} \tag{27}$$

is the mixed reduced gradient of the density and the kinetic-energy density, which depends of the quantity $\iota_{\sigma\varsigma} = \nabla^{\mathrm{T}}\rho_\sigma\nabla\tau_\varsigma$. The latter in turn explicitly contains the gradient of the kinetic-energy density. The contribution of $\iota_{\sigma\varsigma}$ to the perturbed Fock matrix is

$$F^{\iota,B_k}_{\mu\nu,\sigma} = \int \mathrm{d}\mathbf{r}\left\{[\nabla^{\mathrm{T}}(\omega_\mu^*\omega_\nu)]^{B_k}\left(\nabla\tau_\sigma\frac{\partial f}{\partial \iota_{\sigma\sigma}} + \nabla\tau_{\sigma'}\frac{\partial f}{\partial \iota_{\sigma\sigma'}}\right) + \left(\nabla^{\mathrm{T}}\rho_\sigma\frac{\partial f}{\partial \iota_{\sigma\sigma}} + \nabla^{\mathrm{T}}\rho_{\sigma'}\frac{\partial f}{\partial \iota_{\sigma'\sigma}}\right)\left[\frac{\partial\nabla\tilde{\tau}_\sigma}{\partial D^\sigma_{\mu\nu}}\right]^{B_k}\right\} \tag{28}$$

where the magnetic-field derivative of the quantity $\left[\frac{\partial\nabla\tilde{\tau}_\sigma}{\partial D^\sigma_{\mu\nu}}\right]^{B_k}$ has to be constructed. To render these terms gauge-invariant, we can again replace τ with either τ_{MS} (eq 15) or τ_{D} (eq 16). The first variant results in

$$\begin{aligned}\left[\frac{\partial\nabla\tau_{\mathrm{MS},\sigma}}{\partial D^\sigma_{\mu\nu}}\right]^{B_k} &= \left[\nabla\left[\left(i\nabla + \frac{\mathbf{A}}{c}\right)^{\mathrm{T}}\omega_\mu^*\left(-i\nabla + \frac{\mathbf{A}}{c}\right)\omega_\nu\right]\right]^{B_k} \\ &= \frac{i}{4c}[(\mathbf{B}\times\mathbf{R}_{\mu\nu})^{B_k}\nabla^{\mathrm{T}}\phi_\mu^*\nabla\phi_\nu \\ &\quad + (\mathbf{R}_{\mu\nu}\times\mathbf{r})_k\nabla(\nabla^{\mathrm{T}}\phi_\mu^*\nabla\phi_\nu) \\ &\quad + \nabla\nabla^{\mathrm{T}}\phi_\mu^*(\mathbf{B}\times(\mathbf{r}-\mathbf{R}_\nu))^{B_k}\phi_\nu \\ &\quad - \nabla\nabla^{\mathrm{T}}\phi_\nu(\mathbf{B}\times(\mathbf{r}-\mathbf{R}_\mu))^{B_k}\phi_\mu^* \\ &\quad - \nabla\phi_\mu^*(\mathbf{B}\times(\mathbf{r}-\mathbf{R}_\mu))^{\mathrm{T},B_k}\nabla\phi_\nu \\ &\quad + \nabla\phi_\nu(\mathbf{B}\times(\mathbf{r}-\mathbf{R}_\nu))^{\mathrm{T},B_k}\nabla\phi_\mu^*]\end{aligned} \tag{29}$$

For the physically better-founded τ_{D} variant (eq 16), we get the somewhat more complicated

$$\begin{aligned}\left[\frac{\partial\nabla\tau_{D,\sigma}}{\partial D^\sigma_{\mu\nu}}\right]^{B_k} &= \frac{i}{4c}[(\mathbf{B}\times\mathbf{R}_{\mu\nu})^{B_k}\nabla^{\mathrm{T}}\phi_\mu^*\nabla\phi_\nu + (\mathbf{R}_{\mu\nu}\times\mathbf{r})_k\nabla(\nabla^{\mathrm{T}}\phi_\mu^*\nabla\phi_\nu) \\ &\quad + \nabla\phi_\mu^*(\mathbf{B}\times\mathbf{R}_\mu)^{\mathrm{T},B_k}\nabla\phi_\nu - \nabla\phi_\nu(\mathbf{B}\times\mathbf{R}_\nu)^{\mathrm{T},B_k}\nabla\phi_\mu^* \\ &\quad - \nabla\nabla^{\mathrm{T}}\phi_\mu^*(\mathbf{B}\times\mathbf{R}_\nu)^{B_k}\phi_\nu + \nabla\nabla^{\mathrm{T}}\phi_\nu(\mathbf{B}\times\mathbf{R}_\mu)^{B_k}\phi_\mu^*] \\ &\quad + \frac{i\nabla\rho_\sigma}{2\rho_\sigma^2}[\phi_\nu\nabla^{\mathrm{T}}\phi_\mu^* - \phi_\mu^*\nabla^{\mathrm{T}}\phi_\nu]\mathbf{j}^{B_k}_{p,\sigma} - \frac{i}{2\rho_\sigma}(\nabla\mathbf{j}^{\mathrm{T}}_{p,\sigma})^{B_k}[\phi_\nu\nabla\phi_\mu^* \\ &\quad - \phi_\mu^*\nabla\phi_\nu] - \frac{i}{2\rho_\sigma}[\nabla(\phi_\nu\nabla^{\mathrm{T}}\phi_\mu^* - \phi_\mu^*\nabla^{\mathrm{T}}\phi_\nu)]\mathbf{j}^{B_k}_{p,\sigma}\end{aligned} \tag{30}$$

where we have to construct

$$\begin{aligned}\mathbf{j}^{B_k}_{p,\sigma} &= \frac{i}{2}\sum_{\mu\nu}[D^{\sigma,B_k}_{\mu\nu}(\phi_\nu\nabla\phi_\mu^* - \phi_\mu^*\nabla\phi_\nu) \\ &\quad + \frac{i}{2c}D^\sigma_{\mu\nu}([(\mathbf{B}\times\mathbf{R}_\mu)^{B_k} + (\mathbf{B}\times\mathbf{R}_\nu)^{B_k}]\phi_\mu^*\phi_\nu \\ &\quad + (\mathbf{R}_{\mu\nu}\times\mathbf{r})_k(\phi_\nu\nabla\phi_\mu^* - \phi_\mu^*\nabla\phi_\nu))]\end{aligned} \tag{31}$$

and the contribution from the gradient

$$\begin{aligned}(\nabla\mathbf{j}^{\mathrm{T}}_{p,\sigma})^{B_k} &= \frac{i}{2}\sum_{\mu\nu}[D^{\sigma,B_k}_{\mu\nu}\nabla(\phi_\nu\nabla^{\mathrm{T}}\phi_\mu^* - \phi_\mu^*\nabla^{\mathrm{T}}\phi_\nu) \\ &\quad + \frac{i}{2c}D^\sigma_{\mu\nu}((\mathbf{B}\times\mathbf{R}_{\mu\nu})^{B_k}(\phi_\nu\nabla^{\mathrm{T}}\phi_\mu^* - \phi_\mu^*\nabla^{\mathrm{T}}\phi_\nu) \\ &\quad + \nabla(\phi_\mu^*\phi_\nu)((\mathbf{B}\times\mathbf{R}_\mu)^{\mathrm{T},B_k} + (\mathbf{B}\times\mathbf{R}_\nu)^{\mathrm{T},B_k}) \\ &\quad + (\mathbf{R}_{\mu\nu}\times\mathbf{r})_k\nabla(\phi_\nu\nabla^{\mathrm{T}}\phi_\mu^* - \phi_\mu^*\nabla^{\mathrm{T}}\phi_\nu))]\end{aligned} \tag{32}$$

■ ASSOCIATED CONTENT

Supporting Information

The Supporting Information is available free of charge at https://pubs.acs.org/doi/10.1021/acs.jpca.1c01135.

Tables with additional shielding results and statistics and figures with statistical distributions (PDF)

■ AUTHOR INFORMATION

Corresponding Author

Martin Kaupp − *Theoretische Chemie/Quantenchemie, Institut für Chemie, Technische Universität Berlin, D-10623 Berlin, Germany*; orcid.org/0000-0003-1582-2819; Email: martin.kaupp@tu-berlin.de

Author

Caspar Jonas Schattenberg − *Theoretische Chemie/Quantenchemie, Institut für Chemie, Technische Universität Berlin, D-10623 Berlin, Germany*

Complete contact information is available at: https://pubs.acs.org/10.1021/acs.jpca.1c01135

Notes

The authors declare no competing financial interest.

■ ACKNOWLEDGMENTS

C.J.S. is grateful for a scholarship that was provided by Studienstiftung des deutschen Volkes. This work was funded by the German Research Foundation (Deutsche Forschungsgemeinschaft, DFG) within project KA1187/14-1 and furthermore by Project-ID 387284271-SFB 1349.

■ REFERENCES

(1) *Calculation of NMR and EPR Parameters*, 1st ed.; Kaupp, M., Bühl, M., Malkin, V. G., Eds.; Wiley-VCH Verlag GmbH & Co. KGaA: Weinheim, Germany, 2004.

(2) Reiter, K.; Mack, F.; Weigend, F. Calculation of Magnetic Shielding Constants with meta-GGA Functionals Employing the Multipole-Accelerated Resolution of the Identity: Implementation and Assessment of Accuracy and Efficiency. *J. Chem. Theory Comput.* **2018**, *14*, 191−197.

(3) Stoychev, G. L.; Auer, A. A.; Izsàk, R.; Neese, F. Self-Consistent Field Calculation of Nuclear Magnetic Resonance Chemical Shielding Constants Using Gauge-Including Atomic Orbitals and Approximate Two-Electron Integrals. *J. Chem. Theory Comput.* **2018**, *14*, 619−637.

(4) Furness, J. W.; Verbeke, J.; Tellgren, E. I.; Stopkowicz, S.; Ekström, U.; Helgaker, T.; Teale, A. M. Current Density Functional Theory Using Meta-Generalized Gradient Exchange-Correlation Functionals. *J. Chem. Theory Comput.* **2015**, *11*, 4169−4181.
(5) Stoychev, G. L.; Auer, A. A.; Neese, F. Efficient and Accurate Prediction of Nuclear Magnetic Resonance Shielding Tensors with Double-Hybrid Density Functional Theory. *J. Chem. Theory Comput.* **2018**, *14*, 4756−4771.
(6) Franzke, Y. J.; Weigend, F. NMR Shielding Tensors and Chemical Shifts in Scalar-Relativistic Local Exact Two-Component Theory. *J. Chem. Theory Comput.* **2019**, *15*, 1028−1043.
(7) Auer, A. A.; Gauss, J.; Stanton, J. F. Quantitative prediction of gas-phase ^{13}C nuclear magnetic shielding constants. *J. Chem. Phys.* **2003**, *118*, 10407−10417.
(8) Harding, M. E.; Lenhart, M.; Auer, A. A.; Gauss, J. Quantitative prediction of gas-phase ^{19}F nuclear magnetic shielding constants. *J. Chem. Phys.* **2008**, *128*, 244111.
(9) Auer, A. A. Quantitative prediction of gas-phase ^{17}O nuclear magnetic shielding constants. *J. Chem. Phys.* **2009**, *131*, 024116.
(10) Prochnow, E.; Auer, A. A. Quantitative prediction of gas-phase ^{15}N and ^{31}P nuclear magnetic shielding constants. *J. Chem. Phys.* **2010**, *132*, 064109.
(11) Gregusova, A.; Perera, A.; Bartlett, R. J. Accuracy of Computed ^{15}N Nuclear Magnetic Resonance Chemical Shifts. *J. Chem. Theory Comput.* **2010**, *6*, 1228−1239.
(12) Kupka, T.; Stachów, M.; Nieradka, M.; Kaminsky, J.; Pluta, T.; Sauer, S. P. A. From CCSD(T)/aug-cc-pVTZ-J to CCSD(T) complete basis set limit isotropic nuclear magnetic shieldings via affordable DFT/CBS calculations. *Magn. Reson. Chem.* **2011**, *49*, 231−236.
(13) Teale, A. M.; Lutnaes, O. B.; Helgaker, T.; Tozer, D. J.; Gauss, J. Benchmarking density-functional theory calculations of NMR shielding constants and spin-rotation constants using accurate coupled-cluster calculations. *J. Chem. Phys.* **2013**, *138*, 024111.
(14) Flaig, D.; Maurer, M.; Hanni, M.; Braunger, K.; Kick, L.; Thubauville, M.; Ochsenfeld, C. Benchmarking Hydrogen and Carbon NMR Chemical Shifts at HF, DFT, and MP2 Levels. *J. Chem. Theory Comput.* **2014**, *10*, 572−578.
(15) Maurer, M.; Ochsenfeld, C. Spin Component-Scaled Second-Order Møller-Plesset Perturbation Theory for Calculating NMR Shieldings. *J. Chem. Theory Comput.* **2015**, *11*, 37−44.
(16) Reimann, S.; Ekström, U.; Stopkowicz, S.; Teale, A. M.; Borgoo, A.; Helgaker, T. The importance of current contributions to shielding constants in density-functional theory. *Phys. Chem. Chem. Phys.* **2015**, *17*, 18834−18842.
(17) Iron, M. A. Evaluation of the Factors Impacting the Accuracy of ^{13}C NMR Chemical Shift Predictions using Density Functional Theory-The Advantage of Long-Range Corrected Functionals. *J. Chem. Theory Comput.* **2017**, *13*, 5798−5819.
(18) Kupka, T. Theory and computation of nuclear shielding. *Nucl. Magn. Reson.* **2020**, *46*, 1−33.
(19) Prokopiou, G.; Autschbach, J.; Kronik, L. Assessment of the Performance of Optimally Tuned Range-Separated Hybrid Functionals for Nuclear Magnetic Shielding Calculations. *Adv. Theory Simul.* **2020**, *3*, 2000083.
(20) Grimme, S.; Bannwarth, C.; Dohm, S.; Hansen, A.; Pisarek, J.; Pracht, P.; Seibert, J.; Neese, F. Fully Automated Quantum-Chemistry-Based Computation of Spin-Spin-Coupled Nuclear Magnetic Resonance Spectra. *Angew. Chem., Int. Ed.* **2017**, *56*, 14763−14769.
(21) London, F. Théorie quantique des courants interatomiques dans les combinaisons aromatiques. *J. Phys. Radium* **1937**, *8*, 397−409.
(22) Ditchfield, R. Self-consistent perturbation theory of diamagnetism. *Mol. Phys.* **1974**, *27*, 789−807.
(23) Wolinski, K.; Hinton, J. F.; Pulay, P. Efficient Implementation of the Gauge-Independent Atomic Orbital Method for NMR Chemical Shift Calculations. *J. Am. Chem. Soc.* **1990**, *112*, 8251−8260.
(24) Perdew, J. P.; Schmidt, K. Jacob's ladder of density functional approximations for the exchange-correlation energy. *AIP Conf. Proc.* **2001**, *577*, 1−20.
(25) Cruz, F. G.; Lam, K.-C.; Burke, K. Exchange-Correlation Energy Density from Virial Theorem. *J. Phys. Chem. A* **1998**, *102*, 4911−4917.
(26) Jaramillo, J.; Scuseria, G. E.; Ernzerhof, M. Local hybrid functionals. *J. Chem. Phys.* **2003**, *118*, 1068−1073.
(27) Maier, T. M.; Arbuznikov, A. V.; Kaupp, M. Local Hybrid Functionals: Theory, Implementation, and Performance of an Emerging New Tool in Quantum Chemistry and Beyond. *WIREs Comp. Mol. Sci.* **2019**, *9*, e1378.
(28) Schattenberg, C. J.; Reiter, K.; Weigend, F.; Kaupp, M. An Efficient Coupled-Perturbed Kohn-Sham Implementation of NMR Chemical Shift Computations with Local Hybrid Functionals and Gauge-Including Atomic Orbitals. *J. Chem. Theory Comput.* **2020**, *16*, 931−943.
(29) Mack, F.; Schattenberg, C. J.; Kaupp, M.; Weigend, F. Nuclear Spin-Spin Couplings: Efficient Evaluation of Exact Exchange and Extension to Local Hybrid Functionals. *J. Phys. Chem. A* **2020**, *124*, 8529−8539.
(30) Kaupp, M.; Bahmann, H.; Arbuznikov, A. V. Local hybrid functionals: An assessment for thermochemical kinetics. *J. Chem. Phys.* **2007**, *127*, 194102.
(31) Bahmann, H.; Rodenberg, A.; Arbuznikov, A. V.; Kaupp, M. A thermochemically competitive local hybrid functional without gradient corrections. *J. Chem. Phys.* **2007**, *126*, 011103.
(32) Arbuznikov, A. V.; Kaupp, M. Local hybrid exchange-correlation functionals based on the dimensionless density gradient. *Chem. Phys. Lett.* **2007**, *440*, 160−168.
(33) Schattenberg, C. J.; Kaupp, M. Effect of the current dependence of tau-dependent exchange-correlation functionals on nuclear shielding calculations. *J. Chem. Theory Comput.* **2021**, *17*, 1469−1479.
(34) Maximoff, S. N.; Scuseria, G. E. Nuclear magnetic resonance shielding tensors calculated with kinetic energy density-dependent exchange-correlation functionals. *Chem. Phys. Lett.* **2004**, *390*, 408−412.
(35) Dobson, J. F. Spin-density functionals for the electron correlation energy with automatic freedom from orbital self-interaction. *J. Phys.: Condens. Matter* **1992**, *4*, 7877−7890.
(36) Dobson, J. F. Alternative expressions for the Fermi hole curvature. *J. Chem. Phys.* **1993**, *98*, 8870−8872.
(37) Tao, J.; Staroverov, V. N.; Scuseria, G. E.; Perdew, J. P. Exact-exchange energy density in the gauge of a semilocal density-functional approximation. *Phys. Rev. A: At., Mol., Opt. Phys.* **2008**, *77*, 012509.
(38) Arbuznikov, A. V.; Kaupp, M. Towards improved local hybrid functionals by calibration of exchange-energy densities. *J. Chem. Phys.* **2014**, *141*, 204101.
(39) Maier, T. M.; Haasler, M.; Arbuznikov, A. V.; Kaupp, M. New approaches for the calibration of exchange energy densities in local hybrid functionals. *Phys. Chem. Chem. Phys.* **2016**, *18*, 21133−21144.
(40) Haasler, M.; Maier, T. M.; Grotjahn, R.; Gückel, S.; Arbuznikov, A. V.; Kaupp, M. A Local Hybrid Functional with Wide Applicability and Good Balance between (De)Localization and Left-Right Correlation. *J. Chem. Theory Comput.* **2020**, *16*, 5645−5657.
(41) Theilacker, K.; Arbuznikov, A. V.; Kaupp, M. Gauge effects in local hybrid functionals evaluated for weak interactions and the GMTKN30 test set. *Mol. Phys.* **2016**, *114*, 1118−1127.
(42) Klawohn, S.; Kaupp, M.; Karton, A. MVO-10: AGas-Phase Oxide Benchmark for Localization/Delocalization in Mixed-Valence Systems. *J. Chem. Theory Comput.* **2018**, *14*, 3512−3523.
(43) Burke, K.; Cruz, F. G.; Lam, K.-C. Unambiguous exchange-correlation energy density. *J. Chem. Phys.* **1998**, *109*, 8161−8167.
(44) Becke, A. D. Density-functional exchange-energy approximation with correct asymptotic behavior. *Phys. Rev. A: At., Mol., Opt. Phys.* **1988**, *38*, 3098−3100.
(45) Perdew, J. P.; Burke, K.; Ernzerhof, M. Generalized Gradient Approximation Made Simple. *Phys. Rev. Lett.* **1996**, *77*, 3865−3868.

https://doi.org/10.1021/acs.jpca.1c01135
J. Phys. Chem. A 2021, 125, 2697−2707

(46) Becke, A. D. A new inhomogeneity parameter in density-functional theory. *J. Chem. Phys.* **1998**, *109*, 2092−2098.
(47) Helgaker, T.; Jaszuński, M.; Ruud, K. Ab Initio Methods for the Calculation of NMR Shielding and Indirect Spin-Spin Coupling Constants. *Chem. Rev.* **1999**, *99*, 293−352.
(48) Neese, F. Prediction of molecular properties and molecular spectroscopy with density functional theory: From fundamental theory to exchange-coupling. *Coord. Chem. Rev.* **2009**, *253*, 526−563.
(49) Bates, J. E.; Furche, F. Harnessing the meta-generalized gradient approximation for time-dependent density functional theory. *J. Chem. Phys.* **2012**, *137*, 164105.
(50) *TURBOMOLE*, release 7.5.1; TURBOMOLE GmbH: Karlsruhe, Germany, 2019.
(51) Becke, A. D. Current density in exchange-correlation functionals: Application to atomic states. *J. Chem. Phys.* **2002**, *117*, 6935−6938.
(52) Neese, F.; Wennmohs, F.; Hansen, A.; Becker, U. Efficient, approximate and parallel Hartree-Fock and hybrid DFT calculations. A 'chain-of-spheres' algorithm for the Hartree-Fock exchange. *Chem. Phys.* **2009**, *356*, 98−109.
(53) Plessow, P.; Weigend, F. Seminumerical Calculation of the Hartree-Fock Exchange Matrix: Application to Two-Component Procedures and Efficient Evaluation of Local Hybrid Density Functionals. *J. Comput. Chem.* **2012**, *33*, 810−816.
(54) Bahmann, H.; Kaupp, M. Efficient Self-Consistent Implementation of Local Hybrid Functionals. *J. Chem. Theory Comput.* **2015**, *11*, 1540−1548.
(55) Maier, T. M.; Bahmann, H.; Kaupp, M. Efficient Seminumerical Implementation of Global and Local Hybrid Functionals for Time-Dependent Density Functional Theory. *J. Chem. Theory Comput.* **2015**, *11*, 4226−4237.
(56) Klawohn, S.; Bahmann, H.; Kaupp, M. Implementation of Molecular Gradients for Local Hybrid Density Functionals Using Seminumerical Integration Techniques. *J. Chem. Theory Comput.* **2016**, *12*, 4254−4262.
(57) Jensen, F. Segmented Contracted Basis Sets Optimized for Nuclear Magnetic Shielding. *J. Chem. Theory Comput.* **2015**, *11*, 132−138.
(58) Weigend, F. Accurate Coulomb-fitting basis sets for H to Rn. *Phys. Chem. Chem. Phys.* **2006**, *8*, 1057−1065.
(59) Arbuznikov, A. V.; Kaupp, M. Importance of the correlation contribution for local hybrid functionals: Range separation and self-interaction corrections. *J. Chem. Phys.* **2012**, *136*, 014111.
(60) Staroverov, V. N.; Scuseria, G. E.; Tao, J.; Perdew, J. P. Comparative assessment of a new nonempirical density functional: Molecules and hydrogen-bonded complexes. *J. Chem. Phys.* **2003**, *119*, 12129−12137.
(61) Kupka, T.; Leszczyńska, M.; Ejsmont, K.; Mnich, A.; Broda, M.; Thangavel, K.; Kaminský, J. Phosphorus mononitride: A difficult case for theory. *Int. J. Quantum Chem.* **2019**, No. e26032, DOI: 10.1002/qua.26032.

https://doi.org/10.1021/acs.jpca.1c01135
J. Phys. Chem. A 2021, 125, 2697−2707

V

Reprinted with permission from

C. J. Schattenberg and M. Kaupp,
"*Extended Benchmark Set of Main-Group Nuclear Shielding Constants and NMR Chemical Shifts and Its Use to Evaluate Modern DFT Methods*",
J. Chem. Theory Comput., **2021**, *17*, 7602–7621.
DOI: 10.1021/acs.jctc.1c00919

JCTC Journal of Chemical Theory and Computation

pubs.acs.org/JCTC Article

Extended Benchmark Set of Main-Group Nuclear Shielding Constants and NMR Chemical Shifts and Its Use to Evaluate Modern DFT Methods

Caspar Jonas Schattenberg and Martin Kaupp*

Cite This: J. Chem. Theory Comput. 2021, 17, 7602−7621 Read Online

ACCESS | Metrics & More | Article Recommendations | Supporting Information

ABSTRACT: An extended theoretical benchmark set, NS372, for light main-group nuclear shieldings and NMR shifts has been constructed based on high-level GIAO-CCSD(T)/pcSseg-3//CCSD(T)/cc-pVQZ reference data. After removal of the large static-correlation cases O_3, F_3^-, and BH from the statistical evaluations for the ^{17}O, ^{19}F, and ^{11}B subsets, the benchmark comprises overall 372 shielding values in 117 molecules with a wide range of electronic-structure situations, containing 124 ^{1}H, 14 ^{11}B, 93 ^{13}C, 43 ^{15}N, 31 ^{17}O, 47 ^{19}F, 14 ^{31}P, and 6 ^{33}S shielding constants. The CCSD(T)/pcSseg-3 data are shown to be close to the basis-set and method limit and thus provide an excellent benchmark to evaluate more approximate methods, such as density functional approaches. This dataset has been used to evaluate Hartree−Fock (HF) and MP2, and a wide range of exchange−correlation functionals from local density approximation (LDA) to generalized gradient approximations (GGAs) and meta-GGAs (focusing on their current-density functional implementations), as well as global hybrid, range-separated hybrid, local hybrid, and double-hybrid functionals. Starting with absolute shielding constants, the DSD-PBEP86 double hybrid is confirmed to provide the highest accuracy, with an aggregate relative mean absolute error (rel. MAE) of only 0.9%, followed by MP2 (1.1%). MP2 and double hybrids only show larger errors for a few systems with the largest static-correlation effects. The double-hybrid B2GP-PLYP, the two local hybrids cLH12ct-SsirPW92 and cLH12ct-SsifPW92, and the current-density functional meta-GGA cB97M-V follow closely behind (all 1.5%), as do some further functionals, cLH20t and cMN15-L (both 1.6%), as well as B2PLYP and KT3 (both 2.0%). Functionals on the lower rungs of the usual ladder offer the advantage of lower computational cost and access to larger molecules. Closer examination also reveals the best-performing methods for individual nuclei in the test set. Different ways of treating τ-dependent functionals are evaluated. When moving from absolute shielding constants to chemical shifts, some of the methods can benefit from systematic error compensation, and the overall error range somewhat narrows. Further methods now achieve the 2% threshold of relative MAEs, including functionals based on TPSS (TPSSh, cmPSTS).

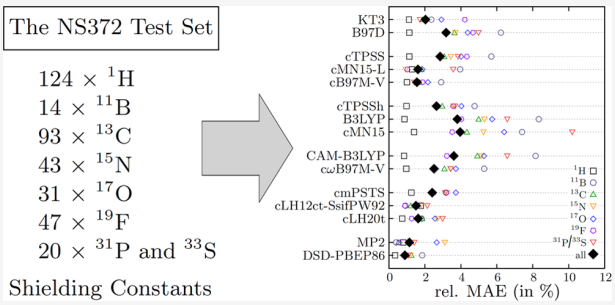

1. INTRODUCTION

Due the central importance of NMR spectroscopy in many areas of natural sciences, quantum-chemical computation of its spectroscopic parameters is increasingly in demand. We focus here on nuclear shieldings and the related NMR chemical shifts. The development of post-Hartree−Fock (post-HF) methodologies has been an important part of the progress here, providing unrivaled accuracy.[1−4] CCSD(T) in combination with gauge-including atomic orbitals (GIAOs[5−7]) is currently the gold standard except for cases with large static-correlation effects. However, due to the substantial computational effort involved with such post-HF methods, the vast majority of practical applications of quantum-chemical methods to NMR shifts, in particular for larger molecules and solids, use the computationally much more expedient methods of the Kohn−Sham density functional theory (KS-DFT). For the latter, the approximate exchange−correlation (XC) functional largely determines the achievable accuracy. Indeed, such approximate DFT methods for nuclear shieldings, while being used widely, frequently do not yet achieve the accuracy desired for some sophisticated spectroscopic problems,[8−11] and thus the search for improved XC functionals is an ongoing and active endeavor.

Currently, it appears that the shieldings of main-group systems, on which we concentrate in this work, are best reproduced by some so-called double-hybrid functionals

Received: September 14, 2021
Published: November 19, 2021

(DHs) on the fifth rung of Perdew's ladder of XC functionals,[12] in particular, the DSD-PBEP86 functional[13,14] based on spin-component-scaled (SCS) MP2[15] (a recent comparison with experimental ^{1}H shifts comes to a different conclusion but suffers from methodological inadequacies[16]). The nonlocal MP2-type correlation of DHs in conjunction with GIAOs introduces substantial computational demands (estimated to be 1−2 orders of magnitude larger than a regular DFT shielding calculation), however, placing this class of functionals in an accuracy and cost range intermediate between the more standard DFT approaches and the CCSD(T) reference method. This limits the accessible system sizes with DHs and emphasizes the need for further accuracy improvements on the lower rungs of the ladder (we note, however, promising efforts to extend DH approaches to local correlation methods[17]). A point in case is provided by a recent computational protocol that combines cheap conformational dynamics simulations with DFT computations of NMR shifts and spin−spin coupling constants to simulate full NMR spectra from first principles.[18] Here, the need for many computations for different conformers on larger systems limits the applicability of DHs. The limited accuracy of NMR shifts obtained with more standard DFT functionals on the lower rungs of the ladder is a decisive obstacle that might be overcome by accuracy improvements.

An area we have started to focus on is the use of local hybrid functionals (LHs[19,20]) with position-dependent (Hartree−Fock-type) exact-exchange (EXX) admixture (rung 4) for which the first efficient implementation of nuclear shieldings has been reported recently.[21] After considering the proper treatment of local kinetic-energy contributions to the local mixing functions (LMFs) that govern the position dependence[22] and introducing more advanced LHs with calibration functions (CFs) to deal with the ambiguity of exchange-energy densities,[23] very promising results have been found in initial evaluations on a relatively small main-group shielding test set when using the most recent LH20t functional,[24] with promising data obtained also with some earlier variants of LHs. Part of the advantages of LHs in this field relate to their larger EXX admixture in the core and semicore regions that may allow induced-current contributions to the magnetic-field response to be covered more accurately than with standard global hybrids (GHs), an aspect that has recently received increased attention.[25] A related notable aspect of refs 22 and 23 is that the implementation of functionals depending on local kinetic energy τ using Dobson's current density functional (CDFT) framework[26,27] cures some artifacts of the widely used Maximoff−Scuseria scheme[28] to render τ gauge-invariant, and it can affect the nuclear shielding results substantially for some meta-GGAs, meta-GGA based GHs, and for τ-dependent LHs. A wider screening of LHs, and of CDFT versions of meta-GGA-based functionals, for nuclear shieldings and chemical shifts thus seems in order.

A completely systematic improvement of approximate XC functionals toward an exact functional is not possible while retaining the computational advantages of DFT. Although we can attempt to use physical reasoning to construct improved functionals, the path forward always typically involves some type of validation and benchmarking to establish that a given functional performs well for a given property. This can be done by comparing approximative calculations to experimental data or to data computed using high-level ab initio methodologies. The latter helps to eliminate a number of factors that often complicate the direct comparison against experiment, such as environmental, ro-vibrational, or thermal contributions (possibly also relativistic effects, see below). This makes a theory-against-theory comparison preferable, provided a benchmark level with sufficiently high accuracy is available. For main-group nuclear shieldings, a number of high-level benchmarks have been put forward, typically based on CCSD(T) "gold standard" data for small molecules.[10,11,15,29−38] However, these data sets usually have been based on a relatively small number of values for a given nucleus, and the different sets often used different basis sets, which may lead to variable accuracy. We therefore decided to construct a larger benchmark set of light main-group nuclear shieldings at a uniform computational level to be used in validation studies of more approximate methods. CCSD(T)/pcSseg-3 benchmark data have been generated for 377 nuclei in 119 molecules, containing 124 ^{1}H, 15 ^{11}B, 93 ^{13}C, 43 ^{15}N, 33 ^{17}O, 49 ^{19}F, 14 ^{31}P, and 6 ^{33}S shielding constants. For a large subset of 297 nuclei in 104 molecules, where this has been computationally feasible, additional CCSD(T)/pcSseg-4 data have been computed to ensure basis-set convergence at the CCSD(T)/pcSseg-3 level. This extended dataset includes light main-group systems with widely different electronic structures and computational requirements, including cases with larger static correlation. It is used here to validate a large number of quantum-chemical methods, from HF and MP2 to a wide range of XC functionals representing all five rungs of the ladder.

2. THEORY

In this study, we include some meta-GGAs, global and range-separated hybrids based on meta-GGAs, and also LHs that may depend on the kinetic energy ($\tau = (1/2)\sum_i \nabla\phi_i^* \nabla\phi_i$) via their LMF. Since τ is not a priori gauge-invariant in the presence of an external magnetic field, the correct handling of gauge dependence is important for these functionals. We will briefly recall some of the relevant aspects. The so far most widely used model to correct the gauge dependence of τ is that proposed by Maximoff and Scuseria (τ_{MS}),[28] which is also the standard implementation in many quantum-chemical program codes

$$\tau \rightarrow \tau_{MS} = \tau + \frac{\mathbf{A}^T}{c}\mathbf{j}_p + \frac{|\mathbf{A}|^2}{2c^2}\rho \tag{1}$$

where

$$\mathbf{j}_p = \frac{i}{2}\sum_i (\phi_i \nabla\phi_i^* - \phi_i^* \nabla\phi_i) \tag{2}$$

is the paramagnetic current density and $\mathbf{A}$ is the vector potential of the magnetic field. Such a treatment keeps the magnetic Hessian diagonal, while removing the gauge dependence. Hence, no iterative procedure is required to solve for the shielding constants in the case of semilocal functionals, i.e., for pure meta-GGAs. However, τ_{MS} does not provide a proper iso-orbital indicator in the presence of an external magnetic field[39,40] and due to its explicit dependence on the vector potential, it is nonuniversal.[41] More importantly, we recently found paramagnetic shielding artifacts for atoms and for the parallel tensor contribution in linear molecules, which are also related to a deterioration of the overall results with, for example, certain τ-dependent LHs, in particular, for proton shieldings and for seemingly simple electronic-structure situations.[22,23]

https://doi.org/10.1021/acs.jctc.1c00919
J. Chem. Theory Comput. 2021, 17, 7602−7621

To overcome these limitations, a physically motivated and intrinsically current-dependent correction as proposed by Dobson[26,27]

$$\tau \rightarrow \tau_D = \tau - \frac{|\mathbf{j}_p|^2}{2\rho} \quad (3)$$

was implemented. This model has been used before in various contexts,[25,39,42,43] It renders the XC functional explicitly dependent on the induced paramagnetic current density, providing a CDFT framework via the τ dependence. And it provides a gauge-invariant treatment. In a linear-response framework, the correction affects only the magnetic-field response. While this generates moderate additional computational burden for meta-GGAs, it hardly affects the computational times for τ-dependent hybrids. We will use the prefix "c" for a given functional to denote the use of τ_D and thus of the CDFT framework, following previous works (cf. refs 25, 43, and 44).

For comparison, data for two additional models for τ will be provided in the Supporting Information: (i) use of the gauge-dependent τ, with the gauge origin placed at the center of mass (termed τ_C), and (ii) the ad hoc gauge-independent model[22,36] used currently as a default method in the ORCA program,[45,46] in the following called τ_0.

In addition to the direct comparison of nuclear shieldings to benchmark CCSD(T) data, we will look at chemical shifts (δ), obtained by referencing the isotropic shielding value

$$\sigma^{iso} = \frac{1}{3}\mathrm{Tr}(\boldsymbol{\sigma}) \quad (4)$$

to the shielding of a known standard compound

$$\delta_{calc.} = \sigma_{ref.} - \sigma_{calc.} + \delta_{ref.} \quad (5)$$

3. THE NEW NS372 BENCHMARK SET

Various test sets for main-group nuclear shieldings and chemical shifts have been put forward,[10,11,29−37] differing in the level of theory used for structure optimization and shielding calculation. Usually, a test set covers one or two nuclei, which makes a comprehensive comparison difficult, even if we want to restrict ourselves to light main-group species for the time being to avoid complications from relativistic effects. This has motivated us to construct a larger benchmark set at uniform CCSD(T) levels of theory for both structures and shielding computations, consisting of overall 377 shielding values in 119 molecules (see Tables S1 and S2 in the Supporting Information), containing 124 ^{1}H, 15 ^{11}B, 93 ^{13}C, 43 ^{15}N, 33 ^{17}O, 49 ^{19}F, 14 ^{31}P, and 6 ^{33}S shielding constants. As we exclude O_3 from the ^{17}O, F_3^- from the ^{19}F, and BH from the ^{11}B subset for statistical evaluations of approximate methods (see the Results section), the number of values used for such purposes reduces to 372, including 14 ^{11}B, 31 ^{17}O, and 47 ^{19}F nuclei. In the interest of including a sufficiently wide and diverse range of molecules containing up to 13 atoms, we settled on the use of the pcSseg-3 basis set.[47] The possible remaining basis-set or method errors of this benchmark level will be evaluated below. As the structures used for the shielding calculations are also of major importance, we have optimized all structures at the high CCSD(T)/cc-pVQZ level.[48,49] We note in passing that we include here only ^{31}P/^{33}S as the third-row nuclei while neglecting other important nuclei like ^{29}Si and ^{27}Al. On the one hand, we expect these nuclei to provide relatively similar, moderate demands on the electronic-structure methods as ^{11}B or ^{13}C shieldings/shifts. On the other hand, a large ^{29}Si shift benchmark based on experimental data has just appeared, which can be utilized for method evaluations.[50] A further extension of the present CCSD(T)-based benchmark to other main-group nuclei is in any case planned.

4. COMPUTATIONAL DETAILS

4.1. Benchmark Calculations. The CCSD(T) structure optimizations and vibrational-frequency analyses (to ensure minima) with cc-pVQZ and cc-pVTZ basis sets,[48,49,51,52] as well as the benchmark GIAO-CCSD(T) and GIAO-CCSD calculations of nuclear shieldings at these structures with the pcSseg-3, pcSseg-4, and pcSseg-4(unc) basis sets,[47] were all carried out with the CFOUR program package, version 1.2.[53] Unless stated otherwise, the CCSD(T)/pcSseg-3//CCSD(T)/cc-pVQZ benchmark data are used, and the CCSD(T)/cc-pVQZ structures are also used for the shielding calculations at lower levels. We note in passing that small imaginary frequencies remain for the used C_s-symmetrical structures of CMe_3^+ and BMe_3, corresponding to free rotations of the methyl groups. The true minima have a C_1 symmetry, which leads to prohibitively costly CCSD(T) shielding calculations and difficult convergence issues. As lower-level computations show negligible effects of symmetry-lowering on the computed shieldings, we use the C_s structures throughout.

The question of systems with large static-correlation effects has already been mentioned. In extreme cases, the reliability of the single-reference CCDS(T) level as the benchmark method may be called into question. We have therefore computed T_1,[54] D_1,[55] and percent total atomization energy[56,57] (%TAE) diagnostics (with the cc-pVQZ basis) using the MOLPRO program[58] to test for multireference character. Standard thresholds[59] for closed-shell main-group species of ≥0.02 (T_1), ≥0.06 (D_1), and ≥10% (|%TAE|) were used. The full CC diagnostics are listed in Table S3 in the Supporting Information. We furthermore use the comparison between MP2 results and the benchmark CCSD(T) data to detect difficult cases (as listed in the last row of Tables S6−S12 in the Supporting Information, next to the shielding overviews for full MP2 results). That is, relative deviations of MP2 by more than 2% for ^{1}H and more than 4% for the other nuclei from the CCSD(T) benchmark data are taken to indicate large static-correlation cases (see below).

To estimate the importance of relativistic effects for a few of the most pertinent systems containing third-row elements, additional four-component (4c) calculations were performed for a subset of molecules (see below) using the ReSpect program code.[60] All calculations employ the KT2 functional in the matrix Dirac−Kohn−Sham (mDKS) Hamiltonian,[61,62] uncontracted pcS-3 basis sets,[63] GIAOs, and a finite size Gaussian charge model for the nucleus. To estimate the magnitude of the relativistic effects (and to avoid cross-program deviations), calculations approaching the nonrelativistic limit were performed by scaling the speed of light by a factor of 50 (the largest recommended scaling factor in ReSpect), while keeping the other parameters as in the relativistic setting.

4.2. Evaluation of DFT Methods. Unless stated otherwise, nuclear shielding constants at DFT levels up to rung 4 on Perdew's "Jacobs Ladder" of XC functionals have been calculated using a local developers' version of the

https://doi.org/10.1021/acs.jctc.1c00919
J. Chem. Theory Comput. 2021, 17, 7602−7621

Table 1. Specifications of LH Functionals of the Present Work

functional	LMF	scal.	CF	exchange	correlation	refs
mPSTS	*a*			TPSS	TPSS	44 and 67
LHJ14	*z*	0.096		B88[68]	B88[69]	70
LH07s-SVWN	*s*	0.220		LSDA	VWN	71
LH07t-SVWN	*t*	0.480		LSDA	VWN	72
LH12ct-SsirPW92	*t*	0.646		LSDA	sir-PW92	73
LH12ct-SsifPW92	*t*	0.709		LSDA	sif-PW92	73
LH14t-calPBE	*t*	0.500	pig1	0.49 LSDA + 0.51 PBE	modified B95	74
LH20t	*t*	0.715	pig2	0.22 LSDA + 0.78 PBE	modified B95	24

TURBOMOLE program package, updated to release 7.5.[64] Self-consistent field (SCF) convergence was set to 10^{-9}, ensuring converged results by additionally enforcing the density matrix change to be smaller than 10^{-7}. Likewise, the shielding coupled-perturbed Kohn−Sham convergence was set to a threshold of 10^{-7} (convergence of the Euclidean norm of the residual vectors). TURBOMOLE standard grids of size "3" have been used throughout, except for the SCAN series of functionals where larger grids (grid setting "5" and enhanced radial grids of size "40") have been employed to ensure convergence. The resolution of the identity approximation was used for both SCF and shielding parts in its multipole accelerated version (MARIJ),[65] with auxiliary basis sets ("universal"), specified in ref 66. pcSseg-3 basis sets[47] have been used, which are essentially at the basis-set limit for DFT shielding computations. Calculations using double hybrids (rung 5) and MP2 are performed with the ORCA 4.2.1 program package,[45,46] using the same settings as in ref 15. Unless stated otherwise, the DFT and MP2 GIAO shielding calculations are reported with pcSseg-3 basis sets, but we also obtained shieldings using pcSseg-4 basis sets. The full pcSseg-3 shielding data are reported in Tables S6−S12, accompanied by statistical results in Table S13, whereas a comparison of statistical results of pcSseg-3 and pcSseg-4 shieldings is provided in Table S14. Hartree−Fock shielding calculations, which are also reported, give almost identical results with TURBOMOLE and ORCA, within the margins expected from different convergence criteria in the two codes.

In addition to HF and MP2 results, data for a wide range of exchange−correlation functionals from all rungs of the ladder will be provided. SVWN[75,76] represents the local density approximation (LDA, rung 1). Rung 2 (generalized gradient approximation, GGA) is represented by PBE,[77] BLYP,[68,78] BP86,[68,79,80] HCTH,[81,82] and B97D,[83] as well as Tozer's three functionals KT1−KT3 aimed specifically at light main-group shieldings.[84,85]

The meta-GGA rung 3 level includes TPSS,[86,87] VSXC,[88] τ-HCTH,[89] B97M-V,[90] SCAN,[91] and its regularized and reregularized versions rSCAN[92] and r^{2}SCAN,[93] as well as the highly parameterized M06-L[94] and MN15-L.[95] For these τ-dependent meta-GGAs, as well as for related GHs, RSHs, and τ-dependent LHs, we will first report results for their theoretically most satisfactory CDFT implementation, as indicated by the prefix "c", but other treatments of τ will also be mentioned.

On rung 4 ("hyper-GGA"), we evaluate a selection of GHs with or without τ-dependence, from simple to more parameterized functionals. This includes (in order of increasing EXX admixture) TPSSh (10%),[96] B3LYP (20%),[97] B97-2 (21%),[98] PBE0 (25%),[99,100] M06 (27%),[101] PW6B95 (28%),[102] MN15 (44%),[103] BHLYP (50%),[104] and M06-2X (54%).[101] Also on rung 4, we have evaluated the four RSHs CAM-B3LYP,[105] ωB97X-D,[106] ωB97X-V,[107] and ωB97M-V.[108] The latter is τ-dependent, and as all other τ-dependent functionals, it will be evaluated in its CDFT variant and other implementations.

All LHs available in TURBOMOLE are evaluated (an overview of the relevant details of the employed LH functionals is shown in Table 1). This includes the first-generation LDA-based LH07s-SVWN,[71] LH07t-SVWN,[72] LH12ct-SsirPW92, and LH12ct-SsifPW92.[73] Except for the first one, which is based on an "s-LMF" depending on the reduced density gradient, these functionals use a t-LMF, defined as the scaled ratio of the von-Weizsäcker and Pauli kinetic energies.[19,72,109] The same holds for the more advanced LH14t-calPBE[74] and LH20t,[24] which make use of GGA-type exchange-energy densities augmented by a so-called calibration function to deal with the ambiguity of exchange-energy densities.[20,110−112] Contrary to a recent statement,[44] the calibration functions in these two functionals do not depend on the gradient of τ and are thus fully implemented. Two additional LHs with other types of LMFs have recently been implemented into TURBOMOLE by Holzer et al.[44] The first is a slightly modified version (mPSTS[44]) of the PSTS functional, which features a more complex LMF.[44,67] The second is Johnson's LHJ14 featuring an LMF based on the correlation length.[70]

Finally, on rung 5, three DHs available in the ORCA code are addressed: B2PLYP,[113] B2GP-PLYP,[114] and DSD-PBEP86.[13,14] The latter functional uses SCS-MP2-type correlation together with a very large EXX admixture of 70% and has been the most accurate functional for main-group shieldings in a recent evaluation for a smaller test set.[36]

The statistical data reported in the present work include standard deviations (SD), mean absolute errors (MAE), and mean signed errors (MSE), and we also report maximum absolute errors (max. AE). To allow comparison between nuclei with different shielding ranges in the present test set, relative deviations normalized to the shielding range covered by the respective CCSD(T) reference for a given nucleus are also given. In addition, the aggregate weighted relative deviations with and without ^{1}H nuclei are given (see Figures 1 and 4; "all" and "all (−^{1}H)"), which are calculated from the sum of the relative data weighted by the number of shieldings in the individual subsets.

5. RESULTS

5.1. Accuracy of the Benchmark Data. Obviously, the ultimate benchmark test of approximate methods would be provided by comparison with experimental shifts. As pointed out in the introduction, this is rendered difficult by a variety of effects not considered in the present nonrelativistic 0 K computations, such as ro-vibrational and thermal effects, and in

https://doi.org/10.1021/acs.jctc.1c00919
J. Chem. Theory Comput. 2021, 17, 7602−7621

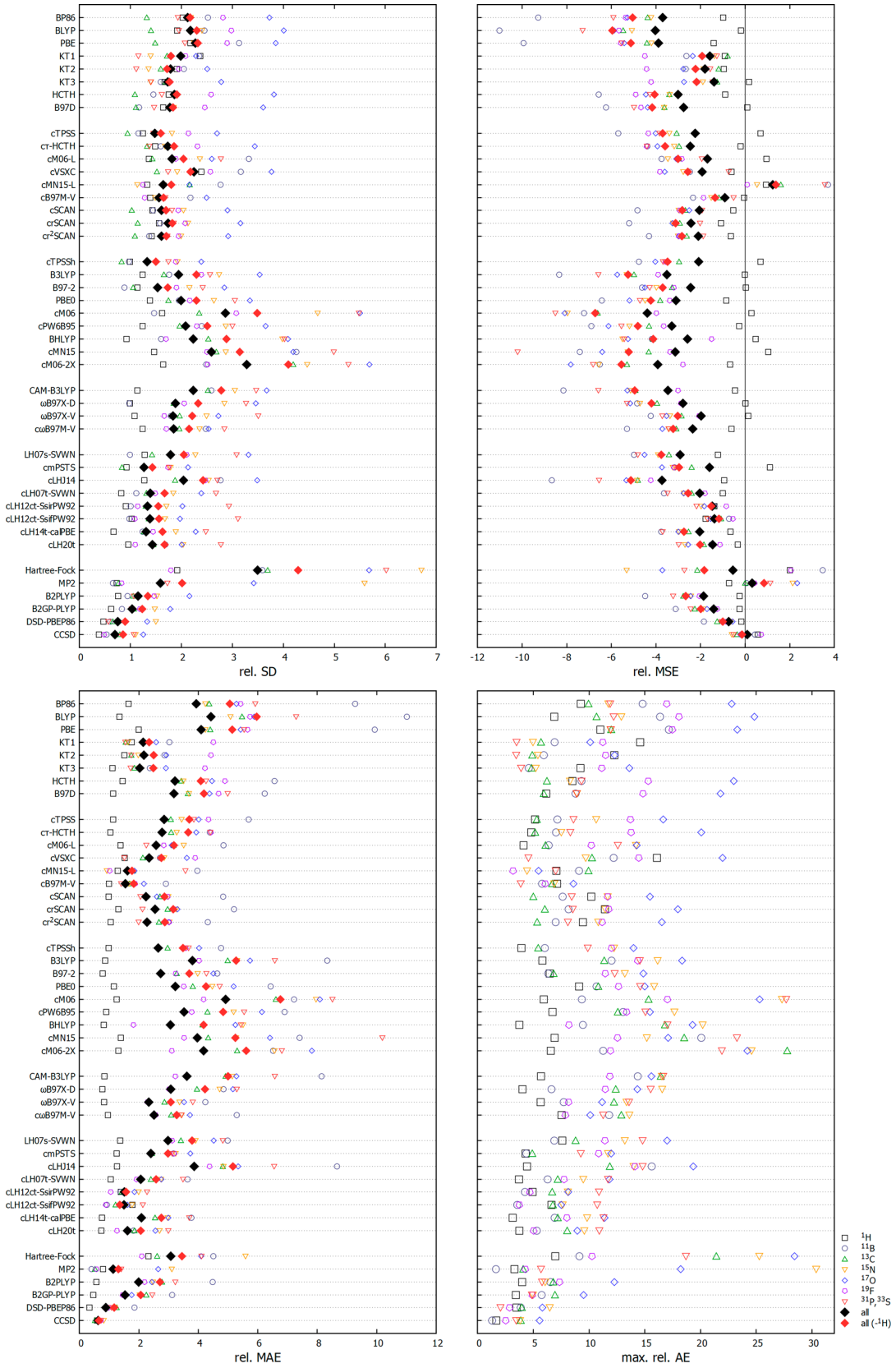

Figure 1. Relative deviations (in %, normalized to the shielding range for a given nucleus) from the CCSD(T)/pcSseg-3 reference data for different methods (with pcSseg-3 basis). Individual nuclei shown as open symbols, weighted aggregate relative deviations across all subsets as black diamonds, and when excluding the ^{1}H shieldings as red diamonds.

https://doi.org/10.1021/acs.jctc.1c00919
J. Chem. Theory Comput. 2021, 17, 7602−7621

some cases, environmental or relativistic contributions. This is the very reason we rely here on a high-level theory benchmark, and why we include light main-group systems only. A comprehensive comparison with experimental shieldings, even for the subset of the present large benchmark for which such data are available, would be prohibitive and of limited usefulness, as the additional corrections needed for such a comparison are themselves not always known with sufficient accuracy or would require extensive computations. We may, however, judge the reliability and accuracy of the present GIAO-CCSD(T)/pcSseg-3 benchmark method by comparing it to some earlier benchmark studies on smaller data sets, where experimental data had been "back-corrected" to be better comparable to isolated 0 K gas-phase computations. Such comparisons are given in Table S4 in the Supporting Information, where CCSD(T)/pcSseg-3 and CCSD(T)/pcSseg-4 results are compared with CCSD(T) calculations with different basis-set sizes from various sources.[29−32,35,37,115−117] The best estimates are the basis-set convergence studies provided in refs 29, 30, 32, and 116 where the uncontracted "13s9p4d3f" basis ("15s12p4d3f2g" for ^{31}P shieldings) basis is considered to be close to the basis-set limit (with a remaining error of about 0.5 parts per million (ppm)).

From these comparisons, we can conclude that the pcSseg-3 basis provides similar accuracy as the "pz3d2f" basis sets with a residual basis-set error of a few ppm in the worst cases (arising for the largest paramagnetic contributions), whereas in many cases the accuracy is in the sub-ppm range, comparable to the larger uncontracted "13s9p4d3f" basis. The even larger pcSseg-4 top-of-the-line basis may be expected to produce essentially converged shielding constants. This can also be seen from Table S5 in the Supporting Information for a smaller subset of molecules. To additionally gauge the remaining basis-set errors at the chosen GIAO-CCSD(T)/pcSseg-3 level, we have also computed CCSD(T)/pcSseg-4 shielding constants for a subset of 104 (smaller) molecules representing 297 nuclei (Table S2 in the Supporting Information). Considering the error ranges of even the most accurate more approximate methods to be evaluated, the basis-set errors of the pcSseg-3 basis may be considered negligible, except possibly for the proton shifts: for the second- and third-row nuclei studied here, the average changes from pcSseg-3 to pcSseg-4 range from −0.2 to −0.4 ppm (^{31}P: −0.6 ppm). The maximum absolute deviations are generally below 3 ppm even for the overall most deshielded cases (e.g., O_3 or F_3^-), which will not even be used for method evaluations (see below). Only for the ^{1}H shieldings, where the overall average differences between methods are below 1 ppm, we need to keep in mind that the larger basis reduces the shieldings by an average of −0.03 ppm and a maximum value of −0.07 ppm (for the S−H proton in CH_3SH). Complete decontraction of the pcSseg-4 basis has essentially negligible further effects (Table S5 in the Supporting Information). Comparison of the statistical data confirms the negligible effects when going from pcSseg-3 to pcSseg-4, with relative deviations in the statistical data below 0.3% for all tested functionals and nuclei (Table S14 in the Supporting Information). Overall, these data show that the somewhat smaller pcSseg-3 basis set, for which data are available for the entire test set, is perfectly sufficient for generating accurate CCSD(T) benchmark data against which we may evaluate more approximate approaches. We note in passing that for regular DFT calculations, the pcSseg-3 level can be considered as converged.

The underlying structures obtained at the CCSD(T)/cc-pVQZ level are known to exhibit close agreement with experimental data for light main-group species, with mean deviations of 0.19 pm in distances. Even the smaller cc-pVTZ basis gives very small deviations.[118] We have nevertheless analyzed the effect of this change of the input-structure level for a subset of our dataset, using either pcSseg-3 or pcSseg-4 basis sets for the shielding computations (Table S5 in the Supporting Information). While the effects are in most cases small and not relevant for the statistical evaluations, they can reach several ppm for the most extreme cases with large static-correlation effects and paramagnetic contributions. Pertinent examples are the ^{15}N and ^{31}P values in PN, where a change of 0.81 pm in the bond length affects the shieldings by ca. 6−7 ppm. An even larger effect is seen for the ^{33}S shielding in SO_2, where a change of 0.94 pm in the bond length causes a change in shielding of ca. 17 ppm. The terminal ^{17}O shielding in O_3 changes even by about 25 ppm. In all of these cases, the effect of changing the basis for the structure optimization is clearly more important than that of changing the basis for the shielding computations. In spite of the overall insignificant changes in the overall statistical results for various nuclei, we decided to use the larger cc-pVQZ basis in the structure optimizations for the entire benchmark set.

Table 2. Shielding Results for F_3^- Obtained at Different Levels of Coupled-Cluster Theory Using the pcSseg-3 Basis Set

	F_3^- (^{19}F)	
	(cent.)	(term.)
CCSD	−297.7	−136.9
CCSD(T)	−203.0	−265.9
CCSDT	−104.5	−286.9

Due to the extreme computational demand involved, the expected effects of full triple excitations are studied less frequently. They typically amount to just 1−1.5 ppm in "normal" main-group cases like BH, HF, CO, N_2O, N_2, or CH_3OH,[116,119] and up to 3−8 ppm for the ^{19}F shieldings in F_2 or F_2O.[30,31] Larger changes are found for the most extreme multireference cases like O_3 and F_3^-. For O_3 the transition from CCSD(T)/qz2p to CCSDT/qz2p was found to be 77 ppm for the terminal atom and 50 ppm for the central oxygen atom.[119] For F_3^-, our own comparison of CCSD(T)/pcSseg-3 with CCSDT/pcSseg-3 data indicates a shift of 99 ppm for the central and 31 ppm for the terminal fluorine atoms, on top of the even larger changes from CCSD to CCSD(T) (Table 2).

Relativistic effects on absolute shieldings can be substantial, but those on the shielding of the heavier atom itself often tend to cancel in relative shifts.[120] The largest relativistic effects for relative shifts are expected here from spin−orbit contributions to neighbor-atom shifts for atoms bonded to chlorine or sulfur. We have evaluated a few of the most pertinent systems by relativistic DFT computations, and the magnitude of the effects is consistent with the literature values.[121−123] The largest effects relative to the overall shielding range of a given nucleus apply to the ^{1}H shieldings in HCl (+0.82 ppm) and H_2S (+0.51 ppm). Effects on the ^{13}C shielding in CS_2 (+5.4 ppm) are also notable. For most systems, the effects are much smaller than this, clearly less important than the intrinsic errors of the electronic-structure methods evaluated in this work. In any case, the comparison against nonrelativistic CCSD(T)

https://doi.org/10.1021/acs.jctc.1c00919
J. Chem. Theory Comput. 2021, 17, 7602−7621

benchmark data allows us to disregard these effects in method evaluations.

Table 3. Overview of Molecules from the Benchmark Set, Where At Least One of the Multireference Diagnostic Thresholds Is Exceeded (CC/cc-pVQZ Results)

	T_1	D_1	|%TAE|
CF_3^+	0.015	0.062	5.3
CH_3NO_2	0.018	0.065	2.2
ClF_3	0.016	0.050	13.1
F_2	0.011	0.029	19.5
F_3^-	0.030	0.133	16.6
FNO	0.021	0.060	4.5
NO_3^-	0.018	0.070	4.4
O_3	0.027	0.075	17.6
OF_2	0.015	0.040	14.4
SO_2	0.021	0.054	6.2
threshold	0.020	0.060	10.0

5.2. Special Cases with Strong Static Correlation. As has been done in several previous studies,[30,31,84,124,125] we decided to exclude a few systems from the statistical evaluations for some nuclei in the main text, essentially the molecules or ions with the largest static-correlation effects and consequently with the by far largest paramagnetic shielding contributions (statistics with these systems included can, however, be found in Table S13 in the Supporting Information). The reason is that, otherwise, these systems tend to dominate the overall deviations and override other trends and insights. Furthermore, in some of these cases, the accuracy of the CCSD(T) benchmark data is lower or in doubt, as single-reference coupled-cluster theory is pushed to or beyond its limits (as also visible from the T_1, D_1, and |% TAE| diagnostics in Table 3, a more complete set of these diagnostics is given in Table S3 in the Supporting Information). We also discuss two molecules, which may be viewed as borderline cases but which we ultimately decided to include in the statistical evaluations in the main text. For the relevant eight nuclei in five molecules/ions, Table 4 summarizes the relative deviations of the results with various functionals from the CCSD(T)/pcSseg-3 data.

O_3 is commonly excluded from statistical evaluations, as otherwise its extreme static-correlation effects (see above) would dominate the comparison. Together with F_3^-, it is also the only molecule of the test set, where all diagnostic thresholds for multireference systems are exceeded (Table 3). Obviously, any Hartree−Fock exchange admixture deteriorates agreement with the benchmark data by providing too deshielded values between several hundreds and more than a thousand of ppm for both distinct ^{17}O nuclei (Table 4; even semilocal functionals produce large deviations, but less so). As Hartree−Fock fails completely for ozone, MP2 also performs catastrophically, giving large positive shieldings for both central and terminal atoms (see Table S10 in the Supporting Information). DSD-PBEP86 is now not able to adequately correct for this failure of MP2, while the deviations of B2PLYP and B2GP-PLYP from the CCSD(T) reference data are less dramatic but still large. Notably, even the reference CCSD(T) method provides about 100 ppm too shielded values for the terminal and somewhat too deshielded values for the central oxygen atom of ozone (in comparison with the experiment, see Table S2 in the Supporting Information). As discussed above, the influence of triple excitations accounts for several hundreds of ppm, and even going from CCSD(T) to full CCSDT has substantial effects for both nuclei. We note in passing that ^{17}O shielding cases with similar or even stronger static-correlation effects are known for transition-metal oxo complexes.[126,127]

An even more extreme case of static correlation (on a relative scale given the overall less dramatic variations for ^{19}F shieldings), which we thought worth presenting but exclude from the statistical evaluations, is provided by F_3^-. Similar to O_3, all diagnostics point to the multireference character (Table 3), and the effects of full triple excitations are large (see Table 2). MP2 exhibits large deviations for both nuclei.

Static-correlation effects for the ^{11}B shieldings of BH are not as pronounced, with MP2 too deshielded by about 16% and none of the multireference thresholds exceeded (note that here the CCSD(T) reference is thought to be quite reliable[119]). Nevertheless, inclusion of this system in the ^{11}B subset would dominate the statistics. The reason is that its reference shielding of −188.3 ppm is more than 205 ppm lower than the next most deshielded system (BH_3) in this still relatively small subset of 15 molecules. That is, this system would extend the shielding range covered for this nucleus from 141.6 to 344.3 ppm. As a consequence, relative deviations will look overall smaller but will often be dominated by BH. We therefore decided to omit the ^{11}B value of BH also from the statistical evaluations. As for O_3 and F_3^-, we provide additional statistics including these systems in Table S13 in the Supporting Information.

Another system with extremely large paramagnetic contributions but without a distinct multireference character, which we considered leaving out of the statistics for the ^{15}N and ^{31}P subsets, is PN. The deviations shown in Table 4 indicate that this is obviously also a difficult system for many methods. Its reference ^{15}N shielding value of −339 ppm is more than 100 ppm lower than the second negative value (−236 ppm, FNO), thereby extending the overall ^{15}N shielding range covered from 523 to 626 ppm. However, the deviations are consistent with the behavior of the methods for the other molecules in the subset, and inclusion of PN does not alter the results of the statistical evaluations unacceptably, given the relatively large number of nuclei (43) in the present ^{15}N subset. The ^{31}P subset is smaller (14 nuclei), and PN also stands out in this subset (its reference shielding of ca. 59 ppm is lower than the nearest value (PF_3) by 170 ppm, extending the overall shielding range covered from 660 to 830 ppm. Its inclusion in the statistics of the combined ^{31}P/^{33}S subset will favor methods that show relatively small deviations in Table 4 (MP2, the DHs, the KT1−KT3 series, cM06-L, cVSXC) and will disfavor most GHs, RSHs, and LHs. We decided in any case to include PN also in this subset. The same considerations hold for SO_2 (Table 4), which also has a moderate multireference character. Table S13 in the Supporting Information provides additional statistics excluding these two molecules.

Table 3 includes further systems for which at least one of the multireference thresholds is exceeded. However, in three of them (F_2, OF_2, ClF_3), the T_1/D_1 diagnostics remain low, indicating good performance of coupled-cluster theory. Only |%TAE| is above the 10% mark, which indicates large importance of triple excitations. Indeed, CCSD(T) data for F_2 and OF_2 were found to deviate from the experiment by almost 20 ppm (after application of ro-vibrational and thermal

https://doi.org/10.1021/acs.jctc.1c00919
J. Chem. Theory Comput. 2021, 17, 7602−7621

Table 4. Relative Deviations to CCSD(T) Reference Data for Some Particularly Difficult Molecules[a]

	O_3		F_3^-		BH	PN		SO_2
	$^{17}O_{cent.}$	$^{17}O_{term.}$	$^{19}F_{cent.}$	$^{19}F_{term.}$	^{11}B	^{15}N	^{31}P	^{33}S
SVWN	−10.8	−19.7	5.6	−22.6	−44.6	−14.2	−16.6	−10.5
BP86	−8.4	−14.8	2.7	−17.2	−19.1	−11.7	−11.9	−7.0
BLYP	−9.6	−16.0	1.6	−17.0	−21.8	−12.9	−12.2	−8.2
PBE	−8.5	−15.3	2.7	−17.8	−24.5	−11.9	−11.9	−6.6
KT1	−2.6	−1.7	6.0	−5.1	−9.2	−5.0	−2.1	1.3
KT2	−3.4	−3.8	3.8	−8.2	−7.3	−5.4	−2.2	0.4
KT3	−3.4	−5.4	0.9	−10.5	−2.7	−4.9	−2.1	0.6
HCTH	−7.2	−14.6	−0.5	−19.9	−10.8	−8.3	−9.3	−5.1
B97D	−7.5	−13.6	0.3	−17.7	−6.4	−8.9	−8.9	−5.8
cTPSS	−8.1	−11.9	1.4	−12.2	−7.4	−10.6	−8.6	−4.5
cτ-HCTH	−6.9	−13.0	−0.7	−18.3	0.7	−7.5	−8.3	−5.7
cM06-L	−14.3	−24.3	−2.3	−10.3	0.0	−14.2	−12.6	−2.1
cVSXC	−10.8	−17.1	0.7	−20.2	−12.9	−9.7	−4.5	−0.6
cMN15-L	−12.9	−12.4	−4.4	1.8	0.0	−0.2	3.2	5.3
cB97M-V	−10.4	−13.0	−2.8	−4.4	−8.6	−6.9	−3.9	0.5
cSCAN	−14.3	−21.0	−1.1	−11.2	−23.1	−11.7	−8.4	−2.6
crSCAN	−12.8	−19.2	−1.4	−12.7	−24.8	−11.5	−8.5	−2.9
cr^{2}SCAN	−12.7	−18.4	−1.4	−11.3	−20.8	−10.8	−8.1	−2.8
cTPSSh	−14.3	−17.9	−6.0	−6.8	−9.5	−12.2	−9.9	−6.2
B3LYP	−23.4	−29.3	−14.7	−5.0	−24.7	−16.2	−14.6	−11.5
B97-2	−21.6	−27.2	−16.0	−4.3	−14.0	−13.2	−12.3	−9.1
PBE0	−25.9	−31.9	−18.7	−1.8	−26.2	−15.8	−14.6	−10.5
cM06	−45.2	−66.1	−26.3	−11.4	−6.5	−27.3	−27.7	−17.9
cPW6B95	−27.9	−33.2	−21.4	−1.0	−23.8	−17.7	−15.1	−11.6
BHLYP	−49.9	−50.5	−49.8	17.1	−27.4	−20.2	−17.0	−15.4
cMN15	−31.6	−33.1	−27.3	3.7	−28.3	−15.2	−21.0	−23.3
cM06-2X	−46.9	−48.3	−49.0	15.2	−29.7	−24.6	−21.9	−17.2
CAM-B3LYP	−29.7	−33.4	−26.0	5.4	−35.4	−16.5	−16.7	−13.4
ωB97X-D	−28.5	−33.7	−27.0	3.3	−16.2	−16.5	−15.5	−11.9
ωB97X-V	−27.8	−28.7	−29.7	12.0	−27.0	−13.3	−13.6	−10.2
cωB97M-V	−26.1	−25.9	−28.7	13.3	−29.5	−13.6	−11.3	−8.0
LH07s-SVWN	−22.7	−29.9	−12.5	−3.8	−19.0	−13.2	−14.8	−10.1
cmPSTS	−15.3	−18.7	−8.1	−4.8	−4.2	−11.7	−9.3	−5.8
cLHJ14	−17.5	−22.9	−5.1	−8.5	−23.1	−14.0	−14.8	−10.9
cLH07t-SVWN	−17.8	−20.4	−10.9	2.7	−22.7	−9.5	−11.7	−8.1
cLH12ct-SsirPW92	−20.1	−21.0	−16.0	9.2	−24.1	−8.1	−10.9	−7.4
cLH12ct-SsifPW92	−21.0	−21.4	−17.9	11.4	−26.3	−7.6	−10.7	−7.3
cLH14t-calPBE	−17.7	−19.7	−11.7	3.2	−19.2	−9.8	−11.3	−8.2
cLH20t	−21.2	−20.0	−18.3	10.9	−13.8	−9.6	−10.9	−8.7
HF	−120.2	−96.0	−160.6	60.9	−23.4	−25.3	−18.4	−18.7
MP2	200.3	131.2	221.1	−30.7	−16.0	12.2	5.7	4.4
B2PLYP	15.7	6.4	23.7	−11.1	−20.4	−5.2	−5.8	−4.7
B2GP-PLYP	27.7	14.9	35.0	−9.1	−20.5	−3.7	−4.9	−4.2
DSD-PBEP86	49.6	33.6	62.9	−15.7	−15.1	0.2	−1.7	−1.0

[a]O_3, F_3^-, and BH are left out from the general statistical evaluations in the main text (for ^{17}O, ^{19}F, and ^{11}B shieldings); PN and SO_2 are included.

corrections).[30,32] However, relative to the ^{19}F shielding range covered here, these deviations are below 3%. For CF_3^+, CH_3NO_2, FNO, and NO_3^-, T_1 and/or D_1 are above threshold but the coupled-cluster energies are accurate and the shieldings look unsuspicious.

5.3. General Statistical Method Overview for Shielding Constants. Before discussing the performance of different methods for the different nuclei of the test set, we take a bird's eye view across the entire shielding test set of 372 values (which excludes O_3, F_3^-, and the ^{11}B shielding of BH). This is enabled by looking at relative (percentage) deviations normalized by the shielding ranges covered by the benchmark data for each nucleus, weighted by the number of values in the various subsets. Figure 1 shows rel. SDs, rel. MSEs, rel. MAEs, and max. rel. AEs in percentage for the individual nuclei, and the weighted deviations for all nuclei (black diamonds). We also show weighted deviations obtained by excluding the ^1H shieldings (red diamonds), as the latter represent rather different demands on the methods than the second- and third-period elements due to the absence of a core shell. For better representation, we had to limit the plots to ≤7% for the relative SDs, ≥−12% and ≤5% for the relative MSEs and ≤12% for the relative MAEs. The results for SVWN have thus been excluded from the plot (but the values can be found in Table S13 in the Supporting Information), as values for some nuclei exceeded these limits. For τ-dependent functionals, we show only their

https://doi.org/10.1021/acs.jctc.1c00919
J. Chem. Theory Comput. 2021, 17, 7602−7621

CDFT-based results (using τ_D), as indicated by the "c" suffix, and postpone a discussion of different models to include τ to a later section. The relative deviations are shown in Figure 1, while data are summarized in Table S13 in the Supporting Information.

Starting with the aggregate rel. MAEs (and implicitly the rel. MSEs, which for most functionals are systematically negative, approaching the negative of the rel. MAE values, see below), we note first that a number of functionals, as well as the MP2 method, provide deviations below 2% from the benchmark data. The lowest combined MAE of the more approximate methods is found with the DH DSD-PBEP86 (0.9%), only slightly behind CCSD (0.6%), confirming its top performance noted in an earlier study on a smaller main-group shielding test set.[36] This is followed by MP2 (1.1%), by the DH B2GP-PLYP, the two LH functionals cLH12ct-SsirPW92 and cLH12ct-SsifPW92, the CDFT meta-GGA cB97M-V (all 1.5%), by the LH cLH20t and the meta-GGA cMN15-L (1.6%). Further functionals in the list are the DH B2PLYP, and by the specialized GGA KT3 (both 2.0%), as well as by two further LHs (cLH07t-SVWN and cLH14t-calPBE) and the GGA KT1 (all 2.1%). As will be discussed in detail further below, the remarkable results for cB97M-V and cMN15-L, which stand out among all functionals up to rung 3, are observed for their CDFT variants. For MN15-L, other treatments of τ are drastically worse and for B97M-V the CDFT treatment is also most accurate but to a lesser extent. The treatment of τ is less determinative for the LHs.

But a number of further functionals also provide relatively good results for the overall test set. Starting with the GGA functionals, the already mentioned specialized functionals KT1, KT2, and KT3 stand out with rel. MAEs around 2%, clearly superior to the simpler GGAs BLYP, BP86, and PBE around 4% as well as the more recent HCTH and B97D around 3%. It has been shown that this improved performance of the KTx series of functionals, which have all been constructed with an emphasis on improving light main-group shieldings, relies on the compensation of errors for the dia- and paramagnetic shielding contributions.[25] As can be seen from the positions of the red vs black diamonds for this subset of functionals, the performance of the simpler GGAs is significantly worse when the moderately good ^{1}H shielding constants are excluded, as errors for some of the second- and third-period nuclei are larger (e.g., up to 11% rel. MAE for ^{11}B with BLYP). This is not the case for the KTx functionals. As for most DFT functionals (but see below), the rel. MSEs of the GGAs are systematically negative, approaching or reaching the amount of the rel. MAEs (for all but the ^{1}H shieldings), reflecting the systematic overestimate of the (usually negative) paramagnetic contributions.

Turning to the CDFT mGGA functionals, we have already noted the outstanding performance of cB97M-V and cMN15-L. The cSCAN series of functionals (between 2.2 and 2.5%), cVSXC (2.3%), and cM06-L (2.6%) also perform rather well. In previous works, a particularly good performance of M06-L had been noted for some main-group nuclei.[15,36,128] However, these results had been obtained using either probably a gauge-dependent τ in the Gaussian03 program[129] or the ad hoc τ_0 treatment in ORCA, and they seem to reflect error compensation to some extent. The same appears to hold for VSXC (both functionals have rel. MAEs near 1.7−1.9% for τ_0 and 1.9−2.2% with τ_C, see Table S13 in the Supporting Information). We postpone a broader discussion of these aspects to a later section. The remaining CDFT meta-GGAs cTPSS and cτ-HCTH trail somewhat behind (2.8%) and perform only slightly better than the HCTH and B97D GGAs. It is worth noting that cB97M-V is the only CDFT meta-GGA, which exhibits rel. MAEs below 3% for all nuclei studied here. cMN15-L deviates more for the ^{11}B (4.0%) and ^{31}P/^{33}S (3.6%) subsets but is better for some other nuclei. One particularly striking observation for cMN15-L is that it is the only DFT functional, and together with MP2, the only method evaluated which gives a clearly positive aggregate rel. MSE (in fact positive MSEs for all subsets). That is, the common overestimate of the (usually negative, except for the ^{19}F shielding in ClF) paramagnetic contributions is reversed. Due to the highly parameterized character of this functional, it seems difficult to find a physical explanation for this observation. However, recent evaluations of transition-metal hyperfine couplings[130] have indicated wide variations and deviations from other methods in the description of electron densities in the core region for several of the Minnesota functionals, including MN15-L.

As has been pointed out before,[125] inclusion of constant exact-exchange admixture in GHs does not necessarily help in the calculation of main-group shielding constants. Indeed, the GHs tend to be overall less accurate than the best (CDFT) meta-GGAs and partly even than the (nonspecialized) GGAs discussed above. The lowest aggregate MAE is observed with cTPSSh (2.6%), slightly better than the underlying CDFT meta-GGA cTPSS. This is followed by B97-2 (2.7%). Moderate overall improvement by constant EXX admixture can be seen for the series of the related BLYP (4.4%), B3LYP (3.8%), and BHLYP (3.1%). Improvements for the latter functional arise mostly from the values for the ^{11}B, ^{19}F, and ^{31}P/^{33}S subsets (see below). It is notable that the widely used B3LYP is far from being a top-performing functional for the present large main-group shielding test set. PBE0 and cPW6B95 are intermediate examples with aggregate rel. MAEs of 3.2 and 3.5%, respectively, followed by the Minnesota functionals cMN15 (4.0%, with large deviations of 10.2% for ^{31}P/^{33}S) and cM06-2X (4.2%). The remaining Minnesota functional cM06 (4.9%) performs worst, in fact worse than all semilocal functionals. We note in passing that PBE0 had been advocated earlier for nuclear shieldings,[99] but it clearly falls behind many other functionals studied here.

The best RSHs ωB97X-V (2.3%) and cωB97M-V (2.5%) improve only slightly over the best GHs. ωB97X-D (3.1%) and CAM-B3LYP (3.6%) are somewhat inferior. Notably, even these relatively sophisticated rung 4 functionals do not outperform the best rung 3 functionals, nor the specialized KTx rung 2 ones. We note in passing the possibility of "optimal tuning" of the range-separation parameter. While this may help improve excitation spectra, its usefulness for nuclear shieldings appears to be limited.[38]

As noted already above, matters are different for the LH functionals. Apart from the top-performing LH12ct-SsirPW92 (1.5%), LH12ct-SsifPW92 (1.5%), and LH20t (1.6%), several other LHs perform relatively well. This includes two further t-LMF-based ones, cLH07t-SVWN and cLH14t-calPBE (both 2.1%), followed by the sophisticated cmPSTS (2.4%). The s-LMF-based LH07s-SVWN (3.0%) only performs comparably to the better GHs, while cLHJ14 (3.9%) falls clearly behind. These differences are not too surprising when one examines the shape of the LMFs, particularly in the core regions around the nuclei of interest (Figure 2): while the t-LMF clearly

https://doi.org/10.1021/acs.jctc.1c00919
J. Chem. Theory Comput. 2021, 17, 7602−7621

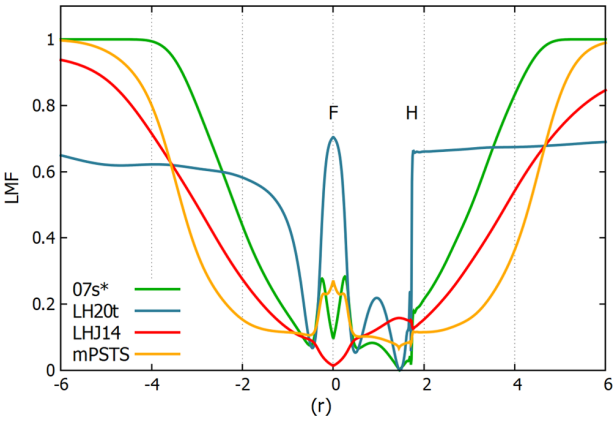

Figure 2. Plots of local mixing functions (LMFs) along the F−H bond in the HF molecule for various LH functionals; F is placed at the origin and H at 1.729 b (*07s corresponds to LH07s-SVWN).

increases toward the fluorine nucleus in the HF molecule shown, and the complicated LMF of mPSTS approaches this behavior, the s-LMF is known to have negative cusps at the nuclei and less pronounced wiggles in the bond. Finally, the "z-LMF" of LHJ14 actually presents low EXX admixture in the entire fluorine core region, which is clearly undesirable for nuclear shieldings, where larger EXX admixtures in the core and semicore regions are expected to enhance useful induced-current contributions and reduce delocalization errors. The shielding results clearly confirm the importance of the shape of the LMF in the core and semicore regions, motivating currently ongoing further developments of improved LMFs in our research group. Only LH20t and LH14t-calPBE exhibit calibrated exchange-energy densities. While this does not have an apparent effect on the aggregate rel. MAEs, we will see below that proton shieldings are improved (see, e.g., distances between red and black diamonds in Figure 1), and the best uncalibrated first-generation LDA-based LH12ct-SsirPW92 and LH12ct-SsifPW92 perform somewhat better for several of the other nuclei. Similar to cB97M-V, discussed above, the best-performing LHs cLH12ct-SsirPW92, cLH12ct-SsifPW92, and LH20t also give individual rel. MAEs below 3% for all subsets. Remarkably, the two former LHs even give rel. MAEs below 2% except for the $^{31}P/^{33}S$ subset.

Coming to rung 5, it seems appropriate to discuss the DH functionals together with MP2, as they all exhibit some form of MP2-type correlation contribution, as well as relatively high constant EXX contributions. As the performance of MP2 depends on how good Hartree−Fock is as a starting point, here we also discuss the HF results. The fact that HF exhibits a rel. MAE of only 3.1% for our overall test set, better than many DFT functionals, indicates that static-correlation cases do not determine the statistical evaluations in this work across the overall test set. This is clearly different when static correlation becomes large, as found in a parallel benchmark study on the NMR shifts of 3d transition-metal nuclei,[131] where HF and MP2 fail completely and thus DHs as well. Indeed, as mentioned already above, here MP2 (1.1%) only trails slightly behind DSD-PBEB86 (0.9%), while B2PG-PLYP (1.5%) falls into the range of the best LHs and CDFT meta-GGAs (see above) and B2PLYP (2.0%) is only slightly behind. Notably, together with cMN15-L (see above), MP2 is the only method here with overall aggregate positive MSE (Figure 1). Interestingly, this is reversed for the DHs, moderately so for DSD-PBEP86, more notably so for the other two functionals. That is, the DHs benefit to some extent from error compensation between too shielded values of MP2 and the commonly too deshielded ones of the DFT approaches. DSD-PBEP86 does this in the clearly most accurate way and is thus the overall frontrunner in the present comparison. We note the SCS-MP2-type correlation part and the 70% EXX admixture of this DH as possibly important factors for this performance. As will be discussed further below, DSD-PBEP86 manages simultaneously to largely conserve the outstanding performance of MP2 for some of the subsets with overall low static correlation (^{11}B, ^{13}C, ^{19}F) and to correct for deficiencies of MP2 for those with somewhat more static-correlation cases mixed in (^{15}N, ^{17}O). We should of course note here as well the substantially higher computational burden and the resulting limitation to smaller systems of MP2 and DHs compared to the DFT functionals on the lower rungs of the ladder.

In principle, the ^{1}H shielding constants are clearly the least critical, reflected by the small rel. MAEs in all functionals tested here (generally below 2% for all functionals evaluated in Figure 1, in contrast to HF). Accordingly, the aggregate rel. MAE deteriorates for most functionals when the ^{1}H shieldings are removed from the statistical data (see red diamonds relative to black diamonds). Hydrogen does not have a core shell and is dominated by the 1s shell with only some deformation of the electron density due to bonding. Consequently, paramagnetic contributions are smaller, and even relative shifts (see below) can be affected by both para- and diamagnetic terms. Only for those methods where the relative deviations for the nonhydrogen nuclei are already relatively small, we see the rel. MAEs to be similar with and without ^{1}H shieldings included. For cLH12ct-SsifPW92 the order is even reversed. This is due to somewhat larger deviations for ^{1}H shieldings (e.g., compared to the calibrated cLH20t) and the rather low deviations for the other nuclei.

So far, we have concentrated on the rel. MAEs and implicitly on the rel. MSEs. The rel. SDs indicate how narrow or wide the distributions of errors are. This is particularly important in the context of relative chemical shifts, where the absolute shielding is subtracted from that of a reference compound. This allows for the elimination of systematic constant errors in the absolute shieldings, for example arising from errors in the diamagnetic shielding term. We will discuss such relative shifts in a later section, but we can already anticipate methods for which such error compensation may be beneficial by examining the rel. SDs for the shieldings (which are equivalent to those for the shifts). That is, we should look for methods that have an SD significantly below the MAE.

Such examples, in particular with narrow SDs, are provided by a number of functionals. cTPSS (rel. SD 1.5%) and the related GH cTPSSh (1.3%), as well as the LH cmPSTS (1.3%), clearly point to such systematic deviations in the absolute shieldings, as do many of the simpler GGAs (with rel. SDs from 1.7 to 2.3%), as well as the meta-GGA $c\tau$-HCTH 1.7%, and many further GHs (B97-2 1.5%, B3LYP 1.9%, PBE0 2.0%, cM06 2.9%, cPW6B95 2.1%, cMN15 2.6%) and RSHs (CAM-B3LYP 2.2% and ωB97X-D 1.9%).

Among the LHs, those with the lowest rel. MAEs (see above) seem to have matchingly low rel. SDs, while some others seem to have narrower distributions than would appear from their MAEs. Apart from cmPSTS (see above), these are particularly LH07s-SVWN (1.8%), cLH07t-SVWN (1.4%),

https://doi.org/10.1021/acs.jctc.1c00919
J. Chem. Theory Comput. 2021, 17, 7602−7621

Table 5. The Ten Functionals with the Lowest MAE for Absolute Shieldings of Each Nucleus with Their Relative MAE (in %), MAE (in ppm), and Max. AE (in ppm), GIAO-DFT/pcSseg-3 vs GIAO-CCSD(T)/pcSseg-3

		functional	rel. MAE	MAE	max. AE
^{1}H	1	DSD-PBEP86	0.34	0.06	0.59
	2	B2GP-PLYP	0.47	0.08	0.58
	3	B2PLYP	0.56	0.09	0.67
	4	cLH20t	0.74	0.12	0.63
	5	cLH14t-calPBE	0.75	0.13	0.53
	6	ωB97X-D	0.77	0.13	0.68
	7	B97-2	0.78	0.13	1.09
	8	MP2	0.80	0.13	0.55
	9	BHLYP	0.82	0.14	0.63
	10	ωB97X-V	0.83	0.14	0.95
^{11}B	1	MP2	0.4	0.6	2.3
	2	cLH12ct-SsifPW92	0.9	1.3	5.0
	3	cLH12ct-SsirPW92	1.4	1.9	6.0
	4	cLH20t	1.8	2.6	7.5
	5	DSD-PBEP86	1.9	2.6	5.5
	6	KT3	2.4	3.3	6.5
	7	cVSXC	2.7	3.8	17.3
	8	KT2	2.9	4.0	8.4
	9	cB97M-V	2.9	4.1	8.2
	10	KT1	3.0	4.3	9.8
^{13}C	1	MP2	0.5	2.1	16.4
	2	cLH12ct-SsifPW92	1.2	4.9	27.2
	3	DSD-PBEP86	1.3	5.0	16.0
	4	cLH12ct-SsirPW92	1.4	5.7	26.9
	5	KT1	1.6	6.3	22.9
	6	cB97M-V	1.7	6.8	26.9
	7	KT2	1.7	7.0	19.8
	8	cMN15-L	1.8	7.2	40.0
	9	cLH20t	1.8	7.4	32.3
	10	KT3	1.9	7.5	19.5
^{15}N	1	cMN15-L	0.9	5.8	27.9
	2	DSD-PBEP86	1.2	7.5	40.5
	3	KT1	1.6	10.2	31.2
	4	cB97M-V	1.7	10.4	43.1
	5	cLH12ct-SsifPW92	1.8	11.1	47.8
	6	KT2	2.0	12.4	33.8
	7	cLH12ct-SsirPW92	2.0	12.5	50.7
	8	KT3	2.0	12.6	32.7
	9	B2GP-PLYP	2.0	12.7	31.1
	10	B2PLYP	2.5	15.5	37.9
^{17}O	1	DSD-PBEP86	0.9	7.0	36.4
	2	cLH12ct-SsifPW92	1.6	13.0	47.0
	3	B2GP-PLYP	1.8	14.0	59.6
	4	cLH12ct-SsirPW92	1.8	14.8	50.9
	5	cMN15-L	1.9	14.8	34.3
	6	cB97M-V	2.2	17.3	53.8
	7	B2PLYP	2.4	19.5	76.8
	8	cLH20t	2.6	20.5	56.1
	9	KT1	2.6	20.6	63.3
	10	cSCAN	2.6	20.9	96.9
^{19}F	1	MP2	0.6	5.2	34.2
	2	cLH12ct-SsifPW92	0.9	8.2	30.0
	3	DSD-PBEP86	1.0	9.0	22.9
	4	cMN15-L	1.0	9.4	25.5
	5	cLH12ct-SsirPW92	1.1	9.7	37.4
	6	cLH20t	1.3	11.6	40.2
	7	B2GP-PLYP	1.5	13.4	39.2
	8	BHLYP	1.8	16.7	65.5
	9	cB97M-V	1.9	17.3	48.4
	10	cLH07t-SVWN	1.9	17.8	61.9
^{31}P/^{33}S	1	DSD-PBEP86	1.1	9.2	17.2
	2	cB97M-V	1.4	12.2	32.3
	3	MP2	1.4	12.6	47.2
	4	cVSXC	1.5	13.2	37.8
	5	KT1	1.5	13.4	29.0
	6	KT3	1.7	15.2	35.3
	7	KT2	1.7	15.3	28.8
	8	cr^{2}SCAN	2.0	17.2	67.1
	9	cSCAN	2.1	17.7	70.1
	10	crSCAN	2.1	18.3	70.9

and cLH14t-calPBE (1.3%). Among the DHs, B2PLYP (1.1%) may benefit most from a compensation of systematic errors. We postpone the actual discussion of relative shifts to a later section.

The right bottom panel of Figure 1 gives also the max. rel. AE for each of the nuclei, providing additional insights into the robustness of a given approach. For example, in spite of its overall excellent performance, MP2 shows cases of particularly large maximum errors for the ^{15}N and ^{17}O subsets, reflecting cases with appreciable static correlation. This is largely corrected with the DSD-PBEP86 DH, which does not show particularly large max. AEs for any of the subsets. Overall, relatively small max. AEs are also seen for a number of functionals from rungs 3 and 4, with cB97M-V being particularly notable, but cMN15-L and several LHs also give a robust performance, followed by, e.g., KT2. We note in passing that some methods (including KT1) also exhibit surprisingly large max. rel. AEs of around 10% for ^{1}H shieldings, contrasting the overall relatively low average deviations for this nucleus.

The overall statistical evaluation given above should provide useful guidelines if one is interested, e.g., in applications to aide multinuclear NMR studies. Often we may be asked, however, to suggest best methods for one specific NMR nucleus. This benchmark also provides extensive information on this question. In the interest of conciseness, we give a more detailed discussion for the individual nuclei in the Supporting Information (see Section S1) and instead briefly focus here on the list of the 10 best-performing functionals (including MP2 as alternative approximate method) for each nucleus shown in Table 5 based on their MAEs (rel. MAEs in percentage and max. AEs in ppm are also provided). For the least critical ^{1}H shieldings, most methods give MAEs below the 0.34 ppm corresponding to 2% rel. MAE, and the best methods in Table 5 even come close to or pass the 0.1 ppm mark, with the top-performing DSD-PBEP86 significantly below. In contrast to the other nuclei, here even two GHs and two RSHs make it into the top-10 list.

Absolute ^{11}B shieldings are more challenging, albeit not very sensitive to static correlation, and the best performer MP2 is

https://doi.org/10.1021/acs.jctc.1c00919
J. Chem. Theory Comput. 2021, 17, 7602−7621

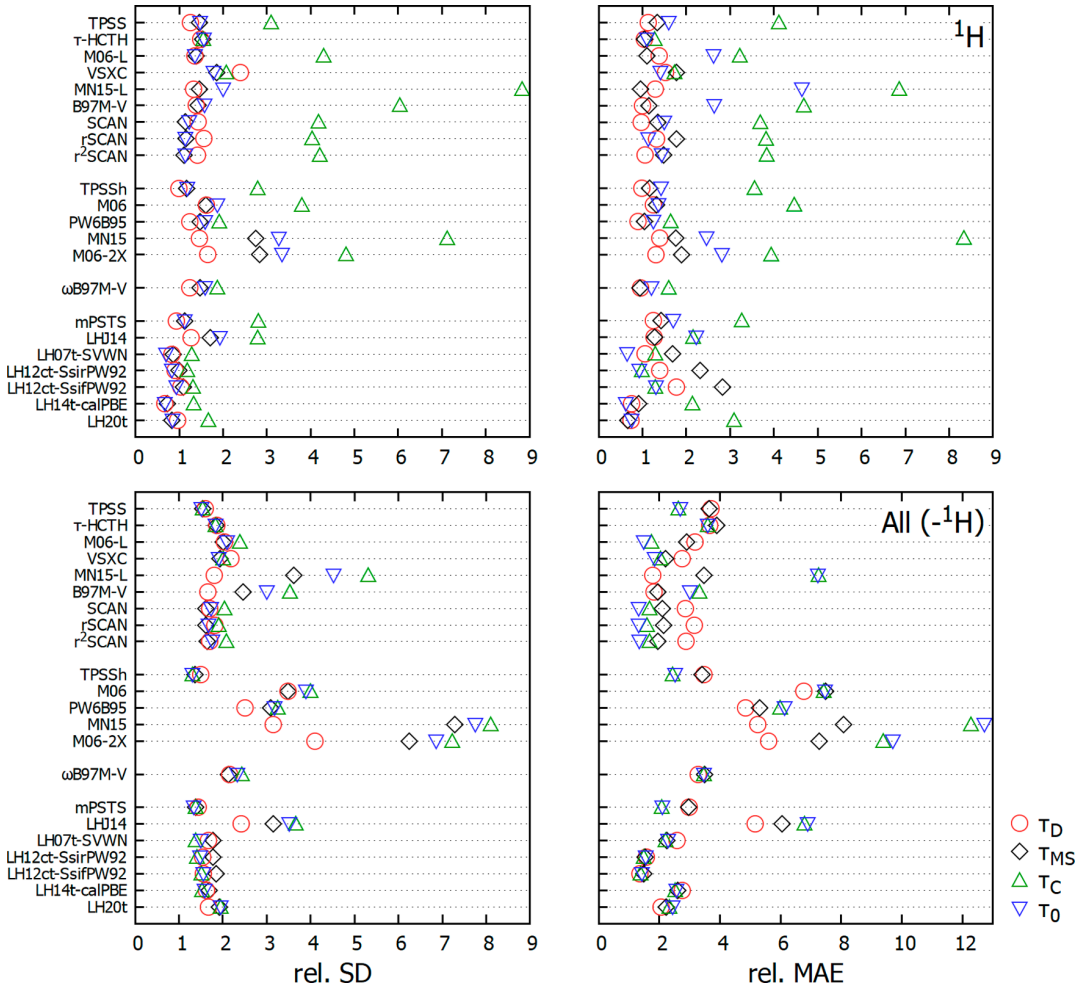

Figure 3. Comparison of relative standard deviations and relative mean absolute errors for four different treatments and implementations of τ-dependent functionals: top, ^{1}H shielding subset; bottom, aggregate deviations for the nonhydrogen shielding subsets.

followed by some LHs even before the more demanding DSD-PBEP86 DH. The much larger ^{13}C shielding subset is also excellently suited for MP2, which shows again an outstanding performance. Several LHs and the DSD-PBEP86 DH (which has the smallest max. AE) compete closely for the second position, with a number of other functionals not too far behind.

For ^{15}N shieldings, where static correlation plays a larger role, the CDFT meta-GGA cMN15-L strikingly takes the lead just before DSD-PBEP86 (MP2 is now far behind, not among the top 10 functionals, see the Supporting Information), followed by a number of functionals from rungs 2−5. Significant static-correlation effects hold also for the ^{17}O shieldings, even after exclusion of O_3. While this deteriorates the performance of MP2, which does not appear among the 10 best functionals, the DSD-PBEP86 DH is still the clear top-performer for this subset, followed by a number of functionals from different rungs, which can also be recommended for oxygen shielding constants (note the small max. AE of cMN15-L).

Static correlation is of lesser importance for the ^{19}F shielding subset (after excluding F_3^-), and MP2 appears again as the clear top-performer. Interestingly, two LHs and the cMN15-L CDFT meta-GGA compete with DSD-PBEP86 for the second place (the DH has, however, the smallest max. AE), and a number of further functionals from rungs 3 and 4 perform reasonably well too (including the BHLYP GH advocated before for ^{19}F shifts[132−135]). Finally, the small subset of third-period nuclei ^{31}P and ^{33}S is intermediate with regard to static correlation. Here, DSD-PBEP86 is the top-performer. Interestingly, the CDFT meta-GGA cB97M-V outperforms MP2 for the second place, at much lower computational cost, followed by a number of other functionals from rungs 2−4. The tested LHs perform only moderately well for this subset and do not make it into the top 10. This is potentially due to the fact that the t-LMF does not respect the high-density limit, which may become more important for heavier nuclei[136] (see further discussion in Section S1, Supporting Information).

Only DSD-PBEP86 appears in the top 10 functionals for all seven subsets. cB97M-V achieves this for six subsets and cLH12ct-SsifPW92, cLH12ct-SsirPW92, and KT1 for five subsets. The two remaining DHs B2GP-PLYP and B2PLYP appear in the list only in four subsets.

5.4. Comparison of Different Ways to Treat τ-Dependent Functionals. We have so far deliberately concentrated on the CDFT variants of the τ-dependent functionals using Dobson's τ_D model. The reason is that this is the physically best justified treatment. We had already pointed

https://doi.org/10.1021/acs.jctc.1c00919
J. Chem. Theory Comput. 2021, 17, 7602−7621

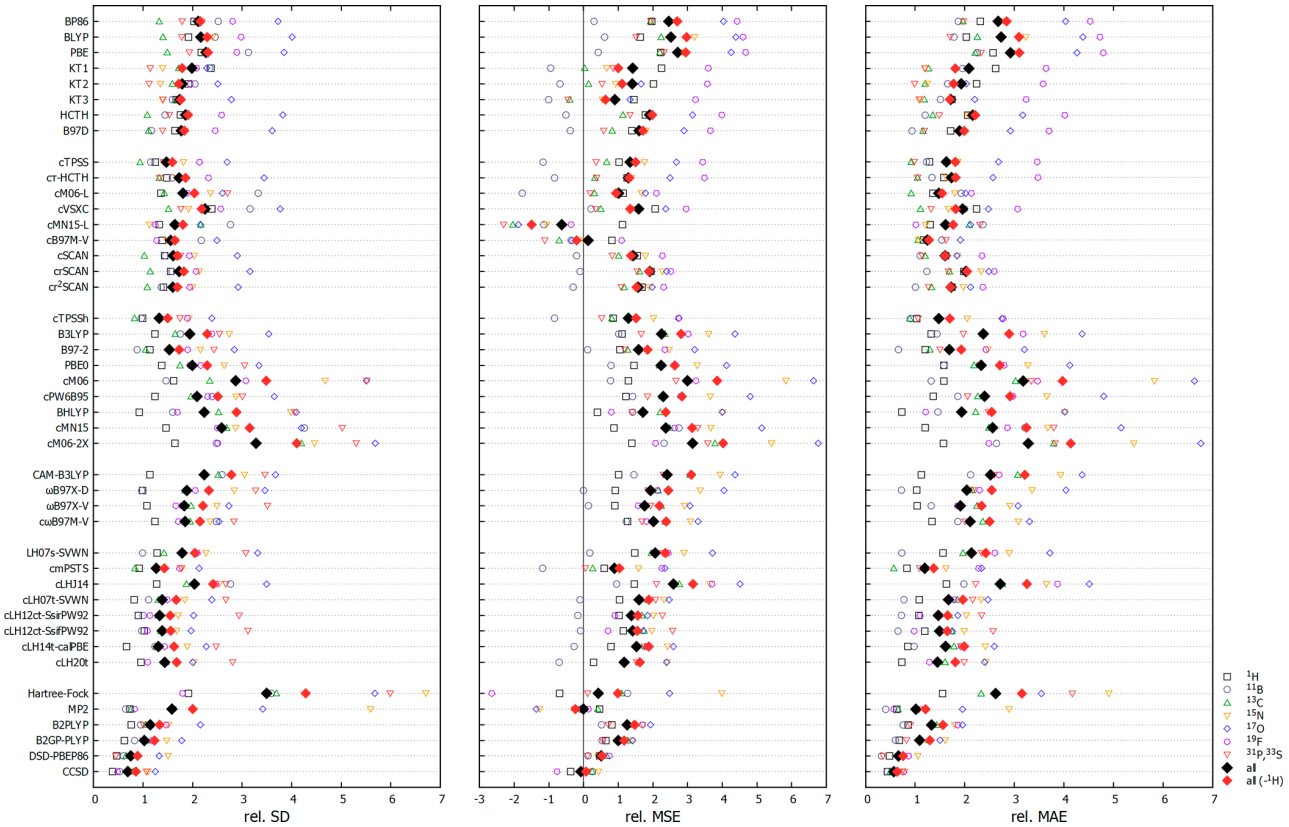

Figure 4. Relative deviations (in %, normalized to the shift range for a given nucleus) from the relative CCSD(T)/pcSseg-3 chemical shifts for different methods (with pcSseg-3 basis). Individual nuclei shown as open symbols, weighted aggregate relative deviations across all subsets as black diamonds, and when excluding the ^{1}H shieldings as red diamonds.

out theoretical disadvantages and paramagnetic artifacts of the widely used τ_{MS} model, the gauge dependence of using unmodified τ (leading to the τ_C model), as well as the ad hoc character of the truncated τ_0 model used so far as default ansatz in the ORCA code. However, as already discussed before,[22,23] this does not mean that the τ_D CDFT treatment gives the overall best agreement with the reference data for all functionals and subsets. Error compensation obviously can become important here, and we had already mentioned some cases where the other models seem to provide smaller deviations and have been touted in previous works. Here, we provide some more analyses on this point. Figure 3 gives rel. SDs and rel. MAEs for ^{1}H shieldings on top and the aggregate rel. deviations for the remaining nuclei at the bottom for all four treatments of τ mentioned here.

The rel. SDs and rel. MAEs provide rather similar information here, and we will not discuss them much separately. Starting with the ^{1}H shieldings, we see that for several meta-GGAs (MN15-L, TPSS, M06-L, B97M-V, SCAN, rSCAN, r^{2}SCAN), meta-GGA GHs (MN15, M06, TPSSh, M06-2X), and some LHs (mPSTS, LHJ14, LH20t, LH14t-calPBE), the gauge-dependent τ_C treatment provides by far larger errors than the other models. This suggests that the gauge dependence is a problem particularly for the hydrogen atoms on the periphery of the molecules when the gauge origin is placed at the center of mass. The ad hoc τ_0 treatment removes this gauge dependence and thereby improves matters, but does not do so completely in all cases (e.g., MN15-L, M06-L, B97M-V, MN15, M06-2X, LHJ14). Other functionals do not exhibit large deviations for τ_C (τHCTH, VSXC, partly PW6B95, ωB97M-V, LH07t-SVWN, LH12ct-SsirPW92, LH12ct-SsifPW92), showing that the construction of the τ-dependent functional plays a role in this context. Artifacts for ^{1}H shieldings of τ_{MS} with t-LMF-based LHs with uncalibrated exchange-energy densities (LH07t-SVWN, LH12ct-SsirPW92, LH12ct-SsifPW92) have been noted previously,[22,23] and are confirmed here for the much larger test set. This problem does not exist for the calibrated LHs (LH20t, LH14t-calPBE) and for mPSTS and LHJ14. Interestingly, for the three above-mentioned uncalibrated t-LMF-based LHs, the τ_0 and partly the τ_C treatments actually provide somewhat better agreement with the reference data, in a clear case of error compensation.

Turning to the nonhydrogen shieldings, we start by noting that induced paramagnetic currents[25] are now expected to play a more important role. Their τ-contributions are properly accounted for by the CDFT treatment (τ_D), but clearly neither by τ_C nor by τ_0. However, as noted above, this does not mean that τ_D will provide the smallest deviations for all functionals, as different factors may compensate each other. MN15-L is the most clearcut case where the CDFT treatment does indeed provide by far the best results. The same holds for MN15 and M06-2X (partly also for LHJ14), but with overall much larger deviations, while B97M-V shows smaller effects but still in favor of τ_D. For MN15-L, the rel. MSEs are generally positive (see Table S13 in the Supporting Information) and are reduced by the CDFT treatment, providing the noted improvements. For MN15, M06-2X, and LHJ14, the rel. MSEs become less negative. Cases where τ_C or τ_0 provide

https://doi.org/10.1021/acs.jctc.1c00919
J. Chem. Theory Comput. 2021, 17, 7602−7621

lower deviations than τ_D and τ_{MS} are the related TPSS, TPSSh, and mPSTS, but particularly also M06-L (and less so VSXC). For M06-L, this explains why some previous studies provided very accurate shielding and shift results with this functional for some main-group nuclei,[15,36,101] as the computations used either a gauge-dependent τ_C or τ_0. However, we do not want to recommend this procedure for a best-practice computational protocol due to (a) the already mentioned theoretical arguments that clearly favor τ_D and (b) the problems arising particularly for the ^{1}H shieldings (see above). Moreover, this work shows that better-performing methods with good theoretical justification are available. On the other hand, the CDFT versions cM06-L and cVSXC also perform reasonably well, albeit somewhat worse than their non-CDFT variants. Finally, we also note relatively small effects of the τ model on the nonhydrogen shieldings for various functionals (all t-LMF-based LHs, ωB97M-V). Here, we suspect that induced-current contributions to the XC response part are mainly covered by position-dependent or range-separated Hartree−Fock exchange, and the τ contributions are less important.

5.5. Method Performance for Relative NMR Shifts. Comparison with the experiment is most often done for relative chemical shifts, as absolute shieldings are rarely available for comparison. Computation of shifts allows some compensation of systematic errors to be made use of, for example if the electronic environment of the nucleus in the reference compound is chosen similar to the compounds to be studied. If we are interested, for example, in ^{13}C shifts in aromatic hydrocarbons, it may be preferable to use benzene as a reference compound rather than tetramethylsilane (TMS) or CH_4. Then, errors in the treatment of the paramagnetic terms, e.g., the typical overestimate made by many DFT methods, cancel out for the relative shifts. One may then easily shift the results back to the scale used by experimentalists, e.g., using the experimental shift of benzene relative to TMS. For a diverse shielding benchmark such as the one presented in this work, this provides only limited extra information of this type, as the molecules studied have been specifically selected to cover many different electronic situations for a given nucleus as well as very large shielding ranges (see above). The potential for beneficial error compensation thus arises only in cases where some constant errors are contained in the computed absolute shielding data for a given method, which are largely removed by subtracting the same error for the reference compound. The most likely candidate for such a constant error to be canceled is the diamagnetic term, which depends on the description of the spherical core shells. While a preliminary inspection of our data confirms this to be the case, the complications of identifying the relevant diamagnetic and paramagnetic contributions for GIAO-based computations let us refrain from a detailed analysis of such compensations in the present benchmark paper.

In the general statistical overview of the shielding part, we had already identified methods for which we expect such elimination of systematic errors. These should be the ones where the rel. SDs are smaller than the rel. MAEs, indicating a relatively narrow error distribution shifted from the origin. We will show below that this is indeed the case. The SDs are essentially the same here for the shifts (except for a small technical change for the ^{31}P/^{33}S subset due to the joint normalization of the deviations for two nuclei), so we should focus on the rel. MAEs (and rel. MSEs) for the shifts in comparison with those discussed already for the shieldings. These are shown in Figure 4 using CH_4 (^{1}H and ^{13}C), BF_3, NH_3, H_2O, HF, PH_3, and H_2S as the respective computational reference standards. Note that the signs of the MSEs are different due to the different sign convention of shieldings and shifts. As these are still comparisons against the GIAO-CCSD(T)/pcSseg-3 data, we do not need to apply any corrections and are free to use convenient standards with small paramagnetic contributions, without having to rely on experimental shift standards. See also Tables S15−S21 in the Supporting Information for full shift results of all nuclei and functionals and the complete statistical evaluation in Table S22.

While we mention the most accurate methods for which changes are small, the main focus will be on methods where accuracy for relative shifts is improved significantly. Starting with MP2 and the three DHs, we see that DSD-PBEP86 (rel. MAE 0.7%, rel. MSE +0.5%) and MP2 (rel. MAE 1.0%) are still the best methods, affected relatively little. Among the two remaining DHs B2PLYP (1.3%) and B2GP-PLYP (1.1%), the improvement by error compensation for the former is more pronounced. The best LHs are still only a bit behind, but now some LHs that had not been at the top for the shieldings (but had narrow SDs) also benefit: cmPSTS (1.2%) is now the top-performer, cLH20t, cLH12ct-SsirPW92, and cLH12ct-SsifPW92 (all 1.5%), cLH14t-calPBE (1.6%), and cLH07t-SVWN (1.7%) follow closely behind. cLHJ14 (2.7%) still gives the poorest performance, but it also benefits from error compensation for the shifts, as do essentially all simpler semilocal functionals (see below).

While the KT1, KT2, and KT3 functionals (2.1, 1.9, 1.7%) are still among the best GGAs, the distance to some of the others is now smaller (e.g., B97D 1.9%, HCTH 2.1%). The same holds for the CDFT meta-GGAs, where cB97M-V is now clearly the top-performing functional (1.2%, rel. MSE +0.1%), while cMN15-L (1.6%, rel. MSE −0.6%) still performs very well but is now rivaled by others: cM06-L (1.5%), cTPSS and cSCAN (both 1.6%), cτ-HCTH and cr^{2}SCAN (both 1.7%), and cVSXC and crSCAN (both 2.0%). The small SDs for the TPSS-related functionals (see also cmPSTS above) also help reduce the rel. MAE of TPSSh (1.5%), which is now the best GH, with only B97-2 (1.7%) and BHLYP (1.9%) also below 2%. While many of the other GHs also benefit from error compensation for the shifts, they are clearly still less accurate (from PBE0 2.3% to cM06-2X 3.3%). The RSHs also benefit, with rel. MAEs from 1.9% (ωB97M-V) to 2.5% (CAM-B3LYP). HF (2.6%) is now in the range of the less well-performing GGAs. Overall, we thus see that, due to the partial elimination of systematic errors, we have now more methods with rel. MAEs below 2% than for absolute shieldings. Those methods that perform already very well for absolute shieldings (see further above) and do not benefit particularly for this error compensation likely give particularly good descriptions of the inner core regions contributing to the diamagnetic term. We note in passing that maximum relative errors for the shifts of the various methods are similar to those for the shieldings. Therefore, we do not discuss them separately here but provide some additional information in the Supporting Information (Section S3).

As for the shieldings above, we can also get detailed information on the performance of the various functionals (again including MP2) for the shifts of the different subsets, and again we provide a detailed discussion in the Supporting Information (Section S2). A short overview of the 10 best-

https://doi.org/10.1021/acs.jctc.1c00919
J. Chem. Theory Comput. 2021, 17, 7602−7621

Table 6. The Ten Functionals with the Lowest MAE for Relative Shifts of Each Nucleus with Their Relative MAE (in %), MAE (in ppm), and Max. AE (in ppm) (GIAO-DFT/pcSseg-3 vs GIAO-CCSD(T)/pcSseg-3)

		functional	rel. MAE	MAE	max. AE
^{1}H	1	DSD-PBEP86	0.48	0.08	0.64
	2	MP2	0.63	0.11	0.51
	3	B2GP-PLYP	0.68	0.11	0.64
	4	cLH20t	0.73	0.12	0.63
	5	BHLYP	0.73	0.12	0.78
	6	cmPSTS	0.83	0.14	0.71
	7	cLH14t-calPBE	0.85	0.14	0.55
	8.	B2PLYP	0.86	0.15	0.77
	9	cTPSSh	1.03	0.17	0.82
	10	ωB97X-D	1.03	0.17	0.84
^{11}B	1	DSD-PBEP86	0.3	0.4	3.0
	2	MP2	0.4	0.6	2.3
	3	B2GP-PLYP	0.6	0.9	4.5
	4	cLH12ct-SsifPW92	0.7	0.9	3.9
	5	B97-2	0.7	0.9	2.6
	6	ωB97X-D	0.7	1.0	2.7
	7	cLH12ct-SsirPW92	0.7	1.0	3.8
	8	LH07s-SVWN	0.7	1.0	2.9
	9	B2PLYP	0.8	1.1	3.7
	10	cLH07t-SVWN	0.8	1.1	3.6
^{13}C	1	cmPSTS	0.6	2.3	15.0
	2	MP2	0.7	2.6	14.8
	3	DSD-PBEP86	0.7	2.8	13.6
	4	cTPSSh	0.9	3.6	13.3
	5	cTPSS	0.9	3.7	11.8
	6	cM06-L	0.9	3.7	35.2
	7	cτ-HCTH	1.0	4.2	21.6
	8	cB97M-V	1.1	4.2	34.4
	9	cVSXC	1.1	4.5	35.6
	10	B97D	1.2	4.6	14.5
^{15}N	1	DSD-PBEP86	1.1	6.6	41.9
	2	cB97M-V	1.1	6.6	33.6
	3	KT3	1.1	7.0	24.6
	4	KT1	1.2	7.4	26.7
	5	cMN15-L	1.2	7.6	31.2
	6	KT2	1.2	7.8	28.0
	7	B2GP-PLYP	1.6	10.1	28.2
	8	cmPSTS	1.6	10.2	62.9
	9	cτ-HCTH	1.6	10.2	35.7
	10	cVSXC	1.7	10.4	52.7
^{17}O	1	DSD-PBEP86	0.8	6.2	45.4
	2	B2GP-PLYP	1.5	12.0	73.8
	3	cLH12ct-SsifPW92	1.8	14.0	61.4
	4	KT1	1.8	14.6	72.9
	5	cSCAN	1.8	14.7	115.6
	6	cLH12ct-SsirPW92	1.9	14.9	65.1
	7	cB97M-V	1.9	15.3	58.2
	8	MP2	2.0	15.6	138.0
	9	B2PLYP	2.0	15.6	93.9
	10	cM06-L	2.0	16.1	103.8
^{19}F	1	MP2	0.6	5.3	34.1
	2	DSD-PBEP86	0.9	8.0	25.3
	3	cLH12ct-SsifPW92	1.0	9.0	36.0
	4	cMN15-L	1.0	9.4	31.9
	5	cLH12ct-SsirPW92	1.1	10.1	43.7
	6	BHLYP	1.2	11.2	69.2
	7	cB97M-V	1.3	11.8	48.8
	8	cLH20t	1.3	11.9	46.8
	9	B2GP-PLYP	1.3	11.9	43.6
	10	cLH07t-SVWN	1.8	16.5	70.1
^{31}P/^{33}S	1	DSD-PBEP86	0.4	3.1	9.7
	2	B2GP-PLYP	0.8	7.2	28.1
	3	B2PLYP	0.9	7.9	26.4
	4	cTPSS	1.0	8.6	41.1
	5	KT2	1.0	8.8	22.5
	6	cτ-HCTH	1.0	9.2	33.7
	7	cTPSSh	1.1	9.2	54.6
	8	MP2	1.1	9.3	42.4
	9	KT3	1.1	9.6	38.5
	10	cmPSTS	1.1	9.4	50.6

performing functionals for the relative shifts of each nucleus is provided in Table 6 in the same manner as Table 5 gave for shieldings. Note that the abovementioned error compensation does not work in most cases for the ^{1}H shifts, due to the absence of a core shell. Here, the rel. MAEs for the shifts are often even somewhat larger than those discussed further above for the shieldings. Compensation of some systematic errors is, however, seen for a few cases like cLH12ct-SsirPW92, cLH12ct-SsifPW92, cmPSTS, HF, and SVWN. The cLH20t LH provides the best performance for the ^{1}H shifts below rung 5.

Massive improvements for a number of methods are seen upon going from shieldings to shifts for the ^{11}B subset. DSD-PBEP86, which had been clearly behind MP2 for absolute shieldings, now gives the lowest MAE, below 0.5 ppm! MP2 is then followed closely by a number of functionals from rungs 2−5 with MAEs around the 1 ppm mark. Somewhat less pronounced but still notable differences between shieldings and shifts apply to the ^{13}C subset. Now, the cmPSTS LH slightly outperforms even MP2 and DSD-PBEP86, and several functionals from rungs 3 and 4 are not far behind, including TPSS and TPSSh.

Error compensation is less pronounced for the ^{15}N shifts, due to the larger paramagnetic terms. cB97M-V and DSD-PBEP86 give the lowest MAEs, closely followed by cMN15-L and the KT*x* family of functionals. Small error compensation is seen also for the ^{17}O shifts. DSD-PBEP86 clearly performs best, followed by B2GP-PLYP and a number of functionals from rungs 2−4 (Table 6). Error compensation is probably smallest for the ^{19}F shifts, where MP2 and DSD-PBEP86 still perform best, and the other top performers still follow a similar order as for the shieldings, including a number of LHs, DHs, CDFT meta-GGAs, and the GH BHLYP.

For the third-row nuclei ^{31}P and ^{33}S, the systematic errors of some functionals in the diamagnetic part seem to be particularly large, and performance can change significantly upon going to the shifts. Indeed, for several functionals, the deviations for shifts are much smaller than for shieldings. Several functionals from rungs 2−5 now outperform MP2, with DSD-PBEP86 again being clearly the top-performer.

https://doi.org/10.1021/acs.jctc.1c00919
J. Chem. Theory Comput. 2021, 17, 7602−7621

6. CONCLUSIONS

An extended benchmark set of light main-group nuclear shielding constants and NMR shifts, NS372, with 372 shielding constants for 117 molecules has been constructed, uniformly based on accurate ab initio data at the GIAO-CCSD(T)/pcSseg-3//CCSD(T)/cc-pVQZ level. The test set combines many molecules contained in earlier, smaller sets, typically for only one or two nuclei, and it adds many more systems that cover a wide range of electronic-structure situations. This allows an unprecedentedly detailed evaluation of more approximate quantum-chemical methods, in particular, different exchange−correlation functionals of Kohn−Sham density functional theory. Adding up weighted relative deviations normalized to the shielding range of a given nucleus has allowed us to compare different methods across the entire ^{1}H, ^{11}B, ^{13}C, ^{15}N, ^{17}O, ^{19}F, and ^{31}P/^{33}S test set, comparing HF, MP2, and CCSD, as well as density functionals from all five rungs of the usual ladder.

As HF is found to be a reasonable starting point for the ^{11}B, ^{13}C, ^{19}F, and ^{31}P/^{33}S subsets, MP2 performs excellently in those cases, and double hybrids (rung 5) that incorporate MP2 correlation are also outstanding, with the spin-scaling-DH DSD-PBEP86 confirmed as the best DFT method for light main-group shieldings and shifts. The latter functional is also able to correct the somewhat larger errors of MP2 in the ^{15}N and ^{17}O subsets that feature more cases with larger static correlation (even while excluding O_3 for the ^{17}O subset). Two further double hybrids evaluated, B2PLYP and particularly B2GP-PLYP, also perform well but not as consistently. Given the large computational demands of GIAO computations with MP2 and double hybrids, and the resulting limitations in the sizes of molecules to which these methods are applicable, it is gratifying that a number of DFT functionals on the lower rungs of the ladder could be identified, that also provide accurate shieldings and shifts. We note that, due to compensation of errors resulting from diamagnetic shielding contributions, a number of methods perform even better for relative shifts. Looking for methods that work well across the entire test set we find, in addition to specialized GGA functionals (KT1−KT3) fitted explicitly for main-group shifts (rung 2), current density functional implementations of several meta-GGA functionals (rung 3; in particular cB97M-V, cMN15-L) and local hybrid functionals with position-dependent exact-exchange admixtures (rung 4; several functionals from our group with t-LMFs and the more complicated mPSTS) to provide promising alternatives to the computationally more expensive methods. Indeed, the CDFT meta-GGA cB97M-V makes it into the list of the 10 best functionals for the shifts for six out of seven subsets, and the cLH12ct-SsifPW92 and cLH12ct-SsifPW92 LHs achieve this for five subsets. The fact that these functionals do not exhibit large maximum absolute errors for any of the subsets (in contrast to, e.g., MP2 for some cases with significant static correlation) also attests to their robustness.

This work is considered an important step in a more extensive benchmarking of quantum-chemical methods for the computation of NMR parameters, aiming toward accurate and computationally expedient methods that work across the periodic table. Obviously, this will also need to include spin−spin coupling constants, and it has to extend to heavier main-group systems, as well as to d- and f-element compounds (including both metal and ligand NMR parameters). This will require us to go beyond the present nonrelativistic framework, and to also include environmental effects in the condensed phase. Work along these lines has been initiated. The long-term goal is to combine the resulting approaches also with conformational averaging procedures as described by Grimme and co-workers (see Introduction) to arrive at the accurate and reliable quantum-chemical simulation of full NMR spectra.

■ ASSOCIATED CONTENT

Supporting Information

The Supporting Information is available free of charge at https://pubs.acs.org/doi/10.1021/acs.jctc.1c00919.

Detailed discussions on the performance of the different methods for shieldings and shifts of individual subsets and a short discussion of maximum relative errors for the shifts of different subsets (PDF)

Overview of the molecules of the benchmark set, the available CCSD and CCSD(T) data, the complete CC diagnostics for all molecules, estimates of the accuracy of the GIAO-CCSD(T) shielding results and the effect of the input structures, full shielding, and shift results, as well as statistics for all functionals including additional τ models; comparisons of the statistical results for a subset of functionals using pcSseg-3 vs pcSseg-4 basis sets, and the CCSD(T)/cc-pVQZ input structures (XLSX)

■ AUTHOR INFORMATION

Corresponding Author

Martin Kaupp − *Technische Universität Berlin, Institut für Chemie, Theoretische Chemie/Quantenchemie, D-10623 Berlin, Germany;* orcid.org/0000-0003-1582-2819; Email: martin.kaupp@tu-berlin.de

Author

Caspar Jonas Schattenberg − *Technische Universität Berlin, Institut für Chemie, Theoretische Chemie/Quantenchemie, D-10623 Berlin, Germany*

Complete contact information is available at: https://pubs.acs.org/10.1021/acs.jctc.1c00919

Notes

The authors declare no competing financial interest.

■ ACKNOWLEDGMENTS

This work has been supported by Deutsche Forschungsgemeinschaft within CRC 1349 (SFB 1349) "Fluorine Specific Interactions"—Project ID 387284271. C.J.S. is grateful for a Ph.D. scholarship provided by Studienstiftung des deutschen Volkes.

■ REFERENCES

(1) Gauss, J.; Stanton, J. F. Coupled-cluster calculations of nuclear magnetic resonance chemical shifts. *J. Chem. Phys.* **1995**, *103*, 3561−3577.

(2) Gauss, J.; Stanton, J. F. Perturbative treatment of triple excitations in coupled-cluster calculations of nuclear magnetic shielding constants. *J. Chem. Phys.* **1996**, *104*, 2574−2583.

(3) Helgaker, T.; Jaszuński, M.; Ruud, K. Ab Initio Methods for the Calculation of NMR Shielding and Indirect Spin-Spin Coupling Constants. *Chem. Rev.* **1999**, *99*, 293−352.

(4) Helgaker, T.; Coriani, S.; Jørgensen, P.; Kristensen, K.; Olsen, J.; Ruud, K. Recent Advances in Wave Function-Based Methods of Molecular-Property Calculations. *Chem. Rev.* **2012**, *112*, 543−631.

(5) London, F. Théorie quantique des courants interatomiques dans les combinaisons aromatiques. *J. Phys. Radium* **1937**, *8*, 397−409.
(6) Ditchfield, R. Self-consistent perturbation theory of diamagnetism. *Mol. Phys.* **1974**, *27*, 789−807.
(7) Wolinski, K.; Hinton, J. F.; Pulay, P. Efficient Implementation of the Gauge-Independent Atomic Orbital Method for NMR Chemical Shift Calculations. *J. Am. Chem. Soc.* **1990**, *112*, 8251−8260.
(8) Bühl, M.; van Mourik, T. NMR spectroscopy: quantum-chemical calculations. *Wiley Interdiscip. Rev.: Comput. Mol. Sci.* **2011**, *1*, 634−647.
(9) Lodewyk, M. W.; Siebert, M. R.; Tantillo, D. J. Computational Prediction of ^{1}H and ^{13}C Chemical Shifts: A Useful Tool for Natural Product, Mechanistic, and Synthetic Organic Chemistry. *Chem. Rev.* **2012**, *112*, 1839−1862.
(10) Flaig, D.; Maurer, M.; Hanni, M.; Braunger, K.; Kick, L.; Thubauville, M.; Ochsenfeld, C. Benchmarking Hydrogen and Carbon NMR Chemical Shifts at HF, DFT, and MP2 Levels. *J. Chem. Theory Comput.* **2014**, *10*, 572−578.
(11) Maurer, M.; Ochsenfeld, C. Spin Component-Scaled Second-Order Møller-Plesset Perturbation Theory for Calculating NMR Shieldings. *J. Chem. Theory Comput.* **2015**, *11*, 37−44.
(12) Perdew, J. P.; Schmidt, K. Jacob's ladder of density functional approximations for the exchange-correlation energy. *AIP Conf. Proc.* **2001**, *577*, 1−20.
(13) Kozuch, S.; Martin, J. M. L. DSD-PBEP86: In search of the best double-hybrid DFT with spin-component scaled MP2 and dispersion corrections. *Phys. Chem. Chem. Phys.* **2011**, *13*, 20104−20107.
(14) Kozuch, S.; Martin, J. M. L. Spin-Component-Scaled Double Hybrids: An Extensive Search for the Best Fifth-Rung Functionals Blending DFT and Perturbation Theory. *J. Comput. Chem.* **2013**, *34*, 2327−2344.
(15) Stoychev, G. L.; Auer, A. A.; Neese, F. Efficient and Accurate Prediction of Nuclear Magnetic Resonance Shielding Tensors with Double-Hybrid Density Functional Theory. *J. Chem. Theory Comput.* **2018**, *14*, 4756−4771.
(16) de Oliveira, M. T.; Alves, J. M. A.; Braga, A. A. C.; Wilson, D. J. D.; Barboza, C. A. Do Double-Hybrid Exchange-Correlation Functionals Provide Accurate Chemical Shifts? A Benchmark Assessment for Proton NMR. *J. Chem. Theory Comput.* **2021**, 6876−6885.
(17) Stoychev, G. L.; Auer, A. A.; Gauss, J.; Neese, F. DLPNO-MP2 second derivatives for the computation of polarizabilities and NMR shieldings. *J. Chem. Phys.* **2021**, *154*, No. 164110.
(18) Grimme, S.; Bannwarth, C.; Dohm, S.; Hansen, A.; Pisarek, J.; Pracht, P.; Seibert, J.; Neese, F. Fully Automated Quantum-Chemistry-Based Computation of Spin-Spin-Coupled Nuclear Magnetic Resonance Spectra. *Angew. Chem., Int. Ed.* **2017**, *56*, 14763−14769.
(19) Jaramillo, J.; Scuseria, G. E.; Ernzerhof, M. Local hybrid functionals. *J. Chem. Phys.* **2003**, *118*, 1068−1073.
(20) Maier, T. M.; Arbuznikov, A. V.; Kaupp, M. Local hybrid functionals: Theory, implementation, and performance of an emerging new tool in quantum chemistry and beyond. *Wiley Interdiscip. Rev.: Comput. Mol. Sci.* **2019**, *9*, No. e1378.
(21) Schattenberg, C. J.; Reiter, K.; Weigend, F.; Kaupp, M. An Efficient Coupled-Perturbed Kohn-Sham Implementation of NMR Chemical Shift Computations with Local Hybrid Functionals and Gauge-Including Atomic Orbitals. *J. Chem. Theory Comput.* **2020**, *16*, 931−943.
(22) Schattenberg, C. J.; Kaupp, M. Effect of the Current Dependence of Tau-Dependent Exchange-Correlation Functionals on Nuclear Shielding Calculations. *J. Chem. Theory Comput.* **2021**, *17*, 1469−1479.
(23) Schattenberg, C. J.; Kaupp, M. Implementation and Validation of Local Hybrid Functionals with Calibrated Exchange-Energy Densities for Nuclear Shielding Constants. *J. Chem. Phys. A* **2021**, 2697−2707.
(24) Haasler, M.; Maier, T. M.; Grotjahn, R.; Gückel, S.; Arbuznikov, A. V.; Kaupp, M. A Local Hybrid Functional with Wide Applicability and Good Balance between (De)Localization and Left-Right Correlation. *J. Chem. Theory Comput.* **2020**, *16*, 5645−5657.
(25) Reimann, S.; Ekström, U.; Stopkowicz, S.; Teale, A. M.; Borgoo, A.; Helgaker, T. The importance of current contributions to shielding constants in density-functional theory. *Phys. Chem. Chem. Phys.* **2015**, *17*, 18834−18842.
(26) Dobson, J. F. Spin-density functionals for the electron correlation energy with automatic freedom from orbital self-interaction. *J. Phys.: Condens. Matter* **1992**, *4*, 7877−7890.
(27) Dobson, J. F. Alternative expressions for the Fermi hole curvature. *J. Chem. Phys.* **1993**, *98*, 8870−8872.
(28) Maximoff, S. N.; Scuseria, G. E. Nuclear magnetic resonance shielding tensors calculated with kinetic energy density-dependent exchange-correlation functionals. *Chem. Phys. Lett.* **2004**, *390*, 408−412.
(29) Auer, A. A.; Gauss, J.; Stanton, J. F. Quantitative prediction of gas-phase ^{13}C nuclear magnetic shielding constants. *J. Chem. Phys.* **2003**, *118*, 10407−10417.
(30) Harding, M. E.; Lenhart, M.; Auer, A. A.; Gauss, J. Quantitative prediction of gas-phase ^{19}F nuclear magnetic shielding constants. *J. Chem. Phys.* **2008**, *128*, No. 244111.
(31) Auer, A. A. Quantitative prediction of gas-phase ^{17}O nuclear magnetic shielding constants. *J. Chem. Phys.* **2009**, *131*, No. 024116.
(32) Prochnow, E.; Auer, A. A. Quantitative prediction of gas-phase ^{15}N and ^{31}P nuclear magnetic shielding constants. *J. Chem. Phys.* **2010**, *132*, No. 064109.
(33) Gregušová, A.; Perera, A.; Bartlett, R. J. Accuracy of Computed ^{15}N Nuclear Magnetic Resonance Chemical Shifts. *J. Chem. Theory Comput.* **2010**, *6*, 1228−1239.
(34) Kupka, T.; Stachów, M.; Nieradka, M.; Kaminsky, J.; Pluta, T. Convergence of Nuclear Magnetic Shieldings in the Kohn-Sham Limit for Several Small Molecules. *J. Chem. Theory Comput.* **2010**, *6*, 1580−1589.
(35) Teale, A. M.; Lutnaes, O. B.; Helgaker, T.; Tozer, D. J.; Gauss, J. Benchmarking density-functional theory calculations of NMR shielding constants and spin-rotation constants using accurate coupled-cluster calculations. *J. Chem. Phys.* **2013**, *138*, No. 024111.
(36) Stoychev, G. L.; Auer, A. A.; Izsàk, R.; Neese, F. Self-Consistent Field Calculation of Nuclear Magnetic Resonance Chemical Shielding Constants Using Gauge-Including Atomic Orbitals and Approximate Two-Electron Integrals. *J. Chem. Theory Comput.* **2018**, *14*, 619−637.
(37) Kupka, T.; Leszczyńska, M.; Ejsmont, K.; Mnich, A.; Broda, M.; Thangavel, K.; Kaminský, J. Phosphorus mononitride: A difficult case for theory. *Int. J. Quantum Chem.* **2019**, No. e26032.
(38) Prokopiou, G.; Autschbach, J.; Kronik, L. Assessment of the Performance of Optimally Tuned Range-Separated Hybrid Functionals for Nuclear Magnetic Shielding Calculations. *Adv. Theory Simul.* **2020**, *3*, No. 2000083.
(39) Bates, J. E.; Furche, F. Harnessing the meta-generalized gradient approximation for time-dependent density functional theory. *J. Chem. Phys.* **2012**, *137*, No. 164105.
(40) Sagvolden, E.; Ekström, U.; Tellgren, E. I. Isoorbital indicators for current density functional theory. *Mol. Phys.* **2013**, *111*, 1295−1302.
(41) Tao, J. Explicit inclusion of paramagnetic current density in the exchange-correlation functionals of current-density functional theory. *Phys. Rev. B* **2005**, *71*, No. 205107.
(42) Becke, A. D. Current density in exchange-correlation functionals: Application to atomic states. *J. Chem. Phys.* **2002**, *117*, 6935−6938.
(43) Furness, J. W.; Verbeke, J.; Tellgren, E. I.; Stopkowicz, S.; Ekström, U.; Helgaker, T.; Teale, A. M. Current Density Functional Theory Using Meta-Generalized Gradient Exchange-Correlation Functionals. *J. Chem. Theory Comput.* **2015**, *11*, 4169−4181.
(44) Holzer, C.; Franzke, Y. J.; Kehry, M. Assessing the Accuracy of Local Hybrid Density Functional Approximations for Molecular Response Properties. *J. Chem. Theory Comput.* **2021**, *17*, 2928−2947.
(45) Neese, F. Software update: the ORCA program system, version 4.0. *Wiley Interdiscip. Rev.: Comput. Mol. Sci.* **2017**, *8*, No. e1327.

https://doi.org/10.1021/acs.jctc.1c00919
J. Chem. Theory Comput. 2021, 17, 7602−7621

(46) Neese, F.; Wennmohs, F.; Becker, U.; Riplinger, C. The ORCA quantum chemistry program package. *J. Chem. Phys.* **2020**, *152*, No. 224108.
(47) Jensen, F. Segmented Contracted Basis Sets Optimized for Nuclear Magnetic Shielding. *J. Chem. Theory Comput.* **2015**, *11*, 132−138.
(48) Dunning, T. H. Gaussian basis sets for use in correlated molecular calculations. I. The atoms boron through neon and hydrogen. *J. Chem. Phys.* **1989**, *90*, 1007−1023.
(49) Woon, D. E.; Dunning, T. H. Gaussian basis sets for use in correlated molecular calculations. III. The atoms aluminum through argon. *J. Chem. Phys.* **1993**, *98*, 1358−1371.
(50) Bursch, M.; Gasevic, T.; Stückrath, J. B.; Grimme, S. Comprehensive Benchmark Study on the Calculation of ^{29}Si NMR Chemical Shifts. *Inorg. Chem.* **2021**, *60*, 272−285.
(51) Kendall, R. A.; Dunning, T. H.; Harrison, R. J. Electron affinities of the first-row atoms revisited. Systematic basis sets and wave functions. *J. Chem. Phys.* **1992**, *96*, 6796−6806.
(52) Prascher, B. P.; Woon, D. E.; Peterson, K. A.; Dunning, T. H., Jr.; Wilson, A. K. Gaussian basis sets for use in correlated molecular calculations. VII. Valence, core-valence, and scalar relativistic basis sets for Li, Be, Na, and Mg. *Theor. Chem. Acc.* **2011**, *128*, 69−82.
(53) CFOUR, a Quantum Chemical Program Package written by Stanton, J. F.; Gauss, J.; Cheng, L.; Harding, M. E.; Matthews, D. A.; Szalay, P. G. with contributions from Auer, A. A., Bartlett, R. J., Benedikt, U., Berger, C., Bernholdt, D. E., Bomble, Y. J., Christiansen, O., Engel, F., Faber, R., Heckert, M., Heun, O., Hilgenberg, M., Huber, C., Jagau, T.-C., Jonsson, D., Jusélius, J., Kirsch, T., Klein, K., Lauderdale, W. J., Lipparini, F., Metzroth, T., Mück, L. A., O'Neill, D. P., Price, D. R., Prochnow, E., Puzzarini, C., Ruud, K., Schiffmann, F., Schwalbach, W., Simmons, C., Stopkowicz, S., Tajti, A., Vázquez, J., Wang, F., Watts, J. D. http://www.cfour.de.
(54) Lee, T. J.; Taylor, P. R. A diagnostic for determining the quality of single-reference electron correlation methods. *Int. J. Quantum Chem.* **1989**, *36*, 199−207.
(55) Janssen, C. L.; Nielsen, I. M. B. New diagnostics for coupled-cluster and Møller-Plesset perturbation theory. *Chem. Phys. Lett.* **1998**, *290*, 423−430.
(56) Karton, A.; Rabinovich, E.; Martin, J. M. L.; Ruscic, B. W4 theory for computational thermochemistry: In pursuit of confident sub-kJ/mol predictions. *J. Chem. Phys.* **2006**, *125*, No. 144108.
(57) Karton, A.; Daon, S.; Martin, J. M. L. W4-11: A high-confidence benchmark dataset for computational thermochemistry derived from first-principles W4 data. *Chem. Phys. Lett.* **2011**, *510*, 165−178.
(58) Werner, H.-J.; Knowles, P. J.; Knizia, G.; Manby, F. R.; Schütz, M.; Celani, P.; Györffy, W.; Kats, D.; Korona, T.; Lindh, R.; Mitrushenkov, A.; Rauhut, G.; Shamasundar, K. R.; Adler, T. B.; Amos, R. D.; Bennie, S. J.; Bernhardsson, A.; Berning, A.; Cooper, D. L.; Deegan, M. J. O.; Dobbyn, A. J.; Eckert, F.; Goll, E.; Hampel, C.; Hesselmann, A.; Hetzer, G.; Hrenar, T.; Jansen, G.; Köppl, C.; Lee, S. J. R.; Liu, Y.; Lloyd, A. W.; Ma, Q.; Mata, R. A.; May, A. J.; McNicholas, S. J.; Meyer, W.; Miller, T. F.; Mura, M. E.; Nicklass, A.; O'Neill, D. P.; Palmieri, P.; Peng, D.; Pflüger, K.; Pitzer, R.; Reiher, M.; Shiozaki, T.; Stoll, H.; Stone, A. J.; Tarroni, R.; Thorsteinsson, T.; Wang, M.; Welborn, M. *MOLPRO, a Package of Ab Initio Programs*, version 2019.2; MOLPRO, 2019. https://www.molpro.net.
(59) Jiang, W.; DeYonker, N. J.; Wilson, A. K. Multireference Character for 3d Transition-Metal-Containing Molecules. *J. Chem. Theory Comput.* **2012**, *8*, 460−468.
(60) Repisky, M.; Komorovsky, S.; Kadek, M.; Konecny, L.; Ekström, U.; Malkin, E.; Kaupp, M.; Ruud, K.; Malkina, O. L.; Malkin, V. G. ReSpect: Relativistic spectroscopy DFT program package. *J. Chem. Phys.* **2020**, *152*, No. 184101.
(61) Komorovský, S.; Repiský, M.; Malkina, O. L.; Malkin, V. G.; Malkin Ondík, I.; Kaupp, M. A fully relativistic method for calculation of nuclear magnetic shielding tensors with a restricted magnetically balanced basis in the framework of the matrix Dirac-Kohn-Sham equation. *J. Chem. Phys.* **2008**, *128*, No. 104101.
(62) Komorovský, S.; Repiský, M.; Malkina, O. L.; Malkin, V. G. Fully relativistic calculations of NMR shielding tensors using restricted magnetically balanced basis and gauge including atomic orbitals. *J. Chem. Phys.* **2010**, *132*, No. 154101.
(63) Jensen, F. Basis Set Convergence of Nuclear Magnetic Shielding Constants Calculated by Density Functional Methods. *J. Chem. Theory Comput.* **2008**, *4*, 719−727.
(64) Local version derived from TURBOMOLE version 7.5, TURBOMOLE GmbH, 2020. TURBOMOLE is a development of University of Karlsruhe and Forschungszentrum Karlsruhe 1989−2007, TURBOMOLE GmbH since 2007.
(65) Reiter, K.; Mack, F.; Weigend, F. Calculation of Magnetic Shielding Constants with meta-GGA Functionals Employing the Multipole-Accelerated Resolution of the Identity: Implementation and Assessment of Accuracy and Efficiency. *J. Chem. Theory Comput.* **2018**, *14*, 191−197.
(66) Weigend, F. Accurate Coulomb-fitting basis sets for H to Rn. *Phys. Chem. Chem. Phys.* **2006**, *8*, 1057−1065.
(67) Perdew, J. P.; Staroverov, V. N.; Tao, J.; Scuseria, G. E. Density functional with full exact exchange, balanced nonlocality of correlation, and constraint satisfaction. *Phys. Rev. A* **2008**, *78*, No. 052513.
(68) Becke, A. D. Density-functional exchange-energy approximation with correct asymptotic behavior. *Phys. Rev. A* **1988**, *38*, 3098−3100.
(69) Becke, A. D. Correlation energy of an inhomogeneous electron gas: A coordinate-space model. *J. Chem. Phys.* **1988**, *88*, 1053−1062.
(70) Johnson, E. R. Local-hybrid functional based on the correlation length. *J. Chem. Phys.* **2014**, *141*, No. 124120.
(71) Arbuznikov, A. V.; Kaupp, M. Local hybrid exchange-correlation functionals based on the dimensionless density gradient. *Chem. Phys. Lett.* **2007**, *440*, 160−168.
(72) Kaupp, M.; Bahmann, H.; Arbuznikov, A. V. Local hybrid functionals: An assessment for thermochemical kinetics. *J. Chem. Phys.* **2007**, *127*, No. 194102.
(73) Arbuznikov, A. V.; Kaupp, M. Importance of the correlation contribution for local hybrid functionals: Range separation and self-interaction corrections. *J. Chem. Phys.* **2012**, *136*, No. 014111.
(74) Arbuznikov, A. V.; Kaupp, M. Towards improved local hybrid functionals by calibration of exchange-energy densities. *J. Chem. Phys.* **2014**, *141*, No. 204101.
(75) Slater, J. C. A Simplification of the Hartree-Fock Method. *Phys. Rev.* **1951**, *81*, 385−390.
(76) Vosko, S. H.; Wilk, L.; Nusair, M. Accurate spin-dependent electron liquid correlation energies for local spin density calculations: a critical analysis. *Can. J. Phys.* **1980**, *58*, 1200−1211.
(77) Perdew, J. P.; Burke, K.; Ernzerhof, M. Generalized Gradient Approximation Made Simple. *Phys. Rev. Lett.* **1996**, *77*, 3865−3868.
(78) Lee, C.; Yang, W.; Parr, R. G. Development of the Colle-Salvetti correlation-energy formula into a functional of the electron density. *Phys. Rev. B* **1988**, *37*, 785−789.
(79) Perdew, J. P. Density-functional approximation for the correlation energy of the inhomogeneous electron gas. *Phys. Rev. B* **1986**, *33*, 8822−8824.
(80) Perdew, J. P. Erratum: Density-functional approximation for the correlation energy of the inhomogeneous electron gas. *Phys. Rev. B* **1986**, *34*, 7406.
(81) Hamprecht, F. A.; Cohen, A. J.; Tozer, D. J.; Handy, N. C. Development and assessment of new exchange-correlation functionals. *J. Chem. Phys.* **1998**, *109*, 6264−6271.
(82) Boese, A. D.; Handy, N. C. A new parametrization of exchange-correlation generalized gradient approximation functionals. *J. Chem. Phys.* **2001**, *114*, 5497−5503.
(83) Grimme, S. Semiempirical GGA-Type Density Functional Constructed with a Long-Range Dispersion Correction. *J. Comput. Chem.* **2006**, *27*, 1787−1799.
(84) Keal, T. W.; Tozer, D. J. The exchange-correlation potential in Kohn-Sham nuclear magnetic resonance shielding calculations. *J. Chem. Phys.* **2003**, *119*, 3015−3024.

https://doi.org/10.1021/acs.jctc.1c00919
J. Chem. Theory Comput. 2021, 17, 7602−7621

(85) Keal, T. W.; Tozer, D. J. A semiempirical generalized gradient approximation exchange-correlation functional. *J. Chem. Phys.* **2004**, *121*, 5654−5660.
(86) Tao, J.; Perdew, J. P.; Staroverov, V. N.; Scuseria, G. E. Climbing the Density Functional Ladder: Nonempirical Meta-Generalized Gradient Approximation Designed for Molecules and Solids. *Phys. Rev. Lett.* **2003**, *91*, No. 146401.
(87) Perdew, J. P.; Tao, J.; Staroverov, V. N.; Scuseria, G. E. Meta-generalized gradient approximation: Explanation of a realistic nonempirical density functional. *J. Chem. Phys.* **2004**, *120*, 6898−6911.
(88) Van Voorhis, T.; Scuseria, G. E. A novel form for the exchange-correlation energy functional. *J. Chem. Phys.* **1998**, *109*, 400−410.
(89) Boese, A. D.; Handy, N. C. New exchange-correlation density functionals: The role of the kinetic-energy density. *J. Chem. Phys.* **2002**, *116*, 9559−9569.
(90) Mardirossian, N.; Head-Gordon, M. Mapping the genome of meta-generalized gradient approximation density functionals: The search for B97M-V. *J. Chem. Phys.* **2015**, *142*, No. 074111.
(91) Sun, J.; Ruzsinszky, A.; Perdew, J. P. Strongly Constrained and Appropriately Normed Semilocal Density Functional. *Phys. Rev. Lett.* **2015**, *115*, No. 036402.
(92) Bartók, A. P.; Yates, J. R. Regularized SCAN functional. *J. Chem. Phys.* **2019**, *150*, No. 161101.
(93) Furness, J. W.; Kaplan, A. D.; Ning, J.; Perdew, J. P.; Sun, J. Accurate and Numerically Efficient r^{2}SCAN Meta-Generalized Gradient Approximation. *J. Phys. Chem. Lett.* **2020**, *11*, 8208−8215.
(94) Zhao, Y.; Truhlar, D. G. A new local density functional for main-group thermochemistry, transition metal bonding, thermochemical kinetics, and noncovalent interactions. *J. Chem. Phys.* **2006**, *125*, No. 194101.
(95) Yu, H. S.; He, X.; Truhlar, D. G. MN15-L: ANew Local Exchange-Correlation Functional for Kohn-Sham Density Functional Theory with Broad Accuracy for Atoms, Molecules, and Solids. *J. Chem. Theory Comput.* **2016**, *12*, 1280−1293.
(96) Staroverov, V. N.; Scuseria, G. E.; Tao, J.; Perdew, J. P. Comparative assessment of a new nonempirical density functional: Molecules and hydrogen-bonded complexes. *J. Chem. Phys.* **2003**, *119*, 12129−12137.
(97) Becke, A. D. Density-functional thermochemistry. III. *J. Chem. Phys.* **1993**, *98*, 5648−5652.
(98) Wilson, P. J.; Bradley, T. J.; Tozer, D. J. Hybrid exchange-correlation functional determined from thermochemical data and *ab initio* potentials. *J. Chem. Phys.* **2001**, *115*, 9233−9242.
(99) Adamo, C.; Barone, V. Toward chemical accuracy in the computation of NMR shieldings: the PBE0 model. *Chem. Phys. Lett.* **1998**, *298*, 113−119.
(100) Adamo, C.; Barone, V. Toward reliable density functional methods without adjustable parameters: The PBE0 model. *J. Chem. Phys.* **1999**, *110*, 6158−6170.
(101) Zhao, Y.; Truhlar, D. G. The M06 suite of density functionals for main group thermochemistry, thermochemical kinetics, noncovalent interactions, excited states, and transition elements: two new functionals and systematic testing of four M06-class functionals and 12 other functionals. *Theor. Chem. Acc.* **2008**, *120*, 215−241.
(102) Zhao, Y.; Truhlar, D. G. Design of Density Functionals That Are Broadly Accurate for Thermochemistry, Thermochemical Kinetics, and Nonbonded Interactions. *J. Phys. Chem. A* **2005**, *109*, 5656−5667.
(103) Yu, H. S.; He, X.; Li, S. L.; Truhlar, D. G. MN15: A Kohn-Sham global-hybrid exchange-correlation density functional with broad accuracy for multi-reference and single-reference systems and noncovalent interactions. *Chem. Sci.* **2016**, *7*, 5032−5051.
(104) Becke, A. D. A new mixing of Hartree-Fock and local density-functional theories. *J. Chem. Phys.* **1993**, *98*, 1372−1377.
(105) Yanai, T.; Tew, D. P.; N Handy, N. C. A new hybrid exchange-correlation functional using the Coulomb-attenuating method (CAM-B3LYP). *Chem. Phys. Lett.* **2004**, *393*, 51−57.
(106) Chai, J.-D.; Head-Gordon, M. Long-range corrected hybrid density functionals with damped atom-atom dispersion corrections. *Phys. Chem. Chem. Phys.* **2008**, *10*, 6615−6620.
(107) Mardirossian, N.; Head-Gordon, M. ωB97X-V: A 10-parameter, range-separated hybrid, generalized gradient approximation density functional with nonlocal correlation, designed by a survival-of-the-fittest strategy. *Phys. Chem. Chem. Phys.* **2014**, *16*, 9904−9924.
(108) Mardirossian, N.; Head-Gordon, M. ωB97M-V: A combinatorially optimized, range-separated hybrid, meta-GGA density functional with VV10 nonlocal correlation. *J. Chem. Phys.* **2016**, *144*, No. 214110.
(109) Bahmann, H.; Rodenberg, A.; Arbuznikov, A. V.; Kaupp, M. A thermochemically competitive local hybrid functional without gradient corrections. *J. Chem. Phys.* **2007**, *126*, No. 011103.
(110) Burke, K.; Cruz, F. G.; Lam, K.-C. Unambiguous exchange-correlation energy density. *J. Chem. Phys.* **1998**, *109*, 8161−8167.
(111) Cruz, F. G.; Lam, K.-C.; Burke, K. Exchange-Correlation Energy Density from Virial Theorem. *J. Phys. Chem. A* **1998**, *102*, 4911−4917.
(112) Maier, T. M.; Haasler, M.; Arbuznikov, A. V.; Kaupp, M. New approaches for the calibration of exchange energy densities in local hybrid functionals. *Phys. Chem. Chem. Phys.* **2016**, *18*, 21133−21144.
(113) Grimme, S. Semiempirical hybrid density functional with perturbative second-order correlation. *J. Chem. Phys.* **2006**, *124*, No. 034108.
(114) Karton, A.; Tarnopolsky, A.; Lamere, J. F.; Schatz, G. C.; Martin, J. M. L. Highly accurate first-principles benchmark data sets for the parametrization and validation of density functional and other approximate methods. Derivation of a robust, generally applicable, double-hybrid functional for thermochemistry and thermochemical kinetics. *J. Phys. Chem. A* **2008**, *112*, 12868−12886.
(115) Antušek, A.; Jaszuński, M. Coupled cluster study of NMR shielding constants and spin-rotation constants in SiH_4, PH_3 and H_2S molecules. *Mol. Phys.* **2006**, *104*, 1463−1474.
(116) Auer, A. A. High-level ab-initio calculation of gas-phase NMR chemical shifts and secondary isotope effects of methanol. *Chem. Phys. Lett.* **2009**, *467*, 230−232.
(117) Jaszuński, M.; Demissie, T. B.; Ruud, K. Spin-Rotation and NMR Shielding Constants in XF Molecules (X = B, Al, Ga, In, and Tl). *J. Phys. Chem. A* **2014**, *118*, 9588−9595.
(118) Helgaker, T.; Gauss, J.; Jørgensen, P.; Olsen, J. The prediction of molecular equilibrium structures by the standard electronic wavefunctions. *J. Chem. Phys.* **1997**, *106*, 6430−6440.
(119) Gauss, J. Analytic second derivatives for the full coupled-cluster singles, doubles, and triples model: Nuclear magnetic shielding constants for BH, HF, CO, N_2, N_2O, and O_3. *J. Chem. Phys.* **2002**, *116*, 4773−4776.
(120) Vícha, J.; Novotný, J.; Komorovsky, S.; Straka, M.; Kaupp, M.; Marek, R. Relativistic Heavy-Neighbor-Atom Effects on NMR Shifts: Concepts and Trends Across the Periodic Table. *Chem. Rev.* **2020**, *120*, 7065−7103.
(121) Lantto, P.; Vaara, J.; Kantola, A. M.; Telkki, V.; Schimmelpfennig, B.; Ruud, K.; Jokisaari, J. Relativistic Spin-Orbit Coupling Effects on Secondary Isotope Shifts of ^{13}C Nuclear Shielding in CX_2 (X = O, S, Se, Te). *J. Am. Chem. Soc.* **2002**, *124*, 2762−2771.
(122) Rusakov, Y. Y.; Rusakova, I. L.; Krivdin, L. B. On the HALA eff ect in the NMR carbon shielding constants of the compounds containing heavy p-elements. *Int. J. Quantum Chem.* **2016**, *116*, 1404−1412.
(123) Malkina, O. L.; Schimmelpfennig, B.; Kaupp, M.; Hess, B. A.; Chandra, P.; Wahlgren, u.; Malkin, V. G. Spin-orbit corrections to NMR shielding constants from density functional theory. How important are the two-electron terms. *Chem. Phys. Lett.* **1998**, *296*, 93−104.
(124) Wilson, P. J.; Tozer, D. J. NMR shielding constants from ab initio and Kohn-Sham electron densities. *Chem. Phys. Lett.* **2001**, *337*, 341−348.

https://doi.org/10.1021/acs.jctc.1c00919
J. Chem. Theory Comput. 2021, 17, 7602−7621

(125) Wilson, P. J.; Tozer, D. J. Varying the fraction of orbital exchange in density functional theory: Influence on nuclear magnetic resonance shielding constants. *J. Chem. Phys.* **2002**, *116*, 10139−10147.
(126) Kaupp, M.; Malkin, V. G.; Malkina, O. L.; Salahub, D. R. Scalar Relativistic Effects on ^{17}O NMR Chemical Shifts in Transition-Metal Oxo Complexes. An ab Initio ECP/DFT Study. *J. Am. Chem. Soc.* **1995**, *117*, 1851−1852.
(127) Kaupp, M.; Malkina, O. L.; Malkin, V. G. The calculation of ^{17}O chemical shielding in transition metal oxo complexes. I. Comparison of DFT and ab initio approaches, and mechanisms of relativity-induced shielding. *J. Chem. Phys.* **1997**, *106*, 9201−9212.
(128) Zhao, Y.; Truhlar, D. G. Improved Description of Nuclear Magnetic Resonance Chemical Shielding Constants Using the M06-L Meta-Generalized-Gradient-Approximation Density Functional. *J. Phys. Chem. A* **2008**, *112*, 6794−6799.
(129) Cheeseman, J. R.; Trucks, G. W.; Keith, T. A.; Frisch, M. J. A comparison of models for calculating nuclear magnetic resonance shielding tensors. *J. Chem. Phys.* **1996**, *104*, 5497−5509.
(130) Schattenberg, C. J.; Maier, T.; Kaupp, M. Lessons from the Spin-Polarization/Spin-Contamination Dilemma of Transition-Metal Hyperfine Couplings for the Construction of Exchange-Correlation Functionals. *J. Chem. Theory. Comput.* **2018**, *14*, 5653−5672.
(131) Schattenberg, C. J.; Lehmann, M.; Bühl, M.; Kaupp, M. Systematic evaluation of modern density functional methods for the computation of NMR shifts of 3d transition-metal nuclei. *J. Chem. Theory Comput.* Submitted.
(132) Kupka, T. H_2O, H_2, HF, F_2 and F_2O nuclear magnetic shielding constants and indirect nuclear spin-spin coupling constants (SSCCs) in the BHandH/pcJ-n and BHandH/XZP Kohn-Sham limits. *Magn. Reson. Chem.* **2009**, *47*, 959−970.
(133) Alkan, F.; Holmes, S. T.; Dybowski, C. Role of Exact Exchange and Relativistic Approximations in Calculating ^{19}F Magnetic Shielding in Solids Using a Cluster Ansatz. *J. Chem. Theory Comput.* **2017**, *13*, 4741−4752.
(134) Dahanayake, J. N.; Kasireddy, C.; Ellis, J. M.; Hildebrandt, D.; Hull, O. A.; Karnes, J. P.; Morlan, D.; Mitchell-Koch, K. R. Evaluating electronic structure methods for accurate calculation of ^{19}F chemical shifts in fluorinated amino acids. *J. Comput. Chem.* **2017**, *38*, 2605−2617.
(135) Fedorov, S. V.; Krivdin, L. B. Computational Protocols for the ^{19}F NMR Chemical Shifts. Part 1: Methodological Aspects. *J. Fluorine Chem.* **2020**, *238*, No. 109625.
(136) Wodyński, A.; Kaupp, M. Noncollinear Relativistic Two-Component X2C Calculations of Hyperfine Couplings Using Local Hybrid Functionals. Importance of the High-Density Coordinate Scaling Limit. *J. Chem. Theory Comput.* **2020**, *16*, 314−325.

https://doi.org/10.1021/acs.jctc.1c00919
J. Chem. Theory Comput. 2021, 17, 7602−7621

VI

Reprinted with permission from

C. J. Schattenberg, M. Lehmann, M. Bühl and M. Kaupp,
"*Systematic Evaluation of Modern Density Functional Methods for the Computation of NMR Shifts of 3d Transition-Metal Nuclei*",
J. Chem. Theory Comput., **2022**, *18*, 273–292.
DOI: 10.1021/acs.jctc.1c00964

JCTC Journal of Chemical Theory and Computation

pubs.acs.org/JCTC Article

Systematic Evaluation of Modern Density Functional Methods for the Computation of NMR Shifts of 3d Transition-Metal Nuclei

Caspar Jonas Schattenberg, Morten Lehmann, Michael Bühl, and Martin Kaupp*

Cite This: J. Chem. Theory Comput. 2022, 18, 273−292 Read Online

ACCESS | Metrics & More | Article Recommendations | Supporting Information

ABSTRACT: A wide range of density functionals from all rungs of Jacob's ladder have been evaluated systematically for a set of experimental 3d transition-metal NMR shifts of 70 complexes encompassing 12 × ^{49}Ti, 10 × ^{51}V, 10 × ^{53}Cr, 11 × ^{55}Mn, 9 × ^{57}Fe, 9 × ^{59}Co, and 9 × ^{61}Ni shift values, as well as a diverse range of electronic structure characteristics. The overall 39 functionals evaluated include one LDA, eight GGAs, seven meta-GGAs (including their current-density-functional—CDFT—versions), nine global hybrids, four range-separated hybrids, eight local hybrids, and two double hybrids, and we also include Hartree−Fock and MP2 calculations. While recent evaluations of the same functionals for a very large coupled-cluster-based benchmark of main-group shieldings and shifts achieved in some cases aggregate percentage mean absolute errors clearly below 2%, the best results for the present 3d-nuclei set are in the range between 4 and 5%. Strikingly, the overall best-performing functionals are the recently implemented CDFT versions of two meta-GGAs, namely cM06-L (4.0%) and cVSXC (4.3%), followed by cLH14t-calPBE (4.9%), B3LYP (5.0%), and cLH07t-SVWN (5.1%), i.e., the previously best-performing global hybrid and two local hybrids. A number of further functionals achieve aggregate deviations in the range 5−6%. Range-separated hybrids offer no particular advantage over global hybrids. Due to the overall poor performance of Hartree−Fock theory for all systems except the titanium complexes, MP2 and double-hybrid functionals are unsuitable for these 3d-nucleus shifts and provide large errors. Global hybrid functionals with larger EXX admixtures, such as BHLYP or M06-2X, also perform poorly, and some other highly parametrized global hybrids also are unsuitable. For many functionals depending on local kinetic energy τ, their CDFT variants perform much better than their "non-CDFT" versions. This holds notably also for the above-mentioned M06-L and VSXC, while the effect is small for τ-dependent local hybrids and can even be somewhat detrimental to the agreement with experiment for a few other cases. The separation between well-performing and more poorly performing functionals is mainly determined by their results for the most critical nuclei ^{55}Mn, ^{57}Fe, and ^{59}Co. Here either moderate exact-exchange admixtures or CDFT versions of meta-GGAs are beneficial for the accuracy. The overall deviations of the better-performing global or local hybrids are then typically dominated by the ^{53}Cr shifts, where triplet instabilities appear to disfavor exact-exchange admixture. Further detailed analyses help to pinpoint specific nuclei and specific types of complexes that are challenges for a given functional.

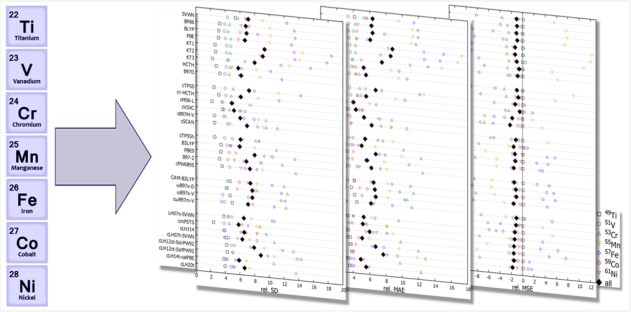

1. INTRODUCTION

The NMR chemical shifts of transition-metal nuclei have a long history, dating back to some of the very first NMR experiments in the early 1950s, on the ^{59}Co isotope.[1,2] While some of the relevant nuclei are difficult to observe,[3] others are easily accessible, and many of them cover a rather large range of chemical shifts of many thousands of ppm.[2,4] This large range and the importance of transition-metal complexes in many areas of research, from organometallic catalysis via materials to bioinorganic chemistry, makes NMR spectroscopy of transition-metal (TM) nuclei an important tool in chemistry. As with main-group NMR,[5−7] quantum-chemical computations of transition-metal NMR parameters have thus been of substantial interest.[7−13]

One of us (M.B.) had initiated systematic studies of DFT approaches to compute TM NMR shifts about 25 years ago, with one of the aims being the correlation with reactivity, and an appreciable knowledge base has been accumulated over the years. Apart from structural, environmental, and ro-vibrational effects, the choice of the exchange-correlation (XC) functional has been crucial to obtain reasonable predictive-quality TM NMR shifts. Initially, (global) hybrid functionals (GHs) with a moderate admixture of Hartree−Fock exchange, such as the B3LYP functional (20%), were found to improve the obtained

Received: September 24, 2021
Published: December 30, 2021

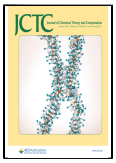

shifts for many TM nuclei, compared to pure semilocal functionals. This holds in particular for nuclei in the second half of the 3d series, such as ^{57}Fe or ^{59}Co[14−16] and to a lesser extent also for ^{55}Mn[17] and ^{61}Ni[18] and for some late 4d nuclei, ^{99}Ru and ^{103}Rh.[15,19−21] Different rationalizations can be put forward for these observations. Delocalization errors of semilocal functionals are known to render metal−ligand bonds too covalent, as also shown for EPR parameters of open-shell complexes.[22,23] Potentially too low excitation energies of semilocal functionals and the coupling terms introduced by nonlocal exchange are additional aspects.[24] Later, studies for some 4d nuclei such as ^{95}Mo or ^{99}Tc,[25,26] or for the 3d nucleus ^{53}Cr,[27] suggested better performance of semilocal functionals and detrimental effects of exact-exchange (EXX) admixture for such elements in the middle of the TM rows. Relatively small dependencies on the EXX admixtures were identified for early TMs, such as ^{49}Ti, ^{51}V, or ^{91}Zr.[28−30]

Many results for main-group nuclei also suggest that different amounts of EXX admixture of global hybrids may be preferable for different nuclei. For example, the BHLYP functional with 50% EXX admixture has been suggested[31] to be among the best choices for ^{19}F shifts (double hybrid functionals (DHs) like DSD-PBEP86 perform even better,[32] but these require computationally demanding MP2-type correlation contributions and have similarly high EXX admixtures). On the other hand, BHLYP dramatically overestimates chemical shifts for many other main-group nuclei[33,34] (and for transition metals,[35] see also below). Indeed, it appears that the optimal amount of EXX admixture depends not only on the nucleus studied but also on the electronic structure of the given compound. That is, large EXX admixtures are known to be problematic in many cases exhibiting large static correlation contributions and in case of triplet instabilities of the generalized ground-state Kohn−Sham wave function.[36,37] This brings us back to the main topic of transition-metal compounds, which are known to often exhibit large static correlation effects as well as spin-symmetry breaking of Hartree−Fock wave functions, depending on oxidation and charge state, as well as on other characteristics of their electronic structure.

In view of these limitations of global hybrid functionals in terms of their flexibility of being able to treat different situations, more flexible extensions of the concept of hybrid functionals obviously are of interest, not exclusively but distinctly also in the context of NMR chemical shifts. So far, the use of range-separated hybrids (RSHs) has been studied to a limited degree, and the results did not seem to provide a significant improvement over global hybrids. This brings us to local hybrid functionals (local hybrids, LHs) with position-dependent EXX admixture, governed by a so-called local mixing function (LMF).[38] An early attempt to use LHs for nuclear shieldings based on an uncoupled scheme on top of an approximate optimized-effective-potential (OEP) treatment within the localized-Hartree−Fock (LHF) approach[39] suffered from the sensitivity of nuclear shieldings to the underlying approximations used.[40,41] Recently we have reported a full and efficient coupled-perturbed Kohn−Sham (CPKS) implementation of nuclear shieldings with LHs within the TURBOMOLE code, based on generalized Kohn−Sham ground-state wave functions.[33] The first evaluations for main-group nucleus shieldings of some first-generation LHs were very encouraging, confirming the potential advantages of having large EXX admixtures in the core region but lower ones in the valence region. In particular, the systematic underestimate of shieldings by semilocal or global hybrid XC functionals for non-hydrogen nuclei, which in part seems to be related to the neglect of current terms in the XC functionals,[42] was reduced significantly. Some limitations noted initially for ^{1}H shieldings, and for the shieldings of nuclei in direct neighborhood of hydrogen atoms, were found[43,44] to be related to the gauge correction of the kinetic energy τ by the widely used Maximoff-Scuseria model.[45] They vanish almost completely when using the Dobson[46−49] current-density functional (CDFT) extension of τ.[43] Further improvements for hydrogen shieldings were found[44] when using more advanced LHs with calibrated exchange-energy densities, such as LH20t.[50] Subsequent evaluations of main-group NMR shifts as part of a more diverse evaluation of local hybrids for response properties by Holzer et al.[51] included the same LHs and in addition a modified variant (mPSTS) of the rather involved PSTS functional,[52] as well as an LH (LHJ14) by Johnson and co-workers[53] with an LMF based on correlation length. Good performance of LHs was generally found, even though the selected test sets in part may have been too limited to distinguish the advantages and disadvantages of different functionals in granular detail. To obtain a more meaningful extensive comparison of a wide variety of XC functionals and other methods for main-group shieldings and shifts, we have very recently constructed and used[34] a very large benchmark set containing 372 shielding values for ^{1}H, ^{11}B, ^{13}C, ^{15}N, ^{17}O, ^{19}F, ^{31}P, and ^{33}S nuclei in 117 molecules and ions, based on CCSD(T)/pcSseg-3//CCSD(T)/cc-pVQC data and used it to evaluate a wide variety of different functionals from all five rungs of Perdew's "Jacob's ladder of functionals"[54] plus HF and MP2 calculations. The DSD-PBEP86 DH[55,56] was confirmed to provide the overall most accurate results. Several LHs performed excellently and were competitive with the other DHs evaluated, at appreciably lower computational cost. A number of further important insights were obtained on other functionals. This includes in particular the excellent performance of parametrized meta-GGAs like B97M-V and MN15-L, when used in their CDFT implementations based on Dobson's scheme ("cB97M-V", "cMN15-L").[34]

A more diverse evaluation of XC functionals for NMR shifts clearly should extend beyond main-group nuclei. Many of the functionals mentioned above, that have recently been evaluated in detail for main-group shieldings, have so far not been applied to transition-metal shifts. Here we work toward filling this gap and provide a systematic study of the NMR shifts of 3d nuclei, as more data are available for comparison here than for the heavier TM nuclei, complications due to relativistic effects (or potentially to violations of the high-density limit for certain functionals[57]) are expected to be small, but the potential importance of static correlation is largest. The latter point reflects the often found stretched-bond situations related to the large Pauli repulsion with semicore−shells, exacerbated by the small 3d shell that lacks a radial node.[58,59] We include 70 shifts of ^{49}Ti, ^{51}V, ^{53}Cr, ^{55}Mn, ^{57}Fe, ^{59}Co, and ^{61}Ni nuclei, where experimental data are available. The selection includes complexes that have been studied previously by computations, and we concentrate largely on systems where environmental effects are not expected to affect the shifts very much (see below). As the generation of high-level coupled-cluster benchmark data of comparable quality as provided for main-group systems in ref 34 would be prohibitive and might not provide the required accuracy in all cases, we compare here to carefully selected experimental data.

Beyond the first evaluations of LHs for transition-metal NMR shifts, we include some GGAs geared specifically toward nuclear

https://doi.org/10.1021/acs.jctc.1c00964
J. Chem. Theory Comput. 2022, 18, 273−292

shieldings of main-group nuclei (KT1, KT2, KT3), more recent meta-GGA functionals (e.g., B97M-V, M06-L, MN15-L, VSXC, τ-HCTH), a number of more recent and highly parametrized GHs, and four RSHs (CAM-B3LYP, ωB97X-D, ωB97X-V, ωB97M-V). We also evaluate HF and MP2 calculations and two DHs, B2PLYP and DSD-PBEB86, even though we expected these approaches to face difficulties for many transition-metal complexes where appreciable static correlation and triplet instabilities are common. Yet MP2 and DSD-PBEP86 excel for most main-group shieldings,[34] and so it is only fair to evaluate them also for transition-metal shifts. Overall, 41 methods are evaluated for the entire test set, without counting different ways of treating local kinetic energy, τ. In the section Theory, we describe the issue of the proper treatment of τ for those functionals that depend on it,[43,44] as this will turn out to be a major aspect for the success of some of the best-performing functionals in this work.

2. THEORY

As many of the functionals evaluated here, meta-GGAs, meta-GGA-based GHs and RSHs, and LHs with certain local mixing functions (LMFs), depend on local kinetic energy τ, the proper treatment of the latter becomes important and shall be briefly discussed here. τ itself is not invariant to gauge transformations of the vector potential in the presence of a magnetic field and has to be adjusted accordingly. In most nuclear shielding implementations used today, a gauge-invariant extension due to Maximoff and Scuseria[45] is used (τ_{MS} in the following)

$$\tau \rightarrow \tau_{MS} = \tau + \frac{\mathbf{A}^{\mathrm{T}}}{c}\mathbf{j}_p + \frac{|\mathbf{A}|^2}{2c^2}\rho \tag{1}$$

where

$$\mathbf{j}_p = \frac{i}{2}\sum_i (\varphi_i \nabla \varphi_i^* - \varphi_i^* \nabla \varphi_i) \tag{2}$$

is the paramagnetic current density, and $\mathbf{A}$ is the vector potential of the magnetic field. However, use of the physical current does not generate a proper isoorbital indicator,[47,48] as τ is in the absence of a field, and this treatment renders τ explicitly field-dependent, which is considered theoretically disadvantageous.[49] More importantly, we have found the model to introduce unphysical paramagnetic artifacts for atoms and for the parallel shielding tensor component in linear molecules,[43] which also turned out to be responsible for a poor description of proton shieldings (and for some other artifacts) by first-generation LHs. It is advantageous to use instead the more physically motivated induced paramagnetic current density. This gives a model proposed by Dobson[46] that has been used also in other contexts (e.g., for gauge invariance of τ-dependent functionals in TDDFT computations,[47] to describe current-carrying atomic states[48] or molecules in strong magnetic fields,[60] to study magnetically induced currents,[61] or to compute spin−spin coupling constants[51,62]):

$$\tau \rightarrow \tau_D = \tau - \frac{|\mathbf{j}_p|^2}{2\rho} \tag{3}$$

Use of τ_D eliminates the above-mentioned artifacts of τ_{MS} and provides a proper current-density functional theory (CDFT) framework for τ-dependent XC functionals. This entails coupling terms in the response treatment also for meta-GGA functionals.[43] We will in the following denote these CDFT implementations of the functionals by a small "c" prefix, as has been done in several previous works.[34,51,60,61] We note in passing that, in the present linear-response treatment, τ_D applies only to the response terms, while a variational treatment of the magnetic field will also turn the ground-state functionals into CDFT functionals.[60] While both τ_{MS} and τ_D frameworks will be considered in this work, we regard τ_D as the physically better founded one and will place central focus on its results. A gauge-dependent model with an unmodified τ (with the gauge origin placed at the center of mass of the molecule, τ_C), as well as the *ad hoc* gauge invariant solution implemented in ORCA[63−65] (τ_0; see discussion in ref 43) will also be mentioned or reported where we find it useful to discuss the role of current-density dependence in τ_D.

While nuclear shielding is a tensor property, for the purpose of the present work we will concentrate on the isotropic shielding

$$\sigma_{iso} = \frac{1}{3}Tr(\boldsymbol{\sigma}) \tag{4}$$

As no reference-quality computed shielding data are available, in contrast to the main-group case (see Introduction), we will have to compare our results to experimental chemical shifts. The NMR chemical shift is usually reported (approximately) as the difference between the shielding of a reference compound and that of the nucleus of interest

$$\delta = \sigma_{iso,\mathrm{ref.}} - \sigma_{iso} \tag{5}$$

In the case of transition-metal nuclei and complexes, the choice of reference compound becomes particularly important, as some complexes may be more difficult to compute than others regarding static correlation or environmental effects. To exclude as far as possible artifacts arising from such errors, one can try to use "benign" reference compounds that are comparably easy to compute accurately. In those cases where the choice differs from that made by the experimentalists for a given nucleus, one can map the computed results back to the experimental shift scale by using the experimental shift of the chosen secondary reference standard relative to the experimentally used one

$$\delta = \sigma_{iso,\mathrm{ref.calc.}} - \sigma_{iso,\mathrm{calc.}} + \delta_{\mathrm{ref.exp.}} \tag{6}$$

We will discuss the chosen reference standards at the beginning of the Results section, in comparison with the alternative approach of referencing via the Y-intercept of the linear regression of computed σ_{iso} against experimental δ values at a given computational level.[18] The latter will be our central choice for statistical analyses.

3. COMPUTATIONAL DETAILS

All regular DFT calculations (except double hybrid shielding calculations) were carried out with a developers' version of the TURBOMOLE program suite.[66,67] Structures of all complexes were optimized at the BP86-D3(BJ)/def2-TZVP(D)[68,69] level of theory, i.e., using a def2-TZVPD basis for the metal centers and def2-TZVP for the main group atoms, which is similar to the structures used in many earlier transition-metal NMR shift studies.[15−21,28−30] To evaluate the role of the structures for the shift computations, we also evaluated TPSSh-D3(BJ)[70]/def2-TZVP(D) structures for comparison. D3(BJ) represents D3 atom-additive dispersion corrections,[71,72] with Becke−Johnson damping.[73−75] The maximum norm of Cartesian gradients was converged to 10^{-5}, with an energy convergence criterion of 10^{-8}. Grids were set to "5" for BP86 optimizations and to "3" in

https://doi.org/10.1021/acs.jctc.1c00964
J. Chem. Theory Comput. 2022, 18, 273−292

Table 1. Shielding Constants and Paramagnetic Contributions for Iso-electronic Atomic Systems with Closed-Shell d^{10} Configuration (with the pcSseg-3 Basis)[a]

			CCSD(T)	TPSS	M06-L	VSXC	B97M-V	SCAN	TPSSh	M06	PW6B95	M06-2X	ωB97M-V	12sif[b]	LH20t
τ_{MS}	Fe^{2-}	σ	n.c.[c]	2075.7	1912.9	829.2	1863.1	2112.1	2076.6	946.6	1733.5	-2549.5	1439.5	2172.8	1925.6
		σ^p		10.6	-152.2	-1237.7	-202.0	46.3	11.3	-1118.7	-332.8	-4616.6	-626.0	107.9	-140.2
	Co^-	σ	2175.5	2197.1	2090.5	1856.1	2153.2	2150.2	2195.8	1722.2	2136.6	1757.1	1888.0	2300.8	2165.7
		σ^p	0.0	21.3	-85.2	-321.2	-22.4	-26.2	19.8	-453.5	-40.5	-420.4	-288.0	125.1	-10.8
	Ni	σ	2288.4	2297.1	2180.2	2455.6	2306.0	2282.6	2296.3	2133.8	2286.7	2196.1	2166.9	2377.7	2295.5
		σ^p	0.0	10.1	-107.0	166.6	19.1	-5.0	9.1	-153.3	-1.7	-92.8	-120.2	90.9	7.9
	Cu^+	σ	2397.5	2409.3	2359.3	2516.0	2418.8	2414.5	2408.5	2336.5	2399.7	2360.2	2347.8	2453.9	2404.7
		σ^p	0.0	11.8	-38.6	116.2	21.2	16.3	10.8	-61.3	0.9	-39.2	-49.8	56.6	6.7
τ_D	Fe^{2-}	σ	n.c.[c]	2065.1	2065.1	2066.8	2065.2	2065.8	2065.3	2065.3	2066.3	2067.1	2065.5	2065.0	2065.8
		σ^p		0.0	0.0	0.0	0.0	0.0	0.0	0.0	0.0	0.0	0.0	0.0	0.0
	Co^-	σ	2175.5	2175.7	2175.8	2177.3	2175.7	2176.4	2175.9	2175.7	2177.2	2177.5	2176.0	2175.7	2176.5
		σ^p	0.0	0.0	0.0	0.0	0.0	0.0	0.0	0.0	0.0	0.0	0.0	0.0	0.0
	Ni	σ	2288.4	2287.0	2287.2	2289.0	2286.9	2287.6	2287.2	2287.2	2288.4	2288.9	2287.1	2286.9	2287.6
		σ^p	0.0	0.0	0.0	0.0	0.0	0.0	0.0	0.0	0.0	0.0	0.0	0.0	0.0
	Cu^+	σ	2397.5	2397.5	2397.9	2399.8	2397.6	2398.2	2397.7	2397.8	2398.8	2399.4	2397.6	2397.3	2398.0
		σ^p	0.0	0.0	0.0	0.0	0.0	0.0	0.0	0.0	0.0	0.0	0.0	0.0	0.0

[a]Gray font indicates cases where the converged closed-shell d^{10} configuration exhibits a negative HOMO−LUMO gap. [b]Abbreviation for LH12ct-SsifPW92. [c]No convergence to a diamagnetic solution was achieved.

TPSSh optimizations (internal TURBOMOLE settings). All structures were characterized as true minima by subsequent harmonic vibrational frequency analyses.

Some truncated model complexes, $VOMe_3$, $VOMe_2(OMe)$, $VOMe(OMe)_2$, $VO(OMe)_3$, and $Fe(CO)_4(CH_2CHOMe)$, have been used throughout the present work, while the experimental shifts were reported for the larger $VO(CH_2SiMe_3)_3$, $VO(CH_2SiMe_3)_2(O^tBu)$, $VO(CH_2SiMe_3)(O^tBu)_2$, $VO(O^tBu)_3$, and $Fe(CO)_4(CH_2CHOEt)$.[76,77] To study the effect of the truncation, the full-sized complexes have been optimized by the Conformer-Rotamer Ensemble Sampling Tool (CREST)[78,79] followed by a BP86-D3(BJ)/def2-TZVP(D) optimization of all relevant conformers. We selected the energetic minimum of this search and evaluated the shielding constants for a small subset of functionals. Comparisons of the results for three functionals are reported in Table S13 in the Supporting Information. Changes of the NMR shifts compared to the truncated complexes are below 50 ppm. Relative to the experimental shift scale the changes do not exceed 2.1%, whereas the relative statistical results are affected by a maximum of 0.3% for the evaluated functionals. Due to the small effects on the overall statistics, and to be consistent with previous publications (see refs 15 and 29), we use the truncated models throughout.

DFT shielding calculations with TURBOMOLE used gauge-including atomic orbitals (GIAOs),[80−82] pcSseg-3[83] basis sets, SCF energy convergence criteria of 10^{-9}, a ground-state density convergence of 10^{-7}, and a grid setting "3". Convergence thresholds for the CPKS iterations were set to 10^{-7} (convergence of the Euclidean vectors).

GIAO−CCSD(T)/pcSseg-3 results for some atoms (see Table 1 below) were computed using the CFOUR program.[84] All double hybrid and MP2 GIAO shielding calculations have been performed using the ORCA program, version 4.2.1.[32,63,64] Due to the much larger computational requirements of such computations compared to regular DFT shielding calculations, the basis sets have been reduced somewhat in a locally dense basis-set approximation to still be able to carry out these calculations for all complexes in reasonable time. pcSseg-3 basis sets were then used only on the transition metal nuclei themselves, while pcSseg-2 basis sets were used on the ligand atoms. The RI approximation (resolution of the identity) has been used employing the def2-universal[85,86] auxiliary basis for the Coulomb and exchange part (RI-JK, AuxJ/AuxJK) and the "AutoAux" option with size setting "1" was used for the auxiliary basis within the MP2 correlation part (AuxC).[87] For one double hybrid (DSD-PBEP86), we have tested the full pcSseg-3 basis set and practically complete auxiliary basis sets (using the "AutoAux" option with setting "3" and the additional setting "AutoAuxLMax = True") for a subset of the smaller complexes. While the differences to the mixed-basis results are non-negligible, they do not affect the overall judgment on the lack of suitability of MP2 and the DHs for the present 3d shift test set (except for ^{49}Ti). Shifts at Hartree−Fock level have also been computed, using both TURBOMOLE and ORCA, with closely similar results.

We do not include thermal corrections or solvent effects in the benchmark statistics. Previous analyses have found the former to be quite small in comparison to the shift ranges of the involved nuclei and possible errors of the XC functionals, and the latter in most cases too,[88,89] at least for the types of complexes studied here. Indeed, larger effects are typically found from possible errors in the optimized structures.[16,90] Exceptionally large solvent influences are expected for some highly charged species in aqueous solution, in particular for nuclei with large shift ranges, due to a shortening of the average metal−ligand distances by the solvent environment. One of us (M.B.) has investigated this previously for a number of Co complexes from the present test set. Based on snapshots from ab initio MD simulations (CPMD level), or based on polarizable continuum models (PCM), the effects on aqueous $[Co(H_2O)_6]^{3+}$, $[Co(NH_3)_6]^{3+}$, $[Co(CN)_6]^{3-}$, and $[Co(CO)_4]^-$ have been estimated.[91] The shifts of these charged systems are reduced compared to their gas-phase values, which can of course alter the comparison between computational methods and experiment. Table S7 and Figure S2 in the Supporting Information show how the statistics for the ^{59}Co subset and those for the entire test set are altered if we consider the two types of correction schemes (PCM vs CPMD) for the four complexes to back-correct their experimental shifts to obtain approximate gas-phase values. The effects on the individual ^{59}Co subset are indeed non-negligible. Notably, the deviations with several (global, local, and range-separated) hybrid functionals tend to be reduced to some extent, in particular with larger EXX admixtures. The reason is, that

https://doi.org/10.1021/acs.jctc.1c00964
J. Chem. Theory Comput. 2022, 18, 273−292

many of these functionals, when used in gas-phase calculations, tend to overestimate the large shifts of these charged species. Semilocal functionals tend to benefit much less from the solvent corrections (for cSCAN the CPMD correction even overshoots), while agreement for SVWN is also improved. The overall trends for the different types of functionals remain similar, but a few changes in the order of the best-performing functionals are found (B3LYP becomes now the best-performing functional for the ^{59}Co subset, and several LHs perform similarly well, in particular cLH20t; Table S7). For the combined test set of all nuclei, the changes are small, however, with the largest shifts below 0.5% in rel SDs and below 0.3% in relative MAEs compared to the uncorrected data (Figure S2). We find even smaller effects of both explicit and implicit solvent modeling for aqueous $Cr_2O_7^{2-}$ (Figure S3 and Tables S8 and S9). Another potential source of larger solvent effects could be explicit coordination of donor solvent molecules to unsaturated metal sites. We examined this for a number of complexes for which the experimental data had been taken in the potential donor solvent acetonitrile. However, even in cases where the computations suggest solvent coordination, the effects on the metal shifts are very small. Neither solvent effects for the charged complexes in aqueous solution nor explicit solvent coordination to the metal center are large enough to modify our conclusions on the suitability of different electronic-structure methods notably. The tremendous effort of modeling the solvent environment for all relevant species would be clearly outside the scope of the present work.

Likewise, no relativistic corrections are included. Scalar relativistic computations using the X2C Hamiltonian[92] have been carried out at the cM06-L level and are provided in Table S12 in the Supporting Information. The largest effect on absolute shieldings is ca. 75 ppm, and variations within a given subset are less than 50 ppm. Given the much larger shift ranges covered for each nucleus, these are negligible contributions. At first sight, spin−orbit effects due to heavy ligand atoms might be expected to be significant for complexes like $TiBr_4$. However, due to the small metal s-character in the metal−ligand bonds, these effects should be small.[93−95]

As triplet instabilities are an issue for some of the complexes in case of hybrid functionals with larger EXX admixtures and for Hartree−Fock and MP2, we carried out stability analyses of the wave functions. In Turbomole, triplet instabilities can be investigated in the escf module by calculating the lowest eigenvalues of all irreducible representations of the electronic Hessian. In ORCA the keyword "stabperform" was employed for the same purpose. In that case, we could also follow the eigenvector associated with the most negative eigenvalue and get unrestricted solutions and, in some cases, also their shieldings. Instabilities are indicated by red color in the full shielding results in Tables S43−S55 in the Supporting Information. While the instability analyses for the mPSTS LH did also indicate instabilities, this appears to be to be an artifact of the recent implementation of this functional (see below) in the analysis rather than true instabilities. We did not pursue UKS solutions for general shielding analyses at a larger scale but report the RKS-based results. However, we did additional analyses of the UKS solutions for the BHLYP functional with 50% EXX admixture to estimate the importance of the symmetry breaking for a method where a larger number of unstable RKS solutions were found (see Section S4 and Table S10 in the Supporting Information). For most complexes studied, the UKS solutions did not show strong symmetry breaking (see S^2 expectation values of zero). For the few cases with spin-broken UKS solutions, somewhat larger deviations are seen, but on a scale that would not affect significantly the overall performance of BHLYP in the statistical evaluations. The same is expected to hold for other hybrid functionals with similar or lower EXX admixtures, where triplet instabilities are seen. Matters are different for HF and consequently for MP2: here the negative eigenvalues are much larger for a given complex than for BHLYP, and to some extent this holds already for the DSD-PBEP86 DH (Table S11). UHF solutions tend to exhibit large symmetry breaking, and their associated shielding values can be very different from those obtained for the unstable RKS solutions. Consequently, we have to consider HF and MP2 results, as well as double-hybrid data, to be meaningless in many cases, and we keep them in the Supporting Information only as an illustration of the failure of these methods. The differences between BHLYP and HF instabilities can be inferred from the magnitude of the negative eigenvalues of the electronic Hessian: these are much smaller with 50% EXX admxiture than for 100% (Table S11). The Turbomole and ORCA stability analyses for HF wave functions do not align to 100%, but this does not affect the main conclusions drawn.

The XC functionals evaluated in the Turbomole shielding and shift calculations include SVWN[96,97] as an example of an LDA functional (rung 1), the rung 2 GGA functionals BLYP,[98,99] BP86,[98,100,101] PBE,[102] KT1,[103] KT2,[103] KT3,[104] B97D,[105] and HCTH,[106,107] and the rung 3 meta-GGA functionals TPSS,[108] M06-L,[109] MN15-L,[110] VSXC,[111] τ-HCTH,[112] B97M-V,[113] and SCAN.[114] Global hybrid functionals (GHs, rung 4) include TPSSh,[70] B3LYP,[115] PBE0,[116] B97-2,[117] BHLYP,[118] PW6B95,[119] M06,[120] MN15,[121] and M06-2X.[120] We additionally tested the four range-separated hybrids (RSHs, rung 4) CAM-B3LYP,[122] ωB97X-D,[123] ωB97X-V,[124] and ωB97M-V,[125] as well as the local hybrid functionals (LHs, also rung 4) LH07s-SVWN,[126] LH07t-SVWN,[127] LH12ct-SsirPW92,[128] LH12ct-SsifPW92,[128] LH14t-calPBE,[129] LH20t,[50] mPSTS,[51,52] and LHJ14.[53] LH14t-calPBE and the recent LH20t are the only local hybrids here that include calibrated exchange-energy densities. mPSTS and LHJ14 have been recently implemented into Turbomole by Holzer et al.[51] mPSTS is a slightly modified version of the PSTS functional[52] that has been suggested to exhibit better SCF convergence than the original functional. Note that for τ-dependent functionals we generally include in particular the CDFT versions (using τ_D) that we will denote with the prefix "c".

Computations with the ORCA program contribute additional results for MP2[130] as well as for the double hybrids (DHs, rung 5) B2PLYP[131] and DSD-PBEP86[55,56] (these data are collected in the Supporting Information). In general, we will not present data for all functionals at length in the main text but will largely concentrate on statistical analyses for the better-performing functionals. Full shifts and shielding results for all functionals and complexes are given in Tables S17−S29 and S43−S55 in the Supporting Information, and further statistical data can be found in Tables S30−S42.

Statistical analyses have been carried out relative to the experimental chemical shifts (as reported in Table S1), using standard deviation (SD), mean signed error (MSE), and mean absolute error (MAE) in ppm, as well as the slope of the linear regression when using the Y-intercept method. To be able to compare performances across different nuclei, we will additionally use dimensionless percentage (relative) deviations normalized to the experimental shift range covered for a given

https://doi.org/10.1021/acs.jctc.1c00964
J. Chem. Theory Comput. 2022, 18, 273−292

nucleus. Adding these relative statistical measures up (including the slopes), weighted by the number of values for a given nucleus, provides us also with final aggregate relative deviations for the entire test set (aggregate relative SD, aggregate relative MSE, aggregate relative MAE, and aggregate slope) for all complexes ("all"). A direct linear regression of shifts across the entire test is of course also possible but would be dominated by the nucleus with the largest shift range, ^{59}Co, and thus be less informative. We furthermore will use histogram plots of relative deviations to trace the origins of the largest deviations for a given method, and we also provide maximum relative absolute errors for each method and nucleus (Figure S4 in Supporting Infromation).

4. RESULTS

Comparison of the Structures Obtained at BP86-D3(BJ) and TPSSh-D3(BJ) Levels. In the following, we will largely focus on the results obtained with BP86-D3(BJ) structures to maintain consistency with previous publications. However, different input structures are known to result in (partly large) deviations in the final shifts (see, e.g., ref 90). For a subset of functionals we therefore also computed shifts using TPSSh-D3(BJ) structures, which have been found to agree somewhat better with experimental structures.[132] The results are provided in the Supporting Information, where statistical comparisons are in Figure S1, while the full numerical data are given in Tables S2−S6.

The relative performance of the functionals in the NMR calculations is essentially the same for both sets of input structures (Figure S1). However, the use of moderate exact-exchange admixture (10%) in the optimizations tends to overall improve agreement with experimental shifts, particularly when hybrid functionals, CDFT variants of τ-dependent functionals or highly parametrized functionals are used for the shielding calculations. That is, the performance of most GGAs and mGGAs is affected insignificantly, with the changes in statistical data mostly below 0.3%. Two exceptions here are cM06-L and cVSXC where the differences between the two structure sets are larger but still below 1.0% in relative deviations. Relative SDs and MAEs are reduced somewhat when using the TPSSh structures. Somewhat larger differences are found for rung 4 functionals. In case of GHs the differences between the two sets increase with exact-exchange admixture: that is, for cTPSSh deviations are still below 0.3% in SD and MAE, for B3LYP they are ca. 1.2%/0.9%, for cPW6B95 1.8%/1.4%, for BHLYP 3.7%/3.2% (reducing the relative SD from 20.4% to 16.7% and the relative MAE from 18.7% to 15.5%). Differences for RSHs and LHs are below 2%. That is, while individual shift values may change significantly with input structure, the overall statistical significance is more limited. We can thus in the following concentrate on the BP86-D3(BJ) structures with some confidence, keeping in mind that the TPSSh-D3(BJ) structures may give overall somewhat improved statistical agreement with experiment. We note additionally that while TPSSh was the top-performer in a systematic evaluation of the structures of 3d-complexes, BP86 was not far behind.[132]

Choice of Reference Standards. We have evaluated different choices of reference standards, as these can affect statistical evaluations for transition-metal nuclei substantially.[17,18] One set of evaluations, for which we provide statistical data in Tables S14−S16 in the Supporting Information, uses shifts relative to the following reference standards for the different 3d nuclei: $TiCl_4$ ($\delta_{ref.exp.}$ = 0 ppm), $VOCl_3$ ($\delta_{ref.exp.}$ = 0 ppm), CrO_2F_2 ($\delta_{ref.exp.}$ = −87 ppm), $MnCp(C_6H_6)$ ($\delta_{ref.exp.}$ = −180 ppm), $Fe(CO)_5$ ($\delta_{ref.exp.}$ = 0 ppm), $Co(CO)_4H$ ($\delta_{ref.exp.}$ = −3721 ppm), and $Ni(PMe_3)_4$ ($\delta_{ref.exp.}$ = 40 ppm). Some of these compounds differ from the usual standards used in the NMR experiments and were chosen because they are either neutral molecules (where the experimental standards are ions) or easier to calculate from an electronic-structure point of view. In these cases, the chemical shifts were converted back to the usual scales using the experimental chemical shifts of the chosen reference compounds. We finally decided, however, to follow earlier precedent for transition-metal nucleus shifts and will focus our main discussion on the *Y*-intercept method, based on the linear regression of computed shielding constants at a given level against the experimental shift data. The intercept on the *Y*-axis of this linear fit provides a new reference shift at the given level. The relative performances of different XC functionals are affected only weakly by this choice, also for additional choices of reference standards (even when using "more difficult" reference complexes[17]). The *Y*-intercept method gives overall the smallest statistical deviations, as it produces a "best linear fit" of the computed shieldings to the experimental shift data for any given method. We assume this to provide the smallest bias. This choice also provides us with slopes of the linear-regression lines as a measure of how well a given method reproduces overall the experimental spread of shifts. We implicitly accept the known disadvantage of this approach: in principle, the chemical shifts need to be re-evaluated each time a new compound is added to the test set. For the current sizable (and chemically diverse) test sets, we feel that the *Y*-intercept method provides us with the best measure of the relative performances of different XC functionals.

Artifacts of Using τ_{MS}. The τ_{MS} scheme (eq 1) for rendering the local kinetic energy gauge-invariant is still the most widely used approach to shielding computations with τ-dependent XC functionals. As we had reported,[43,44] we found the scheme to give unphysical paramagnetic contributions for atoms and for the parallel shielding tensor component in linear molecules. While these artifacts clearly also extend to general molecules, the replacement of τ_{MS} by the better founded τ_D (eq 3) did by no means generally improve the agreement with benchmark data for main-group shieldings. In fact, the previously observed excellent performance of the M06-L meta-GGA, obtained with τ_{MS}, clearly deteriorated with τ_D for the initially studied small main-group shielding test set studied.[43] While the differences were in fact less pronounced for the much larger and diverse main-group benchmark set of ref 34, τ_{MS} still gave somewhat smaller MAEs and less negative MSEs. Similar observations held for the VSXC meta-GGA, while matters were dramatically reversed for MN15-L, with much closer agreement with reference data provided within the τ_D framework (with a reduced positive MSE), and τ_D also gave somewhat better agreement with the benchmark data for B97M-V.[34] Small effects on the overall statistics were found for some other meta-GGAs like TPSS, effects for τ-dependent GHs varied. On the other hand, results with several τ-dependent LHs were clearly improved for proton shieldings and for some other situations considered in refs 34, 43, and 44.

We will discuss the situation for the molecular 3d complexes of the present study further below and find a number of substantial differences for the relative performance of different schemes compared to the main-group case. In this subsection we want to only show for some spherical atoms and ions with d^{10} configuration that the same artifacts exist for transition-metal

https://doi.org/10.1021/acs.jctc.1c00964
J. Chem. Theory Comput. 2022, 18, 273−292

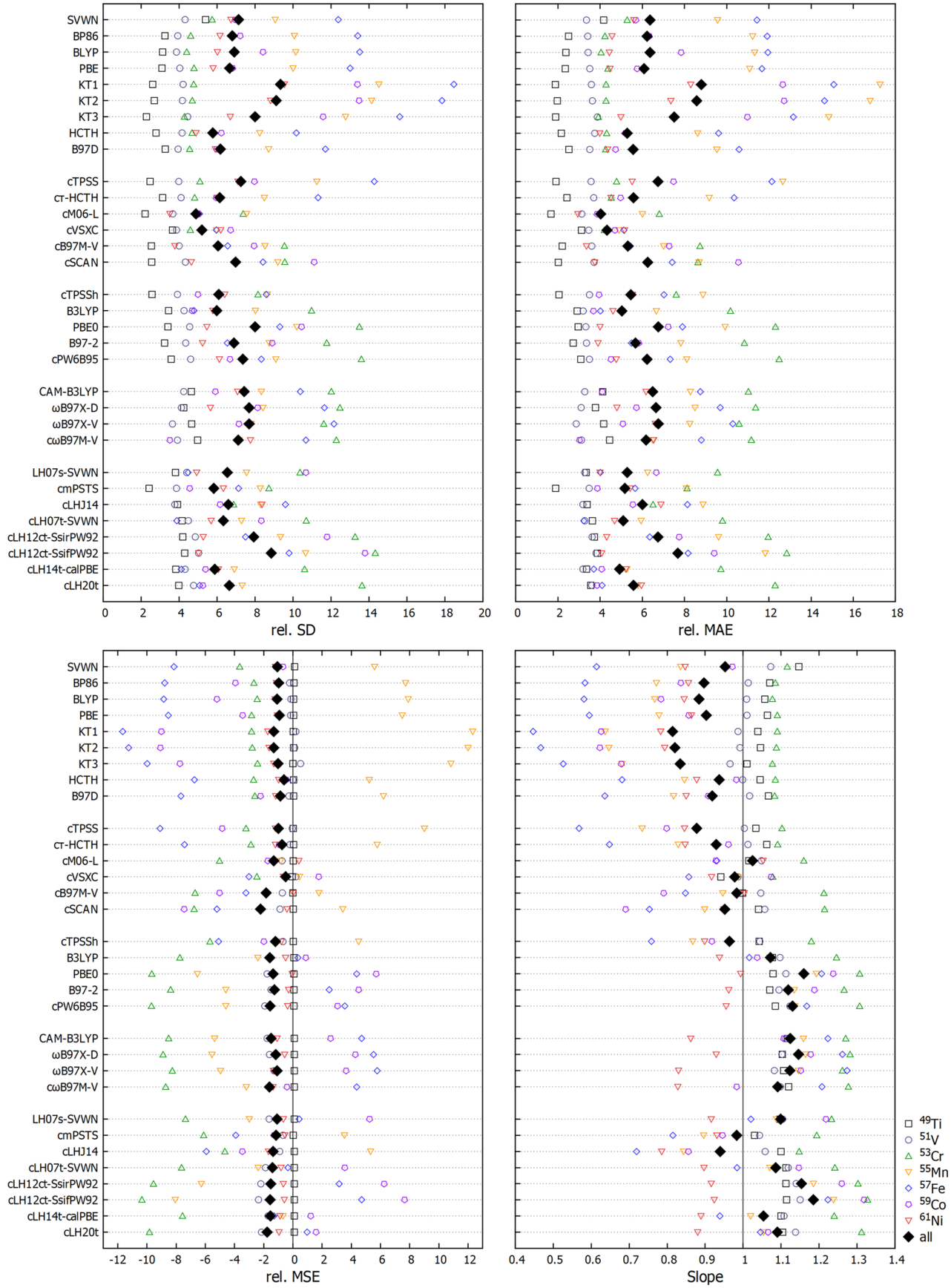

Figure 1. Relative standard deviations, mean signed errors, mean absolute errors in percent, as well as slopes of the linear regression for the individual nuclei (hollow symbols) and their weighted aggregate (filled black symbols) for various XC functionals (using τ_D for τ-dependent functionals).

https://doi.org/10.1021/acs.jctc.1c00964
J. Chem. Theory Comput. 2022, 18, 273−292

nuclei, that they can be even much larger in terms of their shift contributions, and that they are completely eliminated when using τ_D. Table 1 shows total shieldings and paramagnetic contributions for Fe^{2-}, Co^{-}, Ni, and Cu^{+} with τ_{MS} and τ_D for a series of τ-dependent functionals compared to CCSD(T) data. Throughout this analysis, we enforce iso-electronic diamagnetic ($[Ar]3d^{10}$) configurations for all four atomic systems, irrespective of the actual ground state (for Fe^{2-} the CCSD(T) computations produced a symmetry-broken solution only, and the diamagnetic state could not be converged). τ_{MS} gives generally artificial σ^p contributions for all four systems, but the magnitude varies substantially with the overall charge and with the XC functional. The contributions are by far largest for Fe^{2-} and decrease substantially toward Cu^{+}. We may attribute this trend to particularly small energy denominators and low-lying virtual orbitals for the anionic systems.

In agreement with observations for main-group systems,[43,44] the artifacts of the τ_{MS} scheme are by far smallest (with positive sign) for TPSS and TPSSh. SCAN also gives relatively small artifacts, as do B97M-V, PW6B95, and LH20t (except for Fe^{2-}), with varying signs. For LH20t, we note the calibrated exchange-energy densities involved, which appear to reduce such artifacts compared to "uncalibrated" LHs.[44] While M06-L exhibited rather large effects in the main-group case,[43] it occupies an intermediate position for the present 3d systems, together with ωB97M-V and LH12ct-SsifPW92. Particularly large artifacts are seen for VSXC, M06 and, most notably, M06-2X. In some of these latter cases, the paramagnetic artifacts for Fe^{2-} dominate the overall shielding. Fe^{2-} and Co^{-} may be unrealistic examples, however. The case of the Ni atom may be the best glimpse into the magnitude of these artifacts in a realistic situation, as all Ni complexes studied here have a formal Ni(0) oxidation state (see below). Even here the artifacts are substantial with many of the functionals evaluated. This suggests that the τ_{MS} scheme should be viewed with caution for the 3d nuclei studied here. Calculations with τ_D eliminate the artifacts completely. Now the overall shieldings are exclusively due to the diamagnetic term, and they match the CCSD(T) reference data excellently. We will see below that the fact that τ_D includes also current dependencies for τ in a physically reasonable way becomes an additional asset for the molecular transition-metal complexes studied here.

General Statistical Evaluation of 3d-Nucleus NMR Chemical Shifts. We start with a bird-eye's view on the statistical evaluation, focusing first on the relative deviations for the weighted average over all 70 complexes, consisting of 12 × ^{49}Ti, 10 × ^{51}V, 10 × ^{53}Cr, 11 × ^{55}Mn, 9 × ^{57}Fe, 9 × ^{59}Co, and 9 × ^{61}Ni shifts. The relative statistical data for the individual nuclei and the combined weighted values are shown in Figure 1, using the *Y*-intercept method for each nucleus. In this graphic we include only methods where relative MAEs below 18%, relative MSEs between −13% and +13%, relative SDs below 20%, and slopes between 0.4 and 1.4 are achieved for all nuclei. Statistical evaluations for all methods by the *Y*-intercept method can be found in Tables S30−S42 in the Supporting Information, data for the alternative referencing scheme (see above) are in Tables S14−S16, while Tables S17−S29 provide full numerical shifts and Tables S43−S55 the corresponding shielding data. As differences between BP86-D3(BJ) and TPSSh-D3(BJ) structures for the shielding results are insignificant for the overall statistical comparison of the different methods (see above), we focus exclusively on the former set of structures. For τ-dependent functionals, we will focus on the better justified τ_D model only (using prefixes "c" as is common for the CDFT treatment) and postpone a discussion of the treatment of τ to a later section. We note already, however, that τ_D provides generally the best agreement with experiment, sometimes dramatically so, except for MN15-L (see below).

We first discuss the aggregate weighted relative MAEs for the different categories of XC functionals (Figure 1, top right). For orientation we note that for the large main-group absolute shielding benchmark of ref 34 based on CCSD(T)/pcSseg-3 data, several functionals achieved combined relative MAEs below 2%, 0.9% in case of the overall best-performing DH DSD-PBEP86 (1.1% for MP2), 1.5% in case of the currently best rung 4 (cLH12ct-SsifPW92) and rung 3 (cB97M-V) functionals. Even a few more functionals made the 1.5% threshold when going to relative shifts.[34] For the present 3d shift evaluations, the best functionals are generally still above 4% aggregate relative MAE, indicating a generally more challenging situation. We lump the only LDA on rung 1 (SVWN) with the rung 2 GGAs and find that two of the latter, B97D and HCTH, give relatively low relative MAEs of 5.6% and 5.3%, respectively. The SVWN LDA and the standard GGAs BLYP, BP86, and PBE perform only somewhat more poorly with relative MAEs of 6.1−6.4%. Strikingly, the "specialized" KT1-KT3 functionals designed for (main-group) nuclear shieldings give clearly inferior results here (relative MAEs 7.5−8.8%), in spite of their relatively good overall performance for main-group nuclei.[34] Indeed, even SVWN clearly outperforms these three functionals. This shows that their narrow parametrization does not carry over to the present 3d nuclei, consistent with observations that the good performance of these functionals for light main-group shieldings is essentially based on a compensation between errors in the dia- and paramagnetic contributions.[42]

Turning to the meta-GGA functionals (rung 3), we see widely divergent performance. cMN15-L, which performed very well in the main-group case (see above),[34] has been excluded from Figure 1, as it exceeds the boundaries set (see above), mainly due to its rather poor performance for the critical nuclei ^{55}Mn, ^{57}Fe, and ^{59}Co (Table S32). Its final weighted relative MAE is 13.2%. On the other hand, cM06-L and cVSXC provide the best performances (but only in their τ_D CDFT versions, see further below), with a final relative MAE of only 4.0% and 4.3%, respectively. Indeed, these are not only the lowest relative MAEs for rung 3 but for any functional studied here! This is notable, as it defies the usual expectation that the performances of XC functionals usually improve as one moves up the rungs of "Jacob's ladder". In the present case, this has to do with clearly detrimental effects of EXX admixture for certain transition-metal systems (in particular for ^{53}Cr shifts, see below) and also with the ability of the CDFT framework to cover important current contributions (see below). The remaining CDFT meta-GGAs, cTPSS, cτ-HCTH, cB97M-V, and cSCAN exhibit intermediate relative MAEs between 5.3% and 6.7%, which is in the range of the GGAs discussed above. In fact, the rather reasonable performance of cτ-HCTH is slightly inferior to its GGA analogue HCTH, and the exceptionally good performance of cB97M-V for main-group shieldings[34] carries over only partially to the present 3d shift set (relative MAE 5.3%).

Proceeding to rung 4, we start with the GHs. Only five out of the nine GHs evaluated here are included in Figure 1. Most of the Minnesota functionals exhibit extremely large deviations (Tables S35−S37 in Supporting Information), with weighted relative MAEs of 16.7% (cM06-2X), 18.7% (cM06), and 9.9% (cMN15), still much larger deviations are found with other τ

https://doi.org/10.1021/acs.jctc.1c00964
J. Chem. Theory Comput. 2022, 18, 273−292

frameworks. Again the by far largest deviations are accumulated for ^{55}Mn, ^{57}Fe, and ^{59}Co. In case of cM06-2X, the large deviations for these three nuclei can at least in part be attributed to the very large global EXX admixture (54%), as BHLYP exhibits similar deviations (relative MAE 18.7%). For cM06 and cMN15, other shortcomings related to the description of electron density response in the core and semicore regions have to be considered as important factors, as found previously for 3d transition-metal hyperfine couplings.[133] B3LYP, cTPSSh, and B97-2 are the best-performing GHs (relative MAEs 5.0%, 5.5%, 5.7%, respectively), as they perform rather well for the three critical nuclei (they exhibit larger deviations for ^{53}Cr, see below). B3LYP had so far been considered the best functional for the later 3d nuclei,[15−18] and it does indeed belong to the overall best-performing functionals. Nevertheless, its overall relative MAE is larger than those of cVSXC, cM06-L and comparable to those of several LHs (see below) and even to one GGA (HCTH). cPW6B95 (6.2%), and PBE0 (6.8%) follow as intermediate performers among the GHs. We included four RSHs on rung 4, even though previous experience did not suggest them to have any notable advantages over GHs for nuclear shieldings. This is borne out by the results for CAM-B3LYP (6.5%), ωB97X-D (6.7%), ωB97X-V (6.8%), and cωB97M-V (6.2%), which are comparable to, e.g., cPW6B95 or PBE0. For cωB97M-V, the CDFT variant actually deteriorates the results very slightly in comparison to the other τ models.

This brings us to the LHs, where position-dependent EXX admixture indeed has been considered and previously found to be[34,43,44] an advantage for nuclear shieldings in the main-group case. While cLH12ct-SsifPW92 and cLH12ct-SsirPW92 had been found to perform best overall for non-hydrogen main-group nuclei in these studies (followed by cLH20t, which performs better for proton shieldings), in the present case LHs with a smaller prefactor of the t-LMF and thus lower overall EXX admixtures perform better. That is, cLH14t-calPBE (4.9%) and cLH07t-SVWN (5.1%) show the overall lowest relative MAEs, together with cmPSTS that features a more complicated LMF (5.2%). These values are comparable to those for B3LYP and HCTH but remain somewhat above those of the best-performing cVSXC and cM06-L (see above), attributable to the ^{53}Cr values (see below). Interestingly, LH07s-SVWN with an s-LMF based on the reduced density gradient is not far behind here (5.3%), followed by the general-purpose cLH20t (5.6%). The larger deviations for cLH12ct-SsifPW92 (7.7%) and cLH12ct-SsirPW92 (6.7%) are due to larger deviations for several nuclei and related to the large EXX admixture. cLHJ14 (6.0%) based on correlation length is intermediate among the LHs.

The current representatives of rung 5 on the ladder, the B2PLYP and DSD-PBEP86 DHs, are not at all suitable for the 3d-nucleus shifts studied here (see Table S29 in Supporting Information). As expected, their combination of large constant EXX admixtures and MP2 correlation make them largely useless for transition-metal shifts, in contrast to the clearly best performance over all functionals in the main-group case by DSD-PBEP86.[32,34] The DHs and MP2, as well as the underlying HF method, are not included in Figure 1, as they exceed the set boundaries by far for all nuclei except for ^{49}Ti. As HF is a very poor starting point, MP2 fails completely as well, and this failure is only partly corrected in the DHs (somewhat better with B2PLYP than with DSD-PBEP86, which has a larger EXX admixture of 70%).

Based mainly on the aggregated relative MAE values the overall top-performing functionals for the entire set are cM06-L, cVSXC, cLH14t-calPBE, and B3LYP (with values up to 5%), closely followed by LH07t-SVWN, LH07s-SVWN, cmPSTS, HCTH, cB97M-V, cTPSSh, and LH20t (with values up to 5.6%). A closer understanding of what drives these overall trends requires looking at the individual nuclei, as we will do below. This will also involve the relative MSEs (Figure 1, bottom left) and the slopes of the regression lines (Figure 1, bottom right). The aggregates of these two quantities are less informative, and particularly the slopes are of more interest when analyzed for the individual nuclei (see below). We note only here that the aggregate relative MSEs are small and negative (by not more than −2% for semilocal functionals, a bit more when EXX admixture is present), and they arise from a compensation between positive and negative values for different nuclei (see below). The widths of the distributions of errors are indicated by the relative SDs (Figure 1, top left). These give largely the same order of functionals as the relative MAEs.

A Closer Look at the Most Critical Nuclei: ^{55}Mn, ^{57}Fe, and ^{59}Co. These nuclei, as well as ^{61}Ni discussed below, are the best-known examples for the advantage of GHs with moderate EXX admixture such as B3LYP over simple GGAs,[15−18] while GGAs gave better agreement with experiment for earlier 3d nuclei like ^{53}Cr and some earlier 4d nuclei.[25−27,134] We have mentioned in the introduction some of the arguments put forward to explain these observations. Yet we find these three later 3d nuclei to also dominate the aggregated relative deviations discussed in the previous subsection, at least for those functionals that do not make it into the top group. It seems thus important to have a closer look at these critical nuclei, focusing again on the better-performing functionals. Starting again with the rung 1−2 functionals, we see that indeed ^{55}Mn and ^{57}Fe account for the largest relative MAEs, on the order of 9−12% for the simpler functionals (SVWN, BLYP, PBE, B97D, HCTH), and to 13−17% for the "specialized" KT1-KT3. For ^{59}Co, the relative MAEs are lower, about 5−8% for the simple LDA/GGA functionals, 11−13% for KT1-KT3. It is notable, that the relative MSEs often reach substantial fractions of these values, with a positive sign for ^{55}Mn but with a negative sign for ^{57}Fe and ^{59}Co. These opposite signs seem to generally contribute to the overall relatively small negative aggregate relative MSEs that we discussed above. The relatively good performance of HCTH and B97D among the GGAs is reflected in relatively low deviations for these nuclei and is consistent with earlier findings on a smaller set of TM complexes.[135] Note also that the GGAs all give too small slopes of the regression lines for these three nuclei.

While several CDFT meta-GGAs give similar (cτ-HCTH, cTPSSh) or much larger (cMN15-L) deviations for the same nuclei, the top-performing cM06-L and cVSXC are clear outliers and improve the MAEs and MSEs, giving relative MAEs of 3.9−6.0% (but only in their CDFT implementations), comparable to the less critical nuclei (see below), and with slopes close to 1.0. This is indeed the reason for their overall top performance. Notably, these two functionals also give very small relative MSEs (and low SDs). In contrast, the very poor performance of cMN15-L for the overall test set is closely linked to its large deviations for these three nuclei. cB97M-V performs only somewhat inferior (relative MAEs 5.4−7.3%) to the top-performing cM06-L and cVSXC.

The better-performing GHs in the general overview above, such as B3LYP, cTPSSh or B97-2, also reduce the deviations

https://doi.org/10.1021/acs.jctc.1c00964
J. Chem. Theory Comput. 2022, 18, 273−292

most notably for these three nuclei (to 3.7−7.8% relative MAE, 8.9% for ^{55}Mn in case of cTPSSh), to the extent that the relative MAEs of other nuclei are typically larger (see below). The slopes are again close to 1.0 (up to 1.19 with B97-2 for ^{59}Co) for these three functionals. cPW6B95 also has fairly low relative MAEs for these three nuclei (4.5−8.1%), PBE0 and three of the RSHs also remain generally below 10%. All other GHs (BHLYP, cM06, cMN15, cM06-2X) exhibit much larger deviations, including dramatically overestimated slopes. Even larger deviations are seen for HF, MP2 and the DHs, largely indicating erratic behavior.

Among the best-performing LHs, cLH14t-calPBE, cLH07t-SVWN, and cLH20t all have relative MAEs below 6% for these three nuclei, comparable to cM06-L or cVSXC. LH07s-SVWN, cmPSTS, cLHJ14, cLH12ct-SsifPW92, and cLH12ct-SsifPW92 give slightly larger values. For all of these LHs, as well as for cM06-L, cVSXC, and B3LYP, and indeed for most hybrids, the largest relative MAEs are now contributed by other nuclei (see below). Indeed, we can define the best-performing functionals as those where this is the case, i.e., where the deviations for the most critical nuclei ^{55}Mn, ^{57}Fe, and ^{59}Co have been reduced below those for some seemingly less demanding ones. When taking a weighted average of the relative MAEs for just these challenging three later 3d nuclei, we find six functionals competing closely with values below 5%, in the order cLH14t-calPBE < cLH20t = cM06-L < cLH07t-SVWN < cVSXC < B3LYP. It is notable that this includes not only three LHs, the B3LYP GH but also two CDFT meta-GGAs.

The spread of shifts, the slope of the regression lines, and the scatter, as well as the dependence on the electronic-structure method for a given nucleus is typically dominated by the systems with the largest paramagnetic (de)shielding contributions. This holds even more so for transition-metal complexes where the incomplete metal d-shells give rise to large paratropic currents around a given metal nucleus. Indeed, our analyses confirm that the performance of a given method for a given subset is governed largely by the complexes with the most negative absolute shielding values, even though small deviations from this notion can be found. The *Y*-intercept method tends to hide somewhat these effects, as the reference shift value is adapted for a given method. Other choices of reference values may also be misleading. Therefore, it is best to examine the absolute shielding values provided in Tables S43−S55 in the Supporting Information for better understanding.

The subset for the prototypical late 3d nucleus ^{57}Fe consists exclusively of organometallic systems, which typically are considered to provide strong ligand fields. Nevertheless, considerable paramagnetic contributions are found, for example in case of Cp ligands. The relative MSE and the slope of the linear regression are largely dominated by [$FeCp_2$], followed by [$FeCp(CO)_2iPr$] and [$FeCp(CO)_2Me$]. [$Fe(CO)_3(CH_2CHCHO)$] exhibits the second largest shift after [$FeCp_2$] but has a smaller dependence on the functional than the three Cp complexes, potentially due to the lack of support for delocalized currents by a Cp ligand. While functionals that enhance paramagnetic contributions by (a) EXX admixture or (b) CDFT τ contributions also lead to more deshielding for the remaining complexes, they do so to a lesser extent. This explains the effects on slope and MSE. Indeed, [$FeCp_2$] has been chosen earlier for closer analysis of the effects of EXX admixture for this very reason,[24] and we have already mentioned the rationalizations, i.e., energy gaps and CPKS coupling terms on one hand and delocalization errors on metal−ligand covalency reducing the PSO matrix elements on the other hand. Just as an example, the computed absolute shielding constants for [$FeCp_2$] grow more negative with increasing EXX admixture in the series BLYP, B3LYP, and BHLYP as −2747.3 ppm > −4518.8 ppm > −9395.9 ppm. Combined with similar trends for the two further Cp complexes and much smaller changes for the less deshielded systems, this controls MSEs and slopes, with the middle value for B3LYP giving the best representation. Similarly, cM06-L gives a shielding value of −4057.2 ppm, while its non-CDFT variants give much less deshielded values in the range −2300 to −2600 ppm, similar to simple GGAs (similar but less dramatic effects of τ_D are found for VSXC). We can thus conclude that current-dependencies of the response functionals are of major importance here, be it via EXX admixture or via the CDFT treatment of τ.

The ^{59}Co subset is represented by complexes with a much more diverse range of electronic structures and ligand types, and it exhibits the by far largest shift range of any of the nuclei studied here. This has made ^{59}Co NMR such an important subfield. The most deshielded values are found for classical Werner-type ligands with a relatively weak ligand field, which give rise to small ligand-field splittings and consequently low-lying excited states. The complexes dominating the MSEs and slopes are $[Co(H_2O)_6]^{3+}$, $[Co(acac)_3]$, $[Co(NH_3)_4(CO_3)]^+$, and $[Co(NH_3)_6]^{3+}$. As described above for the iron complexes, these systems exhibit the largest dependencies on the functional, and for example both EXX admixture and CDFT τ contributions in the two mentioned CDFT meta-GGAs provide more negative shieldings (larger shifts). The least deshielded values and thus smallest dependencies on the functionals are represented by the carbonyl complexes $[Co(CO)_4H]$ and $[Co(CO)_4]^-$. That is, in spite of the rather more diverse electronic-structure characteristics of the Co complexes, the mechanisms that determine the dependencies on the functional are comparable as for the Fe systems discussed above. Recall that some of the charged species from this subset also exhibit the largest solvent effects on the shifts, reducing the largest values to some extent, but they are not considered in this comparison of functionals (cf. Computational Details above, as well as Table S7 and Figure S2 in Supporting Information).

A somewhat mixed situation pertains to the ^{55}Mn subset, where the most deshielded values represent both high ($[MnO_4]^-$) and lower ($[MnCp(C_7H_8)]$, $[MnCp(C_6H_6)]$) oxidation states. It appears that similar effects of extended paratropic currents as discussed above for [$FeCp_2$] are relevant for the two Cp complexes. In contrast, the permanganate ion represents high-oxidation-state situations with d^0 configuration that are also of importance for the earlier 3d elements, e.g., for ^{53}Cr (see below). Nevertheless, both EXX admixture and CDFT τ contributions lead to more deshielded values for both types of systems. The less deshielded end with smaller dependences on the functional is in this case represented by several carbonyl complexes. The dominance of the most deshielded systems can again be exemplified by the slopes of the regression lines as a function of EXX admixture. For the entire subset they increase overall steeply, e.g., as 0.77 (BLYP), 1.07 (B3LYP), and 1.77 (BHLYP). Removing the three most critical complexes alters this substantially to 0.61 (BLYP), 0.81 (B3LYP), and 1.07 (BHLYP). Now the larger EXX admixture of BHLYP might even seem more favorable. This makes it even more obvious that part of the challenge of these later 3d nuclei indeed arises from some complexes with extremely large paramagnetic shielding contributions. Clearly, the best-performing functionals also

https://doi.org/10.1021/acs.jctc.1c00964
J. Chem. Theory Comput. 2022, 18, 273−292

benefit from some error compensation. Nevertheless, standard GGA functionals tend to underestimate the paramagnetic contributions for these three subsets systematically, and this can be cured partly by moderate (constant or position-dependent) EXX admixture or by CDFT τ contributions. The latter can be exemplified by the shielding value for [MnCp-(C_7H_8)], which is −5392.5 ppm for cM06-L (only somewhat less negative than the B3LYP value of −5814.6 ppm, comparable to the cLH14t-calPBE value of −5268.7 ppm), while it is in the range −3300 to −3600 ppm for the non-CDFT variants of this functional. Similar trends hold for $[MnO_4]^-$ or [MnCp(C_6H_6)].

Note also, that some of the most deshielded systems for these three nuclei do already exhibit substantial triplet instabilities when larger EXX admixtures are used, as with BHLYP. This pertains, e.g., to $[FeCp_2]$, $[Co(H_2O)_6]^{3+}$, and [MnCp(C_7H_8)] (the same holds for $[Mn(NO)_3(CO)]$). This will be a larger issue for the discussion of the ^{53}Cr subset (see below).

Examination of Results for ^{61}Ni, Which Is Represented by Electronically Less Diverse Complexes. The reason for a somewhat diminished diversity of electronic structures for the ^{61}Ni complexes is, that all of the experimentally measured ones correspond to the Ni(0) formal oxidation state and a relatively symmetrical coordination environment. The likely origin for this limitation appears to be the large electric quadrupole moment of ^{61}Ni,[136] when combined with large electric field gradients of the common square-planar Ni(+II) complexes, as well as a low natural abundance.[3] This leads probably to very broad lines, rendering experimental observation very difficult.

^{61}Ni is another nucleus for which the initial computational evaluation by one of us had suggested the B3LYP GH to outperform the BPW91 GGA as well as the BHLYP GH with higher global EXX admixture.[18] The GGA was found to underestimate somewhat the spread of shifts, while BHLYP gave larger scatter. The present broader evaluation confirms this to some extent but provides further insights. We start by noting that most semilocal functionals exhibit small negative relative MSEs between −1.7% and −1.1% and too low slopes, between 0.78 and 0.88. Exceptions are again caused by several CDFT meta-GGAs, such as cM06-L (relative MSE +0.4%, slope 1.05), cMN15-L (relative MSE +0.1%, slope 1.02), cVSXC (relative MSE −0.7%, slope 0.92), cSCAN (relative MSE −0.4%, slope 0.95), and cB97M-V (relative MSE +0.0%, slope 1.00). This leads to an improvement of the relative MAEs from about 4−6% for the simpler GGAs and LDA and up to 8% for KT1 and KT2 to only 2.9% for cM06-L, and 3.3%−3.7% for cB97M-V, cMN15-L, and cSCAN (cVSCX lags somewhat behind, 5.2%). Obviously, the underestimate of the slope by semilocal functionals is much less pronounced here than for the above three critical nuclei, likely due to the narrow range of electronic structures of the Ni(0) complexes, and due to the resulting overall smaller shielding range of less than 2000 ppm. The most deshielded values arise from $[Ni(cod)_2]$, [Ni-t,t,t-cdt(PMe_3)], and [Ni-t,t,t-cdt(CO)], and the most shielded one arises from $[Ni(C_2H_4)_2PMe_3]$. EXX admixture does improve the spread moderately. Here even somewhat larger admixture is tolerated in the GHs (e.g., slope 0.94 for B3LYP, 0.96 for B97-2, 0.99 for PBE0, 1.03 for BHLYP), and most GHs, RSHs or LHs give slopes that are still below unity. Indeed, now the LHs that performed best for the non-hydrogen main-group shieldings, cLH12ct-SsifPW92 and cLH12ct-SsifPW92, are competitive as well but still inferior to cM06-L. CDFT τ contributions for the latter functional (somewhat less so for cVSXC) have similarly moderate effects that increase the slope and improve the MSEs.

Overall the picture is less clear-cut than for some of the other nuclei, as most semilocal functionals and even hybrids with moderate EXX admixtures give somewhat too small slopes, but many of these functionals still have reasonably low relative MAEs and small negative relative MSEs for ^{61}Ni. The poorer performances of cM06-2X and cMN15 should be mentioned, as should the again very poor performances of HF, MP2, and the DHs (see full shift results in Tables S23, S24, and S29, and statistical data in Tables S36, S37, and S42 in Supporting Information). Triplet instabilities play a minor role here. Except for Hartree−Fock, MP2, and DSD-PBEP86, where several Ni complexes feature instabilities, only $[Ni(cod)_2]$ seems to be sensitive for functionals with large EXX admixtures like BHLYP or M06-2X.

Results for ^{53}Cr and the Issue of Triplet Instabilities. ^{53}Cr is the 3d nucleus where EXX admixture most clearly has been found to be detrimental in a past study, with B3LYP giving a too large spread of values as well as more scatter than the BPW91 GGA.[27] We note that the complexes for which data are available fall into the two categories of very low (0) and very high (+VI) oxidation states. In agreement with the earlier work, we find LDA and all GGAs to give comparably small relative MAEs on the order of ca. 4−5% (5.3% for SVWN), with small negative relative MSEs between −2.4% and −3.6%. This suggests that the reasons that render EXX admixture important for the aforementioned nuclei do not apply here to the same extent. As we move to the CDFT versions of the meta-GGAs, this picture is modified somewhat, in an interesting way: now the overall top-performing cM06-L (6.8%) actually gives larger relative MAEs than its otherwise inferior counterparts cTPSS (4.8%) or cτ-HCTH (4.5%). cB97M-V, cSCAN and cMN15-L give relative MAE of 8.7%, 8.6%, and 12.3%, respectively, in this case clearly poorer than their non-CDFT variants (see Tables S32 and S33, as well as discussion below). But cVSXC still performs excellently (relative MAE 4.2%, relative MSE −2.5%) in this case.

We clearly confirm the notion that Hartree−Fock exchange is detrimental for the treatment of the ^{53}Cr shifts: all GHs exhibit larger relative MAEs than the GGAs, increasingly so with growing EXX admixture. That is, cTPSSh (7.6%) performs worse than its underlying cTPSS meta-GGA but better than B3LYP (10.2%), B97-2 (10.8%), PBE0 (12.3%), cM06 (11.5%), or cPW6B95 (12.5%). GHs with larger EXX admixtures, such as BHLYP or cM06-2X, perform even much worse here, with the notable exception of cMN15, which is comparable to B3LYP in this case (relative MAE 10.1%, but only in its CDFT variant), in spite of a larger global EXX admixture of 44%. The RSHs perform comparably as the PBE0 or cM06 GHs in this case. The detrimental effect of Hartree−Fock exchange is particularly apparent in the HF calculation, which fails completely here and gives larger deviations than for any of the other nuclei (see Table S29 for shifts vs experimental data and Table S42 for statistical data). Consequently, MP2 or the DHs also fail completely for ^{53}Cr. Notably, the HF calculations give dramatically negative MSEs, and this carries over in reduced form to negative relative MSEs for all (global, range-separated or local) hybrid functionals. In contrast, MP2 exhibits catastrophically positive relative MSEs, which carries over to the DHs. From the viewpoint of the spread of values, all semilocal functionals already have slopes above one, and this is aggravated by EXX admixture.

Closer analysis has to again focus on the absolute shieldings, as the *Y*-intercept-based shifts cloud which systems actually

https://doi.org/10.1021/acs.jctc.1c00964
J. Chem. Theory Comput. 2022, 18, 273−292

cause the overall largest variations, given that the reference value also changes from method to method. The most deshielded values and the largest variations with the functional arise clearly from the six Cr(+VI) complexes, while the most shielded end is represented by the four Cr(0) carbonyl complexes. The experimental shifts of these two groups of complexes are separated by approximately 2000 ppm, while the variations within a given group are below 350 ppm. It is thus clear that the performances of the different functionals are largely controlled by how well they represent the shielding differences between the two groups, and this is largely determined by how well the Cr(+VI) d^0 complexes and their low-lying LMCT-type excited states are described. We may use $[CrO_2Cl_2]$ as a good example for a Cr(+VI) complex with large deshielding and a large dependence on the functional and contrast it with $[Cr(CO)_6]$ on the most shielded side (see Tables S43−S55). The difference in experimental shifts between these two complexes is 2058 ppm. Already the simplest semilocal functionals give a too large difference of about 2300−2400 ppm, due to a too negative shielding for $[CrO_2Cl_2]$, consistent with an overestimated slope in the range 1.11−1.17, which is slightly more than the corresponding slope of the regression for the entire subset. The difference is further increased by EXX admixture as well as CDFT τ contributions. For example, B3LYP gives a difference between the two shieldings of 2753 ppm, cLH14t-calPBE 2703 ppm, and cM06-L 2517 ppm (compared to 2100−2200 ppm for its non-CDFT variants). The detrimental effect of even small EXX admixtures is thus immediately apparent from just the differences between those two complexes. As the CDFT τ contributions also increase the difference somewhat, they also lead to too large slopes and even more negative MSEs in the final shifts. Indeed, it may well be that the diversity of the ^{53}Cr subset is insufficient to get a more balanced description. This is not easy to correct, however, as any experimental data available fall into either the tetrahedral Cr(+VI) oxo or the octahedral Cr(0) carbonyl category. Less symmetrical complexes pose difficulties for experimental detection due to large electric-field gradients and thus line-broadening for the quadrupolar ^{53}Cr nucleus. For example, Hafner et al. examined a larger series of more than 50 Cr(0) carbonyl and phosphine complexes, most of them (46) with carbene ligands.[137] However, their shifts span a range of less than 300 ppm. Similarly, the range of shifts for experimentally accessible Cr(+VI) oxo complexes is also small so far. Consideration of a larger number of complexes would thus likely not cure the basic problem of the too large relative shifts between Cr(+VI) and Cr(0) complexes.

One may wonder to what extent triplet instabilities are the reason for the unfavorable effect of EXX admixture on the ^{53}Cr shifts. Hartree−Fock exhibits triplet instabilities for *all* chromium complexes studied here, and consequently HF, MP2 and DH shift results are completely erratic. Following ref 36, we may consider this as an artificial spin-symmetry breaking, as GHs with lower EXX admixture, such as B3LYP, or LHs and RSHs produce stable spin-restricted solutions. Yet BHLYP is triplet-unstable for the three Cr(+VI) complexes $[CrO_2Cl_2]$, $[CrO_2F_2]$, and $[CrO_3Cl]^-$, i.e., for several of the systems with the largest paramagnetic contributions. It seems possible that "incipient" or "latent" spin-symmetry breaking could be invoked in this context to rationalize the detrimental effects of EXX admixture. While BHLYP also exhibits triplet instabilities for several Mn, Fe, and Co complexes, in those cases the effects seem to be partly compensated due to the more diverse nature of the electronic-structure characteristics making up the given subset of complexes.

The Less Difficult Earlier 3d Nuclei ^{51}V and ^{49}Ti. The two early 3d nuclei represent smaller dependences on the XC functional than those discussed so far. Indeed, the ^{49}Ti subset is the only one for which even HF, MP2, and the DHs perform reasonably well (see below).

We start our discussion with the slightly more demanding ^{51}V subset. Here the relative MAE values for the semilocal functionals range from 3.1% (cM06-L) to 3.9% (KT3), excluding some of the non-CDFT variants, which give poorer results. The relative MSEs for these functionals are small and can be negative or positive, and slopes close to 1.0 are found. The relative MAEs are also between 3.1%−3.8% for all GHs, RSHs, and LHs, except for a few cases, most notably ωB97X-V with a relative MAE of 2.9%, the top performing functional in this subset. cM06-2X (4.3%), cM06 (5.6%), and BHLYP (5.8%) give clearly larger deviations. Relative MSEs also tend to remain small in many cases except for a few functionals (including some non-CDFT variants of τ-dependent functionals), but they tend to become more consistently negative. Indeed, slopes are now around 1.10 (larger ones are obtained for the less well-performing GHs). Hartree−Fock and particularly MP2 perform nevertheless clearly worse here too, with large negative MSEs, particularly for MP2. Indeed, the majority of vanadium complexes studied here exhibits triplet instabilities at HF level (Table S55). Most of these are cured for the DHs, which perform indeed much better than HF or MP2 while still falling behind most other functionals.

Overall the ^{51}V subset is dominated by V(+V) oxo complexes and VF_5, while the two V(−I) carbonyl complexes bring in additional diversity. It seems, however, that the different ligand types available for the V(+V) complexes improve the balance of the overall set, which may be an advantage over the available ^{53}Cr data discussed above. The largest paramagnetic contributions arise for the model complex $[VOMe_3]$ (and the experimentally studied counterpart $[VO(CH_2SiMe_3)_3]$), as the pure σ-donor methyl ligands leave the system coordinatively unsaturated with low-lying vanadium 3d-type virtual orbitals (additional π-donor ligands like fluoride or chloride help increase the HOMO−LUMO-gap and thus reduce the paramagnetic contributions somewhat). The least deshielded value is represented by $[V(CO)_6]^-$. As discussed in several cases above, EXX admixture and CDFT τ contributions increase the differences between these extreme cases, and the changes for the oxomethyl complex are most important in this context. However, the dependencies are much less pronounced than those discussed so far, and the overall somewhat too large difference for hybrid functionals like B3LYP is in part outweighed by the smaller statistical scatter over the entire subset, giving low relative MAEs.

Turning finally to the ^{49}Ti shifts, we find this to be the only subset, where Hartree−Fock is not a catastrophical starting point, and where thus also MP2 or the DHs do not deviate much from the other functionals. Incidentally the first calculations of ^{49}Ti chemical shifts had been reported at the IGLO-HF level - in hindsight a serendipitously good choice of target systems for this method.[138] Except for some non-CDFT variants of certain τ-dependent functionals (see Tables S32, S33, and S35−S38), all functionals have relative MAEs below 5%, including HF, MP2, and the DHs. Now even the KT1-KT3 functionals perform well with relative MAEs of around 2%, while cM06-L (1.7%) is the top performer. cTPSSh (2.0%) has the lowest value for a GH,

https://doi.org/10.1021/acs.jctc.1c00964
J. Chem. Theory Comput. 2022, 18, 273−292

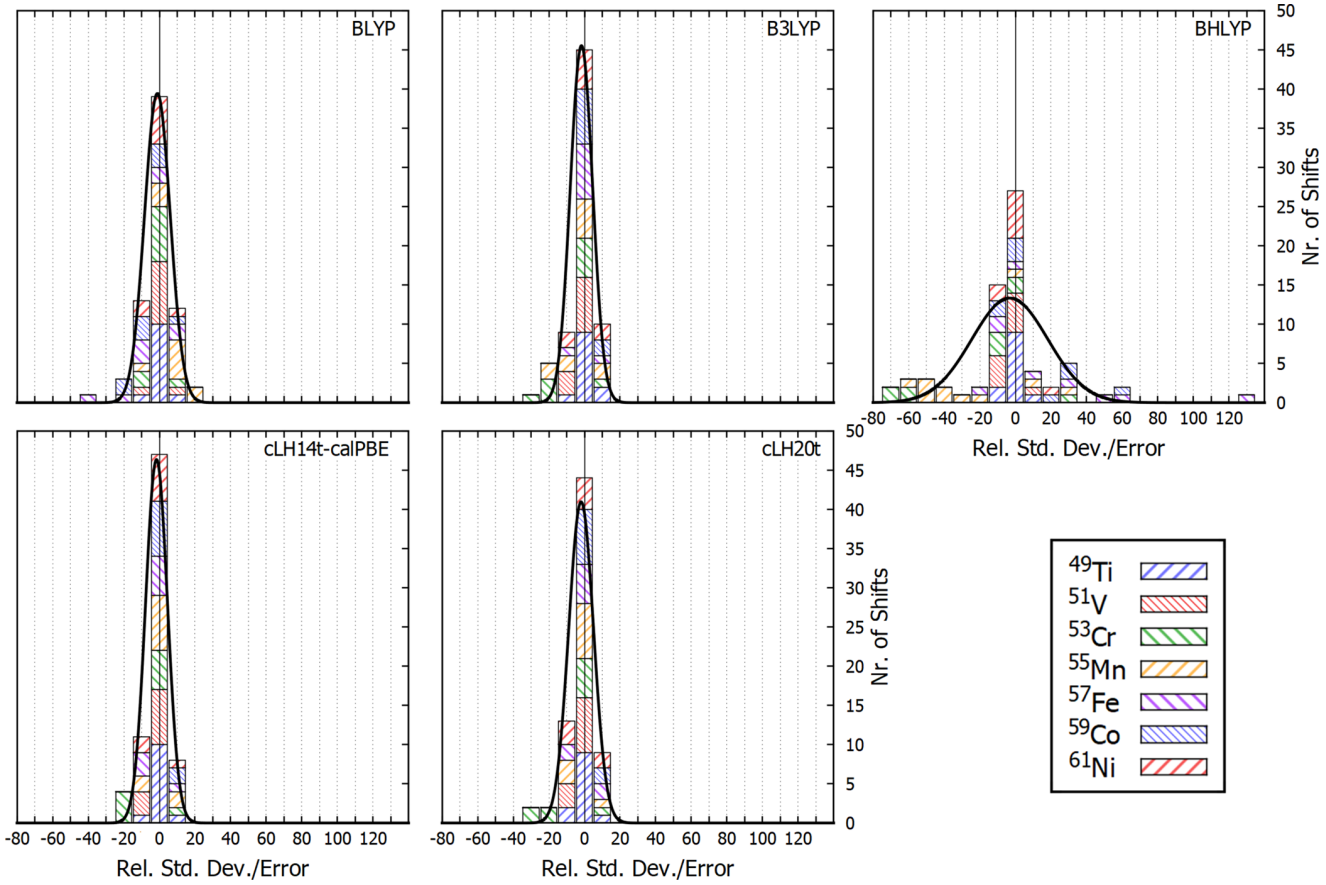

Figure 2. Standard deviation plots (solid black line) on top of histogram deviation plots of the individual 3d transition metal test sets, comparing BLYP to B3LYP and BHLYP (top), and cLH14t-calPBE to cLH20t (bottom) within the range from −60% to +140% in blocks of 10%.

cmPSTS (1.9%) for an LH, while most GHs, RSHs or LHs tend to have somewhat larger relative MAEs above 3%. These observations are consistent with previous work on a much smaller sample of functionals.[28] A few worse performances of highly parametrized functionals should also be mentioned, such as cMN15 or cM06, which exhibit a relative MAE of 5%, while LDA (SVWN) gives 4.2%. Most functionals also give slopes relatively close to one, except for a few (SVWN 1.15, cM06 1.17, cMN15 1.16, MP2 1.15, and some non-CDFT variants of τ-dependent functionals).

A Closer Look at the Role of Exact-Exchange Admixture for Error Distributions (Figure 2). To provide some further insights into how EXX admixture in GHs and LHs shifts the performances for the different 3d nuclei, in Figure 2 we use relative SD curves (black solid line) on top of histogram plots of the number of shifts of all subsets in the error ranges from −80% to 140% in 10% blocks. We compare the series of the closely related BLYP, B3LYP and BHLYP with constant EXX admixtures of 0%, 20%, and 50%, as well as the two cLHs cLH14t-calPBE and cLH20t, which are both based on calibrated exchange-energy densities. They have t-LMF prefactors of 0.500 and 0.715, respectively, and thus also represent different EXX admixtures. The histogram representation allows us to follow how the overall width of the aggregate relative SD distribution over the entire test set is dominated by certain nuclei. Similar information is provided by the maximum relative AEs (see Figure S4 in Supporting Information).

Starting with the BLYP curve, we see its medium width to be caused by positive deviations in the 20% block for ^{55}Mn shifts and a few negative deviations in the −40% and −20% blocks for ^{57}Fe (and ^{59}Co) shifts. This is consistent with the observation that these critical nuclei dominate the errors for most semilocal functionals (with the exception of some CDFT meta-GGAs), with positive MSEs for ^{55}Mn and negative ones for ^{57}Fe. As we move to 20% EXX admixture in B3LYP, the distribution narrows noticeably, larger errors for the three critical nuclei are removed, but now negative deviations in the −30% and −20% blocks occur for ^{53}Cr and ^{55}Mn, consistent with the generally negative MSEs of hybrid functionals for these two nuclei. As we increase the EXX admixture to 50% for BHLYP, the distribution widens dramatically. Now deviations for ^{53}Cr in the −70% and −60% blocks and for ^{55}Mn in the −60% through −20% blocks dominate the negative flank of the curve, while overshooting for ^{57}Fe in the +50%, + 60% and even +130% blocks is seen, together with positive deviations for ^{59}Co in the +30% and +60% blocks. It is thus clear that too high constant EXX admixture enhances the negative MSEs for the early nuclei ^{53}Cr and ^{55}Mn, but positive deviations start to appear for ^{57}Fe and ^{59}Co, which are absent for the more moderate EXX admixture of B3LYP. We may trace this potentially to triplet instabilities, in particular for certain ^{53}Cr and ^{55}Mn complexes (see above). We noted already the smaller dependencies of the ^{49}Ti, ^{51}V and ^{61}Ni shifts on the EXX admixture. In consequence, these nuclei do not dominate the widths of the distributions.

Similar observations can be made for the two cLHs: both functionals have relatively narrow distributions and do not differ much on the side of positive deviations (shifts of all nuclei except

https://doi.org/10.1021/acs.jctc.1c00964
J. Chem. Theory Comput. 2022, 18, 273−292

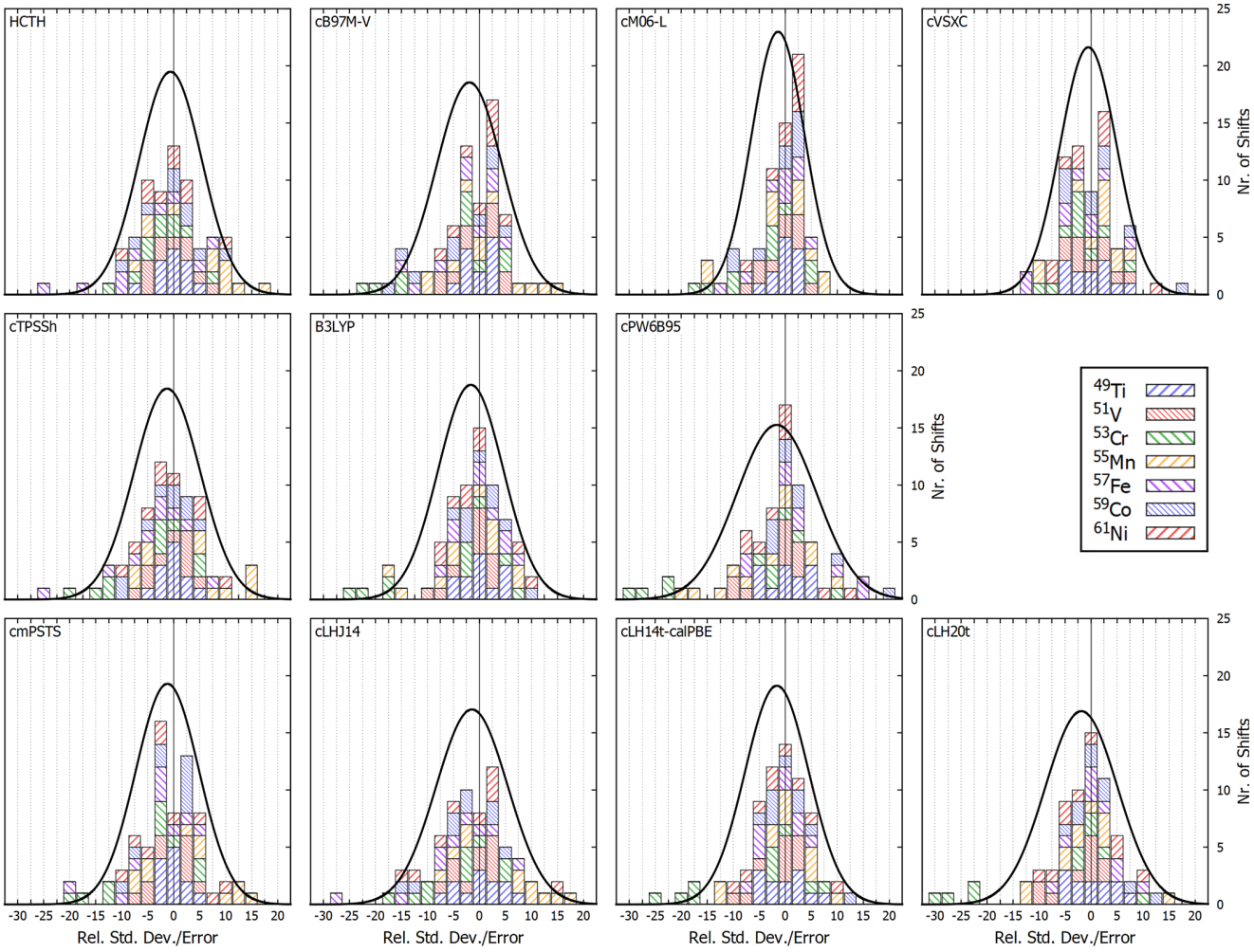

Figure 3. Standard deviation plots (solid black line) on top of histogram deviation plots of the individual 3d transition metal test sets for a larger selection of better-performing functionals within the range −45% to +40% in blocks of 5%.

^{51}V appear in the +10% block). Similarly to the B3LYP GH, for both LHs the negative flank of the distribution curve is dominated by some ^{53}Cr shifts, to a lesser extent by ^{55}Mn shifts (again, except for ^{53}Cr and ^{59}Co, all nuclei appear in the −10% block). These deviations increase somewhat with increased t-LMF prefactor for cLH20t (the ^{53}Cr error margins increase from −24% to −30%, compared to −26% for B3LYP), explaining why this functional arrives at a slightly inferior overall performance and a slightly wider distribution of errors compared to cLH14t-calPBE for the entire test set, while being entirely competitive for the later 3d nuclei. We note, however, that the average EXX admixture of LH20t might be compared best to a GH with around 30−35% EXX admixture (as indicated, e.g., by its performance for mixed-valence (de)localization[50]). In spite of this, its problems caused by triplet instabilities are much less pronounced than for comparable GHs (see above). Yet we also see that the flexibility of position-dependent EXX admixture for the present LHs is not yet sufficient to allow an improvement of the performance for the later 3d nuclei without any deterioration for the earlier ones. This represents a goal for the currently ongoing construction of more sophisticated local mixing functions for LHs.

Figure 3 widens the lens to a larger selection of the better-performing functionals and can correspondingly narrow the scale of the error distributions. Starting with the semilocal functionals, the plots for HCTH and cB97M-V confirm that the widths of the distributions are dominated by positive deviations from ^{55}Mn complexes (and a few ^{59}Co and ^{61}Ni systems) and by both negative and positive deviations from ^{57}Fe and ^{53}Cr complexes (some ^{61}Ni and ^{59}Co systems also appear). The two CDFT meta GGAs cM06-L and cVSXC change the picture decisively in terms of the much smaller magnitude of the deviations for ^{55}Mn, ^{57}Fe and in terms of the nature of the also reduced negative deviations: for cM06-L these are now contributed by some ^{53}Cr, ^{57}Fe, and ^{59}Co complexes and even a few ^{55}Mn systems, and for cVSXC, these smaller negative deviations are now also distributed over different nuclei, including ^{53}Cr, ^{57}Fe and ^{61}Ni. The consequence for the latter functional is, that relative MAEs are below 5.2% for all nuclei, indicating a particularly balanced behavior (see above).

The three GHs cTPSSh, B3LYP, and cPW6B95 can be used to look again at the role of (constant) EXX admixture. As mentioned above, the largest (moderate) negative deviations for B3LYP arise from ^{53}Cr shifts, to a lesser extent from ^{55}Mn. The largest positive deviations come from ^{61}Ni and ^{59}Co, but they reach only into the +10.0 block (ranging from +8.75%−11.25%). In contrast, cTPSSh (10% EXX admixture) is somewhat closer to the semilocal functionals, as its slightly wider distribution is dominated by positive deviations for ^{55}Mn

https://doi.org/10.1021/acs.jctc.1c00964
J. Chem. Theory Comput. 2022, 18, 273−292

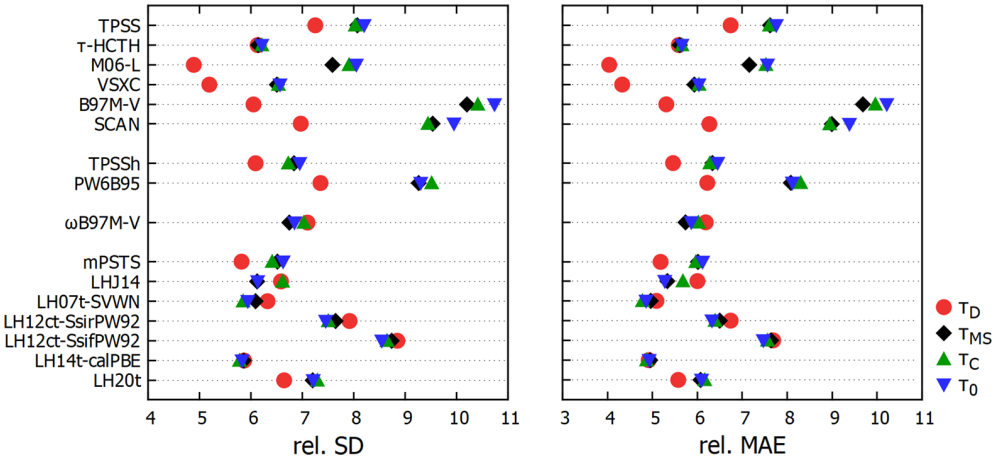

Figure 4. Effects of different treatments of τ on aggregate relative SDs and relative MAEs for different τ-dependent functionals.

and by a less structured mix of negative deviations that include ^{53}Cr and ^{57}Fe. The larger EXX admixture (28%) of cPW6B95 also widens the error distribution compared to B3LYP but retains the typical origins for hybrids: negative deviations for ^{53}Cr and ^{55}Mn, positive ones for ^{59}Co, ^{57}Fe, ^{61}Ni, now ranging from −30% to +20%. In addition to the already discussed LHs cLH14t-calPBE and cLH20t, Figure 3 also includes cmPSTS and cLHJ14, which are both not based on a t-LMF. The most notable feature of the somewhat wider distribution of cLHJ14 are positive deviations for ^{55}Mn. Interestingly, the negative deviations are covered by some ^{57}Fe, ^{53}Cr, ^{59}Co, and ^{61}Ni shifts, which differs from the typical behavior of most of the hybrid functionals. This results from an overall low EXX admixture for this LH in the core region.[34] cmPSTS, which has a similarly narrow distribution as cLH14t-calPBE, differs from the behavior of the latter by clearly having a larger positive deviation for ^{55}Mn (the relative MSE of 3.5% for cmPSTS should be compared to −0.7% in cLH14t-calPBE). The largest negative deviations arise from some ^{53}Cr and ^{57}Fe complexes.

Role of Current-Dependency in the τ-Dependent Functionals for Their Overall Performance. So far we have concentrated on the CDFT variants of the τ-dependent functionals using the τ_D scheme, but we mentioned from time to time the non-CDFT variants. As has been discussed previously,[42−44,47−49,60] τ_D is the physically most appropriate way of using these functionals for magnetic properties, as this turns them into proper CDFTs, if only via their τ-dependence. It is difficult to derive meaningful CDFT functionals at LDA or GGA levels, while EXX admixture is of course a way to bring in current contributions to some extent. Indeed, we have argued previously that the position-dependent EXX admixture of LHs is helpful for this purpose.[43,44]

We also showed above and in refs 43 and 44 that the τ_{MS} scheme, while rendering τ gauge invariant, also introduces paramagnetic artifacts that are easy to demonstrate for atoms but are more difficult to identify for general molecules. We can partly disentangle these artifacts from the genuine current contributions by comparing also to two further models to treat τ, (a) by using the original gauge-dependent τ (with the gauge origin placed at the center of mass, termed τ_C) and (b) by eliminating the gauge dependence in an *ad hoc* way[43] as done in the ORCA code (τ_0). These two models do not generate paramagnetic artifacts for atoms, but they lack of course current contributions arising from τ. Figure 4 compares the aggregate relative SDs and relative MAEs for the entire test set obtained from these overall four treatments for several τ-dependent functionals (MN15-L, M06, MN15, and M06-2X are not shown, as their deviations would be too large to fit properly into the plots; see Tables S32 and S35−S37). The statistical measures for individual nuclei are available in Tables S30−S42 in Supporting Information.

We note first of all, that the performances for τ_{MS}, τ_C, and τ_0 are generally very similar, while the τ_D CDFT results differ substantially from these data for several but not for all functionals. This suggests that the main differences do *not* arise from the τ_{MS} artifacts discussed further above, but that they reflect genuine current contributions provided by the τ_D CDFT framework. This outcome differs somewhat from previous analyses for main-group nuclei,[34,43,44] where sometimes the differences of τ_{MS} compared to τ_C and τ_0 were of similar magnitude as those relative to τ_D. The obvious reason for the large effects of explicit current contributions for some of the functionals in the present case seems to be the genuinely very large paratropic currents determining the shieldings and relative shifts for the transition-metal nuclei.

Indeed, for those functionals in Figure 4, where the differences between τ_D and the other three models are significant, the CDFT framework generally improves the agreement with experiment, as indicated by lower relative SDs and relative MAEs. This is particularly notable for the meta-GGAs M06-L, VSXC, B97M-V, and SCAN: while all these functionals perform rather well, and the first two functionals were even the top performers for the entire test set, when used in their CDFT variants, they are much less convincing otherwise. Closer analyses (Tables S32−S34) show that this holds for almost all nuclei, except for ^{53}Cr where the larger deshielding brought in by the CDFT contributions in fact deteriorates somewhat agreement with experiment, as was found for the main-group case.[34,43,44] For the three critical nuclei ^{55}Mn, ^{57}Fe, and ^{59}Co the improvements by the CDFT terms are dramatic, to some extent comparable to the effects of moderate EXX admixture. Indeed, without the CDFT framework the best-performing meta-GGAs M06-L and VSXC (and partly B97M-V) would not offer any notable advantage over other semilocal functionals. Significant error reductions pertain also to SCAN. Smaller but still notable improvements are seen for TPSS, while the differences are very small for τ-HCTH.

For one meta-GGA not shown in Figure 4, MN15-L, the CDFT framework is actually overall detrimental to the

https://doi.org/10.1021/acs.jctc.1c00964
J. Chem. Theory Comput. 2022, 18, 273−292

agreement with experiment (Table S32). While cMN15-L improves somewhat over the other three schemes for ^{49}Ti, ^{51}V, ^{57}Fe, and ^{61}Ni, it gets significantly worse for ^{53}Cr, for ^{55}Mn, and particularly for ^{59}Co. As a result, the overall relative MAE increases from about 9%−10% for the other three schemes to about 13% for cMN15-L. It appears that here the current contributions overshoot for several nuclei, while they are more moderate and thus mostly improve matters for cM06-L or cVSXC (see above). This should be viewed against the backdrop that cMN15-L is strikingly improved over its non-CDFT variants for main-group shieldings, where it is in fact superior to both cM06-L and cVSXC.[34]

The performance of the two GHs TPSSh and PW6B95 also benefits very notably from the CDFT treatment, even though their EXX admixture does also bring in some current contributions. For TPSSh, the CDFT treatment gives slightly larger deviations for ^{53}Cr, which are outweighed by the improvements for the other nuclei. That is, the effects here also parallel those brought about by EXX admixture. For PW6B95 the improvements extend to essentially all nuclei except ^{61}Ni, which remains almost unaffected. Some improvements are found also for M06 (Table S35), even though the resulting deviations are still too large to fit the scale of Figure 4 (^{55}Mn shifts are improved most notably). In case of M06-2X and of MN15, the non-CDFT variants are even more strikingly worse than the already poorly performing CDFT variants. Indeed, for MN15 the deviations without CDFT treatment reach several hundreds of percent for the critical nuclei ^{55}Mn, ^{57}Fe, and ^{59}Co, suggesting extremely large current contributions needed to reach even moderately accurate results (Table S36). Nevertheless all of the just mentioned, highly parametrized, meta-GGA-based GHs are not competitive even when used in the CDFT framework.

The only RSH that depends on τ is ωB97M-V. Here the overall effects of the CDFT contributions are relatively small and tend to deteriorate the overall agreement with experiment slightly for most nuclei, except for ^{59}Co and ^{61}Ni (see Table S41). A smaller influence of the CDFT treatment is seen also for most LHs, and the overall effects may be somewhat favorable (LH20t) or very slightly unfavorable (LHJ14, LH07t-SVWN, LH12ct-SsirPW92, and LH12ct-SsifPW92). Only mPSTS exhibits a larger improvement by the CDFT contributions for all nuclei except ^{61}Ni. For most LHs, we find moderate improvement for some nuclei and moderate deterioration for others adding up to the observed trend. LH20t shows small improvements for all nuclei, LH14t-calPBE exhibits generally negligible changes. The overall smaller effects of τ_D for most LHs are consistent with the argument that position-dependent EXX admixture, in particular in the core and semicore regions around the NMR nucleus, helps to cover some current-dependencies that are absent for semilocal functionals or insufficiently described by most GHs.[43,44]

5. CONCLUSIONS

This report extends substantially earlier work on the quantum-chemical computation of the NMR chemical shifts of the 3d transition-metal nuclei. On one hand, the composed benchmark set covers 70 NMR shift values for both early and late 3d nuclei from ^{49}Ti, ^{51}V, ^{53}Cr, ^{55}Mn, ^{57}Fe, and ^{59}Co to ^{61}Ni. This provides a systematic comparative look at systems that so far had been evaluated separately at different levels. On the other hand, the overall 41 methods (plus different treatments of τ) evaluated here cover many approaches that had so far not been tested for transition-metal nuclei, in particular many more recent DFT methods. This includes current-density functional (CDFT) implementations of τ-dependent meta-GGAs and of other τ-dependent functionals based on Dobson's extension of τ in comparison with other treatments. In addition to a variety of semilocal functionals, a wide selection of global, range-separated, and local hybrid functionals have been compared, as well as Hartree−Fock, MP2 and two double-hybrid functionals. The same methods have recently been evaluated in an extended screening for main-group shieldings and shifts. In combination, the two evaluations give an unprecedentedly detailed account of the performance of DFT methods for NMR shieldings and shifts.

One particularly striking result of the present study is, that two CDFT versions of meta-GGA functionals, cM06-L and cVSXC, are the top performers when evaluated across the entire 3d-nucleus test set. It appears that the CDFT-extension brings in advantages for the later nuclei ^{55}Mn, ^{57}Fe, ^{59}Co that otherwise can only be provided by moderate Hartree−Fock exchange admixtures in hybrid functionals. On the other hand, the disadvantages of Hartree−Fock exchange for ^{53}Cr are only partly mimicked by these functionals. In general, the effect of the CDFT extension of τ-dependent functionals can have a much larger effect in the present evaluations than for main-group nuclei. Performance is improved overall significantly (i.e., averaged over all nuclei), except for cMN15-L. This suggests that inclusion of current-dependence into a functional via τ contributions is particularly important for nuclei like ^{55}Mn, ^{57}Fe, and ^{59}Co, which exhibit particularly large paratropic currents in their complexes.

Hartree−Fock admixture in different types of hybrid functionals may also be beneficial for these same nuclei for the same reason, i.e., to bring in current contributions. This is the case for moderate constant admixtures as in B3LYP, confirming the excellent performance of this functional for the later 3d nuclei (cTPSSh, B97-2, and partly cPW6B95, also belong to the better-performing global hybrids). But it holds also for several local hybrids, which also perform particularly well for these later nuclei. Too large Hartree−Fock exchange admixtures, either global, range-separated, or local, deteriorate performance for ^{53}Cr. This can probably be traced back to triplet instabilities in high-oxidation-state complexes of these elements at Hartree−Fock level, and possibly to some lack of nuance in the ^{53}Cr set caused by experimental limitations. While most hybrid functionals do not show such instabilities, it seems that their remnants may still deteriorate the performance for the chromium subset increasingly with larger admixtures of Hartree−Fock exchange. Among the local hybrids, functionals with lower admixtures (cLH14t-calPBE, cLH07t-SVWN, and cmPSTS) tend to perform best, changing somewhat the order of the best local hybrids compared to the main-group case. Some of the local hybrids, such as cLH14t-calPBE, may be particularly suitable for multinuclear NMR studies on transition-metal complexes, where simultaneously high accuracy for metal and ligand shifts is desired.

Too high EXX admixtures in global or range-separated hybrids deteriorate even the behavior for the later 3d elements, where Hartree−Fock fails completely. MP2 cannot correct this and also is not applicable here, except for the uncritical ^{49}Ti case. MP2 contributions and large exact-exchange admixtures also make double hybrid functionals unsuitable for 3d transition-metal shifts, while some of them are known to be top performers

https://doi.org/10.1021/acs.jctc.1c00964
J. Chem. Theory Comput. 2022, 18, 273−292

in main-group shielding evaluations (in particular DSD-PBEP86). Overall, we can recommend cM06-L, cVSXC, cLH14t-calPBE, cLH07t-SVWN, cmPSTS, and B3LYP as particularly suitable functionals for 3d-nucleus NMR shifts. The systematic evaluation also provides hints for an even more fine-grained selection of methods for particular nuclei. These insights should be helpful in aiding NMR studies on transition-metal nuclei. In particular, an improved selection of methods for combined computational studies of metal and ligand NMR shifts in the context multinuclear NMR experiments should be enabled. The construction of more advanced local mixing functions for local hybrids is an area from which further improvements can be expected, including for heavier nuclei, where coordinate scaling in the high-density limit becomes important.

We close with a short take-home summary:

- An extended benchmark of experimental NMR shifts for 3d nuclei was used to evaluate more than 40 DFT functionals from all rungs.
- Overall, the top performance was found for current-density-response implementations of two meta-GGAs, cM06-L and cVSXC.
- This is followed closely by two local hybrids (LH14t-calPBE and LH07t-SVWN) and by the B3LYP global hybrid.
- Hartree−Fock, MP2, and double-hybrid functionals are completely unsuitable for the 3d shifts, except for ^{49}Ti, due to large static correlation effects and triplet instabilities.
- Some CDFT meta-GGAs and some local hybrids are suggested for multinuclear NMR studies on 3d transition-metal complexes.

■ ASSOCIATED CONTENT

Supporting Information

The Supporting Information is available free of charge at https://pubs.acs.org/doi/10.1021/acs.jctc.1c00964.

Comparison of shift results with BP86-D3(BJ)/def2-TZVP(D) and TPSSh-D3(BJ)/def2-TZVP(D) structures for a subset of functionals, estimates of solvent effects on the shifts of some selected complexes, evaluation of UKS solutions for triplet-unstable BHLYP wave functions using ORCA in comparison to RKS values with ORCA and TURBOMOLE, the maximum relative AEs, estimates of scalar relativistic effects for all complexes with the best performing cM06-L functional, shieldings, shifts, and statistical results for nontruncated vs model complexes (see text), mean statistical data for the Y-intercept vs referenced shift calculations, as well as full shifts, shieldings, and statistical results for all functionals, including all τ-models with BP86-D3(BJ)/def2-TZVP-(D) structures, as well as comparisons of relevant structural parameters of the BP86-D3(BJ)/def2-TZVP-(D) and TPSSh-D3(BJ)/def2-TZVP(D) structures, and Cartesian input files for all complexes of the present study (PDF)

Raw shielding results for all functionals at BP86-optimized structures and experimental reference shifts used (XLSX)

■ AUTHOR INFORMATION

Corresponding Author

Martin Kaupp − *Institut für Chemie, Theoretische Chemie/Quantenchemie Sekretariat C7, Technische Universität Berlin, D-10623 Berlin, Germany;* orcid.org/0000-0003-1582-2819; Email: martin.kaupp@tu-berlin.de

Authors

Caspar Jonas Schattenberg − *Institut für Chemie, Theoretische Chemie/Quantenchemie Sekretariat C7, Technische Universität Berlin, D-10623 Berlin, Germany*

Morten Lehmann − *Institut für Chemie, Theoretische Chemie/Quantenchemie Sekretariat C7, Technische Universität Berlin, D-10623 Berlin, Germany*

Michael Bühl − *School of Chemistry, University of St. Andrews, St Andrews KY16 9ST Fife, U.K.;* orcid.org/0000-0002-1095-7143

Complete contact information is available at: https://pubs.acs.org/10.1021/acs.jctc.1c00964

Notes

The authors declare no competing financial interest.

■ ACKNOWLEDGMENTS

C.J.S. is grateful for a scholarship that was provided by the Studienstiftung des deutschen Volkes. This work has been funded by the German Research Foundation (Deutsche Forschungsgemeinschaft, DFG) within Project KA1187/14-1. M.B. gratefully acknowledges support from EaStCHEM and the School of Chemistry in St Andrews.

■ REFERENCES

(1) Proctor, W. G.; Yu, F. C. On the Nuclear Magnetic Moments of Several Stable Isotopes. *Phys. Rev.* **1951**, *81*, 20−30.

(2) Mason, J. *Multinuclear NMR*; Plenum Press: New York, 1987.

(3) Werhun, P.; Bryce, D. L. Structural and Crystallographic Information from ^{61}Ni Solid-State NMR Spectroscopy: Diamagnetic Nickel Compounds. *Inorg. Chem.* **2017**, *56*, 9996−10006.

(4) Autschbach, J. In *Principles and Applications of Density Functional Theory in Inorganic Chemistry I*; Kaltsoyannis, N., McGrady, J. E., Eds.; Structure and Bonding; Springer: Heidelberg, Germany, 2004; Vol. *112*; pp 1−43.

(5) Flaig, D.; Maurer, M.; Hanni, M.; Braunger, K.; Kick, L.; Thubauville, M.; Ochsenfeld, C. Benchmarking Hydrogen and Carbon NMR Chemical Shifts at HF, DFT, and MP2 Levels. *J. Chem. Theory Comput.* **2014**, *10*, 572−578.

(6) Maurer, M.; Ochsenfeld, C. Spin Component-Scaled Second-Order Møller-Plesset Perturbation Theory for Calculating NMR Shieldings. *J. Chem. Theory Comput.* **2015**, *11*, 37−44.

(7) Kaupp, M.; Bühl, M.; Malkin, V. G. *Calculation of NMR and EPR Parameters*, 1st ed.; Wiley-VCH: Weinheim, Germany, 2004.

(8) Schreckenbach, G.; Ziegler, T. Density functional calculations of NMR chemical shifts and ESR g-tensors. *Theor. Chem. Acc.* **1998**, *99*, 71−82.

(9) Bühl, M.; Kaupp, M.; Malkina, O. L.; Malkin, V. G. The DFT Route to NMR Chemical Shifts. *J. Comput. Chem.* **1999**, *20*, 91−105.

(10) Kaupp, M.; Bühl, M. In Computational Inorganic and Bioinorganic Chemistry. *Encyclopedia of Inorganic Chemistry*; Solomon, E., King, R. B., Scott, R. A., Eds.; Wiley: Chichester, U.K,, 2009; pp 91−107.

(11) Kaupp, M.; Malkina, O. L.; Malkin, V. G. In *Encyclopedia of Computational Chemistry*; Schleyer, P. v. R., Ed.; Wiley Interscience: New York, 1998; pp 1857−1866.

(12) Bühl, M. DFT Computations of Transition-Metal Chemical Shifts. *Annu. Rep. NMR Spectrosc.* **2008**, *64*, 77−126.

(13) Autschbach, J. Density functional theory applied to calculating optical and spectroscopic properties of metal complexes: NMR and optical activity. *Coord. Chem. Rev.* **2007**, *251*, 1796−1821.
(14) Chan, J. C. C.; Au-Yeung, S. C. F. Density Functional Study of ^{59}Co Chemical Shielding Tensors Using Gauge-Including Atomic Orbitals. *J. Phys. Chem. A* **1997**, *101*, 3637−3640.
(15) Bühl, M. Density functional computations of transition metal NMR chemical shifts: dramatic effects of Hartree-Fock exchange. *Chem. Phys. Lett.* **1997**, *267*, 251−257.
(16) Grigoleit, S.; Bühl, M. Computational ^{59}Co NMR Spectroscopy: Beyond Static Molecules. *J. Chem. Theory Comput.* **2005**, *1*, 181−193.
(17) Bühl, M. Density functional computation of ^{55}Mn NMR parameters. *Theor. Chem. Acc.* **2002**, *107*, 336−342.
(18) Bühl, M.; Peters, D.; Herges, R. Substituent effects on ^{61}Ni NMR chemical shifts. *Dalton Trans.* **2009**, 6037−6044.
(19) Bühl, M.; Gaemers, S.; Elsevier, C. J. Density-Functional Computation of ^{99}Ru NMR Parameters. *Chem. Eur. J.* **2000**, *6*, 3272−3280.
(20) Bühl, M.; Håkansson, M.; Mahmoudkhani, A. H.; Öhrström, L. X-ray Structures and DFT Calculations on Rhodium-Olefin Complexes: Comments on the ^{103}Rh NMR Shift-Stability Correlation. *Organometallics* **2000**, *19*, 5589−5596.
(21) Ramalho, T. C.; Bühl, M.; Figueroa-Villar, J. D.; de Alencastro, R. B. Computational NMR Spectroscopy of Transition-Metal/Nitroimidazole Complexes: Theoretical Investigation of Potential Radiosensitizers. *Helv. Chim. Acta* **2005**, *88*, 2705−2721.
(22) Kaupp, M.; Reviakine, R.; Malkina, O. L.; Arbuznikov, A.; Schimmelpfennig, B.; Malkin, V. G. Calculation of electronic g-tensors for transition metal complexes using hybrid density functionals and atomic meanfield spin-orbit operators. *J. Comput. Chem.* **2002**, *23*, 794−803.
(23) Frantz, S.; Hartmann, H.; Doslik, N.; Wanner, M.; Kaim, W.; Kümmerer, H.-J.; Denninger, G.; Barra, A.-L.; Duboc-Toia, C.; Fiedler, J.; Ciofini, I.; Urban, C.; Kaupp, M. Multifrequency EPR Study and Density Functional g-Tensor Calculations of Persistent Organorhenium Radical Complexes. *J. Am. Chem. Soc.* **2002**, *124*, 10563−10571.
(24) Schreckenbach, G. The ^{57}Fe nuclear magnetic resonance shielding in ferrocene revisited. A density-functional study of orbital energies, shielding mechanisms, and the influence of the exchange-correlation functional. *J. Chem. Phys.* **1999**, *110*, 11936−11949.
(25) Bühl, M. Density Functional Calculations of ^{95}Mo NMR Chemical Shifts: Applications to Model Catalysts for Imine Metathesis. *Chem. Eur. J.* **1999**, *5*, 3514−3522.
(26) Bühl, M.; Golubnychiy, V. Density-functional computation of ^{99}Tc NMR chemical shifts. *Magn. Reson. Chem.* **2008**, *46*, S36−S44.
(27) Bühl, M. Density-functional computation of ^{53}Cr NMR chemical shifts. *Magn. Reson. Chem.* **2006**, *44*, 661−668.
(28) Bühl, M.; Mauschick, F. T. Density functional computation of ^{49}Ti NMR chemical shifts. *Magn. Reson. Chem.* **2004**, *42*, 737−744.
(29) Bühl, M.; Hamprecht, F. A. Theoretical Investigations of NMR Chemical Shifts and Reactivities of Oxovanadium(V) Compounds. *J. Comput. Chem.* **1998**, *19*, 113−122.
(30) Bühl, M. NMR Chemical Shifts of Zr@C28. How Shielded Can ^{91}Zr Get? *J. Phys. Chem. A* **1997**, *101*, 2514−2517.
(31) Kupka, T. H_2O, H_2, HF, F_2 and F_2O nuclear magnetic shielding constants and indirect nuclear spin-spin coupling constants (SSCCs) in the BHandH/pcJ-n and BHandH/XZP Kohn−Sham limits. *J. Chem. Theory Comput.* **2009**, *47*, 959−970.
(32) Stoychev, G. L.; Auer, A. A.; Neese, F. Efficient and Accurate Prediction of Nuclear Magnetic Resonance Shielding Tensors with Double-Hybrid Density Functional Theory. *J. Chem. Theory Comput.* **2018**, *14*, 4756−4771.
(33) Schattenberg, C. J.; Reiter, K.; Weigend, F.; Kaupp, M. An Efficient Coupled-Perturbed Kohn-Sham Implementation of NMR Chemical Shift Computations with Local Hybrid Functionals and Gauge-Including Atomic Orbitals. *J. Chem. Theory Comput.* **2020**, *16*, 931−943.
(34) Schattenberg, C. J.; Kaupp, M. Extended Benchmark Set of Main-Group Nuclear Shielding Constants and NMR Chemical Shifts and Its Use to Evaluate Modern DFT Methods. *J. Chem. Theory Comput.* **2021**, *17*, 7602−7621.
(35) Srebro, M.; Autschbach, J. Computational Analysis of $^{47/49}$Ti NMR Shifts and Electric Field Gradient Tensors of Half-Titanocene Complexes: Structure−Bonding−Property Relationships. *Chem. Eur. J.* **2013**, *19*, 12018−12033.
(36) Lee, J.; Head-Gordon, M. Distinguishing artificial and essential symmetry breaking in a single determinant: approach and application to the C_{60}, C_{36}, and C_{20} fullerenes. *Phys. Chem. Chem. Phys.* **2019**, *21*, 4763−4778.
(37) Shee, J.; Loipersberger, M.; Hait, D.; Lee, J.; Head-Gordon, M. Revealing the nature of electron correlation in transition metal complexes with symmetry breaking and chemical intuition. *J. Chem. Phys.* **2021**, *154*, 194109.
(38) Maier, T. M.; Arbuznikov, A. V.; Kaupp, M. Local hybrid functionals: Theory, implementation, and performance of an emerging new tool in quantum chemistry and beyond. *WIREs Comp. Mol. Sci.* **2019**, *9*, e1378.
(39) Arbuznikov, A. V.; Kaupp, M. Nuclear shielding constants from localized local hybrid exchange-correlation potentials. *Chem. Phys. Lett.* **2007**, *442*, 496−503.
(40) Teale, A. M.; Tozer, D. J. Exchange representations in Kohn−Sham NMR shielding calculations. *Chem. Phys. Lett.* **2004**, *383*, 109−114.
(41) Wilson, P. J.; Tozer, D. J. Varying the fraction of orbital exchange in density functional theory: Influence on nuclear magnetic resonance shielding constants. *J. Chem. Phys.* **2002**, *116*, 10139−10147.
(42) Reimann, S.; Ekström, U.; Stopkowicz, S.; Teale, A. M.; Borgoo, A.; Helgaker, T. The importance of current contributions to shielding constants in density-functional theory. *Phys. Chem. Chem. Phys.* **2015**, *17*, 18834−18842.
(43) Schattenberg, C. J.; Kaupp, M. Effect of the Current Dependence of Tau-Dependent Exchange-Correlation Functionals on Nuclear Shielding Calculations. *J. Chem. Theory Comput.* **2021**, *17*, 1469−1479.
(44) Schattenberg, C. J.; Kaupp, M. Implementation and Validation of Local Hybrid Functionals with Calibrated Exchange-Energy Densities for Nuclear Shielding Constants. *J. Phys. Chem. A* **2021**, *125*, 2697−2707.
(45) Maximoff, S. N.; Scuseria, G. E. Nuclear magnetic resonance shielding tensors calculated with kinetic energy density-dependent exchange-correlation functionals. *Chem. Phys. Lett.* **2004**, *390*, 408−412.
(46) Dobson, J. F. Spin-density functionals for the electron correlation energy with automatic freedom from orbital self-interaction. *J. Phys.: Condens. Matter* **1992**, *4*, 7877−7890.
(47) Bates, J. E.; Furche, F. Harnessing the meta-generalized gradient approximation for time-dependent density functional theory. *J. Chem. Phys.* **2012**, *137*, 164105.
(48) Becke, A. D. Current density in exchange-correlation functionals: Application to atomic states. *J. Chem. Phys.* **2002**, *117*, 6935−6938.
(49) Tao, J. Explicit inclusion of paramagnetic current density in the exchange-correlation functionals of current-density functional theory. *Phys. Rev. B* **2005**, *71*, 205107.
(50) Haasler, M.; Maier, T. M.; Grotjahn, R.; Gückel, S.; Arbuznikov, A. V.; Kaupp, M. A Local Hybrid Functional with Wide Applicability and Good Balance between (De)Localization and Left-Right Correlation. *J. Chem. Theory Comput.* **2020**, *16*, 5645−5657.
(51) Holzer, C.; Franzke, Y. J.; Kehry, M. Assessing the Accuracy of Local Hybrid Density Functional Approximations for Molecular Response Properties. *J. Chem. Theory Comput.* **2021**, *17*, 2928−2947.
(52) Perdew, J. P.; Staroverov, V. N.; Tao, J.; Scuseria, G. E. Density functional with full exact exchange, balanced nonlocality of correlation, and constraint satisfaction. *Phys. Rev. A* **2008**, *78*, 052513.
(53) Johnson, E. R. Local-hybrid functional based on the correlation length. *J. Chem. Phys.* **2014**, *141*, 124120.

https://doi.org/10.1021/acs.jctc.1c00964
J. Chem. Theory Comput. 2022, 18, 273−292

(54) Perdew, J. P.; Schmidt, K. Jacob's ladder of density functional approximations for the exchange-correlation energy. *AIP Conf. Proc.* **2000**, *577*, 1−20.
(55) Kozuch, S.; Martin, J. M. L. DSD-PBEP86: In search of the best double-hybrid DFT with spin-component scaled MP2 and dispersion corrections. *Phys. Chem. Chem. Phys.* **2011**, *13*, 20104−20107.
(56) Kozuch, S.; Martin, J. M. L. Spin-Component-Scaled Double Hybrids: An Extensive Search for the Best Fifth-Rung Functionals Blending DFT and Perturbation Theory. *J. Comput. Chem.* **2013**, *34*, 2327−2344.
(57) Wodyński, A.; Kaupp, M. Noncollinear Relativistic Two-Component X2C Calculations of Hyperfine Couplings Using Local Hybrid Functionals. Importance of the High-Density Coordinate Scaling Limit. *J. Chem. Theory Comput.* **2020**, *16*, 314−325.
(58) Kaupp, M. The role of radial nodes of atomic orbitals for chemical bonding and the periodic table. *J. Comput. Chem.* **2007**, *28*, 320−325.
(59) Joy, J.; Danovich, D.; Kaupp, M.; Shaik, S. A Unified Understanding on the Covalent vs. Charge-Shift Nature of the Metal-Metal Bond in Transition Metal Complexes. *J. Am. Chem. Soc.* **2020**, *142*, 12277−12287.
(60) Furness, J. W.; Verbeke, J.; Tellgren, E. I.; Stopkowicz, S.; Ekström, U.; Helgaker, T.; Teale, A. M. Current Density Functional Theory Using Meta-Generalized Gradient Exchange-Correlation Functionals. *J. Chem. Theory Comput.* **2015**, *11*, 4169−4181.
(61) Irons, T. J. P.; Spence, L.; David, G.; Speake, B. T.; Helgaker, T.; Teale, A. M. Analyzing Magnetically Induced Currents in Molecular Systems Using Current-Density-Functional Theory. *J. Phys. Chem. A* **2020**, *124*, 1321−1333.
(62) Franzke, Y. J.; Mack, F.; Weigend, F. NMR Indirect Spin-Spin Coupling Constants in a Modern Quasirelativistic Density Functional Framework. *J. Chem. Theory Comput.* **2021**, *17*, 3974−3994.
(63) Neese, F. Software update: the ORCA program system, version 4.0. *Wiley Interdisciplinary Reviews: Computational Molecular Science* **2018**, *8*, e1327.
(64) Neese, F.; Wennmohs, F.; Becker, U.; Riplinger, C. The ORCA quantum chemistry program package. *J. Chem. Phys.* **2020**, *152*, 224108.
(65) Stoychev, G. L.; Auer, A. A.; Izsàk, R.; Neese, F. Self-Consistent Field Calculation of Nuclear Magnetic Resonance Chemical Shielding Constants Using Gauge-Including Atomic Orbitals and Approximate Two-Electron Integrals. *J. Chem. Theory Comput.* **2018**, *14*, 619−637.
(66) Local version derived from TURBOMOLE version 7.5, TURBOMOLE GmbH, 2020. TURBOMOLE is a development of University of Karlsruhe and Forschungszentrum Karlsruhe 1989−2007, TURBOMOLE GmbH since 2007.
(67) Balasubramani, S. G.; Chen, G. P.; Coriani, S.; Diedenhofen, M.; Frank, M. S.; Franzke, Y. J.; Furche, F.; Grotjahn, R.; Harding, M. E.; Hättig, C.; et al. TURBOMOLE. *J. Chem. Phys.* **2020**, *152*, 184107.
(68) Weigend, F.; Ahlrichs, R. Balanced basis sets of split valence, triple zeta valence and quadruple zeta valence quality for H to Rn: Design and assessment of accuracy. *Phys. Chem. Chem. Phys.* **2005**, *7*, 3297−3305.
(69) Rappoport, D.; Furche, F. Property-optimized Gaussian basis sets for molecular response calculations. *J. Chem. Phys.* **2010**, *133*, 134105.
(70) Staroverov, V. N.; Scuseria, G. E.; Tao, J.; Perdew, J. P. Comparative assessment of a new nonempirical density functional: Molecules and hydrogen-bonded complexes. *J. Chem. Phys.* **2003**, *119*, 12129−12137.
(71) Grimme, S.; Antony, J.; Ehrlich, S.; Krieg, H. A consistent and accurate ab initio parametrization of density functional dispersion correction (DFT-D) for the 94 elements H-Pu. *J. Chem. Phys.* **2010**, *132*, 154104.
(72) Grimme, S.; Ehrlich, S.; Goerigk, L. Effect of the damping function in dispersion corrected density functional theory. *J. Comput. Chem.* **2011**, *32*, 1456−1465.
(73) Becke, A. D.; Johnson, E. R. A density-functional model of the dispersion interaction. *J. Chem. Phys.* **2005**, *123*, 154101.
(74) Johnson, E. R.; Becke, A. D. A post-Hartree-Fock model of intermolecular interactions. *J. Chem. Phys.* **2005**, *123*, 024101.
(75) Johnson, E. R.; Becke, A. D. A post-Hartree-Fock model of intermolecular interactions: Inclusion of higher-order corrections. *J. Chem. Phys.* **2006**, *124*, 174104.
(76) Feher, F. J.; Blanski, R. L. Lewis Acid Adducts of Oxovanadium(V) Alkyl and Triphenylsiloxy Complexes: Synthesis, Characterization, and Reactivity toward Ethylene. *Organometallics* **1993**, *12*, 958−963.
(77) Koller, M. W. CO-Austauschreaktionen an Metallcarbonyl-(Olefin)-Komplexen: I. Synthese optisch aktiver Organoeisenkomplexe; II. Korrelation zwischen Metallkernresonanz und Reaktivität. Dissertation, Universität Zürich: 1993.
(78) Grimme, S. Exploration of Chemical Compound, Conformer, and Reaction Space with Meta-Dynamics Simulations Based on Tight-Binding Quantum Chemical Calculations. *J. Chem. Theory Comput.* **2019**, *15*, 2847−2862.
(79) Pracht, P.; Bohle, F.; Grimme, S. Automated exploration of the low-energy chemical space with fast quantum chemical methods. *Phys. Chem. Chem. Phys.* **2020**, *22*, 7169−7192.
(80) London, F. Théorie quantique des courants interatomiques dans les combinaisons aromatiques. *J. Phys. Radium* **1937**, *8*, 397−409.
(81) Ditchfield, R. Self-consistent perturbation theory of diamagnetism. *Mol. Phys.* **1974**, *27*, 789−807.
(82) Wolinski, K.; Hinton, J. F.; Pulay, P. Efficient Implementation of the Gauge-Independent Atomic Orbital Method for NMR Chemical Shift Calculations. *J. Am. Chem. Soc.* **1990**, *112*, 8251−8260.
(83) Jensen, F. Segmented Contracted Basis Sets Optimized for Nuclear Magnetic Shielding. *J. Chem. Theory Comput.* **2015**, *11*, 132−138.
(84) CFOUR, a quantum chemical program package written by Stanton, J. F.; Gauss, J.; Cheng, L.; Harding, M. E.; Matthews, D. A.; Szalay, P. G., with contributions from Auer, A. A., Bartlett, R. J., Benedikt, U., Berger, C., Bernholdt, D. E., Bomble, Y. J., Christiansen, O., Engel, F., Faber, R., Heckert, M., Heun, O., Hilgenberg, M., Huber, C., Jagau, T.-C., Jonsson, D., Jusélius, J., Kirsch, T., Klein, K., Lauderdale, W. J., Lipparini, F., Metzroth, T., Mück, L. A., OaNeill, D. P., Price, D. R., Prochnow, E., Puzzarini, C., Ruud, K., Schiffmann, F., Schwalbach, W., Simmons, C., Stopkowicz, S., Tajti, A., Vázquez, J., Wang, F.; Watts, J.D. and the integral packages MOLECULE (J. Almlöf and P. R. Taylor), PROPS (P .R. Taylor), ABACUS (T. Helgaker, H. J. Aa. Jensen, P. Jørgensen, and J. Olsen), and ECP routines by A. V. Mitin and C. van Wüllen. For the current version, see http://www.cfour.de.
(85) Weigend, F. Accurate Coulomb-fitting basis sets for H to Rn. *Phys. Chem. Chem. Phys.* **2006**, *8*, 1057−1065.
(86) Weigend, F. Hartree−Fock exchange fitting basis sets for H to Rn. *J. Comput. Chem.* **2008**, *29*, 167−175.
(87) Stoychev, G. L.; Auer, A. A.; Neese, F. Automatic Generation of Auxiliary Basis Sets. *J. Chem. Theory Comput.* **2017**, *13*, 554−562.
(88) Bühl, M.; Parrinello, M. Medium Effects on ^{51}V NMR Chemical Shifts: A Density Functional Study. *Chem. Eur. J.* **2001**, *7*, 4487−4494.
(89) Bühl, M.; Mauschick, F. T. Thermal and solvent effects on ^{57}Fe NMR chemical shifts. *Phys. Chem. Chem. Phys.* **2002**, *4*, 5508−5514.
(90) Bühl, M.; Mauschick, F. T.; Terstegen, F.; Wrackmeyer, B. Remarkably Large Geometry Dependence of ^{57}Fe NMR Chemical Shifts. *Angew. Chem., Int. Ed.* **2002**, *41*, 2312−2315.
(91) Bühl, M.; Grigoleit, S.; Kabrede, H.; Mauschick, T. Simulation of ^{59}Co NMR Chemical Shifts in Aqueous Solution. *Chem. Eur. J.* **2006**, *12*, 477−488.
(92) Franzke, Y. J.; Weigend, F. NMR Shielding Tensors and Chemical Shifts in Scalar-Relativistic Local Exact Two-Component Theory. *J. Chem. Theory Comput.* **2019**, *15*, 1028−1043.
(93) Vícha, J.; Novotný, J.; Komorovsky, S.; Straka, M.; Kaupp, M.; Marek, R. Relativistic Heavy-Neighbor-Atom Effects on NMR Shifts: Concepts and Trends Across the Periodic Table. *Chem. Rev.* **2020**, *120*, 7065−7103.
(94) Kaupp, M.; Malkina, O. L.; Malkin, V. G.; Pyykkö, P. How Do Spin-Orbit-Induced Heavy-Atom Effects on NMR Chemical Shifts Function? Validation of a Simple Analogy to Spin-Spin Coupling by

https://doi.org/10.1021/acs.jctc.1c00964
J. Chem. Theory Comput. 2022, 18, 273−292

Density Functional Theory (DFT) Calculations on Some Iodo Compounds. *Chem. Eur. J.* **1998**, *4*, 118−126.
(95) Kaupp, M. In *Relativistic Electronic Structure Theory II: Applications*; Schwerdtfeger, P., Ed.; Theoretical and Computational Chemistry; Elsevier: Amsterdam, 2004; Chapter 9, pp 552−597.
(96) Slater, J. C. A Simplification of the Hartree−Fock Method. *Phys. Rev.* **1951**, *81*, 385−390.
(97) Vosko, S. H.; Wilk, L.; Nusair, M. Accurate spin-dependent electron liquid correlation energies for local spin density calculations: a critical analysis. *Can. J. Phys.* **1980**, *58*, 1200−1211.
(98) Becke, A. D. Density-functional exchange-energy approximation with correct asymptotic behavior. *Phys. Rev. A* **1988**, *38*, 3098−3100.
(99) Lee, C.; Yang, W.; Parr, R. G. Development of the Colle-Salvetti correlation-energy formula into a functional of the electron density. *Phys. Rev. B* **1988**, *37*, 785−789.
(100) Perdew, J. P. Density-functional approximation for the correlation energy of the inhomogeneous electron gas. *Phys. Rev. B* **1986**, *33*, 8822−8824.
(101) Perdew, J. P. Erratum: Density-functional approximation for the correlation energy of the inhomogeneous electron gas. *Phys. Rev. B* **1986**, *34*, 7406.
(102) Perdew, J. P.; Burke, K.; Ernzerhof, M. Generalized Gradient Approximation Made Simple. *Phys. Rev. Lett.* **1996**, *77*, 3865−3868.
(103) Keal, T. W.; Tozer, D. J. The exchange-correlation potential in Kohn−Sham nuclear magnetic resonance shielding calculations. *J. Chem. Phys.* **2003**, *119*, 3015−3024.
(104) Keal, T. W.; Tozer, D. J. A semiempirical generalized gradient approximation exchange-correlation functional. *J. Chem. Phys.* **2004**, *121*, 5654−5660.
(105) Grimme, S. Semiempirical GGA-Type Density Functional Constructed with a Long-Range Dispersion Correction. *J. Comput. Chem.* **2006**, *27*, 1787−1799.
(106) Hamprecht, F. A.; Cohen, A. J.; Tozer, D. J.; Handy, N. C. Development and assessment of new exchange-correlation functionals. *J. Chem. Phys.* **1998**, *109*, 6264−6271.
(107) Boese, A. D.; Handy, N. C. A new parametrization of exchange-correlation generalized gradient approximation functionals. *J. Chem. Phys.* **2001**, *114*, 5497−5503.
(108) Tao, J.; Perdew, J. P.; Staroverov, V. N.; Scuseria, G. E. Climbing the Density Functional Ladder: Nonempirical Meta-Generalized Gradient Approximation Designed for Molecules and Solids. *Phys. Rev. Lett.* **2003**, *91*, 146401.
(109) Zhao, Y.; Truhlar, D. G. A new local density functional for main-group thermochemistry, transition metal bonding, thermochemical kinetics, and noncovalent interactions. *J. Chem. Phys.* **2006**, *125*, 194101.
(110) Yu, H. S.; He, X.; Truhlar, D. G. MN15-L: A New Local Exchange-Correlation Functional for Kohn-Sham Density Functional Theory with Broad Accuracy for Atoms, Molecules, and Solids. *J. Chem. Theory Comput.* **2016**, *12*, 1280−1293.
(111) Van Voorhis, T.; Scuseria, G. E. A novel form for the exchange-correlation energy functional. *J. Chem. Phys.* **1998**, *109*, 400−410.
(112) Boese, A. D.; Handy, N. C. New exchange-correlation density functionals: The role of the kinetic-energy density. *J. Chem. Phys.* **2002**, *116*, 9559−9569.
(113) Mardirossian, N.; Head-Gordon, M. Mapping the genome of meta-generalized gradient approximation density functionals: The search for B97M-V. *J. Chem. Phys.* **2015**, *142*, 074111.
(114) Sun, J.; Ruzsinszky, A.; Perdew, J. P. Strongly Constrained and Appropriately Normed Semilocal Density Functional. *Phys. Rev. Lett.* **2015**, *115*, 036402.
(115) Becke, A. D. Density-functional thermochemistry. III. *J. Chem. Phys.* **1993**, *98*, 5648−5652.
(116) Adamo, C.; Barone, V. Toward reliable density functional methods without adjustable parameters: The PBE0 model. *J. Chem. Phys.* **1999**, *110*, 6158−6170.
(117) Wilson, P. J.; Bradley, T. J.; Tozer, D. J. Hybrid exchange-correlation functional determined from thermochemical data and *ab initio* potentials. *J. Chem. Phys.* **2001**, *115*, 9233−9242.
(118) Becke, A. D. A new mixing of Hartree-Fock and local density-functional theories. *J. Chem. Phys.* **1993**, *98*, 1372−1377.
(119) Zhao, Y.; Truhlar, D. G. Design of Density Functionals That Are Broadly Accurate for Thermochemistry, Thermochemical Kinetics, and Nonbonded Interactions. *J. Phys. Chem. A* **2005**, *109*, 5656−5667.
(120) Zhao, Y.; Truhlar, D. G. The M06 suite of density functionals for main group thermochemistry, thermochemical kinetics, noncovalent interactions, excited states, and transition elements: two new functionals and systematic testing of four M06-class functionals and 12 other functionals. *Theor. Chem. Acc.* **2008**, *120*, 215−241.
(121) Yu, H. S.; He, X.; Li, S. L.; Truhlar, D. G. MN15: A Kohn-Sham global-hybrid exchange-correlation density functional with broad accuracy for multi-reference and single-reference systems and noncovalent interactions. *Chem. Sci.* **2016**, *7*, 5032−5051.
(122) Yanai, T.; Tew, D. P.; Handy, N. C. A new hybrid exchange-correlation functional using the Coulomb-attenuating method (CAM-B3LYP). *Chem. Phys. Lett.* **2004**, *393*, 51−57.
(123) Chai, J.-D.; Head-Gordon, M. Long-range corrected hybrid density functionals with damped atom-atom dispersion corrections. *Phys. Chem. Chem. Phys.* **2008**, *10*, 6615−6620.
(124) Mardirossian, N.; Head-Gordon, M. ωB97X-V: A 10-parameter, range-separated hybrid, generalized gradient approximation density functional with nonlocal correlation, designed by a survival-of-the-fittest strategy. *Phys. Chem. Chem. Phys.* **2014**, *16*, 9904−9924.
(125) Mardirossian, N.; Head-Gordon, M. ωB97M-V: A combinatorially optimized, range-separated hybrid, meta-GGA density functional with VV10 nonlocal correlation. *J. Chem. Phys.* **2016**, *144*, 214110.
(126) Arbuznikov, A. V.; Kaupp, M. Local hybrid exchange-correlation functionals based on the dimensionless density gradient. *Chem. Phys. Lett.* **2007**, *440*, 160−168.
(127) Kaupp, M.; Bahmann, H.; Arbuznikov, A. V. Local hybrid functionals: An assessment for thermochemical kinetics. *J. Chem. Phys.* **2007**, *127*, 194102.
(128) Arbuznikov, A. V.; Kaupp, M. Importance of the correlation contribution for local hybrid functionals: Range separation and self-interaction corrections. *J. Chem. Phys.* **2012**, *136*, 014111.
(129) Arbuznikov, A. V.; Kaupp, M. Towards improved local hybrid functionals by calibration of exchange-energy densities. *J. Chem. Phys.* **2014**, *141*, 204101.
(130) Møller, C.; Plesset, M. S. Note on an approximation treatment for many-electron systems. *Phys. Rev.* **1934**, *46*, 618−622.
(131) Grimme, S. Semiempirical hybrid density functional with perturbative second-order correlation. *J. Chem. Phys.* **2006**, *124*, 034108.
(132) Bühl, M.; Kabrede, H. Geometries of Transition-Metal Complexes from Density-Functional Theory. *J. Chem. Theroy Comput.* **2006**, *2*, 1282−1290.
(133) Schattenberg, C. J.; Maier, T.; Kaupp, M. Lessons from the Spin-Polarization/Spin-Contamination Dilemma of Transition-Metal Hyperfine Couplings for the Construction of Exchange-Correlation Functionals. *J. Chem. Theory. Comput.* **2018**, *14*, 5653−5672.
(134) Bühl, M.; Wrackmeyer, B. Density-functional computation of ^{93}Nb NMR chemical shifts. *Magn. Reson. Chem.* **2010**, *48*, S61−S68.
(135) Wilson, P. J.; Amos, R. D.; Handy, N. C. Density functional predictions for metal and ligand nuclear shielding constants in diamagnetic closed-shell first-row transition-metal complexes. *Phys. Chem. Chem. Phys.* **2000**, *2*, 187−194.
(136) Benn, R.; Rufińska, A. Indirect Two-Dimensional Heteronuclear NMR Spectroscopy of Low-γ Metal Nuclei (M = ^{183}W, ^{57}Fe, ^{103}Rh, ^{61}Ni). *Magn. Reson. Chem.* **1988**, *26*, 895−902.
(137) Hafner, A.; Hegedus, L. S.; deWeck, G.; Hawkins, B.; Dötz, K. H. Chromium-53 Nuclear Magnetic Resonance Studies of Pentacarbonylchromium-Carbene Complexes. *J. Am. Chem. Soc.* **1988**, *110*, 8413−8421.
(138) Berger, S.; Bock, W.; Frenking, G.; Jonas, V.; Müller, F. NMR Data of Methyltitanium Trichloride and Related Organometallic Compounds, A Combined Experimental and Theoretical Study of Me_nXCl_{4-n} (n = 0−4; X = C, Si, Sn, Pb, Ti). *J. Am. Chem. Soc.* **1995**, *117*, 3820−3829.

https://doi.org/10.1021/acs.jctc.1c00964
J. Chem. Theory Comput. 2022, 18, 273−292

VII

Reprinted from

P. Pröhm, J. R. Schmid, K. Sonnenberg, P. Voßnacker, S. Steinhauer, C. J. Schattenberg, R. Müller, M. Kaupp and S. Riedel,
"*Improved Access to Organo-Soluble Di- and Tetrafluoridochlorate(I)/(III) Salts*",
Angew. Chem. Int. Ed., **2020**, 59, 16002–16006,
DOI: 10.1002/anie.202006268

How to cite: *Angew. Chem. Int. Ed.* **2020**, *59*, 16002–16006
International Edition: doi.org/10.1002/anie.202006268
German Edition: doi.org/10.1002/ange.202006268

Chlorine Fluorides

Improved Access to Organo-Soluble Di- and Tetrafluoridochlorate-(I)/(III) Salts

*P. Pröhm, J. R. Schmid, K. Sonnenberg, P. Voßnacker, S. Steinhauer, C. J. Schattenberg, R. Müller, M. Kaupp, and S. Riedel**

Abstract: *A facile one-pot gram-scale synthesis of tetraalkylammonium tetrafluoridochlorate(III) [cat][ClF_4] ([cat] = [NEt_3Me]$^+$, [NEt_4]$^+$) is described. An acetonitrile solution of the corresponding alkylammonium chloride salt is fluorinated with diluted fluorine at low temperatures. The reaction proceeds via the [ClF_2]$^-$ anion which is structurally characterized for the first time. The potential application of [ClF_4]$^-$ salts as fluorinating agents is evaluated by the reaction with diphenyl disulfide, Ph_2S_2, to pentafluorosulfanyl benzene, $PhSF_5$. The CN moieties in acetonitrile and [$B(CN)_4$]$^-$ are transferred in CF_3 groups. Exposure of carbon monoxide, CO, leads to the formation of carbonyl fluoride, COF_2, and elemental gold is dissolved under the formation of tetrafluoridoaurate [AuF_4]$^-$.*

Chlorine fluorides (ClF, ClF_3, ClF_5) are amongst the most reactive compounds known.[1] These very strongly oxidizing gases should only be handled in special equipment made from metal, including stainless steel, copper, nickel, Monel and other Cu/Ni alloys or from perfluorinated polymers such as PTFE, KEL-F or PFA. Especially ClF_3 and ClF_5 can under certain conditions exceed the reactivity of elemental fluorine. Exposure to organic material leads to violent reactions in many cases and only carefully chosen reaction conditions (especially dilution of the chlorine fluoride) can avoid dangerous explosions; however, acetonitrile is known to be resistant against bromo and chloro fluorine compounds.[2] ClF_3 reacts with nitrosyl fluoride or alkali metal fluorides under formation of the corresponding tetrafluoridochlorate-(III) salts.[3,4] Alkali metal tetrafluoridochlorates can also be formed via exposure of the corresponding alkali metal chlorides (CsCl, RbCl, KCl) towards elemental fluorine at elevated temperatures.[5] More soluble tetrafluoridochlorate-(III) salts, for example, alkylammonium salts, can be obtained by salt metathesis with the corresponding alkylammonium fluorides in propionitrile at low temperatures.[3] However, only few examples of stable anhydrous alkylammonium fluorides are known.[6] Nevertheless, cation metathesis was used to synthesize the tetramethylammonium and *1,1,3,3,5,5*-hexamethylpiperidinium (pip) tetrafluoridochlorate(III) salts.[3,7] Additionally, [NMe_4][ClF_4] was observed as a decomposition product of [NMe_4][ClF_6].[8] The difluoridochlorate(I) anion, [ClF_2]$^-$, is so-far only reported with a limited amount of counter ions (K^+, Rb^+, Cs^+, NO^+) and only characterized by vibrational spectroscopy.[9,10] To the best of our knowledge the chemistry of di- and tetrafluoridochlorates was only studied rudimentarily. Hence, we present a ClF_3-free, gram scale synthesis of organo-soluble tetraalkylammonium tetrafluoridochlorate and explore its chemical properties. We exposed triethylmethylammonium chloride [NEt_3Me]Cl to dilute fluorine (10 % in argon) in acetonitrile or propionitrile at low temperatures [Equation (1)]. In the beginning of the fluorination a slight yellow color of the solution was observed. We hypothesize that small amounts of chlorine are formed. However, it was not possible to detect any vibrational band of Cl_2 via Raman spectroscopy. In the process of further fluorination the solution decolorized again. For the synthesis of highly concentrated solutions we used [NEt_3Me][Cl_3][11] as a starting material due to its enhanced solubility in acetonitrile in comparison to tertraalkylammonium chlorides like [NEt_4]Cl or [NMe_4]Cl. It is worth mentioning that all starting materials are commercially available and the reaction proceeds in standard laboratory glassware in contrast to the reported synthesis with ClF_3.

$$[NEt_3Me]Cl + 2\,F_2 \xrightarrow[-35\,^\circ C,\,R=Me,Et]{RCN} [NEt_3Me][ClF_4] \quad (1)$$

We characterized the obtained solution by Raman and ^{19}F NMR spectroscopy. The ^{19}F NMR spectrum (Figure S2 in the Supporting Information) shows one main resonance at 67 ppm for [ClF_4]$^-$ which is in good agreement with previously reported values (66.8 ppm).[7] The Raman spectrum (Figure 1) measured at −196 °C shows, besides the bands of the cation and solvent, three bands at 500 cm^{-1}, 408 cm^{-1} and 278 cm^{-1}, which are attributed to the a_{1g}, the b_{1g}, and the b_{2g} vibration in the D_{4h} symmetric molecule in agreement with literature values (508 cm^{-1}, 415 cm^{-1}, 278 cm^{-1}).[7,12]

By exchange of the cation to tetraethylammonium [NEt_4]$^+$ we were able to grow single crystals suitable for single crystal X-Ray diffraction. [NEt_4][ClF_4] crystallizes in

[*] M. Sc. P. Pröhm, J. R. Schmid, Dr. K. Sonnenberg, M. Sc. P. Voßnacker, Dr. S. Steinhauer, Prof. Dr. S. Riedel
Freie Universität Berlin, Institut of Chemistry and Biochemistry
Fabeckstr. 34/36, 14195 Berlin (Germany)
E-mail: s.riedel@fu-berlin.de
M. Sc. C. J. Schattenberg, Dr. R. Müller, Prof. Dr. M. Kaupp
Technische Universität Berlin, Department of Chemistry: Theoretical Chemistry
Sekr. C7, Strasse des 17. Juni 135, 10623 Berlin (Germany)
E-mail: martin.kaupp@tu-berlin.de
Supporting information and the ORCID identification number(s) for the author(s) of this article can be found under: https://doi.org/10.1002/anie.202006268.

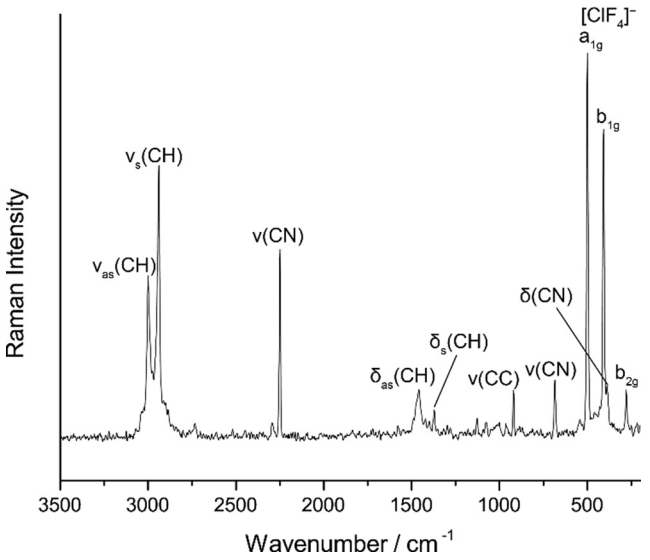

Figure 1. Raman spectrum of $[NEt_3Me][ClF_4]$ in acetonitrile at −196 °C.

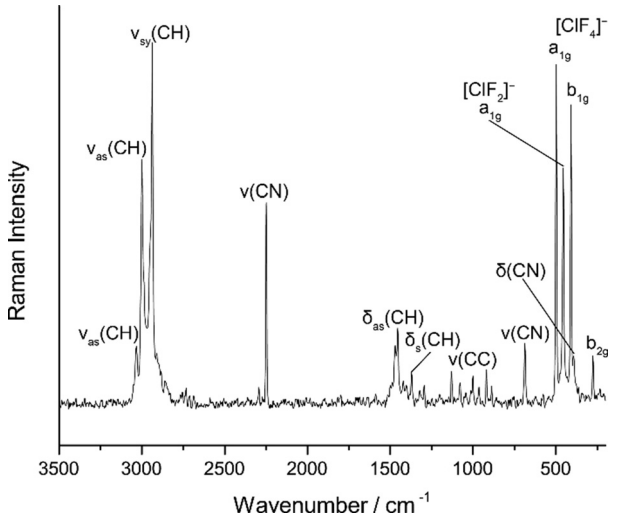

Figure 3. Raman spectrum of $[NEt_3Me]_3[ClF_4][ClF_2]_2$ in acetonitrile at −196 °C.

the space group *C*2/*c*. The chlorine atom occupies the Wyckhoff position 4*c* (site symmetry $P\bar{1}$). The $[ClF_4]^-$ is only slightly distorted from D_{4h} symmetry with two crystallographically inequivalent Cl−F bonds, d(Cl−F1) = 180.6(2) pm and d(Cl−F2) = 179.3(2) pm and rectangular bond angles ∡(F1-Cl-F2) = 90.01(5)° and ∡(F2-Cl-F1′) = 89.99(5)°, see Figure 2. Overall, the anion is in good agreement with the structures reported in the literature ([cat][ClF_4], [cat] = K^+, Rb^+, Cs^+, NO^+, $[pip]^+$) and is only slightly less distorted than in the reported structures of [pip][ClF_4] and [NO][ClF_4] (see Table S2).[3] The shortest cation anion contact is an F−H hydrogen bridge and was determined to 242.3(1) pm, the corresponding F···(H)−C distance was determined to 336.5(3) pm. Additionally, we calculated the Hirshfeld surface which is also showing a short cation anion contact (Figure S16).

The addition of 1.2 equiv. fluorine to a solution of $[NEt_3Me]Cl$ in acetonitrile yields a mixture of $[ClF_2]^-$ and $[ClF_4]^-$ anions. Again, we were able to characterize this mixture by vibrational and ^{19}F NMR spectroscopy. The Raman spectrum (Figure 3) of this mixture at −196 °C shows the characteristic bands of $[ClF_4]^-$ and additionally one band at 455 cm^{-1} which can be assigned to the symmetric stretch vibration of $[ClF_2]^-$, similar to those reported for solid $KClF_2$ (475 cm^{-1}) and $RbClF_2$ (476 cm^{-1}).[10] The harmonic frequency of the symmetric stretching mode for free $[ClF_2]^-$ is calculated to 453 cm^{-1} (CCSD(T)/def2-TZVPP) which is in good agreement with our assignment.[13] The differences between the value reported by us and the literature values can be explained by the stronger coordination of the alkali metal cation in the solid-state in comparison with the tetraalkylammonium cation.

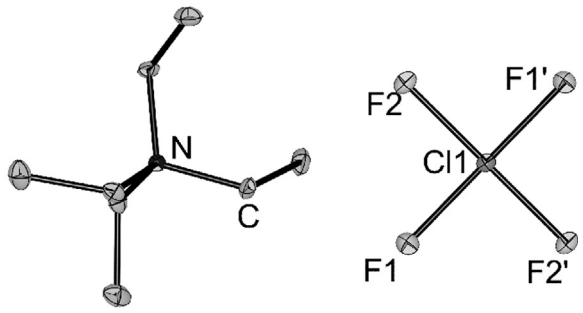

Figure 2. Crystal structure $[NEt_4][ClF_4]$. Displacement ellipsoids are shown at 50% probability at 100 K. Selected bond lengths [pm] and bond angles [°]: F1–Cl1 179.2(2), F2–Cl1 180.6(2) F1-Cl1-F2 89.99(5), F2-Cl1-F1′ 90.01(5). Hydrogen atoms omitted for clarity.[29]

The ^{19}F NMR spectrum (Figure S3) shows two signals. The one at 67 ppm can be assigned to the $[ClF_4]^-$ anion (see above). We assigned the second signal at −125 ppm to the $[ClF_2]^-$ anion since the Raman spectrum showed the corresponding band at 455 cm^{-1} before and after the measurement of the NMR spectrum.

Table 1 provides our computed ^{19}F shifts for the full series of anions $[XF_n]^-$ (X = Cl, Br, I; n = 2, 4, 6), using two functionals (the BHLYP global hybrid and the LH12ct-SsifPW92 local hybrid) that have been shown to provide superior ^{19}F shieldings compared to B3LYP.[14,15] The computations used BP86-D3(BJ)(COSMO,CH_3CN))/def2-TZVPPD structures and DFT(COSMO,CH_3CN)-GIAO//pcSseg-4/ANO-RCC-unc shielding computations (with pcSseg-4 basis sets for F, Cl, Br and the uncontracted ANO-RCC basis for I; see Supporting Information for further computational details and additional data). The available experimental data for n = 4, 6 are reproduced rather well at the two levels used. As shown by separate four-component relativistic computations (Table S5 in Supporting Information), both spin-orbit and scalar relativistic effects are small, in most cases a few ppm, at most about 13 ppm for $[IF_2]^-$. The small spin-orbit effects can be understood from an inefficient transfer mechanism to the fluoride nuclei.[16] However, the computed ^{19}F shifts for the difluoridohalide anions are too shielded by 60–100 ppm (more so for BHLYP than for LH12ct-SsifPW92). This is clearly outside the error margins of these two density functionals or of relativistic contribu-

Table 1: Calculated ^{19}F NMR chemical shifts relative to $CFCl_3$ (in ppm) of $[XF_n]^-$ (X = Cl, Br, I; n = 2, 4, 6) in comparison with experimental values.

Molecule	δ_{exp}	δ_{BHLYP}[a]	$\delta_{LH12ct\text{-}sifPW92}$[a]
$[ClF_2]^-$	−125[b]	−202	−174
$[ClF_4]^-$	67[7]	68	61
$[ClF_6]^-$	–	278	249
$[BrF_2]^-$	−210[3a]	−296	−273
$[BrF_4]^-$	−37[8]	−42	−45
$[BrF_6]^-$	94[8]	129	112
$[IF_2]^-$	−286, −282[3a,17]	−360	−348
$[IF_4]^-$	−106[3a,18]	−111	−117
$[IF_6]^-$	13[19]	30	14

[a] DFT(COSMO,CH_3CN)-GIAO/pcSseg-4/ANO-RCC-unc//BP86-D3-(BJ)(COSMO,CH_3CN))/def2-TZVPPD data. [b] This work.

tions. Closer inspection reveals that the highly negative fluorine charges in the difluorido anions give rise to specific F···H–C interactions with the acetonitrile solvent, which is not the case for the four- and six-coordinate cases. These strong interactions are not covered by the implicit COSMO solvent model but become apparent when using more explicit treatments of solvation. Detailed studies of these interesting fluoro-specific interactions are underway and will be reported elsewhere.

By slowly cooling a reaction mixture of $[NEt_3Me]Cl$ with 1.2 equiv. fluorine in acetonitrile, single crystals of $[NEt_3Me]_3[ClF_4][ClF_2]_2$ were obtained (for further details see Supporting Information, Figure S17). Replacing F_2 by ClF as a fluorination agent we were able to synthesize neat $[NEt_3Me][ClF_2]$. The Raman spectrum (Figure S6) shows one main band at 457 cm^{-1} which is in good agreement with data from $[NEt_3Me]_3[ClF_4][ClF_2]_2$ (455 cm^{-1}). The compound crystallizes in the space group $P12_1/c1$ (Figure 4). The two anionic moieties F1Cl1F1′ and F2ACl2F2A′ are both half occupied with Cl1 on Wyckhoff position 2b (site symmetry $P\bar{1}$) and Cl2 on Wyckhoff position 2c (site symmetry $P\bar{1}$). The Cl–F bond lengths are 185.24(6) pm (Cl1–F1) and 184.6(2) (Cl2–F2A). The calculated bond length of the free $[ClF_2]^-$ is 186.8 pm (CCSD(T)/def2-TZVPP).[13] The bonding situation

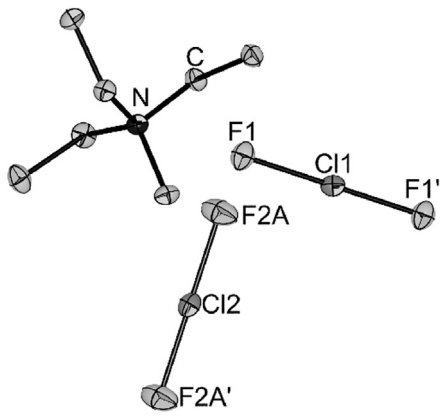

Figure 4. Crystal structure of $[NEt_3Me][ClF_2]$. Displacement ellipsoids are shown at 50% probability at 100 K. Selected bond lengths [pm]: F1–Cl1 185.24(6), F2A–Cl2 184.6(2). Hydrogen atoms omitted for clarity.[29]

is best described by a 3-center-4-electron bond. The Cl–F bond lengths in $[ClF_2]^-$ are significantly elongated in comparison with solid ClF (162.8(1) pm).[20] It is well-known from polyhalide chemistry that the bond length of a dihalogen is elongated upon coordination by a Lewis base due to the donation of electron density into the σ*(Cl–F) orbital.[12,21] As anticipated, the $[ClF_2]^-$ anion is computed to be more thermochemically stable towards halogen loss than $[Cl_3]^-$ and $[F(Cl)_2]^-$ which is due to more ionic interactions of the ClF moiety in comparison to Cl_2.[12,22]

We examined the stability of $[NEt_3Me][ClF_4]$ in acetonitrile solution via ^{19}F NMR spectroscopy. Surprisingly, it showed only slow decomposition at room temperature over a month via fluorination of the organic solvent and the cation. However, the isolated solid is significantly more reactive. We observed explosions in several cases at temperatures above −40 °C. Consequently, we avoided the isolation of larger quantities of $[NEt_3Me][ClF_4]$ and instead worked with solutions in propionitrile or acetonitrile with concentrations in the range of 0.66 $mol\,l^{-1}$ to 8.8 $mol\,l^{-1}$.

We envisioned $[NEt_3Me][ClF_4]$ as a fluorinating and oxidation reagent for the synthesis of highly fluorinated moieties such as trifluoromethyl (-CF_3), pentafluorosulfanyl (-SF_5) or fluoridometallates ($[MF_x]^-$). Trifluoromethyl and pentafluorosulfanyl derivatives have a growing importance in pharmaceutical- and agrochemistry.[23,24,25] Recently, Togni and co-workers reported on a non-gaseous reagent to access aryl tetrafluorido-λ⁶-sulfanyl chlorides (Ar-SF_4Cl), a key intermediate for the synthesis of pentafluorosulfanyl aryls (Ar-SF_5).[24] Beier and co-workers recently studied the direct fluorination with dilute elemental fluorine and disulfides to directly obtain pentafluorosulfanyl aryls, a process with industrial application.[25] As a proof of concept we exposed diphenyl disulfide, Ph_2S_2, to a solution of $[NEt_3Me][ClF_4]$ in propionitrile at −50 °C to directly obtain phenylsulfur pentafluoride, $PhSF_5$. As by-products the *cis*- and *trans*-$PhSF_4Cl$ were observed (Table 2 Entry 1, for further details see Supporting Information). $PhSF_5$ can be prepared in pure form by removal of both $PhSF_4Cl$ isomers by hydrolysis. Simultaneously, residual fluorochlorates are hydrolysed.[26]

Addition of the Lewis acid boron trifluoride, BF_3, to a solution of $[NEt_3Me][ClF_4]$ in acetonitrile led to the formation of CH_3CF_3, the CN activation product of the solvent acetonitrile, amongst other components. To increase the selectivity of this reaction, we synthesized the acetonitrile-BF_3 complex and substituted the solvent, from nitrile-based solvents to chlorofluorocarbons. Dichlorofluoromethane ($CHFCl_2$, R-21) turns out to be sufficiently stable towards

Table 2: Reactivity Studies with $[NEt_3Me][ClF_4]$.

Entry	Substrate	Lewis acid	Product
1	Ph_2S_2	–	$PhSF_5$, $PhSF_4Cl$
2	MeCN	BF_3	$MeCF_3$
3	$[B(CN)_4]^-$	BF_3	$[B(CF_3)_x(CN)_{4-x}]^-$
4	$[Au(CN)_2]^-$	BF_3	*cis*-$[AuF_2(CF_3)(CN)]^-$[a]
5	Au	–	$[AuF_4]^-$
6	CO	–	COF_2

[a] Minor product.

F_2 and $[ClF_4]^-$ and also dissolves the starting material $[NEt_3Me]Cl$. Combination of two dichlorofluoromethane solutions containing $[NEt_3Me][ClF_4]$ and $MeCN{\cdot}BF_3$ leads to the formation of CH_3CF_3 (Table 2 Entry 2, for further details see Supporting Information). This is reminiscent of the reaction between succinonitrile and BrF_3.[27] We also examined the reactivity towards the tetracyanidoborate anion $[B(CN)_4]^-$. With addition of the Lewis acid BF_3 we observed the conversion of the cyanido ligands to trifluoromethyl ligands. This result is analogous to the synthesis of $[B(CF_3)_4]^-$ from $[B(CN)_4]^-$ and ClF_3 in anhydrous HF.[28] However, we did not achieve full conversion but a distribution of different borate anions with trifluormethyl and cyanido ligands $[B(CF_3)_x(CN)_{4-x}]^-$ (Table 2 Entry 3, for further details see Supporting Information). Additionally, we exposed the $[BF_3(CN)]^-$ anion to $[NEt_3Me][ClF_4]$ but only fluorination to $[BF_4]^-$ was observed. The reaction of $[NEt_3Me][ClF_4]$ with dicyanidoaurate(I) $[Au(CN)_2]^-$ is not selective, however, we were able to identify one Au-CF_3 containing product in the reaction mixture via NMR spectroscopy, that is, *cis*-$[AuF_2(CF_3)(CN)]^-$ (Table 2 Entry 4, for further details see Supporting Information). Another promising application for $[NEt_3Me][ClF_4]$ is the dissolution of noble metals such as gold. After the addition of a piece of elemental gold, the solution containing $[ClF_4]^-$ turns yellow. The ^{19}F NMR spectroscopic analysis reveals the formation of mainly $[AuF_4]^-$ (Table 2 Entry 5, for further details see Supporting Information) and traces of other chloridofluoridoaurates ($[AuF_3Cl]^-$ and *cis*-$[AuF_2Cl_2]^-$ see Figure S12). Exposure of $[NEt_3Me][ClF_4]$ in propionitrile to an atmosphere of CO results in the formation of carbonyl fluoride (COF_2) within 30 min (Table 2 Entry 6, for further details see Supporting Information).

In conclusion, we developed a facile and fast synthetic procedure to obtain a soluble source of highly reactive $[ClF_4]^-$ in the form of $[NEt_3Me][ClF_4]$ avoiding gaseous ClF_3 which tends to react explosively when exposed to organic matter. We characterized this compound by NMR and Raman spectroscopy and, additionally, single crystal X-Ray diffraction for the analogous $[NEt_4][ClF_4]$. Furthermore, we presented the first structural and ^{19}F NMR spectroscopic proof of the $[ClF_2]^-$ anion. All experimental results are supported by quantum-chemical calculations. Additionally, we showed several applications of $[NEt_3Me][ClF_4]$ as a highly reactive fluorinating agent for the transformation of aryl disulfides into the corresponding pentafluorosulfanyl aryls, nitriles and cyanido complexes into the corresponding trifluoromethyl compounds, carbon monoxide into carbonyl fluoride and the dissolution of elemental gold. In further studies we will explore a broader substrate scope to develop a widely applicable fluorinating reagent for organic and inorganic chemists.

Caution! Fluorine, even under dilute conditions, is extraordinarily reactive and can react violently with organic materials under the formation of HF. Similarly, tetrafluoridochlorate(III) and difluoridochlorate(I) are strongly oxidizing compounds, which can decompose violently under certain conditions when exposed to organic materials. Exposure to acidic compounds (e.g. water or boron trifluoride) greatly enhances the reactivity due to the in situ formation of ClF_3. Additionally, precipitation also greatly enhances the reactivity of tetrafluoridochlorate(III) and difluoridochlorate(I) compounds, leading to explosions at temperatures above −40 °C. Usage of PFA, FEP or PTFE may lower the risk of injury.

Acknowledgements

We gratefully acknowledge the ZEDAT at Freie Universität Berlin for providing computing resources. Additionally, we are grateful for donations of chemicals from the Solvay company. SPP 1708 is acknowledged for funding. Furthermore, PP acknowledges VCI for providing PhD funding (Kekulé Fellowship). Funded by the Deutsche Forschungsgemeinschaft (DFG, German Research Foundation)—Project-ID 387284271—SFB 1349. Open access funding enabled and organized by Projekt DEAL.

Conflict of interest

The authors declare no conflict of interest.

Keywords: chlorine fluorides · fluorination reagents · strong oxidizers

[1] D. Naumann, *Fluor und Fluorverbindungen*, Steinkopff, Heidelberg, **1980**.
[2] a) K. R. Brower, *J. Fluorine Chem.* **1986**, *31*, 333; b) F. Kraus, *Nachr. Chem.* **2019**, *67*, 17; c) G. Schiemann, K. Bromme, B. Cornils, *Chem. Ber.* **1965**, *98*, 3410; d) G. Schiemann, M. Kühnhold, B. Cornils, *Liebigs Ann. Chem.* **1968**, *714*, 62; e) H. Meinert, U. Groβ, *Z. Chem.* **1969**, *9*, 190.
[3] a) X. Zhang, K. Seppelt, *Z. Anorg. Allg. Chem.* **1997**, *623*, 491; b) B. Scheibe, S. I. Ivlev, A. J. Karttunen, F. Kraus, *Eur. J. Inorg. Chem.* **2020**, 1319.
[4] a) E. D. Whitney, R. O. MacLaren, T. J. Hurley, C. E. Fogle, *J. Am. Chem. Soc.* **1964**, *86*, 4340; b) E. D. Whitney, R. O. MacLaren, C. E. Fogle, T. J. Hurley, *J. Am. Chem. Soc.* **1964**, *86*, 2583; c) K. O. Christe, J. P. Guertin, *Inorg. Chem.* **1966**, *5*, 473; d) K. O. Christe in *IUPAC*, *XXIVth Int. Cong. Pure Appl. Chem.* **1974**, 115.
[5] a) L. B. Asprey, J. L. Margrave, M. E. Silverthorn, *J. Am. Chem. Soc.* **1961**, *83*, 2955; b) D. H. Kelly, B. Post, R. W. Mason, *J. Am. Chem. Soc.* **1963**, *85*, 307.
[6] a) K. O. Christe, W. W. Wilson, R. D. Wilson, R. Bau, J. A. Feng, *J. Am. Chem. Soc.* **1990**, *112*, 7619; b) A. R. Mahjoub, X. Zhang, K. Seppelt, *Chem. Eur. J.* **1995**, *1*, 261; c) H. Sun, S. G. DiMagno, *J. Am. Chem. Soc.* **2005**, *127*, 2050; d) S. Elias, N. Karton-Lifshin, L. Yehezkel, N. Ashkenazi, I. Columbus, Y. Zafrani, *Org. Lett.* **2017**, *19*, 3039.
[7] W. W. Wilson, K. O. Christe, *Inorg. Chem.* **1989**, *28*, 4172.
[8] K. O. Christe, W. W. Wilson, R. V. Chirakal, J. C. P. Sanders, G. J. Schrobilgen, *Inorg. Chem.* **1990**, *29*, 3506.
[9] a) K. O. Christe, J. P. Guertin, *Inorg. Chem.* **1965**, *4*, 905; b) K. O. Christe, J. P. Guertin, *Inorg. Chem.* **1965**, *4*, 1785.
[10] K. O. Christe, W. Sawodny, J. P. Guertin, *Inorg. Chem.* **1967**, *6*, 1159.
[11] R. Brückner, *Dissertation*, Freie Universität Berlin, Berlin, **2016**.
[12] K. O. Christe, W. Sawodny, *Z. Anorg. Allg. Chem.* **1968**, *357*, 125.
[13] F. A. Redeker, A. Kropman, C. Müller, S. E. Zewge, H. Beckers, B. Paulus, S. Riedel, *J. Fluorine Chem.* **2018**, *216*, 81.

[14] C. J. Schattenberg, K. Reiter, F. Weigend, M. Kaupp, *J. Chem. Theory Comput.* **2020**, *16*, 931.
[15] T. Kupka, *Magn. Reson. Chem.* **2009**, *47*, 959.
[16] M. Kaupp, O. L. Malkina, V. G. Malkin, P. Pyykkö, *Chem. Eur. J.* **1998**, *4*, 118.
[17] K. O. Christe, W. W. Wilson, G. W. Drake, M. A. Petrie, J. A. Boatz, *J. Fluorine Chem.* **1998**, *88*, 185.
[18] K. O. Christe, W. W. Wilson, G. W. Drake, D. A. Dixon, J. A. Boatz, R. Z. Gnann, *J. Am. Chem. Soc.* **1998**, *120*, 4711.
[19] K. O. Christe, W. W. Wilson, *Inorg. Chem.* **1989**, *28*, 3275.
[20] R. Boese, A. D. Boese, D. Bläser, M. Y. Antipin, A. Ellern, K. Seppelt, *Angew. Chem. Int. Ed. Engl.* **1997**, *36*, 1489; *Angew. Chem.* **1997**, *109*, 1538.
[21] a) B. Schmidt, K. Sonnenberg, H. Beckers, S. Steinhauer, S. Riedel, *Angew. Chem. Int. Ed.* **2018**, *57*, 9141; *Angew. Chem.* **2018**, *130*, 9279; b) K. Sonnenberg, P. Pröhm, N. Schwarze, C. Müller, H. Beckers, S. Riedel, *Angew. Chem. Int. Ed.* **2018**, *57*, 9136; *Angew. Chem.* **2018**, *130*, 9274; c) S. I. Ivlev, A. J. Karttunen, R. Ostvald, F. Kraus, *Z. Anorg. Allg. Chem.* **2015**, *641*, 2593; d) S. I. Ivlev, A. J. Karttunen, R. V. Ostvald, F. Kraus, *Chem. Commun.* **2016**, *52*, 12040; e) K. Sonnenberg, L. Mann, F. A. Redeker, B. Schmidt, S. Riedel, *Angew. Chem. Int. Ed.* **2020**, *59*, 5464; *Angew. Chem.* **2020**, *132*, 5506.
[22] a) T. J. Van Huis, J. M. Galbraith, H. F. Schaeffer, *Mol. Phys.* **1996**, *89*, 607; b) A. B. Sannigrahi, S. D. Peyerimhoff, *Chem. Phys. Lett.* **1985**, *119*, 119; c) L. Chen, D. E. Woon, T. H. Dunning, *Comput. Theor. Chem.* **2017**, *1116*, 73; d) K. S. Thanthiriwatte, J. M. Spruell, D. A. Dixon, K. O. Christe, H. D. B. Jenkins, *Inorg. Chem.* **2014**, *53*, 8136.
[23] a) D. Lentz, K. Seppelt in *Chemistry of hypervalent compounds* (Ed.: K.′y. Akiba), Wiley-VCH, Weinheim, **1999**; b) H. L. Yale, *J. Med. Chem.* **1959**, *1*, 121; c) T. Umemoto, L. M. Garrick, N. Saito, *Beilstein J. Org. Chem.* **2012**, *8*, 461; d) P. R. Savoie, J. T. Welch, *Chem. Rev.* **2015**, *115*, 1130.
[24] C. R. Pitts, D. Bornemann, P. Liebing, N. Santschi, A. Togni, *Angew. Chem. Int. Ed.* **2019**, *58*, 1950; *Angew. Chem.* **2019**, *131*, 1970.
[25] J. Ajenjo, B. Klepetářová, M. Greenhall, D. Bím, M. Culka, L. Rulíšek, P. Beier, *Chem. Eur. J.* **2019**, *25*, 11375.
[26] W.-T. Tsai, *J. Hazard. Mater.* **2011**, *190*, 1.
[27] M. T. Baker, J. A. Ruzicka, J. H. Tinker, *J. Fluorine Chem.* **1999**, *94*, 123.
[28] E. Bernhardt, G. Henkel, H. Willner, G. Pawelke, H. Bürger, *Chem. Eur. J.* **2001**, *7*, 4696.
[29] Deposition Number(s) 1948998 (for $[NEt_4][ClF_4]$) and 2004243 (for $[NEt_3Me][ClF_2]$) contain(s) the supplementary crystallographic data for this paper. These data are provided free of charge by the joint Cambridge Crystallographic Data Centre and Fachinformationszentrum Karlsruhe Access Structures service www.ccdc.cam.ac.uk/structures.

Manuscript received: April 30, 2020
Revised manuscript received: May 18, 2020
Accepted manuscript online: May 27, 2020
Version of record online: July 15, 2020

VIII

Reprinted from

M. Kaupp, C. J. Schattenberg, R. Müller and M. Reimann,
"*Unusually Large Effects of Charge-assisted C–H$\cdots$F Hydrogen Bonds to Anionic Fluorine in Organic Solvents: Computational Study of ^{19}F NMR Shifts versus Thermochemistry*",
ChemistryOpen, **2022**, e202200146,
DOI: 10.1002/open.202200146

ChemistryOpen

Research Article
doi.org/10.1002/open.202200146

Chemistry Europe
European Chemical Societies Publishing

www.chemistryopen.org

Unusually Large Effects of Charge-assisted C–H···F Hydrogen Bonds to Anionic Fluorine in Organic Solvents: Computational Study of ^{19}F NMR Shifts versus Thermochemistry

Martin Kaupp,* Caspar J. Schattenberg, Robert Müller, and Marc Reimann[a]

A comparison of computed ^{19}F NMR chemical shifts and experiment provides evidence for large specific solvent effects for fluoride-type anions interacting with the σ*(C–H) orbitals in organic solvents like MeCN or CH_2Cl_2. We show this for systems ranging from the fluoride ion and the bifluoride ion $[FHF]^-$ to polyhalogen anions $[ClF_x]^-$. Discrepancies between computed and experimental shifts when using continuum solvent models like COSMO or force-field-based descriptions like the 3D-RISM-SCF model show specific orbital interactions that require a quantum-mechanical treatment of the solvent molecules. This is confirmed by orbital analyses of the shielding constants, while less negatively charged fluorine atoms (e.g., in $[EF_4]^-$) do not require such quantum-mechanical treatments to achieve reasonable accuracy. The larger ^{19}F solvent shift of fluoride in MeCN compared to water is due to the larger coordination number in the former. These observations are due to unusually strong charge-assisted C–H···F^- hydrogen bonds, which manifest beyond some threshold negative natural charge on fluorine of ca. < -0.6 e. The interactions are accompanied by sizable free energies of solvation, in the order $F^- \gg [FHF]^- > [ClF_2]^- > [ClF_4]^-$. COSMO-RS solvation free energies tend to moderately underestimate those from the micro-solvated cluster treatment. Red-shifted and intense vibrational C–H stretching bands, potentially accessible in bulk solution, are further spectroscopic finger prints.

Introduction

CH bonds acting as hydrogen-bond donors have a long and varied history going back to a 1937 suggestion by Glasstone to explain the formation of mixtures of CX_3H (X = Cl, Br, I) with acetone or quinoline.[1] From the controversial early history of such suggestions, we mention here only the X-ray diffraction studies of short CH···O distances in crystals by Suton[2] and first definitive IR experiments by Allerhand and Schleyer.[3] Meanwhile the existence of such interactions is very well established, with too many facets and applications to be mentioned here in detail. They even form the central basis for a book on weak hydrogen bonds.[4] The latter implies that usually such interactions tend to be weaker than regular hydrogen bonds with more electronegative donor atoms like N, O, or F. And indeed, often CH···O hydrogen bonds tend to exhibit blue-shifted CH vibrations with reduced intensities and have been (improperly) termed "improper hydrogen bonds", as the charge-transfer component is small, and electrostatic and rehybridization effects can lead to shortened CH bonds with enhanced force constants and reduced bond dipoles.[5,6]

However, the strength of CH···X hydrogen bonds can be enhanced by various factors: a) a net positive charge on the donor in cationic species, for example by protonation, metal coordination or involvement in an ammonium-ion framework;[7] b) employing sp^2 or sp hybridized carbon donors, which increases their electronegativity;[8] c) a more gradual increase of the electronegativity and donor strength by attaching electronegative substituents to the carbon atom (this explains the predominant early observation of such interactions for haloforms); and d) a negative charge on the hydrogen-bond acceptor.[9,10,11] All of these aspects have been utilized, for example, in the design of supramolecular anion receptors,[12] including those for halide ions, or, for example, in catalysis.[13] The term "charge-assisted hydrogen bonding" has been used in this context.[14]

While these types of studies of specific anion receptors benefit from well-defined structural arrangements, the CH bonds of many common solvents also should be expected to form rather strong CH···X hydrogen bonds with anionic solutes. This is supported by a number of recent computational studies at various levels.[9,10,11] While little experimental solution data is available, these computational studies indeed suggest strong CH···X interactions to contribute to the microsolvation of anions in many common organic solvents. This certainly should hold for aliphatic CH groups not only in the haloforms (which have been used in previous computational studies[9]) but also in solvents like acetonitrile (MeCN) or dichloromethane (DCM), which all bear electronegative substituents on the donor carbon

[a] Prof. Dr. M. Kaupp, C. J. Schattenberg, Dr. R. Müller, M. Reimann
Technische Universität Berlin
Institut für Chemie, Theoretische Chemie/Quantenchemie
Sekr. C7, Strasse des 17. Juni 135, 10623 Berlin (Germany)
E-mail: martin.kaupp@tu-berlin.de

Supporting information for this article is available on the WWW under https://doi.org/10.1002/open.202200146

atom. It should also hold for the more electronegative aromatic CH groups as in benzene or toluene, even in the absence of electronegative substituents,[15] but enhanced in their presence.[16]

If we discard small, multiply charged anions,[10a] which are unlikely to dissolve in organic solvents, fluoride-like species may be expected to exhibit the largest CH···X solvent-solute interactions,[9] as fluoride concentrates negative charge density on the smallest conceivable volume. In a recent combined experimental and computational study[17] of polyhalogen anions $[EF_x]^-$ (E = Cl, Br, I; X = 2, 4, 6) we found that using suitable DFT approaches and continuum solvent models allowed us to reproduce well the ^{19}F NMR shifts with X = 4, 6 to within about 10–15 ppm but not with X = 2. In the latter case our computations underestimated the shifts systematically by about 50–60 ppm at our best DFT level used (with the LH12ct-SsifPW92 local hybrid functional[18] and large basis sets). As relativistic effects were found to be small, and such discrepancies are clearly outside the expected accuracy of functional and basis set,[19,20] we suspected that specific solvent interactions in the experimentally used MeCN, that are not covered adequately by the standard COSMO solvent model[21] used, are responsible for the differences. We will show this to be the case below by using microsolvated cluster models. The differences between X = 2 versus X = 4, 6 in these systems intrigued us, as they suggested that the negative charge on fluorine may determine how well or how poorly standard solvent models may reproduce these effects. Similar specific solvent interactions can be inferred from recent ab initio molecular dynamics studies of the bifluoride ion $[FHF]^-$ in deuterated dichloromethane (CD_2Cl_2).[22] Here an explicit quantum-mechanical treatment of solvent molecules was found as well to be necessary to reproduce the experimental ^{19}F NMR shifts in solution, even though the main focus of that work was on the (a-)symmetry of hydrogen bonding within the anion.

Properties like NMR shifts are important probes of molecular interactions, and the need to include solute-solvent interactions quantum-mechanically in some but not in other cases signals a more general challenge for computational studies in that field. Consider, for example, a chemical reaction where the anionic character on a fluorine atom (or on some other very electronegative atom) varies for different intermediates or transition states. Then standard computational treatments using continuum solvent models will certainly not be adequate, and an appropriate treatment of microsolvation becomes mandatory. As we will see below, a force-field based treatment of the solvent, as in QM/MM simulations or related approaches, is also insufficient.

To obtain more insight, we use here microsolvated model clusters for anionic fluorine species and select MeCN as organic solvent and CH-bond donor, as it is often used to dissolve such species (see Ref. [11] for a recent computational study of interactions between one acetonitrile molecule and chloride). In addition to the anions $[ClF_x]^-$ (X = 2, 4) that were part of the abovementioned study,[17] we will evaluate such effects for the free fluoride ion, and for the bifluoride ion. We will concentrate on MeCN, to avoid complications due to halogen bonding, as is possible for DCM. For the fluoride ion we will compare also to aqueous solution, as experimental evidence suggests a larger deshielding solvent effect on the ^{19}F shift in organic solvents such as MeCN compared to water,[23] which seems interesting to understand.

Computational Details

Initial estimates of the average number of solvent molecules expected around a given species were obtained using 3D-RISM-SCF calculations,[24] where the solute is treated at the BP86-D3(BJ)/TZ2P level[25,26,27] and the solvent at the 3D-RISM level based on OPLS force field parameters, either using a united atom (UA) approach[28] or the parameters obtained from the LigParGen web server[29,30] employing 1.14*CM1A-LBCC[31] charges and the all-atoms (AA) approach. All these computations used a modified version of our recent 3D-RISM-SCF implementation[32] in the ADF engine[33] of the AMS program package[34] – a code based on Slater-type-orbital basis sets. These modifications are part of the 2022.1 release. In all calculations, the 3D-RISM equations were solved on a Cartesian grid with 128 points in each direction and a spacing of 0.25 Å using the KH closure[35] and solvent susceptibility functions obtained from DRISM calculations[36] employing the hypernetted chain (HNC) closure.[37] The Lennard-Jones parameters of the solute atoms were taken from Ref. [38], using special parameters for the H in FHF^- (σ = 1.0 Å, ε = 0.056 kcal/mol). The electrostatic potential obtained from the fitted electron density of the solute at the given DFT level has been used.[32] The estimated average coordination number was obtained by integrating the pair distribution function – either spherically averaged around a fluorine atom or around the molecular center of mass – up to the first minimum.

The computed average solvation numbers provided the basis for fast meta-dynamics runs using the GFN2-xTB tight-binding approach[39] as implemented in the CREST tool of the xtb program.[40] Optimized structures from the latter simulations were used as starting points for DFT structure optimizations of clusters of the solute with varying numbers of solvent molecules. These optimizations were done within a COSMO solvent environment (ε = 35.688 for MeCN, ε = 78.355 for water) at MARIJ-BP86-D3(BJ)/def2-TZVPP[41] level (MARIJ stands for "multipole-accelerated resolution of the identity"), using the Turbomole program,[42,43] version 7.5.1 and newer.

Free energies of solvation were computed from the microsolvated cluster energies following a cluster cycle[44] corresponding to the reaction $[X^-(MeCN)_n]_{solv} \rightleftharpoons X^-(g) + [(MeCN)_n]_{solv}$ (and analogously for $F^-(H_2O)_n$). Contributions to the free energies were obtained from the optimized clusters by including their vibrational contributions at the same level plus additional solvation contributions at COSMO-RS(MeCN) level for $X^-(MeCN)_n$ as well as for $(MeCN)_n$.[45] To this end, additional single-point calculations at the COSMO and gas-phase optimized structures were carried out. These calculations were performed at MARIJ-BP86 level (omitting the D3(BJ) corrections) with COSMO, setting an infinite permittivity and using the refined COSMO cavity construction algorithm (keyword $cosmo_isorad),[45b] as well as in the gas phase, employing def2-TZVPD[41a] basis sets for all atoms. Based on these single-point calculations, subsequent COSMO-RS computations to obtain ΔG_{solv} used the COSMOtherm program, version C30_1201, and a BP-TZVPD-FINE level parameterization (BP_TZVPD_FINE_HB2012_C30_1201). Electronic energy contributions were refined by single-point energy calculations at the DLPNO-SCS-MP2/aug-cc-pVTZ[46,47] level and, where computationally feasible for smaller clusters, at the DLPNO-CCSD(T)-F12/cc-pVTZ-F12 level as reference.[48,49] These calculations used the ORCA

program, version 4.2.1.[50] For comparison, electronic energies have also been computed by single-point energy calculations at the ωB97M-V/def2-TZVPP[51] DFT level. Furthermore, free energies of solvation without the presence of explicit solvent molecules have been computed directly with COSMO-RS at MARIJ-BP86/def2-TZVPD level for comparison, using the settings given above. Free energies were computed at standard conditions, i.e. 298.15 K and 0.1 MPa, and standard-state corrections were computed as SScorr = $-RTln(V_m)$; $V_m = 24.46$ mol l^{-1}.

Using the clusters optimized at MARIJ-BP86-D3(BJ)/def2-TZVPP/COSMO level, calculations of ^{19}F shieldings were done with a number of different DFT functionals that have recently been established to perform well for the ^{19}F shielding and shift subset (47 nuclei) of the large coupled-cluster-based NS372 benchmark.[20] That is, we used the three local hybrid functionals cLH12ct-SsirPW92,[18] LH12ct-SsifPW92,[18] and LH20t[52] including their current-density response[53,54] within Dobson's scheme[55] (denoted cLH12ct-SsirPW92, cLH12ct-SsifPW92 and cLH20t) and with gauge-including atomic orbitals (GIAOs[56]) as implemented in the Turbomole code, version 7.6. pcSseg-3 basis sets were employed for all atoms, and the computations used COSMO (MeCN, ε = 35.688; H_2O, ε = 8.93), as well as the MARIJ approach for the Coulomb contribution (using "universal" auxiliary basis sets[57]). We will preferably focus on results obtained with the cLH12ct-SsirPW92 local hybrid functional. For free F^- and for HF, it provides ^{19}F shielding constants that agree with high-level CCSD(T)/pcSseg-3[58] results to within about 1 ppm, and for LiF to within ca. 3 ppm.[20] Its mean absolute error for the full ^{19}F subset of the recent NS372 benchmark is 9.7 ppm.[20] This should be compared to 5.2 ppm for MP2 and to 9.0 ppm for the top-performing[20,59] double hybrid DSD-PBEP86,[60] which both require substantially higher computational effort and indeed exhibit somewhat larger deviations from the benchmark data for HF (in the latter case also for LiF). For comparison we also used the BHLYP global hybrid functional[61] that has previously been used often for ^{19}F NMR parameter computations[62] but does not perform as well as the three local hybrids.[19,20,53,54] Computations without explicit microsolvation using COSMO or the self-consistent version of COSMO-RS, D-COSMO-RS,[63] were also done for comparison at the otherwise identical levels. Additional computations of ^{19}F shieldings using 3D-RISM-SCF as solvent model without explicit solvent molecules used ADF/AMS at BHLYP/QZ4P-J//BP86-D3(BJ)/TZ2P level.

To transform computed ^{19}F absolute shielding constants σ into chemical shifts δ requires a value for the absolute shielding σ_{ref} of the reference standard used experimentally. For ^{19}F NMR this is nontrivial, as a direct computation of the absolute shielding constant of neat liquid $CFCl_3$ is required. In this work we decided to indeed use reference shieldings for $CFCl_3$ computed directly at the given level, using structures optimized at the MARIJ-BP86-D3(BJ)/def2-TZVPP level with COSMO (ε = 2.315 for liquid $CFCl_3$[64]) to model the liquid environment. Shielding computations also used COSMO($CFCl_3$). The obtained reference values are: 186.3 ppm (cLH12ct-SsirPW92), 189.5 ppm (cLH12ct-SsifPW92), 184.6 ppm (cLH20 t), and 187.2 ppm (BHLYP).

We have carefully considered but ultimately not applied an alternative scheme for obtaining a shielding for liquid $CFCl_3$ indirectly via the secondary standard of gaseous dilute HF at 300 K that we want to share here for scientists interested in computing ^{19}F NMR shifts in other contexts: the relative shift of HF(g, 300 K) with respect to neat liquid $CFCl_3$ can be inferred to be 217.02 ppm from a relative shift of HF(g, 300 K) against SiF_4(g, 300 K) of 46.85 ± 0.35 ppm,[65] and a more recent relative shift of SiF_4(g, 300 K) versus $CFCl_3$(l, 300 K) of 170.17 ppm.[66] For the absolute shielding of HF(g, 300 K) we use a nonrelativistic value of 409.7 ppm computed from an equilibrium shielding of 419.384 ppm obtained at CCSDTQ/CBS level (with corrections for quintuple excitations) and 300 K rovibrational corrections at CCSD(T)/CBS level of −9.677 ppm.[67] Using this shielding value provides us with a reference shielding value of 192.7 ppm for neat liquid $CFCl_3$. We assume that this is an appropriate reference for shielding computations that neglect relativistic effects, as we expect computed relativistic effects of ca. +4.6 ppm[67] to be essentially atomic in nature (a so-called heavy-atom effect on the heavy-atom shielding, HAHA[68]) and to therefore cancel out by taking the experimental shift of HF(g) vs. $CFCl_3$(l) into account to obtain our reference shielding. When relativistic corrections would be included in the actual shielding computations, the reference value would have to be increased accordingly. Note that this alternative reference shielding value is a few ppm larger than the directly computed ones (see above), and it would thus lead to slightly lower relative shifts. We note furthermore in passing that all σ_{ref} values discussed here are much lower than the MP2-based gas-phase value of 217.9 ppm used in the MP2 computations of fluoride solvent shifts in Ref. [23], explaining our more negative shifts for free fluoride compared to the −260 ppm given in that work.

Natural population analyses (NPA) and natural bond orbital analyses (NBO)[69] for the clusters $F^-(H_2O)_6$ and $F^-(MeCN)_8$ were carried out at the BP86-D3(BJ)/def2-TZVPP level using the NBO3.1 routines available in the Gaussian16 program, revision A.03.[70] MO-based analyses of the shielding constants computed at GIAO-BP86/pcSseg-2//MARIJ-BP86-D3(BJ)/def2-TZVPP level with Turbomole were carried out by interfacing to the in-house MAG code.[71] Alternative analyses using localized MOs at IGLO-level (individual gauges for localized orbitals[72]) were not as informative, and we will thus concentrate on the GIAO-based canonical MO analyses. The Turbomole MOs have been generated with convergence criteria scfconv 10^{-9}, convergence of the density matrix to 10^{-7}, and gridsize m5 (internal settings). Harmonic vibrational spectra for cluster models were computed using the NumForce subroutine at MARIJ/BP86-D3(BJ)/def2-TZVPP/COSMO level with displacements of 0.02 a.u. Spectra are obtained with Gaussian broadening and a full width at half maximum of 4 cm^{-1} using the Gallier tool included in Turbomole.

Results

Fluoride in acetonitrile compared to water

We start with the fluoride ion as the simplest solute. For F^- in MeCN our 3D-RISM-SCF computations suggest an average coordination by 9–10 MeCN methyl groups in the first solvation shell for both UA and AA approaches. All-atom calculations show that a bit more than 1 in 3 of the attached H atoms is in close contact with the fluoride ion (using a maximum F···H distance of 2.7 Å), suggesting each methyl group to contribute one CH bond oriented towards the fluoride (see Figures S1, S2 in Supporting Information for the computed radial distribution functions). This rather large coordination number is indeed confirmed by the GFN2-xTB MD simulations and preoptimizations, which show binding of up to eight or nine solvent molecules in the first shell. DFT- and DFT-COSMO-optimized clusters tend to retain this picture. The $F^-(MeCN)_9$ cluster has all nine MeCN molecules contributing to the coordination (Figure 1). For n = 10, 11 we see only eight molecules coordinating directly to fluoride, with 3–4 somewhat shorter CH···F contacts of around 1.98 Å and the others somewhat longer, 2.04 Å (see

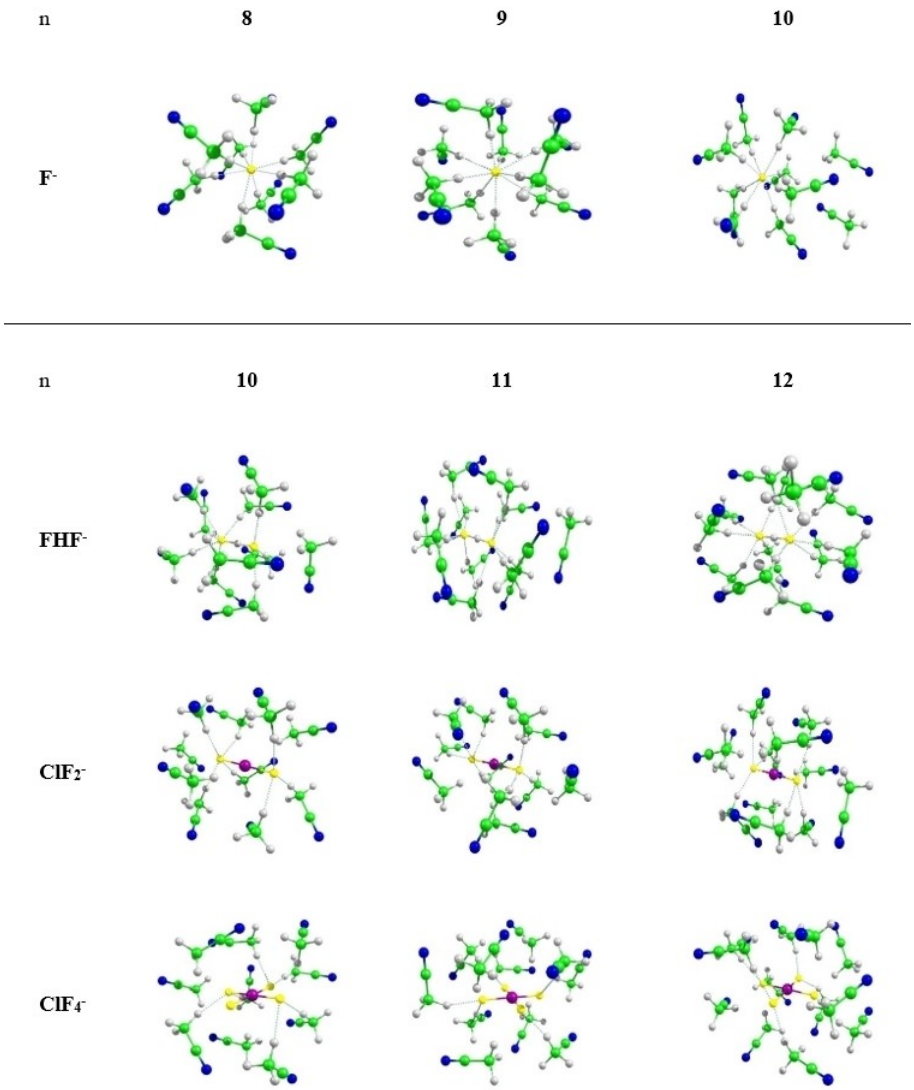

Figure 1. Examples of microsolvated clusters $X^-(MeCN)_n$ with relevant sizes (structures optimized at COSMO-MARIJ/BP86-D3(BJ)/def2-TZVPP level).

Figure 1 and Table S1; for n = 9 a somewhat different arrangement with overall longer distances is found).

The exergonicity of the free binding energies of the solvent molecules in the $F^-(MeCN)_n$ clusters increases very quickly for smaller n and then more slowly (Figure 2 and Table S2). The curve dips at around n = 7–9, confirming completion of the first solvation shell at around this number. Note that the embedding of both the clusters and the cluster of MeCN molecules without fluoride by the COSMO-RS solvent model is required to obtain these qualitatively correct curves, and it is mandatory to use a "cluster cycle" (see Computational Details). If one uses a "monomer cycle" according to the reaction $[X^-(MeCN)_n]_{solv} \rightleftharpoons X^-(g) + n[(MeCN)]_{solv}$ rather than the cluster cycle, the most negative free energies (Table S3) are obtained for smaller n (around n = 5 for F^-), and the curves then bend up towards zero for larger n values. This incorrect behavior, which is shown in Figures S3, S4 (without and with COSMO-RS embedding; see also Table S3) in Supporting Information and is similar to curves obtained for microsolvation of anions by CHF_3,[9] is an artefact of an exaggerated translational entropy for the monomer treatment. The even slightly larger coordination number given by 3D-RISM-SCF might be attributed to the somewhat larger CH···F bond length (maximum of the RDF, Figure S1). What is also noticeable is the rather steep negative slope from n = 1 to n = 2, which is consistent with the steep positive slope in that area for the ^{19}F shift changes (Figure 2). A direct computation of the solvation free energy of F^- in MeCN with COSMO-RS, without explicit solvent molecules, gives $-375.2\ kJ\,mol^{-1}$. This is somewhat below the expected asymptote of the cluster-based free-energy curve in Figure 2, and it agrees well with an experimental solvation free energy range of $-383\ kJ\,mol^{-1}$ to $-389\ kJ\,mol^{-1}$ for F^- in MeCN obtained from the known range in aqueous solution ($-454\ kJ\,mol^{-1}$[73] to $-460\ kJ\,mol^{-1}$[74]) and the standard Gibbs free energy for the transfer of fluoride from water to MeCN ($+71\ kJ\,mol^{-1}$ at 298 K).[75] Given the uncertainties involved in the explicit calculations on the microsolvated cluster models (e.g., neglected dynamical averaging, see below, or configurational entropies) as well as in the parametrization of

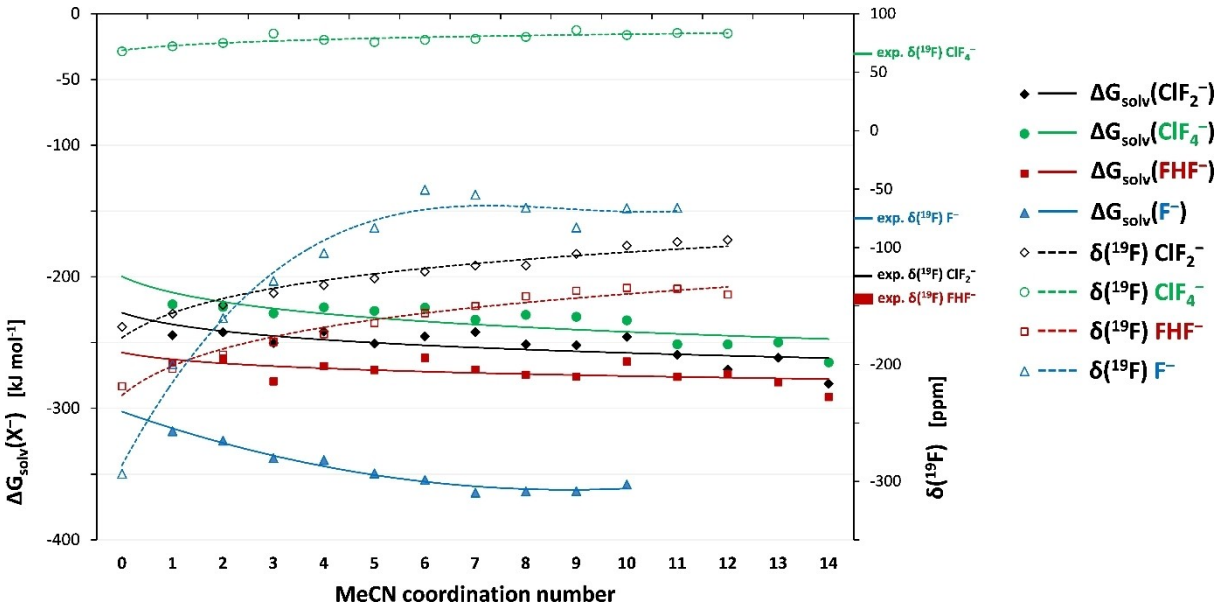

Figure 2. A comparison of computed solvation free energies ΔG_{solv} (DLPNO-SCS-MP2/aug-cc-pVTZ/COSMO-RS//MARIJ-BP86-D3(BJ)/def2-TZVPP[/COSMO(MeCN)] level using a cluster cycle) and ^{19}F NMR chemical shifts (GIAO-cLH12ct-SsirPW92/pcSseg-3/COSMO(MeCN)//MARIJ-BP86-D3(BJ)/def2-TZVPP/COSMO(MeCN) level) of microsolvated anions in MeCN as a function of cluster size. See Supporting Information Table S2 for thermochemical data, Table S4 for NMR shifts, and Table S3 for comparative thermochemical data using a monomer cycle. Experimental shifts and shift ranges are shown at the right-hand y-axis.

COSMO-RS, this may be considered close agreement. We note in passing that DLPNO-CCSD(T)-F12 gives about 13 kJ mol^{-1} more negative solvation free energies for a given n than the DLPNO-MP2 values used to draw the curves in Figure 2 (compare Figure S5 in Supporting Information for electronic binding energies; BP86-D3(BJ) and ωB97X-D give still larger binding energies; see also Table S2), bringing the microsolvated-cluster value to around −365 kJ mol^{-1}, into even closer agreement with the implicit COSMO-RS value and experiment. We note in passing that only for fluoride, the COSMO-RS value is more negative than the (COSMO-RS-embedded) microsolvated cluster value, while this reverts for the other anions discussed below (see Figure S6).

The experimental ^{19}F NMR shifts of fluoride in different solvents have been studied by Christe and coworkers (based on dissolving tetramethylammonium fluoride),[76] and by others,[77] and have been summarized and compared to MP2 calculations of fluoride with one coordinated solvent molecule (and up to six coordinated molecules for water) in Ref. [23]. Interestingly, the measured ^{19}F shifts of fluoride in organic solvents are larger (less negative) than those in water or in alcoholic solvents (e.g. −74 ppm in MeCN, −109 ppm in DCM, −119 ppm in water, and −149 ppm in MeOH). That is, the deshielding solvent contribution in MeCN is particularly large. It was pointed out that these solvent shifts do not correlate with the binding energies of the corresponding solvent molecules to fluoride.[23] The MP2 calculations of the monocoordinated clusters reproduce the trends but of course underestimate the solvent shifts. Our computed shifts for n = 8 (−65.9 ppm) and n = 9 (−82.8 ppm) at LH12ct-SsirPW92/pcSseg-3 level bracket the −74 ppm[23] experimental shift value in solution and are clearly within the expected accuracy margin of the method.[20] This corresponds to a remarkable solvent shift of more than 200 ppm.

The shifts at n = 8, 9 are thought to realistically reflect the most probable situation in solution. This is borne out by additional computations for all clusters obtained in xTB metadynamics simulations with 12 MeCN molecules, which we summarize in Figure S7 in Supporting Information. Energies at either the BP86-D3/def2-TZVPP/COSMO level used for the optimizations, or in LH12ct-SsirPW92-D3/pcSseg-3/COSMO single-point calculations to match the level used for the shift computations, clearly show that clusters with n = 8, 9 provide the lowest energies, by about 10 kJ mol^{-1} compared to n = 7 (the few n = 6 clusters have even higher energies). The BP86-D3 energies favor somewhat structures with n = 8, giving shifts centered around ca. −65 ppm. The LH12ct-SsirPW92-D3 energies favor more structures with n = 9, which lead to shifts closer to −80 ppm. I.e. the two coordination numbers give shifts slightly above or below the experimental value of −74 ppm and generally match experiment to within the accuracy of the method used in the shift computations. They are reasonably well represented by the single-structure results shown in Figure 2, given that the shifts for a given n only show a small spread with different structures. This supports the approximation of using the "best" static cluster in this case, an approximation made also for the other ions, given that to carry out full MD simulations for all cases is beyond the scope of the present work. We note that during revision of this paper, Spicher et al.[78] reported a new, automated workflow for the generation of microsolvated clusters, called "quantum cluster growth". Such algorithms provide more freedom to include

conformer averaging in a computationally affordable manner, and we will investigate its use in our ongoing work.

Shifts for DFT-optimized clusters have been computed with increasing cluster size up to n = 9 (Table S4, Figure 2). In Ref. [23] the solvent deshielding was linked to the larger shielding anisotropy in the monosolvated complexes used to model the effects. However, as we see in Table S5, the anisotropy only reflects the unsymmetrical coordination (see Figure 1 for some example cluster structures) and overall decreases with increasing coordination number, albeit in an uneven way due to the symmetry and structure of the given static solvate complex used. Yet, the isotropic shifts increase up to n = 6, 7 before levelling off only slightly for n = 8, 9 (Figure 2). Moreover, the computed shielding anisotropies for the larger clusters are much smaller (Table S4) than the overall solvent shifts (Table S4, Figure 2) and thus cannot be the major reason for the latter. Indeed, in isotropic solution the shielding anisotropy of a fluoride ion will vanish in the dynamical average. The mechanism by which solvation leads to low-frequency shifts thus clearly must operate also in the absence of anisotropy, and we will analyze it in more detail below.

In aqueous solution, which we also studied for comparison, 3D-RISM-SCF suggests an average of six hydrogen bonds from water molecules to fluoride (see Figure S8), while previous ab initio MD simulations give results closer to n = 5.[79] Other microsolvated cluster models even suggest n = 4 to be the predominant number of OH···F hydrogen bonds in the first solvation shell.[80] Our computations on $F^-(H_2O)_n$ cluster models embedded in COSMO-RS surroundings show the Gibbs free energies of solvation to still drop after n = 6, but in an irregular fashion (Figure S9, Table S6 in Supporting Information), even though closer inspection of the clusters suggest that indeed only four water molecules are coordinated to F^- in the larger clusters. This suggests that the contributions from the COSMO-RS model are somewhat smaller than those contributed by adding more explicit solvent molecules to the clusters in the second solvation shell. However, the large scatter in the curve suggests that the static clusters in any case do not provide an as good description as they did for MeCN (see above). Free solvation energies approach the experimental range of around −460 kJ mol^{-1} (see above) but do not quite get there (Table S6, Figure S9). The "pure" COSMO-RS value of −437.2 kJ mol^{-1} agrees well with the cluster-based numbers but is also slightly too small in absolute value. We note in passing, that also in this case the free energies of the "monomer cycle" agree much less with experiment (Table S6) than those of the "cluster cycle" shown in Figure S9.

The ^{19}F shifts increase sharply for small n and seem almost saturated at around n = 6 (Figure S9, Table S7). At this n, the chosen cLH12ct-SsirPW92/pcSseg-3 level provides a shift of −150 ppm. Further deshielding by up to 10–15 ppm is seen for the larger n values. This brings us to around −130 ppm to −140 ppm, still somewhat below the experimental shift of −119 ppm of fluoride in aqueous solution.[23] Overall, the solvent shift of around 140–150 ppm is in any case overall less pronounced than the more than 200 ppm we find for MeCN (see above). An explanation will be provided below.

Computations of F^- with only a COSMO or D-COSMO-RS solvent model fail completely to capture the solvent shifts, both in MeCN and in water. They give less than 2 ppm solvent shift for both solvents (−1.4 ppm in water for COSMO, −1.7 ppm for D-COSMO-RS). A 3D-RISM-SCF treatment of the solvents does not give any solvent effects on the ^{19}F shifts. This is to be expected, since the spherical symmetry of the solute gives a spherical solvation potential, which in turn creates no polarization of the electron density of the fluoride ion compared to the gas phase.

That is, as previously noticed for the gas-liquid ^{17}O shift of water,[32] electronic coupling of the solute and solvent orbitals in the magnetic field must play a decisive role for the solvent shifts in such strong-interaction cases. We have analyzed these effects in more detail using the $F^-(MeCN)_8$ and $F^-(H_2O)_6$ clusters (the latter cluster with S_6 symmetry, taken from Ref. [23], is not a minimum but gives a good overall solvent shift and renders analyses relatively transparent). We first note that the solvent shifts arise purely from paramagnetic shielding contributions σ^p (Table S8). For further analyses, we have used a breakdown into orbital contributions using the implemented tools in the MAG code,[71] at the quantitatively less accurate GIAO-BP86/pcSseg-2[58] level (the more accurate functionals are not implemented in that code). For the $F^-(H_2O)_6$ cluster, the deshielding compared to free fluoride ion is distributed over a substantial number of occupied canonical MOs (some MO plots are provided in Figure S10 in Supporting Information). All of them have some fluorine p-orbital character mixed with various water oxygen-based orbitals. This reflects the similar electronegativity of fluorine and oxygen, which places their valence orbitals in a similar energy range and thus leads to extensively delocalized canonical MOs for the cluster. While it confirms extensive solute-solvent orbital mixing, further analyses in terms of occupied-virtual MO couplings turn out to be complicated.

Analyses are more straightforward for the $F^-(MeCN)_8$ cluster, where the fluorine p-orbital character concentrates more in the three highest, almost degenerate occupied canonical MOs, which indeed dominate the large deshielding compared to free fluoride (in particular the HOMO and HOMO-1; see Figure 3 for MO plots). The dominant contributions to σ^p from occupied/virtual MO couplings arise from these three occupied MOs and from three virtual MOs. The latter do indeed have substantial σ^*(C–H) character in the CH-bonds coordinating to fluoride, albeit mixed with π^*(C≡N) character of these coordinated MeCN molecules (Figure S10). Alternative analyses using Boys-localized MOs[81] within an IGLO[72]-BP86-based scheme confirm the dominance of occupied LMOs with fluorine p-orbital character, but the couplings tend to be smeared over a larger number of (canonical) virtual MOs, rendering the analyses less transparent. Overall, our analyses clearly confirm couplings between fluorine lone pair orbitals and low-lying solvent based virtuals for MeCN solvates. This holds also analogously for the interpretation of the ^{19}F solvent shifts of the other species covered in this work (see below). We will not discuss extensive shielding analyses for these other species. We note here already that both the free solvation energies and the shift effects in

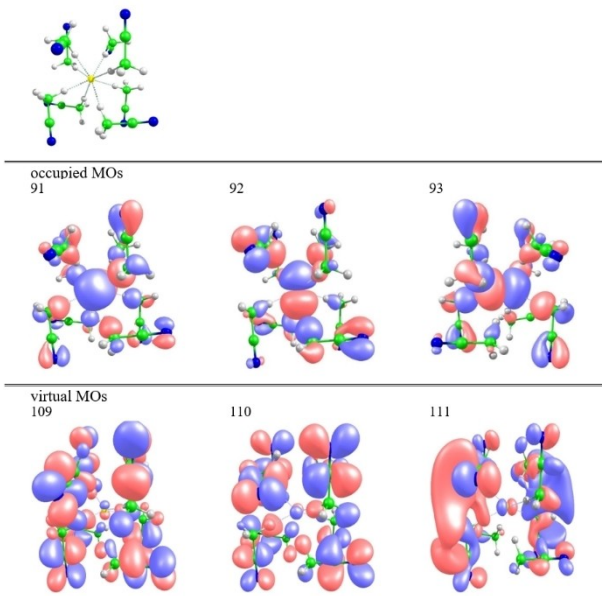

Figure 3. Structure of the optimized $F^-(MeCN)_8$ cluster used and isosurface plots (0.03 a.u.) of relevant occupied and virtual canonical molecular orbitals contributing to the ^{19}F shielding tensor.

MeCN are largest for fluoride compared to the solutes discussed further below.

Bifluoride anion

Turning to the bifluoride ion FHF^-, we note that its solvation in CH_2Cl_2 and CCl_4 has been subject to recent AIMD simulations.[22] While that work had its main focus on changes to the potential of the strong hydrogen bond within the solute, computed ^{19}F shift results clearly also confirmed appreciable deshielding in both solvents even for symmetrical structures of the solute, on which we focus in the present work. Note that those authors found that the average coordination of CH bonds to the fluorine atoms tended to be close to two for each of the fluorine atoms,[22] corresponding to n = 4 in the present context. It was speculated that steric interactions between the coordinated solvent molecules determine average dihedral angles between their CH···F vectors and thereby limit the average coordination.

Here we focus on solvation in MeCN. 3D-RISM-SCF suggests an average number of CH···F interactions n = 10 when integrating to the minimum after the second maximum (Figure S2b, the second maximum includes the sites coordinating to the other F atom, assuming 1 in 3 H sites to form a CH···F contact), that is, five hydrogen bonds per fluorine atom. Integrating only to the first minimum results in an average of 3 close interactions (again assuming 1 in 3 H sites to form a CH···F contact). The GFN2-xTB preoptimizations and the subsequent DFT and DFT + COSMO optimizations with up to 12 solvent molecules agree with this notion, as maximally 10–11 short CH···F contacts below 2.3 Å are found, and there is a tendency of solvent molecules to bind in a second solvation shell when higher coordination numbers are explored (Table S1 in Supporting Information). The DLPNO-SCS-MP2-based free energies behave similarly as for F^- but progress more slowly down to ca. $-290\ kJ\,mol^{-1}$ (Figure 2, Table S2), while DLPNO-CCSD(T)-F12 gives even about $20\ kJ\,mol^{-1}$ more negative free energies. COSMO-RS without explicit solvent molecules provides a somewhat less negative free solvation energy of $-263\ kJ\,mol^{-1}$, again (see above for fluoride) in agreement with the observation that the free energies of the microsolvated cluster models still grow more negative at n = 14, even though this involves already solvent molecules in a second shell. That is, the "pure" COSMO-RS treatment seems to underestimate slightly the overall binding. "Monomer-cycle" free energies again exhibit an incorrect behavior (Table S3, Figures S4, S5)

The ^{19}F NMR shifts tend to increase slowly up to n = 10, 11 (Figure 2, Table S4), where they reach ca. −135 ppm (compared to experimental shifts of −145 ppm to −148 ppm[82]), a solvent shift of about +84 ppm compared to the gas-phase anion (Table S4), less than half the solvent shift found for fluoride (see above). This may be compared to an average solvent ^{19}F shift in CH_2Cl_2 of +79 ppm from the AIMD simulations in Ref. [22]. COSMO and D-COSMO-RS give a solvent shift of about 3 ppm, 3D-RISM-SCF of less than 2 ppm, both methods again failing completely to capture the orbital couplings and thus the explicit solvent effects on the shifts, as can be expected. Note that we have not varied the asymmetry of the F–H–F moiety, in contrast to the AIMD simulations in Ref. [22], which showed a coupling of an asymmetry in that nominally symmetrical hydrogen bond and an asymmetric solvation shell. We conclude thus that the bifluoride ion also exhibits large solvation shifts in MeCN, but less so than fluoride, consistent with the overall smaller binding/solvation energies.

ClF_2^- compared to ClF_4^-

For the ClF_2^- anion, which originally stimulated our interest in these types of interactions of fluoride-type fluorine atoms with the CH-bonds of organic solvents,[17] 3D-RISM-SCF gives a lower average number n = 2 of close CH···F interactions (see also Figure S2, assuming 1 in 3 H sites to form a CH···F contact) than for the related FHF^- anion, where an identical analysis gives n = 3 (see above). The second minimum in the RDF would accommodate 9 contacts. Overall, the RDF shows less pronounced structure than for FHF^-. This trend is consistent with the cluster models, which provide only up to 6–7 short F···H distances below 2.3 Å, with additional solvent molecules moving further away from the fluorine sites (Table S1 in Supporting Information). The computed free energies for the microsolvated clusters nevertheless also go down further, even at n = 12, beyond $-260\ kJ\,mol^{-1}$ (Figure 2, Table S2), where they have clearly not yet converged. "Pure" COSMO-RS suggests a free solvation energy of $-240.9\ kJ\,mol^{-1}$, so the shape of the curve is again consistent with the microsolvation beyond the first solvent shell providing a slightly larger stabilization than

the COSMO-RS embedding. Overall the solvation energies are only slightly smaller than those discussed above for FHF^-.

The solvent effects on the ^{19}F NMR shifts still increase slowly up to n = 11 (Figure 2, Table S3) where the calculations would suggest them to be about 73 ppm, also only slightly less than those for FHF^- (see above). However, possibly adding further solvent molecules to the second solvation shell beyond n = 6, 7 leads to an unbalanced coordination sphere. It thus seems prudent to focus on the shifts obtained for n = 6, 7. Then we arrive at shifts between −115 ppm and −121 ppm, which is reasonably close to the experimental shift of −125 ppm. This corresponds to a somewhat smaller and more realistic and still appreciable solvation shift of 47–53 ppm. COSMO and D-COSMO-RS give a solvent shift of −4.8 and +0.5 ppm, respectively, while 3D-RISM-SCF gives about +5 ppm. All of these methods are thus again unable to recover most of the actual solvent shifts. We note that our previous computations using COSMO(MeCN) in Ref. [17] for this and related EF_2^- anions left deviations from the experimental shifts in solution of about 50–70 ppm using a similar local hybrid (LH12ct-SsifPW92, still without current response). The present computations clearly show that this is due to the orbital couplings caused by specific CH···F hydrogen bonds not being covered by implicit or force-field-based solvent models.

In that same work, the ^{19}F shifts of anions EF_4^- in MeCN could be reproduced to within ca. 10 ppm using a COSMO model for the solvent.[17] This suggests that the specific CH···F interactions are much less pronounced for the tetrafluoro species (as well as for the hexafluoro anions studied in the same paper), and it was argued that this reflects a less negative charge on fluorine (see below). 3D-RISM-SCF indeed suggests only an average of 1.5 close CH···F contacts for ClF_4^- in MeCN overall for the four fluorine sites, and a much shallower RDF overall than for the other three anions (Figure S2). This is consistent with a much less structured solvation shell. While cluster models can be constructed for many more solvent molecules, they tend to feature only 6 short contacts below 2.3 Å (Table S1), about 8–10 below 2.5 Å. The free binding energies still go down at n = 12 (DLPNO-SCS-MP2 ca. −251 kJ mol^{-1}), but this also again involves second-shell micro-solvation (Figure 2, Table S2), and the "pure" COSMO-RS value of −223.6 kJ mol^{-1} indicates again less binding. For both ClF_2^- and ClF_4^- the "monomer cycle" is again unsuitable (Table S3, Figures S3, S4).

The solvent effects on the ^{19}F shifts in ClF_4^- are much smaller than those for ClF_2^-, peaking at about 18 ppm at n = 9, while at a more realistic n = 6 the solvation shift is 10 ppm (Figure 2, Table S4), leading to a shift of 78 ppm compared to the experimental value of 67 ppm. This explains why even a COSMO-based calculation without explicit inclusion of solvent molecules gave already reasonable agreement with experiment in Ref. [17]. In the present work, COSMO gives a solvent shift of −4.9 ppm, D-COSMO-RS −2.0 ppm, 3D-RISM-SCF (OPLS-AA) ca. +11 ppm.

NMR shifts of solvent nuclei

While the effects on the shifts of the coordinating MeCN molecules will be difficult or impossible to observe experimentally, due to the expected fast exchange on the NMR time scale and the likely dominance of the bulk solvent signals, we summarize the computed data nevertheless in Tables S9–S13 in Supporting Information. As one might expect, the effects due to the charge transfer from the anion to a given solvate molecule decrease with increasing cluster size, as the effects are somewhat "diluted" over more interactions. The ^1H shifts of the coordinating hydrogen atoms are computed to have increased shifts compared to the noncoordinating ones by about 2–3 ppm for F^-, by about 0.8 ppm for FHF^- and by about 0.4 ppm for ClF_2^- (Tables S9, S10), while noncoordinating hydrogens show very small deviations from an $(MeCN)_n$ cluster. The computed methyl and nitrile ^{13}C shifts are within less than 1 ppm from a pure solvent cluster $(CH_3CN)_8$ (Tables S11, S12), the nitrile ^{15}N shifts within less than 2.5 ppm (Table S13). Any ion-induced shifts for these nuclei are thus even less likely to be observable experimentally.

IR spectroscopic fingerprints for the interaction

While weak CH···X hydrogen bonds tend to give blue-shifted CH stretching frequencies in vibrational spectra,[83] the larger charge transfer into the σ*(C–H) orbitals for stronger charge-assisted interactions with anionic acceptors is expected to lead to strongly red-shifted bands with enhanced intensity.[5,6] This should certainly hold for simple halide ions in organic solvents, and the only question is, whether these shifted bands are sufficiently strong in comparison with the bulk spectra. As an exploratory computational examination, we have computed the harmonic vibrational spectra of the $F^-(MeCN)_8$ cluster in comparison with clusters of the heavier halides Cl^- and Br^- and a cluster $(MeCN)_8$ without a halide ion as a rough approximation for the bulk liquid. The simulated spectra at BP86-D3(BJ)/def2-TZVPP/COSMO level are compared in Figure 4. It is clear that

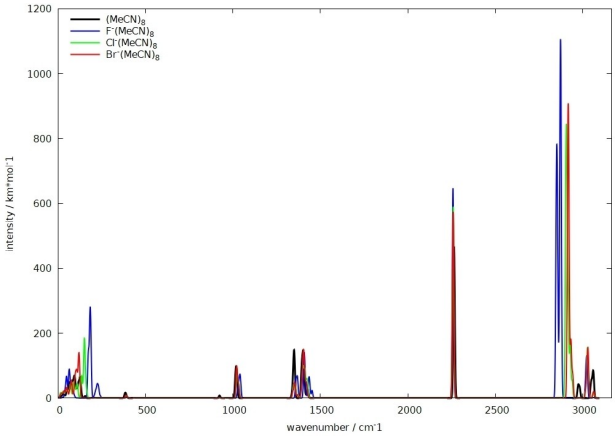

Figure 4. Computed harmonic IR Spectra of $X^-(MeCN)_8$ clusters (X = F, Cl, Br) in comparison with an $(MeCN)_8$ cluster (BP86-D3(BJ)/def2-TZVPP/COSMO).

the halide ions generate red-shifted, very intense C–H stretching bands that are not present in the $(MeCN)_8$ cluster (nor in an isolated MeCN molecule). Both the red-shift by several hundreds of cm^{-1} and the intensity increase by an order of magnitude are clearly most pronounced for fluoride. Such bands might well be observable even in the presence of the bulk vibrations. We note in passing that similar computational frequency and intensity shifts have also been found for molecular complexes of halide ions with fluoro- or chloroform, with fluoride again causing the largest effects.[10d]

Comparison of charge transfer and polarization in $F^-(MeCN)_8$ and $F^-(H_2O)_6$ clusters by NPA/NBO analyses

The fact that the ^{19}F NMR solvent shifts of fluoride in MeCN are larger than in water prompted us to compare the amount of charge transfer in the respective cluster models by NBO analyses (BP86/pcSseg-2//BP86-D3(BJ)/def2-TZVPP level, Table 1). Nuclear shieldings are a response property and thus do not necessarily follow the ground-state charge on the NMR atom of interest.[84] Still, such charge analyses can be useful. Interestingly, the negative NPA charge on fluorine is indeed smaller for the MeCN-based cluster. However, the average charge transferred to one solvent ligand is slightly larger for the aqueous cluster (0.026 e) compared to the MeCN-based cluster (0.023 e), and it is the larger number of solvent molecules that are able to coordinate for the organic solvent that overall depletes somewhat more charge from the fluoride than for the aqueous case (note that the actual n in water may be 4 or 5,[79,80] so the disparity in the average coordination may even be slightly larger than for the chosen cluster sizes).

For the latter, we see a redistribution of negative charge to the water oxygen atoms within the coordinated molecules, and the coordinating hydrogen ends up with an even more positive charge than for a free water molecule. This behavior is consistent with the behavior for a typical hydrogen bond, which enhances the ionicity of the bond within the hydrogen-bond donor. That is, in addition to moderate charge transfer from the solute to the solvent molecules, charge becomes more polarized within the coordinating solvent, accumulating more negative charge on oxygen (which in turn will enhance further interactions with the next solvent shell, not covered by the cluster model). The same observations can be made for the MeCN case: in addition to the charge transfer from fluoride to the solvent molecules, the charge within the solvent molecules becomes more polarized, accumulating charge on the nitrogen and methyl carbon (C2) atom, while depleting charge from C1 and the hydrogen atoms, particularly on the coordinating ones (H1). This underscores the character of a strong CH···F hydrogen bond with an essentially conventional build. Perturbation-theoretical analyses of the interactions between the strictly localized NBOs and the composition of the resulting natural localized MOs[69] (NLMOs) confirm expectations that the charge transfer from fluoride to the solvent molecules involves donation into the σ*(H–O) and σ*(H–C) antibonding orbitals of the coordinating OH or CH units, respectively, consistent with the MO couplings responsible for the ^{19}F solvation shifts (see above).

The interactions for the other anions are analogous albeit less pronounced, regarding both the charge-transfer and the polarization within the MeCN molecules, consistent with the reduced negative fluorine NPA charges for the free gas-phase anions of −0.756 (FHF^-), −0.591 (ClF_2^-) and −0.529 (ClF_4^-).

Table 1. Relevant NPA charges of atoms and fragments for the solvent complexes and the free solvent molecules (BP86/pcSseg-2//BP86-D3(BJ)/def2-TZVPP)[a]

	MeCN	$F^-(MeCN)_8$		H_2O	$F^-(H_2O)_6$
Q(F)	–	−0.819	Q(F)	–	−0.843
Q(N)	−0.308	−0.368	Q(O)	−0.905	−0.975
Q(C1)	+0.263	+0.294	Q(H1)[b]	+0.452	+0.484
Q(C2)	−0.733	−0.785	Q(H2)	+0.452	+0.465
Q(H1)[b]	+0.259	+0.308			
Q(H2)	+0.259	+0.264			
Q(H3)	+0.260	+0.264			
Q(MeCN)	0.000	−0.023 (8x)	$Q(H_2O)$	0.000	−0.026 (6x)

[a] Averaged over the eight and six solvent molecules, respectively.
[b] Hydrogen atom coordinating to fluoride in the cluster.

Conclusions

The element fluorine occupies a special place in the Periodic Table, not only as the most electronegative element but also due to its compact charge concentration within a small radial space. Once the accumulation of negative charge becomes very large, the resulting fluoride-like units exhibit particularly strong CH···F hydrogen-bonding interactions with the CH-bonds of organic solvents, which are not captured by the usual continuum solvation models nor by force-field-based models. In this work we have largely concentrated on acetonitrile, but the effects are clearly observable for other CH-bond containing solvents as well, CH_2Cl_2 or the haloforms being other examples.

Computational studies have already pointed out that anionic acceptors X^- can enhance CH···X^- interactions to the extent that they have to be considered strong, charge-assisted hydrogen bonds (see literature pointed out in the Introduction). The focus of the present work has been on the extremely large and characteristic solvent effects on ^{19}F NMR shifts generated by these types of hydrogen bonds. It had been known that ^{19}F solvent shifts of fluoride in many organic solvents are larger than in aqueous solution. Our analyses show that this is largely due to the fact that a solvent like acetonitrile can form more CH···F hydrogen bonds to fluoride than possible in aqueous solution (8–9 rather than 4–6). In contrast to previous interpretations, it is this larger number of (slightly weaker) hydrogen-bonding interactions that leads to a larger solvation shift, in spite of an overall somewhat smaller solvation free energy. This is why Christe had noted that the ^{19}F shift of fluoride cannot be used as an indicator of its "nakedness".

However, we do confirm that for a given solvent the ^{19}F solvation shifts of different anionic fluorine species correlate with the magnitude of their solvation free energies, which are

in turn determined by the strengths of the CH···F hydrogen bonds that correlate with the amount of negative charge on the given fluorine atom. That is, both the solvation ^{19}F shifts and the solvation free energies in acetonitrile decrease along the series $F^- \gg FHF^- > ClF_2^- > ClF_4^-$ studied in the present work. The ^{19}F solvation shifts reach astounding +227 ppm for F^- and clearly require a proper quantum-chemical treatment of microsolvation to be reproduced accurately. In contrast, the effects of microsolvation are close to +10 ppm for ClF_4^-, where the negative charge is more delocalized and thus smaller on a given fluorine atom. In the latter case these specific solvation effects are still relatively close to the error margins of even rather advanced DFT approaches but might be needed accounting for in more accurate benchmark-level treatments. And more delocalized fluoridic ions will exhibit even less pronounced effects of microsolvation. But already for ClF_2^-, the ^{19}F solvation shifts of 50–60 ppm are far outside practically achievable DFT accuracies and thus clearly have to be dealt with.

None of the implicit or force-field-based solvent models studied here, COSMO, D-COSMO-RS or 3D-RISM-SCF, can reproduce these microsolvation effects on the ^{19}F shifts, as these involve a coupling of solute and solvent orbitals in the magnetic-field response. This clearly requires an accurate quantum-mechanical treatment of the directly bound solvent molecules. In the present work, we have pre-generated the static DFT cluster models used for the computation of both shifts and solvation free energies by cheap tight-binding (xTB) meta-dynamics methods available in Grimme's CREST program, followed by DFT optimizations. In the present case of relatively simple anionic species, this has still led to probably reasonable estimates of the microsolvation effects. Clearly, matters will become less tractable for routine computational treatment for more complicated systems that one may encounter in various chemical applications (also for other electronegative elements like oxygen or chlorine when they exhibit large negative charge). This puts more emphasis on improved and expedient methods for the generation of microsolvated clusters (as, for example, the recent QCG algorithm, see above), short of the costs of full AIMD simulations, to be used in mechanistic studies of chemical reactions where the "fluoridic" character may vary along a reaction coordinate. Thermochemistry and kinetics of such reactions are expected to be strongly affected by differential microsolvation contributions not only in protic but also in "aprotic" organic solvents. In contrast to the NMR shift case, in this case we have semi-empirical methods like COSMO-RS as reasonable albeit not perfect alternatives to obtain estimates of solvation free energies. Finally, microsolvated cluster models are also required to access computationally the fingerprints that such CH···X hydrogen bonds may cause in the vibrational frequencies and intensities of C–H vibrations of the coordinated solvent molecules.

Supporting Information Summary

Tables with additional data on structures, thermochemistry and NMR chemical shifts, Figures on 3D-RISM-SCF radial distribution functions, cluster models, free energies and NMR shifts as functions of cluster size, relevant MOs for analyzing solvent NMR shifts.

Acknowledgments

We acknowledge financial support from the CRC1349 funded by the Deutsche Forschungsgemeinschaft (German Research Foundation; Gefördert durch die Deutsche Forschungsgemeinschaft (DFG) – Projektnummer 387284271–SFB 1349). We thank our experimentalist colleagues in SFB1349 on "Fluoro-Specific Interactions" for motivating our interest in this topic.

Conflict of Interest

The authors declare no conflict of interest.

Data Availability Statement

The data that support the findings of this study are available in the supplementary material of this article.

Keywords: NMR chemical shifts · solvation effects · hydrogen bonding · density functional theory · solvation free energy

[1] S. Glasstone, *Trans. Faraday Soc.* **1937**, *33*, 200–206.
[2] Siehe z. B.: D. J. Sutor, *Nature* **1962**, 68–69.
[3] A. Allerhand, P. v. R. Schleyer, *J. Am. Chem. Soc.* **1963**, *85*, 1715–1723.
[4] G. Desiraju, T. Steiner, *The Weak Hydrogen Bond: In Structural Chemistry and Biology* Oxford University Press, Oxford, **2001**.
[5] X. Li, L. Liu, H. B. Schlegel, *J. Am. Chem. Soc.* **2002**, *124*, 9639–9647.
[6] I. V. Alabugin, M. Manoharan, S. Peabody, F. Weinhold, *J. Am. Chem. Soc.* **2003**, *125*, 5973–5987.
[7] See, for example: a) N. Sreerama, S. Vishveshwara, *J. Mol. Struct.* **1985**, *133*, 139–146; b) A. Schmiedekamp, V. Nanda, *J. Inorg. Biochem.* **2009**, *103*, 1054–1060; c) C. D. Tatko, M. L. Waters, *J. Am. Chem. Soc.* **2004**, *126*, 2028–2034; d) U. Adhikari, S. Scheiner, *J. Phys. Chem. A* **2013**, *117*, 10551–10562; e) E. S. Kryachko, M. T. Nguyen, *J. Phys. Chem. A* **2001**, *105*, 153–155; f) F. M. Raymo, M. D. Bartberger, K. N. Houk, J. F. Stoddart, *J. Am. Chem. Soc.* **2001**, *123*, 9264–9267; g) K. S. Kim, J. Y. Lee, S. J. Lee, T.-K. Ha, D. H. Kim, *J. Am. Chem. Soc.* **1994**, *116*, 7399–7400; h) C. E. Cannizzaro, K. N. Houk, *J. Am. Chem. Soc.* **2002**, *124*, 7163–7169; i) S. Scheiner, T. Kar, J. Pattanayak, *J. Am. Chem. Soc.* **2002**, *124*, 13257–13264.
[8] See, for example: V. S. Bryantsev, B. P. Hay, *J. Am. Chem. Soc.* **2005**, *127*, 8282–8283.
[9] B. Nepal, S. Scheiner, *Chem. Phys.* **2015**, *463*, 137–144.
[10] See, for example: a) B. Nepal, S. Scheiner, *Chem. Eur. J.* **2015**, *21*, 1474–1481; b) B. Nepal, S. Scheiner, *Chem. Phys. Lett.* **2015**, *630*, 6–11; c) B. Nepal, S. Scheiner, *Chem. Eur. J.* **2015**, *21*, 13330–13335; d) E. S. Kryachko, T. Zeegers-Huyskens, *J. Phys. Chem. A* **2002**, *106*, 6832–6838; e) P. Botschwina, R. Oswald, V. Dyczmons, *Int. J. Mass Spectrom.* **2007**, *267*, 308–314.
[11] L. Pedzisa, B. P. Hay, *J. Org. Chem.* **2009**, *74*, 2554–2560.
[12] See, for example: a) C. A. Ilioudis, D. A. Tocher, J. W. Steed, *J. Am. Chem. Soc.* **2004**, *126*, 12395–12402; b) P. A. Gale, *Acc. Chem. Res.* **2006**, *39*,

465–475; c) O. B. Berryman, V. S. Bryantsev, D. P. Stay, D. W. Johnson, B. P. Hay, *J. Am. Chem. Soc.* **2006**, *128*, 48–58; d) J. Cai, B. P. Hay, N. J. Young, X. Yang, J. L. Sessler, *Chem. Sci.* **2013**, *4*, 1560–1567; e) P. A. Gale, N. Busschaert, C. J. E. Haynes, L. E. Karagiannidis, I. L. Kirby, *Chem. Soc. Rev.* **2014**, *43*, 205–241; f) S. Lee, C.-H. Chen, A. H. Flood, *Nat. Chem.* **2013**, *5*, 704–710; g) E. A. Katayev, G. V. Kolesnikov, J. L. Sessler, *Chem. Soc. Rev.* **2009**, *38*, 1572–1586; h) K. P. McDonald, Y. Hua, S. Lee, A. H. Flood, *Chem. Commun.* **2012**, *48*, 5065–5075; i) Y. Hua, A. H. Flood, *Chem. Soc. Rev.* **2010**, *39*, 1262–1271; j) S. S. Zhu, H. Staats, K. Brandhorst, J. Grunenberg, F. Gruppi, E. Dalcanale, A. Lützen, K. Rissanen, C. A. Schalley, *Angew. Chem. Int. Ed.* **2008**, *47*, 788–792; *Angew. Chem.* **2008**, *120*, 800–804; k) W. B. Farnham, D. C. Roe, D. A. Dixon, J. C. Calabrese, R. L. Harlow, *J. Am. Chem. Soc.* **1990**, *112*, 7707–7718; l) I. El Drubi Vega, P. A. Gale, M. E. Light, S. J. Loeb, *Chem. Commun.* **2005**, 4913–4915; m) B. W. Tresca, R. J. Hansen, C. V. Chau, B. P. Hay, L. N. Zakharov, M. M. Haley, D. W. Johnson, *J. Am. Chem. Soc.* **2015**, *137*, 14959–14967.
[13] H. Yang, M. W. Wong, *J. Am. Chem. Soc.* **2013**, *135*, 5808–5818.
[14] See, for example: S. A. Katsyuba, M. V. Vener, E. E. Zvereva, Z. Fei, R. Scopelliti, J. G. Brandenburg, S. Siankevich, P. J. Dyson, *J. Phys. Chem. Lett.* **2015**, *6*, 4431–4436.
[15] C. Coletti, N. Re, *J. Phys. Chem. A* **2009**, *113*, 1578–1585.
[16] V. S. Bryantsev, B. P. Hay, *Org. Lett.* **2005**, *7*, 5031–5034.
[17] P. Pröhm, J. R. Schmid, K. Sonnenberg, P. Voßnacker, S. Steinhauer, C. J. Schattenberg, R. Müller, M. Kaupp, S. Riedel, *Angew. Chem. Int. Ed. Engl.* **2020**, *59*, 16002–16006.
[18] A. V. Arbuznikov, M. Kaupp, *J. Chem. Phys.* **2012**, *136*, 014111.
[19] C. J. Schattenberg, K. Reiter, F. Weigend, M. Kaupp, *J. Chem. Theory Comput.* **2020**, *16*, 931–943.
[20] C. J. Schattenberg, M. Kaupp, *J. Chem. Theory Comput.* **2021**, *17*, 7602–7621.
[21] A. Klamt, G. Schüürmann, *J. Chem. Soc.-Perkin Trans.* **1993**, *2*, 799–805.
[22] S. A. Pylaeva, H. Elgabarty, D. Sebastiani, P. M. Tolstoy, *Phys. Chem. Chem. Phys.* **2017**, *19*, 26107–21620.
[23] M. Gerken, J. A. Boatz, A. Kornath, R. Haiges, S. Schneider, T. Schroer, K. O. Christe, *J. Fluorine Chem.* **2002**, *116*, 49–58.
[24] See, for example: H. Sato, *Phys. Chem. Chem. Phys.* **2013**, *15*, 7450–7465, and references therein.
[25] a) A. D. Becke, *Phys. Rev. A* **1998**, *38*, 3098–3100; b) J. P. Perdew, *Phys. Rev. B* **1986**, *33*, 8822–8824.
[26] a) S. Grimme, J. Antony, S. Ehrlich, H. Krieg, *J. Chem. Phys.* **2010**, *132*, 154104; b) S. Grimme, S. Ehrlich, L. Goerigk, *J. Comput. Chem.* **2011**, *32*, 1456–1465.
[27] E. Van Lenthe, E. J. Baerends, *J. Comput. Chem.* **2003**, *24*, 1142–1156.
[28] W. L. Jorgensen, J. M. Briggs, *Mol. Phys.* **1988**, *63*, 547–558.
[29] W. L. Jorgensen, J. Tirado-Rives, *Proc. Natl. Acad. Sci. USA* **2005**, *102*, 6665–6670.
[30] L. S. Dodda, I. Cabeza de Vaca, J. Tirado-Rives, W. L. Jorgensen, *Nucleic Acids Res.* **2018**, *45*, W331–W336.
[31] L. S. Dodda, J. Z. Vilseck, J. Tirado-Rives, W. L. Jorgensen, *J. Phys. Chem. B* **2017**, *121*, 3864–3870.
[32] M. Reimann, M. Kaupp, *J. Phys. Chem. A* **2020**, *124*, 7439–7452.
[33] a) *ADF 2021.1*, SCM, Theoretical Chemistry, Vrije Universiteit: Amsterdam, The Netherlands, http://www.scm.com; b) G. te Velde, F. M. Bickelhaupt, E. J. Baerends, C. Fonseca Guerra, S. J. A. van Gisbergen, J. G. Snijders, T. Ziegler, *J. Comput. Chem.* **2001**, *22*, 931–967.
[34] *AMS 2021.1*, SCM, Theoretical Chemistry, Vrije Universiteit: Amsterdam, The Netherlands, http://www.scm.com.
[35] A. Kovalenko, A. F. Hirata, *J. Chem. Phys.* **1999**, *110*, 10095–10112.
[36] See, for example: J. S. Perkyns, B. M. Pettitt, *Chem. Phys. Lett.* **1992**, *190*, 626–630.
[37] See, for example: Q. Du, D. Beglov, B. Roux, *J. Phys. Chem. B* **2000**, *104*, 796–805, and references therein.
[38] H. Sato, F. Hirata, *J. Am. Chem. Soc.* **1999**, *121*, 3460–3467.
[39] C. Bannwarth, S. Ehlert, S. Grimme, *J. Chem. Theory Comput.* **2019**, *15*, 1652–1671.
[40] a) S. Grimme, C. Bannwarth, S. Dohm, A. Hansen, J. Pisarek, P. Pracht, J. Seibert, F. Neese, *Angew. Chem. Int. Ed. Engl.* **2017**, *56*, 14763–14769; b) S. Grimme, *J. Chem. Theory Comput.* **2019**, *15*, 2847–2862; c) P. Pracht, F. Bohle, S. Grimme, *Phys. Chem. Chem. Phys.* **2020**, *22*, 7169–7192.
[41] a) F. Weigend, R. Ahlrichs, *Phys. Chem. Chem. Phys.* **2005**, *7*, 3297–3305.
[42] S. G. Balasubramani, G. P. Chen, S. Coriani, M. Diedenhofen, M. S. Frank, Y. J. Franzke, F. Furche, R. Grotjahn, M. E. Harding, C. Hättig, A Hellweg, B. Helmich-Paris, C. Holzer, U. Huniar, M. Kaupp, A. M. Khah, S. K. Khani, T. Müller, F. Mack, B. D. Nguyen, S. M. Parker, E. Perlt, D. Rappoport, K. Reiter, S. Roy, M. Rückert, G. Schmitz, M. Sierka, E. Tapavicza, D. P. Tew, C. van Wüllen, V. K. Voora, F. Weigend, A. Wodynski, J. M. Yu, *J. Chem. Phys.* **2020**, *152*, 184107.
[43] Local version derived from Turbomole, release 7.5.1, Turbomole GmbH, 2017. Turbomole is a development of University of Karlsruhe and Forschungszentrum Karlsruhe 1989–2007, Turbomole GmbH since 2007.
[44] V. S. Bryantsev, M. S. Diallo, W. A. Goddard III, *J. Phys. Chem. B* **2008**, *112*, 9709–9719.
[45] See, for example: a) F. Eckert, A. Klamt, *AIChE J.* **2002**, *45*, 369–385; b) A. Klamt, *WIREs Comput. Mol. Sci.* **2011**, *1*, 699–709; c) A. Klamt, M. Diedenhofen, *J. Phys. Chem. A* **2015**, *119*, 5439–5445; d) A. Hellweg, F. Eckert, *AIChE J.* **2017**, *63*, 3944–3954.
[46] S. Grimme, *J. Chem. Phys.* **2003**, *118*, 9095–9102.
[47] a) T. H. Dunning, *J. Chem. Phys.* **1989**, *90*, 1007–1023; b) R. A. Kendall, T. H. Dunning, R. J. Harrison, *J. Chem. Phys.* **1992**, *96*, 6796–6806; c) D. E. Woon, T. H. Dunning, *J. Chem. Phys.* **1993**, *98*, 1358–1371.
[48] a) C. Riplinger, B. Sandhofer, A. Hansen, F. Neese, *J. Chem. Phys.* **2013**, *139*, 134101; b) C. Riplinger, F. Neese, *J. Chem. Phys.* **2013**, *138*, 034106; c) A. Kumar, F. Neese, E. F. Valeev, *J. Chem. Phys.* **2020**, *153*, 094105.
[49] K. A. Peterson, T. B. Adler, H.-J. Werner, *J. Chem. Phys.* **2008**, *128*, 84102.
[50] a) *ORCA An Ab Initio, DFT, and Semiempirical Electronic Structure Package, Ver. 4.2.1*; Max-Planck-Institut für Kohlenforschung: Mühlheim a. d. Ruhr, Germany, **2019**; b) F. Neese, F. Wennmohs, U. Becker, C. Riplinger, *J. Chem. Phys.* **2020**, *152*, 224108.
[51] N. Mardirossian, M. Head-Gordon, *J. Chem. Phys.* **2016**, *144*, 214110.
[52] M. Haasler, T. M. Maier, R. Grotjahn, S. Gückel, A. V. Arbuznikov, M. Kaupp, *J. Chem. Theory Comput.* **2020**, *16*, 5645–5657.
[53] C. J. Schattenberg, M. Kaupp, *J. Chem. Theory Comput.* **2021**, *17*, 1469–1479.
[54] C. J. Schattenberg, M. Kaupp, *J. Phys. Chem. A* **2021**, *125*, 2697–2707.
[55] J. F. Dobson, *J. Chem. Phys.* **1993**, *98*, 8870–8872.
[56] a) R. Ditchfield, *Mol. Phys.* **1974**, *27*, 789–807; b) K. Wolinski, J. F. Hinton, P. Pulay, *J. Am. Chem. Soc.* **1990**, *112*, 8251–8260.
[57] F. Weigend, *Phys. Chem. Chem. Phys.* **2006**, *8*, 1057–1065.
[58] F. Jensen, *J. Chem. Theory Comput.* **2015**, *11*, 132–138.
[59] G. L. Stoychev, A. A. Auer, F. Neese, *J. Chem. Theory Comput.* **2018**, *14*, 4756–4771.
[60] S. Kozuch, J. M. L. Martin, *Phys. Chem. Chem. Phys.* **2011**, *13*, 20104–20107.
[61] a) A. D. Becke, *J. Chem. Phys.* **1993**, *98*, 1372–1377; b) C. Lee, W. Yang, R. G. Parr, *Phys. Rev. B* **1988**, *37*, 785–789.
[62] See, for example: T. Kupka, *Magn. Reson. Chem.* **2009**, *47*, 959–970.
[63] See, for example: a) M. Renz, M. Kess, M. Diedenhofen, A. Klamt, M. Kaupp, *J. Chem. Theory Comput.* **2012**, *8*, 4189–4203; b) S. Sinnecker, A. Rajendran, A. Klamt, M. Diedenhofen, F. Neese, *J. Phys. Chem. A* **2006**, *110*, 2235–2245.
[64] C. Wohlfarth, D. Lechner, *Landolt-Börnstein IV/17: Static Dielectric Constants of Pure Liquids and Binary Liquid Mixtures* Springer, Heidelberg/Berlin, **2008**.
[65] D. K. Hindermann, C. D. Cornwell, *J. Chem. Phys.* **1968**, *48*, 2017–2025.
[66] W. Makulski, *J. Mol. Struct.* **2013**, *1036*, 168–173.
[67] T. Kemp, *Master Thesis*, La Trobe University, Australia, **2021**.
[68] J. Vícha, J. Novotný, S. Komorovsky, M. Straka, M. Kaupp, R. Marek, *Chem. Rev.* **2020**, *120*, 7065–7103.
[69] A. E. Reed, L. A. Curtiss, F. Weinhold, *Chem. Rev.* **1988**, *88*, 899–926.
[70] *Gaussian 16*, Revision A.03, M. J. Frisch, G. W. Trucks, H. B. Schlegel, G. E. Scuseria, M. A. Robb, J. R. Cheeseman, G. Scalmani, V. Barone, G. A. Petersson, H. Nakatsuji, X. Li, M. Caricato, A. V. Marenich, J. Bloino, B. G. Janesko, R. Gomperts, B. Mennucci, H. P. Hratchian, J. V. Ortiz, A. F. Izmaylov, J. L. Sonnenberg, D. Williams-Young, F. Ding, F. Lipparini, F. Egidi, J. Goings, B. Peng, A. Petrone, T. Henderson, D. Ranasinghe, V. G. Zakrzewski, J. Gao, N. Rega, G. Zheng, W. Liang, M. Hada, M. Ehara, K. Toyota, R. Fukuda, J. Hasegawa, M. Ishida, T. Nakajima, Y. Honda, O. Kitao, H. Nakai, T. Vreven, K. Throssell, J. A. Montgomery, Jr., J. E. Peralta, F. Ogliaro, M. J. Bearpark, J. J. Heyd, E. N. Brothers, K. N. Kudin, V. N. Staroverov, T. A. Keith, R. Kobayashi, J. Normand, K. Raghavachari, A. P. Rendell, J. C. Burant, S. S. Iyengar, J. Tomasi, M. Cossi, J. M. Millam, M. Klene, C. Adamo, R. Cammi, J. W. Ochterski, R. L. Martin, K. Morokuma, O. Farkas, J. B. Foresman, D. J. Fox, Gaussian, Inc., Wallingford CT, **2016**.
[71] V. G. Malkin, O. L. Malkina, R. Reviakine, A. V. Arbuznikov, M. Kaupp, B. Schimmelpfennig, I. Malkin, T. Helgaker, K. Ruud, *MAG-ReSpect* (Ver. 1.1); **2003**.
[72] W. Kutzelnigg, U. Fleischer, M. Schindler, in *The IGLO-Method: Ab-initio Calculation and Interpretation of NMR Chemical Shifts and Magnetic Susceptibilities in NMR Basic Principles and Progress* (Eds.: P. Diehl, E.

Fluck, H. Günther, R. Kosfeld, J. Seelig), Springer, Berlin, **1991**, pp. 165–262.
[73] P. Hunenberger, M. Reif, in *Single-Ion Solvation: Experimental and Theoretical Approaches to Elusive Thermodynamic Quantities*, The Royal Society of Chemistry, London, **2011**.
[74] Y. Marcus, *Biophys. Chem.* **1994**, *51*, 111–127.
[75] Y. Marcus, M. J. Kamlet, R. W. Taft, *J. Phys. Chem.* **1988**, *92*, 3613–3622.
[76] K. O. Christe, W. W. Wilson, R. D. Wilson, R. Ban, J. Feng, *J. Am. Chem. Soc.* **1990**, *112*, 7619–7625.
[77] a) B. K. Bennett, R. G. Harrisson, T. G. Richmond, *J. Am. Chem. Soc.* **1994**, 116, 11165–11166; b) V. V. Grishin, *Angew. Chem. Int. Ed. Engl.* **1998**, *37*, 994–996.
[78] S. Spicher, C. Plett, P. Pracht, A. Hansen, S. Grimme, *J. Chem. Theory Comput.* **2022**, *18*, 3174–3189.
[79] See, for example: a) J. M. Heuft, E. J. Meijer, *J. Chem. Phys.* **2004**, *122*, 094501; b) E. Pluhařová, O. Marsalek, B. Schmidt, P. Jungwirth, *J. Phys. Chem. Lett.* **2013**, *4*, 4177–4181.
[80] See, for example: a) C.-G. Zhan, D. A. Dixon, *J. Phys. Chem. A* **2004**, *108*, 2020–2029; b) R. Shi, P. Wang, L. Tang, X. Huang, Y. Chen, Y. Su, J. Zhao, *J. Phys. Chem. A* **2018**, *122*, 3413–3422.
[81] S. F. Boys, in *Quantum Theory of Atoms, Molecules and the Solid State*, O. Löwdin (Ed.), Academic Press, New York, **1966**, pp. 253 ff.
[82] K. O. Christe, W. W. Wilson, *J. Fluorine Chem.* **1990**, *47*, 117–120.
[83] See, for example: S. Scheiner, T. Kar, *J. Phys. Chem. A* **2002**, *106*, 1784–1789.
[84] M. Kaupp, *Interpretation of NMR Chemical Shifts in Calculation of NMR and EPR Parameters. Theory and Applications* (Eds. M. Kaupp, M. Bühl, V. G. Malkin) Wiley-VCH, Weinheim **2004**, Ch. 18, pp. 293–306.

Manuscript received: June 27, 2022
Revised manuscript received: July 26, 2022

A Appendix

A.1 SI-I

A.1.1 Statistical Quantities

$$\text{MSE/MSD} = \frac{1}{N}\sum_{i}^{N} x_i - x_{i,\text{ref.}}, \tag{A.1}$$

$$\text{MAE/MAD} = \frac{1}{N}\sum_{i}^{N} |x_i - x_{i,\text{ref.}}|, \tag{A.2}$$

$$\text{StD} = \sqrt{\frac{1}{N}\sum_{i}^{N}\left(x_i - x_{i,\text{ref.}}\right)^2 - \text{MSE/MSD}^2}. \tag{A.3}$$

$$\text{MARE/MAPD} = \left(\frac{1}{N}\sum_{i}^{N}\frac{|x_i - x_{i,\text{ref.}}|}{|x_{i,\text{ref.}}|}\right)\cdot 100, \tag{A.4}$$

where x denotes either shielding or spin–spin coupling constants.

A.1.2 The Perturbed A-Matrix

For one component ($\mathbf{B}_x$) of the magnetic field, the perturbed A-matrix at a point on the numerical grid $\mathbf{r}_g$ is given by

$$\begin{aligned} A^{\mathbf{B}_x}_{\mu\nu,g} &= \frac{i}{2c}\int \left[\mathbf{R}_{\mu\nu}\times\mathbf{r}'\right]_x \frac{\phi^*_\mu(\mathbf{r}')\phi_\nu(\mathbf{r}')}{|\mathbf{r}_g-\mathbf{r}'|}\mathrm{d}\mathbf{r}', \\ &= \frac{i}{2c}\left\{R_{\mu\nu,y}\int z'\cdot\frac{\phi^*_\mu(\mathbf{r}')\phi_\nu(\mathbf{r}')}{|\mathbf{r}_g-\mathbf{r}'|}\mathrm{d}\mathbf{r}' - R_{\mu\nu,z}\int y'\cdot\frac{\phi^*_\mu(\mathbf{r}')\phi_\nu(\mathbf{r}')}{|\mathbf{r}_g-\mathbf{r}'|}\mathrm{d}\mathbf{r}'\right\}. \end{aligned} \tag{A.5}$$

Due to the GIAO derivative (see Eq. 3.57) an additional dependence on the grid vector $\mathbf{r}'$ arises, which can be projected onto the position of the Gaussian basis function ($\mathbf{r}' = \mathbf{r}'_K + \mathbf{R}_K$, with $\mathbf{r}'_K = \mathbf{r}' - \mathbf{R}_K$, where $\mathbf{R}_K$ is the position of nucleus K; The same condition holds also for the Cartesian components). For simplicity, an uncontracted basis set is chosen and the Gaussian function is separated into its Cartesian components,[269]

$$\begin{aligned}\gamma_K(\mathbf{r}) &= x_K^i \exp(-\alpha x_K^2) \cdot y_K^j \exp(-\alpha y_K^2) \cdot z_K^k \exp(-\alpha z_K^2),\\ &= G_{iK}^x \cdot G_{jK}^y \cdot G_{kK}^z,\\ &= \tilde{G}_{ijk,K}^{r'}. \end{aligned} \tag{A.6}$$

It is noted in passing, that atom-centered basis functions are assumed, therefore the position of nucleus K is also the center of the Gaussian. Inserting the projection of the Gaussian basis function and the Cartesian expansion into Eq. A.5 results in

$$\begin{aligned}A_{\mu\nu,g}^{\mathbf{B}_x} &= \frac{i}{2c}\Bigg\{ R_{\mu\nu,y} \int (z'_K + Z_K) \cdot \frac{\left(\tilde{G}_{ijk,K}^{r'}\right)\left(\tilde{G}_{lmn,L}^{r'}\right)}{|\mathbf{r}_g - \mathbf{r}'|} \mathrm{d}\mathbf{r}' \\ &\qquad - R_{\mu\nu,z} \int (y' + Y_K) \cdot \frac{\left(\tilde{G}_{ijk,K}^{r'}\right)\left(\tilde{G}_{lmn,L}^{r'}\right)}{|\mathbf{r}_g - \mathbf{r}'|} \mathrm{d}\mathbf{r}', \Bigg\} \\ &= \frac{i}{2c}\Big\{ R_{\mu\nu,y}\left(A_{\mu\nu,g}^{k+1} + Z_K \cdot A_{\mu\nu,g}\right) - R_{\mu\nu,z}\left(A_{\mu\nu,g}^{j+1} + Y_K \cdot A_{\mu\nu,g}\right) \Big\}, \end{aligned} \tag{A.7}$$

where $A_{\mu\nu,g}^{r+1}$ is the A-matrix with an enlarged l-quantum number. The expression can be generalized to

$$A_{\mu\nu,g}^{\mathbf{B}_k} = \frac{i}{2c}\Big\{ \mathbf{R}_{\mu\nu} \times (\mathbf{A}_{\mu\nu,g}^{l_k+1} + \mathbf{R}_K A_{\mu\nu,g}) \Big\}_k. \tag{A.8}$$

The vector $\mathbf{A}_{\mu\nu,g}^{\mathbf{l}_k+1}$ contains the three A-matrices with an enlarged quantum number l of the Gaussian with Cartesian component k.

A.1.3 Grid Dependence of LH Shielding Calculations

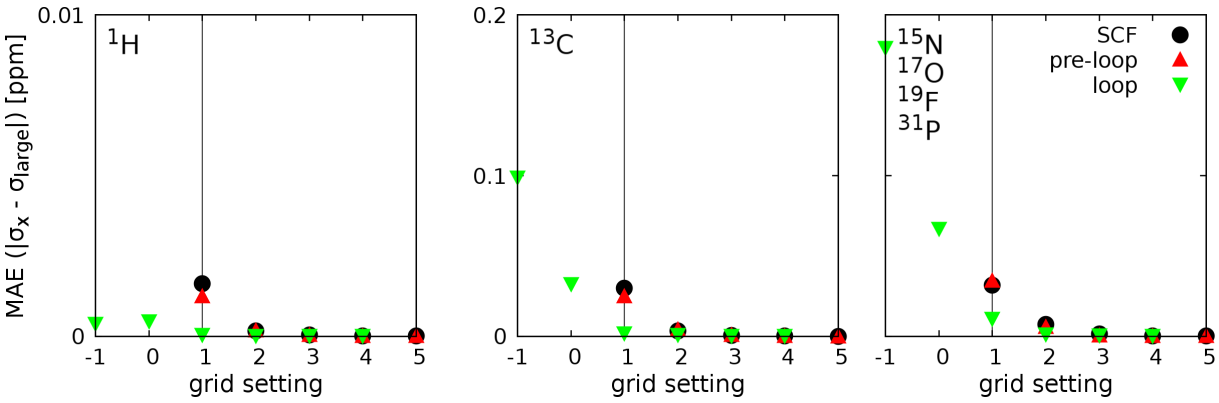

Figure A.1.: MAEs of shieldings obtained with various grid sizes relative to the extra-large (7/25) grid at LH07t-SVWN/pcSseg-4/MARI-J level of theory for ^{1}H (left), ^{13}C (middle), and the other nuclei (^{15}N, ^{17}O, ^{19}F and ^{31}P, right) for the test-set of Ref. 13.

A.1.4 Validation of Semi-Numerical Integration

Table A.1.: Top: Comparison of selected isotropic shielding constants obtained with analytical vs. semi-numerical EXX integration (B3LYP/pcSseg-4). Bottom: Mean absolute errors (MAE) of the semi-numerical results compared to the analytical program code (in ppm, results for pcSseg-4 and grid setting 5) for various functionals.

B3LYP				
	molecule	analyt.	sem.-num. (Eq.(27) P-I)	sem.-num. $A^{\mathbf{B}}$ (Eq.(26) P-I)
^{1}H	furan (C2/5)	23.998	23.998	23.998
	furan (C3/4)	24.995	24.995	24.995
	$(CH_3)_2CO$	29.800	29.800	29.800
	CH_4	31.592	31.592	31.592
	NH_3	31.720	31.720	31.720
	H_2O	31.042	31.042	31.042
	HF	29.334	29.334	29.334
	PH_3	29.631	29.631	29.631
^{13}C	furan (C2/5)	26.504	26.504	26.504
	furan (C3/4)	61.627	61.627	61.627
	$(CH_3)_2\underline{C}O$	-39.810	-39.810	-39.810
	$(\underline{C}H_3)_2CO$	148.840	148.840	148.840
	CH_4	188.822	188.822	188.822
	CF_4	44.642	44.642	44.642
	CO	-22.925	-22.925	-22.925
^{15}N	N_2	-97.205	-97.205	-97.205
	NH_3	259.679	259.679	259.679
	N$\underline{N}$O	-14.516	-14.516	-14.516
	$\underline{N}$NO	79.013	79.013	79.013
	PN	-447.495	-447.495	-447.495
^{17}O	furan	15.031	15.031	15.031
	$(CH_3)_2CO$	-356.208	-356.208	-356.208
	H_2O	326.534	326.534	326.534
	CO	-88.066	-88.066	-88.066
	OF_2	-593.761	-593.761	-593.761
	NNO	171.304	171.304	171.304
^{19}F	HF	411.486	411.486	411.486
	F_2	-259.918	-259.918	-259.918
	CF_4	241.329	241.329	241.329
	OF_2	-76.603	-76.603	-76.603
	PF_3	199.155	199.155	199.155
^{31}P	PH_3	560.987	560.988	560.987
	PF_3	168.069	168.069	168.069
	PN	-70.298	-70.298	-70.298

	functional	MAE (Eq.(27) P-I)	MAE $A^{\mathbf{B}}$ (Eq.(26) P-I)
	B3LYP	0.00001	0.00001
	BHLYP	0.00005	0.00003
	TPSSh	0.00001	0.00001
	PBE0	0.00002	0.00001
	Hartree-Fock	0.00004	0.00002

A.1.5 Test of the Gauge Independence of Initial LH Implementation

Table A.2.: Coordinate files of NH_3 used to test gauge dependence of the implementation (top) and corresponding isotropic shielding constants (in ppm, results for def2-TZVP and pcSseg-4 with grid setting 5) for various functionals (bottom).

centered	0.000000	0.000000	0.069289
	0.807968	0.466482	-0.320910
	0.000002	-0.932962	-0.320910
	-0.807969	0.466479	-0.320910
rotated	0.069289	0.000000	0.000000
	-0.320910	0.807968	0.466482
	-0.320910	0.000002	-0.932962
	-0.320910	-0.807969	0.466479
translated	100.000000	100.000000	100.069289
	100.807968	100.466482	99.679090
	100.000002	99.067038	99.679090
	99.192031	100.466479	99.679090

		def2-TZVP			pcSseg-4		
	functional	cent.	rot.	transl.	cent.	rot.	transl.
^{1}H	SVWN	32.096	32.096	32.096	31.382	31.382	31.382
	BLYP	32.600	32.600	32.600	31.833	31.833	31.833
	PBE	32.477	32.477	32.477	31.758	31.758	31.758
	TPSS	32.616	32.616	32.616	31.945	31.945	31.945
	TPSSh	32.548	32.548	32.548	31.883	31.883	31.882
	B3LYP	32.456	32.456	32.456	31.720	31.720	31.719
	PBE0	32.339	32.339	32.339	31.654	31.654	31.654
	BHLYP	32.307	32.307	32.307	31.594	31.594	31.594
	LH07s-SVWN	32.316	32.316	32.316	31.575	31.575	31.574
	LH07t-SVWN	32.076	32.076	32.076	31.326	31.326	31.326
	LH12ct-SsirPW92	31.951	31.951	31.951	31.175	31.175	31.175
	LH12ct-SsifPW92	31.882	31.882	31.882	31.094	31.094	31.094
^{15}N	SVWN	272.722	272.722	272.724	266.383	266.383	266.385
	BLYP	265.682	265.682	265.684	258.450	258.450	258.453
	PBE	268.840	268.840	268.842	261.877	261.877	261.880
	TPSS	265.878	265.878	265.881	259.258	259.258	259.261
	TPSSh	266.260	266.260	266.261	259.988	259.988	259.980
	B3LYP	266.122	266.122	266.115	259.679	259.679	259.660
	PBE0	268.803	268.803	268.796	262.834	262.834	262.812
	BHLYP	266.593	266.593	266.566	261.062	261.062	260.975
	LH07s-SVWN	270.172	270.172	270.167	263.877	263.877	263.833
	LH07t-SVWN	280.812	280.812	280.806	275.845	275.845	275.838
	LH12ct-SsirPW92	285.085	285.085	285.082	280.429	280.429	280.417
	LH12ct-SsifPW92	286.944	286.944	286.937	282.390	282.390	282.376

A.2 SI-II

A.2.1 Evaluation of LH Grid Dependency in SSCCs

Table A.3.: Grid dependency in SSCC calculations using the meta-GGA hybrid TPSSh and several LH functionals.

SSCC	grid	TPSSh	LH07t-SVWN	LH12ct-SsifPW92	LH14t-calPBE
$^1J_{CO}$ (CO)	1	19.78	19.55	24.32	18.70
	1–2[a]	20.72	19.56	24.32	17.37
	1–3[a]	20.73	19.56	24.32	17.78
	2	20.71	19.55	24.32	17.36
	2–3[a]	20.73	19.56	24.32	17.77
	3	20.73	19.56	24.32	17.78
	4	20.51	19.56	24.32	17.87
	5	20.52	19.56	24.32	17.88
	7–25[a]	20.52	19.56	24.32	17.88
$^1J_{HF}$ (HF)	1	404.95	438.85	421.63	436.90
	1–2[a]	401.54	439.20	421.57	445.31
	1–3[a]	398.72	439.29	421.64	448.89
	2	401.81	439.04	421.51	445.34
	2–3[a]	398.99	439.10	421.54	448.79
	3	399.10	439.13	421.54	448.79
	4	396.54	439.12	421.54	449.96
	5	396.59	439.12	421.53	449.93
	7–25[a]	396.60	439.12	421.53	449.93
$^1J_{NN}$ (N_2)	1	1.35	1.75	3.10	1.42
	1–2[a]	1.84	1.75	3.09	0.91
	1–3[a]	1.90	1.75	3.10	0.97
	2	1.83	1.75	3.10	0.92
	2–3[a]	1.90	1.75	3.10	0.97
	3	1.90	1.75	3.10	0.97
	4	1.84	1.75	3.10	1.00
	5	1.83	1.75	3.10	1.00
	7–25[a]	1.84	1.75	3.10	1.00

[a] With enlarged radial grid (radsize 2, 3 or 25).

A.2.2 SSCCs with Various DFAs

Table A.4.: Comparison of computed SSCCs (in Hz) with various density functionals against CC3/aug-ccJ-pVTZ and MCSCF/BS2 reference data.

Molecule	Coupling	Exp.	Rovib.[b]	CC3[a]	MCSCF[b]	TPSS	TPSSh	B3LYP	PBE0	BHLYP	LH07t[c]	LH12ct[c]	LH14t[c]
CH_4	$^1J_{HC}$	125.30[b]	4.43		121.07	139.61	140.41	133.06	123.72	141.62	114.32	97.51	122.70
	$^2J_{HH}$	-12.57[b]	-0.58		-12.89	-10.28	-11.38	-13.38	-13.94	-16.16	-15.19	-10.40	-13.37
CH_3F	$^1J_{HC}$	149.1[b]			144.35	163.64	164.91	154.61	144.69	165.68	135.42	115.73	144.89
	$^1J_{CF}$	-157.5[b]	5.1		-161.68	-255.28	-243.86	-226.99	-220.40	-190.22	-207.87	-185.11	-209.30
	$^2J_{HH}$	-9.5[b]			-10.74	-5.12	-6.39	-10.06	-10.62	-12.63	-12.43	-8.47	-10.09
	$^2J_{HF}$	46.4[b]			48.09	57.05	57.65	53.67	51.65	58.92	50.25	35.53	53.91
C_2H_4	$^1J_{HC}$	156.302[b]	5.1		153.57	172.73	174.27	166.70	156.44	178.56	145.43	125.47	154.62
	$^1J_{CC}$	67.457[b]	0.9		69.63	71.78	74.33	73.39	70.53	87.10	65.51	48.72	72.73
	$^2J_{HH}$	2.394[b]	0.3		1.06	8.32	7.15	3.28	1.36	0.59	-1.27	1.48	1.37
	$^2J_{HC}$	-2.403[b]	-1.2		-2.24	-0.67	-1.76	-1.42	-2.88	-5.53	-2.24	0.41	-2.33
	$^3J_{HH}$ (trans)	19.015[b]	2.3		18.25	22.54	22.85	20.53	20.15	22.97	17.71	14.90	18.57
	$^3J_{HH}$ (cis)	11.657[b]	1.2		11.72	12.53	12.97	13.37	13.11	15.20	12.40	10.29	12.29
C_2H_6	$^1J_{HC}$	125.206[b]			124.56	139.71	140.77	133.33	124.63	142.62	115.75	98.48	124.00
	$^1J_{CC}$	34.521[b]			35.51	34.70	36.14	33.79	31.53	41.92	29.82	18.23	34.40
	$^2J_{HH}$	-13.12[b]			-14.63	-10.17	-11.36	-13.75	-14.19	-16.61	-15.41	-10.79	-13.51
	$^2J_{HC}$	-4.657[b]			-5.01	-3.34	-3.89	-3.47	-4.15	-5.14	-4.25	-2.53	-4.12
	$^3J_{HH}$ (gauche)	3.92[b]			3.61	3.80	3.93	4.36	4.07	4.73	3.86	3.23	3.87
	$^3J_{HH}$ (trans)	16.92[b]			15.79	19.35	19.29	17.85	16.64	18.77	14.94	13.22	15.91
C_3H_4	$^1J_{HC}$ (CH)	228.2[b]	4.5		229.75	249.97	252.23	245.36	231.47	260.31	215.22	190.16	226.80
	$^1J_{HC}$ (CH_2)	167[b]	5.0		168.49	185.16	186.45	178.70	167.66	189.45	156.57	136.42	166.02
	$^1J_{CC}$ ($\underline{C}H{=}\underline{C}H$)	57.1[b]	-0.2		66.34	64.16	67.13	68.68	66.87	83.16	61.43	47.89	68.32
	$^1J_{CC}$ ($\underline{C}H{-}\underline{C}H_2$)				10.55	7.24	8.77	8.82	8.03	15.62	7.09	0.77	10.10
	$^2J_{HH}$				2.03	14.99	14.20	9.51	8.10	9.01	4.73	6.11	7.34
	$^2J_{HC}$ ($C\underline{H}{=}\underline{C}H$)				3.15	4.76	3.97	3.66	2.64	-0.01	3.64	5.69	3.67
	$^2J_{HC}$ ($C\underline{H}{-}\underline{C}H_2$)				2.39	4.31	4.38	3.30	3.03	4.06	2.35	1.48	3.17
	$^2J_{HC}$ ($C\underline{H}_2$-$\underline{C}H$)				-2.86	-0.87	-1.24	-1.74	-2.24	-2.73	-2.38	-1.54	-1.91
	$^3J_{HH}$ ($C\underline{H}{=}C\underline{H}$)	1.3[b]	0.3		6.48	1.11	1.53	2.28	2.59	4.30	2.41	1.71	2.25
	$^3J_{HH}$ ($C\underline{H}{-}C\underline{H}_2$)	-1.4[b]	0.0		-2.15	-2.31	-2.45	-2.11	-2.21	-2.58	-2.10	-1.45	-2.04
CO	$^1J_{CO}$	16.4[a,b]	0.76	14.62	15.17	22.26	20.81	18.70	20.61	11.51	19.84	24.58	18.16
CO_2	$^1J_{CO}$	16.1[b]	2.8		15.67	29.22	27.05	23.45	24.17	15.64	23.92	26.99	22.08
	$^2J_{OO}$				2.36	-0.22	0.89	2.43	2.48	6.60	1.20	0.87	2.12
H_2CO	$^1J_{HC}$	172[a]		167.89		190.47	192.45	185.30	173.25	198.15	165.03	143.48	174.01
	$^1J_{CO}$			26.98		37.58	35.43	35.37	35.21	24.61	33.61	36.20	31.66
	$^2J_{HH}$	40.2[a]		37.29		56.18	54.85	45.00	41.01	44.66	33.43	30.63	38.24
	$^2J_{HO}$			-3.01		-3.69	-3.77	-2.91	-2.50	-2.95	-3.13	-1.96	-3.70

Continuing Table A.4

HFCO	$^1J_{HC}$	267[a]		242.4		281.90	283.92	270.37	254.00	284.99	241.54	212.67	254.39
	$^1J_{CF}$	369[a]		-352.41		-478.08	-464.21	-450.35	-439.08	-407.59	-420.58	-376.70	-426.38
	$^1J_{CO}$			14.67		26.82	24.36	22.31	22.33	12.09	22.09	25.46	19.80
	$^2J_{HF}$	182[a]		182.86		203.25	201.86	200.48	188.51	203.27	182.94	152.35	188.80
	$^2J_{HO}$			-10.01		-10.56	-10.57	-10.61	-9.90	-10.12	-10.71	-9.73	-10.85
	$^2J_{OF}$			48.74		72.75	67.78	71.10	69.78	47.98	64.54	74.12	58.24
F_2CO	$^1J_{CF}$	-308[a]		-294.39		-438.45	-420.71	-403.13	-393.67	-348.15	-385.34	-352.34	-386.38
	$^1J_{CO}$			12.08		28.11	25.04	21.30	21.36	10.52	21.36	24.35	19.15
	$^2J_{FF}$			-100.2		-266.49	-247.59	-232.95	-233.29	-162.91	-194.74	-222.14	-180.89
	$^2J_{OF}$			39.78		57.38	54.02	53.97	53.39	39.62	49.21	54.24	45.83
HCN	$^1J_{HC}$	267.3[a,b]	5.1	249.95	257.92	288.22	291.83	286.19	267.09	306.03	249.20	219.51	263.28
	$^1J_{CN}$	-19.1[a], -18.5[b]	2	-18.19	-19.07	-12.17	-14.84	-18.20	-16.94	-30.32	-16.04	-10.83	-19.24
	$^2J_{HN}$	-8.7[a], -7.4[b]	0.8	-7.47	-8.24	-5.17	-5.98	-7.52	-7.40	-8.50	-8.94	-9.75	-8.83
FCN	$^1J_{CF}$			-403		-601.90	-579.21	-550.19	-544.01	-493.90	-526.75	-479.85	-530.25
	$^1J_{CN}$			-5.63		10.13	5.77	-0.56	0.52	-17.55	1.38	5.78	-2.08
	$^2J_{NF}$			53.12		64.88	59.22	54.89	53.42	34.57	52.42	49.52	49.90
C_2H_2	$^1J_{HC}$	247.56[a,b]	4.86	240.44	247.65	284.94	286.65	275.36	258.82	291.34	237.51	208.30	251.83
	$^1J_{CC}$	174.78[a,b]	-10.26	180.96	185.66	190.92	194.22	205.74	198.36	222.26	186.83	162.95	195.50
	$^2J_{HC}$	50.14[a,b]	-3.68	53.07	53.63	58.87	58.27	56.66	54.09	54.72	52.14	50.70	53.69
	$^3J_{HH}$	9.62[a,b]	-1.27	9.95	10.72	12.22	12.90	11.57	12.67	15.10	10.73	8.65	10.71
CHCF	$^1J_{HC}$			270.08		320.17	321.40	307.87	290.36	324.10	266.06	234.86	281.56
	$^1J_{CC}$			268.11		276.92	281.46	296.68	287.21	316.95	271.96	239.28	283.16
	$^1J_{CF}$			-277.68		-439.04	-427.71	-405.99	-406.69	-371.26	-391.07	-363.17	-393.82
	$^2J_{HC}$			68.53		80.08	78.89	74.78	71.69	72.33	67.93	65.34	70.05
	$^2J_{CF}$			25.56		20.69	27.51	28.72	30.50	58.19	30.62	14.88	38.53
	$^3J_{HF}$	21[a]		14.45		19.34	16.87	18.55	16.74	9.32	16.09	20.85	15.03
C_2F_2	$^1J_{CC}$			401.65		424.21	429.03	445.28	433.67	467.70	413.20	367.76	427.41
	$^1J_{CF}$	-287.3[a]		-256.58		-424.45	-413.66	-389.28	-390.26	-354.26	-372.52	-345.44	-375.96
	$^2J_{CF}$			45.54		41.66	47.27	48.00	49.85	74.00	48.85	29.42	57.03
	$^3J_{FF}$	2.1[a]		2.56		4.58	11.27	26.43	20.19	48.70	24.57	-1.27	31.51
FNO	$^1J_{NF}$			152.73		170.40	180.83	187.76	190.94	233.88	165.55	139.34	175.60
	$^1J_{NO}$			-34.14		-41.96	-41.12	-41.94	-41.52	-34.42	-40.02	-42.12	-38.82
	$^2J_{OF}$			130.22		175.70	174.24	191.14	190.28	156.96	166.28	176.76	158.70
HD	$^1J_{HD}$	42.94[b]	1.81		41.22	41.10	41.66	49.35	45.10	51.56	40.38	39.53	42.90
HF	$^1J_{HF}$	500[b]	-25		538.40	372.21	396.59	449.25	433.75	530.16	439.12	421.53	449.93
N_2	$^1J_{NN}$ (^{14}N–^{15}N)	1.8[b]	0.43		1.30	2.42	1.83	1.04	1.41	-1.98	1.75	3.10	1.00
NH_3	$^1J_{HN}$	-61.4[b*]	-0.3		-61.65*	-64.67	-65.38	-64.43	-60.28	-69.40	-57.42	-50.10	-60.78
	$^2J_{HH}$	-9.6[b]	0.7		-10.60	-7.12	-8.33	-10.18	-10.17	-13.59	-10.52	-7.59	-9.07
H_2O	$^1J_{HO}$	-80.6[a,b]	4.58	-81.19	-81.19	-71.21	-73.58	-77.63	-73.63	-87.18	-72.93	-66.09	-75.96
	$^2J_{HH}$	-7.11[a], -7.34[b]	0.67	-7.84	-8.31	-4.05	-5.32	-7.37	-7.26	-11.35	-7.40	-5.71	-6.25
OHF	$^1J_{HO}$			-49.7		-27.41	-31.49	-35.52	-32.91	-49.66	-37.00	-33.56	-39.73
	$^1J_{OF}$			-565.79		-659.75	-680.53	-731.44	-743.10	-813.24	-630.95	-600.29	-651.23
	$^2J_{HF}$			89.93		102.12	104.18	113.07	114.64	115.33	103.05	94.83	101.97
OF_2	$^1J_{OF}$	300[a]		-251.99		-251.74	-286.46	-319.03	-339.78	-441.27	-269.96	-270.27	-285.50
	$^2J_{FF}$			1327.34		1808.58	1766.85	1790.41	1777.09	1734.41	1537.74	1291.74	1602.44

[a] Ref. 388; [b] Ref. 387 (and references therein); [c] LH07t-SVWN, LH12ct-SsifPW92, LH14t-calPBE; * Recalculated for ^{15}N.

A.2.3 Additional, More Detailed Evaluations of LHs for Different Types of Couplings

Full data for the comparison of various functionals against the reference data are provided in Tab. A.4 (individual FC, SD, PSO, and DSO terms are analyzed in Tabs. A.5–A.8 below). We will attempt to understand the statistical results presented in the main text better by discussing different types of couplings in turn, focussing in particular on one-bond couplings for different combinations of nuclei. We start with cases dominated clearly by the FC term, followed by cases with sizeable PSO and/or SD contributions. A rather diverse set of 11 relatively large and positive (ca. 120-250 Hz) $^1J_{CH}$ couplings is contained in the tests. Here most standard functionals tend to overshoot by about 20 Hz or more (B3LYP somewhat less), only PBE0 gets within a few Hz of the reference values for pure hydrocarbons and overshoots a bit more for more difficult heteroatom systems or acetylene (and FCCH). Among the LHs, the calibrated LH14t-calPBE performs best, on par with PBE0. LH07t-SVWN performs almost as well but gives lower values, which deteriorates matters for the simplest hydrocarbons but improves agreement for the heteroatom systems. LH12ct-SsifPW92 values are systematically lower (about 30-40 Hz below the reference values), while BHLYP generally overshoots, by ca. 20 Hz for the simpler systems up to ca. 50 Hz for the acetylenes.

$^1J_{CC}$ couplings (7 couplings in the test sets) are also FC-dominated and do not involve lone pairs. They might thus be expected to behave the same as $^1J_{CH}$. Here most standard functionals, as well as LH14t-calPBE and LH07t-SVWN, provide values close to the references for the simpler hydrocarbons, with a somewhat larger overestimate for FCCF. BHLYP overshoots again, moderately so for simple hydrocarbons, notably so for highly unsaturated systems like the acetylenes. LH12ct-SsifPW92 undershoots again systematically.

We have only four $^1J_{EH}$ couplings in the test set in which E contains one or more lone pairs (NH_3, H_2O, HOF, HF). HF is special by exhibiting a sizeable PSO contribution, the other three are clearly FC-dominated. As differences between the PSO terms for the various functionals are comparably small in this case too, the trends are in all cases anyway clearly controlled by the FC term. The large positive $^1J_{FH}$ in HF is a challenge for the DFT methods, most of which strongly underestimate it. Only BHLYP reproduces this coupling well. The LHs perform comparably to B3LYP or PBE0, while TPSS and TPSSh give even lower values. The negative $^1J_{OH}$ couplings in H_2O and HOF (note the negative gyromagnetic ratio of ^{17}O) are also best reproduced by BHLYP. All other functionals, including the three LHs, give somewhat too large values. In contrast, the

negative $^1J_{NH}$ in ammonia is reproduced well by most functionals, with LH14t-calPBE and PBE0 performing best. Here BHLYP gives a too low, LH12ct-SsifPW92 a too high value.

The remaining one-bond SSCCs exhibit more important PSO and partly SD contributions than the previously discussed ones. We may start with $^1J_{CO}$, which is represented in the test sets by five relatively small positive couplings (CO, CO_2, F_2CO, H_2CO, FHCO; Tab. A.4). BHLYP provides the best agreement with the reference values, while standard functionals with lower exact-exchange admixtures clearly overshoot. The LHs also overshoot, in the order LH14t-calPBE < LH07t-SVWN < LH12ct-SsifPW92. The excellent performance of BHLYP arises again from a particularly good agreement for the FC term, combined with some error compensation between a somewhat too positive PSO and a somewhat too negative SD term. Two $^1J_{CN}$ values (HCN, FCN) are included in Tab. A.4. Here LH14t-calPBE and B3LYP produce values closest to the reference data, followed by PBE0 and LH07t-SVWN. BHLYP gives clearly too negative values, while LH12ct-SsifPW92, TPSS, and TPSSh overshoot somewhat. Obviously BHLYP does not always perform well for couplings involving lone pairs. For the two C–N couplings discussed here, this may relate to the highly unsaturated nature of the bonds.

The two examples of $^1J_{OF}$ couplings (F_2O, FHO) differ distinctly from most other couplings in the two test sets by exhibiting large positive FC, negative PSO, and negative SD contributions that add up to overall negative SSCCs. Appreciable static correlation complicates the description by global hybrid functionals, which exhibit increasingly too negative values with increasing exact-exchange admixture. This leaves TPSS the best-performing standard functional in this case. Here position-dependent exact-exchange admixture allows keeping triplet instabilities low, and thus the LHs perform well, with LH12ct-SsifPW92 on average closest to the reference values.

The FNO molecule is the sole representative for $^1J_{NF}$ and $^1J_{NO}$ couplings and also clearly a static-correlation case. This is seen for $^1J_{NF}$, where increasing constant exact-exchange admixture leads to an increasing overestimate of the sizeable positive SSCC, while TPSS and the three LHs are closest to the reference value (LH12ct-SsifPW92 is the only functional that underestimates it somewhat). In contrast, the much smaller negative $^1J_{NO}$ coupling is best reproduced by BHLYP and underestimated somewhat by all other functionals (least so for LH14t-calPBE). HD and NN couplings are the remaining one-bond couplings not covered yet. They do not offer much further insight (the t-LMF is a constant for H_2 or HD, and the coupling in N_2 is extremely small).

We turn to two-bond SSCCs but discuss them more briefly than the larger and more diverse set of one-bond couplings. Starting with $^2J_{HH}$ (8 values), no clearcut best-performing

functional can be identified. Couplings in saturated systems (CH_4, C_2H_6, CH_3F) are reproduced well by a number of functionals, including LHs. The very small couplings in ethylene and cyclopropene give a more variable picture with no clearcut trends. The larger positive value in H_2CO is best reproduced by LH14t-calPBE. The other LHs and PBE0 are somewhat too low, TPSS and TPSSh clearly too high, while BHLYP and B3LYP rank in the middle. Finally the couplings involving lone pairs (H_2O, NH_3) are best reproduced by LH14t-calPBE, LH07t-SVWN, B3LYP, and PBE0, but variations are overall small. Two distinct groups of $^2J_{CH}$ couplings are marked by five very small couplings of either sign (C_2H_4, C_2H_6, 3x C_3H_4) and by two larger positive couplings in acetylenes (HCCH, FCCH). The former couplings are reproduced reasonably well by several functionals, including LH14t-calPBE and LH07t-SVWN, but also B3LYP or PBE0. The two larger couplings are also not too sensitive, only TPSS and TPSSh overshoot more notably. For the three relatively large $^2J_{HF}$ couplings we only note that BHLYP overestimates them most notably, while several other functionals, including the LHs, perform better. The two $^2J_{OH}$ couplings (H_2CO, HFCO) are small and do not exhibit enough variation with the functional to allow meaningful conclusions. Two $^2J_{CF}$ couplings (FCCF, FCCH) reveal a strong overestimate by BHLYP (a smaller one by LH14t-calPBE and an underestimate by LH12ct-SsifPW92) and better performance by functionals like B3LYP or TPSSh. Very different behavior because of very different electronic structures is found for the two $^2J_{CF}$ couplings in the test set (F_2CO, OF_2). Finally, LH14t-calPBE and LH07t-SVWN are among the best performers for $^2J_{NF}$, $^2J_{OF}$, and $^2J_{OO}$ couplings (overall 5 values). We refrain from analyzing the three-bond couplings (9 values) in further detail, as they are relatively small and show only weak dependencies on the functionals.

A.2.4 Contribution to the SSCCs with Various DFAs

Table A.5.: Comparison of computed FC contribution to SSCCs (in Hz) with various density functionals against CC3/aug-ccJ-pVTZ and MCSCF/BS2 reference data

Molecule	Coupling	CC3[a]	MCSCF[b]	TPSS	TPSSh	B3LYP	PBE0	BHLYP	LH07t[c]	LH12ct[c]	LH14t[c]
CH_4	$^1J_{HC}$		119.21	137.65	138.48	130.84	121.55	139.61	112.28	95.47	120.74
	$^2J_{HH}$		-13.50	-10.93	-12.04	-14.07	-14.64	-16.86	-15.83	-11.01	-14.01
CH_3F	$^1J_{HC}$		143.82	162.96	164.25	153.81	143.93	165.02	134.73	115.04	144.26
	$^1J_{CF}$		-218.12	-309.33	-298.73	-285.86	-279.88	-249.97	-265.32	-241.43	-267.82
	$^2J_{HH}$		-11.29	-5.67	-6.95	-10.65	-11.24	-13.26	-12.98	-9.01	-10.63
	$^2J_{HF}$		41.00	49.90	50.63	45.27	43.19	51.47	42.62	27.74	46.63
C_2H_4	$^1J_{HC}$		152.59	171.49	173.12	165.41	155.32	177.63	144.29	124.41	153.55
	$^1J_{CC}$		75.76	76.75	78.97	79.45	75.79	91.40	71.43	55.17	78.15
	$^2J_{HH}$		0.44	7.61	6.33	2.50	0.56	-0.28	-1.91	0.85	0.71
	$^2J_{HC}$		-0.66	0.95	-0.15	0.31	-1.20	-3.88	-0.54	2.09	-0.68
	$^3J_{HH}$ (trans)		18.44	22.68	22.95	20.58	20.17	22.82	17.81	15.12	18.65
	$^3J_{HH}$ (cis)		12.07	12.89	13.33	13.72	13.46	15.58	12.75	10.63	12.65
C_2H_6	$^1J_{HC}$		123.03	137.92	139.01	131.29	122.66	140.78	113.88	96.60	122.21
	$^1J_{CC}$		34.28	33.33	34.77	32.42	30.20	40.53	28.42	16.91	32.93
	$^2J_{HH}$		-15.00	-10.90	-12.07	-14.41	-14.85	-17.26	-16.03	-11.39	-14.11
	$^2J_{HC}$		-5.11	-3.45	-4.00	-3.59	-4.29	-5.26	-4.36	-2.65	-4.24
	$^3J_{HH}$ (gauche)		3.65	3.76	3.86	4.27	3.99	4.63	3.82	3.18	3.82
	$^3J_{HH}$ (trans)		15.80	19.37	19.38	17.89	16.69	18.85	15.00	13.27	15.96
C_3H_4	$^1J_{HC}$ (CH)		229.67	249.44	251.82	244.96	231.26	260.35	214.96	190.05	226.61
	$^1J_{HC}$ (CH_2)		167.10	183.63	184.95	176.97	166.03	187.91	155.02	134.91	164.54
	$^1J_{CC}$ ($\underline{C}H{=}\underline{C}H$)		67.87	64.95	67.47	69.85	67.37	82.26	63.13	50.14	69.50
	$^1J_{CC}$ ($\underline{C}H{-}\underline{C}H_2$)		11.32	8.22	9.78	9.90	9.07	16.81	7.83	1.39	10.88
	$^2J_{HH}$		2.22	14.42	13.62	8.84	7.33	8.35	4.08	5.44	6.70
	$^2J_{HC}$ ($C\underline{H}{=}\underline{C}H$)		2.96	4.58	3.75	3.47	2.38	-0.38	3.52	5.60	3.51
	$^2J_{HC}$ ($C\underline{H}{-}\underline{C}H_2$)		1.98	3.79	3.86	2.80	2.55	3.55	1.90	1.10	2.70
	$^2J_{HC}$ ($C\underline{H}_2$-$\underline{C}H$)		-2.62	-0.66	-1.02	-1.52	-2.01	-2.46	-2.17	-1.34	-1.69
	$^3J_{HH}$ ($C\underline{H}{=}C\underline{H}$)		5.93	1.33	1.76	2.41	2.73	4.49	2.58	1.80	2.42
	$^3J_{HH}$ ($C\underline{H}{-}C\underline{H}_2$)		-2.21	-2.19	-2.32	-2.04	-2.13	-2.47	-1.99	-1.36	-1.92
CO	$^1J_{CO}$	6.34		14.34	13.16	10.86	12.77	5.06	11.98	16.53	10.71
CO_2	$^1J_{CO}$		12.87	28.03	25.59	21.54	22.21	13.02	21.92	24.65	20.18
	$^2J_{OO}$		-5.00	-8.34	-7.74	-7.45	-7.13	-4.87	-7.31	-6.89	-6.81
H_2CO	$^1J_{HC}$	167.75		190.09	192.14	185.07	173.10	198.20	164.84	143.35	173.83
	$^1J_{CO}$	8.21		18.80	16.85	14.53	14.92	5.87	14.24	17.06	12.60
	$^2J_{HH}$	36.92		55.83	54.47	44.54	40.48	44.18	33.02	30.15	37.92
	$^2J_{HO}$	-5.88		-6.14	-6.21	-5.84	-5.33	-5.69	-5.84	-4.76	-6.26

Continuing Table A.5

HFCO	$^{1}J_{HC}$	241.67		280.94	283.01	269.47	253.16	284.27	240.79	211.98	253.65
	$^{1}J_{CF}$	-314.60		-427.18	-413.57	-397.83	-387.22	-357.29	-374.17	-333.84	-379.56
	$^{1}J_{CO}$	6.49		19.51	17.13	14.23	14.60	4.85	14.10	17.21	12.10
	$^{2}J_{HF}$	190.06		212.20	210.58	208.89	196.95	210.99	190.78	159.83	196.61
	$^{2}J_{HO}$	-10.39		-10.82	-10.79	-10.95	-10.18	-10.31	-11.03	-10.09	-11.10
	$^{2}J_{OF}$	-19.32		-0.84	-5.60	-7.54	-8.53	-27.33	-6.39	5.40	-12.93
F_2CO	$^{1}J_{CF}$	-256.94		-394.57	-375.72	-355.19	-346.15	-298.65	-342.54	-311.56	-342.84
	$^{1}J_{CO}$	8.96		26.21	23.14	18.90	19.18	8.44	18.67	21.23	16.75
	$^{2}J_{FF}$	144.15		15.34	28.86	54.63	49.94	105.48	64.56	23.27	79.43
	$^{2}J_{OF}$	-3.61		13.42	9.58	6.75	6.03	-7.48	5.71	11.10	2.14
HCN	$^{1}J_{HC}$	249.63		287.49	291.36	286.06	267.17	306.94	249.08	219.75	263.28
	$^{1}J_{CN}$	-13.13		-4.81	-6.71	-9.79	-8.18	-18.27	-9.24	-4.48	-11.62
	$^{2}J_{HN}$	-3.98		-1.48	-2.10	-3.29	-3.10	-3.55	-5.09	-5.81	-4.88
FCN	$^{1}J_{CF}$	-365.36		-556.46	-527.63	-493.85	-484.74	-418.39	-477.93	-432.60	-478.88
	$^{1}J_{CN}$	4.64		22.90	19.19	13.38	14.59	-0.64	13.26	16.93	10.60
	$^{2}J_{NF}$	44.98		61.18	56.32	53.42	51.42	37.51	50.02	45.55	48.13
C_2H_2	$^{1}J_{HC}$	240.39		284.51	286.49	275.54	259.25	292.64	237.68	208.87	252.13
	$^{1}J_{CC}$	165.83		171.29	173.49	184.41	176.46	196.26	168.70	146.12	176.04
	$^{2}J_{HC}$	47.86		53.40	52.57	50.38	47.72	47.59	46.51	44.93	47.91
	$^{3}J_{HH}$	8.30		10.38	10.96	9.37	10.48	12.64	8.72	6.69	8.72
CHCF	$^{1}J_{HC}$	269.90		319.65	321.15	307.83	290.57	325.06	266.03	235.14	281.67
	$^{1}J_{CC}$	247.28		251.91	255.39	269.48	259.87	285.59	248.55	217.44	258.46
	$^{1}J_{CF}$	-247.47		-398.12	-381.47	-356.20	-353.56	-305.58	-349.14	-323.82	-349.57
	$^{2}J_{HC}$	63.04		74.50	73.07	68.39	65.23	65.11	62.21	59.51	64.19
	$^{2}J_{CF}$	13.02		-3.01	2.80	2.73	4.52	27.06	9.86	-1.59	16.00
	$^{3}J_{HF}$	0.21		2.04	-0.44	0.37	-1.54	-9.03	0.18	5.25	-1.20
C_2F_2	$^{1}J_{CC}$	376.08		394.98	398.66	413.22	401.81	431.66	385.49	341.80	398.44
	$^{1}J_{CF}$	-241.57		-400.36	-384.67	-357.81	-355.82	-308.95	-348.08	-323.51	-349.35
	$^{2}J_{CF}$	19.99		1.31	6.89	6.95	9.15	30.63	14.95	0.90	21.27
	$^{3}J_{FF}$	8.17		5.68	10.05	4.08	6.52	23.28	6.12	-6.63	13.89
FNO	$^{1}J_{NF}$	124.98		120.22	137.43	146.99	154.50	225.78	130.52	112.12	141.93
	$^{1}J_{NO}$	-18.90		-24.99	-23.70	-23.29	-22.87	-15.80	-22.93	-25.50	-21.57
	$^{2}J_{OF}$	-34.13		-13.56	-20.30	-21.60	-22.84	-60.25	-17.93	2.56	-28.89
HD	$^{1}J_{HD}$		40.22	41.18	41.73	48.38	44.10	50.52	39.44	38.48	41.95
HF	$^{1}J_{HF}$		348.62	178.07	203.23	244.44	233.28	331.29	251.60	238.88	264.03
N_2	$^{1}J_{NN}$ (^{14}N–^{15}N)		0.20	1.99	1.70	1.01	1.45	-0.50	1.42	2.77	0.95
NH_3	$^{1}J_{HN}$		-58.50	-61.37	-62.09	-60.81	-56.75	-65.91	-54.07	-46.84	-57.50
	$^{2}J_{HH}$		-12.14	-8.76	-9.98	-11.98	-11.99	-15.40	-12.19	-9.17	-10.69
H_2O	$^{1}J_{HO}$	-68.88		-58.64	-61.00	-64.07	-60.36	-73.86	-60.39	-53.86	-63.59
	$^{2}J_{HH}$	-10.93		-7.28	-8.53	-10.83	-10.70	-14.61	-10.52	-8.59	-9.36
OHF	$^{1}J_{HO}$	-55.55		-34.46	-38.76	-43.63	-41.43	-58.15	-44.10	-40.25	-47.08
	$^{1}J_{OF}$	106.09		126.34	127.65	134.27	129.79	130.27	117.74	96.69	122.57
	$^{2}J_{HF}$	23.01		30.02	32.47	32.69	33.47	41.30	32.72	27.11	32.07
OF_2	$^{1}J_{OF}$	120.58		134.16	136.61	147.62	142.24	137.63	128.81	112.44	132.10
	$^{2}J_{FF}$	97.68		29.22	34.44	30.97	26.18	41.04	26.33	-33.24	54.75

[a] Ref. 388; [b] Ref. 387 (and references therein); [c] LH07t-SVWN, LH12ct-SsifPW92, LH14t-calPBE.

Table A.6.: Comparison of computed SD contribution to SSCCs (in Hz) with various density functionals against CC3/aug-ccJ-pVTZ and MCSCF/BS2 reference data

Molecule	Coupling	CC3[a]	MCSCF[b]	TPSS	TPSSh	B3LYP	PBE0	BHLYP	LH07t[c]	LH12ct[c]	LH14t[c]
CH_4	$^1J_{HC}$		0.07	0.09	0.06	0.18	0.14	0.05	0.13	0.13	0.09
	$^2J_{HH}$		0.40	0.42	0.42	0.35	0.35	0.38	0.37	0.31	0.39
CH_3F	$^1J_{HC}$		0.05	0.20	0.16	0.20	0.18	0.07	0.16	0.16	0.15
	$^1J_{CF}$		20.22	23.82	23.95	24.15	24.10	24.53	22.10	20.60	23.19
	$^2J_{HH}$		0.52	0.57	0.58	0.49	0.52	0.54	0.52	0.46	0.53
	$^2J_{HF}$		-3.12	-4.11	-4.17	-3.32	-3.52	-3.62	-3.19	-2.82	-3.46
C_2H_4	$^1J_{HC}$		0.13	0.31	0.25	0.29	0.21	0.07	0.26	0.22	0.24
	$^1J_{CC}$		2.85	4.23	4.68	4.13	4.71	6.00	3.51	2.74	4.03
	$^2J_{HH}$		0.36	0.44	0.55	0.40	0.43	0.46	0.35	0.28	0.40
	$^2J_{HC}$		0.11	0.12	0.14	0.12	0.19	0.22	0.08	0.10	0.11
	$^3J_{HH}$ (trans)		0.24	0.29	0.33	0.35	0.39	0.55	0.35	0.19	0.36
	$^3J_{HH}$ (cis)		-0.04	-0.06	-0.07	-0.07	-0.07	-0.11	0.01	-0.03	-0.07
C_2H_6	$^1J_{HC}$		-0.11	0.03	0.00	0.12	0.09	-0.01	0.09	0.11	0.06
	$^1J_{CC}$		1.02	1.27	1.26	1.21	1.17	1.23	1.10	0.98	1.17
	$^2J_{HH}$		0.34	0.51	0.49	0.34	0.35	0.34	0.36	0.30	0.37
	$^2J_{HC}$		0.06	0.07	0.07	0.07	0.07	0.07	0.06	0.06	0.06
	$^3J_{HH}$ (gauche)		0.08	0.08	0.11	0.10	0.10	0.11	0.08	0.08	0.08
	$^3J_{HH}$ (trans)		0.02	0.02	-0.06	-0.06	-0.06	-0.12	-0.03	-0.04	-0.02
C_3H_4	$^1J_{HC}$ (CH)		0.31	0.56	0.52	0.50	0.42	0.35	0.48	0.39	0.46
	$^1J_{HC}$ (CH_2)		0.14	0.29	0.25	0.32	0.28	0.20	0.27	0.25	0.25
	$^1J_{CC}$ ($\underline{C}H{=}\underline{C}H$)		3.77	4.86	5.28	4.88	5.40	6.71	3.96	3.20	4.49
	$^1J_{CC}$ ($\underline{C}H{-}\underline{C}H_2$)		-0.36	-0.48	-0.49	-0.43	-0.43	-0.50	-0.35	-0.26	-0.38
	$^2J_{HH}$		-0.20	0.37	0.38	0.36	0.46	0.36	0.42	0.40	0.41
	$^2J_{HC}$ ($C\underline{H}{=}\underline{C}H$)		0.42	0.54	0.56	0.49	0.55	0.58	0.42	0.38	0.47
	$^2J_{HC}$ ($C\underline{H}{-}\underline{C}H_2$)		0.35	0.40	0.41	0.37	0.36	0.40	0.37	0.30	0.38
	$^2J_{HC}$ ($C\underline{H}_2$-$\underline{C}H$)		-0.17	-0.18	-0.18	-0.16	-0.17	-0.18	-0.15	-0.14	-0.16
	$^3J_{HH}$ ($C\underline{H}{=}C\underline{H}$)		0.32	-0.19	-0.21	-0.19	-0.20	-0.29	-0.19	-0.14	-0.20
	$^3J_{HH}$ ($C\underline{H}{-}C\underline{H}_2$)		-0.06	-0.07	-0.08	-0.07	-0.07	-0.09	-0.07	-0.06	-0.07
CO	$^1J_{CO}$	-4.94		-6.04	-6.28	-6.66	-6.65	-7.46	-5.72	-5.17	-6.10
CO_2	$^1J_{CO}$		-2.11	-3.14	-3.08	-3.10	-3.02	-2.93	-2.67	-2.35	-2.80
	$^2J_{OO}$		5.30	6.32	6.59	6.82	6.75	7.73	5.96	5.29	6.33
H_2CO	$^1J_{HC}$	0.30		0.63	0.58	0.48	0.46	0.29	0.45	0.38	0.47
	$^1J_{CO}$	-1.64		-2.18	-2.70	-2.66	-3.07	-5.10	-2.06	-1.82	-2.42
	$^2J_{HH}$	0.40		0.42	0.43	0.40	0.48	0.41	0.40	0.44	0.33
	$^2J_{HO}$	-0.73		-1.28	-1.32	-1.11	-1.24	-1.28	-0.98	-0.83	-1.12

Continuing Table A.6

HFCO	$^{1}J_{HC}$	0.46		0.75	0.74	0.62	0.62	0.54	0.57	0.51	0.61
	$^{1}J_{CF}$	1.18		-0.54	-1.13	-1.06	-1.68	-2.66	-0.64	0.07	-0.96
	$^{1}J_{CO}$	-3.13		-4.23	-4.52	-4.57	-4.74	-5.81	-3.79	-3.29	-4.16
	$^{2}J_{HF}$	-1.50		-1.23	-1.37	-1.23	-1.41	-1.62	-1.23	-1.28	-1.28
	$^{2}J_{HO}$	-0.61		-0.86	-0.89	-0.78	-0.83	-0.89	-0.71	-0.64	-0.79
	$^{2}J_{OF}$	-2.87		-3.62	-4.05	-4.16	-4.31	-6.23	-3.52	-3.02	-3.72
F_2CO	$^{1}J_{CF}$	0.00		-0.91	-1.42	-1.46	-1.97	-2.78	-1.12	-0.62	-1.48
	$^{1}J_{CO}$	-3.50		-4.69	-4.88	-4.95	-4.99	-5.69	-4.18	-3.63	-4.53
	$^{2}J_{FF}$	24.72		31.45	29.97	26.96	27.23	23.24	25.34	23.69	25.68
	$^{2}J_{OF}$	-4.84		-6.82	-6.93	-6.79	-6.82	-7.66	-5.84	-4.90	-6.20
HCN	$^{1}J_{HC}$	0.52		0.72	0.68	0.53	0.46	0.38	0.61	0.47	0.58
	$^{1}J_{CN}$	-5.02		-7.42	-7.87	-7.63	-7.94	-9.64	-6.34	-5.58	-7.02
	$^{2}J_{HN}$	-0.71		-1.00	-1.02	-0.93	-0.99	-1.04	-0.73	-0.71	-0.84
FCN	$^{1}J_{CF}$	-9.67		-14.78	-17.42	-16.98	-18.73	-25.59	-14.04	-11.26	-16.08
	$^{1}J_{CN}$	-5.50		-7.90	-8.27	-8.08	-8.25	-9.70	-6.71	-5.90	-7.36
	$^{2}J_{NF}$	-10.20		-14.43	-14.98	-15.18	-15.25	-17.77	-13.15	-11.17	-13.96
C_2H_2	$^{1}J_{HC}$	0.48		0.65	0.60	0.49	0.40	0.31	0.58	0.42	0.53
	$^{1}J_{CC}$	8.54		13.06	13.58	12.81	13.40	15.07	10.72	9.15	11.83
	$^{2}J_{HC}$	1.01		1.34	1.36	1.33	1.41	1.43	1.01	1.00	1.15
	$^{3}J_{HH}$	0.55		0.71	0.75	0.81	0.75	0.87	0.70	0.59	0.71
CHCF	$^{1}J_{HC}$	0.48		0.61	0.57	0.52	0.43	0.35	0.57	0.43	0.53
	$^{1}J_{CC}$	9.31		13.55	14.04	13.48	13.82	15.42	11.23	9.65	12.28
	$^{1}J_{CF}$	-9.73		-16.60	-18.81	-17.40	-19.64	-24.34	-14.31	-10.72	-16.34
	$^{2}J_{HC}$	0.98		1.24	1.27	1.24	1.31	1.33	0.95	0.94	1.08
	$^{2}J_{CF}$	17.95		27.49	28.09	27.06	27.65	29.81	23.16	18.96	24.80
	$^{3}J_{HF}$	3.07		4.79	4.65	4.11	4.29	3.84	3.15	3.03	3.54
C_2F_2	$^{1}J_{CC}$	10.18		14.19	14.68	14.31	14.49	16.07	11.91	10.31	12.91
	$^{1}J_{CF}$	-7.52		-13.41	-15.32	-14.00	-15.91	-19.60	-11.04	-7.92	-12.76
	$^{2}J_{CF}$	19.10		29.69	29.92	28.77	29.05	30.43	24.36	19.92	25.96
	$^{3}J_{FF}$	34.45		45.92	46.94	51.24	50.32	53.20	46.69	35.92	47.40
FNO	$^{1}J_{NF}$	-12.16		-8.24	-10.78	-12.83	-13.88	-28.28	-11.18	-12.23	-12.35
	$^{1}J_{NO}$	0.69		-0.14	-0.06	0.34	0.25	1.30	0.24	0.47	0.22
	$^{2}J_{OF}$	-2.45		8.04	9.80	7.21	9.04	6.59	4.27	1.29	6.65
HD	$^{1}J_{HD}$		0.51	-0.38	-0.38	0.46	0.48	0.52	0.47	0.48	0.50
HF	$^{1}J_{HF}$		-1.52	-1.50	-2.65	-0.74	-2.36	-4.94	-0.35	-0.39	-2.16
N_2	$^{1}J_{NN}$ (^{14}N–^{15}N)		-1.86	-2.49	-2.70	-2.74	-2.80	-3.65	-2.30	-2.11	-2.53
NH_3	$^{1}J_{HN}$		-0.14	-0.16	-0.14	-0.27	-0.23	-0.18	-0.23	-0.21	-0.19
	$^{2}J_{HH}$		0.64	0.67	0.67	0.64	0.69	0.72	0.69	0.60	0.67
H_2O	$^{1}J_{HO}$	-0.60		-0.45	-0.39	-0.68	-0.57	-0.43	-0.62	-0.55	-0.50
	$^{2}J_{HH}$	0.99		0.98	1.00	1.02	1.05	0.99	1.01	0.82	1.01
OHF	$^{1}J_{HO}$	0.91		2.04	2.03	1.64	1.84	1.61	1.25	0.90	1.51
	$^{1}J_{OF}$	-211.71		-318.67	-329.79	-314.21	-324.13	-377.77	-259.27	-221.65	-285.41
	$^{2}J_{HF}$	-7.26		-5.16	-6.28	-6.55	-6.52	-11.96	-7.03	-7.45	-7.07
OF_2	$^{1}J_{OF}$	-146.51		-200.71	-216.78	-210.24	-219.28	-277.66	-172.31	-151.50	-191.07
	$^{2}J_{FF}$	431.61		787.51	770.68	705.82	709.76	758.13	592.82	476.80	640.02

[a] Ref. 388; [b] Ref. 387 (and references therein); [c] LH07t-SVWN, LH12ct-SsifPW92, LH14t-calPBE.

Table A.7.: Comparison of computed PSO contribution to SSCCs (in Hz) with various density functionals against CC3/aug-ccJ-pVTZ and MCSCF/BS2 reference data

Molecule	Coupling	CC3[a]	MCSCF[b]	TPSS	TPSSh	B3LYP	PBE0	BHLYP	LH07t[c]	LH12ct[c]	LH14t[c]
CH_4	$^1J_{HC}$		1.54	1.63	1.63	1.80	1.77	1.72	1.67	1.65	1.62
	$^2J_{HH}$		3.74	3.78	3.79	3.90	3.89	3.90	3.81	3.84	3.80
CH_3F	$^1J_{HC}$		-0.17	-0.16	-0.15	-0.03	-0.07	-0.03	-0.12	-0.11	-0.15
	$^1J_{CF}$		35.84	29.84	30.53	34.34	35.00	34.83	34.97	35.34	34.95
	$^2J_{HH}$		3.05	3.01	3.03	3.14	3.13	3.16	3.07	3.11	3.06
	$^2J_{HF}$		12.12	13.16	13.09	13.63	13.88	12.98	12.73	12.52	12.66
C_2H_4	$^1J_{HC}$		0.42	0.50	0.47	0.58	0.49	0.46	0.45	0.42	0.41
	$^1J_{CC}$		-8.98	-9.27	-9.38	-10.25	-10.04	-10.36	-9.49	-9.26	-9.52
	$^2J_{HH}$		4.13	4.16	4.17	4.30	4.27	4.33	4.18	4.24	4.16
	$^2J_{HC}$		-1.00	-1.05	-1.06	-1.16	-1.17	-1.17	-1.08	-1.09	-1.07
	$^3J_{HH}$ (trans)		3.15	3.15	3.15	3.20	3.18	3.20	3.14	3.17	3.15
	$^3J_{HH}$ (cis)		0.77	0.78	0.79	0.82	0.81	0.83	0.80	0.78	0.80
C_2H_6	$^1J_{HC}$		1.15	1.28	1.28	1.45	1.40	1.39	1.31	1.30	1.27
	$^1J_{CC}$		0.14	-0.01	0.00	0.05	0.05	0.06	0.19	0.23	0.20
	$^2J_{HH}$		2.91	3.13	3.14	3.24	3.23	3.25	3.17	3.20	3.15
	$^2J_{HC}$		0.38	0.39	0.40	0.40	0.41	0.40	0.41	0.41	0.41
	$^3J_{HH}$ (gauche)		0.80	0.89	0.89	0.92	0.91	0.92	0.90	0.90	0.89
	$^3J_{HH}$ (trans)		3.04	3.03	3.04	3.09	3.09	3.12	3.05	3.06	3.04
C_3H_4	$^1J_{HC}$ (CH)		-0.88	-0.68	-0.75	-0.74	-0.85	-1.01	-0.85	-0.92	-0.91
	$^1J_{HC}$ (CH_2)		0.61	0.61	0.61	0.77	0.70	0.71	0.64	0.63	0.59
	$^1J_{CC}$ ($\underline{C}H{=}\underline{C}H$)		-5.35	-5.76	-5.74	-6.16	-6.00	-5.91	-5.77	-5.56	-5.78
	$^1J_{CC}$ ($\underline{C}H{-}\underline{C}H_2$)		-0.52	-0.62	-0.64	-0.76	-0.72	-0.80	-0.51	-0.47	-0.51
	$^2J_{HH}$		2.75	3.48	3.49	3.61	3.59	3.61	3.52	3.56	3.52
	$^2J_{HC}$ ($C\underline{H}{=}\underline{C}H$)		0.75	0.62	0.65	0.69	0.69	0.78	0.68	0.70	0.68
	$^2J_{HC}$ ($C\underline{H}{-}\underline{C}H_2$)		0.78	0.84	0.84	0.85	0.84	0.83	0.80	0.79	0.81
	$^2J_{HC}$ ($C\underline{H}_2$-$\underline{C}H$)		0.39	0.43	0.42	0.41	0.41	0.38	0.41	0.40	0.41
	$^3J_{HH}$ ($C\underline{H}{=}C\underline{H}$)		3.58	2.70	2.72	2.80	2.80	2.84	2.76	2.79	2.76
	$^3J_{HH}$ ($C\underline{H}{-}C\underline{H}_2$)		2.31	2.15	2.15	2.20	2.19	2.19	2.16	2.17	2.16
CO	$^1J_{CO}$	13.12		13.86	13.83	14.39	14.39	13.80	13.47	13.11	13.45
CO_2	$^1J_{CO}$		5.00	4.39	4.60	5.08	5.03	5.61	4.73	4.74	4.75
	$^2J_{OO}$		2.15	1.89	2.13	3.16	2.95	3.83	2.64	2.57	2.70
H_2CO	$^1J_{HC}$	-0.78		-0.88	-0.90	-0.87	-0.95	-0.94	-0.88	-0.87	-0.91
	$^1J_{CO}$	20.41		20.96	21.28	23.49	23.36	23.84	21.43	20.95	21.49
	$^2J_{HH}$	3.49		3.46	3.48	3.60	3.59	3.64	3.55	3.57	3.53
	$^2J_{HO}$	3.11		3.23	3.26	3.54	3.57	3.52	3.18	3.13	3.17

Continuing Table A.7

HFCO	$^{1}J_{HC}$	-0.91		-0.98	-1.00	-0.89	-0.95	-0.95	-0.99	-0.99	-1.04
	$^{1}J_{CF}$	-39.70		-51.07	-50.22	-52.17	-50.89	-48.35	-46.47	-43.65	-46.58
	$^{1}J_{CO}$	11.36		11.59	11.80	12.71	12.52	13.10	11.83	11.60	11.91
	$^{2}J_{HF}$	-3.87		-5.88	-5.50	-5.33	-5.18	-4.25	-4.77	-4.36	-4.69
	$^{2}J_{HO}$	0.47		0.60	0.59	0.60	0.60	0.56	0.51	0.48	0.52
	$^{2}J_{OF}$	70.60		76.88	77.10	82.46	82.28	81.20	74.11	71.41	74.56
F_2CO	$^{1}J_{CF}$	-38.61		-44.14	-44.74	-47.63	-46.71	-47.89	-42.84	-41.32	-43.22
	$^{1}J_{CO}$	6.76		6.73	6.92	7.48	7.30	7.90	7.00	6.89	7.06
	$^{2}J_{FF}$	-267.98		-312.18	-305.33	-313.45	-309.37	-290.53	-283.55	-268.01	-284.90
	$^{2}J_{OF}$	47.91		50.46	51.05	53.69	53.86	54.44	49.02	47.72	49.57
HCN	$^{1}J_{HC}$	-0.60		-0.40	-0.61	-0.78	-0.94	-1.65	-0.89	-1.10	-0.97
	$^{1}J_{CN}$	-0.07		0.02	-0.30	-0.82	-0.86	-2.45	-0.50	-0.80	-0.64
	$^{2}J_{HN}$	-3.40		-3.31	-3.48	-3.92	-3.93	-4.52	-3.73	-3.85	-3.73
FCN	$^{1}J_{CF}$	-28.55		-31.23	-34.72	-39.91	-41.11	-50.47	-35.33	-36.54	-35.84
	$^{1}J_{CN}$	-4.73		-4.84	-5.12	-5.83	-5.79	-7.19	-5.13	-5.22	-5.29
	$^{2}J_{NF}$	17.92		17.71	17.46	16.24	16.84	14.41	15.13	14.73	15.31
C_2H_2	$^{1}J_{HC}$	-0.73		-0.51	-0.74	-0.95	-1.13	-1.88	-1.05	-1.29	-1.13
	$^{1}J_{CC}$	6.57		6.56	7.14	8.52	8.49	10.93	7.40	7.67	7.62
	$^{2}J_{HC}$	5.54		5.47	5.69	6.31	6.32	7.06	5.97	6.11	5.97
	$^{3}J_{HH}$	4.69		4.72	4.78	4.99	5.04	5.20	4.89	4.96	4.86
CHCF	$^{1}J_{HC}$	-0.74		-0.54	-0.75	-0.90	-1.07	-1.72	-0.98	-1.16	-1.07
	$^{1}J_{CC}$	11.35		11.30	11.87	13.57	13.36	15.78	12.02	12.02	12.26
	$^{1}J_{CF}$	-20.96		-24.81	-27.92	-32.86	-33.96	-41.81	-28.08	-29.10	-28.38
	$^{2}J_{HC}$	5.63		5.46	5.68	6.29	6.28	7.01	5.90	6.01	5.91
	$^{2}J_{CF}$	-4.53		-2.91	-2.50	-0.19	-0.79	2.21	-1.52	-1.61	-1.38
	$^{3}J_{HF}$	13.78		15.12	15.28	16.69	16.60	17.12	15.37	15.18	15.30
C_2F_2	$^{1}J_{CC}$	15.09		14.73	15.37	17.44	17.07	19.67	15.50	15.34	15.75
	$^{1}J_{CF}$	-8.08		-11.27	-14.26	-18.04	-19.12	-26.29	-13.98	-14.58	-14.43
	$^{2}J_{CF}$	7.14		11.36	11.16	12.97	12.34	13.64	10.23	9.30	10.49
	$^{3}J_{FF}$	-38.22		-45.18	-43.87	-27.04	-34.80	-25.93	-26.39	-28.71	-27.93
FNO	$^{1}J_{NF}$	40.17		58.69	54.46	53.87	50.59	36.66	46.48	39.72	46.28
	$^{1}J_{NO}$	-15.93		-16.82	-17.35	-18.97	-18.89	-19.91	-17.33	-17.08	-17.46
	$^{2}J_{OF}$	166.55		180.96	184.48	205.26	203.82	210.35	179.68	172.65	180.67
HD	$^{1}J_{HD}$		0.79	0.62	0.62	0.85	0.83	0.86	0.80	0.90	0.78
HF	$^{1}J_{HF}$		191.41	195.78	196.17	205.78	203.05	204.09	188.18	183.39	188.36
N_2	$^{1}J_{NN}$ (^{14}N–^{15}N)		2.93	2.90	2.81	2.74	2.73	2.14	2.59	2.41	2.56
NH_3	$^{1}J_{HN}$		-2.97	-3.08	-3.09	-3.30	-3.24	-3.25	-3.06	-3.00	-3.03
	$^{2}J_{HH}$		6.15	6.23	6.24	6.43	6.40	6.40	6.25	6.27	6.24
H_2O	$^{1}J_{HO}$	-11.67		-12.09	-12.16	-12.87	-12.68	-12.87	-11.90	-11.66	-11.86
	$^{2}J_{HH}$	9.29		9.42	9.40	9.66	9.60	9.54	9.32	9.30	9.32
OHF	$^{1}J_{HO}$	5.05		5.12	5.35	6.57	6.79	6.96	5.96	5.88	5.94
	$^{1}J_{OF}$	-459.91		-467.16	-478.14	-551.23	-548.51	-565.47	-489.17	-475.08	-488.13
	$^{2}J_{HF}$	76.15		79.22	79.95	88.91	89.67	87.98	79.34	77.17	78.96
OF_2	$^{1}J_{OF}$	-225.66		-184.79	-205.89	-256.01	-262.35	-300.83	-226.07	-230.81	-226.13
	$^{2}J_{FF}$	799.05		992.85	962.73	1054.62	1042.16	936.25	919.60	849.18	908.67

[a] Ref. 388; [b] Ref. 387 (and references therein); [c] LH07t-SVWN, LH12ct-SsifPW92, LH14t-calPBE.

Table A.8.: Comparison of computed DSO contribution to SSCCs (in Hz) with various density functionals against CC3/aug-ccJ-pVTZ and MCSCF/BS2 reference data

Molecule	Coupling	CC3[a]	MCSCF[b]	TPSS	TPSSh	B3LYP	PBE0	BHLYP	LH07t[c]	LH12ct[c]	LH14t[c]
CH_4	$^1J_{HC}$		0.25	0.25	0.24	0.24	0.25	0.23	0.25	0.25	0.24
	$^2J_{HH}$		-3.53	-3.54	-3.55	-3.56	-3.55	-3.57	-3.55	-3.55	-3.55
CH_3F	$^1J_{HC}$		0.65	0.65	0.64	0.64	0.65	0.63	0.64	0.65	0.64
	$^1J_{CF}$		0.39	0.39	0.39	0.39	0.39	0.39	0.38	0.39	0.39
	$^2J_{HH}$		-3.02	-3.03	-3.04	-3.05	-3.04	-3.07	-3.04	-3.04	-3.04
	$^2J_{HF}$		-1.90	-1.91	-1.91	-1.91	-1.91	-1.92	-1.91	-1.91	-1.91
C_2H_4	$^1J_{HC}$		0.43	0.43	0.43	0.42	0.43	0.41	0.42	0.42	0.42
	$^1J_{CC}$		0.07	0.07	0.07	0.07	0.07	0.06	0.07	0.07	0.07
	$^2J_{HH}$		-3.88	-3.89	-3.90	-3.91	-3.89	-3.93	-3.89	-3.89	-3.90
	$^2J_{HC}$		-0.69	-0.69	-0.70	-0.70	-0.70	-0.70	-0.70	-0.69	-0.70
	$^3J_{HH}$ (trans)		-3.58	-3.58	-3.59	-3.59	-3.59	-3.60	-3.58	-3.58	-3.59
	$^3J_{HH}$ (cis)		-1.08	-1.09	-1.09	-1.09	-1.09	-1.10	-1.09	-1.09	-1.09
C_2H_6	$^1J_{HC}$		0.49	0.47	0.47	0.46	0.48	0.46	0.47	0.47	0.47
	$^1J_{CC}$		0.11	0.11	0.11	0.11	0.11	0.11	0.11	0.11	0.11
	$^2J_{HH}$		-2.88	-2.91	-2.91	-2.92	-2.91	-2.94	-2.91	-2.91	-2.92
	$^2J_{HC}$		-0.34	-0.35	-0.35	-0.35	-0.35	-0.35	-0.35	-0.35	-0.35
	$^3J_{HH}$ (gauche)		-0.92	-0.93	-0.93	-0.93	-0.93	-0.94	-0.93	-0.93	-0.93
	$^3J_{HH}$ (trans)		-3.06	-3.07	-3.07	-3.08	-3.07	-3.08	-3.07	-3.07	-3.08
C_3H_4	$^1J_{HC}$ (CH)		0.65	0.65	0.64	0.64	0.65	0.62	0.64	0.64	0.64
	$^1J_{HC}$ (CH_2)		0.65	0.64	0.64	0.64	0.65	0.63	0.64	0.64	0.64
	$^1J_{CC}$ ($\underline{C}H{=}\underline{C}H$)		0.11	0.11	0.11	0.11	0.11	0.11	0.11	0.11	0.11
	$^1J_{CC}$ ($\underline{C}H{-}\underline{C}H_2$)		0.12	0.12	0.12	0.12	0.12	0.12	0.12	0.12	0.12
	$^2J_{HH}$		-2.74	-3.28	-3.29	-3.30	-3.28	-3.32	-3.29	-3.28	-3.29
	$^2J_{HC}$ ($C\underline{H}{=}\underline{C}H$)		-0.98	-0.98	-0.99	-0.99	-0.98	-0.99	-0.98	-0.98	-0.99
	$^2J_{HC}$ ($C\underline{H}{-}\underline{C}H_2$)		-0.72	-0.72	-0.72	-0.72	-0.72	-0.72	-0.72	-0.72	-0.72
	$^2J_{HC}$ ($C\underline{H}_2$-$\underline{C}H$)		-0.46	-0.47	-0.47	-0.47	-0.47	-0.47	-0.47	-0.47	-0.47
	$^3J_{HH}$ ($C\underline{H}{=}C\underline{H}$)		-3.36	-2.74	-2.74	-2.74	-2.74	-2.75	-2.74	-2.73	-2.74
	$^3J_{HH}$ ($C\underline{H}{-}C\underline{H}_2$)		-2.19	-2.20	-2.20	-2.21	-2.20	-2.21	-2.20	-2.20	-2.20
CO	$^1J_{CO}$	0.10		0.10	0.10	0.11	0.10	0.11	0.10	0.10	0.10
CO_2	$^1J_{CO}$		-0.06	-0.06	-0.06	-0.06	-0.06	-0.05	-0.06	-0.06	-0.06
	$^2J_{OO}$		-0.09	-0.09	-0.09	-0.09	-0.09	-0.09	-0.09	-0.09	-0.09
H_2CO	$^1J_{HC}$	0.63		0.63	0.63	0.62	0.63	0.60	0.62	0.62	0.62
	$^1J_{CO}$	0.00		0.00	0.00	0.01	0.01	0.01	0.01	0.01	0.01
	$^2J_{HH}$	-3.53		-3.52	-3.53	-3.54	-3.53	-3.57	-3.53	-3.53	-3.54
	$^2J_{HO}$	0.50		0.50	0.50	0.50	0.50	0.50	0.50	0.50	0.50

Continuing Table A.8

HFCO	$^{1}J_{HC}$	1.18		1.19	1.18	1.17	1.18	1.14	1.17	1.17	1.17
	$^{1}J_{CF}$	0.72		0.72	0.72	0.71	0.72	0.71	0.71	0.71	0.71
	$^{1}J_{CO}$	-0.05		-0.05	-0.05	-0.05	-0.05	-0.05	-0.05	-0.05	-0.05
	$^{2}J_{HF}$	-1.83		-1.84	-1.84	-1.84	-1.84	-1.86	-1.84	-1.84	-1.85
	$^{2}J_{HO}$	0.51		0.51	0.52	0.52	0.52	0.52	0.52	0.52	0.52
	$^{2}J_{OF}$	0.33		0.33	0.33	0.33	0.33	0.33	0.33	0.33	0.33
F_2CO	$^{1}J_{CF}$	1.17		1.17	1.17	1.16	1.16	1.15	1.16	1.16	1.16
	$^{1}J_{CO}$	-0.13		-0.13	-0.13	-0.13	-0.13	-0.13	-0.13	-0.13	-0.13
	$^{2}J_{FF}$	-1.09		-1.09	-1.09	-1.10	-1.10	-1.10	-1.10	-1.10	-1.10
	$^{2}J_{OF}$	0.32		0.32	0.32	0.32	0.32	0.32	0.32	0.32	0.32
HCN	$^{1}J_{HC}$	0.41		0.41	0.40	0.39	0.40	0.36	0.39	0.39	0.39
	$^{1}J_{CN}$	0.03		0.04	0.04	0.04	0.04	0.04	0.04	0.04	0.04
	$^{2}J_{HN}$	0.62		0.62	0.62	0.62	0.62	0.62	0.62	0.62	0.62
FCN	$^{1}J_{CF}$	0.57		0.57	0.56	0.55	0.56	0.54	0.55	0.55	0.55
	$^{1}J_{CN}$	-0.04		-0.04	-0.03	-0.03	-0.03	-0.03	-0.03	-0.03	-0.03
	$^{2}J_{NF}$	0.41		0.41	0.41	0.41	0.41	0.41	0.41	0.41	0.41
C_2H_2	$^{1}J_{HC}$	0.30		0.30	0.30	0.28	0.30	0.27	0.30	0.30	0.29
	$^{1}J_{CC}$	0.01		0.01	0.01	0.00	0.01	0.00	0.01	0.01	0.01
	$^{2}J_{HC}$	-1.35		-1.35	-1.35	-1.35	-1.35	-1.35	-1.35	-1.34	-1.35
	$^{3}J_{HH}$	-3.59		-3.59	-3.60	-3.60	-3.59	-3.60	-3.59	-3.58	-3.59
CHCF	$^{1}J_{HC}$	0.44		0.44	0.44	0.42	0.44	0.40	0.44	0.44	0.43
	$^{1}J_{CC}$	0.16		0.16	0.16	0.16	0.16	0.15	0.16	0.16	0.16
	$^{1}J_{CF}$	0.49		0.49	0.49	0.48	0.48	0.47	0.47	0.47	0.48
	$^{2}J_{HC}$	-1.12		-1.12	-1.12	-1.13	-1.12	-1.13	-1.12	-1.12	-1.12
	$^{2}J_{CF}$	-0.88		-0.88	-0.88	-0.88	-0.88	-0.88	-0.88	-0.88	-0.88
	$^{3}J_{HF}$	-2.61		-2.62	-2.62	-2.62	-2.62	-2.62	-2.61	-2.61	-2.62
C_2F_2	$^{1}J_{CC}$	0.31		0.31	0.31	0.30	0.31	0.30	0.31	0.31	0.31
	$^{1}J_{CF}$	0.59		0.59	0.59	0.58	0.58	0.58	0.58	0.58	0.58
	$^{2}J_{CF}$	-0.69		-0.69	-0.69	-0.69	-0.69	-0.69	-0.69	-0.69	-0.69
	$^{3}J_{FF}$	-1.84		-1.85	-1.85	-1.85	-1.85	-1.85	-1.85	-1.85	-1.85
FNO	$^{1}J_{NF}$	-0.27		-0.27	-0.27	-0.27	-0.27	-0.27	-0.27	-0.27	-0.27
	$^{1}J_{NO}$	-0.01		-0.01	-0.01	-0.01	-0.01	-0.01	-0.01	-0.01	-0.01
	$^{2}J_{OF}$	0.26		0.26	0.26	0.26	0.26	0.26	0.26	0.26	0.26
HD	$^{1}J_{HD}$		-0.30	-0.31	-0.32	-0.34	-0.32	-0.35	-0.33	-0.33	-0.33
HF	$^{1}J_{HF}$		-0.09	-0.14	-0.16	-0.23	-0.21	-0.29	-0.31	-0.35	-0.30
N_2	$^{1}J_{NN}$ (^{14}N–^{15}N)		0.03	0.03	0.03	0.03	0.03	0.03	0.03	0.03	0.03
NH_3	$^{1}J_{HN}$		-0.07	-0.06	-0.06	-0.06	-0.06	-0.06	-0.06	-0.06	-0.06
	$^{2}J_{HH}$		-5.25	-5.25	-5.26	-5.28	-5.27	-5.31	-5.27	-5.28	-5.28
H_2O	$^{1}J_{HO}$	-0.03		-0.03	-0.03	-0.02	-0.02	-0.01	-0.02	-0.01	-0.02
	$^{2}J_{HH}$	-7.18		-7.17	-7.19	-7.21	-7.22	-7.27	-7.22	-7.24	-7.22
OHF	$^{1}J_{HO}$	-0.12		-0.12	-0.11	-0.10	-0.11	-0.09	-0.10	-0.09	-0.10
	$^{1}J_{OF}$	-0.26		-0.26	-0.26	-0.26	-0.26	-0.27	-0.26	-0.26	-0.26
	$^{2}J_{HF}$	-1.97		-1.96	-1.97	-1.97	-1.98	-1.99	-1.99	-1.99	-1.98
OF_2	$^{1}J_{OF}$	-0.40		-0.40	-0.40	-0.40	-0.40	-0.40	-0.39	-0.39	-0.40
	$^{2}J_{FF}$	-1.00		-1.00	-1.00	-1.00	-1.01	-1.00	-1.01	-1.01	-1.01

[a] Ref. 388; [b] Ref. 387 (and references therein); [c] LH07t-SVWN, LH12ct-SsifPW92, LH14t-calPBE.

A.3 SI-III

A.3.1 Action of an Angular Momentum Operator Around the x-Axis on p-Orbitals in an Atom

In case of an atomic system at the origin, the contribution to the Fock matrix for the τ_{MS} model is given by

$$F_{\mu\nu,XC}^{\tau_{MS},\mathbf{B}_k} = \frac{i}{4c}\int \frac{\delta f}{\delta \tau}\Big[\phi_\nu \left(\mathbf{r}\times\nabla\phi_\mu^*\right)_k - \phi_\mu^* \left(\mathbf{r}\times\nabla\phi_\nu\right)_k\Big], \tag{A.9}$$

where f is an arbitrary functional and the the x component of the rotation operator is given by

$$\left(\mathbf{r}\times\nabla\phi\right)_x = y\cdot\frac{\partial\phi}{\partial z} - z\cdot\frac{\partial\phi}{\partial y} \tag{A.10}$$

It is noted in passing, that for atoms at the origin $y = y_K$, since $\mathbf{R}_K = 0$. Using Gaussian basis functions (see also Eq. A.6), the above definition and the recurrence relation [269]

$$\frac{\partial G_{iK}^x}{\partial X_K} = -\frac{\partial G_{iK}^x}{\partial x} = 2\alpha G_{i+1K}^x - iG_{i-1K}^x, \tag{A.11}$$

the rotation operator of Eq. A.10 gives

$$\begin{aligned}\left(\mathbf{r}\times\nabla\phi\right)_x &= -y_K\cdot\left(2\alpha\tilde{G}_{ijk+1,K}^r - k\tilde{G}_{ijk-1,K}^r\right) + z_K\cdot\left(2\alpha\tilde{G}_{ij+1k,K}^r - j\tilde{G}_{ij-1k,K}^r\right)\\ &= k\tilde{G}_{ij+1k-1,K}^r - j\tilde{G}_{ij-1k+1,K}^r\end{aligned} \tag{A.12}$$

That is, if ϕ is of p_y character, a p_z orbital is obtained, and vice versa. s-Orbitals, as well as p_x orbitals vanish under application of the x rotation operator. It should be noted, that within the CPKS equations the MO indices run over the occupied and virtual block, respectively. If no $m_l \geq 1$ orbital is present in either of the sets, the contributions vanish.

A.3.2 Models for the Kinetic Energy Density

Within the context of the present work, four different models for the kinetic energy density have been employed. The two gauge-corrected τ_D (Eq. 3.87) and τ_{MS} (Eq. 3.86), but also an uncorrected explicitly gauge dependent version (τ_C), related to the common kinetic

energy density (Eq. 2.42) and the ad-hoc corrected variant implemented within the ORCA program code. Using the general derivative operator of Eq. 2.80, and applying the direct derivative with respect to magnetic field, the contributions due to the kinetic energy density within the perturbed potential are obtained (here, f is an arbitrary functional with $f = f[\tilde{\tau}]$)

$$F_{\mu\nu,XC}^{\tilde{\tau},\mathbf{B}_k} = \int \frac{\delta f}{\delta \tilde{\tau}} \frac{\partial}{\partial \mathbf{B}_k} \left[\frac{\partial \tilde{\tau}}{\partial D_{\mu\nu}} \right] \mathrm{d}\mathbf{r}. \tag{A.13}$$

The contribution to the Fock matrix of the uncorrected energy density is given by

$$\begin{aligned} F_{\mu\nu,XC}^{\tau_C,\mathbf{B}_k} = \frac{i}{4c} \int \frac{\delta f}{\delta \tau} \Big[& \left(\mathbf{R}_{\mu\nu} \times \mathbf{r}\right)_k \nabla\phi_\mu^* \nabla\phi_\nu \\ & - \phi_\nu \left(\left(\mathbf{R}_\nu - \mathbf{R}_G\right) \times \nabla\phi_\mu^* \right)_k + \phi_\mu^* \left(\left(\mathbf{R}_\mu - \mathbf{R}_G\right) \times \nabla\phi_\nu \right)_k \Big] \mathrm{d}\mathbf{r}, \end{aligned} \tag{A.14}$$

which is gauge dependent due to the presence of $\mathbf{R}_G$. The ad-oc corrected variant (τ_0) sets $\mathbf{R}_\nu - \mathbf{R}_G = 0$ and $\mathbf{R}_\mu - \mathbf{R}_G = 0$, and thus only the first contribution on the right hand side remains. The contribution of the gauge-corrected model by Maximoff and Scuseria is given by

$$\begin{aligned} F_{\mu\nu,XC}^{\tau_{MS},\mathbf{B}_k} = \frac{i}{4c} \int \frac{\delta f}{\delta \tau} \Big[& \left(\mathbf{R}_{\mu\nu} \times \mathbf{r}\right)_k \nabla\phi_\mu^* \nabla\phi_\nu \\ & + \phi_\nu \left(\left(\mathbf{r} - \mathbf{R}_\nu\right) \times \nabla\phi_\mu^* \right)_k + \phi_\mu^* \left(\left(\mathbf{r} - \mathbf{R}_\mu\right) \times \nabla\phi_\nu \right)_k \Big] \mathrm{d}\mathbf{r}, \end{aligned} \tag{A.15}$$

without any gauge dependence as shown in Eq. A.14. For the model by Dobson the contribution to the Fock matrix is given by

$$\begin{aligned} F_{\mu\nu,XC}^{\tau_D,\mathbf{B}_k} = \int \frac{\delta f}{\delta \tau} \Bigg[\frac{i}{4c} \Big(& \left(\mathbf{R}_{\mu\nu} \times \mathbf{r}\right)_k \nabla\phi_\mu^* \nabla\phi_\nu \\ & - \phi_\nu \left(\left(\mathbf{R}_\nu - \mathbf{R}_G\right) \times \nabla\phi_\mu^* \right)_k + \phi_\mu^* \left(\left(\mathbf{R}_\mu - \mathbf{R}_G\right) \times \nabla\phi_\nu \right)_k \Big) \\ & - \frac{i}{2\rho} \mathbf{j}_p^{\mathbf{B}_k} \left[\phi_\nu \nabla\phi_\mu^* - \phi_\mu^* \nabla\phi_\nu \right] \Bigg] \mathrm{d}\mathbf{r}, \end{aligned} \tag{A.16}$$

where the last term on the right-hand side corrects the gauge dependence of the model and $\mathbf{j}_p^{\mathbf{B}_k}$ is given in Eq. (18) of P-III.

A.3.3 Test of the Gauge Independence of the CDFT LH Implementation

Table A.9.: Tests of the gauge influence on isotropic shielding constants for NH_3 (in ppm, DFT/pcSseg-4 with grid setting 5) for one meta-GGA and one LH functional (input structure as indicated on the left hand side). The table on the top displays gauge independence using different models for τ (see Eqs. 3.86 and 3.87 within the present work), whereas the table on the bottom shows gauge dependence using an uncorrected (explicitly gauge-dependent) model for τ (see Eq. A.14) with different choices for the gauge origin.

				TPSS			LH12ct-SsifPW92		
Nucleus	x	y	z	τ_{MS}	τ_D	τ_0	τ_{MS}	τ_D	τ_0
N	0.000000	0.000000	0.000000	259.6	260.3	264.2	282.7	272.3	272.3
H	0.933748	0.000000	-0.385356	31.96	31.89	32.13	31.11	31.34	31.32
H	-0.466874	-0.808650	-0.385356	31.958	31.89	32.13	31.11	31.34	31.32
H	-0.466874	0.808650	-0.385356	31.958	31.89	32.13	31.11	31.34	31.32
N	0.000000	0.000000	0.000000	259.6	260.3	264.2	282.7	272.3	272.3
H	0.000000	0.000000	1.010141	31.96	31.89	32.13	31.11	31.34	31.32
H	0.969231	0.000000	-0.284562	31.96	31.89	32.13	31.11	31.34	31.32
H	-0.380116	0.891586	-0.284553	31.96	31.89	32.13	31.11	31.34	31.32
N	-100.000000	-100.000000	-100.000000	259.6	260.3	264.2	282.7	272.4	272.3
H	-99.066252	-100.000000	-100.385356	31.96	31.89	32.13	31.11	31.34	31.32
H	-100.466874	-100.808650	-100.385356	31.96	31.89	32.13	31.11	31.34	31.32
H	-100.466874	-99.191350	-100.385356	31.96	31.89	32.13	31.11	31.34	31.32
N	100.000000	100.000000	100.000000	259.6	260.2	264.2	282.6	272.3	272.3
H	100.933748	100.000000	99.614644	31.96	31.89	32.13	31.11	31.34	31.32
H	99.533126	99.191350	99.614644	31.96	31.89	32.13	31.11	31.34	31.32
H	99.533126	100.808650	99.614644	31.96	31.89	32.13	31.11	31.34	31.32

			TPSS			LH12ct-SsifPW92		
			τ	τ	τ_C	τ	τ	τ_C
	$\mathbf{R}_G$	x	100.000000	0.000000	0.000000	100.000000	0.000000	0.000000
		y	100.000000	0.000000	0.000000	100.000000	0.000000	0.000000
		z	100.000000	0.000000	-0.068423	100.000000	0.000000	-0.068423
x	y	z				Nucleus		
N 0.000000	0.000000	0.000000	143.2	261.0	261.1	256.7	271.9	271.9
H 0.933748	0.000000	-0.385356	120.94	31.59	31.62	33.15	31.44	31.44
H -0.466874	-0.808650	-0.385356	-205.34	31.59	31.62	20.05	31.44	31.44
H -0.466874	0.808650	-0.385356	33.52	31.59	31.62	29.64	31.44	31.44

A.4 SI-V

A.4.1 Detailed Analysis of Shieldings for Individual Nuclei of the Test Set

As we see some variation of the best-performing methods for the different nuclei, here we scrutinize them separately for the subsets. We reiterate that the ^{1}H shieldings exhibit different, on average lower demands on the electronic-structure methods than the other nuclei studied here. Furthermore, the ^{11}B, ^{13}C and ^{19}F subsets exhibit relatively moderate demands, as they include less systems with appreciable static correlation in comparison with the more demanding ^{15}N and ^{17}O subsets. The ^{31}B/^{33}S subset appears to be less critical in terms of static correlation but might already pose higher demands to some functionals regarding the high-density core regions of these third-row atoms. Note that we still look at absolute shieldings and do not yet take into account the compensation of systematic errors enabled by going to relative shifts.

^{1}H shieldings. As we will discuss deviations relative to the shielding range covered by the reference data, we note that for the ^{1}H subset this range is 16.84 ppm. That is, 1% relative deviation corresponds to ca. 0.17 ppm. Most methods give give rel. MAEs below 2% (0.34 ppm). Exceptions are (a) the SVWN LDA (4.5%), (b) HF (2.3%), (c) some τ_C and τ_0 implementations of τ-dependent meta-GGAs and GHs, and of the LHs LH14t-calPBE, LH20t, mPSTS and LHJ14, and (d) the τ_{MS} implementations of the LHs LH12ct-SsirPW92 and LH12ct-SsifPW92 (data for the latter two categories are provided in Tab. S13 in Supporting Information of SI-V). The poor performances of some τ_C variants likely reflect the fact that the gauge dependence of τ may be most detrimental for the ^{1}H shieldings, as the hydrogen atoms in question may be far from the center of mass used as a gauge. While the *ad hoc* τ_0 model removes the gauge dependence, it apparently does not eliminate the problems with ^{1}H shieldings for all τ-dependent functionals (even though the results for some other nuclei at this level may benefit from error compensation with some functionals like M06-L or VSXC). The τ_{MS} treatment has been shown earlier to deteriorate the ^{1}H shielding results for some t-LMF-based LHs without calibration function, with LH12ct-SsirPW92 and LH12ct-SsifPW92 being the most extreme cases (see also P-III). Several methods provide rel. MAEs below 1%, including DSD-PBEP86 (0.3%), B2GP-PLYP (0.5%), B2PLYP (0.6%), cLH20t (0.7%), B97-2, BHLYP, CAM-B3LYP, ωB97X-D, ωB97X-V, cLH14t-calPBE, MP2 (all 0.8%), B3LYP, cPW6B95 (both 0.9%). Here the specialized KTx GGAs are not among the

best performers, and the otherwise well-performing LHs cLH12ct-SsirPW92 and cLH12ct-SsifPW92 also fall slightly behind.

We can compare the present results to a previous benchmark on relative ^{1}H shifts, encompassing a narrower set of 48 values (the present subset contains 124 nuclei in more widely varying environments) and fewer DFT methods, against CCSD(T)/cc-pVQZ reference data.[65] The lowest MAD in that work was provided by MP2 (0.08 ppm), while HF (0.17 ppm) and the best-performing DFT methods (KT2 0.15 ppm, B97-2 0.16 ppm) were roughly on par. The more diverse set studied here gives a somewhat different perspective, where MP2 exhibits an MAE of 0.13 ppm and is outperformed by the DHs DSD-PBEP86 (0.06 ppm), B2GP-PLYP (0.08 ppm), B2PLYP (0.09 ppm) and matched by several LHs (cLH20t 0.12 ppm, cLH14t-calPBE 0.13 ppm), and a number of other functionals from rungs 2-4 (including B97-2, 0.13 ppm) are not far behind. The former top-performing KT2 (0.25 ppm) does not belong to them. Of course the DHs and LHs had not yet been available for evaluation at the time of Ref. 65, and the present ^{1}H shielding set features somewhat more demanding bond environments for the hydrogen atoms.

^{11}B shieldings. Here the shielding range covered (without BH) is 141.5 ppm, and 1% relative deviation thus corresponds to 1.4 ppm. This is a smaller value than for the other second- and third-period nuclei. We find that the rel. MAEs for some functionals can be rather large for this subset (this changes partly for relative shifts, see below). Static correlation plays a relatively small role (after removal of BH). Hartree-Fock is thus a more reasonable starting point (rel. MAE 4.5%), and MP2 is clearly excellent (rel. MAE 0.4%, rel. MSE +0.1%). In fact, BF gives the largest deviation of MP2 from the reference data (1.7% or 2.3 ppm). Given that almost all DFT functionals suffer from the systematically too large paramagnetic contributions (negative MSEs, except for cMN15-L), none of them can compete here with MP2. Even the DSD-PBEP86 DH falls behind (rel. MAE 1.9%, rel. MSE -1.9%), the other DHs much more so (rel. MSE: B2PLYP -4.5%, B2PG-PLYP -3.1%).

The otherwise best-performing functionals are those that minimize this systematic deshielding. Disregarding some τ_C and τ_0 variants of τ-dependent functionals (see discussion further below), only a few functionals keep this systematic underestimate to less than -3%: apart from DSD-PBEP86, these are cLH12ct-SsifPW92 (-0.7%), cLH12ct-SsirPW92 (-1.4%), cLH20t (-1.5%), KT3 (-2.2%), cB97M-V (-2.3%), cVSXC (-2.5%), KT1 (-2.6%), and KT2 (-2.7%). For the most part, these rel. MSEs translate into rel. MAEs of the same magnitude or very slightly larger. cMN15-L stands out with a positive rel. MSE of +3.7%. Many standard functionals exhibit much more negative rel. MSEs than the better-performing functionals (see Tab. S13 in Supporting Information of SI-V). The rel.

MSEs of the non-specialized GGAs range from -6.2% (B97D) to -11.0% (BLYP) (SVWN LDA: -14.0%). Apart from the better-performing cB97M-V and cVSXC (-2.3% and -2.5%, see above) and the unusual cMN15-L, those for the CDFT meta-GGAs range from -3.8% (cM06-L) to -5.7% (cTPSS). The GHs range from -4.2% (BHLYP) to -8.3% (B3LYP), the RSHs from -4.2% (ωB97X-V) to -8.1% (CAM-B3LYP). We have already mentioned the top-performing LHs above. Most of the remaining LHs fall into the range of the GHs or RSHs, from -3.2% (cmPSTS) to -5.0% (LH07s-SVWN), with cLHJ14 (-8.7%) standing out negatively, in line with the above discussion of the shape of its LMF. We can thus conclude that in this case the functionals that come closest to the MP2 performance, without being able to reach it, are not the DHs but several LHs (in particular cLH12ct-SsifPW92, cLH12ct-SsirPW92). This is notable in view of the much lower computational effort involved for the LH computations.

^{13}C shieldings. This much larger subset (93 nuclei) covers a shielding range of 402 ppm. A 1% relative deviation corresponds thus to ca. 4 ppm. As for the ^{11}B subset, static correlation cases tend to be of minor importance here. The CS_2 molecule provides the largest deviation of MP2 from CCSD(T) (16.4 ppm, 4.1%). Therefore, Hartree-Fock is a very reasonable starting point (rel. MAE 2.6%, rel. MSE -2.2%), and MP2 performs outstandingly (rel. MAE 0.5%, rel. MSE 0.0%). For most functionals, systematically too low shieldings can again be noted, and thus the negative MSE often equals or approaches the MAE value. Given the larger shielding range, the relative deviations tend to be smaller here than for the ^{11}B subset.

cMN15-L again holds a special position by being the only functional with a positive rel. MSE (+1.6%, rel. MAE 1.8%). Mentioning otherwise only functionals with rel. MSEs less negative than -2%, we get the following rel. MAEs: cLH12ct-SsifPW92 (1.2%), DSD-PBEB86 (1.3%), cLH12ct-SsirPW92 (1.4%), KT1 (1.6%), cB97M-V and KT2 (1.7%), cLH20t (1.8%), KT3 (1.9%), cVSXC (2.1%). All other functionals give larger deviations. In the range of rel. MAEs below 3% we find the two other DHs, several of the remaining LHs, the ωB97X-V RSH, cSCAN, and cr^{2}SCAN. The largest rel. MAEs are represented by cM06 (6.6%) and SVWN (5.7%). The widely used B3LYP is also among the worse-performing functionals (5.0%) for the ^{13}C shieldings.

As for the ^{1}H shieldings (see above), we may compare to the relative ^{13}C shift set for 40 nuclei of ref. 65 (cc-pVQZ data). In that work, MP2 also outperformed all DFT approaches, giving an MAD of 1.9 ppm (HF 8.0 ppm), while the best functionals were B97-2 (3.9 ppm) and KT2 (4.2 ppm). For the present, more diverse and larger ^{13}C shielding set, MP2 gives an only slightly larger MAE of 2.1 ppm (HF 10.5 ppm). As discussed above, the best DFT methods do not reach the MP2 performance for this

subset, confirming the results of the previous work. The lowest MAEs correspond to 4.9 ppm (cLH12ct-SsifPW92) and 5.0 ppm (DSD-PBEP86), while the best functionals from ref. 65 trail somewhat behind (KT2 7.0 ppm, B97-2 13.2 ppm) but at least for KT2 are still in the range of the better-performing functionals for this nucleus.
Clearly, the ^{11}B and ^{13}C subsets are ideal for MP2, but the best LH cLH12ct-SsifPW92 offers a reasonably accurate alternative at substantially lower computational cost. We will see below that relative shifts provide an easier target for many methods.
^{15}N shieldings. Including the PN molecule, this subset (43 nuclei) covers a shielding range of 626 ppm. That is, a 1% relative deviation corresponds to 6.3 ppm. Together with the ^{17}O subset discussed below, the ^{15}N set exhibits the largest demands regarding cases with static correlation. In addition to PN, further molecules with larger static correlation are, e.g., H_2CN_2, CH_3NO_2, HN_3, and NO_3^-. Consequently, Hartree-Fock starts out with a rel. MAE of 5.6%, and MP2 (3.1%) is clearly inferior to the best DFT approaches for the ^{15}N shieldings. The latter are represented by cMN15-L (0.9%, rel. MSE +0.5%) and DSD-PBEP86 (1.2%, rel. MSE -0.7%), with several further functionals with rel. MAEs below or equal 2.0% (KT1, cB97M-V, cLH12ct-SsifPW92, cLH12ct-SsirPW92, B2GP-PLYP, KT2, KT3), and others below the 3% mark, i.e. still competitive with MP2 (B2PLYP, cLH20t, cLH07t-SVWN, cVSXC). The functionals with the largest negative rel. MSEs are cM06 (-8.0%) and cM06-2X (-6.6%). The fact that DFT can outperform MP2 for ^{15}N shifts or shieldings has been noted before for typically much smaller or less definite benchmark sets.[39,401,402] Translating the relative MAEs for the best-performing functionals into ppm values, we can conclude that modern DFT methods allow the computation of ^{15}N shieldings with mean absolute errors of about 5-10 ppm for a diverse and demanding data set, better than the ca. 20 ppm MAE provided by MP2.
^{17}O shieldings. Excluding O_3, the ^{17}O shielding subset (32 nuclei) covers a range of 800 ppm. A relative deviation of 1% in this case corresponds already to 8 ppm. As for the ^{15}N subset discussed above, the nature of typical oxygen compounds also guarantees that cases with larger static correlation are present, even though the by far most severe case ozone (see above) is excluded from the statistics. Other typical systems included with static correlation and large paramagnetic contributions are, e.g., CH_3NO_2, FNO, H_2CO, CH_3CHO, SO_2, and OF_2. As a result, Hartree-Fock (rel. MAE 4.1%, rel. MSE -3.7%) provides an only moderately good starting point, and MP2 (rel. MAE 2.7%, rel. MSE +2.3%) is reasonable but not outstanding. Clearly lower rel. MAEs below 2% are provided by DSD-PBEP86 (0.9%), cLH12ct-SsifPW92 (1.6%), B2GP-PLYP and cLH12ct-SsirPW92 (1.8%), and cMN15-L (1.9%). The latter functional is again the only one with a positive rel. MSE (+1.3%), while the negative ones for the other functionals tend to be

close in magnitude to the MAEs (except DSD-PBEP86 -0.6%). Further functionals that provide lower rel. MAEs than MP2 are cB97M-V (2.2%), B2PLYP (2.4%), cLH20t, KT1 and cSCAN (all 2.6%). The worst performers are cM06 (8.1%) and cM06-2X (7.8%). In conclusion, several DFT functionals outperform MP2 also for the relatively difficult ^{17}O shieldings of the present test set. DSD-PBEP86 reproduces the reference ^{17}O shieldings with an MAE of ca. 7 ppm, and several other functionals (two LHs, one DH, one CDFT meta-GGA) give relatively low MAEs of 12-15 ppm.

^{19}F shieldings. The reference shieldings of the ^{19}F subset cover a range of 923 ppm, from FNO (-276 ppm) to ClF (+647 ppm). A relative deviation of 1% corresponds thus to ca. 9.2 ppm. While the subset contains a number of systems with larger paramagnetic contributions (e.g. F_2, FNO, OF_2; see Tab. S11 in Supporting Information of SI-V), static correlation does not play a crucial role, if F_3^- is excluded. Interestingly, the largest deviation of MP2 results from the CCSD(T) (39.4 ppm, 4.3%) is seen for the most shielded ClF (more shielded than F^-!). This large shielding has long been known to arise from off-center paramagnetic currents.[403–405] That is, while the induced local paramagnetic currents are paratropic around Cl, they turn diatropic around the fluorine nucleus. MP2 works well for the entire ^{19}F subset (except for the excluded F_3^-, see above) and exhibits a rel. MAE (rel. MSE) of 0.6% (+0.4%). Indeed, the underlying HF method is already a reasonable starting point (rel. MAE 2.1%, rel. MSE +2.1%). Given their tendency to overestimate the (negative) paramagnetic contributions, it is difficult for the DFT methods to outperform MP2 for this subset, as we discussed above for the ^{11}B and ^{13}C subsets. We note in passing that due to the positive paramagnetic shielding of the special case of ClF the negative MSEs of most DFT functionals tend to be slightly smaller than the negative of the corresponding MAE values, in contrast to the other nonhydrogen subsets of this work.

Given the good performance of MP2, the DHs perform well but do not outperform MP2. Notably, however, some LHs are as good here as the best DH (DSD-PBEP86). In the order of increasing rel. MAE, the best-performing functionals with values below 2% are: cLH12ct-SsifPW92 (0.9%), DSD-PBEP86, cMN15-L (1.0%), cLH12ct-SsirPW92 (1.1%), cLH20t (1.3%), B2GP-PLYP (1.5%), BHLYP (1.8%), cB97M-V and cLH07t-SVWN (1.9%). Further functionals with rel. MAEs below or equal to 3% (in addition to HF) are: cLH14t-calPBE (2.1%), B2PLYP (2.2%), ωB97X-V (2.3%), cωB97M-V (2.6%), cM06-L (2.8%), cSCAN and ωB97X-D (3.0%). GGA functionals feature rel. MAEs of 4.2-5.7% (the SVWN LDA gives 6.3%). Notably, here the specialized KT1-KT3 set is still best among the GGAs (4.2-4.5%) but not by as much as for the other nuclei of this work. Most GHs range from 3.5% (PBE0) to 4.2% (cM06). Interestingly, in spite of

its large EXX admixture of 54% cM06-2X is one of the better-performing GHs (3.1%), closely followed by B97-2 (3.2%), and only behind BHLYP (see above). In a way this confirms that static correlation is not a particular issue for the ^{19}F subset. Nevertheless, fluorine NMR shifts have often been considered particularly difficult for DFT methods. Indeed, in view of the larger cost of MP2 or DHs, GHs with large EXX admixture, such as BHLYP or related constructions (or sometimes even Hartree-Fock), had been suggested to be the method of choice in the field.[406–409] The relatively high and compact electron-density distributions around the ^{19}F nuclei and the related induced currents seem to be an important aspect explaining why larger EXX admixtures are favorable in this case. Notably, however, the best LHs, DHs, and the CDFT meta-GGA cMN15-L, reduce the relative MAE by a factor of up to 2 compared to the so far recommended BHLYP, and they perform well also for the other nuclei in this overall test set, while BHLYP becomes much worse in the presence of more static correlation (e.g. for ^{15}N, ^{17}O), and even for the ^{13}C shieldings. The best LHs and cMN15-L (which exhibits a rel. MSE of +0.1%) achieve this improvement without increasing the computational effort, and they can thus be recommended for routine use in the field.

^{31}P/^{33}S shieldings. Given that the subsets for the two third-row nuclei contain only 14 (6) nuclei for ^{31}P (^{33}S) and exhibit rather comparable shielding ranges (830 ppm for ^{31}P, 984 ppm for ^{33}S), we lump them together to one subset of 20 nuclei (including PN and SO_2), and their weighted relative deviations are discussed. That is, for ^{31}P 1% relative deviation corresponds to 8.3 ppm, for ^{33}S to 9.8 ppm. As expected, the largest deviations of MP2 results from the CCSD(T) reference data occur for PN (47.2 ppm, 5.7%) and SO_2 (43.3 ppm, 4.4%). The overall rel. MAE (rel. MSE) of MP2 for the combined subset is 1.4% (+1.1%). This is closer to the subsets with the smallest importance of static correlation than to those with the largest ones. Hartree-Fock performs only moderately well (4.1%, -2.7%).

The only DFT methods that outperform MP2 here are the DSD-PBEP86 DH (rel. MAE 1.1%) and cB97M-V (1.4%). While several LHs are still among the better-performing functionals, they fall behind MP2, and a number of other functionals also provide lower deviations. In the order of increasing rel. MAE, the further best-performing functionals below 3% are: cVSXC, KT1 (1.5%), KT2, KT3 (1.7%), cr^{2}SCAN (2.0%), cSCAN, crSCAN, cLH12ct-SsifPW92 (2.1%), cM06-L (2.2%), cLH12ct-SsirPW92 (2.3%), B2PG-PLYP (2.4%), cLH20t (3.0%). Of course the inclusion of the static-correlation cases PN and SO_2 *does* influence this order to some extent. Excluding them (see Tab. S13 in Supporting Information of SI-V for these modified statistical data) would bring the best LHs (1.8%, 1.9%) closer to MP2 and DSD-PBEP86 (both 1.3%), on par with cVSXC (1.8%)

and in front of the KTx functionals (2.0-2.3%). This demonstrates the importance of the makeup of test sets. Nevertheless, it seems that the t-LMF-based LHs perform slightly less well for these two third-row nuclei than for the second-row ones discussed above. In view of recent analyses for the hyperfine couplings of 3d, 4d, and 5d transition metal complexes,[410] it appears possible that the t-LMF, which does not respect the high-density coordinate-scaling limit,[238] does not provide a sufficient increase of EXX admixture in the core when going to the larger core densities of the heavier atoms. These aspects are obviously of importance in constructing improved LMFs.
Non-specialized GGAs range from 4.3% (HCTH) to 7.3% (BLYP), with the latter only slightly below SVWN (7.4%). As mentioned above, cB97M-V and cVSXC are the best-performing CDFT meta-GGAs for this subset. Interestingly, in contrast to the other subsets, here cMN15-L does not perform particularly well and overestimates the shieldings systematically (rel. MAE 3.6%, rel. MSE +3.6%). With rel. MAEs comparable to this, cTPSSh (3.7%) is the best GH, followed by B97-2 (4.3%) (with several others performing much worse, up to 10.2% for the overall worst-performing cMN15). ωB97X-V (3.4%) and cωB97M-V (3.8%) are again the best RSHs.

A.4.2 Detailed Analysis of Shifts for Individual Nuclei of the Test Set

Due to the error compensation discussed in the main text, some methods reach a higher ranking for the shifts than for absolute shieldings. Here we also extend the discussion for the individual subsets for the shifts beyond what has already been stated in the main text.
^{1}H shifts. Note that the abovementioned error compensation does not work in most cases for the ^{1}H shifts, due to the absence of a core shell. Here the rel. MAEs for the shifts are often even somewhat larger than those discussed further above for the shieldings. Compensation of some systematic errors is, however, seen for a few cases like cLH12ct-SsirPW92, cLH12ct-SsifPW92, cmPSTS, HF, and SVWN. cLH20t is now the best-performing functional on rungs 1-4.
^{11}B shifts. Massive improvements of a number of methods are seen upon going from shieldings to shifts for the ^{11}B subset. DSD-PBEP86, which had been clearly behind MP2 for absolute shieldings, now gives the lowest rel. MAE (0.3%; note that this corresponds to less than 0.5 ppm!). This is followed by B2GP-PLYP (0.6%), LH07s-SVWN, cLH12ct-SsirPW92, cLH12ct-SsifPW92, B97-2, ωB97X-D (all 0.7%), B2PLYP, cLH07t-SVWN (0.8%), B97D, cTPSSh (0.9%), cLH14t-calPBE and cr^{2}SCAN (1.0%), with an

appreciable number of further functionals below the threshold of 2%. That is, the error compensation when going to relative shifts is large for ^{11}B, rendering this subset overall relatively uncritical for shifts. We also note that some of the advantages of the specialized KT1-KT3 functionals over other GGAs are removed for these relative ^{11}B shifts.

^{13}C shifts. Somewhat less pronounced but still notable differences between shieldings and shifts apply to the ^{13}C subset: while MP2 had clearly outperformed all DFT methods for the absolute shieldings, none of the DFT methods giving rel. MAEs below 1% (4 ppm) and only a relatively small number below 2% (8 ppm), matters change for the relative shifts: now cmPSTS (0.6%) outperforms MP2 and DSD-PBEP86 (0.7%), and some of the functionals from the lower rungs also perform strikingly well (cTPSS, cTPSSh, cM06-L, all 0.9%), cτ-HCTH (1.0%). The remaining DHs, the remaining LHs (except cLHJ14), the KT1-KT3 specialized functionals, B86, HCTH, B97D, the remaining CDFT meta-GGAs (except cMN15-L), and B97-2 all give values below 2%. Many functionals with large deviations for absolute shieldings also exhibit lower relative errors for the shifts. The largest outliers are still SVWN (4.2%) and cM06-2X (3.8%).

^{15}N shifts. Given the much larger importance of paramagnetic contributions and static correlation for the ^{15}N shieldings (see above), here the compensation of errors in the core contributions has a lower impact. Nevertheless, a few changes of "best methods" occur compared to the shieldings. MP2 (2.9%) clearly is still not the top-performing method for this subset. DSD-PBEP86 (1.1%) and cMN15-L (1.2%) still belong to the methods with the smallest rel. MAE but have reversed their order, and cB97M-V performs now comparably well (1.1%). What becomes more clear for the relative ^{15}N shifts is the advantage that the absence of EXX admixture provides for some semi-local functionals in view of many systems with appreciable static correlation: KT3 (1.1%), KT1, KT2 (1.2%), cτ-HCTH (1.6%), cVSXC (1.7%), cM06-L (1.8%), cSCAN (1.9%) B97D and cr^{2}SCAN (2.0%), and HCTH (2.1%) are pertinent examples. Several of these outperform the remaining two DHs B2GP-PLYP (1.6%) and B2PLYP (1.8%). Among the LHs, cmPSTS (1.6%) now stands out, while cLH12ct-SsirPW92 and cLH12ct-SsifPW92 (2.0%) still perform reasonably well and the other LHs (except cLHJ14, 3.6%) still are in the range below 3%. Apart from cTPSSh (see above) the only GH below 3% is B97-2 (2.5%), while all others perform distinctly worse. ωB97X-V (2.9%) is the best RSH.

^{17}O shifts. Even after removal of O_3 from the statistical evaluations, many systems with large paramagnetic contributions in this subset suggest that here the compensation of errors for the diamagnetic part should also have a smaller impact in going to relative shifts. This is confirmed by the data, as is the potential of some semi-local functionals to perform well. MP2 (2.0%) performs moderately well here, but DSD-PBEP86 (0.8%) and

B2GP-PLYP (1.5%) are still the best-performing methods, followed by KT1, cSCAN and cLH12ct-SsifPW92 (1.8%), cLH12ct-SsifPW92 and cB97M-V (1.9%), KT2, cM06-L and B2PLYP (2.0%). Further functionals with rel. MAEs up to 2.5% are cMN15-L, cr^{2}SCAN (both 2.1%), KT3 (2.2%), cmPSTS (2.3%), cLH20t (2.4%), and cLH07t-SVWN (2.5%). Problems with constant and range-separated EXX admixture are shown by the fact that cTPSSh (2.8%) is clearly the best GH and ωB97X-V (3.1%) the best RSH. The largest deviations are exhibited by cM06-2X (6.8%), cM06 (6.6%), and SVWN (6.0%).

^{19}F shifts. As noted already for the shieldings, here Hartree-Fock (2.6%) is a reasonable starting point, and MP2 (0.6%) is the top performer, followed by DSD-PBEP86 (0.9%). The error compensation in going from shieldings to shifts is probably the least pronounced among the second- and third-period nuclei, and the order of the best-performing functionals is largely retained, with cMN15-L, cLH12ct-SsirPW92 (1.0%), cLH12ct-SsifPW92 (1.1%) right behind DSD-PBEP86. The largest benefits of error compensation are seen with for BHLYP (1.2%) and cB97M-V (1.3%), which range now before B2GP-PLYP and cLH20t (1.3%), cLH07t-SVWN (1.8%), cLH14t-calPBE, ωB97X-V, B2PLYP (1.9%), cM06-L, cωB97M-V (2.1%), cSCAN, ωB97X-D, cmPSTS (all 2.3%). As noted already for the absolute shieldings (see above), here the specialized KT1-KT3 functionals (3.2-3.6%) perform still slightly better than the standard GGAs, but not by very much, and they are no match for the best-performing functionals. Apart from the excellent value of BHLYP, the GHs do not perform particularly well, with only a few functionals somewhat below 3% (B97-2, cM06-2X, cTPSSh, PBE0, cMN15, cPW6B95).

^{31}P/^{33}S shifts. For these two third-row nuclei, the systematic errors of some functionals in the diamagnetic part seem to be particularly large, and performance can change significantly upon going to the shifts. Indeed, for several functionals the deviations for shifts are much smaller than for shieldings. All three DHs, DSD-PBEP86 (0.4%), B2GP-PLYP (0.8%) and B2PLYP (0.9%) do now outperform MP2 (1.1%), as do KT2, cτ-HCTH and cTPSS (1.0%). Further functionals with rel. MAEs below or equal to 2% are KT3, cTPSSh, cmPSTS, cSCAN (all 1.1%), KT1, B97D (1.2%), cVSXC, cr^{2}SCAN (1.3%), HCTH, cM06-L, B97-2 (1.5%), cB97M-V (1.6%), BLYP, crSCAN (1.7%), cLH14t-calPBE (1.9%), BP86, B3LYP, cωB97M-V, cLH20t (2.0%). As observed already for the shieldings, the LHs perform overall somewhat less well here than for the other nuclei in the test set, with the notable exception now of cmPSTS. Given this relatively small subset of 20 values, further investigations of third-row shieldings and shifts will probably be required to pinpoint some of the decisive factors determining the accuracy of DFT approaches. In the case of LHs this clearly includes the shape of the LMF in the core and semi-core regions of heavier atoms.

A.4.3 Estimates of Basis-Set and Structure Convergence of the CCSD(T) Shielding Reference Data

Table A.10.: GIAO-CCSD(T) shielding data (in ppm) using various basis sets in the calculation of the input structures and NMR shielding constants to estimate the convergence with respect to the employed input structures and basis-set size.

CCSD(T)	Structure	cc-pVTZ		cc-pVQZ		
	NMR	pcSseg-3	pcSseg-4	pcSseg-3	pcSseg-4	pcSseg-4(unc)
^{1}H	BH	25.07	25.05	25.03	25.02	25.02
	Furan (C_2, C_5)	24.06	24.03	24.04	24.02	
	Furan (C_3, C_4)	25.04	25.02	25.02	25.00	
	CH_4	31.30	31.29	31.32	31.31	31.31
	H_2O	30.69	30.65	30.72	30.68	30.68
	HCCH	30.17	30.16	30.10	30.09	30.09
	HF	28.88	28.82	28.92	28.86	28.86
	NH_3	31.46	31.44	31.48	31.45	31.45
	HOF	19.68	19.61	19.78	19.70	19.70
	PH_3	29.50	29.46	29.56	29.52	29.53
	HCN	29.01	29.00	28.92	28.90	
	H_2S	30.56	30.49	30.57	30.50	
^{11}B	BH	-188.8	-190.3	-188.3	-189.7	-189.4
	BF	82.1	82.0	82.2	82.1	
^{13}C	Furan (C_2, C_5)	47.6	47.4	48.0	47.8	
	Furan (C_3, C_4)	81.8	81.7	82.0	81.8	
	CH_4	198.7	198.8	198.9	198.9	198.9
	CO	2.6	2.2	4.0	3.7	3.7
	CO_2	60.1	60.0	60.8	60.7	
	HCCH	122.5	122.3	122.6	122.4	122.5
	HCN	84.8	84.5	85.3	85.1	
^{15}N	N_2	-61.2	-61.2	-59.3	-59.3	-59.3
	NNO	106.7	106.2	107.5	107.0	107.1
	NNO	12.2	11.7	12.9	12.5	12.5
	NH_3	270.4	270.4	270.7	270.7	270.6
	PN	-345.7	-344.7	-339.1	-338.1	-338.0
	HCN	-14.3	-14.7	-13.1	-13.4	
^{17}O	Furan	65.1	64.8	65.8	65.6	
	CO	-56.0	-56.1	-52.9	-53.0	-53.0
	CO_2	231.4	231.3	233.7	233.6	
	H_2O	337.5	337.6	338.2	338.3	338.3
	NNO	198.9	198.8	200.9	200.8	200.8
	O_3 (cent.)	-770.6	-772.2	-760.7	-762.2	
	O_3	-1224.9	-1227.9	-1200.0	-1202.9	
	OF_2	-444.0	-446.3	-435.7	-438.0	
	HOF	-67.6	-68.7	-64.5	-65.6	-65.6
	SO_2	-243.4	-243.2	-225.2	-225.1	-225.3
^{19}F	F_2	-190.5	-192.8	-183.7	-185.9	-185.9
	F_3^- (cent.)	-208.7	-211.9	-203.0	-206.1	
	F_3^-	-272.8	-276.3	-265.9	-269.5	
	HF	419.6	419.9	420.0	420.3	420.3
	OF_2	-22.5	-24.3	-17.2	-18.9	
	HOF	190.9	191.2	193.3	193.6	193.6
	BF	123.3	123.4	124.3	124.4	
^{31}P	PH_3	604.1	604.5	604.7	605.1	605.4
	PN	51.2	51.6	58.6	59.1	59.4
^{33}S	SO_2	-199.0	-200.2	-182.6	-183.8	-183.2
	H_2S	737.8	738.4	738.1	738.8	

A.4.4 Maximum Relative Deviations for Main Group Shieldings and Shifts

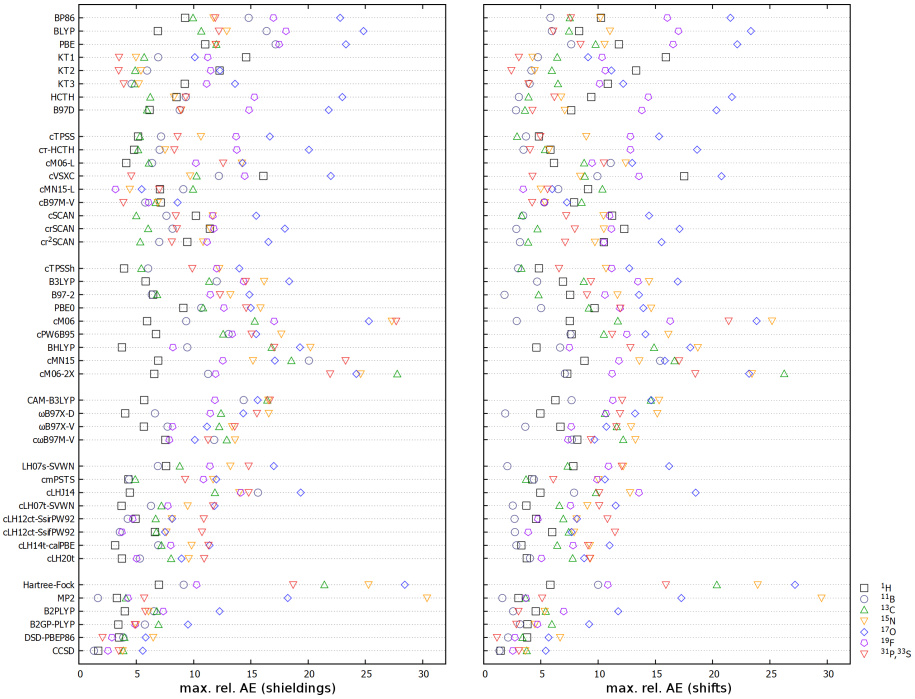

Figure A.2.: Maximum relative AEs (in %, normalized to the shielding and shift range for a given nucleus) from the relative CCSD(T)/pcSseg-3 shieldings (left) and chemical shifts (right) for different methods (with pcSseg-3 basis).

The right hand side of Fig. A.2 summarizes the max. rel. AEs of the shifts for each of the nuclei, similar to what is provided in panel 4 of Fig. 1 in P-V for absolute shieldings. The overall behavior for the different methods is similar to the shieldings, but some details differ. Among the various DFT functionals and MP2, DSD-PBEP86 gives the smallest maximum value (6.7% in the ^{15}N set), followed by cB97M-V (8.6% for ^{13}C), B2GP-PLYP (9.2% for ^{17}O), cLH20t (9.3% for ^{31}P/^{33}S), cMN15-L (10.4% for ^{13}C), cmPSTS (10.6% for ^{17}O), cLH12ct-SsirPW92 (10.8% for ^{31}P/^{33}S), cLH14t-calPBE (11.0% for ^{17}O), cLH12ct-SsifPW92 (11.5% for ^{31}P/^{33}S), cLH07t-SVWN (11.5% for ^{17}O), and B2PLYP (11.7% for ^{17}O). That is, the overall most robust functionals in terms of maximum deviations identified for the shieldings can also be confirmed for the shifts, with slight differences in their relative ranking. Large max. rel. AEs pertain to methods which are sensitive to static-correlation cases. This includes HF (27.2% for ^{17}O) and MP2 (29.5% for ^{15}N). As for the shieldings, these are the two methods with the largest maximum errors.

Table A.11.: GIAO-CCSD(T)/pcSseg-3 and pcSseg-4 shielding data (in ppm) in comparison to previously published data (literature estimates) estimating the CBS.

Structure	Nucleus	Molecule	pcSseg-3*	pcSseg-4*	literature estimates
CCSD(T)/cc-pVTZ	^{1}H	CH_4	31.30	31.29	31.25[a]
		H_2O	30.69	30.65	30.77[a]
		HF	28.88	28.82	28.96[a]
		NH_3	31.46	31.44	31.52[a]
		OHF	19.68	19.61	19.57[a]
		HCN	29.01	29.00	29.04[a]
		H_2S	30.56	30.49	30.767, 30.564;[b] 30.55[a]
		PH_3	29.50	29.46	29.638, 29.514[b]
	^{13}C	HCN	84.8	84.5	86.9, 85.9, 85.1, 85.0;[c] 85.71[a]
		CO_2	60.1	60.0	61.1, 61.5, 60.4, 60.2;[c]
		CO	2.6	2.2	6.3, 4.1, 3.0, 3.0;[c] 4.03[a]
		HCCH	122.5	122.3	123.5, 123.3, 122.7, 122.6;[c]
		CH_4	198.7	198.8	199.0, 199.0, 198.8, 198.8;[c] 199.25[a]
	^{15}N	N_2	-61.2	-61.2	-58.76[a]
		NH_3	270.4	270.4	270.79[a]
		HCN	-14.3	-14.7	-12.72[a]
		NNO	106.7	106.2	107.66[a]
		NNO	12.2	11.7	13.62[a]
		PN	-345.7	-344.7	-341.44[a]
	^{17}O	CO	-56.0	-56.1	-52.1, -56.3;[d] -53.63[a]
		CO_2	231.4	231.3	234.6, 232.5;[d]
		H_2O	337.5	337.6	337.0, 338.2;[d] 337.97[a]
		N_2O	198.9	198.8	200.3, 198.2;[d] 200.00[a]
		Furan	65.1	64.8	69.1, 64.7[d]
		OF_2	-444.0	-446.3	-438.3, -439.8;[d] -442.10[a]
		O_3 (cent.)	-770.6	-772.2	-763.52[a]
		O_3	-1224.9	-1227.9	-1215.81[a]
		OHF	-67.6	-68.7	-66.07[a]
		SO_2	-243.4	-243.2	-240.32[a]
	^{19}F	HF	419.6	419.9	418.4, 418.8, 418.9, 419.1;[e] 420.17[a]
		OHF	190.9	191.2	185.8, 188.2, 188.5, 188.4;[e] 193.01[a]
		OF_2	-22.5	-24.3	-18.9, -20.3, -22.6, -25.0[e]
		F_2	-190.5	-192.8	-189.0, -189.7, -191.3, -193.2[e]
	^{31}P	PH_3	604.1	604.5	608.965, 605.831[b]
		PN	51.2	51.6	55.65[a]
	^{33}S	SO_2	-199.0	-200.2	-195.38[a]
		H_2S	737.8	738.4	738.990, 737.923;[b] 739.98[a]
CCSD(T)/cc-pVQZ	^{1}H	CH_3OH	28.12	28.10	28.435, 28.197, 28.175, 28.150[f]
		CH_3OH	31.67	31.62	32.292, 31.839, 31.812, 31.749[f]
	^{13}C	CH_3OH	141.7	141.6	143.17, 142.33, 141.92, 141.82[f]
	^{15}N	N_2	-59.3	-59.3	-55.2, -58.5, -59.8[g]
		NH_3	270.7	270.7	270.4, 271.4, 270.7[g]
		HCN	-13.1	-13.4	-9.3, -12.7, -13.3[g]
		NNO	107.5	107.0	110.9, 108.5, 107.6[g]
		NNO	12.9	12.5	16.1, 14.1, 12.8[g]
		CH_3NH_2	256.2	256.3	255.5, 256.9, 256.2[g]
	^{17}O	OF_2	-435.7	-438.0	-431.6, -435.0[d]
		CH_3OH	344.5	344.8	342.80, 345.22, 344.42, 344.14[f]
	^{31}P	PN	58.6	59.1	73.3, 58.5, 53.4[g]
		PH_3	604.7	605.1	614.2, 609.6, 607.1[g]
		PF_3	228.5	227.2	242.3, 232.4, 230.1[g]
		P_4	888.9	888.0	903.8, 894.4, 889.4[g]
		PMe_3	408.3		427.7, 419.5, 416.8[g]
CCSD(T)/aug-pc-4[h]	^{15}N	PN	-338.7	-337.7	-337.39, -337.27, -336.91, -338.59, -337.72[h]
	^{31}P	PN	59.0	59.5	58.08, 56.92, 59.09, 60.21, 59.99[h]
Exp.[i]	^{11}B	BF	82.3	82.2	85.73, 83.13, 82.36, 82.83[i]
	^{19}F	BF	124.6	124.7	130.56, 126.44, 125.02, 125.18[i]

* work of P-V; [a] Ref. 64; [b] Ref. 411; [c] Ref. 36; [d] Ref. 38; [e] Ref. 37; [f] Ref. 392; [g] Ref. 39; [h] Ref. 35; [i] Ref. 412.

A.5 SI-VI

A.5.1 Estimates of Solvent Effects for Selected TM Complexes

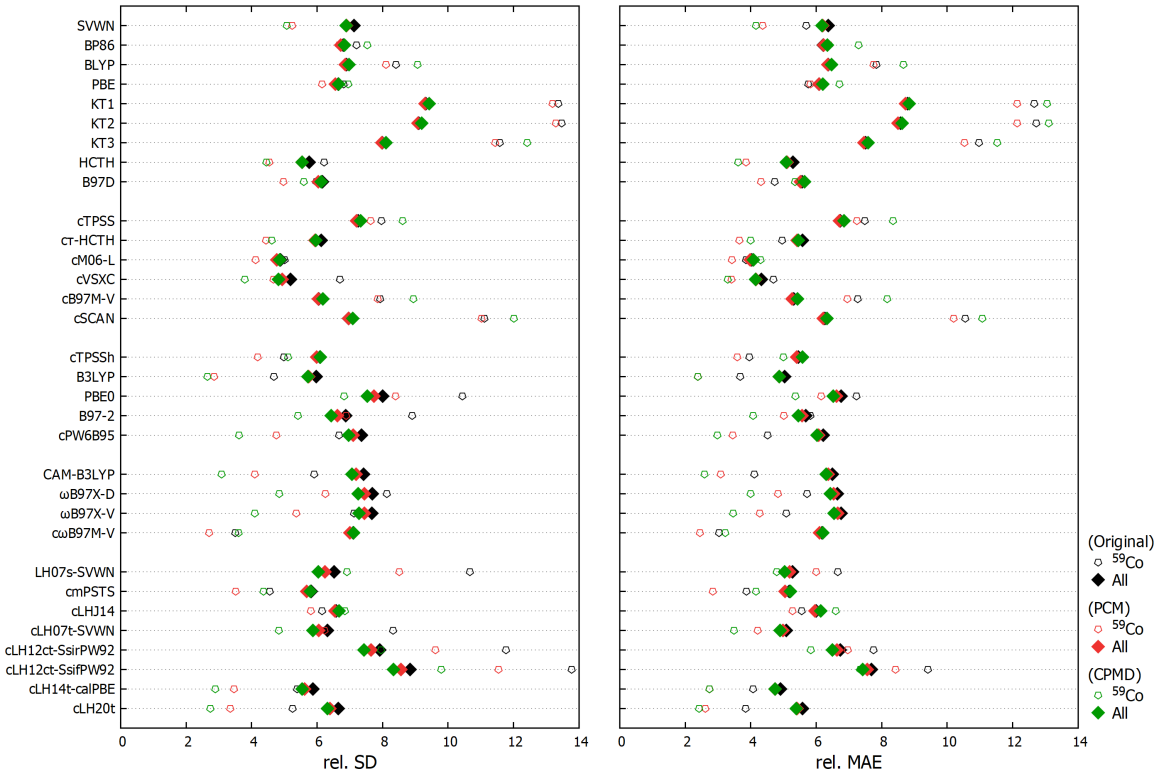

Figure A.3.: Plot of statistical data of the ^{59}Co test set (hollow diamonds) and the combined transition metal test-set (filled diamonds) for various density functionals, either without solvent model (black), a PCM (red) or CPMD (green) solvent correction for four charged cobalt complexes ($[Co(H_2O)_6]^{3+}$, $[Co(NH_3)_6]^{3+}$, $[Co(CN)_6]^{3-}$, and $[Co(CO)_4]^{-}$), see main text.

Beyond literature data probing solvent effects for four charged Co complexes (as shown in Fig. A.3 and Tab. A.12), we have looked at a number of further complexes where solvent effects on the computed shifts might have mattered. This involves aqueous $[Cr_2O_7]^{2-}$ as well as four complexes where the experimental NMR shifts had been obtained in acetonitrile, due to the donor properties of MeCN. Optimization at BP86-D3(BJ)/def2-TZVP(D) level was preceded by evaluation of conformer-rotamer ensembles (CREs) of clusters with 2-4 explicit solvent molecules using the tight-binding methods in the CREST code.[360,413] Subsequently, all relevant conformers, including the explicit solvent molecules, were DFT-optimized without implicit conductor-like screening model, COSMO (gas-phase, "GP"). The best GP structure was then re-optimized at the same BP86-D3(BJ)/def2-TZVP(D)

Table A.12.: Statistical data of the ^{59}Co test set (relative StD and MAE) for various density functionals, either without solvent model, a PCM or CPMD solvent correction for four charged cobalt complexes ($[Co(H_2O)_6]^{3+}$, $[Co(NH_3)_6]^{3+}$, $[Co(CN)_6]^{3-}$, and $[Co(CO)_4]^{-}$), see main text.

^{59}Co	Original		PCM Corrected		CPMD Corrected	
	rel. StD	rel. MAE	rel. StD	rel. MAE	rel. StD	rel. MAE
SVWN	6.9	5.7	5.2	4.4	5.1	4.2
BP86	7.2	6.3	6.7	6.4	7.5	7.3
BLYP	8.4	7.8	8.1	7.7	9.1	8.7
PBE	6.8	5.8	6.2	5.8	6.9	6.7
KT1	13.4	12.7	13.2	12.1	14.1	13.0
KT2	13.5	12.7	13.3	12.1	14.2	13.1
KT3	11.6	11.0	11.4	10.5	12.4	11.5
HCTH	6.2	5.2	4.5	3.9	4.5	3.6
B97D	6.0	4.7	5.0	4.3	5.6	5.4
cTPSS	8.0	7.5	7.6	7.3	8.6	8.3
cτ-HCTH	5.9	5.0	4.4	3.6	4.6	4.0
cM06-L	5.0	3.9	4.1	3.4	4.8	4.3
cVSXC	6.7	4.7	4.7	3.4	3.8	3.3
cMN15-L	59.6	40.1	54.6	37.4	51.4	35.0
cB97M-V	7.9	7.3	7.9	7.0	8.9	8.2
cSCAN	11.1	10.5	11.0	10.2	12.0	11.1
cTPSSh	5.0	4.0	4.2	3.6	5.1	5.0
B3LYP	4.7	3.7	2.8	2.4	2.7	2.4
PBE0	10.4	7.2	8.4	6.1	6.8	5.4
B97-2	8.9	5.8	6.9	5.0	5.4	4.1
cM06	39.8	28.6	36.1	27.2	33.5	24.6
cPW6B95	6.7	4.5	4.8	3.5	3.6	3.0
BHLYP	20.6	16.9	18.1	15.5	16.2	14.1
cMN15	35.3	25.4	31.9	23.7	29.4	21.8
cM06-2X	23.2	19.1	20.6	17.7	18.6	16.1
CAM-B3LYP	5.9	4.1	4.1	3.1	3.1	2.6
ωB97X-D	8.1	5.7	6.3	4.8	4.9	4.0
ωB97X-V	7.1	5.1	5.4	4.3	4.1	3.5
cωB97M-V	3.5	3.0	2.7	2.5	3.6	3.2
LH07s-SVWN	10.7	6.7	8.5	6.0	6.9	4.8
cmPSTS	4.5	3.9	3.5	2.8	4.4	4.2
cLHJ14	6.1	5.6	5.8	5.3	6.9	6.6
cLH07t-SVWN	8.3	5.0	6.2	4.2	4.8	3.5
cLH12ct-SsirPW92	11.8	7.7	9.6	7.0	8.0	5.8
cLH12ct-SsifPW92	13.8	9.4	11.5	8.4	9.8	7.4
cLH14t-calPBE	5.4	4.1	3.5	2.7	2.9	2.7
cLH20t	5.2	3.9	3.4	2.6	2.7	2.4

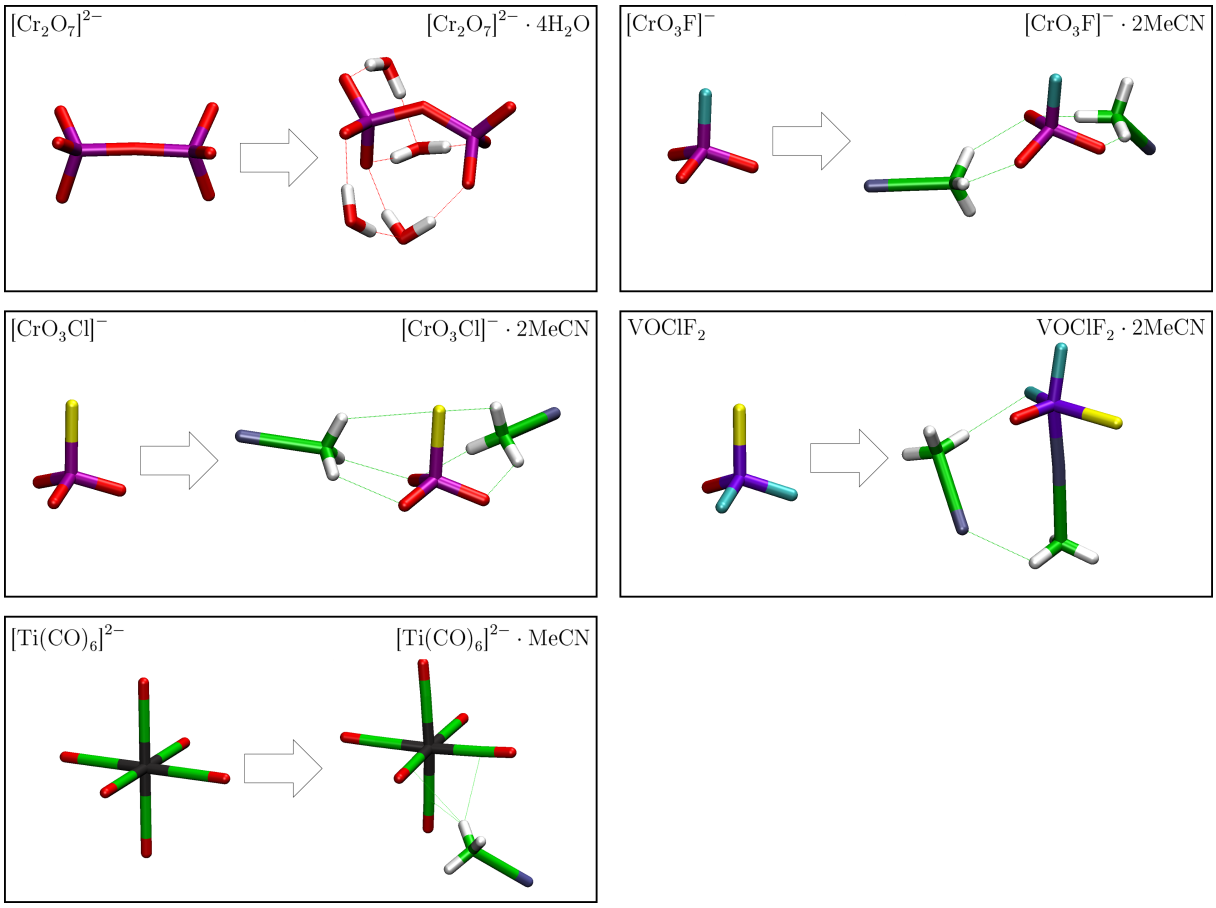

Figure A.4.: Optimized structures (BP86-D3(BJ)/def2-TZVP(D)) without and with explicit coordination by solvent molecules.

Table A.13.: Relevant structural data with and without explicit+implicit solvation (BP86-D3(BJ)/def2-TZVP(D) data).

molecule	Parameter		incl. solv.
$[Ti(CO)_6]^{2-}$ (MeCN,COSMO[a])	r(Ti–C)	2.058	2.044
$VOClF_2$ (2 MeCN,COSMO[a])	av. r(V–F)	1.733	1.778
	r(V–Cl)	2.149	2.226
	r(V–O)	1.574	1.578
	r(V–N)	–	2.118
$[CrO_3Cl]^-$ (2 MeCN,COSMO[a])	av. r(Cr–O)	1.614	1.613
	r(Cr–Cl)	2.237	2.223
	av. ∢(O–Cr–Cl)	107.9	107.5
$[CrO_3F]^-$ (2 MeCN,COSMO[a])	r(Cr–O)	1.617	1.618
	r(Cr–F)	1.793	1.777
	∢(O–Cr–F)	108.2	108.8
$[Cr_2O_7]^{2-}$ (4 H_2O,COSMO[a])	r(Cr–O)bridge	1.781	1.773
	av. r(Cr–O)term	1.630	1.625
	∢(Cr–O–Cr)	175.3	133.4

[a] COSMO dielectric constants, $\varepsilon = 35.688$ (MeCN), 78.3553 (H_2O)

Table A.14.: Nuclear shielding constants (GIAO-DFT/pcSseg-3) with different treatments of solvation in structure optimization and shielding computation (see text).

	molecule	solvent model		cM06-L	cLH14t-calPBE
		opt	nmr		
^{49}Ti	$[Ti(CO)_6]^{2-}$	gas-phase	gas-phase	627.5	642.8
	+1 MeCN	gas-phase	gas-phase	626.5	639.9
	+1 MeCN	COSMO	gas-phase	639.7	657.0
	+1 MeCN	COSMO	COSMO	646.1	659.6
^{51}V	$VOClF_2$	gasphase	gasphase	-1599.3	-1632.3
	+2 MeCN	gasphase	gasphase	-1594.8	-1615.5
	+2 MeCN	COSMO	gasphase	-1602.7	-1622.7
	+2 MeCN	COSMO	COSMO	-1585.2	-1606.4
^{53}Cr	$[CrO_3F]^-$	gasphase	gasphase	-3035.2	-3151.3
	+2 MeCN	gasphase	gasphase	-2995.7	-3099.9
	+2 MeCN	COSMO	gasphase	-2996.8	-3101.2
	+2 MeCN	COSMO	COSMO	-3000.3	-3106.9
	$[CrO_3Cl]^-$	gasphase	gasphase	-3146.0	-3268.8
	+2 MeCN	gasphase	gasphase	-3144.0	-3262.0
	+2 MeCN	COSMO	gasphase	-3144.0	-3262.0
	+2 MeCN	COSMO	COSMO	-3136.9	-3252.4
	$[Cr_2O_7]^{2-}$	gasphase	gasphase	-3032.9	-3143.3
	+4 H_2O	gasphase	gasphase	-3034.7	-3132.5
	+4 H_2O	COSMO	gasphase	-3009.9	-3104.4
	+4 H_2O	COSMO	COSMO	-3014.8	-3110.0

level of theory including COSMO with dielectric constants of $\varepsilon = 35.688$ (MeCN), and 78.3553 (H_2O), respectively. For $[Ti(CO)_6]^{2-}$ the CRE calculations with one MeCN resulted in no solvent coordination, and we therefore optimized a structure directly at DFT level. The resulting structures are shown in Fig. A.4, relevant structural parameters are listed in Tab. A.13. Metal-nucleus NMR shielding results at GIAO-DFT/pcSseg-3/COSMO level were compared for GP structures without any solvent surroundings and with the structures obtained with both explicit and implicit solvantion. Results are shown in Tab. A.14. Overall minor solvent effects are seen.

A.5.2 Estimates of Relativistic Effects in TM Complexes

Table A.15.: Shielding results (GIAO-DFT/pcSseg-3) for cM06-L with and without X2C scalar relativistic corrections (for BP86-D3(BJ) structures).

		Shieldings		
		cM06-L	cM06-L$_{X2C}$	Diff.$_{X2C-NR}$
^{49}Ti	$TiBr_4$	-1358.2	-1309.9	48.3
	$TiMe_4$	-2274.9	-2200.3	74.6
	$TiClMe_3$	-2065.4	-1989.4	76.0
	$TiCl_2Me_2$	-1784.8	-1711.7	73.1
	$TiCl_3Me$	-1412.4	-1349.1	63.3
	$TiCl_4$	-942.6	-896.7	45.9
	$[Ti(CO)_6]^{2-}$	627.5	640.7	13.2
	$TiCp_2Br_2$	-292.7	-257.2	35.4
	$TiCp_2Cl_2$	-151.4	-112.1	39.3
	$TiCp_2F_2$	170.8	201.8	30.9
	$TiCpCl_3$	-538.8	-496.2	42.6
	$TiCp*Cl_3$	-777.6	-724.7	52.9
^{51}V	$[V(CO)_5N_2]^-$	-227.4	-196.1	31.3
	$[V(CO)_6]^-$	22.2	48.4	26.2
	VF_5	-1344.8	-1295.1	49.7
	$VOCl_3$	-2131.4	-2066.9	64.6
	$VOClF_2$	-1599.3	-1545.1	54.1
	VOF_3	-1346.6	-1297.9	48.7
	$VOMe_3$	-3272.3	-3192.0	80.3
	$VOMe_2(OMe)$	-2556.6	-2484.5	72.0
	$VOMe(OMe)_2$	-1953.1	-1889.0	64.1
	$VO(OMe)_3$	-1552.9	-1498.4	54.5
^{53}Cr	$[Cr_2O_7]^{2-}$	-3032.9	-2962.8	70.1
	$Cr(CO)_5(CHNH_2)$	-1123.7	-1079.8	43.9
	$Cr(CO)_5(CMeNMe_2)$	-1189.5	-1144.1	45.4
	$Cr(CO)_5(PF_3)$	-900.1	-862.9	37.1
	$Cr(CO)_6$	-868.2	-826.9	41.4
	CrO_2Cl_2	-3385.1	-3312.0	73.1
	CrO_2F_2	-2922.0	-2853.5	68.5
	$[CrO_3Cl]^-$	-3146.3	-3075.5	70.8
	$[CrO_3F]^-$	-3035.7	-2965.2	70.4
	$[CrO_4]^{2-}$	-3131.7	-3062.5	69.3
^{55}Mn	$Mn_2(CO)_{10}$	-1875.8	-1830.5	45.4
	$Mn(CO)_5Cl$	-2637.8	-2578.9	58.9
	$Mn(CO)_5(COMe)$	-2245.7	-2192.8	52.9
	$Mn(CO)_5H$	-1547.9	-1505.0	42.9
	$[Mn(CO)_5]^-$	-1699.1	-1655.5	43.6
	$[Mn(CO)_6]^+$	-2186.9	-2129.8	57.1
	$Mn(NO)_3(CO)$	-3350.8	-3281.6	69.2
	$MnCp(C_6H_6)$	-4100.8	-3980.0	120.8
	$MnCp(C_7H_8)$	-5392.5	-5264.5	128.0
	$MnCp(CO)_3$	-2097.8	-2041.2	56.6
	$[MnO_4]^-$	-4440.0	-4369.3	70.7
^{57}Fe	$Fe(CO)_3(C_4H_4)$	-2016.2	-1979.7	36.4
	$Fe(CO)_3(CH_2CHCHCH_2)$	-2526.9	-2485.5	41.4
	$Fe(CO)_3(CH_2CHCHO)$	-3570.9	-3518.3	52.6
	$Fe(CO)_4(CH_2CHCN)$	-2689.7	-2646.9	42.8
	$Fe(CO)_4(CH_2CHOMe)$	-2674.9	-2633.2	41.7
	$Fe(CO)_5$	-2464.2	-2425.0	39.2
	$FeCp_2$	-4057.2	-3959.7	97.5
	$FeCp(CO)_2iPr$	-3387.5	-3337.5	50.0
	$FeCp(CO)_2Me$	-3215.7	-3167.5	48.3
^{59}Co	$fac-Co(NH_3)_3(CN)_3$	-7880.8	-7895.5	-14.7
	$Co(acac)_3$	-15848.6	-15876.4	-27.8
	$[Co(CN)_6]^{3-}$	-5531.2	-5508.9	22.4
	$Co(CO)_4H$	-2297.2	-2290.7	6.6
	$[Co(CO)_4]^-$	-2578.8	-2571.5	7.3
	$CoCp(C_2H_4)_2$	-4238.6	-4223.6	15.1
	$[Co(H_2O)_6]^{3+}$	-20837.7	-20887.6	-49.9
	$[Co(NH_3)_4(CO_3)]^+$	-13258.8	-13272.1	-13.2
	$[Co(NH_3)_6]^{3+}$	-13857.1	-13901.3	-44.2
^{61}Ni	$Ni(C_2H_4)_2(PMe_3)$	-911.0	-973.9	-62.8
	$Ni(CO)_4$	-1934.6	-1975.4	-40.8
	$Ni(cod)_2$	-2880.0	-2952.6	-72.6
	$Ni(PCl_3)_4$	-2245.6	-2332.6	-87.0
	$Ni(PF_3)_4$	-1041.5	-1090.3	-48.8
	$Ni(PMe_3)_4$	-1896.7	-1958.3	-61.6
	Ni(t,t,t-cdt)(CO)	-2730.1	-2798.6	-68.5
	Ni(t,t,t-cdt)	-2167.2	-2237.8	-70.6
	Ni(t,t,t-cdt)(PMe_3)	-2894.2	-2969.5	-75.3

A.5.3 Shielding Constants and Shifts for Truncated Models and Full TM Complexes

Table A.16.: Comparison of shielding and shift results, including the y-intercepts, and statistical data for ^{51}V and ^{57}Fe test sets using either the model compounds ($VOMe_3$, $VOMe_2(OMe)$, $VOMe(OMe)_2$,$VO(OMe)_3$ and $Fe(CO)_4(CH_2CHOMe)$) or the experimental complexes ($VO(CH_2SiMe_3)_3$, $VO(CH_2SiMe_3)_2(O^tBu)$, $VO(CH_2SiMe_3)(O^tBu)_2$,$VO(O^tBu)_3$ and $Fe(CO)_4(CH_2CHOEt)$). Only the statistical data and results for the truncated systems are reproduced in the present work, for the full data set see Table S13 of SI-VI.

			Model Complexes			Full Complexes		
			cTPSS	cM06-L	cLH20t	cTPSS	cM06-L	cLH20t
^{51}V	$VOMe_3//VO(CH_2SiMe_3)_3$		-3057.7	-3272.3	-3512.1	-3027.2	-3252.3	-3476.5
	$VOMe_2(OMe)//VO(CH_2SiMe_3)_2(OtBu)$		-2400.4	-2556.6	-2717.8	-2370.6	-2539.6	-2701.6
	$VOMe(OMe)_2//VO(CH_2SiMe_3)(OtBu)_2$		-1827.4	-1953.1	-2025.7	-1790.8	-1915.4	-2007.1
	$VO(OMe)_3//VO(OtBu)_3$		-1462.2	-1552.9	-1562.6	-1403.1	-1488.0	-1518.9
^{57}Fe	$Fe(CO)_4(CH_2CHOMe)//Fe(CO)_4(CH_2CHOEt)$		-2151.6	-2674.9	-2828.3	-2161.0	-2685.6	-2838.6
	y-Intercept	^{51}V	-1987.9	-2115.0	-2226.0	-1967.3	-2097.9	-2210.0
		^{57}Fe	-1991.4	-2540.6	-2736.1	-1992.9	-2542.3	-2737.8

Shift Results		Exp.	cTPSS	cM06-L	cLH20t	cTPSS	cM06-L	cLH20t
^{51}V	$VOMe_3//VO(CH_2SiMe_3)_3$	1205	1069.8	1157.3	1286.1	1059.9	1154.4	1266.5
	$VOMe_2(OMe)//VO(CH_2SiMe_3)_2(OtBu)$	470	412.5	441.6	491.8	403.4	441.7	491.6
	$VOMe(OMe)_2//VO(CH_2SiMe_3)(OtBu)_2$	-210	-160.5	-161.9	-200.3	-176.5	-182.5	-202.9
	$VO(OMe)_3//VO(OtBu)_3$	-676	-525.7	-562.0	-663.4	-564.2	-610.0	-691.1
^{57}Fe	$Fe(CO)_4(CH_2CHOMe)//Fe(CO)_4(CH_2CHOEt)$	5	160.2	134.3	92.3	168.1	143.3	100.8
	rel. StD	^{51}V	4.0	3.7	4.8	3.9	3.4	4.5
		^{57}Fe	14.3	5.1	5.1	14.3	5.2	5.1
	rel. MSE	^{51}V	0.0	-0.8	-2.2	0.1	-0.7	-2.0
		^{57}Fe	-9.1	-1.5	1.0	-9.1	-1.5	1.0
	rel. MAE	^{51}V	3.6	3.1	3.6	3.5	2.9	3.4
		^{57}Fe	12.1	4.0	4.1	12.2	4.0	4.1

A.5.4 Statistical Shift Data of TM Benchmark Set Using the y-Intercept Method and Explicit References

Table A.17.: Comparison of statistical data of GIAO-DFT/pcSseg-3 calculations for various density functionals vs experimental data using BP86-D3(BJ) structures referenced with either the y-Intercept method (see P-VI) or via the complexes $TiCl_4$, $VOCl_3$, CrO_2F_2, $MnCp(C_6H_6)$, $Fe(CO)_5$, $Co(CO)_4H$, and $Ni(PMe_3)_4$.

		SVWN	BP86	BLYP	PBE	KT1	KT2	KT3	B97D	HCTH	TPSS			
											τ_D^a	τ_{MS}	τ_C	τ_0
y-Intercept	mean StD	334.0	333.0	361.0	321.4	530.0	526.5	459.2	289.8	285.2	361.2	436.9	440.6	444.0
	mean MSE	-22.9	-84.0	-112.7	-72.3	-186.5	-189.1	-156.7	-48.2	-7.5	-99.6	-136.0	-135.1	-138.2
	mean MAE	290.6	304.5	340.0	288.8	509.5	505.3	441.3	251.9	253.3	343.3	422.6	427.2	430.0
	mean rel. StD	7.1	6.8	6.9	6.6	9.3	9.1	8.0	6.2	5.8	7.3	8.1	8.0	8.2
	mean rel. MSE	-1.1	-1.0	-1.1	-0.9	-1.3	-1.3	-1.0	-0.8	-0.6	-1.0	-1.0	-0.8	-1.0
	mean rel. MAE	6.4	6.2	6.4	6.1	8.8	8.6	7.5	5.6	5.3	6.7	7.6	7.6	7.8
Referenced	mean StD	338.3	319.2	345.2	309.6	503.1	500.6	436.4	284.1	289.6	343.0	413.7	417.3	420.3
	mean MSE	-181.6	-260.7	-297.3	-243.4	-407.8	-409.1	-359.7	-205.2	-147.7	-268.0	-329.3	-333.3	-334.7
	mean MAE	382.7	456.2	496.4	433.7	749.8	739.2	646.6	364.1	322.5	514.4	627.4	631.2	637.6
	mean rel. StD	7.3	6.8	6.9	6.7	9.2	9.0	7.9	6.3	6.0	7.2	8.0	7.9	8.1
	mean rel. MSE	-2.6	-2.3	-2.2	-2.2	-2.9	-2.9	-2.3	-2.1	-1.7	-1.9	-2.0	-1.8	-2.0
	mean rel. MAE	7.7	7.9	8.1	7.7	12.2	11.9	10.3	6.8	6.2	9.0	10.4	10.3	10.6

		τ-HCTH				M06-L				MN15-L			
		τ_D^a	τ_{MS}	τ_C	τ_0	τ_D^a	τ_{MS}	τ_C	τ_0	τ_D^a	τ_{MS}	τ_C	τ_0
y-Intercept	mean StD	287.8	288.1	289.6	289.8	237.9	511.0	530.6	532.2	1678.5	533.5	572.7	581.9
	mean MSE	-20.2	-22.6	-23.0	-23.4	-68.3	-199.2	-198.0	-203.0	722.1	-164.4	-164.7	-174.8
	mean MAE	256.2	256.7	257.8	257.8	189.7	485.2	506.9	506.1	1205.0	510.3	553.3	561.3
	mean rel. StD	6.1	6.1	6.2	6.2	4.9	7.6	7.9	8.0	16.2	9.7	10.2	10.7
	mean rel. MSE	-0.8	-0.7	-0.8	-0.8	-1.3	-0.9	-0.6	-0.9	1.5	-0.8	-0.2	-0.8
	mean rel. MAE	5.6	5.6	5.7	5.7	4.0	7.2	7.5	7.6	13.2	9.2	9.9	10.3
Referenced	mean StD	288.5	288.0	289.3	289.6	239.5	491.7	511.3	511.7	1695.8	511.2	550.6	555.6
	mean MSE	-168.2	-172.2	-171.6	-172.5	-168.8	-413.1	-422.6	-423.1	908.7	-380.8	-400.1	-405.9
	mean MAE	339.4	342.0	343.9	343.6	253.2	675.1	699.2	706.1	1447.3	722.6	772.2	799.7
	mean rel. StD	6.3	6.3	6.4	6.4	5.0	7.6	7.9	8.1	16.5	9.6	10.2	10.6
	mean rel. MSE	-2.0	-2.0	-2.0	-2.0	-1.6	-1.4	-1.2	-1.7	0.3	-2.5	-1.8	-2.8
	mean rel. MAE	6.7	6.7	6.8	6.8	5.1	9.2	9.5	9.8	17.1	11.9	12.5	13.5

		B97M-V				SCAN				VSXC			
		τ_D^a	τ_{MS}	τ_C	τ_0	τ_D^a	τ_{MS}	τ_C	τ_0	τ_D^a	τ_{MS}	τ_C	τ_0
y-Intercept	mean StD	328.7	683.4	700.1	705.4	418.3	634.4	642.3	652.1	277.4	337.2	345.3	347.9
	mean MSE	-143.0	-263.6	-265.0	-269.8	-198.4	-261.0	-260.6	-265.3	29.2	-99.5	-100.6	-104.1
	mean MAE	293.9	649.8	668.9	672.7	388.8	602.7	613.1	621.3	212.2	309.5	319.5	322.5
	mean rel. StD	6.1	10.2	10.4	10.7	7.0	9.5	9.4	10.0	5.2	6.5	6.5	6.6
	mean rel. MSE	-1.8	-1.1	-0.9	-1.2	-2.2	-1.6	-1.3	-1.6	-0.5	-0.7	-0.5	-0.6
	mean rel. MAE	5.3	9.7	10.0	10.2	6.3	9.0	8.9	9.4	4.3	5.9	6.0	6.0
Referenced	mean StD	322.0	656.3	672.9	675.6	406.0	608.6	616.7	624.6	285.1	323.8	334.4	339.2
	mean MSE	-281.7	-537.4	-537.2	-546.7	-385.5	-518.9	-521.6	-525.4	-56.2	-264.8	-268.2	-235.6
	mean MAE	404.0	905.2	928.8	947.8	534.7	852.4	856.7	881.9	262.0	443.1	444.9	437.7
	mean rel. StD	6.2	10.1	10.4	10.6	7.1	9.5	9.4	9.9	5.2	6.3	6.5	6.7
	mean rel. MSE	-2.9	-2.7	-2.0	-2.8	-3.2	-2.6	-2.2	-2.7	-2.5	-2.9	-2.3	-0.6
	mean rel. MAE	6.6	12.7	13.0	13.7	7.8	12.1	11.7	12.7	5.9	8.3	7.7	7.1

[a] corresponds to the CDFT functional of the main discussion in P-VI.

Table A.18.: Comparison of statistical data of GIAO-DFT/pcSseg-3 calculations for various density functionals vs experimental data using BP86-D3(BJ) structures referenced with either the y-Intercept method (see main text) or via the complexes $TiCl_4$, $VOCl_3$, CrO_2F_2, $MnCp(C_6H_6)$, $Fe(CO)_5$, $Co(CO)_4H$, and $Ni(PMe_3)_4$.

		TPSSh				B3LYP	PBE0	B97-2	BHLYP	M06			
		τ_D^a	τ_{MS}	τ_C	τ_0					τ_D^a	τ_{MS}	τ_C	τ_0
y-Intercept	mean StD	265.6	332.3	334.0	338.8	256.4	429.3	368.3	957.1	1401.8	1621.1	1633.5	1624.8
	mean MSE	-56.2	-99.4	-98.5	-101.5	-22.8	73.5	56.2	142.0	395.5	455.8	454.6	460.2
	mean MAE	229.8	314.6	317.9	321.5	209.7	331.6	272.7	861.0	1156.3	1328.0	1342.2	1331.8
	mean rel. StD	6.1	6.8	6.7	7.0	6.0	8.0	6.9	20.4	20.4	23.2	23.4	23.1
	mean rel. MSE	-1.2	-1.2	-1.0	-1.2	-1.6	-1.4	-1.3	-3.0	-1.1	-1.1	-1.4	-1.1
	mean rel. MAE	5.5	6.3	6.3	6.4	5.0	6.8	5.7	18.7	18.7	21.2	21.5	21.2
Referenced	mean StD	260.9	317.8	319.2	323.7	265.7	436.3	377.1	940.5	1385.0	1601.6	1616.2	1606.4
	mean MSE	-165.4	-237.0	-241.2	-242.7	-81.5	82.8	38.0	364.2	497.8	541.5	557.5	559.8
	mean MAE	329.3	460.3	464.3	471.2	250.7	396.9	324.8	1155.7	1549.7	1780.3	1784.8	1779.4
	mean rel. StD	6.2	6.8	6.7	6.9	6.2	8.1	7.0	20.3	20.1	22.8	23.2	22.8
	mean rel. MSE	-1.9	-1.9	-1.8	-2.0	-2.1	-1.7	-1.8	-1.7	-3.6	-4.6	-4.4	-4.1
	mean rel. MAE	6.9	8.4	8.3	8.6	6.1	8.5	7.2	24.6	25.8	29.5	29.6	29.4

		PW6B95				MN15				M06-2X			
		τ_D^a	τ_{MS}	τ_C	τ_0	τ_D^a	τ_{MS}	τ_C	τ_0	τ_D^a	τ_{MS}	τ_C	τ_0
y-Intercept	mean StD	331.7	479.6	490.5	484.1	1041.1	17940.6	18822.1	19175.2	1004.4	3490.4	3582.8	3583.1
	mean MSE	17.8	77.6	78.0	80.0	446.0	-8329.3	-8719.7	-8827.4	248.4	1298.9	1317.6	1322.1
	mean MAE	257.0	387.0	397.2	391.6	793.7	17005.7	17845.4	18163.8	849.1	2761.1	2844.6	2846.1
	mean rel. StD	7.4	9.3	9.5	9.3	11.6	274.8	289.8	296.1	19.3	47.6	49.3	49.2
	mean rel. MSE	-1.6	-1.6	-1.7	-1.5	0.6	-101.2	-106.3	-106.8	-0.7	3.3	2.9	3.3
	mean rel. MAE	6.2	8.1	8.3	8.1	9.9	258.5	272.6	277.8	16.7	41.4	43.0	43.0
Referenced	mean StD	339.7	484.6	495.8	488.4	1045.9	18609.6	19521.5	19881.9	990.8	3473.0	3566.8	3562.5
	mean MSE	19.0	117.3	122.3	123.2	612.1	-4999.7	-5231.8	-5288.6	480.8	2062.3	2108.0	2108.6
	mean MAE	307.5	469.1	479.2	478.4	984.3	17027.4	17874.5	18232.8	1166.2	3639.9	3730.7	3759.3
	mean rel. StD	7.5	9.4	9.7	9.4	11.7	284.6	300.1	306.4	19.3	47.7	49.5	49.3
	mean rel. MSE	-1.6	-1.6	-1.6	-1.4	1.0	-88.8	-93.6	-94.3	0.6	7.0	6.9	7.4
	mean rel. MAE	7.8	10.1	10.3	10.2	13.2	282.5	298.2	305.2	22.8	54.9	56.5	57.2

		07s*	mPSTS				LHJ14				LH07t-SVWN		
			τ_D^a	τ_{MS}	τ_C	τ_0	τ_D^a	τ_{MS}	τ_C	τ_0	τ_D^a	τ_{MS}	τ_C	τ_0
y-Intercept	mean StD	396.3	249.2	308.2	309.9	314.3	300.6	257.9	269.8	257.6	340.9	298.1	290.8	292.3
	mean MSE	79.8	-43.0	-87.6	-86.8	-89.7	-89.1	-42.5	-44.3	-41.4	37.8	10.5	11.4	10.5
	mean MAE	278.5	219.8	288.2	291.7	295.0	276.3	223.9	232.5	221.5	238.6	218.2	213.9	215.8
	mean rel. StD	6.5	5.8	6.5	6.4	6.6	6.6	6.1	6.6	6.1	6.3	6.1	5.9	5.9
	mean rel. MSE	-1.1	-1.1	-1.1	-1.0	-1.1	-1.4	-1.4	-1.7	-1.5	-1.4	-1.5	-1.4	-1.5
	mean rel. MAE	5.3	5.2	6.0	6.0	6.1	6.0	5.3	5.7	5.3	5.1	5.0	4.8	4.9
Referenced	mean StD	408.2	248.5	296.4	297.8	302.0	291.5	262.3	275.5	263.2	354.1	310.6	302.7	304.6
	mean MSE	36.9	-133.9	-208.3	-212.6	-213.9	-233.1	-158.2	-150.2	-150.1	-22.0	-58.1	-62.1	-61.6
	mean MAE	320.6	286.1	416.6	420.8	427.4	392.0	270.1	279.2	264.6	272.4	259.3	256.8	257.1
	mean rel. StD	6.7	5.9	6.5	6.4	6.6	6.7	6.4	6.9	6.4	6.6	6.3	6.1	6.2
	mean rel. MSE	-1.9	-1.7	-1.7	-1.6	-1.8	-2.5	-2.5	-2.6	-2.3	-2.2	-2.3	-2.2	-2.2
	mean rel. MAE	66.4	6.4	7.9	7.8	8.1	7.3	5.9	6.4	5.8	5.9	5.8	5.6	5.6

* 07s – LH07s-SVWN

[a] corresponds to the CDFT functional of the main discussion in P-VI.

Table A.19.: Comparison of statistical data of GIAO-DFT/pcSseg-3 calculations for various density functionals vs experimental data using BP86-D3(BJ) structures referenced with either the y-Intercept method (see main text) or via the complexes $TiCl_4$, $VOCl_3$, CrO_2F_2, $MnCp(C_6H_6)$, $Fe(CO)_5$, $Co(CO)_4H$, and $Ni(PMe_3)_4$.

		LH12ct-SsirPW92				LH12ct-SsifPW92				LH14t-calPBE			
		τ_D^a	τ_{MS}	τ_C	τ_0	τ_D^a	τ_{MS}	τ_C	τ_0	τ_D^a	τ_{MS}	τ_C	τ_0
y-Intercept	mean StD	455.3	410.5	405.7	402.9	521.9	488.2	485.0	480.6	266.8	255.9	253.5	254.8
	mean MSE	82.4	55.6	56.0	55.8	106.8	83.3	83.3	83.7	-9.8	-21.3	-21.4	-21.8
	mean MAE	342.6	310.3	305.7	302.8	404.8	383.2	379.6	375.6	211.8	210.0	208.1	209.6
	mean rel. StD	7.9	7.6	7.5	7.5	8.8	8.7	8.7	8.5	5.9	5.9	5.8	5.8
	mean rel. MSE	-1.5	-1.7	-1.6	-1.6	-1.6	-1.8	-1.7	-1.7	-1.5	-1.6	-1.6	-1.6
	mean rel. MAE	6.7	6.5	6.4	6.3	7.7	7.6	7.6	7.5	4.9	4.9	4.9	4.9
Referenced	mean StD	464.2	419.6	414.0	411.8	528.8	495.0	491.1	487.1	277.7	265.6	263.0	264.4
	mean MSE	62.7	29.6	25.0	26.0	104.2	76.6	72.1	73.3	-85.6	-100.6	-102.6	-102.6
	mean MAE	408.4	367.6	364.9	359.5	485.7	459.7	458.4	452.0	250.2	248.1	247.1	247.9
	mean rel. StD	8.1	7.8	7.6	7.6	8.9	8.8	8.7	8.6	6.1	6.1	6.0	6.1
	mean rel. MSE	-2.2	-2.3	-2.3	-2.3	-2.2	-2.4	-2.4	-2.3	-2.3	-2.4	-2.4	-2.4
	mean rel. MAE	8.5	8.2	8.1	8.0	9.8	9.7	9.7	9.5	5.7	5.7	5.7	5.7

		LH20t				CAM-B3LYP	ωB97X-D	ωB97X-V	ωB97M-V			
		τ_D^a	τ_{MS}	τ_C	τ_0				τ_D^a	τ_{MS}	τ_C	τ_0
y-Intercept	mean StD	281.7	317.2	320.7	318.0	315.0	368.4	344.0	253.0	322.9	331.5	327.6
	mean MSE	-10.8	2.9	2.4	2.6	7.0	50.2	40.7	-53.1	-128.3	-132.1	-130.6
	mean MAE	223.2	245.3	248.3	246.2	254.9	293.3	280.7	220.2	280.0	289.1	285.5
	mean rel. StD	6.6	7.2	7.3	7.2	7.4	7.7	7.7	7.1	6.8	7.0	6.8
	mean rel. MSE	-1.8	-1.9	-1.9	-1.9	-1.5	-1.2	-1.1	-1.6	-1.6	-1.8	-1.7
	mean rel. MAE	5.6	6.1	6.2	6.1	6.5	6.7	6.8	6.2	5.7	6.0	5.9
Referenced	mean StD	291.4	327.3	330.7	327.9	320.0	372.4	346.9	257.2	317.7	326.2	322.1
	mean MSE	-52.0	-24.5	-24.5	-24.3	-19.7	50.0	30.9	-104.8	-246.6	-245.5	-246.8
	mean MAE	268.0	287.5	291.0	288.8	317.8	364.1	353.2	280.3	388.3	398.5	395.6
	mean rel. StD	6.8	7.4	7.5	7.4	7.5	7.7	7.7	7.2	6.8	7.1	6.9
	mean rel. MSE	-2.1	-2.2	-2.3	-2.2	-1.9	-1.4	-1.3	-2.0	-2.3	-2.3	-2.2
	mean rel. MAE	6.9	7.5	7.6	7.5	8.4	8.7	9.0	8.1	7.7	7.9	7.7

		HF	HF^{b,d}	MP2^{b,d}	B2PLYP^{b,d}	DSD-PBEP86^{b}	DSD-PBEP86^{c,d}
y-Intercept	mean StD	12655.9	8707.1	26262.6	1423.0	6412.9	6562.8
	mean MSE	-1254.5	907.0	-3441.3	582.5	1221.0	1203.4
	mean MAE	10037.3	7785.8	18903.7	1359.4	5080.4	5194.8
	mean rel. StD	303.9	286.9	1095.8	39.1	180.5	182.9
	mean rel. MSE	-39.1	-32.4	-132.5	12.7	29.6	29.7
	mean rel. MAE	256.9	251.0	772.1	35.9	140.8	142.7
Referenced	mean StD	12009.6	7876.5	23715.1	1462.4	6627.7	6676.1
	mean MSE	-1948.6	-4531.9	7600.9	278.4	-768.9	-670.4
	mean MAE	15678.9	13419.0	25617.8	1410.1	4672.9	4635.2
	mean rel. StD	273.8	254.5	972.6	39.7	184.9	181.3
	mean rel. MSE	-318.0	-339.0	363.4	10.8	7.6	15.5
	mean rel. MAE	470.7	465.7	1026.2	43.1	149.2	142.5

[a] corresponds to the CDFT functional of the main discussion in P-VI; [b] ORCA calculation; pcSseg-3 for transition metal, pcSseg-2 other nuclei using the "AutoAux" option with settings AutoAuxSize=1 for the "C" auxiliary basis, as well as def2/J and def2/JK auxiliary basis sets and internal grid setting "Grid5"; [c] ORCA calculation; pcSseg-3 for all nuclei using the "AutoAux" option with settings AutoAuxSize=3 and AutoAuxLMax=TRUE for the "C", "J" and "JK" auxiliary basis and internal grid setting "Grid5"; [d] Calculated from incomplete results.

A.5.5 Comparison of Shifts with BP86 and TPSSh Structures

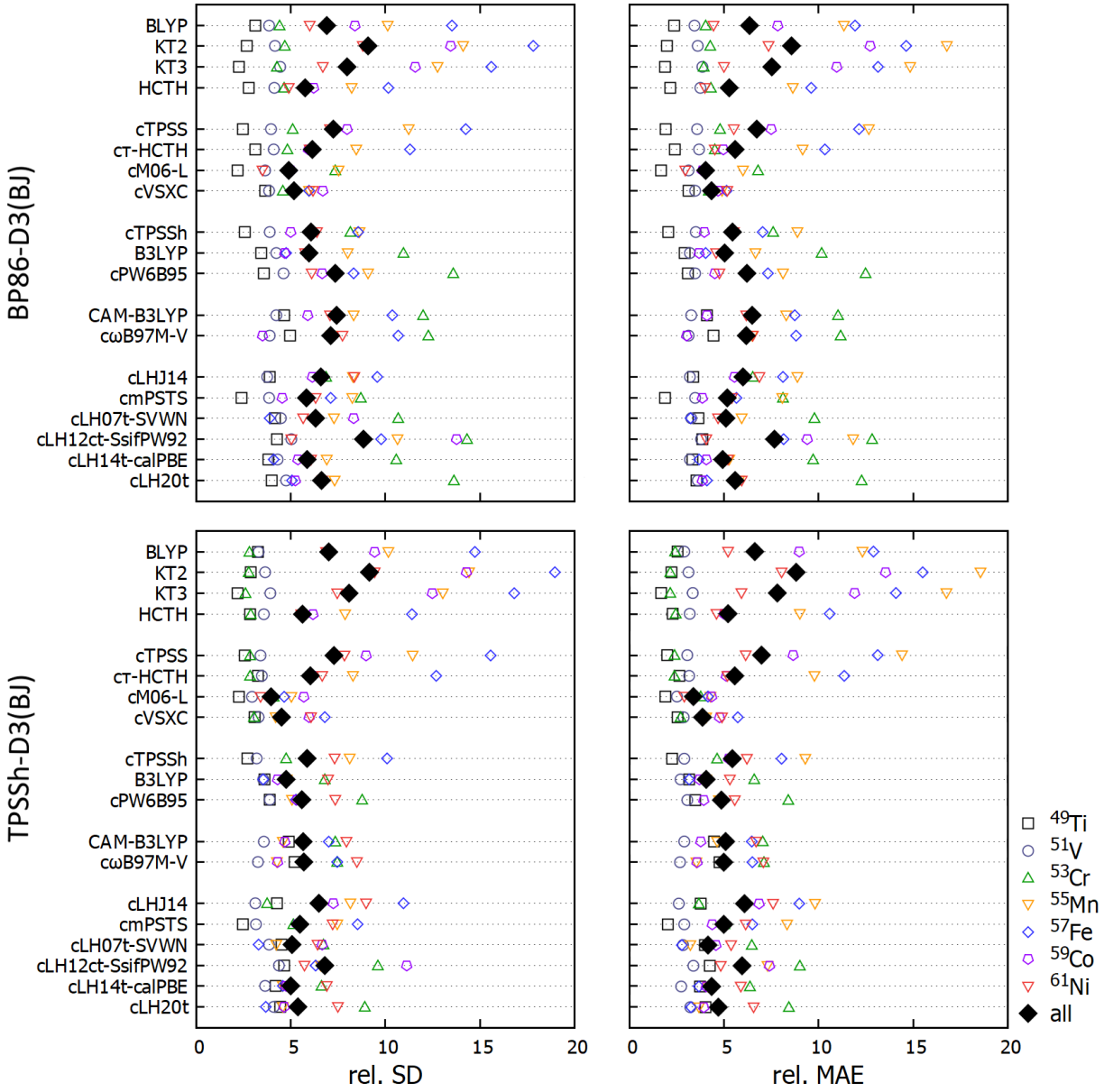

Figure A.5.: Relative standard deviations and mean absolute errors in % for the individual nuclei (hollow symbols) and their weighted aggregate (filled black symbols) for various XC functionals (using τ_D for τ-dependent functionals), with either BP86-D3(BJ) (top) or TPSSh-D3(BJ) structures (bottom).

A.5.6 Studies of Triplet Instabilities and Comparison of RKS and UKS Solutions

Table A.20.: Comparison of shielding results at GIAO-BHYLP/pcSseg-3 level, either calculated with TURBOMOLE or with ORCA. Triplet instabilities were detected for results given in red font. The last two columns give UKS shieldings and total spin expectation values for those cases. In the present work, only cases are included, which show triplet instabilities in one of the calculations. the full data set is provided in Tab. S10 of SI-VI.

		TURBOMOLE	ORCA[a]		
			RKS	UKS	$\langle S^2 \rangle$
^{49}Ti	$[Ti(CO)_6]^{2-}$	661.9	661.9	661.9	0.000
^{51}V	$[V(CO)_6]^{-}$	-155.6	-155.8	-155.8	0.000
^{53}Cr	$Cr(CO)_6$	-1588.7	-1588.9	-1588.9	0.000
	CrO_2Cl_2	-5704.7	-5704.6		
	CrO_2F_2	-4866.4	-4866.2		
	$[CrO_3Cl]^{-}$	-5045.2	-5045.2	-4591.0	0.625
^{55}Mn	$[Mn(CO)_6]^{+}$	-3969.8	-3970.3	-3970.3	0.000
	$Mn(NO)_3(CO)$	-5693.2	-5693.2	-5526.7	2.325
	$MnCp(C_7H_8)$	-9647.5	-9647.2	-9666.7	0.244
^{57}Fe	$FeCp_2$	-9395.9	-9396.7		
^{59}Co	$[Co(CO)_4]^{-}$	-5120.4	-5120.3	-5120.3	0.000
	$CoCp(C_2H_4)_2$	-8060.8	-8061.4	-7998.8	0.197
	$[Co(H_2O)_6]^{3+}$	-35593.1	-35598.6	-35598.6	0.000
	$[Co(NH_3)_6]^{3+}$	-23185.8	-23189.9	-23189.9	0.000
^{61}Ni	$Ni(cod)_2$	-3105.8	-3105.9	-4118.5	0.281

[a] ORCA calculation; pcSseg-3 for all nuclei using the "AutoAux" option with settings AutoAuxSize=3 and AutoAuxLMax=TRUE for "JK" auxiliary basis and internal grid setting "Grid5".

Table A.21.: Triplet-instability analyses and restricted/unrestricted shielding results including lowest eigenvalues of the electronic Hessian for the restricted solutions and $\langle S^2 \rangle$ as a measure of spin-contamination of the unrestricted solutions, comparing BHLYP, HF, and DSD-PBEP86.[a]

		BHLYP	Hartree-Fock	DSD-PBEP86
$[CrO_3Cl]^{-}$	$\langle H \rangle^b$	-0.005	-0.109	-0.049
	$\langle S^2 \rangle$	0.606	2.422	1.827
	$\sigma_{restr.}$	-5042.3	-13520.2	5808.5
	$\sigma_{unrestr.}$	-4604.0	-5851.5	n.a.[c]
$Mn(NO)_3(CO)$	$\langle H \rangle^b$	-0.051	-0.158	-0.092
	$\langle S^2 \rangle$	2.320	3.587	2.875
	$\sigma_{restr.}$	-5662.6	-9700.6	88731.8
	$\sigma_{unrestr.}$	-5512.4	-12946.2	n.a.[c]
$Ni(cod)_2$	$\langle H \rangle^b$	-0.013	-0.159	-0.064
	$\langle S^2 \rangle$	0.275	1.466	0.772
	$\sigma_{restr.}$	-3091.4	-7312.1	2093.6
	$\sigma_{unrestr.}$	-4084.3	-13622.8	n.a.[c]

[a] ORCA calculation; pcSseg-3 for transition metal, pcSseg-2 for other nuclei using the "AutoAux" option with settings AutoAuxSize=1 for the "C" auxiliary basis, as well as def2/J and def2/JK auxiliary basis sets and internal grid setting "Grid3"; $\langle H \rangle$ values according to RHF/RKS solution.
[b] Lowest Hessian eigenvalue. [c] Not available.

A.5.7 Maximum Relative Absolute Errors.

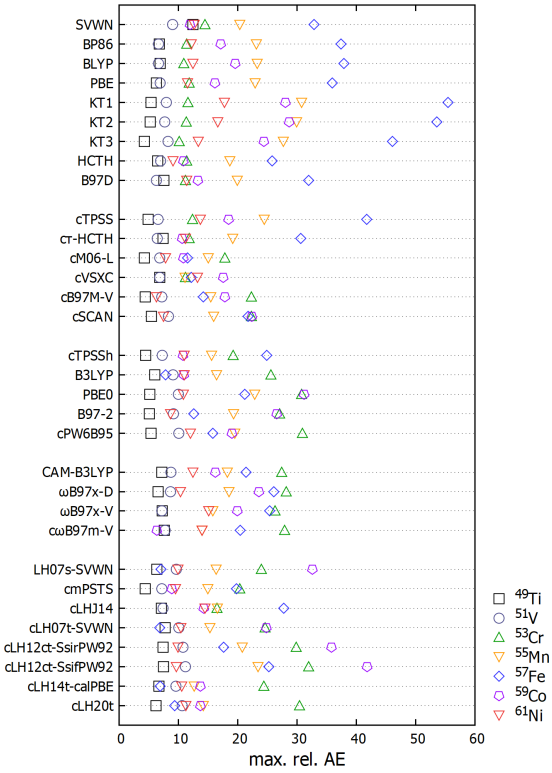

Figure A.6.: Maximum relative AEs (in %) with respect to experimental shift range of the individual nuclei with various density functionals (with pcSseg-3 basis).

As an additional measure for the robustness of different methods, Fig. A.6 shows maximum relative absolute errors (or equivalently maximum relative unsigned errors) for different nuclei. These max. rel. AEs are much larger than what is obtained for light main-group shieldings (as shown in P-V). Further insights on robustness are provided for several methods by histogram plots of relative deviations in the main text.

A.6 SI-VII

Table A.22.: Calculated ^{19}F NMR chemical shifts relative to $CFCl_3$ (in ppm) of $[XF_n]^-$ (X = Cl, Br, I; $n = 2, 4, 6$) in comparison with experimental values, at BP86-D3 structures.[a]

	BHLYP				LH12ct-SsifPW92				
opt.	gas.	gas.	COSMO	COSMO	gas.	gas.	COSMO	COSMO	
NMR	gas.	COSMO	gas.	COSMO	gas.	COSMO	gas.	COSMO	$\delta_{exp.}$
$[ClF_2]^-$	-193.2	-200.0	-196.6	-202.4	-166.3	-170.1	-171.5	-174.4	-125
$[ClF_4]^-$	80.6	76.1	71.9	67.8	71.8	68.6	63.3	60.5	67
$[ClF_6]^-$	284.3	286.8	275.0	277.6	255.1	257.3	246.6	248.9	–
$[BrF_2]^-$	-284.4	-294.6	-286.2	-295.5	-262.6	-270.7	-265.4	-272.7	-210
$[BrF_4]^-$	-32.2	-38.3	-36.3	-42.0	-36.6	-41.6	-40.7	-45.4	-37
$[BrF_6]^-$	131.9	135.0	126.0	129.2	114.6	117.4	109.0	111.9	94
$[IF_2]^-$	-350.1	-359.3	-351.4	-360.1	-338.1	-346.7	-339.5	-347.8	-282
$[IF_4]^-$	-103.1	-109.5	-105.1	-111.1	-109.8	-115.5	-111.8	-117.3	-106
$[IF_6]^-$	31.1	33.3	28.1	30.5	14.8	16.9	11.9	14.1	13
$\sigma(CFCl_3)$	185.4	189.7	183.8	183.8	195.2	198.8	193.7	197.5	

[a] At BP86-D3(BJ)/def2-TZVPPD optimized structures. $CFCl_3$ reference shieldings at the same level have been used to obtain the relative shifts. Nonrelativistic results with pcSseg-4 basis sets for F, Cl, Br, and ANO-RCC-unc for I.

Table A.23.: Calculated ^{19}F NMR chemical shifts relative to $CFCl_3$ (in ppm) of $[XF_n]^-$ (X = Cl, Br, I; $n = 2, 4, 6$) in comparison with experimental values, at B3LYP-D3 structures.[a]

	BHLYP				LH12ct-SsifPW92				
opt.	gas.	gas.	COSMO	COSMO	gas.	gas.	COSMO	COSMO	
NMR	gas.	COSMO	gas.	COSMO	gas.	COSMO	gas.	COSMO	$\delta_{exp.}$
$[ClF_2]^-$	-190.6	-196.4	-193.4	-198.4	-169.8	-171.0	-173.3	-169.8	-125.0
$[ClF_4]^-$	65.3	61.3	58.5	54.9	56.5	53.8	49.9	47.5	67.0
$[ClF_6]^-$	250.8	252.9	243.0	245.3	224.7	226.7	217.5	219.7	–
$[BrF_2]^-$	-279.4	-288.5	-281.1	-289.5	-260.0	-267.1	-262.3	-268.9	-210.0
$[BrF_4]^-$	-38.2	-43.7	-41.5	-46.7	-43.3	-47.8	-46.6	-50.8	-37.0
$[BrF_6]^-$	113.8	116.4	108.5	111.4	97.6	100.0	92.7	95.3	94.0
$[IF_2]^-$	-343.0	-351.5	-344.6	-352.9	-332.4	-340.3	-333.9	-341.8	-282.0
$[IF_4]^-$	-99.5	-105.5	-101.3	-107.1	-107.0	-112.5	-108.8	-114.1	-106.0
$[IF_6]^-$	29.3	31.1	26.5	28.4	12.7	14.4	9.9	11.7	13.0
$\sigma(CFCl_3)$	190.8	194.8	189.1	193.3	200.3	203.6	198.7	202.2	

[a] At B3LYP-D3(BJ)/def2-TZVPPD optimized structures. $CFCl_3$ reference shieldings at the same level have been used to obtain the relative shifts. Nonrelativistic results with pcSseg-4 basis sets for F, Cl, Br, and ANO-RCC-unc for I.

A.7 SI-VIII

A.7.1 CH···F Bond Lengths and Coordination in Microsolvated Clusters

Table A.24.: Optimized CH···F bond lengths in pm in optimized $X^-(MeCN)_n$ ($X = F^-$, FHF^-, ClF_2^-, ClF_4^-) clusters at GFN2-xTB, MARIJ-BP86-D3(BJ)/def2-TZVPP levels (DFT+C uses COSMO, $\varepsilon = 35.688$) levels.

Anion	n	XTB	DFT	DFT+C	Anion	n	XTB	DFT	DFT+C
F-	8	198.9	197.5	198.2	FHF-	10	210.5	206.7	205.4
		198.9	197.5	198.2			219.3	208.3	206.6
		198.9	197.5	199.7			220.0	210.0	206.6
		198.9	197.5	199.7			220.7	213.1	207.4
		214.0	209.0	202.6			221.2	213.4	207.5
		214.0	209.0	202.6			221.5	213.7	208.6
		214.0	209.0	203.2			223.0	215.8	209.5
		214.0	209.0	203.2			223.2	216.4	214.8
							227.2	218.3	(233.9)
							238.4	218.7	(272.2)
	9	201.2	204.9	204.0		11	217.5	208.2	205.9
		201.2	204.9	204.2			220.0	209.5	208.0
		201.8	205.0	204.2			223.3	210.9	210.7
		201.8	211.8	206.6			223.4	211.5	211.5
		206.0	211.9	206.7			224.8	211.9	212.0
		206.0	212.0	206.7			226.1	212.5	212.8
		210.1	214.4	216.1			226.4	213.3	213.2
		213.1	214.5	216.4			227.1	213.8	215.7
		(505.9)	214.5	216.5			228.6	220.9	217.8
							228.6	221.5	218.1
							(231.7)	(513.3)	(484.4)
	10	193.9	192.9	196.0		12	218.7	212.0	210.5
		194.6	199.8	198.3			220.2	214.1	211.4
		202.2	202.5	198.9			222.3	214.8	212.9
		202.6	203.5	202.2			222.4	215.2	215.0
		211.2	203.8	202.5			223.3	217.0	215.8
		212.8	204.0	203.0			225.9	217.0	216.9
		212.9	205.9	203.9			227.7	218.9	218.5
		215.3	206.9	204.2			227.7	220.5	219.0
		(540.6)	(506.2)	(462.5)			228.2	222.3	221.8
		(574.1)	(565.5)	(585.4)			(230.5)	225.2	227.0
							(234.6)	228.1	(235.9)
							(479.0)	(472.3)	(443.6)
ClF2-	10	218.0	208.0	209.1	ClF4-	10	222.3	217.4	215.8
		218.7	208.5	210.1			225.8	222.5	221.6
		219.2	209.2	212.1			226.1	222.7	222.4
		221.8	213.1	213.2			(233.4)	225.9	224.7
		(231.4)	214.1	215.6			(235.9)	228.2	228.8
		(235.4)	217.9	217.5			(238.2)	(237.7)	229.8
		(237.9)	220.8	220.3			(240.9)	(239.7)	(238.1)
		(243.0)	(254.6)	259.6			(244.7)	(243.0)	(242.6)
		(246.3)	(267.6)	265.4			(264.1)	(290.5)	(257.8)
		(247.7)	(299.1)	(315.6)			(284.4)	(294.3)	(280.2)
	11	214.5	209.1	206.6		11	226.7	211.9	215.0
		217.9	209.8	208.8			227.8	224.4	224.8
		218.8	212.5	212.8			(232.1)	226.0	226.2
		220.1	214.4	213.2			(232.2)	(231.1)	229.8
		223.1	214.4	214.6			(234.9)	(244.3)	229.8
		226.4	215.8	215.4			(236.8)	(245.5)	(233.1)
		(239.6)	223.1	220.5			(242.0)	(246.3)	(236.3)
		(259.7)	223.8	(247.5)			(248.6)	(247.6)	(241.5)
		(336.0)	(242.2)	(260.4)			(251.7)	(249.1)	(242.9)
		(342.2)	(283.9)	(277.1)			(257.1)	(251.1)	(246.3)
		(360.1)	(297.9)	(289.6)			(258.3)	(259.3)	(261.5)
	12	218.2	208.9	209.6		12	223.0	217.0	217.7
		219.2	208.9	209.7			223.0	217.1	217.8
		221.2	212.3	209.8			(233.6)	221.2	222.9
		222.6	212.4	209.9			(233.6)	221.2	223.0
		224.4	212.6	214.3			(235.8)	222.6	227.9
		225.5	212.7	214.6			(235.8)	222.7	227.9
		(230.4)	(233.4)	(236.1)			(239.4)	229.9	(231.5)
		(234.6)	(234.6)	(238.8)			(239.4)	(230.6)	(231.5)
		(274.2)	(291.0)	(284.6)			(248.9)	(233.9)	(232.0)
		(297.1)	(291.6)	(284.8)			(248.9)	(233.9)	(232.0)
		(362.9)	(292.7)	(290.3)			(252.0)	(247.4)	(249.2)
		(368.6)	(292.8)	(291.0)			(252.0)	(248.0)	(249.2)

A.7.2 ^{19}F NMR Shift Data

Table A.25.: Computed ^{19}F-NMR shifts in ppm for microsolvated fluoride-like anions in MeCN with increasing cluster size using different functionals.[a]

Anion	n	exp. Shift	BHLYP	cLH12sir	cLH12sif	cLH20t
F^-	0	-74	-293.5	-293.3	-290.1	-295.8
	1		-194.0	-199.8	-198.0	-200.3
	2		-151.8	-160.4	-159.3	-158.6
	3		-117.3	-128.5	-128.0	-125
	4		-93.2	-104.7	-104.7	-99.8
	5		-71.5	-83.1	-83.5	-77.3
	6		-37.0	-50.6	-51.6	-43.3
	7		-44.1	-54.8	-55.9	-46.1
	8		-57.3	-65.9	-66.9	-57.0
	9		-77.5	-82.8	-83.7	-75.4
	10		-58.2	-66.3	-67.2	-57.3
	11		-58.6	-66.1	-67.1	-57.5
FHF^-	0	145–149	-211.6	-218.7	-216.5	-219.1
	1		-195.5	-203.7	-201.7	-203.2
	2		-182.9	-191.6	-189.9	-190.4
	3		-171.5	-180.8	-179.3	-178.7
	4		-164.3	-174.0	-172.7	-171.4
	5		-154.2	-164.6	-163.4	-160.8
	6		-145.5	-156.1	-155.1	-151.8
	7		-139.2	-150.0	-149.1	-145.0
	8		-130.4	-141.7	-140.9	-136.0
	9		-125.3	-136.9	-136.3	-130.7
	10		-124.1	-134.5	-133.9	-128.3
	11		-124.3	-135.2	-134.6	-128.1
	12		-129.7	-140.2	-139.6	-133.2
ClF_2^-	0	-125	-206.3	-167.9	-168.8	-174.7
	1		-193.2	-156.5	-157.4	-162.0
	2		-184.6	-149.1	-150.2	-153.4
	3		-173.9	-139.0	-140.3	-143.3
	4		-166.7	-132.2	-133.7	-136.0
	5		-160.7	-126.5	-128.0	-128.9
	6		-154.0	-120.6	-122.2	-122.0
	7		-147.8	-115.4	-117.2	-116.4
	8		-147.1	-115.4	-117.0	-114.7
	9		-137.3	-105.4	-107.0	-106.3
	10		-130.2	-98.3	-100.0	-98.1
	11		-126.7	-95.1	-96.7	-94.3
	12		-125.5	-93.4	-95.0	-93.6
ClF_4^-	0	67	67.8	67.8	65.4	69.0
	1		73.0	72.2	69.6	73.8
	2		76.2	75.0	72.4	77.4
	3		83.8	83.1	80.4	86.2
	4		78.0	77.7	75.2	81.1
	5		76.2	75.8	73.3	79.0
	6		77.7	77.7	75.1	81.2
	7		78.2	78.5	75.9	82.6
	8		80.7	80.2	77.6	83.9
	9		87.0	86.0	83.3	89.9
	10		81.8	81.8	79.3	85.5
	11		82.8	83.6	81.0	88.3
	12		83.5	83.2	80.5	87.1

[a] MARIJ-GIAO-DFT/pcSseg-3/COSMO//MARIJ-D3(BJ)-BP86/def2-TZVPP/COSMO level. Relative to a computed $CFCl_3$(l) reference shielding of 187.2 ppm (BHLYP), 186.3 ppm (cLH12ct-SsirPW92), 189.5 ppm (cLH12ct-SsifPW92), 184.6 ppm (cLH20t). Experimental data from Refs. 414,415 and P-VII. cLH12sir and cLH12sif abbreviate cLH12ct-SsirPW92 and cLH12ct-SsifPW92, respectively.

A.8 Additional Data

A.8.1 Test of the Gauge Independence of the Implementation of Calibrated LHs

Table A.26.: Tests of the gauge independence of isotropic shielding constants for NH_3 (in ppm, DFT/pcSseg-3 with grid setting 5) for the calibrated LH20t (input structure as indicated on the left hand side) using different models for τ (see Eqs. 3.86 and 3.87).

				LH20t	
Nucleus	x	y	z	τ_{MS}	τ_D
N	0.000000	0.000000	0.000000	270.75	268.93
H	0.933748	0.000000	-0.385356	31.490	31.435
H	-0.466874	-0.808650	-0.385356	31.490	31.435
H	-0.466874	0.808650	-0.385356	31.490	31.435
N	0.000000	0.000000	0.000000	270.75	268.93
H	0.000000	0.000000	1.010141	31.491	31.436
H	0.969231	0.000000	-0.284562	31.490	31.435
H	-0.380116	0.891586	-0.284553	31.490	31.435
N	-100.000000	-100.000000	-100.000000	270.77	268.95
H	-99.066252	-100.000000	-100.385356	31.490	31.435
H	-100.466874	-100.808650	-100.385356	31.490	31.435
H	-100.466874	-99.191350	-100.385356	31.490	31.435
N	100.000000	100.000000	100.000000	270.73	268.91
H	100.933748	100.000000	99.614644	31.490	31.435
H	99.533126	99.191350	99.614644	31.490	31.435
H	99.533126	100.808650	99.614644	31.490	31.435

A.8.2 Grid Dependency of DFT and CDFT Shielding Calculations

Table A.27.: Shielding data (in ppm) for the benchmark set of Ref. 13 using two LH functionals with various grid settings (GIAO-DFT/pcSseg-3 data).

		LH07t								lh20t							
		τ_{MS}				τ_D				τ_{MS}				τ_D			
	grid	5	1	1	1	5	1	1	1	5	1	1	1	5	1	1	1
	cpksgrid	–	–	0	-1	–	–	0	-1	–	–	0	-1	–	–	0	-1
^{1}H	$C_4H_4O(C_2,C_5)$	23.68	23.68	23.68	23.68	23.81	23.81	23.81	23.81	23.92	23.91	23.92	23.91	23.92	23.92	23.92	23.92
	$C_4H_4O(C_3,C_4)$	24.62	24.62	24.62	24.62	24.74	24.74	24.74	24.74	24.87	24.87	24.87	24.87	24.85	24.85	24.85	24.85
	CH_3COCH_3	29.28	29.28	29.28	29.28	29.39	29.40	29.40	29.40	29.50	29.50	29.50	29.50	29.47	29.47	29.47	29.47
	CH_3F	27.14	27.14	27.14	27.14	27.24	27.24	27.24	27.24	27.41	27.41	27.41	27.41	27.40	27.40	27.40	27.40
	CH_4	31.30	31.30	31.30	31.31	31.41	31.41	31.41	31.41	31.44	31.44	31.44	31.44	31.40	31.40	31.40	31.40
	H_2O	30.47	30.47	30.47	30.47	30.64	30.64	30.64	30.64	30.58	30.58	30.58	30.58	30.53	30.53	30.53	30.53
	HF	28.56	28.56	28.56	28.56	28.77	28.77	28.77	28.77	28.56	28.56	28.56	28.56	28.54	28.54	28.54	28.53
	NH_3	31.33	31.33	31.33	31.33	31.46	31.46	31.46	31.46	31.47	31.47	31.47	31.47	31.42	31.42	31.42	31.42
	PH_3	29.25	29.25	29.25	29.25	29.37	29.37	29.37	29.37	29.42	29.42	29.42	29.42	29.40	29.40	29.40	29.40
^{13}C	$C_4H_4O(C_2,C_5)$	38.0	38.0	38.0	37.9	38.2	38.1	38.2	38.0	39.3	39.3	39.3	39.1	40.6	40.6	40.5	40.5
	$C_4H_4O(C_3,C_4)$	72.3	72.3	72.4	72.2	72.0	72.0	72.1	71.9	74.0	74.0	74.1	73.9	75.0	75.0	75.0	75.0
	CF_4	53.4	53.4	53.5	53.4	54.0	54.0	54.1	54.0	57.2	57.2	57.3	57.2	58.1	58.2	58.2	58.2
	$CH_3\underline{C}OCH_3$	-30.3	-30.3	-30.3	-30.5	-29.9	-29.9	-29.9	-30.1	-30.0	-30.0	-30.1	-30.3	-28.2	-28.2	-28.3	-28.4
	$\underline{C}H_3CO\underline{C}H_3$	159.4	159.4	159.4	159.3	158.1	158.0	158.0	158.0	160.2	160.2	160.2	160.2	160.4	160.4	160.4	160.4
	CH_3F	117.0	116.9	116.9	116.9	116.3	116.3	116.3	116.2	119.7	119.7	119.6	119.6	120.2	120.2	120.1	120.1
	CH_4	199.9	199.8	199.8	199.8	197.2	197.1	197.1	197.1	198.7	198.7	198.7	198.6	198.4	198.4	198.4	198.4
	CO	-13.3	-13.3	-13.2	-13.5	-13.3	-13.3	-13.2	-13.6	-14.4	-14.4	-14.3	-14.8	-12.6	-12.6	-12.6	-12.8
^{15}N	N_2	-82.2	-82.2	-82.1	-82.6	-83.9	-83.9	-83.8	-84.4	-86.6	-86.6	-86.5	-87.2	-83.4	-83.4	-83.4	-83.8
	$N\underline{N}O$	-1.5	-1.5	-1.4	-1.6	-1.9	-1.9	-1.9	-2.1	-6.2	-6.2	-6.2	-6.5	-4.6	-4.6	-4.6	-4.7
	$\underline{N}NO$	94.5	94.5	94.5	94.3	92.5	92.5	92.5	92.3	88.7	88.7	88.7	88.4	89.6	89.6	89.6	89.5
	NH_3	275.8	275.8	275.8	275.8	267.8	267.7	267.7	267.7	270.5	270.4	270.4	270.4	268.7	268.6	268.6	268.6
	PN	-403.7	-403.7	-403.7	-404.5	-407.5	-407.4	-407.5	-408.3	-418.9	-418.7	-418.8	-420.0	-409.2	-409.0	-409.3	-409.9
^{17}O	C_4H_4O	37.5	37.4	37.5	37.5	35.7	35.7	35.7	35.8	38.7	38.8	38.9	39.0	40.2	40.3	40.4	40.5
	CH_3COCH_3	-316.8	-316.6	-317.0	-316.7	-322.1	-321.9	-322.3	-322.0	-328.4	-328.4	-329.0	-328.5	-323.0	-323.0	-323.6	-323.3
	CO	-65.2	-65.2	-65.2	-65.2	-71.1	-71.1	-71.1	-71.1	-69.0	-69.0	-69.0	-69.0	-66.5	-66.4	-66.4	-66.4
	F_2O	-538.0	-538.0	-538.1	-537.3	-540.5	-540.5	-540.6	-539.7	-513.1	-513.1	-513.2	-512.0	-503.6	-503.6	-503.6	-502.7
	H_2O	349.3	349.3	349.3	349.3	335.2	335.2	335.2	335.2	339.9	339.9	339.9	339.9	336.2	336.2	336.2	336.2
	NNO	191.2	191.2	191.2	191.2	185.8	185.8	185.8	185.8	182.6	182.6	182.6	182.6	183.4	183.4	183.4	183.4
^{19}F	CH_3F	486.7	486.7	486.7	486.7	476.9	476.9	476.9	476.9	479.8	479.8	479.8	479.8	476.0	476.0	476.1	476.1
	CF_4	262.9	262.9	263.1	263.1	255.8	255.9	256.0	256.0	260.7	260.8	261.0	261.0	258.9	259.0	259.2	259.2
	F_2	-214.2	-214.2	-214.0	-214.0	-221.2	-221.2	-221.0	-220.9	-207.7	-207.7	-207.4	-207.5	-204.7	-204.7	-204.4	-204.6
	F_2O	-33.0	-33.0	-32.8	-33.1	-38.3	-38.3	-38.1	-38.3	-29.7	-29.7	-29.5	-29.9	-29.3	-29.3	-29.1	-29.5
	HF	436.8	436.8	436.8	436.8	418.2	418.2	418.2	418.2	425.7	425.7	425.8	425.8	419.9	419.9	419.9	419.9
	PF_3	227.2	227.2	227.2	227.2	218.9	219.0	218.9	219.0	227.1	227.1	227.1	227.1	224.8	224.9	224.8	224.8
^{31}P	PF_3	189.5	189.5	189.3	189.4	189.6	189.6	189.4	189.6	200.5	200.4	200.2	200.4	200.5	200.5	200.2	200.2
	PH_3	599.2	599.0	599.0	599.1	590.6	590.4	590.4	590.5	592.5	592.2	592.2	592.3	590.6	590.4	590.3	590.4
	PN	-46.5	-46.5	-46.5	-47.0	-49.1	-49.0	-49.1	-49.5	-48.8	-48.7	-48.8	-49.5	-43.9	-43.8	-44.0	-44.5

A.8.3 Statistical Data for SSCC Subsets

Table A.28.: Standard deviation (StD), mean signed (MSE) and mean absolute errors (MAE) in Hz from reference SSCC data for a variety of LH models (DFT/pcJ-4 level of theory).

		c07t[a]	c07ct[a]	c07tx[a]	c07ctx[a]	c12sif[a]	c14t[a]	c14t-nc[a]	c20t[a]	c20t-nc[a]
StD	$^{1}J_{HC}$	4.30	3.55	5.66	3.95	4.52	6.01	5.36	3.18	4.14
	$^{1}J_{CC}$	6.43	2.98	7.11	5.59	7.22	9.61	8.26	3.10	2.49
	$-^{1}J_{CO/CN}$	2.20	1.90	2.72	1.98	1.48	2.54	2.54	1.79	1.61
	$^{1}J_{CF}$	28.62	26.78	31.48	27.82	27.54	28.74	32.00	25.87	24.89
	$^{2}J_{HH}$	1.90	2.34	2.34	2.23	3.28	1.59	1.86	2.78	1.76
	$^{2}J_{HC}$	0.50	1.58	0.93	1.22	2.23	0.49	0.43	0.98	0.76
	$^{3}J_{HH}$	1.54	1.63	1.98	1.55	1.70	1.62	1.68	1.67	1.64
MSE	$^{1}J_{HC}$	-6.43	-19.19	3.84	-17.12	-30.04	4.69	-0.14	-11.00	-4.51
	$^{1}J_{CC}$	0.60	-12.69	8.00	-14.27	-20.87	8.52	3.93	-4.45	-5.65
	$-^{1}J_{CO/CN}$	-6.73	-10.55	-2.34	-8.90	-10.50	-4.35	-6.95	-5.76	-5.98
	$^{1}J_{CF}$	-93.52	-81.19	-81.66	-62.74	-59.88	-96.39	-103.51	-59.70	-58.59
	$^{2}J_{HH}$	-0.90	2.52	-3.79	1.81	1.49	1.46	-1.21	2.06	2.85
	$^{2}J_{HC}$	0.08	0.91	-1.25	0.92	0.40	0.79	0.05	1.68	2.13
	$^{3}J_{HH}$	-0.49	-1.59	0.77	-1.39	-1.83	-0.26	0.07	-1.51	-1.05
MAE	$^{1}J_{HC}$	6.43	19.19	5.45	17.12	30.04	5.77	5.05	11.00	4.79
	$^{1}J_{CC}$	5.88	12.69	8.00	14.27	20.87	8.97	7.01	4.67	5.65
	$-^{1}J_{CO/CN}$	6.73	10.55	3.13	8.90	10.50	4.67	6.95	5.76	5.98
	$^{1}J_{CF}$	93.52	81.19	81.66	62.74	59.88	96.39	103.51	59.70	58.59
	$^{2}J_{HH}$	1.75	3.29	4.06	2.59	3.18	1.56	1.97	3.21	2.86
	$^{2}J_{HC}$	0.42	1.64	1.29	1.30	2.15	0.82	0.36	1.68	2.13
	$^{3}J_{HH}$	1.03	1.76	1.68	1.52	2.04	0.94	1.18	1.70	1.21

[a] abbreviations of LH functionals c07t = cLH07t-SVWN, c12sif = cLH12ct-SsfiPW92, c14t = LH14t-calPBE, c20t = cLH20t; "t" vs. "ct" mark the spin-channel and common t-LMF, "x" denotes functionals with a non standard prefactor ($a = 0.709$), and "nc" is used for uncalibrated models.

A.8.4 Computed SSCCs of Various DFAs with Corrected PSO Contribution

Table A.29.: Comparison of computed SSCCs (in Hz) with various density functionals against CC3/aug-ccJ-pVTZ and MCSCF/BS2 reference data (DFT/pcJ-4 level of theory).

Molecule	Coupling		CC3[a]	MCSCF[b]	TPSS		TPSSh		B3LYP	PBE0	BHLYP
					τ_{MS}^{PSO}	τ_{D}^{PSO}	τ_{MS}^{PSO}	τ_{D}^{PSO}			
CH_4	$^1J_{HC}$			121.07	139.61	139.64	140.41	140.44	133.05	123.72	141.61
	$^2J_{HH}$			-12.89	-10.27	-10.17	-11.37	-11.28	-13.36	-13.90	-16.14
CH_3F	$^1J_{HC}$			144.35	163.64	163.68	164.91	164.94	154.61	144.69	165.68
	$^1J_{CF}$			-161.68	-255.28	-254.29	-243.85	-242.96	-226.99	-220.40	-190.22
	$^2J_{HH}$			-10.74	-5.12	-5.01	-6.38	-6.28	-10.05	-10.61	-12.65
	$^2J_{HF}$			48.09	57.05	57.17	57.65	57.76	53.66	51.63	58.91
C_2H_4	$^1J_{HC}$			153.57	172.73	172.76	174.27	174.29	166.70	156.44	178.56
	$^1J_{CC}$			69.63	71.78	71.58	74.33	74.15	73.38	70.53	87.10
	$^2J_{HH}$			1.06	8.32	8.44	7.06	7.17	3.29	1.37	0.59
	$^2J_{HC}$			-2.24	-0.67	-0.69	-1.77	-1.79	-1.42	-2.88	-5.54
	$^3J_{HH}$	(cis)		11.72	12.52	12.56	12.96	12.99	13.38	13.12	15.22
	$^3J_{HH}$	(trans)		18.25	22.54	22.61	22.85	22.91	20.48	20.11	22.87
C_2H_6	$^1J_{HC}$			124.56	139.70	139.73	140.76	140.79	133.32	124.63	142.61
	$^1J_{CC}$			35.51	34.70	34.70	36.14	36.14	33.79	31.53	41.92
	$^2J_{HH}$			-14.63	-10.21	-10.12	-11.37	-11.28	-13.68	-14.10	-16.51
	$^2J_{HC}$			-5.01	-3.34	-3.34	-3.88	-3.88	-3.47	-4.15	-5.14
	$^3J_{HH}$	(gauche)		3.61	3.80	3.82	3.90	3.93	4.34	4.05	4.69
	$^3J_{HH}$	(trans)		15.79	19.35	19.42	19.38	19.44	17.93	16.74	18.89
C_3H_4	$^1J_{HC}$	(CH)		229.75	249.97	249.98	252.24	252.25	245.36	231.47	260.30
	$^1J_{HC}$	(CH_2)		168.49	185.16	185.21	186.45	186.49	178.69	167.66	189.43
	$^1J_{CC}$	($\underline{C}H$–$\underline{C}H_2$)		10.55	7.24	7.23	8.77	8.76	8.82	8.03	15.62
	$^1J_{CC}$	($\underline{C}H$=$\underline{C}H$)		66.34	64.16	64.05	67.14	67.04	68.69	66.88	83.16
	$^2J_{HH}$			2.03	14.99	15.10	14.22	14.31	9.49	7.99	9.00
	$^2J_{HC}$	(C$\underline{H}$–$\underline{C}H_2$)		2.39	4.31	4.31	4.38	4.38	3.30	3.03	4.06
	$^2J_{HC}$	(C$\underline{H}$=$\underline{C}$H)		3.15	4.76	4.78	3.97	3.99	3.66	2.64	-0.01
	$^2J_{HC}$	(C$\underline{H}_2$-$\underline{C}$H)		-2.86	-0.87	-0.87	-1.24	-1.25	-1.75	-2.24	-2.73
	$^3J_{HH}$	(C$\underline{H}$=C$\underline{H}$)		6.48	1.11	1.18	1.53	1.59	2.28	2.58	4.29
	$^3J_{HH}$	(C$\underline{H}$–C$\underline{H}_2$)		-2.15	-2.31	-2.26	-2.45	-2.41	-2.12	-2.22	-2.58
CO	$^1J_{CO}$		14.62	15.17	22.26	22.66	20.81	21.16	18.70	20.61	11.51
CO_2	$^1J_{CO}$			15.67	29.22	29.23	27.05	27.06	23.45	24.17	15.64
	$^2J_{OO}$			2.36	-0.22	-0.09	0.89	1.02	2.43	2.48	6.60
H_2CO	$^1J_{HC}$		167.89		190.47	190.50	192.45	192.47	185.30	173.25	198.15
	$^1J_{CO}$		26.98		37.58	38.26	35.43	36.05	35.37	35.21	24.61
	$^2J_{HH}$		37.29		56.18	56.31	54.87	54.98	45.00	40.96	44.67
	$^2J_{HO}$		-3.01		-3.69	-3.61	-3.77	-3.69	-2.91	-2.50	-2.95

Continuing Table A.29

HFCO	$^{1}J_{HC}$		242.4		281.90	281.98	283.92	284.00	270.37	254.00	284.99
	$^{1}J_{CO}$		14.67		26.82	26.99	24.36	24.51	22.31	22.33	12.09
	$^{1}J_{CF}$		-352.41		-478.08	-478.93	-464.21	-464.95	-450.35	-439.08	-407.59
	$^{2}J_{HO}$		-10.01		-10.56	-10.58	-10.57	-10.59	-10.61	-9.90	-10.12
	$^{2}J_{HF}$		182.86		203.25	203.34	201.86	201.94	200.48	188.51	203.27
	$^{2}J_{OF}$		48.74		72.75	74.91	67.78	69.77	71.10	69.78	47.98
F_2CO	$^{1}J_{CO}$		12.08		28.11	28.12	25.04	25.05	21.30	21.36	10.52
	$^{1}J_{CF}$		-294.39		-438.45	-439.06	-420.71	-421.27	-403.13	-393.66	-348.15
	$^{2}J_{OF}$		39.78		57.38	58.47	54.02	55.03	53.97	53.39	39.62
	$^{2}J_{FF}$		-100.2		-266.49	-271.29	-247.58	-251.78	-232.94	-233.28	-162.93
HCN	$^{1}J_{HC}$		249.95	257.92	288.22	288.20	291.82	291.80	286.19	267.08	306.03
	$^{1}J_{CN}$		-18.19	-19.07	-12.17	-12.29	-14.84	-14.97	-18.20	-16.94	-30.32
	$^{2}J_{HN}$		-7.47	-8.24	-5.17	-5.29	-5.98	-6.10	-7.52	-7.40	-8.50
FCN	$^{1}J_{CN}$		-5.63		10.13	9.89	5.77	5.53	-0.56	0.51	-17.55
	$^{1}J_{CF}$		-403		-601.90	-603.12	-579.21	-580.41	-550.19	-544.02	-493.90
	$^{2}J_{NF}$		53.12		64.88	65.09	59.22	59.38	54.89	53.42	34.57
C_2H_2	$^{1}J_{HC}$		240.44	247.65	284.95	284.90	286.65	286.60	275.36	258.82	291.34
	$^{1}J_{CC}$		180.96	185.66	190.91	191.30	194.23	194.61	205.74	198.35	222.27
	$^{2}J_{HC}$		53.07	53.63	58.86	59.06	58.27	58.46	56.66	54.09	54.73
	$^{3}J_{HH}$		9.95	10.72	12.22	12.33	12.91	13.02	11.45	12.64	15.09
CHCF	$^{1}J_{HC}$		270.08		320.17	320.14	321.40	321.36	307.86	290.36	324.08
	$^{1}J_{CC}$		268.11		276.92	277.37	281.46	281.89	296.68	287.21	316.95
	$^{1}J_{CF}$		-277.68		-439.04	-440.07	-427.71	-428.74	-405.99	-406.69	-371.28
	$^{2}J_{HC}$		68.53		80.08	80.26	78.89	79.06	74.78	71.70	72.34
	$^{2}J_{CF}$		25.56		20.69	21.13	27.50	27.96	28.72	30.50	58.20
	$^{3}J_{HF}$		14.45		19.34	19.80	16.88	17.31	18.55	16.75	9.35
C_2F_2	$^{1}J_{CC}$		401.65		424.21	424.67	429.03	429.47	445.27	433.67	467.70
	$^{1}J_{CF}$		-256.58		-424.46	-424.99	-413.67	-414.23	-389.28	-390.26	-354.27
	$^{2}J_{CF}$		45.54		41.66	42.29	47.27	47.87	48.00	49.85	74.01
	$^{3}J_{FF}$		2.56		4.57	3.51	11.24	10.42	26.45	20.17	48.70
FNO	$^{1}J_{NO}$		-34.14		-41.96	-42.48	-41.12	-41.62	-41.94	-41.52	-34.42
	$^{1}J_{NF}$		152.73		170.40	172.32	180.83	182.42	187.76	190.94	233.88
	$^{2}J_{OF}$		130.22		175.70	183.40	174.24	181.64	191.14	190.28	156.97
HD	$^{1}J_{DH}$			41.22	41.10	41.21	41.67	41.83	49.38	45.13	51.55
HF	$^{1}J_{HF}$			538.4	372.21	374.18	396.59	398.35	449.25	433.75	530.17
N_2	$^{1}J_{NN}$	^{14}N-^{15}N		1.3	2.42	2.47	1.84	1.87	1.04	1.41	-1.98
NH_3	$^{1}J_{HN}$			-61.65*	-64.67	-64.68	-65.38	-65.39	-64.43	-60.28	-69.39
	$^{2}J_{HH}$			-10.6	-7.11	-6.98	-8.31	-8.20	-10.17	-10.18	-13.59
H_2O	$^{1}J_{HO}$		-81.19	-81.19	-71.21	-71.30	-73.57	-73.65	-77.63	-73.63	-87.18
	$^{2}J_{HH}$		-7.84	-8.31	-4.06	-3.89	-5.32	-5.17	-7.39	-7.28	-11.22
OHF	$^{1}J_{HO}$		-49.7		-27.41	-26.73	-31.49	-30.86	-35.52	-32.91	-49.66
	$^{1}J_{OF}$		-565.79		-659.76	-685.56	-680.53	-704.36	-731.44	-743.11	-813.25
	$^{2}J_{HF}$		89.93		102.12	106.14	104.18	107.86	113.07	114.64	115.33
OF_2	$^{1}J_{OF}$		-251.99		-251.74	-265.60	-286.46	-299.99	-319.03	-339.78	-441.27
	$^{2}J_{FF}$		1327.34		1808.58	1865.06	1766.86	1815.86	1790.42	1777.10	1734.43

[a] Ref. 388; [b] Ref. 387 (and references therein); * Recalculated for ^{15}N.

Table A.30.: Comparison of computed SSCCs (in Hz) with various density functionals against CC3/aug-ccJ-pVTZ and MCSCF/BS2 reference data (DFT/pcJ-4 level of theory).

Molecule	Coupling		CC3[a]	MCSCF[b]	LH07t-SVWN		LH12ct-SsirPW92		LH12ct-SsifPW92		LH14t-calPBE		LH20t	
					τ_{MS}^{PSO}	τ_{D}^{PSO}	τ_{MS}^{PSO}	τ_{D}^{PSO}	τ_{MS}^{PSO}	τ_{D}^{PSO}	τ_{MS}^{PSO}	τ_{D}^{PSO}	τ_{MS}^{PSO}	τ_{D}^{PSO}
CH_4	$^1J_{HC}$			121.07	114.33	114.35	100.49	100.50	97.53	97.53	122.71	122.72	113.02	113.03
	$^2J_{HH}$			-12.89	-15.15	-15.13	-10.32	-10.32	-10.33	-10.35	-13.34	-13.31	-10.24	-10.20
CH_3F	$^1J_{HC}$			144.35	135.42	135.42	118.95	118.94	115.74	115.72	144.89	144.91	131.51	131.55
	$^1J_{CF}$			-161.68	-206.90	-206.62	-188.65	-188.58	-183.71	-183.77	-208.29	-208.11	-179.16	-179.24
	$^2J_{HH}$			-10.74	-12.42	-12.40	-8.21	-8.22	-8.44	-8.47	-10.07	-10.03	-7.56	-7.49
	$^2J_{HF}$			48.09	50.43	50.65	37.12	37.38	35.78	36.06	54.10	54.15	44.22	44.15
C_2H_4	$^1J_{HC}$			153.57	145.43	145.43	128.67	128.66	125.48	125.46	154.61	154.63	142.23	142.28
	$^1J_{CC}$			69.63	65.37	65.33	50.71	50.71	48.54	48.57	72.59	72.57	61.85	61.98
	$^2J_{HH}$			1.06	-1.16	-1.14	1.99	1.98	1.58	1.55	1.42	1.46	2.86	2.91
	$^2J_{HC}$			-2.24	-2.26	-2.27	0.37	0.37	0.37	0.37	-2.35	-2.35	0.30	0.33
	$^3J_{HH}$	(cis)		11.72	12.40	12.40	10.37	10.37	10.31	10.30	12.30	12.31	10.56	10.58
	$^3J_{HH}$	(trans)		18.25	17.69	17.71	15.24	15.24	14.95	14.95	18.56	18.58	15.51	15.54
C_2H_6	$^1J_{HC}$			124.56	115.76	115.77	101.35	101.36	98.49	98.49	124.01	124.02	113.99	114.00
	$^1J_{CC}$			35.51	29.83	29.83	19.77	19.77	18.24	18.24	34.41	34.41	28.84	28.83
	$^2J_{HH}$			-14.63	-15.31	-15.29	-10.62	-10.63	-10.67	-10.70	-13.41	-13.38	-10.47	-10.43
	$^2J_{HC}$			-5.01	-4.24	-4.24	-2.55	-2.55	-2.53	-2.52	-4.11	-4.11	-2.54	-2.54
	$^3J_{HH}$	(gauche)		3.61	3.86	3.87	3.26	3.26	3.23	3.22	3.87	3.87	3.52	3.53
	$^3J_{HH}$	(trans)		15.79	15.03	15.05	13.61	13.61	13.33	13.32	15.99	16.01	14.48	14.50
C_3H_4	$^1J_{HC}$	(CH)		229.75	215.21	215.19	194.02	194.00	190.13	190.10	226.78	226.80	211.08	211.16
	$^1J_{HC}$	(CH_2)		168.49	156.58	156.59	139.73	139.73	136.44	136.43	166.04	166.05	153.83	153.86
	$^1J_{CC}$	($\underline{C}H–\underline{C}H_2$)		10.55	7.08	7.07	1.45	1.45	0.77	0.76	10.10	10.09	6.77	6.78
	$^1J_{CC}$	($\underline{C}H=\underline{C}H$)		66.34	61.36	61.34	49.40	49.41	47.79	47.81	68.24	68.23	57.96	58.02
	$^2J_{HH}$			2.03	4.68	4.70	6.53	6.52	6.07	6.04	7.29	7.32	7.26	7.31
	$^2J_{HC}$	($C\underline{H}–\underline{C}H_2$)		2.39	2.36	2.36	1.65	1.66	1.48	1.49	3.17	3.17	2.94	2.94
	$^2J_{HC}$	($C\underline{H}=\underline{C}H$)		3.15	3.64	3.64	5.63	5.62	5.70	5.69	3.68	3.69	6.02	6.04
	$^2J_{HC}$	($C\underline{H}_2$-$\underline{C}H$)		-2.86	-2.38	-2.38	-1.50	-1.50	-1.54	-1.54	-1.91	-1.91	-0.89	-0.89
	$^3J_{HH}$	($C\underline{H}=C\underline{H}$)		6.48	2.43	2.45	1.69	1.69	1.74	1.73	2.27	2.29	1.64	1.67
	$^3J_{HH}$	($C\underline{H}–C\underline{H}_2$)		-2.15	-2.08	-2.07	-1.47	-1.47	-1.42	-1.43	-2.02	-2.01	-1.48	-1.47
CO	$^1J_{CO}$		14.62	15.17	20.04	20.16	24.49	24.51	24.87	24.83	18.38	18.44	20.98	20.88
CO_2	$^1J_{CO}$			15.67	23.94	23.94	26.93	26.92	27.01	27.01	22.09	22.10	22.80	22.77
	$^2J_{OO}$			2.36	1.34	1.31	1.04	0.97	1.09	1.00	2.27	2.25	2.30	2.27
H_2CO	$^1J_{HC}$		167.89		165.02	165.00	146.66	146.62	143.46	143.41	173.99	174.01	160.71	160.79
	$^1J_{CO}$		26.98		34.33	34.58	37.16	37.26	37.25	37.26	32.42	32.53	32.95	32.71
	$^2J_{HH}$		37.29		33.43	33.45	31.81	31.79	30.59	30.54	38.32	38.36	32.62	32.69
	$^2J_{HO}$		-3.01		-3.03	-2.98	-1.96	-1.92	-1.82	-1.77	-3.60	-3.61	-2.88	-2.97

Continuing Table A.30

HFCO	$^{1}J_{HC}$		242.4		241.56	241.56	217.08	217.04	212.71	212.65	254.42	254.46	231.69	231.78
	$^{1}J_{CO}$		14.67		22.24	22.28	25.59	25.59	25.67	25.65	19.95	19.97	21.06	20.96
	$^{1}J_{CF}$		-352.41		-421.19	-421.32	-384.61	-384.56	-377.55	-377.41	-427.04	-427.08	-386.37	-385.81
	$^{2}J_{HO}$		-10.01		-10.73	-10.74	-9.81	-9.81	-9.75	-9.74	-10.87	-10.89	-10.32	-10.38
	$^{2}J_{HF}$		182.86		182.98	183.07	155.32	155.37	152.42	152.45	188.84	188.96	165.43	165.69
	$^{2}J_{OF}$		48.74		66.46	66.77	76.81	76.71	76.89	76.55	60.25	60.31	68.76	67.87
F_2CO	$^{1}J_{CO}$		12.08		21.36	21.36	24.39	24.38	24.35	24.34	19.15	19.15	19.81	19.75
	$^{1}J_{CF}$		-294.39		-385.74	-385.82	-358.94	-358.90	-352.91	-352.80	-386.80	-386.80	-355.01	-354.44
	$^{2}J_{OF}$		39.78		50.03	50.17	55.64	55.57	55.44	55.25	46.69	46.68	51.46	50.87
	$^{2}J_{FF}$		-100.2		-198.41	-198.23	-229.83	-228.85	-227.24	-225.84	-184.77	-184.37	-200.09	-197.65
HCN	$^{1}J_{HC}$		249.95	257.92	249.17	249.13	224.30	224.26	219.46	219.42	263.25	263.27	241.83	241.96
	$^{1}J_{CN}$		-18.19	-19.07	-16.11	-16.17	-11.32	-11.36	-10.93	-10.94	-19.31	-19.31	-16.61	-16.47
	$^{2}J_{HN}$		-7.47	-8.24	-9.01	-9.06	-9.64	-9.65	-9.86	-9.85	-8.91	-8.94	-9.78	-9.75
FCN	$^{1}J_{CN}$		-5.63		1.24	1.16	5.49	5.48	5.56	5.58	-2.24	-2.24	-0.25	-0.06
	$^{1}J_{CF}$		-403		-527.45	-527.77	-488.08	-488.09	-480.96	-480.78	-530.99	-531.03	-486.54	-485.54
	$^{2}J_{NF}$		53.12		52.58	52.75	50.74	50.93	49.74	49.93	50.07	50.15	48.61	48.53
C_2H_2	$^{1}J_{HC}$		240.44	247.65	237.46	237.40	213.17	213.12	208.22	208.17	251.77	251.79	230.99	231.13
	$^{1}J_{CC}$		180.96	185.66	187.06	187.23	166.31	166.39	163.29	163.30	195.75	195.76	182.06	181.72
	$^{2}J_{HC}$		53.07	53.63	52.26	52.34	51.30	51.33	50.88	50.87	53.81	53.85	53.37	53.30
	$^{3}J_{HH}$		9.95	10.72	10.76	10.80	8.73	8.75	8.72	8.72	10.76	10.79	8.75	8.75
CHCF	$^{1}J_{HC}$		270.08		266.01	265.97	240.15	240.13	234.77	234.75	281.50	281.52	259.88	259.99
	$^{1}J_{CC}$		268.11		272.28	272.43	243.80	243.83	239.76	239.72	283.51	283.52	264.34	263.95
	$^{1}J_{CF}$		-277.68		-391.76	-392.18	-368.49	-368.65	-364.26	-364.25	-394.57	-394.63	-359.61	-358.69
	$^{2}J_{HC}$		68.53		68.06	68.12	66.22	66.23	65.54	65.52	70.19	70.21	69.70	69.63
	$^{2}J_{CF}$		25.56		30.85	30.88	15.68	15.56	15.23	15.02	38.80	38.73	28.16	27.87
	$^{3}J_{HF}$		14.45		16.44	16.63	21.19	21.28	21.37	21.39	15.40	15.50	19.70	19.65
C_2F_2	$^{1}J_{CC}$		401.65		413.61	413.72	373.80	373.79	368.35	368.27	427.84	427.83	400.71	400.28
	$^{1}J_{CF}$		-256.58		-372.97	-373.11	-350.87	-350.84	-346.15	-346.01	-376.44	-376.40	-340.95	-340.22
	$^{2}J_{CF}$		45.54		49.38	49.42	30.93	30.79	30.20	29.95	57.61	57.53	44.54	44.16
	$^{3}J_{FF}$		2.56		22.80	21.32	-1.67	-3.33	-3.71	-5.42	29.70	29.09	3.27	2.98
FNO	$^{1}J_{NO}$		-34.14		-40.51	-40.66	-42.77	-42.80	-42.82	-42.78	-39.33	-39.38	-40.95	-40.69
	$^{1}J_{NF}$		152.73		166.77	167.07	143.29	143.27	140.82	140.64	176.87	176.93	166.88	166.27
	$^{2}J_{OF}$		130.22		174.41	176.02	188.50	188.57	188.73	187.84	167.23	167.54	179.06	175.72
HD	$^{1}J_{DH}$			41.22	40.39	40.41	38.00	37.90	37.95	37.70	42.85	42.93	23.98	24.12
HF	$^{1}J_{HF}$			538.4	441.50	443.24	421.70	423.54	424.89	426.69	452.44	452.77	501.45	500.17
N_2	$^{1}J_{NN}$	^{14}N-^{15}N		1.3	1.77	1.78	3.01	3.01	3.13	3.12	1.03	1.03	1.87	1.87
NH_3	$^{1}J_{HN}$			-61.65*	-57.43	-57.46	-51.21	-51.23	-50.12	-50.15	-60.80	-60.80	-59.51	-59.49
	$^{2}J_{HH}$			-10.6	-10.50	-10.45	-7.58	-7.56	-7.52	-7.52	-9.02	-8.97	-8.30	-8.26
H_2O	$^{1}J_{HO}$		-81.19	-81.19	-73.02	-73.12	-66.69	-66.79	-66.23	-66.33	-76.06	-76.08	-79.03	-78.93
	$^{2}J_{HH}$		-7.84	-8.31	-7.33	-7.25	-5.52	-5.46	-5.53	-5.49	-6.18	-6.12	-6.44	-6.40
OHF	$^{1}J_{HO}$		-49.7		-36.44	-36.31	-32.57	-32.59	-32.75	-32.86	-39.16	-39.11	-45.00	-45.22
	$^{1}J_{OF}$		-565.79		-652.73	-659.09	-632.40	-633.89	-631.39	-629.95	-673.82	-675.75	-639.40	-630.13
	$^{2}J_{HF}$		89.93		106.70	108.07	100.11	100.83	100.07	100.38	105.74	106.09	98.68	97.20
OF_2	$^{1}J_{OF}$		-251.99		-283.09	-286.64	-285.54	-286.10	-289.66	-288.36	-299.09	-300.18	-286.85	-281.61
	$^{2}J_{FF}$		1327.34		1584.60	1594.57	1380.62	1381.18	1355.22	1350.51	1650.62	1653.05	1455.65	1438.89

[a] Ref. 388; [b] Ref. 387 (and references therein); * Recalculated for ^{15}N.

Table A.31.: Comparison of computed SSCCs (in Hz) with various density functionals against CC3/aug-ccJ-pVTZ and MCSCF/BS2 reference data (DFT/pcJ-4 level of theory).

Molecule	Coupling		CC3[a]	MCSCF[b]	c07ct	c07tx	c07ctx	cLH14t-nc	cLH20t-nc
CH_4	$^1J_{HC}$			121.07	105.79	121.71	107.77	118.44	116.66
	$^2J_{HH}$			-12.89	-10.12	-19.31	-11.16	-16.10	-10.55
CH_3F	$^1J_{HC}$			144.35	124.47	145.51	127.65	140.28	137.05
	$^1J_{CF}$			-161.68	-201.27	-193.01	-186.93	-211.14	-180.11
	$^2J_{HH}$			-10.74	-7.63	-16.12	-8.43	-13.17	-7.74
	$^2J_{HF}$			48.09	39.89	55.76	39.92	52.90	44.39
C_2H_4	$^1J_{HC}$			153.57	134.42	154.86	136.40	150.49	147.18
	$^1J_{CC}$			69.63	54.60	74.34	55.87	67.89	61.50
	$^2J_{HH}$			1.06	2.89	-4.68	2.29	-1.64	3.67
	$^2J_{HC}$			-2.24	0.38	-5.16	0.09	-3.01	0.10
	$^3J_{HH}$	(cis)		11.72	10.54	14.12	10.55	13.04	11.22
	$^3J_{HH}$	(trans)		18.25	15.79	19.82	16.09	18.78	16.89
C_2H_6	$^1J_{HC}$			124.56	106.44	123.65	108.48	119.96	117.62
	$^1J_{CC}$			35.51	22.42	36.08	24.04	31.18	28.64
	$^2J_{HH}$			-14.63	-10.33	-19.40	-11.36	-16.25	-10.77
	$^2J_{HC}$			-5.01	-2.55	-5.81	-2.91	-4.57	-2.72
	$^3J_{HH}$	(gauche)		3.61	3.31	4.28	3.34	4.06	3.61
	$^3J_{HH}$	(trans)		15.79	14.17	15.68	14.20	15.58	15.24
C_3H_4	$^1J_{HC}$	(CH)		229.75	201.37	224.88	202.23	222.28	217.68
	$^1J_{HC}$	(CH_2)		168.49	145.60	165.43	147.78	161.81	158.61
	$^1J_{CC}$	($\underline{C}H$–$\underline{C}H_2$)		10.55	2.47	11.58	3.98	8.02	6.79
	$^1J_{CC}$	($\underline{C}H$=$\underline{C}H$)		66.34	52.33	68.95	53.21	64.16	57.69
	$^2J_{HH}$			2.03	7.41	3.10	7.42	4.78	8.61
	$^2J_{HC}$	(C$\underline{H}$–$\underline{C}H_2$)		2.39	1.98	2.54	2.00	2.46	3.01
	$^2J_{HC}$	(C$\underline{H}$=$\underline{C}$H)		3.15	5.51	1.20	5.22	2.95	6.16
	$^2J_{HC}$	(C$\underline{H}_2$-$\underline{C}$H)		-2.86	-1.38	-3.36	-1.61	-2.56	-0.95
	$^3J_{HH}$	(C$\underline{H}$=C$\underline{H}$)		6.48	1.59	3.79	1.85	2.84	1.65
	$^3J_{HH}$	(C$\underline{H}$–C$\underline{H}_2$)		-2.15	-1.53	-2.54	-1.69	-2.20	-1.60
CO	$^1J_{CO}$		14.62	15.17	24.20	16.68	23.16	20.62	21.35
CO_2	$^1J_{CO}$			15.67	26.93	21.56	26.53	24.89	22.68
	$^2J_{OO}$			2.36	0.82	2.20	1.08	1.69	1.96
H_2CO	$^1J_{HC}$		167.89		152.16	176.37	155.29	170.10	166.73
	$^1J_{CO}$		26.98		37.94	29.02	35.10	34.62	32.95
	$^2J_{HH}$		37.29		34.23	32.71	34.19	34.95	37.24
	$^2J_{HO}$		-3.01		-2.08	-3.58	-2.55	-3.24	-2.97

Continuing Table A.31

HFCO	$^{1}J_{HC}$		242.4		225.05	254.64	227.86	249.18	243.09
	$^{1}J_{CO}$		14.67		25.93	17.86	24.18	22.45	21.04
	$^{1}J_{CF}$		-352.41		-404.17	-404.12	-379.18	-428.92	-385.97
	$^{2}J_{HO}$		-10.01		-9.91	-10.99	-10.01	-10.84	-10.65
	$^{2}J_{HF}$		182.86		162.33	188.18	156.50	186.62	170.81
	$^{2}J_{OF}$		48.74		78.77	51.60	70.94	65.51	67.46
F_2CO	$^{1}J_{CO}$		12.08		24.84	17.45	23.49	21.88	19.59
	$^{1}J_{CF}$		-294.39		-375.19	-370.22	-355.74	-393.87	-351.68
	$^{2}J_{OF}$		39.78		57.17	41.06	52.77	49.68	50.28
	$^{2}J_{FF}$		-100.2		-240.55	-149.70	-214.94	-202.17	-188.57
HCN	$^{1}J_{HC}$		249.95	257.92	233.32	261.34	235.17	257.37	250.84
	$^{1}J_{CN}$		-18.19	-19.07	-11.76	-20.94	-13.30	-16.71	-15.95
	$^{2}J_{HN}$		-7.47	-8.24	-9.02	-9.60	-10.04	-9.08	-9.75
FCN	$^{1}J_{CN}$		-5.63		5.98	-5.06	3.37	1.09	0.40
	$^{1}J_{CF}$		-403		-508.07	-515.56	-484.32	-541.14	-484.53
	$^{2}J_{NF}$		53.12		54.09	44.41	48.60	51.84	49.11
C_2H_2	$^{1}J_{HC}$		240.44	247.65	222.50	248.80	223.90	245.81	239.12
	$^{1}J_{CC}$		180.96	185.66	172.80	194.95	170.44	190.71	179.61
	$^{2}J_{HC}$		53.07	53.63	52.02	51.54	52.71	52.94	54.81
	$^{3}J_{HH}$		9.95	10.72	8.68	13.90	9.58	12.01	9.30
CHCF	$^{1}J_{HC}$		270.08		250.36	277.59	251.72	275.31	268.38
	$^{1}J_{CC}$		268.11		252.75	280.89	248.05	277.38	261.22
	$^{1}J_{CF}$		-277.68		-380.69	-385.98	-366.11	-404.83	-358.16
	$^{2}J_{HC}$		68.53		67.45	67.33	67.95	69.15	71.54
	$^{2}J_{CF}$		25.56		15.90	48.25	19.59	34.41	27.69
	$^{3}J_{HF}$		14.45		21.49	9.44	19.47	15.09	20.38
C_2F_2	$^{1}J_{CC}$		401.65		386.54	421.96	377.26	420.95	397.79
	$^{1}J_{CF}$		-256.58		-363.46	-366.81	-349.90	-386.90	-336.85
	$^{2}J_{CF}$		45.54		32.28	65.44	33.51	52.91	44.33
	$^{3}J_{FF}$		2.56		2.59	30.64	-4.63	24.52	-2.01
FNO	$^{1}J_{NO}$		-34.14		-43.21	-37.23	-41.66	-40.86	-40.62
	$^{1}J_{NF}$		152.73		149.09	174.87	144.87	170.61	168.32
	$^{2}J_{OF}$		130.22		192.82	150.62	178.94	176.06	174.77
HD	$^{1}J_{DH}$			41.22	38.14	43.32	39.78	42.97	42.10
HF	$^{1}J_{HF}$			538.4	415.79	462.96	419.30	437.86	479.00
N_2	$^{1}J_{NN}$	^{14}N-^{15}N		1.3	2.89	0.65	2.49	1.66	2.00
NH_3	$^{1}J_{HN}$			-61.65*	-53.27	-59.91	-53.40	-58.61	-58.65
	$^{2}J_{HH}$			-10.6	-7.42	-13.37	-8.51	-11.03	-8.03
H_2O	$^{1}J_{HO}$		-81.19	-81.19	-67.53	-76.45	-67.75	-73.47	-76.07
	$^{2}J_{HH}$		-7.84	-8.31	-5.17	-9.58	-6.26	-7.54	-5.98
OHF	$^{1}J_{HO}$		-49.7		-31.19	-42.58	-34.43	-36.25	-41.87
	$^{1}J_{OF}$		-565.79		-647.66	-640.47	-621.80	-679.12	-624.28
	$^{2}J_{HF}$		89.93		102.84	105.47	98.07	108.60	98.03
OF_2	$^{1}J_{OF}$		-251.99		-279.07	-303.94	-290.84	-304.88	-277.65
	$^{2}J_{FF}$		1327.34		1477.76	1487.31	1320.94	1617.16	1438.96

A.8.5 $^1J_{CF}$ Coupling Constants for Various DFAs with Corrected PSO Contribution

Table A.32.: Comparison of computed contributions to the $^1J_{CF}$ SSCCs with various density functionals against CC3/aug-ccJpVTZ reference data (DFT/pcJ-4 level of theory).

		CC3	TPSS	TPSSh	B3LYP	PBE0	BHLYP	07t[b]	12sir[b]	12sif[b]	14t[b]	LH20t
FCCF	FC	-241.57	-400.36	-384.67	-357.81	-355.82	-308.95	-348.08	-328.19	-323.51	-349.35	-315.39
	SD	-7.52	-13.42	-15.33	-14.01	-15.91	-19.61	-11.05	-8.21	-7.92	-12.77	-8.83
	PSO	-8.08	-11.27	-14.26	-18.04	-19.12	-26.29	-14.42	-15.05	-15.29	-14.91	-17.32
	PSO (τ_D)		-11.80	-14.83	–	–	–	-14.56	-15.02	-15.15	-14.87	-16.59
	DSO	0.59	0.59	0.59	0.58	0.58	0.58	0.58	0.58	0.58	0.58	0.58
	Σ	-256.58	-424.46	-413.67	-389.28	-390.26	-354.27	-372.97	-350.87	-346.15	-376.44	-340.95
	Σ (τ_D)		-424.99	-414.23	–	–	–	-373.11	-350.84	-346.01	-376.40	-340.22
F_2CO	FC	-256.94	-394.57	-375.72	-355.19	-346.15	-298.65	-342.54	-317.24	-311.56	-342.84	-312.29
	SD	0	-0.91	-1.42	-1.46	-1.97	-2.78	-1.12	-0.63	-0.62	-1.48	-0.43
	PSO	-38.61	-44.14	-44.74	-47.63	-46.71	-47.89	-43.24	-42.23	-41.88	-43.64	-43.45
	PSO (τ_D)		-44.75	-45.29	–	–	–	-43.32	-42.19	-41.77	-43.64	-42.89
	DSO	1.17	1.17	1.17	1.16	1.16	1.15	1.16	1.16	1.16	1.16	1.16
	Σ	-294.39	-438.45	-420.71	-403.13	-393.66	-348.15	-385.74	-358.94	-352.91	-386.80	-355.01
	Σ (τ_D)		-439.06	-421.27	–	–	–	-385.82	-358.90	-352.80	-386.80	-354.44
FCCH	FC	-247.47	-398.12	-381.47	-356.20	-353.56	-305.58	-349.14	-328.18	-323.82	-349.57	-316.72
	SD	-9.73	-16.60	-18.81	-17.41	-19.64	-24.35	-14.32	-11.04	-10.73	-16.35	-11.84
	PSO	-20.96	-24.81	-27.92	-32.86	-33.96	-41.81	-28.77	-29.74	-30.18	-29.13	-31.53
	PSO (τ_D)		-25.84	-28.95	–	–	–	-29.20	-29.90	-30.17	-29.19	-30.60
	DSO	0.49	0.49	0.49	0.48	0.48	0.47	0.47	0.47	0.47	0.48	0.48
	Σ	-277.68	-439.04	-427.71	-405.99	-406.69	-371.28	-391.76	-368.49	-364.26	-394.57	-359.61
	Σ (τ_D)		-440.07	-428.74	–	–	–	-392.18	-368.65	-364.25	-394.63	-358.69
FCN	FC	-365.36	-556.46	-527.63	-493.85	-484.74	-418.39	-477.94	-439.97	-432.60	-478.88	-434.61
	SD	-9.67	-14.78	-17.42	-16.98	-18.73	-25.59	-14.04	-11.48	-11.26	-16.09	-12.87
	PSO	-28.55	-31.23	-34.72	-39.91	-41.11	-50.47	-36.02	-37.17	-37.64	-36.57	-39.61
	PSO (τ_D)		-32.45	-35.93	–	–	–	-36.34	-37.19	-37.46	-36.61	-38.61
	DSO	0.57	0.57	0.56	0.55	0.56	0.54	0.55	0.55	0.55	0.55	0.55
	Σ	-403	-601.90	-579.21	-550.19	-544.02	-493.90	-527.45	-488.08	-480.96	-530.99	-486.54
	Σ (τ_D)		-603.12	-580.41	–	–	–	-527.77	-488.09	-480.78	-531.03	-485.54
HFCO	FC	-314.6	-427.18	-413.58	-397.83	-387.22	-357.29	-374.18	-340.26	-333.84	-379.56	-341.79
	SD	1.18	-0.54	-1.13	-1.06	-1.68	-2.66	-0.64	0.06	0.07	-0.96	0.38
	PSO	-39.7	-51.07	-50.22	-52.17	-50.89	-48.35	-47.09	-45.12	-44.50	-47.24	-45.67
	PSO (τ_D)		-51.92	-50.96	–	–	–	-47.22	-45.07	-44.36	-47.29	-45.11
	DSO	0.72	0.72	0.72	0.71	0.72	0.71	0.71	0.71	0.71	0.71	0.71
	Σ	-352.41	-478.08	-464.21	-450.35	-439.08	-407.59	-421.19	-384.61	-377.55	-427.04	-386.37
	Σ (τ_D)		-478.93	-464.95	–	–	–	-421.32	-384.56	-377.41	-427.08	-385.81

[a] see Ref.[388]; [b] Abbreviations for functional acronyms 07t=LH07t-SVWN, 12sir=LH12ct-SsirPW92, 12sif=LH12ct-SsifPW92, 14t=LH14t-calPBE.

Bibliography

[1] Purcell, E. M.; Torrey, H. C.; Pound, R. V. Resonance Absorption by Nuclear Magnetic Moments in a Solid. *Phys. Rev.* **1946**, *69*, 37–38.

[2] Bloch, F.; Hansen, W. W.; Packard, M. Nuclear Induction. *Phys. Rev.* **1946**, *69*, 127.

[3] Bloch, F. Nuclear Induction. *Phys. Rev.* **1946**, *70*, 460–474.

[4] Bloch, F.; Hansen, W. W.; Packard, M. The Nuclear Induction Experiment. *Phys. Rev.* **1946**, *70*, 474–485.

[5] Harris, R. K., Mann, B. E., Eds. *NMR and the Periodic Table*; Academic Press: London, 1978.

[6] Mason, J. *Multinuclear NMR*; Plenum Press: New York, 1987.

[7] Pregosin, P. S., Ed. *Transition metal nuclear magnetic resonance*; Elsevier: Amsterdam u.a., 1991.

[8] Kaupp, M., Bühl, M., Malkin, V. G., Eds. *Calculation of NMR and EPR parameters: theory and applications*; John Wiley & Sons: Weinheim, 2004.

[9] Local version derived from TURBOMOLE version 7.5, TURBOMOLE GmbH, 2020. TURBOMOLE is a development of University of Karlsruhe and Forschungszentrum Karlsruhe 1989-2007, TURBOMOLE GmbH since 2007.

[10] CFOUR, a quantum chemical program package written by J.F. Stanton, J. Gauss, L. Cheng, M.E. Harding, D.A. Matthews, P.G. Szalay, with contributions from A.A. Auer, R.J. Bartlett, U. Benedikt, C. Berger, D.E. Bernholdt, Y.J. Bomble, O. Christiansen, F. Engel, R. Faber, M. Heckert, O. Heun, M. Hilgenberg, C. Huber, T.-C. Jagau, D. Jonsson, J. Jusélius, T. Kirsch, K. Klein, W.J. Lauderdale, F.

Lipparini, T. Metzroth, L.A. Mück, D.P. O'Neill, D.R. Price, E. Prochnow, C. Puzzarini, K. Ruud, F. Schiffmann, W. Schwalbach, C. Simmons, S. Stopkowicz, A. Tajti, J. Vázquez, F. Wang, J.D. Watts and the integral packages MOLECULE (J. Almlöf and P.R. Taylor), PROPS (P.R. Taylor), ABACUS (T. Helgaker, H.J. Aa. Jensen, P. Jørgensen, and J. Olsen), and ECP routines by A. V. Mitin and C. van Wüllen. For the current version, see http://www.cfour.de.

[11] Neese, F. Software update: the ORCA program system, version 4.0. *Wiley Interdiscip. Rev.: Comput. Mol. Sci.* **2017**, *8*, e1327.

[12] Neese, F.; Wennmohs, F.; Becker, U.; Riplinger, C. The ORCA quantum chemistry program package. *J. Chem. Phys.* **2020**, *152*, 224108.

[13] Stoychev, G. L.; Auer, A. A.; Izsàk, R.; Neese, F. Self-Consistent Field Calculation of Nuclear Magnetic Resonance Chemical Shielding Constants Using Gauge-Including Atomic Orbitals and Approximate Two-Electron Integrals. *J. Chem. Theory Comput.* **2018**, *14*, 619–637.

[14] Ramsey, N. F. Magnetic Shielding of Nuclei in Molecules. *Phys. Rev.* **1950**, *78*, 699–703.

[15] Ramsey, N. F.; Purcell, E. M. Interactions between Nuclear Spins in Molecules. *Phys. Rev.* **1952**, *85*, 143–144.

[16] Ramsey, N. F. Electron Coupled Interactions between Nuclear Spins in Molecules. *Phys. Rev.* **1953**, *91*, 303–307.

[17] Pyykkö, P. Perspective on Norman Ramsey's theories of NMR chemical shifts and nuclear spin–spin coupling. *Theor. Chem. Acc.* **2000**, *103*, 214–216.

[18] Hameka, H. F. In *Reviews of Modern Quantum Chemistry*; Sen, K. D., Ed.; World Scientific: Singapore, 2002; pp 1237–1246.

[19] Pyykkö, P. In *Calculation of NMR and EPR parameters: theory and applications*; Kaupp, M., Bühl, M., Malkin, V. G., Eds.; John Wiley & Sons: Weinheim, 2004; Chapter 2, pp 7–19.

[20] Kutzelnigg, W. Theory of Magnetic Susceptibilities and NMR Chemical Shifts in Terms of Localized Quantities. *Isr. J. Chem.* **1980**, *19*, 193–200.

[21] Schindler, M.; Kutzelnigg, W. Theory of magnetic susceptibilities and NMR chemical shifts in terms of localized quantities. II. Application to some simple molecules. *J. Chem. Phys.* **1982**, *76*, 1919–1933.

[22] Kutzelnigg, W. Ab initio calculation of molecular properties. *J. Mol. Struct. Theochem.* **1989**, *202*, 11–61.

[23] Wolinski, K.; Hinton, J. F.; Pulay, P. Efficient Implementation of the Gauge-Independent Atomic Orbital Method for NMR Chemical Shift Calculations. *J. Am. Chem. Soc.* **1990**, *112*, 8251–8260.

[24] Malkin, V. G.; Malkina, O. L.; Salahub, D. R. Calculation of spin–spin coupling constants using density functional theory. *Chem. Phys. Lett.* **1994**, *221*, 91–99.

[25] Schreckenbach, G.; Ziegler, T. Calculation of NMR Shielding Tensors Using Gauge-Including Atomic Orbitals and Modern Density Functional Theory. *J. Phys. Chem.* **1995**, *99*, 606–611.

[26] Lee, A. M.; Handy, N. C.; Colwell, S. M. The density functional calculation of nuclear shielding constants using London atomic orbitals. *J. Chem. Phys.* **1995**, *103*, 10095–10109.

[27] Dickson, R. M.; Ziegler, T. NMR Spin–Spin Coupling Constants from Density Functional Theory with Slater-Type Basis Functions. *J. Phys. Chem.* **1996**, *100*, 5286–5290.

[28] Helgaker, T.; Watson, M.; Handy, N. C. Analytical calculation of nuclear magnetic resonance indirect spin–spin coupling constants at the generalized gradient approximation and hybrid levels of density-functional theory. *J. Chem. Phys.* **2000**, *113*, 9402–9409.

[29] Sychrovský, V.; Gräfenstein, J.; Cremer, D. Nuclear magnetic resonance spin–spin coupling constants from coupled perturbed density functional theory. *J. Chem. Phys.* **2000**, *113*, 3530–3547.

[30] Cheeseman, J. R.; Trucks, G. W.; Keith, T. A.; Frisch, M. J. A comparison of models for calculating nuclear magnetic resonance shielding tensors. *J. Chem. Phys.* **1996**, *104*, 5497–5509.

[31] Wilson, P. J.; Amos, R. D.; Handy, N. C. Density functional predictions for magnetizabilities and nuclear shielding constants. *Mol. Phys.* **1999**, *97*, 757–768.

[32] Gauss, J.; Stanton, J. F. Coupled-cluster calculations of nuclear magnetic resonance chemical shifts. *J. Chem. Phys.* **1995**, *103*, 3561–3577.

[33] Gauss, J.; Stanton, J. F. Perturbative treatment of triple excitations in coupled-cluster calculations of nuclear magnetic shielding constants. *J. Chem. Phys.* **1996**, *104*, 2574–2583.

[34] Gauss, J. Analytic second derivatives for the full coupled-cluster singles, doubles, and triples model: Nuclear magnetic shielding constants for BH, HF, CO, N_2, N_2O, and O_3. *J. Chem. Phys.* **2002**, *116*, 4773–4776.

[35] Kupka, T.; Leszczyńska, M.; Ejsmont, K.; Mnich, A.; Broda, M.; Thangavel, K.; Kaminský, J. Phosphorus mononitride: A difficult case for theory. *Int. J. Quantum Chem.* **2019**, *119*, e26032.

[36] Auer, A. A.; Gauss, J.; Stanton, J. F. Quantitative prediction of gas-phase ^{13}C nuclear magnetic shielding constants. *J. Chem. Phys.* **2003**, *118*, 10407–10417.

[37] Harding, M. E.; Lenhart, M.; Auer, A. A.; Gauss, J. Quantitative prediction of gas-phase ^{19}F nuclear magnetic shielding constants. *J. Chem. Phys.* **2008**, *128*, 244111.

[38] Auer, A. A. Quantitative prediction of gas-phase ^{17}O nuclear magnetic shielding constants. *J. Chem. Phys.* **2009**, *131*, 024116.

[39] Prochnow, E.; Auer, A. A. Quantitative prediction of gas-phase ^{15}N and ^{31}P nuclear magnetic shielding constants. *J. Chem. Phys.* **2010**, *132*, 064109.

[40] Gauss, J. Calculation of NMR chemical shifts at second-order many-body perturbation theory using gauge-including atomic orbitals. *Chem. Phys. Lett.* **1992**, *191*, 614–620.

[41] Gauss, J. Effects of electron correlation in the calculation of nuclear magnetic resonance chemical shifts. *J. Chem. Phys.* **1993**, *99*, 3629–3643.

[42] Stoychev, G. L.; Auer, A. A.; Neese, F. Efficient and Accurate Prediction of Nuclear Magnetic Resonance Shielding Tensors with Double-Hybrid Density Functional Theory. *J. Chem. Theory Comput.* **2018**, *14*, 4756–4771.

[43] Stoychev, G. L.; Auer, A. A.; Gauss, J.; Neese, F. DLPNO-MP2 second derivatives for the computation of polarizabilities and NMR shieldings. *J. Chem. Phys.* **2021**, *154*, 164110.

[44] Grimme, S.; Bannwarth, C.; Dohm, S.; Hansen, A.; Pisarek, J.; Pracht, P.; Seibert, J.; Neese, F. Fully Automated Quantum-Chemistry-Based Computation of Spin–Spin-Coupled Nuclear Magnetic Resonance Spectra. *Angew. Chem. Int. Ed.* **2017**, *56*, 14763–14769.

[45] Hohenberg, P.; Kohn, W. Inhomogeneous Electron Gas. *Phys. Rev.* **1964**, *136*, B864–B871.

[46] Kohn, W.; Sham, L. J. Self-Consistent Equations Including Exchange and Correlation Effects. *Phys. Rev.* **1965**, *140*, A1133–A1138.

[47] Koch, W.; Holthausen, M. C. *A Chemist's Guide to Density Functional Theory*; John Wiley & Sons, Inc.: Weinheim, 2001.

[48] Parr, R. G.; Yang, W. *Density Functional Theory of Atoms and Molecules*; Oxford Univ. Pr. u.a.: New York, NY, 1989.

[49] Burke, K. Perspective on density functional theory. *J. Chem. Phys.* **2012**, *136*, 150901.

[50] Becke, A. D. Perspective: Fifty years of density-functional theory in chemical physics. *J. Chem. Phys.* **2014**, *140*, 18A301.

[51] Mardirossian, N.; Head-Gordon, M. Thirty years of density functional theory in computational chemistry: an overview and extensive assessment of 200 density functionals. *Mol. Phys.* **2017**, *115*, 2315–2372.

[52] Slater, J. C. A Simplification of the Hartree-Fock Method. *Phys. Rev.* **1951**, *81*, 385–390.

[53] Perdew, J. P. Accurate Density Functional for the Energy: Real-Space Cutoff of the Gradient Expansion for the Exchange Hole. *Phys. Rev. Lett.* **1985**, *55*, 1665–1668.

[54] Perdew, J. P.; Yue, W. Accurate and simple density functional for the electronic exchange energy: Generalized gradient approximation. *Phys. Rev. B* **1986**, *33*, 8800–8802.

[55] Becke, A. D. Density functional calculations of molecular bond energies. *J. Chem. Phys.* **1986**, *84*, 4524–4529.

[56] Becke, A. D. Hartree–Fock Exchange Energy of an Inhomogeneous Electron Gas. *Int. J. Quantum Chem.* **1983**, *23*, 1915–1922.

[57] Becke, A. D.; Roussel, M. R. Exchange holes in inhomogeneous systems: A coordinate-space model. *Phys. Rev. A* **1989**, *39*, 3761–3767.

[58] Becke, A. D. A new mixing of Hartree–Fock and local density-functional theories. *J. Chem. Phys.* **1993**, *98*, 1372–1377.

[59] Becke, A. D. Density-functional thermochemistry. III. The role of exact exchange. *J. Chem. Phys.* **1993**, *98*, 5648–5652.

[60] Perdew, J. P.; Zunger, A. Self-interaction correction to density-functional approximations for many-electron systems. *Phys. Rev. B* **1981**, *23*, 5048–5079.

[61] Bühl, M. In *DFT Computations of Transition-Metal Chemical Shifts*; Webb, G. A., Ed.; Annual Reports on NMR Spectroscopy; Academic Press, 2008; Vol. 64; Chapter 3, pp 77–126.

[62] Gregusova, A.; Perera, A.; Bartlett, R. J. Accuracy of Computed ^{15}N Nuclear Magnetic Resonance Chemical Shifts. *J. Chem. Theory Comput.* **2010**, *6*, 1228–1239.

[63] Kupka, T.; Stachów, M.; Nieradka, M.; Kaminsky, J.; Pluta, T. Convergence of Nuclear Magnetic Shieldings in the Kohn–Sham Limit for Several Small Molecules. *J. Chem. Theory Comput.* **2010**, *6*, 1580–1589.

[64] Teale, A. M.; Lutnæs, O. B.; Helgaker, T.; Tozer, D. J.; Gauss, J. Benchmarking density-functional theory calculations of NMR shielding constants and spin-rotation constants using accurate coupled-cluster calculations. *J. Chem. Phys.* **2013**, *138*, 024111.

[65] Flaig, D.; Maurer, M.; Hanni, M.; Braunger, K.; Kick, L.; Thubauville, M.; Ochsenfeld, C. Benchmarking Hydrogen and Carbon NMR Chemical Shifts at HF, DFT, and MP2 Levels. *J. Chem. Theory Comput.* **2014**, *10*, 572–578.

[66] Maurer, M.; Ochsenfeld, C. Spin Component-Scaled Second-Order Møller-Plesset Perturbation Theory for Calculating NMR Shieldings. *J. Chem. Theory Comput.* **2015**, *11*, 37–44.

[67] Bursch, M.; Gasevic, T.; Stückrath, J. B.; Grimme, S. Comprehensive Benchmark Study on the Calculation of ^{29}Si NMR Chemical Shifts. *Inorg. Chem.* **2021**, *60*, 272–285.

[68] Barone, V.; Peralta, J. E.; Contreras, R. H.; Snyder, J. P. DFT Calculation of NMR J_{FF} Spin–Spin Coupling Constants in Fluorinated Pyridines. *J. Phys. Chem. A* **2002**, *106*, 5607–5612.

[69] Maximoff, S. N.; Peralta, J. E.; Barone, V.; Scuseria, G. E. Assessment of Density Functionals for Predicting One-Bond Carbon–Hydrogen NMR Spin–Spin Coupling Constants. *J. Chem. Theory Comput.* **2005**, *1*, 541–545.

[70] Jimeno, M.-L.; Alkorta, I.; Elguero, J.; Del Bene, J. E. Computed coupling constants in $X(CH_3)_nH_{(4-n)}$ moieties where X = ^{13}C and $^{15}N^+$, and n = 0–4: comparisons with experimental data. *Magn. Reson. Chem.* **2006**, *44*, 698–707.

[71] Helgaker, T.; Jaszuński, M.; Pecul, M. The quantum-chemical calculation of NMR indirect spin–spin coupling constants. *Prog. Nucl. Magn. Reson. Spectrosc.* **2008**, *53*, 249–268.

[72] de Giovanetti, M.; Bitencourt, L. F. F.; Cormanich, R.; Sauer, S. P. A. On the Unexpected Accuracy of the M06L Functional in the Calculation of $^1J_{FC}$ Spin–Spin Coupling Constants. *J. Chem. Theory Comput.* **2021**, *17*, 7712–7723.

[73] Vignale, G.; Rasolt, M. Density-Functional Theory in Strong Magnetic Fields. *Phys. Rev. Lett.* **1987**, *59*, 2360–2363.

[74] Reimann, S.; Ekström, U.; Stopkowicz, S.; Teale, A. M.; Borgoo, A.; Helgaker, T. The importance of current contributions to shielding constants in density-functional theory. *Phys. Chem. Chem. Phys.* **2015**, *17*, 18834–18842.

[75] Arbuznikov, A. V.; Kaupp, M. Nuclear shielding constants from localized local hybrid exchange-correlation potentials. *Chem. Phys. Lett.* **2007**, *442*, 496–503.

[76] Wilson, P. J.; Tozer, D. J. Varying the fraction of orbital exchange in density functional theory: Influence on nuclear magnetic resonance shielding constants. *J. Chem. Phys.* **2002**, *116*, 10139–10147.

[77] Arbuznikov, A. V.; Kaupp, M. Construction of local hybrid exchange-correlation potentials and their evaluation for nuclear shielding constants. *Chem. Phys. Lett.* **2004**, *386*, 8–16.

[78] Teale, A. M.; Tozer, D. J. Exchange representations in Kohn–Sham NMR shielding calculations. *Chemical Physics Letters* **2004**, *383*, 109–114.

[79] Hieringer, W.; Della Sala, F.; Görling, A. Density-functional calculations of NMR shielding constants using the localized Hartree–Fock method. *Chem. Phys. Lett.* **2004**, *383*, 115–121.

[80] Teale, A. M.; Cohen, A. J.; Tozer, D. J. Transition metal NMR chemical shifts from optimized effective potentials. *J. Chem. Phys.* **2007**, *126*, 074101.

[81] Arbuznikov, A. V.; Kaupp, M.; Bahmann, H. From local hybrid functionals to "localized local hybrid" potentials: Formalism and thermochemical tests. *J. Chem. Phys.* **2006**, *124*, 204102.

[82] Peach, M. J. G.; Kattirtzi, J. A.; Teale, A. M.; Tozer, D. J. Shielding Constants and Chemical Shifts in DFT: Influence of Optimized Effective Potential and Coulomb-Attenuation. *J. Phys. Chem. A* **2010**, *114*, 7179–7186.

[83] Krykunov, M.; Ziegler, T. On the use of the exact exchange optimized effective potential method for static response properties. *Int. J. Quantum Chem.* **2009**, *109*, 3246–3258.

[84] Ostlund, N. S.; Szabo, A. *Modern Quantum Chemistry: Introduction to Advanced Electronic Structure Theory*; Dover Publications, 2012; Chapter 2, pp 39–107.

[85] Born, M.; Oppenheimer, R. Zur Quantentheorie der Molekeln. *Ann. Phys.* **1927**, *389*, 457–484.

[86] Koch, W.; Holthausen, M. C. *A Chemist's Guide to Density Functional Theory*; John Wiley & Sons, Inc.: Weinheim, 2001; Chapter 1, pp 3–18.

[87] Ostlund, N. S.; Szabo, A. *Modern Quantum Chemistry: Introduction to Advanced Electronic Structure Theory*; Dover Publications, 2012; Chapter 1, pp 1–38.

[88] Ostlund, N. S.; Szabo, A. *Modern Quantum Chemistry: Introduction to Advanced Electronic Structure Theory*; Dover Publications, 2012; Chapter 3, pp 108–229.

[89] Pauli, W. Über den Zusammenhang des Abschlusses der Elektronengruppen im Atom mit der Komplexstruktur der Spektren. *Z. Phys.* **1925**, *31*, 765–783.

[90] Jensen, F. *Introduction to Computational Chemistry*, 2nd ed.; John Wiley & Sons, 2007; Chapter 3, pp 80–132.

[91] Jensen, F. *Introduction to Computational Chemistry*, 2nd ed.; John Wiley & Sons, 2007; Chapter 4, pp 133–191.

[92] Löwdin, P.-O. Quantum Theory of Many-Particle Systems. III. Extension of the Hartree-Fock Scheme to Include Degenerate Systems and Correlation Effects. *Phys. Rev.* **1955**, *97*, 1509–1520.

[93] Pople, J. A.; Binkley, J. S. Correlation energies for AH_n molecules and cations. *Mol. Phys.* **1975**, *29*, 599–611.

[94] Hollett, J. W.; Gill, P. M. W. The two faces of static correlation. *J. Chem. Phys.* **2011**, *134*, 114111.

[95] Ramos-Cordoba, E.; Salvador, P.; Matito, E. Separation of dynamic and nondynamic correlation. *Phys.Chem.Chem.Phys.,* **2016**, *18*, 24015–24023.

[96] Helgaker, T.; Jørgensen, P.; Olsen, J. *Molecular Electronic Structure Theory*; Wiley: Chichester u.a., 2000; Chapter 5, pp 142–200.

[97] Møller, C.; Plesset, M. S. Note on an Approximation Treatment for Many-Electron Systems. *Phys. Rev.* **1934**, *46*, 618–622.

[98] Cremer, D. Møller-Plesset perturbation theory: from small molecule methods to methods for thousands of atoms. *WIREs Comput. Mol. Sci.* **2011**, *1*, 509–530.

[99] Helgaker, T.; Jørgensen, P.; Olsen, J. *Molecular Electronic Structure Theory*; Wiley: Chichester u.a., 2000; Chapter 11, pp 523–597.

[100] Helgaker, T.; Jørgensen, P.; Olsen, J. *Molecular Electronic Structure Theory*; Wiley: Chichester u.a., 2000; Chapter 13, pp 648–723.

[101] Helgaker, T.; Jørgensen, P.; Olsen, J. *Molecular Electronic Structure Theory*; Wiley: Chichester u.a., 2000; Chapter 14, pp 724–816.

[102] Ostlund, N. S. Complex and Unrestricted Hartree–Fock Wavefunctions. *J. Chem. Phys.* **1972**, *57*, 2994–2997.

[103] Helgaker, T.; Jørgensen, P.; Olsen, J. *Molecular Electronic Structure Theory*; Wiley: Chichester u.a., 2000; Chapter 12, pp 598–647.

[104] Olsen, J. The CASSCF Method: A Perspective and Commentary. *Int. J. Quantum Chem.* **2011**, *111*, 3267–3272.

[105] Koch, W.; Holthausen, M. C. *A Chemist's Guide to Density Functional Theory*; John Wiley & Sons, Inc.: Weinheim, 2001; Chapter 2, pp 19–28.

[106] Parr, R. G.; Yang, W. *Density Functional Theory of Atoms and Molecules*; Oxford Univ. Pr. u.a.: New York, NY, 1989; Chapter 1, pp 3–19.

[107] Levy, M. Universal variational functionals of electron densities, first-order density matrices, and natural spin-orbitals and solution of the v-representability problem. *Proc. Natl. Acad. Sci.* **1979**, *76*, 6062–6065.

[108] Parr, R. G.; Yang, W. *Density Functional Theory of Atoms and Molecules*; Oxford Univ. Pr. u.a.: New York, NY, 1989; Chapter 3, pp 47–69.

[109] Jensen, F. *Introduction to Computational Chemistry*, 2nd ed.; John Wiley & Sons, 2007; Chapter 6, pp 232–267.

[110] Teller, E. On the Stability of Molecules in the Thomas-Fermi Theory. *Rev. Mod. Phys.* **1962**, *34*, 627–631.

[111] Parr, R. G.; Yang, W. *Density Functional Theory of Atoms and Molecules*; Oxford Univ. Pr. u.a.: New York, NY, 1989; Chapter 6, pp 105–141.

[112] Salazar, E. X.; Guarderas, P. F.; Ludeña, E. V.; Cornejo, M. H.; Karasiev, V. V. Study of Some Simple Approximations to the Non-Interacting Kinetic Energy Functional. *Int. J. Quantum Chem.* **2016**, *116*, 1313–1321.

[113] Iyengar, S. S.; Ernzerhof, M.; Maximoff, S. N.; Scuseria, G. E. Challenge of creating accurate and effective kinetic-energy functionals. *Phys. Rev. A* **2001**, *63*, 052508.

[114] Koch, W.; Holthausen, M. C. *A Chemist's Guide to Density Functional Theory*; John Wiley & Sons, Inc.: Weinheim, 2001; Chapter 5, pp 41–64.

[115] Parr, R. G.; Yang, W. *Density Functional Theory of Atoms and Molecules*; Oxford Univ. Pr. u.a.: New York, NY, 1989; Chapter 7, pp 142–168.

[116] Seidl, A.; Görling, A.; Vogl, P.; Majewski, J. A.; Levy, M. Generalized Kohn-Sham schemes and the band-gap problem. *Phys. Rev. B* **1996**, *53*, 3764–3774.

[117] Koch, W.; Holthausen, M. C. *A Chemist's Guide to Density Functional Theory*; John Wiley & Sons, Inc.: Weinheim, 2001; Chapter 6, pp 65–92.

[118] Becke, A. D. In *Modern Electronic Structure Theory: Part II*; Yarkony, D. R., Ed.; World Scientific Publishing Company, 1995; Chapter 15, pp 1022–1046.

[119] Gunnarsson, O.; Lundqvist, B. I. Exchange and correlation in atoms, molecules, and solids by the spin-density-functional formalism. *Phys. Rev. B* **1976**, *13*, 4274–4298.

[120] Vosko, S.; Wilk, L.; Nusair, M. Accurate spin-dependent electron liquid correlation energies for local spin density calculations: a critical analysis. *Can. J. Phys.* **1980**, *58*, 1200–1211.

[121] Harris, J.; Jones, R. O. The surface energy of a bounded electron gas. *J. Phys. F: Met. Phys.* **1974**, *4*, 1170–1186.

[122] Langreth, D. C.; Perdew, J. P. Exchange-correlation energy of a metallic surface: Wave-vector analysis. *Phys. Rev. B* **1977**, *15*, 2884–2901.

[123] Harris, J. Adiabatic-connection approach to Kohn-Sham theory. *Phys. Rev. A* **1984**, *29*, 1648–1659.

[124] McWeeny, R. The Nature of Electron Correlation in Molecules. *Int. J. Quantum Chem.* **1967**, *1*, 351–359.

[125] Mcweeny, R. The nature of electron correlation in molecules. *Int. J. Quantum Chem.* **1967**, *1*, 351–359.

[126] Parr, R. G.; Yang, W. *Density Functional Theory of Atoms and Molecules*; Oxford Univ. Pr. u.a.: New York, NY, 1989; Chapter 8, pp 169–200.

[127] Pople, J. A.; Head-Gordon, M.; Fox, D. J.; Raghavachari, K.; Curtiss, L. A. Gaussian-1 theory: A general procedure for prediction of molecular energies. *J. Chem. Phys.* **1989**, *90*, 5622–5629.

[128] Curtiss, L. A.; Raghavachari, K.; Redfern, P. C.; Pople, J. A. Assessment of Gaussian-2 and density functional theories for the computation of enthalpies of formation. *J. Chem. Phys.* **1997**, *106*, 1063–1079.

[129] Curtiss, L. A.; Redfern, P. C.; Raghavachari, K. Assessment of Gaussian-3 and density-functional theories on the G3/05 test set of experimental energies. *J. Chem. Phys.* **2005**, *123*, 124107.

[130] Goerigk, L.; Grimme, S. A thorough benchmark of density functional methods for general main group thermochemistry, kinetics, and noncovalent interactions. *Phys. Chem. Chem. Phys.* **2011**, *13*, 6670–6688.

[131] Korth, M.; Grimme, S. "Mindless" DFT Benchmarking. *J. Chem. Theory Comput.* **2009**, *5*, 993–1003.

[132] Lynch, B. J.; Truhlar, D. G. Small Representative Benchmarks for Thermochemical Calculations. *J. Phys. Chem. A* **2003**, *107*, 8996–8999.

[133] Zhao, Y.; Truhlar, D. G. Benchmark Databases for Nonbonded Interactions and Their Use To Test Density Functional Theory. *J. Chem. Theory Comput.* **2005**, *1*, 415–432.

[134] Zhao, Y.; Truhlar, D. G. The M06 suite of density functionals for main group thermochemistry, thermochemical kinetics, noncovalent interactions, excited states, and transition elements: two new functionals and systematic testing of four M06-class functionals and 12 other functionals. *Theor. Chem. Account* **2008**, *120*, 215–241.

[135] Goerigk, L.; Hansen, A.; Bauer, C.; Ehrlich, S.; Najibi, A.; Grimme, S. A look at the density functional theory zoo with the advanced GMTKN55 database for general main group thermochemistry, kinetics and noncovalent interactions. *Phys. Chem. Chem. Phys.* **2017**, *19*, 32184–32215.

[136] Goerigk, L.; Grimme, S. A General Database for Main Group Thermochemistry, Kinetics, and Noncovalent Interactions - Assessment of Common and Reparameterized (meta-)GGA Density Functionals. *J. Chem. Theory Comput.* **2010**, *6*, 107–126.

[137] Goerigk, L.; Grimme, S. Efficient and Accurate Double-Hybrid-Meta-GGA Density Functionals-Evaluation with the Extended GMTKN30 Database for General Main Group Thermochemistry, Kinetics, and Noncovalent Interactions. *J. Chem. Theory Comput.* **2011**, *7*, 291–309.

[138] Medvedev, M. G.; Bushmarinov, I. S.; Sun, J.; Perdew, J. P.; Lyssenko, K. A. Density functional theory is straying from the path toward the exact functional. *Science* **2017**, *355*, 49–52.

[139] Medvedev, M. G.; Bushmarinov, I. S.; Sun, J.; Perdew, J. P.; Lyssenko, K. A. Response to Comment on "Density functional theory is straying from the path toward the exact functional". *Science* **2017**, *356*, 496c.

[140] Kepp, K. P. Comment on "Density functional theory is straying from the path toward the exact functional". *Science* **2017**, *356*, 496b.

[141] Korth, M. Density Functional Theory: Not Quite the Right Answer for the Right Reason Yet. *Angew. Chem. Int. Ed.* **2017**, *56*, 5396–5398.

[142] Parr, R. G.; Yang, W. *Density Functional Theory of Atoms and Molecules*; Oxford Univ. Pr. u.a.: New York, NY, 1989; Chapter Appendix E, pp 271–275.

[143] Slater, J. C. *The Self-Consistent Field for Molecules and Solids: Quantum Theory of Molecules and Solids, Volume 4*; McGraw-Hill Book Company: New York, NY, 1974; p 21 ff.

[144] Ceperley, D. M.; Alder, B. J. Ground State of the Electron Gas by a Stochastic Method. *Phys. Rev. Lett.* **1980**, *45*, 566–569.

[145] Perdew, J. P.; Wang, Y. Accurate and simple analytic representation of the electron-gas correlation energy. *Phys. Rev. B* **1992**, *45*, 13244–13249.

[146] Perdew, J. P.; Wang, Y. Erratum: Accurate and simple analytic representation of the electron-gas correlation energy [Phys. Rev. B 45, 13244 (1992)]. *Phys. Rev. B* **2018**, *98*, 079904.

[147] von Barth, U.; Hedin, L. A local exchange-correlation potential for the spin polarized case. *J. Phys. C: Solid State Phys.* **1972**, *5*, 1629–1642.

[148] Ziegler, T. Approximate Density Functional Theory as a Practical Tool in Molecular Energetics and Dynamics. *Chem. Rev.* **1991**, *91*, 651–667.

[149] Andzelm, J.; Wimmer, E. Density functional Gaussian-type-orbital approach to molecular geometries, vibrations, and reaction energies. *J. Chem. Phys.* **1992**, *96*, 1280–1303.

[150] Johnson, B. G.; Gill, P. M. W.; Pople, J. A. The performance of a family of density functional methods. *J. Chem. Phys.* **1993**, *98*, 5612–5626.

[151] Jones, R. O.; Gunnarsson, O. Density-functional formalism: Sources of error in local-density approximations. *Phys. Rev. Lett.* **1985**, *55*, 107–110.

[152] Tong, B. Y.; Sham, L. J. Application of a Self-Consistent Scheme Including Exchange and Correlation Effects to Atoms. *Phys. Rev.* **1966**, *144*, 1–4.

[153] Stoll, H.; Pavlidou, C. M. E.; Preuß, H. On the calculation of correlation energies in the spin-density functional formalism. *Theoret. Chim. Acta* **1978**, *149*, 143–149.

[154] Herman, F.; Van Dyke, J. P.; Ortenburger, I. B. Improved Statistical Exchange Approximation for Inhomogeneous Many-Electron Systems. *Phys. Rev. Lett.* **1969**, *22*, 807–811.

[155] Herman, F.; Ortenburger, I. B.; Van Dyke, J. P. A Method for Improving the Physical Realism of First-Principles Band Structure Calculations. *Int. J. Quantum Chem.* **1969**, *4*, 827–846.

[156] Kleinman, L. Exchange density-functional gradient expansion. *Phys. Rev. B* **1984**, *30*, 2223–2225.

[157] Becke, A. D. On the large-gradient behavior of the density functional exchange energy. *J. Chem. Phys.* **1986**, *85*, 7184–7187.

[158] Becke, A. D. Density-functional thermochemistry. V. Systematic optimization of exchange-correlation functionals. *J. Chem. Phys.* **1997**, *107*, 8554–8560.

[159] Becke, A. D. Density-functional exchange-energy approximation with correct asymptotic behavior. *Phys. Rev. A* **1988**, *38*, 3098–3100.

[160] Perdew, J. P.; Burke, K.; Ernzerhof, M. Generalized Gradient Approximation Made Simple. *Phys. Rev. Lett.* **1996**, *77*, 3865–3868.

[161] Lieb, E. H.; Oxford, S. Improved Lower Bound on the Indirect Coulomb Energy. *Int. J. Quantum Chem.* **1981**, *19*, 427–439.

[162] Hamprecht, F. A.; Cohen, A. J.; Tozer, D. J.; Handy, N. C. Development and assessment of new exchange-correlation functionals. *J. Chem. Phys.* **1998**, *109*, 6264–6271.

[163] Boese, A. D.; Doltsinis, N. L.; Handy, N. C.; Sprik, M. New generalized gradient approximation functionals. *J. Chem. Phys.* **2000**, *112*, 1670–1678.

[164] Peverati, R.; Truhlar, D. G. Exchange-Correlation Functional with Good Accuracy for Both Structural and Energetic Properties while Depending Only on the Density and Its Gradient. *J. Chem. Theory Comp.* **2012**, *8*, 2310–2319.

[165] Wilson, P. J.; Tozer, D. J. NMR shielding constants from ab initio and Kohn–Sham electron densities. *Chem. Phys. Lett.* **2001**, *337*, 341–348.

[166] Keal, T. W.; Tozer, D. J. The exchange-correlation potential in Kohn–Sham nuclear magnetic resonance shielding calculations. *J. Chem. Phys.* **2003**, *119*, 3015–3024.

[167] Keal, T. W.; Tozer, D. J. A semiempirical generalized gradient approximation exchange-correlation functional. *J. Chem. Phys.* **2004**, *121*, 5654–5660.

[168] Engel, E.; Chevary, J. A.; Macdonald, L. D.; Vosko, S. H. Asymptotic properties of the exchange energy density and the exchange potential of finite systems: relevance for generalized gradient approximations. *Z. Phys. D: Atoms, Molecules and Clusters* **1992**, *23*, 7–14.

[169] Lee, C.; Yang, W.; Parr, R. G. Development of the Colle-Salvetti correlation-energy formula into a functional of the electron density. *Phys. Rev. B* **1988**, *37*, 785–789.

[170] Perdew, J. P. Density-functional approximation for the correlation energy of the inhomogeneous electron gas. *Phys. Rev. B* **1986**, *33*, 8822–8824.

[171] Perdew, J. P. *Electronic structure of solids '91 : proceedings of the 75. WE-Heraeus-Seminar and 21st Annual International Symposium on Electronic Structure of Solids held in Gaussig (Germany), March 11 - 15, 1991*, 1st ed.; Akad.-Verl.: Berlin, 1991; pp 11–21.

[172] Burke, K.; Perdew, J. P.; Wang, Y. In *Electronic Density Functional Theory: Recent Progress and New Directions*; Dobson, J. F., Vignale, G., Das, M. P., Eds.; Springer US: Boston, MA, 1998; Chapter II, pp 81–111.

[173] Colle, R.; Salvetti, O. Approximate calculation of the correlation energy for the closed shells. *Theoret. Chim. Acta* **1975**, *37*, 329–334.

[174] Results obtained with the correlation energy density functionals of becke and Lee, Yang and Parr. *Chem. Phys. Lett.* **1989**, *157*, 200–206.

[175] Perdew, J. P.; Constantin, L. A. Laplacian-level density functionals for the kinetic energy density and exchange-correlation energy. *Phys. Rev. B* **2007**, *75*, 155109.

[176] Perdew, J. P.; Kurth, S.; Zupan, A.; Blaha, P. Accurate Density Functional with Correct Formal Properties: A Step Beyond the Generalized Gradient Approximation. *Phys. Rev. Lett.* **1999**, *82*, 2544–2547.

[177] Staroverov, V. N.; Scuseria, G. E.; Tao, J.; Perdew, J. P. Tests of a ladder of density functionals for bulk solids and surfaces. *Phys. Rev. B* **2004**, *69*, 075102.

[178] Tao, J.; Perdew, J. P.; Staroverov, V. N.; Scuseria, G. E. Climbing the Density Functional Ladder: Nonempirical Meta–Generalized Gradient Approximation Designed for Molecules and Solids. *Phys. Rev. Lett.* **2003**, *91*, 146401.

[179] Sun, J.; Ruzsinszky, A.; Perdew, J. P. Strongly Constrained and Appropriately Normed Semilocal Density Functional. *Phys. Rev. Lett.* **2015**, *115*, 036402.

[180] Van Voorhis, T.; Scuseria, G. E. A novel form for the exchange-correlation energy functional. *J. Chem. Phys.* **1998**, *109*, 400–410.

[181] Boese, A. D.; Handy, N. C. New exchange-correlation density functionals: The role of the kinetic-energy density. *J. Chem. Phys.* **2002**, *116*, 9559–9569.

[182] Zhao, Y.; Truhlar, D. G. A new local density functional for main-group thermochemistry, transition metal bonding, thermochemical kinetics, and noncovalent interactions. *J. Chem. Phys.* **2006**, *125*, 194101.

[183] Yu, H. S.; He, X.; Truhlar, D. G. MN15-L: A New Local Exchange-Correlation Functional for Kohn–Sham Density Functional Theory with Broad Accuracy for Atoms, Molecules, and Solids. *J. Chem. Theory Comput.* **2016**, *12*, 1280–1293.

[184] Perdew, J. P.; Schmidt, K. Jacob's ladder of density functional approximations for the exchange-correlation energy. *AIP Conf. Proc.* **2001**, *577*, 1–20.

[185] Sharp, R. T.; Horton, G. K. A Variational Approach to the Unipotential Many-Electron Problem. *Phys. Rev.* **1953**, *90*, 317–317.

[186] Talman, J. D.; Shadwick, W. F. Optimized effective atomic central potential. *Phys. Rev. A* **1976**, *14*, 36–40.

[187] Mori-Sánchez, P.; Cohen, A. J.; Yang, W. Many-electron self-interaction error in approximate density functionals. *J. Chem. Phys.* **2006**, *125*, 201102.

[188] Holthausen, M. C.; Heinemann, C.; Cornehl, H. H.; Koch, W.; Schwarz, H. The performance of density-functional/Hartree–Fock hybrid methods: Cationic transition-metal methyl complexes MCH_3^+ (M=Sc–Cu,La,Hf–Au). *J. Chem. Phys.* **1995**, *102*, 4931–4941.

[189] Staroverov, V. N.; Scuseria, G. E.; Tao, J.; Perdew, J. P. Comparative assessment of a new nonempirical density functional: Molecules and hydrogen-bonded complexes. *J. Chem. Phys.* **2003**, *119*, 12129–12137.

[190] Adamo, C.; Barone, V. Toward chemical accuracy in the computation of NMR shieldings: the PBE0 model. *Chem. Phys. Lett.* **1998**, *298*, 113–119.

[191] Adamo, C.; Barone, V. Toward reliable density functional methods without adjustable parameters: The PBE0 model. *J. Chem. Phys.* **1999**, *110*, 6158–6170.

[192] Perdew, J. P.; Ernzerhof, M.; Burke, K. Rationale for mixing exact exchange with density functional approximations. *J. Chem. Phys.* **1996**, *105*, 9982–9985.

[193] Cortona, P. Note: Theoretical mixing coefficients for hybrid functionals. *J. Chem. Phys.* **2012**, *136*, 086101.

[194] Guido, C. A.; Brémond, E.; Adamo, C.; Cortona, P. Communication: One third: A new recipe for the PBE0 paradigm. *J. Chem. Phys.* **2013**, *138*, 021104.

[195] Stephens, P. J.; Devlin, F. J.; Chabalowski, C. F.; Frisch, M. J. Ab Initio Calculation of Vibrational Absorption and Circular Dichroism Spectra Using Density Functional Force Fields. *J. Phys. Chem.* **1994**, *98*, 11623–11627.

[196] Csonka, G. I.; Perdew, J. P.; Ruzsinszky, A. Global Hybrid Functionals: A Look at the Engine under the Hood. *J. Chem. Theory Comput.* **2010**, *6*, 3688–3703.

[197] Schmider, H. L.; Becke, A. D. Optimized density functionals from the extended G2 test set. *J. Chem. Phys.* **1998**, *108*, 9624–9631.

[198] Zhao, Y.; Truhlar, D. G. Density Functional for Spectroscopy: No Long-Range Self-Interaction Error, Good Performance for Rydberg and Charge-Transfer States, and Better Performance on Average than B3LYP for Ground States. *J. Phys. Chem. A* **2006**, *110*, 13126–13130.

[199] Zhao, Y.; Truhlar, D. G. Exploring the Limit of Accuracy of the Global Hybrid Meta Density Functional for Main-Group Thermochemistry, Kinetics, and Noncovalent Interactions. *J. Chem. Theory Comput.* **2008**, *4*, 1849–1868.

[200] Yu, H. S.; He, X.; Li, S. L.; Truhlar, D. G. MN15: A Kohn–Sham global-hybrid exchange–correlation density functional with broad accuracy for multi-reference and single-reference systems and noncovalent interactions. *Chem. Sci.* **2016**, *7*, 5032–5051.

[201] Stoll, H.; Savin, A. In *Density Functional Methods in Physics*; Dreizler, R. M., da Providencia, J., Eds.; Plenum Press: New York and London, 1985; pp 177–207.

[202] Leininger, T.; Stoll, H.; Werner, H.-J.; Savin, A. Combining long-range configuration interaction with short-range density functionals. *Chem. Phys. Lett.* **1997**, *275*, 151–160.

[203] Zhang, M.-Y.; Cui, Z.-H.; Wang, Y.-C.; Jiang, H. Hybrid functionals with system-dependent parameters: Conceptual foundations and methodological developments. *WIREs Comput. Mol. Sci.* **2020**, *10*, e1476.

[204] Iikura, H.; Tsuneda, T.; Yanai, T.; Hirao, K. A long-range correction scheme for generalized-gradient-approximation exchange functionals. *J. Chem. Phys.* **2001**, *115*, 3540–3544.

[205] Chai, J.-D.; Head-Gordon, M. Systematic optimization of long-range corrected hybrid density functionals. *J. Chem. Phys.* **2008**, *128*, 084106.

[206] Yanai, T.; Tew, D. P.; Handy, N. C. A new hybrid exchange-correlation functional using the Coulomb-attenuating method (CAM-B3LYP). *Chem. Phys. Lett.* **2004**, *393*, 51–57.

[207] Livshits, E.; Baer, R. A well-tempered density functional theory of electrons in molecules. *Phys. Chem. Chem. Phys.* **2007**, *9*, 2932–2941.

[208] Stein, T.; Kronik, L.; Baer, R. Reliable Prediction of Charge Transfer Excitations in Molecular Complexes Using Time-Dependent Density Functional Theory. *J. Am. Chem. Soc.* **2009**, *131*, 2818–2820.

[209] Stein, T.; Eisenberg, H.; Kronik, L.; Baer, R. Fundamental Gaps in Finite Systems from Eigenvalues of a Generalized Kohn-Sham Method. *Phys. Rev. Lett.* **2010**, *105*, 266802.

[210] Prokopiou, G.; Autschbach, J.; Kronik, L. Assessment of the Performance of Optimally Tuned Range-Separated Hybrid Functionals for Nuclear Magnetic Shielding Calculations. *Adv. Theory Simul.* **2020**, *3*, 2000083.

[211] Grimme, S.; Hansen, A.; Brandenburg, J. G.; Bannwarth, C. Dispersion-Corrected Mean-Field Electronic Structure Methods. *Chem. Rev.* **2016**, *116*, 5105–5154.

[212] Grimme, S. Semiempirical GGA-type density functional constructed with a long-range dispersion correction. *J. Comput. Chem.* **2006**, *27*, 1787–1799.

[213] Grimme, S.; Antony, J.; Ehrlich, S.; Krieg, H. A consistent and accurate ab initio parametrization of density functional dispersion correction (DFT-D) for the 94 elements H-Pu. *J. Chem. Phys.* **2010**, *132*, 154104.

[214] Grimme, S. Accurate description of van der Waals complexes by density functional theory including empirical corrections. *J. Comput. Chem.* **2004**, *25*, 1463–1473.

[215] Caldeweyher, E.; Ehlert, S.; Hansen, A.; Neugebauer, H.; Spicher, S.; Bannwarth, C.; Grimme, S. A generally applicable atomic-charge dependent London dispersion correction. *J. Chem. Phys.* **2019**, *150*, 154122.

[216] Chai, J.-D.; Head-Gordon, M. Long-range corrected hybrid density functionals with damped atom-atom dispersion corrections. *Phys. Chem. Chem. Phys.* **2008**, *10*, 6615–6620.

[217] Vydrov, O. A.; Van Voorhis, T. Nonlocal van der Waals density functional: The simpler the better. *J. Chem. Phys.* **2010**, *133*, 244103.

[218] Hujo, W.; Grimme, S. Performance of the van der Waals Density Functional VV10 and (hybrid)GGA Variants for Thermochemistry and Noncovalent Interactions. *J. Chem. Theory Comput.* **2011**, *7*, 3866–3871.

[219] Mardirossian, N.; Head-Gordon, M. Mapping the genome of meta-generalized gradient approximation density functionals: The search for B97M-V. *J. Chem. Phys.* **2015**, *142*, 074111.

[220] Mardirossian, N.; Head-Gordon, M. ωB97X-V: A 10-parameter, range-separated hybrid, generalized gradient approximation density functional with nonlocal correlation, designed by a survival-of-the-fittest strategy. *Phys. Chem. Chem. Phys.* **2014**, *16*, 9904–9924.

[221] Mardirossian, N.; Head-Gordon, M. ωB97M-V: A combinatorially optimized, range-separated hybrid, meta-GGA density functional with VV10 nonlocal correlation. *J. Chem. Phys.* **2016**, *144*, 214110.

[222] Dreuw, A.; Head-Gordon, M. Single-Reference ab Initio Methods for the Calculation of Excited States of Large Molecules. *Chem. Rev.* **2005**, *105*, 4009–4037.

[223] Jensen, F. *Introduction to Computational Chemistry*, 2nd ed.; John Wiley & Sons, 2007; Chapter 10, pp 315–349.

[224] Görling, A.; Levy, M. Correlation-energy functional and its high-density limit obtained from a coupling-constant perturbation expansion. *Phys. Rev. B* **1993**, *47*, 13105–13113.

[225] Görling, A.; Levy, M. Exact Kohn–Sham scheme based on perturbation theory. *Phys. Rev. A* **1994**, *50*, 196–204.

[226] Engel, E.; Dreizler, R. M. From explicit to implicit density functionals. *J. Comput. Chem.* **1999**, *20*, 31–50.

[227] Mori-Sánchez, P.; Wu, Q.; Yang, W. Orbital-dependent correlation energy in density-functional theory based on a second-order perturbation approach: Success and failure. *J. Chem. Phys.* **2005**, *123*, 062204.

[228] Goerigk, L.; Grimme, S. Double-hybrid density functionals. *WIREs Comput. Mol. Sci.* **2014**, *4*, 576–600.

[229] Mehta, N.; Casanova-Páez, M.; Goerigk, L. Semi-empirical or non-empirical double-hybrid density functionals: which are more robust? *Phys. Chem. Chem. Phys.* **2018**, *20*, 23175–23194.

[230] Grimme, S. Semiempirical hybrid density functional with perturbative second-order correlation. *J. Chem. Phys.* **2006**, *124*, 034108.

[231] Schwabe, T.; Grimme, S. Double-hybrid density functionals with long-range dispersion corrections: higher accuracy and extended applicability. *Phys. Chem. Chem. Phys.* **2007**, *9*, 3397–3406.

[232] Karton, A.; Tarnopolsky, A.; Lamère, J.-F.; Schatz, G. C.; Martin, J. M. L. Highly Accurate First-Principles Benchmark Data Sets for the Parametrization and Validation of Density Functional and Other Approximate Methods. Derivation of a Robust, Generally Applicable, Double-Hybrid Functional for Thermochemistry and Thermochemical Kinetics. *J. Phys. Chem. A* **2008**, *112*, 12868–12886.

[233] Kozuch, S.; Martin, J. M. L. DSD-PBEP86: in search of the best double-hybrid DFT with spin-component scaled MP2 and dispersion corrections. *Phys. Chem. Chem. Phys.* **2011**, *13*, 20104–20107.

[234] Sharkas, K.; Toulouse, J.; Savin, A. Double-hybrid density-functional theory made rigorous. *J. Chem. Phys.* **2011**, *134*, 064113.

[235] Benighaus, T.; DiStasio, R. A.; Lochan, R. C.; Chai, J.-D.; Head-Gordon, M. Semiempirical Double-Hybrid Density Functional with Improved Description of Long-Range Correlation. *J. Phys. Chem. A* **2008**, *112*, 2702–2712.

[236] Cruz, F. G.; Lam, K.-C.; Burke, K. Exchange–Correlation Energy Density from Virial Theorem. *J. Phys. Chem. A* **1998**, *102*, 4911–4917.

[237] Jaramillo, J.; Scuseria, G. E.; Ernzerhof, M. Local hybrid functionals. *J. Chem. Phys.* **2003**, *118*, 1068–1073.

[238] Maier, T. M.; Arbuznikov, A. V.; Kaupp, M. Local hybrid functionals: Theory, implementation, and performance of an emerging new tool in quantum chemistry and beyond. *WIREs Comput. Mol. Sci.* **2019**, *9*, e1378.

[239] Perdew, J. P.; Staroverov, V. N.; Tao, J.; Scuseria, G. E. Density functional with full exact exchange, balanced nonlocality of correlation, and constraint satisfaction. *Phys. Rev. A* **2008**, *78*, 052513.

[240] Becke, A. D. A new inhomogeneity parameter in density-functional theory. *J. Chem. Phys.* **1998**, *109*, 2092–2098.

[241] Bates, J. E.; Furche, F. Harnessing the meta-generalized gradient approximation for time-dependent density functional theory. *J. Chem. Phys.* **2012**, *137*, 164105.

[242] Kaupp, M.; Bahmann, H.; Arbuznikov, A. V. Local hybrid functionals: An assessment for thermochemical kinetics. *J. Chem. Phys.* **2007**, *127*, 194102.

[243] Arbuznikov, A. V.; Kaupp, M. Importance of the correlation contribution for local hybrid functionals: Range separation and self-interaction corrections. *J. Chem. Phys.* **2012**, *136*, 014111.

[244] Arbuznikov, A. V.; Kaupp, M. Towards improved local hybrid functionals by calibration of exchange-energy densities. *J. Chem. Phys.* **2014**, *141*, 204101.

[245] Haasler, M.; Maier, T. M.; Grotjahn, R.; Gückel, S.; Arbuznikov, A. V.; Kaupp, M. A Local Hybrid Functional with Wide Applicability and Good Balance between (De)Localization and Left-Right Correlation. *J. Chem. Theory Comput.* **2020**, *16*, 5645–5657.

[246] Bahmann, H.; Rodenberg, A.; Arbuznikov, A. V.; Kaupp, M. A thermochemically competitive local hybrid functional without gradient corrections. *J. Chem. Phys.* **2007**, *126*, 011103.

[247] Arbuznikov, A. V.; Kaupp, M. Local hybrid exchange-correlation functionals based on the dimensionless density gradient. *Chem. Phys. Lett.* **2007**, *440*, 160–168.

[248] Becke, A. D. Correlation energy of an inhomogeneous electron gas: A coordinate-space model. *J. Chem. Phys.* **1988**, *88*, 1053–1062.

[249] Johnson, E. R. Local-hybrid functional based on the correlation length. *J. Chem. Phys.* **2014**, *141*, 124120.

[250] Arbuznikov, A. V.; Kaupp, M. What can we learn from the adiabatic connection formalism about local hybrid functionals? *J. Chem. Phys.* **2008**, *128*, 214107.

[251] Arbuznikov, A. V.; Bahmann, H.; Kaupp, M. Local Hybrid Functionals with an Explicit Dependence on Spin Polarization. *J. Phys. Chem. A* **2009**, *113*, 11898–11906.

[252] de Silva, P.; Corminboeuf, C. Simultaneous Visualization of Covalent and Noncovalent Interactions Using Regions of Density Overlap. *J. Chem. Theory Comput.* **2014**, *10*, 3745–3756.

[253] de Silva, P.; Corminboeuf, C. Local hybrid functionals with orbital-free mixing functions and balanced elimination of self-interaction error. *J. Chem. Phys.* **2015**, *142*, 074112.

[254] Schmidt, T.; Kraisler, E.; Makmal, A.; Kronik, L.; Kümmel, S. A self-interaction-free local hybrid functional: Accurate binding energies vis-à-vis accurate ionization potentials from Kohn–Sham eigenvalues. *J. Chem. Phys.* **2014**, *140*, 18A510.

[255] Janesko, B. G.; Scuseria, G. E. Local hybrid functionals based on density matrix products. *J. Chem. Phys.* **2007**, *127*, 164117.

[256] Janesko, B. G.; Scuseria, G. E. Parameterized local hybrid functionals from density-matrix similarity metrics. *J. Chem. Phys.* **2008**, *128*, 084111.

[257] Haunschild, R.; Janesko, B. G.; Scuseria, G. E. Local hybrids as a perturbation to global hybrid functionals. *J. Chem. Phys.* **2009**, *131*, 154112.

[258] Burke, K.; Cruz, F. G.; Lam, K.-C. Unambiguous exchange-correlation energy density. *J. Chem. Phys.* **1998**, *109*, 8161–8167.

[259] Tao, J.; Staroverov, V. N.; Scuseria, G. E.; Perdew, J. P. Exact-exchange energy density in the gauge of a semilocal density-functional approximation. *Phys. Rev. A* **2008**, *77*, 012509.

[260] Theilacker, K.; Arbuznikov, A. V.; Kaupp, M. Gauge effects in local hybrid functionals evaluated for weak interactions and the GMTKN30 test set. *Mol. Phys.* **2016**, *114*, 1118–1127.

[261] Maier, T. M.; Haasler, M.; Arbuznikov, A. V.; Kaupp, M. New approaches for the calibration of exchange-energy densities in local hybrid functionals. *Phys. Chem. Chem. Phys.* **2016**, *18*, 21133–21144.

[262] Holzer, C.; Franzke, Y. J.; Kehry, M. Assessing the Accuracy of Local Hybrid Density Functional Approximations for Molecular Response Properties. *J Chem. Theory Comput.* **2021**, *17*, 2928–2947.

[263] Grotjahn, R.; Lauter, G. J.; Haasler, M.; Kaupp, M. Evaluation of Local Hybrid Functionals for Electric Properties: Dipole Moments and Static and Dynamic Polarizabilities. *J. Phys. Chem. A* **2020**, *124*, 8346–8358.

[264] Curtiss, L. A.; Raghavachari, K.; Redfern, P. C.; Pople, J. A. Assessment of Gaussian-3 and density functional theories for a larger experimental test set. *J. Chem. Phys.* **2000**, *112*, 7374–7383.

[265] Koch, W.; Holthausen, M. C. *A Chemist's Guide to Density Functional Theory*; John Wiley & Sons, Inc.: Weinheim, 2001; Chapter 7, pp 93–116.

[266] Roothaan, C. C. J. New Developments in Molecular Orbital Theory. *Rev. Mod. Phys.* **1951**, *23*, 69–89.

[267] Hall, G. G. The molecular orbital theory of chemical valency VIII. A method of calculating ionization potentials. *Proc. R. Soc.* **1951**, *205*, 541–552.

[268] Pople, J. A.; Nesbet, R. K. Self-Consistent Orbitals for Radicals. *J. Chem. Phys.* **1954**, *22*, 571–572.

[269] Helgaker, T.; Jørgensen, P.; Olsen, J. *Molecular Electronic Structure Theory*; Wiley: Chichester u.a., 2000; Chapter 9, pp 336–432.

[270] Helgaker, T.; Jørgensen, P.; Olsen, J. *Molecular Electronic Structure Theory*; Wiley: Chichester u.a., 2000; Chapter 6, pp 201–255.

[271] Becke, A. D. A multicenter numerical integration scheme for polyatomic molecules. *J. Chem. Phys.* **1988**, *88*, 2547–2553.

[272] Treutler, O.; Ahlrichs, R. Efficient molecular numerical integration schemes. *J. Chem. Phys.* **1995**, *102*, 346–354.

[273] Balasubramani, S. G.; Chen, G. P.; Coriani, S.; Diedenhofen, M.; Frank, M. S.; Franzke, Y. J.; Furche, F.; Grotjahn, R.; Harding, M. E.; Hättig, C.; Hellweg, A.; Helmich-Paris, B.; Holzer, C.; Huniar, U.; Kaupp, M.; Marefat Khah, A.; Karbalaei Khani, S.; Müller, T.; Mack, F.; Nguyen, B. D.; Parker, S. M.; Perlt, E.; Rappoport, D.; Reiter, K.; Roy, S.; Rückert, M.; Schmitz, G.; Sierka, M.; Tapavicza, E.; Tew, D. P.; van Wüllen, C.; Voora, V. K.; Weigend, F.; Wodyński, A.; Yu, J. M. TURBOMOLE: Modular program suite for ab initio quantum-chemical and condensed-matter simulations. *J. Chem. Phys.* **2020**, *152*, 184107.

[274] Sierka, M.; Hogekamp, A.; Ahlrichs, R. Fast evaluation of the Coulomb potential for electron densities using multipole accelerated resolution of identity approximation. *J. Chem. Phys.* **2003**, *118*, 9136–9148.

[275] Neese, F.; Wennmohs, F.; Hansen, A.; Becker, U. Efficient, approximate and parallel Hartree–Fock and hybrid DFT calculations. A 'chain-of-spheres' algorithm for the Hartree–Fock exchange. *Chem. Phys.* **2009**, *356*, 98–109.

[276] Kossmann, S.; Neese, F. Comparison of two efficient approximate Hartee–Fock approaches. *Chem. Phys. Lett.* **2009**, *481*, 240–243.

[277] Vahtras, O.; Almlöf, J.; Feyereisen, M. W. Integral approximations for LCAO-SCF calculations. *Chem. Phys. Lett.* **1993**, *213*, 514–518.

[278] Weigend, F. A fully direct RI-HF algorithm: Implementation, optimised auxiliary basis sets, demonstration of accuracy and efficiency. *Phys. Chem. Chem. Phys.* **2002**, *4*, 4285–4291.

[279] Eichkorn, K.; Treutler, O.; Öhm, H.; Häser, M.; Ahlrichs, R. Auxiliary basis sets to approximate Coulomb potentials. *Chem. Phys. Lett.* **1995**, *240*, 283–290.

[280] White, C. A.; Head-Gordon, M. Derivation and efficient implementation of the fast multipole method. *J. Chem. Phys.* **1994**, *101*, 6593–6605.

[281] Reiter, K.; Mack, F.; Weigend, F. Calculation of Magnetic Shielding Constants with meta-GGA Functionals Employing the Multipole-Accelerated Resolution of the Identity: Implementation and Assessment of Accuracy and Efficiency. *J. Chem. Theory Comput.* **2018**, *14*, 191–197.

[282] Friesner, R. A. Solution of self-consistent field electronic structure equations by a pseudospectral method. *Chem. Phys. Lett.* **1985**, *116*, 39–43.

[283] Friesner, R. A. Solution of the Hartree–Fock equations by a pseudospectral method: Application to diatomic molecules. *J. Chem. Phys.* **1986**, *85*, 1462–1468.

[284] Friesner, R. A. Solution of the Hartree–Fock equations for polyatomic molecules by a pseudospectral method. *J. Chem. Phys.* **1987**, *86*, 3522–3531.

[285] Maier, T. M.; Ikabata, Y.; Nakai, H. Efficient Semi-Numerical Implementation of Relativistic Exact Exchange within the Infinite-Order Two-Component Method Using a Modified Chain-of-Spheres Method. *J. Chem. Theory Comput.* **2019**, *15*, 4745–4763.

[286] Laqua, H.; Kussmann, J.; Ochsenfeld, C. Efficient and Linear-Scaling Seminumerical Method for Local Hybrid Density Functionals. *J. Chem. Theory Comput.* **2018**, *14*, 3451–3458.

[287] Bahmann, H.; Kaupp, M. Efficient Self-Consistent Implementation of Local Hybrid Functionals. *J. Chem. Theory Comput.* **2015**, *11*, 1540–1548.

[288] Klawohn, S. Implementation of Modern Density Functional Methods. Dissertation, Technische Universität Berlin, 2019.

[289] Fukui, H. Theory and calculation of nuclear shielding constants. *Prog. Nucl. Magn. Reson. Spectrosc.* **1997**, *31*, 317–342.

[290] van Wüllen, C. In *Calculation of NMR and EPR parameters: theory and applications*; Kaupp, M., Bühl, M., Malkin, V. G., Eds.; John Wiley & Sons: Weinheim, 2004; Chapter 6, pp 85–100.

[291] Fukui, H. Theory and calculation of nuclear spin–spin coupling constants. *Prog. Nucl. Magn. Reson. Spectrosc.* **1999**, *35*, 267–294.

[292] Helgaker, T.; Jaszuński, M.; Ruud, K. Ab Initio Methods for the Calculation of NMR Shielding and Indirect Spin–Spin Coupling Constants. *Chem. Rev.* **1999**, *99*, 293–352.

[293] Vaara, J. Theory and computation of nuclear magnetic resonance parameters. *Phys. Chem. Chem. Phys.* **2007**, *9*, 5399–5418.

[294] McWeeny, R. *Methods of Molecular Quantum Mechanics*, 2nd ed.; Acad. Press: London u. a., 1989; Chapter 2, pp 25–53.

[295] Gauss, J. In *Modern Methods and Algorithms of Quantum Chemistry*, 2nd ed.; Grotendorst, J., Ed.; NIC series; John von Neumann Institute for Computing: Jülich, 2000; Vol. 3; pp 541–592.

[296] Helgaker, T.; Jørgensen, P. In *Methods in Computational Molecular Physics*; Wilson, S., Diercksen, G. H. F., Eds.; NATO ASI Series; Springer US: Boston, MA, 1992; pp 353–421.

[297] Hellmann, H. Zur Rolle der kinetischen Elektronenenergie für die zwischenatomaren Kräfte. *Z. Physik* **1933**, *85*, 180–190.

[298] Feynman, R. P. Forces in Molecules. *Phys. Rev.* **1939**, *56*, 340–343.

[299] McWeeny, R. *Methods of Molecular Quantum Mechanics*, 2nd ed.; Acad. Press: London u. a., 1989; Chapter 11, pp 357–418.

[300] Mayer, I. *Simple Theorems, Proofs, and Derivations in Quantum Chemistry*; Kluwer Academic: New York u. a., 2003; Chapter 4, pp 69–120.

[301] Jackson, J. D.; Witte, C.; Diestelhorst, M.; Müller, K. *Klassische Elektrodynamic*, 3rd ed.; De Gruyter, Inc: Berlin/Boston, 2013; Chapter 6, pp 275–340.

[302] Kutzelnigg, W. In *Calculation of NMR and EPR parameters: theory and applications*; Kaupp, M., Bühl, M., Malkin, V. G., Eds.; John Wiley & Sons: Weinheim, 2004; Chapter 5, pp 43–82.

[303] Griffiths, D. J. Hyperfine splitting in the ground state of hydrogen. *Am. J. Phys.* **1982**, *50*, 698–703.

[304] Kutzelnigg, W. Origin and meaning of the Fermi contact interaction. *Theor. Chim. Acta* **1988**, *73*, 173–200.

[305] Dirac, P. A. M.; Fowler, R. H. The quantum theory of the electron. *Proc. R. Soc. Lond.* **1928**, *117*, 610–624.

[306] Dirac, P. A. M.; Fowler, R. H. The quantum theory of the electron. Part II. *Proc. R. Soc. Lond.* **1928**, *118*, 351–361.

[307] Benda, L. Determination of structure and dynamics of biomolecules by theoretical calculations of NMR spectroscopic parameters. Dissertation, Charles University Prague, 2012.

[308] Dyall, K. G.; Fægri Jr., K. *Introduction to Relativistic Quantum Chemistry*; Oxford University Press: New York, 2007; Chapter 4, pp 35–53.

[309] Fritscher, J. Quantum Chemical Calculations of EPR Parameters using Density Functional Theory. Dissertation, Johann Wolfgang Goethe-Universität Frankfurt am Main, 2006.

[310] Helgaker, T. In *European Summerschool in Quantum Chemistry Book II*, 10th ed.; Reine, S., Saue, T., Eds.; ESQC committee, 2017; Chapter VIII, pp 463–504.

[311] Kaupp, M. In *Calculation of NMR and EPR parameters: theory and applications*; Kaupp, M., Bühl, M., Malkin, V. G., Eds.; John Wiley & Sons: Weinheim, 2004; Chapter 18, pp 293–306.

[312] Mulder, F. A. A.; Filatov, M. NMR chemical shift data and ab initio shielding calculations: emerging tools for protein structure determination. *Chem. Soc. Rev.* **2010**, *39*, 578–590.

[313] Hansen, A. E.; Bouman, T. D. Localized orbital/local origin method for calculation and analysis of NMR shieldings. Applications to ^{13}C shielding tensors. *J. Chem. Phys.* **1985**, *82*, 5035–5047.

[314] Keith, T. A.; Bader, R. F. W. Calculation of magnetic response properties using atoms in molecules. *Chem. Phys. Lett.* **1992**, *194*, 1–8.

[315] Keith, T. A.; Bader, R. F. W. Calculation of magnetic response properties using a continuous set of gauge transformations. *Chem. Phys. Lett.* **1993**, *210*, 223–231.

[316] Hameka, H. F. Theory of Magnetic Properties of Molecules with Particular Emphasis on the Hydrogen Molecule. *Rev. Mod. Phys.* **1962**, *34*, 87–101.

[317] London, F. Théorie quantique des courants interatomiques dans les combinaisons aromatiques. *J. Phys. Radium* **1937**, *8*, 397–409.

[318] Ditchfield, R. Molecular Orbital Theory of Magnetic Shielding and Magnetic Susceptibility. *J. Chem. Phys.* **1972**, *56*, 5688–5691.

[319] Ditchfield, R. Self-consistent perturbation theory of diamagnetism. *Mol. Phys.* **1974**, *27*, 789–807.

[320] Friedrich, K.; Seifert, G.; Großmann, G. Nuclear magnetic shielding in molecules. The application of GIAO's in LCAO-$X\alpha$-calculations. *Z. Phys. D.* **1990**, *17*, 45–46.

[321] Rauhut, G.; Puyear, S.; Wolinski, K.; Pulay, P. Comparison of NMR Shieldings Calculated from Hartree–Fock and Density Functional Wave Functions Using Gauge-Including Atomic Orbitals. *J. Phys. Chem.* **1996**, *100*, 6310–6316.

[322] Neese, F. Prediction of molecular properties and molecular spectroscopy with density functional theory: From fundamental theory to exchange-coupling. *Coord. Chem. Rev.* **2009**, *253*, 526–563.

[323] Stevens, R. M.; Pitzer, R. M.; Lipscomb, W. N. Perturbed Hartree–Fock Calculations. I. Magnetic Susceptibility and Shielding in the LiH Molecule. *J. Chem. Phys.* **1963**, *38*, 550–560.

[324] Pople, J. A.; Krishnan, R.; Schlegel, H. B.; Binkley, J. S. Derivative Studies in Hartree–Fock and Møller–Plesset Theories. *Int. J. Quantum Chem.* **1979**, *16*, 225–241.

[325] Johnson, B. G.; Fisch, M. J. An implementation of analytic second derivatives of the gradient-corrected density functional energy. *J. Chem. Phys.* **1994**, *100*, 7429–7442.

[326] Beer, M.; Kussmann, J.; Ochsenfeld, C. Nuclei-selected NMR shielding calculations: A sublinear-scaling quantum-chemical method. *J. Chem. Phys.* **2011**, *134*, 074102.

[327] Kumar, C.; Kjærgaard, T.; Helgaker, T.; Fliegl, H. Nuclei-selected atomic-orbital response-theory formulation for the calculation of NMR shielding tensors using density-fitting. *J. Chem. Phys.* **2016**, *145*, 234108.

[328] Neese, F. Prediction of electron paramagnetic resonance g values using coupled perturbed Hartree–Fock and Kohn–Sham theory. *J. Chem. Phys.* **2001**, *115*, 11080–11096.

[329] Cao, Y.; Beachy, M. D.; Braden, D. A.; Morrill, L.; Ringnalda, M. N.; Friesner, R. A. Nuclear-magnetic-resonance shielding constants calculated by pseudospectral methods. *J. Chem. Phys.* **2005**, *122*, 224116.

[330] Helgaker, T.; Pecul, M. In *Calculation of NMR and EPR parameters: theory and applications*; Kaupp, M., Bühl, M., Malkin, V. G., Eds.; John Wiley & Sons: Weinheim, 2004; Chapter 7, pp 101–121.

[331] Rajagopal, A. K.; Callaway, J. Inhomogeneous Electron Gas. *Phys. Rev. B* **1973**, *7*, 1912–1919.

[332] Vignale, G.; Rasolt, M. Current- and spin-density-functional theory for inhomogeneous electronic systems in strong magnetic fields. *Phys. Rev. B* **1988**, *37*, 10685–10696.

[333] Jackson, J. D.; Witte, C.; Diestelhorst, M.; Müller, K. *Klassische Elektrodynamic*, 3rd ed.; De Gruyter, Inc: Berlin/Boston, 2013; Chapter 5, pp 203–274.

[334] Furness, J. W.; Verbeke, J.; Tellgren, E. I.; Stopkowicz, S.; Ekström, U.; Helgaker, T.; Teale, A. M. Current Density Functional Theory Using Meta-Generalized Gradient Exchange-Correlation Functionals. *J. Chem. Theory Comput.* **2015**, *11*, 4169–4181.

[335] Maximoff, S. N.; Scuseria, G. E. Nuclear magnetic resonance shielding tensors calculated with kinetic energy density-dependent exchange-correlation functionals. *Chem. Phys. Lett.* **2004**, *390*, 408–412.

[336] Dobson, J. F. Spin-density functionals for the electron correlation energy with automatic freedom from orbital self-interaction. *J. Phys.: Condens. Matter* **1992**, *4*, 7877–7890.

[337] Dobson, J. F. Alternative expressions for the Fermi hole curvature. *J. Chem. Phys.* **1993**, *98*, 8870–8872.

[338] Becke, A. D. Current-density dependent exchange-correlation functionals. *Can. J. Chem.* **1996**, *74*, 995–997.

[339] Becke, A. D. Current density in exchange-correlation functionals: Application to atomic states. *J. Chem. Phys.* **2002**, *117*, 6935–6938.

[340] Tao, J.; Perdew, J. P. Nonempirical Construction of Current-Density Functionals from Conventional Density-Functional Approximations. *Phys. Rev. Lett.* **2005**, *95*, 196403.

[341] Klawohn, S.; Bahmann, H.; Kaupp, M. Implementation of Molecular Gradients for Local Hybrid Density Functionals Using Seminumerical Integration Techniques. *J. Chem. Theory Comput.* **2016**, *12*, 4254–4262.

[342] Häser, M.; Ahlrichs, R.; Baron, H. P.; Weis, P.; Horn, H. Direct computation of second-order SCF properties of large molecules on workstation computers with an application to large carbon clusters. *Theoret. Chim. Acta* **1992**, *83*, 455–470.

[343] Huniar, U. Berechnung der chemischen Verschiebung der NMR mit Methoden der Dichtefunktionaltheorie (DFT). Diploma Thesis, University of Karlsruhe, 1999.

[344] Kollwitz, M.; Gauss, J. A direct implementation of the GIAO-MBPT(2) method for calculating NMR chemical shifts. Application to the naphthalenium and anthracenium ions. *Chem. Phys. Lett.* **1996**, *260*, 639–646.

[345] Kollwitz, M.; Häser, M.; Gauss, J. Non-Abelian point group symmetry in direct second-order many-body perturbation theory calculations of NMR chemical shifts. *J. Chem. Phys.* **1998**, *108*, 8295–8301.

[346] Klamt, A.; Schüürmann, G. COSMO: a new approach to dielectric screening in solvents with explicit expressions for the screening energy and its gradient. *J. Chem. Soc., Perkin Trans. 2* **1993**, 799–805.

[347] van Wüllen, C. On the use of effective core potentials in the calculation of magnetic properties, such as magnetizabilites and magnetic shieldings. *J. Chem. Phys.* **2012**, *136*, 114110.

[348] Reiter, K.; Kühn, M.; Weigend, F. Vibrational circular dichroism spectra for large molecules and molecules with heavy elements. *J. Chem. Phys.* **2017**, *146*, 054102.

[349] Franzke, Y. J.; Weigend, F. NMR Shielding Tensors and Chemical Shifts in Scalar-Relativistic Local Exact Two-Component Theory. *J. Chem. Theory Comput.* **2019**, *15*, 1028–1043.

[350] Marques, M. A. L.; Oliveira, M. J. T.; Burnus, T. LIBXC: A library of exchange and correlation functionals for density functional theory. *Comput. Phys. Commun.* **2012**, *183*, 2272–2281.

[351] Lehtola, S.; Steigemann, C.; Oliveira, M. J. T.; Marques, M. A. L. Recent developments in LIBXC – A comprehensive library of functionals for density functional theory. *SoftwareX* **2018**, *7*, 1–5.

[352] Weiss, H.; Ahlrichs, R.; Häser, M. A direct algorithm for self-consistent-field linear response theory and application to C_60: Excitation energies, oscillator strengths, and frequency-dependent polarizabilities. *J. Chem. Phys.* **1993**, *99*, 1262–1270.

[353] Maier, T. M.; Bahmann, H.; Kaupp, M. Efficient Semi-numerical Implementation of Global and Local Hybrid Functionals for Time-Dependent Density Functional Theory. *J. Chem. Theory Comput.* **2015**, *11*, 4226–4237.

[354] Maier, T. M. Development of Local Hybrid Functionals for Time-Dependent Density Functional Theory. Dissertation, Technische Universität Berlin, 2016.

[355] Gaussian 09, Revision D.01, M. J. Frisch, G. W. Trucks, H. B. Schlegel, G. E. Scuseria, M. A. Robb, J. R. Cheeseman, G. Scalmani, V. Barone, B. Mennucci, G. A. Petersson, H. Nakatsuji, M. Caricato, X. Li, H. P. Hratchian, A. F. Izmaylov, J. Bloino, G. Zheng, J. L. Sonnenberg, M. Hada, M. Ehara, K. Toyota, R. Fukuda, J. Hasegawa, M. Ishida, T. Nakajima, Y. Honda, O. Kitao, H. Nakai, T. Vreven, J. A. Montgomery, Jr., J. E. Peralta, F. Ogliaro, M. Bearpark, J. J. Heyd, E. Brothers, K. N. Kudin, V. N. Staroverov, T. Keith, R. Kobayashi, J. Normand, K. Raghavachari, A. Rendell, J. C. Burant, S. S. Iyengar, J. Tomasi, M. Cossi, N. Rega, J. M. Millam, M. Klene, J. E. Knox, J. B. Cross, V. Bakken, C. Adamo, J. Jaramillo, R. Gomperts, R. E. Stratmann, O. Yazyev, A. J. Austin, R. Cammi, C. Pomelli, J. W. Ochterski, R. L. Martin, K. Morokuma, V. G. Zakrzewski, G. A. Voth, P. Salvador, J. J. Dannenberg, S. Dapprich, A. D. Daniels, O. Farkas, J. B. Foresman, J. V. Ortiz, J. Cioslowski, and D. J. Fox, Gaussian, Inc., Wallingford CT, 2013.

[356] Gaussian 16, Revision A.03, M. J. Frisch and G. W. Trucks and H. B. Schlegel and G. E. Scuseria and M. A. Robb and J. R. Cheeseman and G. Scalmani and V. Barone and G. A. Petersson and H. Nakatsuji and X. Li and M. Caricato and A. V. Marenich and J. Bloino and B. G. Janesko and R. Gomperts and B. Mennucci and H. P. Hratchian and J. V. Ortiz and A. F. Izmaylov and J. L. Sonnenberg and D. Williams-Young and F. Ding and F. Lipparini and F. Egidi and J. Goings and B. Peng and A. Petrone and T. Henderson and D. Ranasinghe and V. G. Zakrzewski and J. Gao and N. Rega and G. Zheng and W. Liang and M. Hada and M. Ehara and K. Toyota and R. Fukuda and J. Hasegawa and M. Ishida and T. Nakajima and Y. Honda and O. Kitao and H. Nakai and T. Vreven and K. Throssell and Montgomery, Jr., J. A. and J. E. Peralta and F. Ogliaro and M. J. Bearpark and J. J. Heyd and E. N. Brothers and K. N. Kudin and V. N. Staroverov and T. A.

Keith and R. Kobayashi and J. Normand and K. Raghavachari and A. P. Rendell and J. C. Burant and S. S. Iyengar and J. Tomasi and M. Cossi and J. M. Millam and M. Klene and C. Adamo and R. Cammi and J. W. Ochterski and R. L. Martin and K. Morokuma and O. Farkas and J. B. Foresman and D. J. Fox, Gaussian Inc., Wallingford CT, 2016.

[357] Werner, H.-J. et al. MOLPRO, version 2019.2, a package of ab initio programs. 2019; see https://www.molpro.net.

[358] Malkin, V. G.; Malkina, O. L.; Reviakine, R.; Arbuznikov, A. V.; Kaupp, M.; Schimmelpfennig, B.; Malkin, I.; Helgaker, T.; Ruud, K.; Pennanen. O. ReSpect program, Revisited, Version 1.2.1, 2013.

[359] Bannwarth, C.; Caldeweyher, E.; Ehlert, S.; Hansen, A.; Pracht, P.; Seibert, J.; Spicher, S.; Grimme, S. Extended tight-binding quantum chemistry methods. *WIREs Comput. Mol. Sci.* **2021**, *11*, e1493.

[360] Pracht, P.; Bohle, F.; Grimme, S. Automated exploration of the low-energy chemical space with fast quantum chemical methods. *Phys. Chem. Chem. Phys.* **2020**, *22*, 7169–7192.

[361] Perdew, J. P. Erratum: Density-functional approximation for the correlation energy of the inhomogeneous electron gas. *Phys. Rev. B* **1986**, *34*, 7406–7406.

[362] Boese, A. D.; Handy, N. C. A new parametrization of exchange–correlation generalized gradient approximation functionals. *J. Chem. Phys.* **2001**, *114*, 5497–5503.

[363] Perdew, J. P.; Tao, J.; Staroverov, V. N.; Scuseria, G. E. Meta-generalized gradient approximation: Explanation of a realistic nonempirical density functional. *J. Chem. Phys.* **2004**, *120*, 6898–6911.

[364] Bartók, A. P.; Yates, J. R. Regularized SCAN functional. *J. Chem. Phys.* **2019**, *150*, 161101.

[365] Furness, J. W.; Kaplan, A. D.; Ning, J.; Perdew, J. P.; Sun, J. Accurate and Numerically Efficient r^{2}SCAN Meta-Generalized Gradient Approximation. *J. Phys. Chem. Lett.* **2020**, *11*, 8208–8215.

[366] Furness, J. W.; Kaplan, A. D.; Ning, J.; Perdew, J. P.; Sun, J. Correction to "Accurate and Numerically Efficient r^{2}SCAN Meta-Generalized Gradient Approximation". *J. Phys. Chem. Lett.* **2020**, *11*, 9248–9248.

[367] Zhao, Y.; Truhlar, D. G. Design of Density Functionals That Are Broadly Accurate for Thermochemistry, Thermochemical Kinetics, and Nonbonded Interactions. *J. Phys. Chem. A* **2005**, *109*, 5656–5667.

[368] Kozuch, S.; Martin, J. M. L. Spin-component-scaled double hybrids: An extensive search for the best fifth-rung functionals blending DFT and perturbation theory. *J. Comput. Chem.* **2013**, *34*, 2327–2344.

[369] Grimme, S.; Ehrlich, S.; Goerigk, L. Effect of the damping function in dispersion corrected density functional theory. *J. Comput. Chem.* **2011**, *32*, 1456–1465.

[370] Becke, A. D.; Johnson, E. R. A density-functional model of the dispersion interaction. *J. Chem. Phys.* **2005**, *123*, 154101.

[371] Johnson, E. R.; Becke, A. D. A post-Hartree-Fock model of intermolecular interactions. *J. Chem. Phys.* **2005**, *123*, 024101.

[372] Johnson, E. R.; Becke, A. D. A post-Hartree-Fock model of intermolecular interactions: Inclusion of higher-order corrections. *J. Chem. Phys.* **2006**, *124*, 174104.

[373] Sinnecker, S.; Rajendran, A.; Klamt, A.; Diedenhofen, M.; Neese, F. Calculation of Solvent Shifts on Electronic g-Tensors with the Conductor-Like Screening Model (COSMO) and Its Self-Consistent Generalization to Real Solvents (Direct COSMO-RS). *J. Phys. Chem. A* **2006**, *110*, 2235–2245.

[374] Renz, M.; Kess, M.; Diedenhofen, M.; Klamt, A.; Kaupp, M. Reliable Quantum Chemical Prediction of the Localized/Delocalized Character of Organic Mixed-Valence Radical Anions. From Continuum Solvent Models to Direct-COSMO-RS. *J. Chem. Theory Comput.* **2012**, *8*, 4189–4203.

[375] Klamt, A. The COSMO and COSMO-RS solvation models. *WIREs Comput. Mol. Sci.* **2018**, *8*, e1338.

[376] Weigend, F.; Ahlrichs, R. Balanced basis sets of split valence, triple zeta valence and quadruple zeta valence quality for H to Rn: Design and assessment of accuracy. *Phys. Chem. Chem. Phys.* **2005**, *7*, 3297–3305.

[377] Rappoport, D.; Furche, F. Property-optimized Gaussian basis sets for molecular response calculations. *J. Chem. Phys.* **2010**, *133*, 134105.

[378] Dunning, T. H. Gaussian basis sets for use in correlated molecular calculations. I. The atoms boron through neon and hydrogen. *J. Chem. Phys.* **1989**, *90*, 1007–1023.

[379] Kendall, R. A.; Dunning, T. H.; Harrison, R. J. Electron affinities of the first-row atoms revisited. Systematic basis sets and wave functions. *J. Chem. Phys.* **1992**, *96*, 6796–6806.

[380] Woon, D. E.; Dunning, T. H. Gaussian basis sets for use in correlated molecular calculations. III. The atoms aluminum through argon. *J. Chem. Phys.* **1993**, *98*, 1358–1371.

[381] Prascher, B. P.; Woon, D. E.; Peterson, K. A.; Dunning Jr., T. H.; Wilson, A. K. Gaussian basis sets for use in correlated molecular calculations. VII. Valence, core-valence, and scalar relativistic basis sets for Li, Be, Na, and Mg. *Theor. Chem. Acc.* **2011**, *128*, 69–82.

[382] Jensen, F. Segmented Contracted Basis Sets Optimized for Nuclear Magnetic Shielding. *J. Chem. Theory Comput.* **2015**, *11*, 132–138.

[383] Jensen, F. The optimum contraction of basis sets for calculating spin–spin coupling constants. *Theor. Chem. Acc.* **2010**, *126*, 371–382.

[384] Roos, B. O.; Lindh, R.; Malmqvist, P.-Å.; Veryazov, V.; Widmark, P.-O. Main Group Atoms and Dimers Studied with a New Relativistic ANO Basis Set. *J. Phys. Chem. A* **2004**, *108*, 2851–2858.

[385] Weigend, F. Accurate Coulomb-fitting basis sets for H to Rn. *Phys. Chem. Chem. Phys.* **2006**, *8*, 1057–1065.

[386] Franzke, Y. J.; Mack, F.; Weigend, F. NMR Indirect Spin–Spin Coupling Constants in a Modern Quasi-Relativistic Density Functional Framework. *J. Chem. Theory Comput.* **2021**, *17*, 3974–3994.

[387] San Fabián, J.; Díez, E.; García de la Vega, J. M.; Suardíaz, R. Approximating correlation effects in multiconfigurational self-consistent field calculations of spin–spin coupling constants. *J. Chem. Phys.* **2008**, *128*, 084108.

[388] Faber, R.; Sauer, S. P. A.; Gauss, J. Importance of Triples Contributions to NMR Spin–Spin Coupling Constants Computed at the CC3 and CCSDT Levels. *J. Chem. Theory Comput.* **2017**, *13*, 696–709.

[389] Lantto, P.; Vaara, J.; Helgaker, T. Spin–spin coupling tensors by density-functional linear response theory. *J. Chem. Phys.* **2002**, *117*, 5998–6009.

[390] Helgaker, T.; Lutnæs, O. B.; Jaszuński, M. Density-Functional and Coupled-Cluster Singles-and-Doubles Calculations of the Nuclear Shielding and Indirect Nuclear Spin–Spin Coupling Constants of o-Benzyne. *J. Chem. Theory Comput.* **2007**, *3*, 86–94.

[391] Gryff-Keller, A.; Szczeciński, P. An efficient DFT method of predicting the one-, two- and three-bond indirect spin-–spin coupling constants involving a fluorine nucleus in fluoroalkanes. *RSC Adv.* **2016**, *6*, 82783–82792.

[392] Auer, A. A. High-level ab-initio calculation of gas-phase NMR chemical shifts and secondary isotope effects of methanol. *Chem. Phys. Lett.* **2009**, *467*, 230–232.

[393] Bühl, M.; Mauschick, F. T. Density functional computation of ^{49}Ti NMR chemical shifts. *Magn. Reson. Chem.* **2004**, *42*, 737–744.

[394] Srebro, M.; Autschbach, J. Computational Analysis of 47/49Ti NMR Shifts and Electric Field Gradient Tensors of Half-Titanocene Complexes: Structure–Bonding–Property Relationships. *Chem. Eur. J.* **2013**, *19*, 12018–12033.

[395] Bühl, M.; Hamprecht, F. A. Theoretical investigations of NMR chemical shifts and reactivities of oxovanadium(v) compounds. *J. Comput. Chem.* **1998**, *19*, 113–122.

[396] Bühl, M. Density-functional computation of ^{53}Cr NMR chemical shifts. *Magn. Reson. Chem.* **2006**, *44*, 661–668.

[397] Bühl, M. Density functional computation of ^{55}Mn NMR parameters. *Theor. Chem. Acc.* **2002**, *107*, 336–342.

[398] Bühl, M. Density functional computations of transition metal NMR chemical shifts: dramatic effects of Hartree–Fock exchange. *Chem. Phys. Lett.* **1997**, *267*, 251–257.

[399] Grigoleit, S.; Bühl, M. Computational ^{59}Co NMR Spectroscopy: Beyond Static Molecules. *J. Chem. Theory Comput.* **2005**, *1*, 181–193.

[400] Bühl, M.; Peters, D.; Herges, R. Substituent effects on ^{61}Ni NMR chemical shifts. *Dalton Trans.* **2009**, 6037–6044.

[401] Wu, A.; Zhang, Y.; Xu, X.; Yan, Y. Systematic studies on the computation of nuclear magnetic resonance shielding constants and chemical shifts: The density functional models. *J. Comput. Chem.* **2007**, *28*, 2431–2442.

[402] Semenov, V. A.; Samultsev, D. O.; Krivdin, L. B. Calculation of ^{15}N NMR Chemical Shifts in a Diversity of Nitrogen-Containing Compounds Using Composite Method Approximation at the DFT, MP2, and CCSD Levels. *J. Phys. Chem. A* **2019**, *123*, 8417–8426.

[403] Cornwell, C. D. Interpretation of the Chemical Shift of ClF. *J. Chem. Phys.* **1966**, *44*, 874–880.

[404] Kutzelnigg, W.; Fleischer, U.; Schindler, M. The IGLO-Method: Ab-initio Calculation and Interpretation of NMR Chemical Shifts and Magnetic Susceptibilities. Deuterium and Shift Calculation. Berlin, Heidelberg, 1991; pp 165–262.

[405] Wiberg, K. B.; Hammer, J. D.; Zilm, K. W.; Cheeseman, J. R.; Keith, T. A. NMR Chemical Shifts. 1. The Role of Relative Atomic Orbital Phase in Determining the Sign of the Paramagnetic Terms: ClF, CH_3F, $CH_3NH_3^+$, FNH_3^+, HC⋮CF. *J. Phys. Chem. A* **1998**, *102*, 8766–8773.

[406] Kupka, T. H_2O, H_2, HF, F_2 and F_2O nuclear magnetic shielding constants and indirect nuclear spin–spin coupling constants (SSCCs) in the BHandH/pcJ-n and BHandH/XZP Kohn–Sham limits. *Magn. Reson. Chem.* **2009**, *47*, 959–970.

[407] Alkan, F.; Holmes, S. T.; Dybowski, C. Role of Exact Exchange and Relativistic Approximations in Calculating 19F Magnetic Shielding in Solids Using a Cluster Ansatz. *J. Chem. Theory Comput.* **2017**, *13*, 4741–4752.

[408] Dahanayake, J. N.; Kasireddy, C.; Ellis, J. M.; Hildebrandt, D.; Hull, O. A.; Karnes, J. P.; Morlan, D.; Mitchell-Koch, K. R. Evaluating electronic structure methods for accurate calculation of ^{19}F chemical shifts in fluorinated amino acids. *J. Comput. Chem.* **2017**, *38*, 2605–2617.

[409] Fedorov, S. V.; Krivdin, L. B. Computational Protocols for the ^{19}F NMR Chemical Shifts. Part 1: Methodological Aspects. *J. Fluor. Chem.* **2020**, *238*, 109625.

[410] Wodyński, A.; Kaupp, M. Noncollinear Relativistic Two-Component X2C Calculations of Hyperfine Couplings Using Local Hybrid Functionals. Importance of the High-Density Coordinate Scaling Limit. *J. Chem. Theory Comput.* **2020**, *16*, 314–325.

[411] Antušek, A.; Jaszuński, M. Coupled cluster study of NMR shielding constants and spin-rotation constants in SiH_4, PH_3 and H_2S molecules. *Mol. Phys.* **2006**, *104*, 1463–1474.

[412] Jaszuński, M.; Demissie, T. B.; Ruud, K. Spin-Rotation and NMR Shielding Constants in XF Molecules (X = B, Al, Ga, In, and Tl). *J. Phys. Chem. A* **2014**, *118*, 9588–9595.

[413] Grimme, S. Exploration of Chemical Compound, Conformer, and Reaction Space with Meta-Dynamics Simulations Based on Tight-Binding Quantum Chemical Calculations. *J. Chem. Theory Comput.* **2019**, *15*, 2847–2862.

[414] Gerken, M.; Boatz, J. A.; Kornath, A.; Haiges, R.; Schneider, S.; Schroer, T.; Christe, K. O. The ^{19}F NMR shifts are not a measure for the nakedness of the fluoride anion. *J. Fluor. Chem.* **2002**, *116*, 49–58.

[415] Christe, K. O.; Wilson, W. W. Reaction of the fluoride anion with acetonitrile. Chloroform and methylene chloride. *J. Fluor. Chem.* **1990**, *47*, 117–120.